

Accelerate your neuropathology research

Identify novel interactions across 23 key pathways in less than 24 hours

nCounter[®] Neuropathology Gene Expression Panel

23 neurodegenerative pathways and processes

15 mins hands on time, publishable data in less than 24 hours

770 genes with option to add custom content

Profile disease mechanisms, response to drug treatment and biomarker characterization

View the gene list at nanosttring.com/neuro

FOR RESEARCH USE ONLY. Not for use in diagnostic procedures.
© 2017 NanoString Technologies, Inc. All rights reserved.

nanosttring

Neuron

Best of 2016–2017



gibco

Cellvival of the fittest

Increase neuronal cell survival by more than 50%
with the new Gibco B-27 Plus Neuronal Culture System

Cell survival rates are critical to the success and reliability of your neurobiology research. The Gibco™ B-27™ Plus Neuronal Culture System helps improve the reliability of your experiments by increasing the survival of neurons by more than 50%—the highest in the industry.

See the results—request your free sample* at
thermofisher.com/b27plus

* Terms and conditions apply.

For Research Use Only. Not for use in diagnostic procedures. © 2017 Thermo Fisher Scientific Inc. All rights reserved. All trademarks are the property of Thermo Fisher Scientific and its subsidiaries unless otherwise specified. B-27 is a trademark of Southern Illinois University. **COL04954 0917**



ThermoFisher
SCIENTIFIC

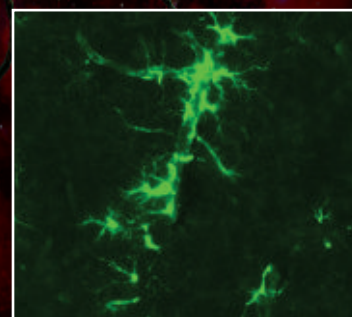
Neuroinflammation: connecting brain disorders to the immune system



BioLegend develops innovative reagents to support research within multiple neuroscience areas with a great focus on the fields of neurodegeneration and neuroinflammation. We offer a wide selection of high quality and specificity antibodies with utility in multiple applications such as IHC, IF, WB, and Flow Cytometry. Choose from a variety of targets covering:

- immune cells
- signaling molecules
- complement system

Learn more at: [biolegend.com/neuroinflammation](https://www.biolegend.com/neuroinflammation)



FFPE mouse brain tissue stained with astrocyte marker anti-GFAP antibody (clone SMI 25).



BioLegend is ISO 13485:2003 Certified

Toll-Free Tel: (US & Canada): 1.877.BIOLEGEND (246.5343)

Tel: 858.768.5800

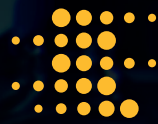
[biolegend.com](https://www.biolegend.com)

08-0069-01

World-Class Quality | Superior Customer Support | Outstanding Value



turning science into solutions



sartorius

No matter the time of day or night,
see exactly what happened
to your cells and when.

Biological processes are dynamic, and a single snapshot in time may not capture rare or transient events, causing you to miss a relevant response. With the IncuCyte® S3 live-cell analysis system and reagents, automatically follow the sequence of biological events continuously, then 'rewind and replay' the experiment to see what really happened to your cells while you were away.

The IncuCyte S3 combines image-based measurements, a physiologically relevant environment, and microplate throughput to enable researchers to visualize and analyze cell behaviors at a scale and in ways that were previously not possible—all without ever removing cells from the incubator.

Visit www.essenbio.com/IncuCyte to learn about the next-generation IncuCyte S3 System and the benefits of real-time, automated live-cell analysis.



IncuCyte®
by SARTORIUS

Accuracy by Design; Not by Chance.

Human XL Cytokine Discovery Luminex® High Performance Assay

- Broad selection – 45 analytes
- Superior accuracy – see the data
- Flexible – choose your analytes
- Easy to order – save time

NEW



Learn more | rndsystems.com/human-xl



Nikon
100th
anniversary

A1ways Evolving

NEW High Definition 1K Resonant Scanner

Open up a world of new imaging strategies and possibilities with the latest upgrade to Nikon's always evolving A1R+ confocal microscope system. The all-new High Definition 1K Resonant Scanner delivers high resolution images at ultra-high speed. The new scanner also provides 4x the field of view at the same resolution usually generated by a normal 512x512 scanner. The wide dynamic range and reduced noise level raises the bar for image quality in resonant scanners.

For more information, go to www.nikoninstruments.com/a1r
or call 1-800-52-NIKON.



Light re-engineered

An Employee-Owned Company

Multiline Laser Illuminator - High Power, Low Cost

LDI^{*}

- Up to 1W of power per channel
- Feedback controlled stability
- Up to 7 wavelengths
- Ultimate price to performance ratio

LDI Applications

- Spinning Disk Confocal
- Photoactivation
- Optogenetics
- TIRF
- PALM / STORM

Works with X-Light V2 & OptoTIRF

www.89north.com
sales@89north.com
+1.802.881.0302
1.877.417.8313

The World's Finest Optical Filters

TIRF Filter Sets

- Highest possible signal to noise
- Custom filter cubes for precise dichroic alignment

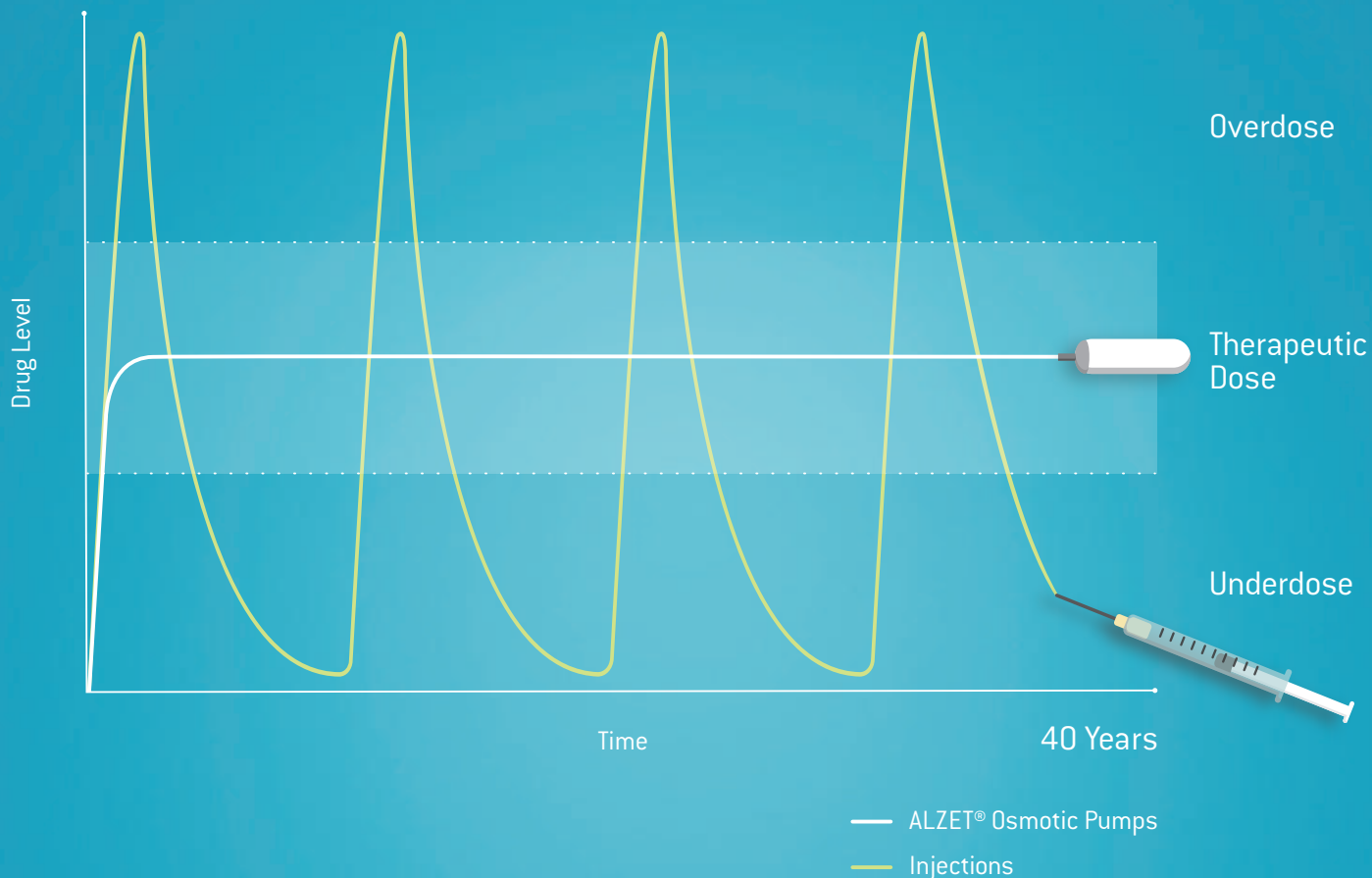
New Multiband Filter Sets

- Dedicated LED engine sets
- 5-band set for new Brilliant Violet™ dyes

Lifetime
Warranty

Filter sets optimized for the LDI

www.chroma.com
sales@chroma.com
+1.802.428.2500
1.800.824.7662



40 years of consistent dosing



ALZET Osmotic Pump, 100 µl
[actual size]

alzet[®]
OSMOTIC PUMPS

Find out more at
alzet.com/40years

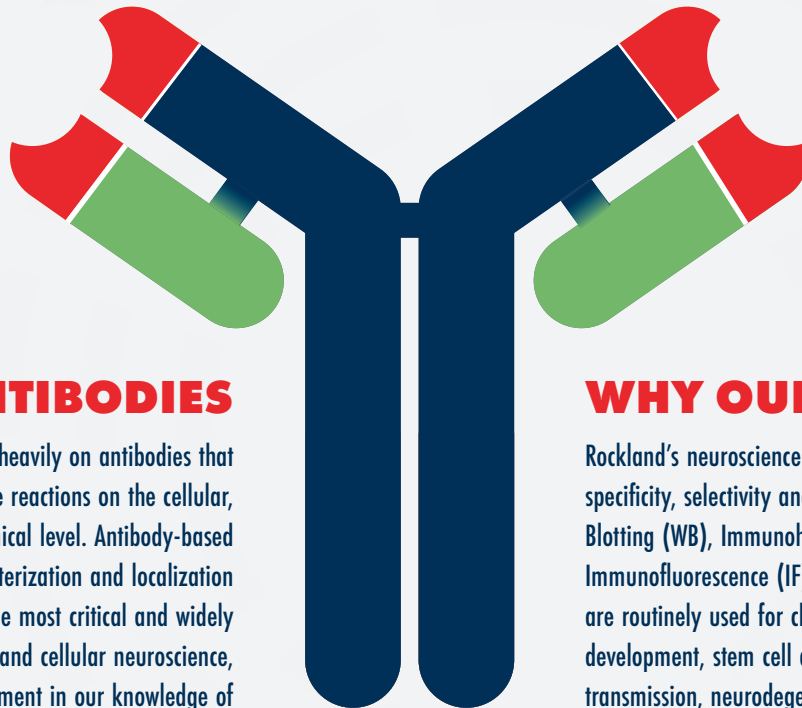
Visit us at
Neuroscience 2017
Exhibit #1316

A product of



©2017 DURECT Corporation
All Rights Reserved

Introducing the
NEUROSCIENCE
ANTIBODY



WHY ANTIBODIES

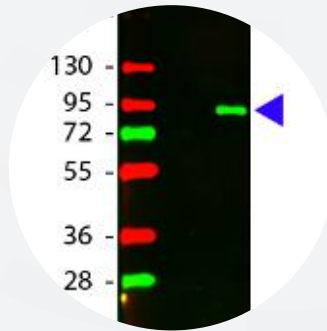
Neurological research relies heavily on antibodies that can help identify and elucidate reactions on the cellular, molecular and biochemical level. Antibody-based approaches for isolation, characterization and localization of target proteins are among the most critical and widely used techniques in molecular and cellular neuroscience, leading to rapid development in our knowledge of protein abundance, distribution, structure, and function.

WHY OURS

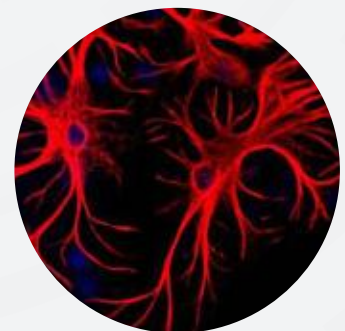
Rockland's neuroscience antibodies exhibit high specificity, selectivity and reproducibility by Western Blotting (WB), Immunohistochemistry (IHC), Immunofluorescence (IF) and ELISA. These antibodies are routinely used for characterization of neural development, stem cell and differentiation, neural transmission, neurodegenerative disease and neuroinflammation.



Anti-Nestin (RABBIT) Antibody
600-401-417



Anti-AKT pT308 (MOUSE) Monoclonal
Antibody DyLight™ 549 Conjugated
200-342-269



Anti-Glial Fibrillary Acidic Protein
(GFAP) (Chicken) Antibody
200-901-D60

Foreword

In 2012, we introduced *Best of Neuron 2011* as one of the first “Best of” reprint collections from Cell Press. Now, we are happy to present the seventh edition in our annual *Best of Neuron* series in time for the Society for Neuroscience annual meeting.

Neuron is published bi-weekly in four volumes each year. In order to account for the amount of time since publication, we have selected a mix of the most highly accessed research articles and perspectives from volumes 92–95, which cover the last quarter of 2016 and the first three quarters of 2017. We use the number of requests for PDF and full-text HTML versions of a given article to identify the “most accessed” articles, taking into consideration the range of topic areas to provide our readers with a clearer sense of *Neuron*’s breadth and scope. Of course, no single measurement can be accurately indicative of “the best” research papers over a given period of time. This is especially true for recently published research, because the community hasn’t had enough time to fully appreciate the relative importance of the findings. That said, we are confident that you will still find this collection informative and exciting.

This edition features two reviews, three NeuroResources, and five full-length articles that have significantly captured our readership’s attention over the last year. A wide range of neuroscience is covered in this collection, including a look at how mutant huntingtin disrupts nuclear pore complexes, an examination of how dopamine neurons modulate arousal and wakefulness, and a review of how neuroscience is helping shape the future of artificial intelligence.

We hope that you will enjoy reading this special collection. You can access the entire “Best of” Cell Press collection online at www.cell.com/bestof. Visit www.cell.com/neuron to learn about the latest findings that *Neuron* has had the privilege to publish and www.cell.com to find other high-quality neuroscience-relevant papers published in the full portfolio of Cell Press journals. Please feel free to contact us at neuron@cell.com to tell us about your latest work or to provide feedback. We look forward to working with you in 2018 and beyond!

As a final note, we are grateful for the generosity of our sponsors, who helped to make this reprint collection possible.

Neuron

Quantitative & Qualitative Data for the Total Cell Picture



Microplate Reader & Imager

DO MORE | GROW IT, READ IT, SEE IT, COUNT IT.

Cytation™5 Cell Imaging Multi-Mode Reader combines ultra-sensitive microplate detection *and* digital imaging in one compact instrument. Now with Gen5™ Image+ software, you have remarkable reader control and data analysis. Isn't it time you got the whole picture?

Get the whole picture, visit www.cytation5.com

Think Possible

BioTek®



www.biotek.com

SPEED OR SENSITIVITY? THE ANSWER IS YES

When analyzing complex cell models, you don't want to compromise on your imaging technologies. And that's what the Opera Phenix™ high-content screening system is all about. Building on over a decade of experience with confocal high-throughput

HCS, the system's new confocal Synchrony™ Optics deliver the speed to image millions of cells per hour in up to four colors – *simultaneously* – without compromising sensitivity. So you can obtain more accurate phenotypic information. Opera Phenix: More physiological relevance. No compromise.

Check out the Opera Phenix High-Content Screening System at www.perkinelmer.com/YES



Opera Phenix High-Content Screening System

Nanoject III

The Smallest Big Deal in Microinjection



Completely programmable nanoliter injection control
expands your capabilities

- User-friendly touchscreen setup for single injections as well as multiple injection cycle recipes
- Advanced hydraulics deliver precise, consistent injection volumes down to 0.6 nanoliters
- Improved chuck design provides simple, secure micropipet attachment without the need for O-rings

Go to **injection.expert** for more details about Nanoject III expanded microinjection capabilities.

**Nanoject III...
a Big Deal in
Microinjection**



Developers of the original Pipet-Aid®

Made  in USA

www.drummondsci.com

500 Parkway, Box 700 • Broomall, PA 19008 • 800.523.7480

Your neurons are
talking.

Are you listening?



Maestro Pro™ microelectrode array (MEA) *in vitro* neural activity analysis

Record network-level neural activity directly on the benchtop with Maestro. Over minutes or months, gain unprecedented access to electrical network function from cultured neural populations.

Straightforward and easy to use, any researcher can measure activity from neurons in 12-, 24-, 48- or 96-well plates. With a Maestro system for every budget, now there's nothing stopping you from exploring life's circuitry.



Maestro Pro MEA platform showing real-time neural activity across a 48-well plate.

Connect to your network.

Learn more: axionbio.com/neuron





Bringing clarity to complex gene targets.

While highly repetitive regions of the genome pose significant hurdles to reliable genetic analysis, their implications in disease are becoming clear.

Asuragen is committed to providing clinical researchers with the kits needed to investigate the most compelling and challenging targets, including genes implicated in Alzheimer's, ALS, FTD, Myotonic Dystrophy and Fragile X Syndrome.

Our clinical research kits overcome target complexity so you can focus on what matters most — scientific breakthroughs that drive better outcomes.

**AmplideX® PCR/CE *FMR1*^{1,2} | *C9orf72*² | *TOMM40*² | *DMPK*³
Xpansion Interpreter® for AGG Interruptions in *FMR1*⁴**

Visit Asuragen at the American Society of Human Genetics Annual Meeting
Booth # 824 | Oct 18-21, 2017 | Orange County Convention Center | Orlando, FL

Sensitive | Accurate | Complete
www.asuragen.com/ComplexityMadeClear



¹CE-IVD. ²RUO. ³In development. ⁴Only available from the Asuragen Clinical Laboratory.

Neuron

Best of 2016–2017

Review

Neuroscience-Inspired Artificial Intelligence

Demis Hassabis, Dharshan Kumaran, Christopher Summerfield, and Matthew Botvinick

Perspective

Cracking the Neural Code for Sensory Perception by Combining Statistics, Intervention, and Behavior

Stefano Panzeri, Christopher D. Harvey, Eugenio Piasini, Peter E. Latham, and Tommaso Fellin

NeuroResources

Flexible Near-Field Wireless Optoelectronics as Subdermal Implants for Broad Applications in Optogenetics

Gunchul Shin, Adrian M. Gomez, Ream Al-Hasani, Yu Ra Jeong, Jeonghyun Kim, Zhaoqian Xie, Anthony Banks, Seung Min Lee, Sang Youn Han, Chul Jong Yoo, Jong-Lam Lee, Seung Hee Lee, Jonas Kurniawan, Jacob Tureb, Zhongzhu Guo, Jangyeol Yoon, Sung-Il Park, Sang Yun Bang, Yoonho Nam, Marie C. Walicki, Vijay K. Samineni, Aaron D. Mickle, Kunhyuk Lee, Seung Yun Heo, Jordan G. McCall, Taisong Pan, Liang Wang, Xue Feng, Tae-il Kim, Jong Kyu Kim, Yuhang Li, Yonggang Huang, Robert W. Gereau IV, Jeong Sook Ha, Michael R. Bruchas, and John A. Rogers

High-Throughput Mapping of Single-Neuron Projections by Sequencing of Barcoded RNA

Justus M. Kebschull, Pedro Garcia da Silva, Ashlan P. Reid, Ian D. Peikon, Dinu F. Albeanu, and Anthony M. Zador

Human Astrocyte Maturation Captured in 3D Cerebral Cortical Spheroids Derived from Pluripotent Stem Cells

Steven A. Sloan, Spyros Darmanis, Nina Huber, Themasap A. Khan, Fikri Birey, Christine Caneda, Richard Reimer, Stephen R. Quake, Ben A. Barres, and Sergiu P. Pașca

Articles

Mutant Huntingtin Disrupts the Nuclear Pore Complex

Jonathan C. Grima, J. Gavin Daigle, Nicolas Arbez, Kathleen C. Cunningham, Ke Zhang, Joseph Ochaba, Charlene Geater, Eva Morozko, Jennifer Stocksdales, Jenna C. Glatzer, Jacqueline T. Pham, Ishrat Ahmed, Qi Peng, Harsh Wadhwa, Olga Pletnikova, Juan C. Troncoso, Wenzhen Duan, Solomon H. Snyder, Laura P.W. Ranum, Leslie M. Thompson, Thomas E. Lloyd, Christopher A. Ross, and Jeffrey D. Rothstein

De Novo Coding Variants Are Strongly Associated with Tourette Disorder

A. Jeremy Willsey, Thomas V. Fernandez, Dongmei Yu, Robert A. King, Andrea Dietrich, Jinchuan Xing, Stephan J. Sanders, Jeffrey D. Mandell, Alden Y. Huang, Petra Richer, Louw Smith, Shan Dong, Kaitlin E. Samocha, Tourette International Collaborative Genetics (TIC Genetics), Tourette Syndrome Association International Consortium for Genetics (TSAICG), Benjamin M. Neale, Giovanni Coppola, Carol A. Mathews, Jay A. Tischfield, Jeremiah M. Scharf, Matthew W. State, and Gary A. Heiman

(continued)

Tau Prion Strains Dictate Patterns of Cell Pathology, Progression Rate, and Regional Vulnerability In Vivo

Sarah K. Kaufman, David W. Sanders, Talitha L. Thomas, Allison J. Ruchinskas, Jaime Vaquer-Alicea, Apurwa M. Sharma, Timothy M. Miller, and Marc I. Diamond

Dorsal Raphe Dopamine Neurons Modulate Arousal and Promote Wakefulness by Salient Stimuli

Jounhong Ryan Cho, Jennifer B. Treweek, J. Elliott Robinson, Cheng Xiao, Lindsay R. Bremner, Alon Greenbaum, and Viviana Gradinaru

A Map of Anticipatory Activity in Mouse Motor Cortex

Tsai-Wen Chen, Nuo Li, Kayvon Daie, and Karel Svoboda

THE HUNT FOR BIOMARKERS HAS NO PEER.

Hone in on proteins and nucleic acids at the femtomolar level with the **Quanterix SR-Plex™ Ultra-Sensitive Biomarker Detection System**.

The new SR-Plex features multiplexed detection of analytes and 1,000 times the sensitivity of ELISA, changing the biomarker detection game one molecule at a time.

Discover the SR-Plex at go.quanterix.com/sr-plex



Quanterix™
The Science of Precision Health

F · S · T[®]
FINE SCIENCE TOOLS

ADVANCING THE FIELD OF RESEARCH

Scissors • Retractors • Magnifiers • Probes & Hooks • Bone Instruments • Animal Identification
Hemostats • Forceps • Surgical & Laboratory Equipment • Feeding Needles • Spatulae & Spoons
Wound Closure • Surgical Plates • Instrument Care & Sterilization • Rongeurs • Scalpels & Knives
Clamps • Pins & Holders • Needles & Needle Holders • Student Quality Instruments & Much More



FINE SURGICAL INSTRUMENTS FOR RESEARCH™

VISIT US AT FINESCIENCE.COM OR CALL 800 521 2109

Accelerate your drug discovery research at every step

GE Healthcare provides innovative tools and analytics to support therapeutic development from target identification, all the way through bioprocessing. Confidently move through the drug development pipeline while reducing costs and maximizing productivity throughout development and biomanufacturing. Learn more at gelifsciences.com.



REDEFINING more

FLUORESCENCE | CHEMILUMINESCENCE | PHOSPHOR IMAGING



With three imaging modalities and outstanding performance, the **Sapphire™ Biomolecular Imager** expands what you can accomplish with a single image scanning instrument.

Find out what more really means—visit
azurebiosystems.com/sapphire



NEW Metabolic Phenotyping Monitor: Oxymax CLAMS-HC

The Columbus Instruments Oxymax - **CLAMS-HC** (Comprehensive Lab Animal Monitoring System for Home Cages) is a versatile device for monitoring metabolic performance of mice and rats in their natural home cage environment.

- VO₂/VCO₂ & RER
- Food Intake
- Drinking Volume
- Body Mass
- Core Body Temp. & Heart Rate
- Breaths / Minute
- Animal Activity
- Sleeping Bouts
- Running Wheel Activity
- **Optional Environmental enclosure with temperature and LED light color control**

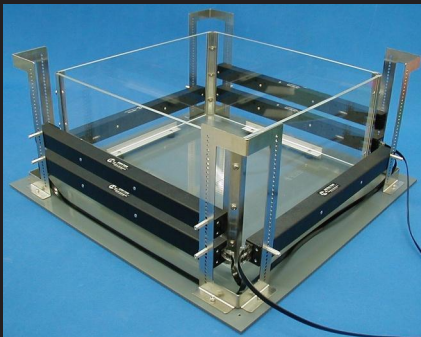


For more information: clams@colinst.com

Animal Activity Monitor

The Columbus Instruments Auto-Track Activity Meter presents the **ultimate flexibility** for measuring in home or special cages. Measures these parameters:

- Distance Traveled
- Path of Movement
- Zone Entries
- Rearing (Vertical)
- Rotations
- Open Field
- Hole Poke
- Light / Dark
- Contextual Place Preference

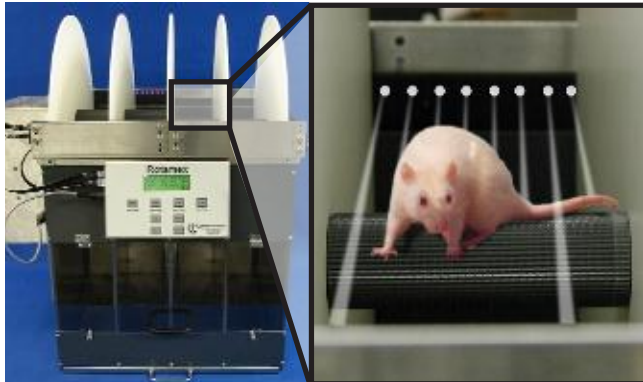


Animal Treadmill

The Exer 3/6 Treadmill provides 6 mouse lanes or 3 rat lanes for general purpose exercise. Adjustable speed, acceleration, and incline on all models. Available with or without electric stimulus or our **NEW Air Puff Stimulus!**



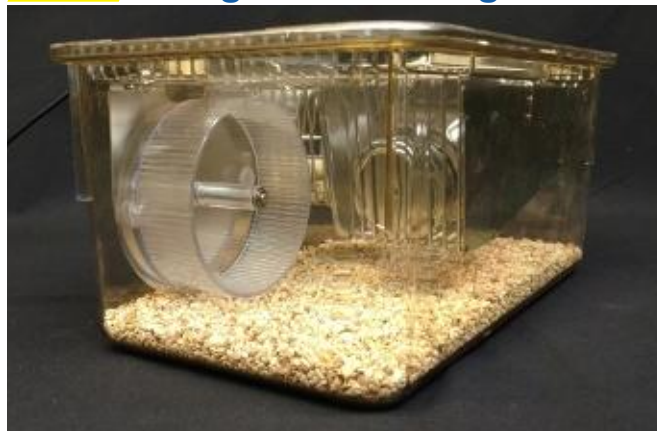
Rota-Rod: Rotamex-5



The Rotamex-5 measures coordination in up to four mice or rats by recording the latency to fall from a spinning rod. Key features include:

- Reports latency time to fall for each subject
- Reports rod speed in RPMin. or in cm/sec.
- Adjustable speed from 0-99.9 RPMin.
- Fully adjustable acceleration 0.1-20 RPMin/sec.
- Fall detection by photocells above the rod
- Detection of passive rotation (looping) in mice

NEW Weighted Running Wheel



The loaded running wheel applies a precise resistance during voluntary running for the purpose of increasing the load and measuring Work.

- Connects to PC via USB
- Software automatically calculates Work
- Adjustable load between 0 - 0.025 Newton-Meters in 0.00000038 Nm increments.

Go figure

With author-narrated animations



Introducing Figure360, an author-narrated animation of select figures in Cell Press primary research and review journals.

A short, digestible synopsis puts the figure in context and helps you zoom in on the most important take-home message in a matter of minutes. Why go it alone when the author can help you figure it out in less than half the time?

Check it out at www.cell.com/figure360

Figure360

CellPress

Neuroscience-Inspired Artificial Intelligence

Demis Hassabis,^{1,2,*} Dharshan Kumaran,^{1,3} Christopher Summerfield,^{1,4} and Matthew Botvinick^{1,2}

¹DeepMind, 5 New Street Square, London, UK

²Gatsby Computational Neuroscience Unit, 25 Howland Street, London, UK

³Institute of Cognitive Neuroscience, University College London, 17 Queen Square, London, UK

⁴Department of Experimental Psychology, University of Oxford, Oxford, UK

*Correspondence: dhcontact@google.com

<http://dx.doi.org/10.1016/j.neuron.2017.06.011>

The fields of neuroscience and artificial intelligence (AI) have a long and intertwined history. In more recent times, however, communication and collaboration between the two fields has become less commonplace. In this article, we argue that better understanding biological brains could play a vital role in building intelligent machines. We survey historical interactions between the AI and neuroscience fields and emphasize current advances in AI that have been inspired by the study of neural computation in humans and other animals. We conclude by highlighting shared themes that may be key for advancing future research in both fields.

In recent years, rapid progress has been made in the related fields of neuroscience and artificial intelligence (AI). At the dawn of the computer age, work on AI was inextricably intertwined with neuroscience and psychology, and many of the early pioneers straddled both fields, with collaborations between these disciplines proving highly productive (Churchland and Sejnowski, 1988; Hebb, 1949; Hinton et al., 1986; Hopfield, 1982; McCulloch and Pitts, 1943; Turing, 1950). However, more recently, the interaction has become much less commonplace, as both subjects have grown enormously in complexity and disciplinary boundaries have solidified. In this review, we argue for the critical and ongoing importance of neuroscience in generating ideas that will accelerate and guide AI research (see Hassabis commentary in Brooks et al., 2012).

We begin with the premise that building human-level general AI (or “Turing-powerful” intelligent systems; Turing, 1936) is a daunting task, because the search space of possible solutions is vast and likely only very sparsely populated. We argue that this therefore underscores the utility of scrutinizing the inner workings of the human brain—the only existing proof that such an intelligence is even possible. Studying animal cognition and its neural implementation also has a vital role to play, as it can provide a window into various important aspects of higher-level general intelligence.

The benefits to developing AI of closely examining biological intelligence are two-fold. First, neuroscience provides a rich source of *inspiration* for new types of algorithms and architectures, independent of and complementary to the mathematical and logic-based methods and ideas that have largely dominated traditional approaches to AI. For example, were a new facet of biological computation found to be critical to supporting a cognitive function, then we would consider it an excellent candidate for incorporation into artificial systems. Second, neuroscience can provide *validation* of AI techniques that already exist. If a known algorithm is subsequently found to be implemented in the brain, then that is strong support for its plausibility as an integral component of an overall general intelligence system. Such clues can be critical to a long-term research program when determining where to allocate resources most produc-

tively. For example, if an algorithm is not quite attaining the level of performance required or expected, but we observe it is core to the functioning of the brain, then we can surmise that redoubled engineering efforts geared to making it work in artificial systems are likely to pay off.

Of course from a practical standpoint of building an AI system, we need not slavishly enforce adherence to biological plausibility. From an engineering perspective, what works is ultimately all that matters. For our purposes then, biological plausibility is a guide, not a strict requirement. What we are interested in is a systems neuroscience-level understanding of the brain, namely the algorithms, architectures, functions, and representations it utilizes. This roughly corresponds to the top two levels of the three levels of analysis that Marr famously stated are required to understand any complex biological system (Marr and Poggio, 1976): the goals of the system (the computational level) and the process and computations that realize this goal (the algorithmic level). The precise mechanisms by which this is physically realized in a biological substrate are less relevant here (the implementation level). Note this is where our approach to neuroscience-inspired AI differs from other initiatives, such as the Blue Brain Project (Markram, 2006) or the field of neuromorphic computing systems (Esser et al., 2016), which attempt to closely mimic or directly reverse engineer the specifics of neural circuits (albeit with different goals in mind). By focusing on the computational and algorithmic levels, we gain transferrable insights into general mechanisms of brain function, while leaving room to accommodate the distinctive opportunities and challenges that arise when building intelligent machines *in silico*.

The following sections unpack these points by considering the past, present, and future of the AI-neuroscience interface. Before beginning, we offer a clarification. Throughout this article, we employ the terms “neuroscience” and “AI.” We use these terms in the widest possible sense. When we say neuroscience, we mean to include all fields that are involved with the study of the brain, the behaviors that it generates, and the mechanisms by which it does so, including cognitive neuroscience, systems neuroscience and psychology. When we say AI, we mean work

in machine learning, statistics, and AI research that aims to build intelligent machines (Legg and Hutter, 2007).

We begin by considering the origins of two fields that are pivotal for current AI research, deep learning and reinforcement learning, both of which took root in ideas from neuroscience. We then turn to the current state of play in AI research, noting many cases where inspiration has been drawn (sometimes without explicit acknowledgment) from concepts and findings in neuroscience. In this section, we particularly emphasize instances where we have combined deep learning with other approaches from across machine learning, such as reinforcement learning (Mnih et al., 2015), Monte Carlo tree search (Silver et al., 2016), or techniques involving an external content-addressable memory (Graves et al., 2016). Next, we consider the potential for neuroscience to support future AI research, looking at both the most likely research challenges and some emerging neuroscience-inspired AI techniques. While our main focus will be on the potential for neuroscience to benefit AI, our final section will briefly consider ways in which AI may be helpful to neuroscience and the broader potential for synergistic interactions between these two fields.

The Past

Deep Learning

As detailed in a number of recent reviews, AI has been revolutionized over the past few years by dramatic advances in neural network, or “deep learning,” methods (LeCun et al., 2015; Schmidhuber, 2014). As the moniker “neural network” might suggest, the origins of these AI methods lie directly in neuroscience. In the 1940s, investigations of neural computation began with the construction of artificial neural networks that could compute logical functions (McCulloch and Pitts, 1943). Not long after, others proposed mechanisms by which networks of neurons might learn incrementally via supervisory feedback (Rosenblatt, 1958) or efficiently encode environmental statistics in an unsupervised fashion (Hebb, 1949). These mechanisms opened up the field of artificial neural network research, and they continue to provide the foundation for contemporary research on deep learning (Schmidhuber, 2014).

Not long after this pioneering work, the development of the backpropagation algorithm allowed learning to occur in networks composed of multiple layers (Rumelhart et al., 1985; Werbos, 1974). Notably, the implications of this method for understanding intelligence, including AI, were first appreciated by a group of neuroscientists and cognitive scientists, working under the banner of parallel distributed processing (PDP) (Rumelhart et al., 1986). At the time, most AI research was focused on building logical processing systems based on serial computation, an approach inspired in part by the notion that human intelligence involves manipulation of symbolic representations (Haugeland, 1985). However, there was a growing sense in some quarters that purely symbolic approaches might be too brittle and inflexible to solve complex real-world problems of the kind that humans routinely handle. Instead, a growing foundation of knowledge about the brain seemed to point in a very different direction, highlighting the role of stochastic and highly parallelized information processing. Building on this, the PDP movement proposed that human cognition and behavior emerge

from dynamic, distributed interactions within networks of simple neuron-like processing units, interactions tuned by learning procedures that adjust system parameters in order to minimize error or maximize reward.

Although the PDP approach was at first applied to relatively small-scale problems, it showed striking success in accounting for a wide range of human behaviors (Hinton et al., 1986). Along the way, PDP research introduced a diverse collection of ideas that have had a sustained influence on AI research. For example, current machine translation research exploits the notion that words and sentences can be represented in a distributed fashion (i.e., as vectors) (LeCun et al., 2015), a principle that was already ingrained in early PDP-inspired models of sentence processing (St. John and McClelland, 1990). Building on the PDP movement’s appeal to biological computation, current state-of-the-art convolutional neural networks (CNNs) incorporate several canonical hallmarks of neural computation, including nonlinear transduction, divisive normalization, and maximum-based pooling of inputs (Yamins and DiCarlo, 2016). These operations were directly inspired by single-cell recordings from the mammalian visual cortex that revealed how visual input is filtered and pooled in simple and complex cells in area V1 (Hubel and Wiesel, 1959). Moreover, current network architectures replicate the hierarchical organization of mammalian cortical systems, with both convergent and divergent information flow in successive, nested processing layers (Krizhevsky et al., 2012; LeCun et al., 1989; Riesenhuber and Poggio, 1999; Serre et al., 2007), following ideas first advanced in early neural network models of visual processing (Fukushima, 1980). In both biological and artificial systems, successive non-linear computations transform raw visual input into an increasingly complex set of features, permitting object recognition that is invariant to transformations of pose, illumination, or scale.

As the field of deep learning evolved out of PDP research into a core area within AI, it was bolstered by new ideas, such as the development of deep belief networks (Hinton et al., 2006) and the introduction of large datasets inspired by research on human language (Deng et al., 2009). During this period, it continued to draw key ideas from neuroscience. For example, biological considerations informed the development of successful regularization schemes that support generalization beyond training data. One such scheme, in which only a subset of units participate in the processing of a given training example (“dropout”), was motivated by the stochasticity that is inherent in biological systems populated by neurons that fire with Poisson-like statistics (Hinton et al., 2012). Here and elsewhere, neuroscience has provided initial guidance toward architectural and algorithmic constraints that lead to successful neural network applications for AI.

Reinforcement Learning

Alongside its important role in the development of deep learning, neuroscience was also instrumental in erecting a second pillar of contemporary AI, stimulating the emergence of the field of reinforcement learning (RL). RL methods address the problem of how to maximize future reward by mapping states in the environment to actions and are among the most widely used tools in AI research (Sutton and Barto, 1998). Although it is not widely appreciated among AI researchers, RL methods were originally

inspired by research into animal learning. In particular, the development of temporal-difference (TD) methods, a critical component of many RL models, was inextricably intertwined with research into animal behavior in conditioning experiments. TD methods are real-time models that learn from differences between temporally successive predictions, rather than having to wait until the actual reward is delivered. Of particular relevance was an effect called second-order conditioning, where affective significance is conferred on a conditioned stimulus (CS) through association with another CS rather than directly via association with the unconditioned stimulus (Sutton and Barto, 1981). TD learning provides a natural explanation for second-order conditioning and indeed has gone on to explain a much wider range of findings from neuroscience, as we discuss below.

Here, as in the case of deep learning, investigations initially inspired by observations from neuroscience led to further developments that have strongly shaped the direction of AI research. From their neuroscience-informed origins, TD methods and related techniques have gone on to supply the core technology for recent advances in AI, ranging from robotic control (Hafner and Riedmiller, 2011) to expert play in backgammon (Tesauro, 1995) and Go (Silver et al., 2016).

The Present

Reading the contemporary AI literature, one gains the impression that the earlier engagement with neuroscience has diminished. However, if one scratches the surface, one can uncover many cases in which recent developments have been inspired and guided by neuroscientific considerations. Here, we look at four specific examples.

Attention

The brain does not learn by implementing a single, global optimization principle within a uniform and undifferentiated neural network (Marblestone et al., 2016). Rather, biological brains are modular, with distinct but interacting subsystems underpinning key functions such as memory, language, and cognitive control (Anderson et al., 2004; Shallice, 1988). This insight from neuroscience has been imported, often in an unspoken way, into many areas of current AI.

One illustrative example is recent AI work on attention. Up until quite lately, most CNN models worked directly on entire images or video frames, with equal priority given to all image pixels at the earliest stage of processing. The primate visual system works differently. Rather than processing all input in parallel, visual attention shifts strategically among locations and objects, centering processing resources and representational coordinates on a series of regions in turn (Koch and Ullman, 1985; Moore and Zirnsak, 2017; Posner and Petersen, 1990). Detailed neurocomputational models have shown how this piecemeal approach benefits behavior, by prioritizing and isolating the information that is relevant at any given moment (Olshausen et al., 1993; Salinas and Abbott, 1997). As such, attentional mechanisms have been a source of inspiration for AI architectures that take “glimpses” of the input image at each step, update internal state representations, and then select the next location to sample (Larochelle and Hinton, 2010; Mnih et al., 2014) (Figure 1A). One such network was able to use this selective attentional mechanism to ignore irrelevant objects in a

scene, allowing it to perform well in challenging object classification tasks in the presence of clutter (Mnih et al., 2014). Further, the attentional mechanism allowed the computational cost (e.g., number of network parameters) to scale favorably with the size of the input image. Extensions of this approach were subsequently shown to produce impressive performance at difficult multi-object recognition tasks, outperforming conventional CNNs that process the entirety of the image, both in terms of accuracy and computational efficiency (Ba et al., 2015), as well as enhancing image-to-caption generation (Xu et al., 2015).

While attention is typically thought of as an orienting mechanism for perception, its “spotlight” can also be focused internally, toward the contents of memory. This idea, a recent focus in neuroscience studies (Summerfield et al., 2006), has also inspired work in AI. In some architectures, attentional mechanisms have been used to select information to be read out from the internal memory of the network. This has helped provide recent successes in machine translation (Bahdanau et al., 2014) and led to important advances on memory and reasoning tasks (Graves et al., 2016). These architectures offer a novel implementation of content-addressable retrieval, which was itself a concept originally introduced to AI from neuroscience (Hopfield, 1982).

One further area of AI where attention mechanisms have recently proven useful focuses on generative models, systems that learn to synthesize or “imagine” images (or other kinds of data) that mimic the structure of examples presented during training. Deep generative models (i.e., generative models implemented as multi-layered neural networks) have recently shown striking successes in producing synthetic outputs that capture the form and structure of real visual scenes via the incorporation of attention-like mechanisms (Hong et al., 2015; Reed et al., 2016). For example, in one state-of-the-art generative model known as DRAW, attention allows the system to build up an image incrementally, attending to one portion of a “mental canvas” at a time (Gregor et al., 2015).

Episodic Memory

A canonical theme in neuroscience is that intelligent behavior relies on multiple memory systems (Tulving, 1985). These will include not only reinforcement-based mechanisms, which allow the value of stimuli and actions to be learned incrementally and through repeated experience, but also instance-based mechanisms, which allow experiences to be encoded rapidly (in “one shot”) in a content-addressable store (Gallistel and King, 2009). The latter form of memory, known as episodic memory (Tulving, 2002), is most often associated with circuits in the medial temporal lobe, prominently including the hippocampus (Squire et al., 2004).

One recent breakthrough in AI has been the successful integration of RL with deep learning (Mnih et al., 2015; Silver et al., 2016). For example, the deep Q-network (DQN) exhibits expert play on Atari 2600 video games by learning to transform a vector of image pixels into a policy for selecting actions (e.g., joystick movements). One key ingredient in DQN is “experience replay,” whereby the network stores a subset of the training data in an instance-based way, and then “replays” it offline, learning anew from successes or failures that occurred in the past. Experience replay is critical to maximizing data efficiency, avoids the

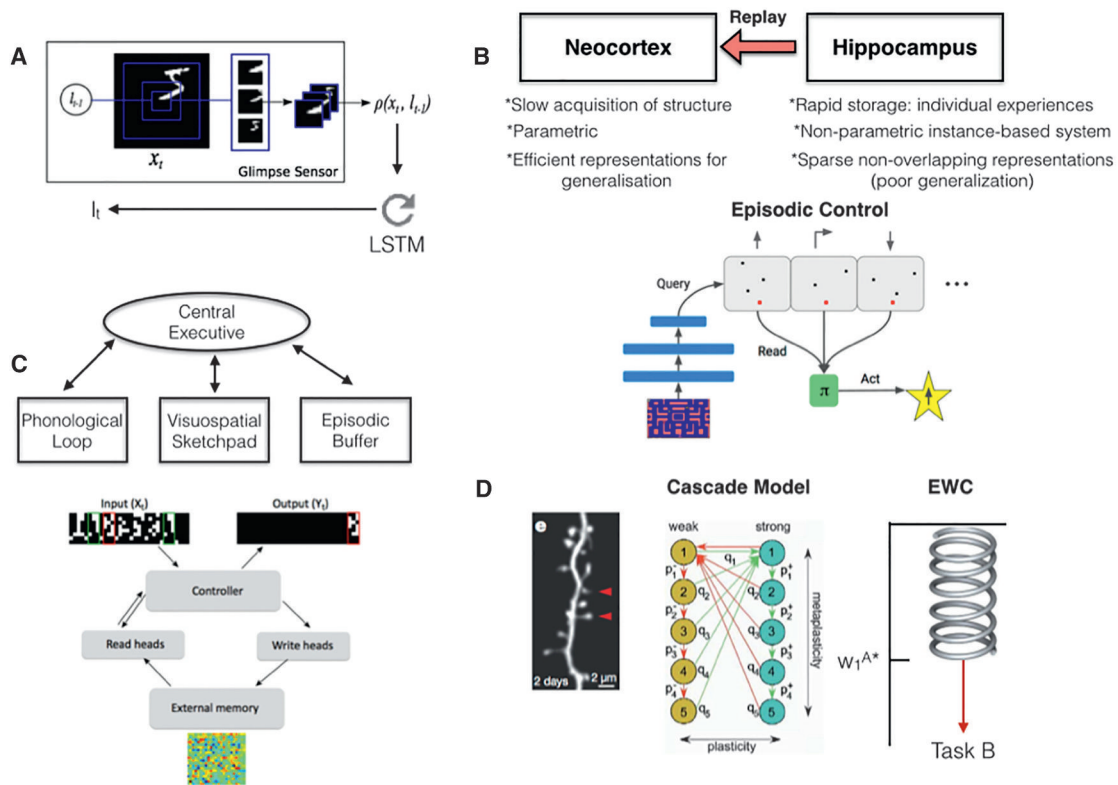


Figure 1. Parallels between AI Systems and Neural Models of Behavior

(A) Attention. Schematic of recurrent attention model (Mnih et al., 2014). Given an input image (x_t) and foveal location (l_{t-1}), the glimpse sensor extracts a multi-resolution “retinal” representation ($p(x_t, l_{t-1})$). This is the input to a glimpse network, which produces a representation that is passed to the LSTM core, which defines the next location to attend to (l_t) (and classification decision).

(B) Schematic of complementary learning systems and episodic control. Top: non-parametric fast learning hippocampal system and parametric slow-learning neocortical system (i.e., parametric: a fixed number of parameters; non-parametric: the number of parameters can grow with the amount of data). Hippocampus/instance-based system supports rapid behavioral adjustment (i.e., episodic control; Blundell et al., 2016) and experience replay, which supports interleaved training (i.e., on random subsets of experiences) of deep neural network (Mnih et al., 2015) or neocortex. Bottom: episodic control (from Blundell et al., 2016). Game states (Atari shown) are stored within buffers (one for each possible action) together with the highest (discounted) return experienced from that state (i.e., Q-value). When experiencing a new state, the policy (π) is determined by averaging the Q-value across the k nearest neighbors in each action buffer and selecting the action with the highest expected return.

(C) Illustration of parallels between macroscopic organization of models of working memory and the differentiable neural computer (Graves et al., 2016) (or Neural Turing Machine). The network controller (typically recurrent) is analogous to the central executive (typically viewed to be instantiated in the prefrontal cortex) and attends/reads/writes to an external memory matrix (phonological loop /sketchpad in working memory model). Architecture is shown performing copy task.

(D) Illustration of parallel between neurobiological models of synaptic consolidation and the elastic weight consolidation (EWC) algorithm. Left: two-photon structural imaging data showing learning-related increase in size of dendrites (each corresponding approximately to a single excitatory synapse) that persists for months (from Yang et al., 2009). Middle: schematic of Cascade model of synaptic consolidation (adapted with permission from Fusi et al., 2005). Binary synapses transition between metaplastic states which are more/less plastic (least plastic states at bottom of diagram), as a function of prior potentiation/depression events. Right panel: schematic of elastic weight consolidation (EWC) algorithm. After training on the first task (A), network parameters are optimized for good performance: single weight (w_1^{A*} illustrated). EWC implements a constraint analogous to a spring that anchors weights to the previously found solution (i.e., for task A), when training on a new task (e.g., task B), with the stiffness of the spring *proportional to the importance* of that parameter for task A performance (Kirkpatrick et al., 2017).

destabilizing effects of learning from consecutive correlated experiences, and allows the network to learn a viable value function even in complex, highly structured sequential environments such as video games.

Critically, experience replay was directly inspired by theories that seek to understand how the multiple memory systems in the mammalian brain might interact. According to a prominent view, animal learning is supported by parallel or “complementary” learning systems in the hippocampus and neocortex (Kumaran et al., 2016; McClelland et al., 1995). The hippocampus acts to encode novel information after a single exposure (one-

shot learning), but this information is gradually consolidated to the neocortex in sleep or resting periods that are interleaved with periods of activity. This consolidation is accompanied by replay in the hippocampus and neocortex, which is observed as a reinstatement of the structured patterns of neural activity that accompanied the learning event (O’Neill et al., 2010; Skaggs and McNaughton, 1996) (Figure 1B). This theory was originally proposed as a solution to the well-known problem that in conventional neural networks, correlated exposure to sequential task settings leads to mutual interference among policies, resulting in catastrophic forgetting of one task as a new one is

learned. The replay buffer in DQN might thus be thought of as a very primitive hippocampus, permitting complementary learning *in silico* much as is proposed for biological brains. Later work showed that the benefits of experience replay in DQN are enhanced when replay of highly rewarding events is prioritized (Schaul et al., 2015), just as hippocampal replay seems to favor events that lead to high levels of reinforcement (Singer and Frank, 2009).

Experiences stored in a memory buffer can not only be used to gradually adjust the parameters of a deep network toward an optimal policy, as in DQN, but can also support rapid behavioral change based on an individual experience. Indeed, theoretical neuroscience has argued for the potential benefits of *episodic control*, whereby rewarded action sequences can be internally re-enacted from a rapidly updateable memory store, implemented in the biological case in the hippocampus (Gershman and Daw, 2017). Further, normative accounts show that episodic control is particularly advantageous over other learning mechanisms when limited experience of the environment has been obtained (Lengyel and Dayan, 2007).

Recent AI research has drawn on these ideas to overcome the slow learning characteristics of deep RL networks, developing architectures that implement episodic control (Blundell et al., 2016). These networks store specific experiences (e.g., actions and reward outcomes associated with particular Atari game screens) and select new actions based on the similarity between the current situation input and the previous events stored in memory, taking the reward associated with those previous events into account (Figure 1B). As predicted from the initial, neuroscience-based work (Lengyel and Dayan, 2007), artificial agents employing episodic control show striking gains in performance over deep RL networks, particularly early on during learning (Blundell et al., 2016). Further, they are able to achieve success on tasks that depend heavily on one-shot learning, where typical deep RL architectures fail. Moreover, episodic-like memory systems more generally have shown considerable promise in allowing new concepts to be learned rapidly based on only a few examples (Vinyals et al., 2016). In the future, it will be interesting to harness the benefits of rapid episodic-like memory and more traditional incremental learning in architectures that incorporate both of these components within an interacting framework that mirrors the complementary learning systems in mammalian brain. We discuss these future perspectives below in more detail later, in “Imagination and planning.”

Working Memory

Human intelligence is characterized by a remarkable ability to maintain and manipulate information within an active store, known as working memory, which is thought to be instantiated within the prefrontal cortex and interconnected areas (Goldman-Rakic, 1990). Classic cognitive theories suggest that this functionality depends on interactions between a central controller (“executive”) and separate, domain-specific memory buffers (e.g., visuo-spatial sketchpad) (Baddeley, 2012). AI research has drawn inspiration from these models, by building architectures that explicitly maintain information over time. Historically, such efforts began with the introduction of recurrent neural network architectures displaying attractor dynamics and rich sequential behavior, work directly inspired by neuroscience

(Elman, 1990; Hopfield and Tank, 1986; Jordan, 1997). This work enabled later, more detailed modeling of human working memory (Botvinick and Plaut, 2006; Durstewitz et al., 2000), but it also laid the foundation for further technical innovations that have proved pivotal in recent AI research. In particular, one can see close parallels between the learning dynamics in these early, neuroscience-inspired networks and those in long-short-term memory (LSTM) networks, which subsequently achieved state of the art performance across a variety of domains. LSTMs allow information to be gated into a fixed activity state and maintained until an appropriate output is required (Hochreiter and Schmidhuber, 1997). Variants of this type of network have shown some striking behaviors in challenging domains, such as learning to respond to queries about the latent state of variables after training on computer code (Zaremba and Sutskever, 2014).

In ordinary LSTM networks, the functions of sequence control and memory storage are closely intertwined. This contrasts with classic models of human working memory, which, as mentioned above, separate these two. This neuroscience-based schema has recently inspired more complex AI architectures where control and storage are supported by distinct modules (Graves et al., 2014, 2016; Weston et al., 2014). For example, the differential neural computer (DNC) involves a neural network controller that attends to and reads/writes from an external memory matrix (Graves et al., 2016). This externalization allows the network controller to learn from scratch (i.e., via end-to-end optimization) to perform a wide range of complex memory and reasoning tasks that currently elude LSTMs, such as finding the shortest path through a graph-like structure, such as a subway map, or manipulating blocks in a variant of the Tower of Hanoi task (Figure 1C). These types of problems were previously argued to depend exclusively on symbol processing and variable binding and therefore beyond the purview of neural networks (Fodor and Pylyshyn, 1988; Marcus, 1998). Of note, although both LSTMs and the DNC are described here in the context of working memory, they have the potential to maintain information over many thousands of training cycles and so may thus be suited to longer-term forms of memory, such as retaining and understanding the contents of a book.

Continual Learning

Intelligent agents must be able to learn and remember many different tasks that are encountered over multiple timescales. Both biological and artificial agents must thus have a capacity for continual learning, that is, an ability to master new tasks without forgetting how to perform prior tasks (Thrun and Mitchell, 1995). While animals appear relatively adept at continual learning, neural networks suffer from the problem of catastrophic forgetting (French, 1999; McClelland et al., 1995). This occurs as the network parameters shift toward the optimal state for performing the second of two successive tasks, overwriting the configuration that allowed them to perform the first. Given the importance of continual learning, this liability of neural networks remains a significant challenge for the development of AI.

In neuroscience, advanced neuroimaging techniques (e.g., two-photon imaging) now allow dynamic *in vivo* visualization of the structure and function of dendritic spines during learning, at the spatial scale of single synapses (Nishiyama and Yasuda, 2015). This approach can be used to study

neocortical plasticity during continual learning (Cichon and Gan, 2015; Hayashi-Takagi et al., 2015; Yang et al., 2009). There is emerging evidence for specialized mechanisms that protect knowledge about previous tasks from interference during learning on a new task. These include decreased synaptic lability (i.e., lower rates of plasticity) in a proportion of strengthened synapses, mediated by enlargements to dendritic spines that persist despite learning of other tasks (Cichon and Gan, 2015; Yang et al., 2009) (Figure 1D). These changes are associated with retention of task performance over several months, and indeed, if they are “erased” with synaptic optogenetics, this leads to forgetting of the task (Hayashi-Takagi et al., 2015). These empirical insights are consistent with theoretical models that suggest that memories can be protected from interference through synapses that transition between a cascade of states with different levels of plasticity (Fusi et al., 2005) (Figure 1D).

Together, these findings from neuroscience have inspired the development of AI algorithms that address the challenge of continual learning in deep networks by implementing a form of “elastic” weight consolidation (EWC) (Kirkpatrick et al., 2017), which acts by slowing down learning in a subset of network weights identified as important to previous tasks, thereby anchoring these parameters to previously found solutions (Figure 1D). This allows multiple tasks to be learned without an increase in network capacity, with weights shared efficiently between tasks with related structure. In this way, the EWC algorithm allows deep RL networks to support continual learning at large scale.

The Future

In AI, the pace of recent research has been remarkable. Artificial systems now match human performance in challenging object recognition tasks (Krizhevsky et al., 2012) and outperform expert humans in dynamic, adversarial environments such as Atari video games (Mnih et al., 2015), the ancient board game of Go (Silver et al., 2016), and imperfect information games such as heads-up poker (Moravčík et al., 2017). Machines can autonomously generate synthetic natural images and simulations of human speech that are almost indistinguishable from their real-world counterparts (Lake et al., 2015; van den Oord et al., 2016), translate between multiple languages (Wu et al., 2016), and create “neural art” in the style of well-known painters (Gatys et al., 2015).

However, much work is still needed to bridge the gap between machine and human-level intelligence. In working toward closing this gap, we believe ideas from neuroscience will become increasingly indispensable. In neuroscience, the advent of new tools for brain imaging and genetic bioengineering have begun to offer a detailed characterization of the computations occurring in neural circuits, promising a revolution in our understanding of mammalian brain function (Deisseroth and Schnitzer, 2013). The relevance of neuroscience, both as a roadmap for the AI research agenda and as a source of computational tools is particularly salient in the following key areas.

Intuitive Understanding of the Physical World

Recent perspectives emphasize key ingredients of human intelligence that are already well developed in human infants but

lacking in most AI systems (Gilmore et al., 2007; Gopnik and Schulz, 2004; Lake et al., 2016). Among these capabilities are knowledge of core concepts relating to the physical world, such as space, number, and objectness, which allow people to construct compositional mental models that can guide inference and prediction (Battaglia et al., 2013; Spelke and Kinzler, 2007).

AI research has begun to explore methods for addressing this challenge. For example, novel neural network architectures have been developed that interpret and reason about scenes in a humanlike way, by decomposing them into individual objects and their relations (Battaglia et al., 2016; Chang et al., 2016; Eslami et al., 2016) (Figures 2A and 2B). In some cases, this has resulted in human-level performance on challenging reasoning tasks (Santoro et al., 2017). In other work, deep RL has been used to capture the processes by which children gain commonsense understanding of the world through interactive experiments (Denil et al., 2016). Relatedly, deep generative models have been developed that are able to construct rich object models from raw sensory inputs (Higgins et al., 2016). These leverage constraints first identified in neuroscience, such as redundancy reduction (Barlow, 1959), which encourage the emergence of disentangled representations of independent factors such as shape and position (Figure 2C). Importantly, the latent representations learned by such generative models exhibit compositional properties, supporting flexible transfer to novel tasks (Eslami et al., 2016; Higgins et al., 2016; Rezende et al., 2016a). In the caption associated with Figure 2, we provide more detailed information about these networks.

Efficient Learning

Human cognition is distinguished by its ability to rapidly learn about new concepts from only a handful of examples, leveraging prior knowledge to enable flexible inductive inferences. In order to highlight this human ability as a challenge for AI, Lake and colleagues recently posed a “characters challenge” (Lake et al., 2016). Here, an observer must distinguish novel instances of an unfamiliar handwritten character from other, similar items after viewing only a single exemplar. Humans can perform this task well, but it is difficult for classical AI systems.

Encouragingly, recent AI algorithms have begun to make progress on tasks like the characters challenge, through both structured probabilistic models (Lake et al., 2015) and deep generative models based on the abovementioned DRAW model (Rezende et al., 2016b). Both classes of system can make inferences about a new concept despite a poverty of data and generate new samples from a single example concept (Figure 2D). Further, recent AI research has developed networks that “learn to learn,” acquiring knowledge on new tasks by leveraging prior experience with related problems, to support one-shot concept learning (Santoro et al., 2016; Vinyals et al., 2016) and accelerating learning in RL tasks (Wang et al., 2016). Once again, this builds on concepts from neuroscience: learning to learn was first explored in studies of animal learning (Harlow, 1949), and has subsequently been studied in developmental psychology (Adolph, 2005; Kemp et al., 2010; Smith, 1995).

Transfer Learning

Humans also excel at generalizing or transferring generalized knowledge gained in one context to novel, previously unseen domains (Barnett and Ceci, 2002; Holyoak and Thagard, 1997). For

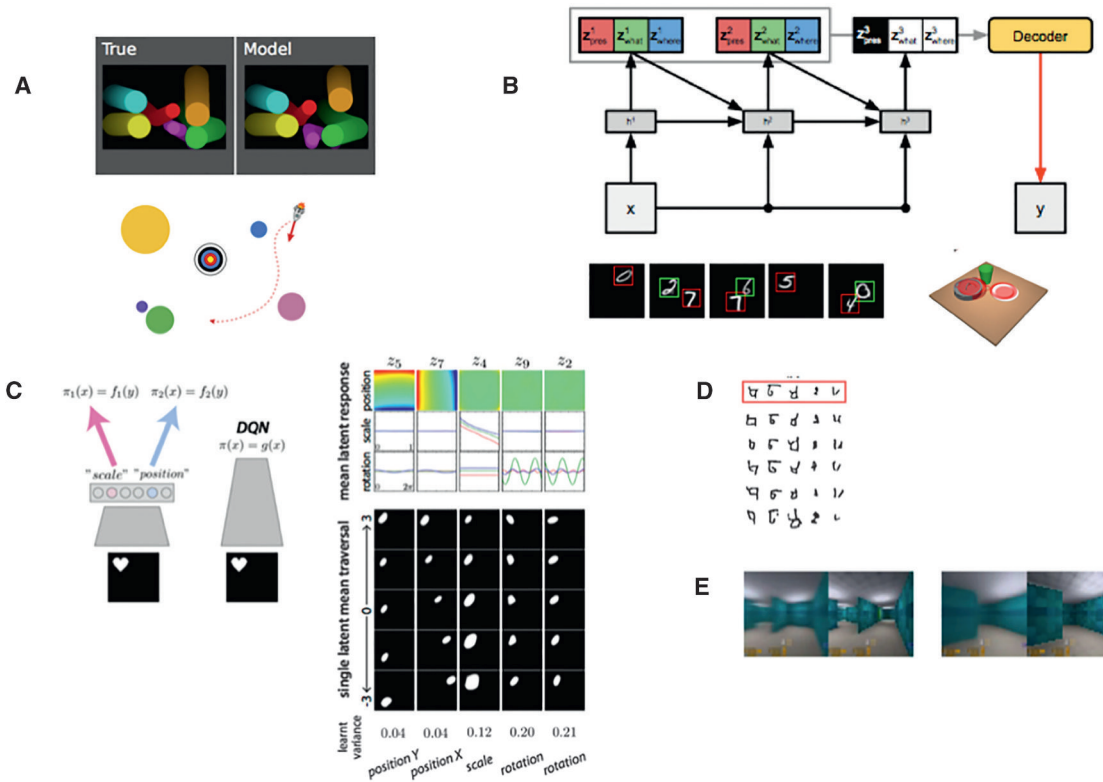


Figure 2. Examples of Recent AI Systems that Have Been Inspired by Neuroscience

(A) Intuitive physics knowledge. Illustration of the ability of the interaction network (Battaglia et al., 2016) to reason and make predictions about the physical interaction between objects in the bouncing ball problem (top) and spaceship problem (bottom). The network takes as input objects and their relations and accurately simulates their trajectories by modeling collisions, gravitational forces, etc., effectively acting as a learned physics engine.

(B) Scene understanding through structured generative models (Eslami et al., 2016). Top: iterative inference in a variational auto-encoder architecture. The recurrent network attends to one object at a time, infers its attributes, and performs the appropriate number of inference steps for each input image (x). Scenes are described in terms of groups of latent variables (Z) that specify presence/absence (z_{pres}), properties such as position (z_{where}), and shape (z_{what}). Inference network (black connections), and the generator network (red arrow), which produces reconstructed image (y). Bottom: illustration of iterative inference in multiple MNIST images (green indicates the first step and red the second step). Right: inference about the position/shape of multiple objects in realistic scene (note that inference is accurate, and hence it is difficult to distinguish inferred positions [red line] from ground truth). Latent representations in this network speed learning on downstream tasks (e.g., addition of MNIST digits) (not depicted; see Eslami et al., 2016).

(C) Unsupervised learning of core object properties (Higgins et al., 2016) is shown. Left: schematic illustrating learning of disentangled factors of sensory input by deep generative model (left: variational auto-encoder [VAE]), whose representations can speed learning on downstream tasks (Eslami et al., 2016), as compared to relatively entangled representation learned by typical deep network (e.g., DQN: right). Right panel illustrates latent representation of VAE; latent units coding for factors of variation, such as object position, rotation, and scale, are shown by effect of independently changing the activity of one latent unit. Such networks can learn intuitive concepts such as “objectness,” being able to support zero-shot transfer (i.e., reasoning about position or scale of an unseen object with a novel shape; Higgins et al., 2016).

(D) One-shot generalization in deep sequential generative models (Rezende et al., 2016b) is shown. Deep generative models specify a causal process for generating the observed data using a hierarchy of latent variables, with attentional mechanisms supporting sequential inference. Illustrated are generated samples from the Rezende et al. model, conditioned on a single novel character from a held-out alphabet from the Omniglot dataset (Lake et al., 2015), demonstrating abilities that mirror human abilities to generalize from a single concept.

(E) Imagination of realistic environments in deep networks (Chiappa et al., 2017) is shown. Generated (left) and real (right) frames from procedural mazes (i.e., new maze layout on each episode) produced by an action-conditional recurrent network model ~ 150 and 200 frames after the last observed image, respectively.

example, a human who can drive a car, use a laptop computer, or chair a committee meeting is usually able act effectively when confronted with an unfamiliar vehicle, operating system, or social situation. Progress is being made in developing AI architectures capable of exhibiting strong generalization or transfer, for example by enabling zero-shot inferences about novel shapes outside the training distribution based on compositional representations (Higgins et al., 2016; Figure 2C). Others have shown that a new class of architecture, known as a progressive network, can leverage knowledge gained in one video game to

learn rapidly in another, promising the sort of “far transfer” that is characteristic of human skill acquisition (Rusu et al., 2016a). Progressive networks have also been successfully employed to transfer knowledge for a simulated robotic environment to a real robot arm, massively reducing the training time required on the real world (Rusu et al., 2016b). Intriguingly, the proposed architecture bears some resemblance to a successful computational model of sequential task learning in humans (Collins and Koechlin, 2012; Donoso et al., 2014). In the neuroscience literature, one hallmark of transfer learning has been the ability to

reason relationally, and AI researchers have also begun to make progress in building deep networks that address problems of this nature, for example by solving visual analogies (Reed et al., 2015). More generally however, how humans or other animals achieve this sort of high-level transfer learning is unknown, and remains a relatively unexplored topic in neuroscience. New advances on this front could provide critical insights to spur AI research toward the goal of lifelong learning in agents, and we encourage neuroscientists to engage more deeply with this question.

At the level of neural coding, this kind of transfer of abstract structured knowledge may rely on the formation of conceptual representations that are invariant to the objects, individuals, or scene elements that populate a sensory domain but code instead for abstract, relational information among patterns of inputs (Doumas et al., 2008). However, we currently lack direct evidence for the existence of such codes in the mammalian brain. Nevertheless, one recent report made the very interesting claim that neural codes thought to be important in the representation of allocentric (map-like) spaces might be critical for abstract reasoning in more general domains (Constantinescu et al., 2016). In the mammalian entorhinal cortex, cells encode the geometry of allocentric space with a periodic “grid” code, with receptive fields that tile the local space in a hexagonal pattern (Rowland et al., 2016). Grid codes may be an excellent candidate for organizing conceptual knowledge, because they allow state spaces to be decomposed efficiently, in a way that could support discovery of subgoals and hierarchical planning (Stachenfeld et al., 2014). Using functional neuroimaging, the researchers provide evidence for the existence of such codes while humans performed an abstract categorization task, supporting the view that periodic encoding is a generalized hallmark of human knowledge organization (Constantinescu et al., 2016). However, much further work is required to substantiate this interesting claim.

Imagination and Planning

Despite their strong performance on goal-directed tasks, deep RL systems such as DQN operate mostly in a reactive way, learning the mapping from perceptual inputs to actions that maximize future value. This “model-free” RL is computationally inexpensive but suffers from two major drawbacks: it is relatively data inefficient, requiring large amounts of experience to derive accurate estimates, and it is inflexible, being insensitive to changes in the value of outcomes (Daw et al., 2005). By contrast, humans can more flexibly select actions based on forecasts of long-term future outcomes through simulation-based planning, which uses predictions generated from an internal model of the environment learned through experience (Daw et al., 2005; Dolan and Dayan, 2013; Tolman, 1948). Moreover, planning is not a uniquely human capacity. For example, when caching food, scrub jays consider the future conditions under which it is likely to be recovered (Raby et al., 2007), and rats use a “cognitive map” when navigating, allowing inductive inferences during wayfinding and facilitating one-shot learning behaviors in maze-like environments (Daw et al., 2005; Tolman, 1948). Of course, this point has not been lost on AI researchers; indeed, early planning algorithms such as Dyna (Sutton, 1991) were inspired by theories that emphasized the importance of “mental models” in generating hypothetical experiences useful for

human learning (Craik, 1943). By now, a large volume of literature exists on AI planning techniques, including model-based RL methods, which seek to implement this forecast-based method of action selection. Furthermore, simulation-based planning, particularly Monte Carlo tree search (MCTS) methods, which use forward search to update a value function and/or policy (Browne et al., 2012), played a key role in recent work in which deep RL attained expert-level performance in the game of Go (Silver et al., 2016).

AI research on planning, however, has yet to capture some of the key characteristics that give human planning abilities their power. In particular, we suggest that a general solution to this problem will require understanding how rich internal models, which in practice will have to be approximate but sufficiently accurate to support planning, can be learned through experience, without strong priors being handcrafted into the network by the experimenter. We also argue that AI research will benefit from a close reading of the related literature on how humans imagine possible scenarios, envision the future, and carry out simulation-based planning, functions that depend on a common neural substrate in the hippocampus (Doll et al., 2015; Hassabis and Maguire, 2007, 2009; Schacter et al., 2012). Although imagination has an intrinsically subjective, unobservable quality, we have reason to believe that it has a conserved role in simulation-based planning across species (Hassabis and Maguire, 2009; Schacter et al., 2012). For example, when paused at a choice point, ripples of neural activity in the rat hippocampus resemble those observed during subsequent navigation of the available trajectories (“preplay”), as if the animal were “imagining” each possible alternative (Johnson and Redish, 2007; Ólafsdóttir et al., 2015; Pfeiffer and Foster, 2013). Further, recent work has suggested a similar process during non-spatial planning in humans (Doll et al., 2015; Kurth-Nelson et al., 2016). We have discussed above the ways in which the introduction of mechanisms that replay and learn offline from past experiences can improve the performance of deep RL agents such as DQN (as discussed above in Episodic Memory).

Some encouraging initial progress toward simulation-based planning has been made using deep generative models (Eslami et al., 2016; Rezende et al., 2016a, 2016b) (Figure 2). In particular, recent work has introduced new architectures that have the capacity to generate temporally consistent sequences of generated samples that reflect the geometric layout of newly experienced realistic environments (Gemici et al., 2017; Oh et al., 2015) (Figure 2E), providing a parallel to the function of the hippocampus in binding together multiple components to create an imagined experience that is spatially and temporally coherent (Hassabis and Maguire, 2007). Deep generative models thus show the potential to capture the rich dynamics of complex realistic environments, but using these models for simulation-based planning in agents remains a challenge for future work.

Insights from neuroscience may provide guidance that facilitates the integration of simulation with control. An emerging picture from neuroscience research suggests that the hippocampus supports planning by instantiating an internal model of the environment, with goal-contingent valuation of simulated outcomes occurring in areas downstream of the hippocampus

such the orbitofrontal cortex or striatum (Redish, 2016). Notably, however, the mechanisms that guide the rolling forward of an internal model of the environment in the hippocampus remain uncertain and merit future scrutiny. One possibility is that this process is initiated by the prefrontal cortex through interactions with the hippocampus. Indeed, this notion has distinct parallels with proposals from AI research that a separate controller interacts with an internal model of the environment in a bidirectional fashion, querying the model based on task-relevant goals and receiving predicted simulated states as input (Schmidhuber, 2014). Further, recent efforts to develop agents have employed architectures that instantiate a separation between controller and environmental model to effect simulation-based planning in problems involving the interaction between physical objects (Hamrick et al., 2017).

In enhancing agent capabilities in simulation-based planning, it will also be important to consider other salient properties of this process in humans (Hassabis and Maguire, 2007, 2009). Research into human imagination emphasizes its constructive nature, with humans able to construct fictitious mental scenarios by recombining familiar elements in novel ways, necessitating compositional/disentangled representations of the form present in certain generative models (Eslami et al., 2016; Higgins et al., 2016; Rezende et al., 2016a). This fits well with the notion that planning in humans involves efficient representations that support generalization and transfer, so that plans forged in one setting (e.g., going through a door to reach a room) can be leveraged in novel environments that share structure. Further, planning and mental simulation in humans are “jumpy,” bridging multiple temporal scales at a time; for example, humans seem to plan hierarchically, by considering in parallel terminal solutions, interim choice points, and piecemeal steps toward the goal (Balaguer et al., 2016; Solway et al., 2014; Huys et al., 2012). We think that ultimately these flexible, combinatorial aspects of planning will form a critical underpinning of what is perhaps the hardest challenge for AI research: to build an agent that can plan hierarchically, is truly creative, and can generate solutions to challenges that currently elude even the human mind.

Virtual Brain Analytics

One rather different way in which neuroscience may serve AI is by furnishing new analytic tools for understanding computation in AI systems. Due to their complexity, the products of AI research often remain “black boxes”; we understand only poorly the nature of the computations that occur, or representations that are formed, during learning of complex tasks. However, by applying tools from neuroscience to AI systems, synthetic equivalents of single-cell recording, neuroimaging, and lesion techniques, we can gain insights into the key drivers of successful learning in AI research and increase the interpretability of these systems. We call this “virtual brain analytics.”

Recent work has made some progress along these lines. For example, visualizing brain states through dimensionality reduction is commonplace in neuroscience, and has recently been applied to neural networks (Zahavy et al., 2016). Receptive field mapping, another standard tool in neuroscience, allows AI researchers to determine the response properties of units in a neural network. One interesting application of this approach in AI is known as activity maximization, in which a network learns

to generate synthetic images by maximizing the activity of certain classes of unit (Nguyen et al., 2016; Simonyan et al., 2013). Elsewhere, neuroscience-inspired analyses of linearized networks have uncovered important principles that may be of general benefit in optimizing learning these networks, and understanding the benefits of network depth and representational structure (McClelland and Rogers, 2003; Saxe et al., 2013).

While this initial progress is encouraging, more work is needed. It remains difficult to characterize the functioning of complex architectures such as networks with external memory (Graves et al., 2016). Nevertheless, AI researchers are in the unique position of having ground truth knowledge of all components of the system, together with the potential to causally manipulate individual elements, an enviable scenario from the perspective of experimental neuroscientists. As such, we encourage AI researchers to use approaches from neuroscience to explore properties of network architectures and agents through analysis, visualization, causal manipulation, not forgetting the need for carefully designed hypothesis-driven experiments (Jonas and Kording, 2017; Krakauer et al., 2017). We think that virtual brain analytics is likely to be an increasingly integral part of the pipeline of algorithmic development as the complexity of architectures increases.

From AI to Neuroscience

Thus far, our review has focused primarily on the role of neuroscience in accelerating AI research rather than vice versa. Historically, however, the flow of information between neuroscience and AI has been reciprocal. Machine learning techniques have transformed the analysis of neuroimaging datasets—for example, in the multivariate analysis of fMRI and magnetoencephalographic (MEG) data (Cichy et al., 2014; Çukur et al., 2013; Kriegeskorte and Kievit, 2013)—with promise for expediting connectomic analysis (Glasser et al., 2016), among other techniques. Going further, we believe that building intelligent algorithms has the potential to offer new ideas about the underpinnings of intelligence in the brains of humans and other animals. In particular, psychologists and neuroscientists often have only quite vague notions of the mechanisms that underlie the concepts they study. AI research can help, by formalizing these concepts in a quantitative language and offering insights into their necessity and sufficiency (or otherwise) for intelligent behavior.

A key illustration of this potential is provided by RL. After ideas from animal psychology helped to give birth to reinforcement learning research, key concepts from the latter fed back to inform neuroscience. In particular, the profile of neural signals observed in midbrain dopaminergic neurons in conditioning paradigms was found to bear a striking resemblance to TD-generated prediction errors, providing neural evidence that the brain implements a form of TD learning (O’Doherty et al., 2003; Schultz et al., 1997). This overall narrative arc provides an excellent illustration of how the exchange of ideas between AI and neuroscience can create a “virtuous circle” advancing the objectives of both fields.

In another domain, work focused on enhancing the performance of CNNs has also yielded new insights into the nature of neural representations in high-level visual areas (Khaligh-Razavi and Kriegeskorte, 2014; Yamins and DiCarlo, 2016). For

example, one group systematically compared the ability of more than 30 network architectures from AI to explain the structure of neural representations observed in the ventral visual stream of humans and monkeys, finding favorable evidence for deep supervised networks (Khaligh-Razavi and Kriegeskorte, 2014). Further, these deep convolutional network architectures offer a computational account of recent neurophysiological data demonstrating that the coding of category-orthogonal properties of objects (e.g., position, size) actually increases as one progresses higher up the ventral visual stream (Hong et al., 2016). While these findings are far from definitive as yet, it shows how state-of-the-art neural networks from AI can be used as plausible simulacra of biological brains, potentially providing detailed explanations of the computations occurring therein (Khaligh-Razavi and Kriegeskorte, 2014; Yamins and DiCarlo, 2016). Relatedly, properties of the LSTM architecture have provided key insights that motivated the development of working memory models that afford gating-based maintenance of task-relevant information in the prefrontal cortex (Lloyd et al., 2012; O'Reilly and Frank, 2006).

We also highlight two recent strands of AI research that may motivate new research in neuroscience. First, neural networks with external memory typically allow the controller to iteratively query or “hop through” the contents of memory. This mechanism is critical for reasoning over multiple supporting input statements that relate to a particular query (Sukhbaatar et al., 2015). Previous proposals in neuroscience have argued for a similar mechanism in human cognition, but any potential neural substrates, potentially in the hippocampus, remain to be described (Kumaran and McClelland, 2012). Second, recent work highlights the potential benefits of “meta-reinforcement learning,” where RL is used to optimize the weights of a recurrent network such that the latter is able to implement a second, emergent RL algorithm that is able to learn faster than the original (Duan et al., 2016; Wang et al., 2016). Intriguingly, these ideas connect with a growing neuroscience literature indicating a role for the prefrontal cortex in RL, alongside more established dopamine-based mechanisms (Schultz et al., 1997). Specifically, they indicate how a relatively slow-learning dopaminergic RL algorithm may support the emergence of a freestanding RL algorithm instantiated with the recurrent activity dynamics of the prefrontal cortex (Tsutsui et al., 2016).

Insights from AI research are also providing novel perspectives on how the brain might implement an algorithmic parallel to backpropagation, the key mechanism that allows weights within multiple layers of a hierarchical network to be optimized toward an objective function (Hinton et al., 1986; Werbos, 1974). Backpropagation offers a powerful solution to the problem of credit assignment within deep networks, allowing efficient representations to be learned from high dimensional data (LeCun et al., 2015). However, until recently, several aspects of the backpropagation algorithm were viewed to be biologically implausible (e.g., see Bengio et al., 2015). One important factor is that backpropagation has typically been thought to require perfectly symmetric feedback and feedforward connectivity, a profile that is not observed in mammalian brains. Recent work, however, has demonstrated that this constraint can in fact be relaxed (Liao et al., 2015; Lillicrap et al., 2016). Random backward con-

nections, even when held fixed throughout network training, are sufficient to allow the backpropagation algorithm to function effectively through a process whereby adjustment of the forward weights allows backward projections to transmit useful teaching signals (Lillicrap et al., 2016).

A second core objection to the biological plausibility of backpropagation is that weight updates in multi-layered networks require access to information that is non-local (i.e., error signals generated by units many layers downstream) (for review, see Bengio et al., 2015). In contrast, plasticity in biological synapses depends primarily on local information (i.e., pre- and post-synaptic neuronal activity) (Bi and Poo, 1998). AI research has begun to address this fundamental issue. In particular, recent work has shown that hierarchical auto-encoder networks and energy-based networks (e.g., continuous Hopfield networks) (Scellier and Bengio, 2016; Whittington and Bogacz, 2017)—models that have strong connections to theoretical neuroscience ideas about predictive coding (Bastos et al., 2012)—are capable of approximating the backpropagation algorithm, based on weight updates that involve purely local information. Indeed, concrete connections have been drawn between learning in such networks and spike-timing dependent plasticity (Scellier and Bengio, 2016), a Hebbian mechanism instantiated widely across the brain (Bi and Poo, 1998). A different class of local learning rule has been shown to allow hierarchical supervised networks to generate high-level invariances characteristic of biological systems, including mirror-symmetric tuning to physically symmetric stimuli, such as faces (Leibo et al., 2017). Taken together, recent AI research offers the promise of discovering mechanisms by which the brain may implement algorithms with the functionality of backpropagation. Moreover, these developments illustrate the potential for synergistic interactions between AI and neuroscience: research aimed to develop biologically plausible forms of backpropagation have also been motivated by the search for alternative learning algorithms. Given the increasingly deep networks (e.g., >20 layer) used in AI research, factors such as the compounding of successive non-linearities pose challenges for optimization using backpropagation (Bengio et al., 2015).

Conclusions

In this perspective, we have reviewed some of the many ways in which neuroscience has made fundamental contributions to advancing AI research, and argued for its increasingly important relevance. In strategizing for the future exchange between the two fields, it is important to appreciate that the past contributions of neuroscience to AI have rarely involved a simple transfer of full-fledged solutions that could be directly re-implemented in machines. Rather, neuroscience has typically been useful in a subtler way, stimulating algorithmic-level questions about facets of animal learning and intelligence of interest to AI researchers and providing initial leads toward relevant mechanisms. As such, our view is that leveraging insights gained from neuroscience research will expedite progress in AI research, and this will be most effective if AI researchers actively initiate collaborations with neuroscientists to highlight key questions that could be addressed by empirical work.

The successful transfer of insights gained from neuroscience to the development of AI algorithms is critically dependent on the interaction between researchers working in both these fields, with insights often developing through a continual handing back and forth of ideas between fields. In the future, we hope that greater collaboration between researchers in neuroscience and AI, and the identification of a common language between the two fields (Marblestone et al., 2016), will permit a virtuous circle whereby research is accelerated through shared theoretical insights and common empirical advances. We believe that the quest to develop AI will ultimately also lead to a better understanding of our own minds and thought processes. Distilling intelligence into an algorithmic construct and comparing it to the human brain might yield insights into some of the deepest and the most enduring mysteries of the mind, such as the nature of creativity, dreams, and perhaps one day, even consciousness.

ACKNOWLEDGMENTS

We thank Peter Battaglia, Koray Kavukcuoglu, Neil Rabinowitz, Adam Santoro, Greg Wayne, Daan Wierstra, Jane Wang, Martin Chadwick, Joel Leibo, and David Barrett for useful discussions and comments.

REFERENCES

- Adolph, K. (2005). Learning to learn in the development of action. In *Action as an organizer of perception and cognition during learning and development*, J. Lockman, J. Reiser, and C.A. Nelson, eds. (Erlbaum Press), pp. 91–122.
- Anderson, J.R., Bothell, D., Byrne, M.D., Douglass, S., Lebiere, C., and Qin, Y. (2004). An integrated theory of the mind. *Psychol. Rev.* *111*, 1036–1060.
- Ba, J.L., Mnih, V., and Kavukcuoglu, K. (2015). Multiple object recognition with visual attention. *arXiv*, arXiv:14127755.
- Baddeley, A. (2012). Working memory: theories, models, and controversies. *Annu. Rev. Psychol.* *63*, 1–29.
- Bahdanau, D., Cho, K., and Bengio, Y. (2014). Neural machine translation by jointly learning to align and translate. *arXiv*, arXiv:14090473.
- Balaguer, J., Spiers, H., Hassabis, D., and Summerfield, C. (2016). Neural Mechanisms of Hierarchical Planning in a Virtual Subway Network. *Neuron* *90*, 893–903.
- Barlow, H. (1959). Sensory mechanisms, the reduction of redundancy, and intelligence. In *The Mechanisation of Thought Processes* (National Physical Laboratory, UK: H.M. Stationery Office), pp. 535–539.
- Barnett, S.M., and Ceci, S.J. (2002). When and where do we apply what we learn? A taxonomy for far transfer. *Psychol. Bull.* *128*, 612–637.
- Bastos, A.M., Usrey, W.M., Adams, R.A., Mangun, G.R., Fries, P., and Friston, K.J. (2012). Canonical microcircuits for predictive coding. *Neuron* *76*, 695–711.
- Battaglia, P.W., Hamrick, J.B., and Tenenbaum, J.B. (2013). Simulation as an engine of physical scene understanding. *Proc. Natl. Acad. Sci. USA* *110*, 18327–18332.
- Battaglia, P., Pascanu, R., Lai, M., Rezende, D., and Kavukcuoglu, K. (2016). Interaction networks for learning about objects, relations and physics. *arXiv*, arXiv:161200222.
- Bengio, Y., Lee, D.H., Bornschein, J., Mesnard, T., and Lin, Z. (2015). Towards biologically plausible deep learning. *arXiv*, arXiv:150204156.
- Bi, G.Q., and Poo, M.M. (1998). Synaptic modifications in cultured hippocampal neurons: dependence on spike timing, synaptic strength, and postsynaptic cell type. *J. Neurosci.* *18*, 10464–10472.
- Blundell, C., Uria, B., Pritzel, A., Yazhe, L., Ruderman, A., Leibo, J.Z., Rae, J., Wierstra, D., and Hassabis, D. (2016). Model-free episodic control. *arXiv*, arXiv:160604460.
- Botvinick, M.M., and Plaut, D.C. (2006). Short-term memory for serial order: a recurrent neural network model. *Psychol. Rev.* *113*, 201–233.
- Brooks, R., Hassabis, D., Bray, D., and Shashua, A. (2012). Turing centenary: is the brain a good model for machine intelligence? *Nature* *482*, 462–463.
- Browne, C., Powley, E., Whitehouse, D., Lucas, S.M., Cowling, P.I., Rohlfshagen, P., Tavener, S., Perez, D., Samothrakis, S., and Colton, S. (2012). A survey of Monte-Carlo tree search methods. *IEEE Trans. Comput. Intell. AI Games* *4*, 1–43.
- Chang, M.B., Ullman, T., Torralba, A., and Tenenbaum, J.B. (2016). A compositional object-based approach to learning physical dynamics. *arXiv*, arXiv:161200341.
- Chiappa, S., Racaniere, S., Wierstra, D., and Mohamed, S. (2017). Recurrent environment simulators. *Proceedings of the 32nd International Conference on Machine Learning*, pp. 1–61.
- Churchland, P.S., and Sejnowski, T.J. (1988). Perspectives on cognitive neuroscience. *Science* *242*, 741–745.
- Cichon, J., and Gan, W.B. (2015). Branch-specific dendritic Ca(2+) spikes cause persistent synaptic plasticity. *Nature* *520*, 180–185.
- Cichy, R.M., Pantazis, D., and Oliva, A. (2014). Resolving human object recognition in space and time. *Nat. Neurosci.* *17*, 455–462.
- Collins, A., and Koechlin, E. (2012). Reasoning, learning, and creativity: frontal lobe function and human decision-making. *PLoS Biol.* *10*, e1001293.
- Constantinescu, A.O., O'Reilly, J.X., and Behrens, T.E. (2016). Organizing conceptual knowledge in humans with a gridlike code. *Science* *352*, 1464–1468.
- Craik, K. (1943). *The Nature of Explanation* (Cambridge University Press).
- Çukur, T., Nishimoto, S., Huth, A.G., and Gallant, J.L. (2013). Attention during natural vision warps semantic representation across the human brain. *Nat. Neurosci.* *16*, 763–770.
- Daw, N.D., Niv, Y., and Dayan, P. (2005). Uncertainty-based competition between prefrontal and dorsolateral striatal systems for behavioral control. *Nat. Neurosci.* *8*, 1704–1711.
- Deisseroth, K., and Schnitzer, M.J. (2013). Engineering approaches to illuminating brain structure and dynamics. *Neuron* *80*, 568–577.
- Deng, J., Dong, W., Socher, R., Li, L.J., Li, K., and Fei-Fei, L. (2009). Imagenet: a large-scale hierarchical image database. In *Computer Vision and Pattern Recognition*, pp. 1–8.
- Denil, M., Agrawal, P., Kulkarni, T.D., Erez, T., Battaglia, P., and de Freitas, N. (2016). Learning to perform physics experiments via deep reinforcement learning. *arXiv*, arXiv:161101843.
- Dolan, R.J., and Dayan, P. (2013). Goals and habits in the brain. *Neuron* *80*, 312–325.
- Doll, B.B., Duncan, K.D., Simon, D.A., Shohamy, D., and Daw, N.D. (2015). Model-based choices involve prospective neural activity. *Nat. Neurosci.* *18*, 767–772.
- Donoso, M., Collins, A.G., and Koechlin, E. (2014). Human cognition. Foundations of human reasoning in the prefrontal cortex. *Science* *344*, 1481–1486.
- Dumas, L.A., Hummel, J.E., and Sandhofer, C.M. (2008). A theory of the discovery and predication of relational concepts. *Psychol. Rev.* *115*, 1–43.
- Duan, Y., Schulman, J., Chen, X., Bartlett, P.L., Sutskever, I., and Abbeel, P. (2016). RL²: fast reinforcement learning via slow reinforcement learning. *arXiv*, arXiv:1611.02779.
- Durstewitz, D., Seamans, J.K., and Sejnowski, T.J. (2000). Neurocomputational models of working memory. *Nat. Neurosci.* *3* (Suppl.), 1184–1191.
- Elman, J.L. (1990). Finding structure in time. *Cogn. Sci.* *14*, 179–211.

- Eslami, A., Heess, N., Weber, T.Y.T., Szepesvari, D., Kavukcuoglu, K., and Hinton, G. (2016). Attend, infer, repeat: fast scene understanding with generative models. arXiv, arXiv:160308575.
- Esser, S.K., Merolla, P.A., Arthur, J.V., Cassidy, A.S., Appuswamy, R., Andreopoulos, A., Berg, D.J., McKinstry, J.L., Melano, T., Barch, D.R., et al. (2016). Convolutional networks for fast, energy-efficient neuromorphic computing. *Proc. Natl. Acad. Sci. USA* *113*, 11441–11446.
- Fodor, J.A., and Pylyshyn, Z.W. (1988). Connectionism and cognitive architecture: a critical analysis. *Cognition* *28*, 3–71.
- French, R.M. (1999). Catastrophic forgetting in connectionist networks. *Trends Cogn. Sci.* *3*, 128–135.
- Fukushima, K. (1980). Neocognitron: a self organizing neural network model for a mechanism of pattern recognition unaffected by shift in position. *Biol. Cybern.* *36*, 193–202.
- Fusi, S., Drew, P.J., and Abbott, L.F. (2005). Cascade models of synaptically stored memories. *Neuron* *45*, 599–611.
- Gallistel, C., and King, A.P. (2009). *Memory and the Computational Brain: Why Cognitive Science will Transform Neuroscience* (Wiley-Blackwell).
- Gatys, L.A., Ecker, A.S., and Bethge, M. (2015). A neural algorithm of artistic style. arXiv, arXiv:1508.06576.
- Gemici, M., Hung, C., Santoro, A., Wayne, G., Mohamed, S., Rezende, D., Amos, D., and Lillicrap, T. (2017). Generative temporal models with memory. arXiv, arXiv:170204649.
- Gershman, S.J., and Daw, N.D. (2017). Reinforcement learning and episodic memory in humans and animals: an integrative framework. *Annu. Rev. Psychol.* *68*, 101–128.
- Gilmore, C.K., McCarthy, S.E., and Spelke, E.S. (2007). Symbolic arithmetic knowledge without instruction. *Nature* *447*, 589–591.
- Glasser, M.F., Smith, S.M., Marcus, D.S., Andersson, J.L., Auerbach, E.J., Behrens, T.E., Coalson, T.S., Harms, M.P., Jenkinson, M., Moeller, S., et al. (2016). The Human Connectome Project's neuroimaging approach. *Nat. Neurosci.* *19*, 1175–1187.
- Goldman-Rakic, P.S. (1990). Cellular and circuit basis of working memory in prefrontal cortex of nonhuman primates. *Prog. Brain Res.* *85*, 325–335.
- Gopnik, A., and Schulz, L. (2004). Mechanisms of theory formation in young children. *Trends Cogn. Sci.* *8*, 371–377.
- Graves, A., Wayne, G., and Danihelka, I. (2014). Neural Turing machines. arXiv, arXiv:1410.5401.
- Graves, A., Wayne, G., Reynolds, M., Harley, T., Danihelka, I., Grabska-Barwińska, A., Colmenarejo, S.G., Grefenstette, E., Ramalho, T., Agapiou, J., et al. (2016). Hybrid computing using a neural network with dynamic external memory. *Nature* *538*, 471–476.
- Gregor, K., Danihelka, I., Graves, A., Renzende, D., and Wierstra, D. (2015). DRAW: a recurrent neural network for image generation. arXiv, arXiv:150204623.
- Hafner, R., and Riedmiller, M. (2011). Reinforcement learning in feedback control. *Mach. Learn.* *84*, 137–169.
- Hamrick, J.B., Ballard, A.J., Pascanu, R., Vinyals, O., Heess, N., and Battaglia, P.W. (2017). Metacontrol for adaptive imagination-based optimization. *Proceedings of the 5th International Conference on Learning Representations (ICLR 2017)*, pp. 1–21.
- Harlow, H.F. (1949). The formation of learning sets. *Psychol. Rev.* *56*, 51–65.
- Hassabis, D., and Maguire, E.A. (2007). Deconstructing episodic memory with construction. *Trends Cogn. Sci.* *11*, 299–306.
- Hassabis, D., and Maguire, E.A. (2009). The construction system of the brain. *Philos. Trans. R. Soc. Lond. B Biol. Sci.* *364*, 1263–1271.
- Haugeland, J. (1985). *Artificial Intelligence: The Very Idea* (MIT Press).
- Hayashi-Takagi, A., Yagishita, S., Nakamura, M., Shirai, F., Wu, Y.I., Loshbaugh, A.L., Kuhlman, B., Hahn, K.M., and Kasai, H. (2015). Labelling and optical erasure of synaptic memory traces in the motor cortex. *Nature* *525*, 333–338.
- Hebb, D.O. (1949). *The Organization of Behavior* (John Wiley & Sons).
- Higgins, I., Matthey, L., Glorot, X., Pal, A., Uria, B., Blundell, C., Mohamed, S., and Lerchner, A. (2016). Early visual concept learning with unsupervised deep learning. arXiv, arXiv:160605579.
- Hinton, G.E., McClelland, J.L., and Rumelhart, D.E. (1986). Distributed Representations. In *Explorations in the Microstructure of Cognition* (MIT Press), pp. 77–109.
- Hinton, G.E., Osindero, S., and Teh, Y.W. (2006). A fast learning algorithm for deep belief nets. *Neural Comput.* *18*, 1527–1554.
- Hinton, G.E., Srivastava, N., Krizhevsky, A., Sutskever, I., and Salakhutdinov, R.R. (2012). Improving neural networks by preventing co-adaptation of feature detectors. arXiv, arXiv:12070580.
- Hochreiter, S., and Schmidhuber, J. (1997). Long short-term memory. *Neural Comput.* *9*, 1735–1780.
- Holyoak, K.J., and Thagard, P. (1997). The analogical mind. *Am. Psychol.* *52*, 35–44.
- Hong, S., Oh, J., Bohyung, H., and Lee, H. (2015). Learning transferrable knowledge for semantic segmentation with deep convolutional neural network. arXiv, arXiv:151207928.
- Hong, H., Yamins, D.L., Majaj, N.J., and DiCarlo, J.J. (2016). Explicit information for category-orthogonal object properties increases along the ventral stream. *Nat. Neurosci.* *19*, 613–622.
- Hopfield, J.J. (1982). Neural networks and physical systems with emergent collective computational abilities. *Proc. Natl. Acad. Sci. USA* *79*, 2554–2558.
- Hopfield, J.J., and Tank, D.W. (1986). Computing with neural circuits: a model. *Science* *233*, 625–633.
- Hubel, D.H., and Wiesel, T.N. (1959). Receptive fields of single neurones in the cat's striate cortex. *J. Physiol.* *148*, 574–591.
- Huys, Q.J., Eshel, N., O'Nions, E., Sheridan, L., Dayan, P., and Roiser, J.P. (2012). Bonsai trees in your head: how the pavlovian system sculpts goal-directed choices by pruning decision trees. *PLoS Comput. Biol.* *8*, e1002410.
- Johnson, A., and Redish, A.D. (2007). Neural ensembles in CA3 transiently encode paths forward of the animal at a decision point. *J. Neurosci.* *27*, 12176–12189.
- Jonas, E., and Kording, K.P. (2017). Could a neuroscientist understand a microprocessor? *PLoS Comput. Biol.* *13*, e1005268.
- Jordan, M.I. (1997). Serial order: a parallel distributed processing approach. *Adv. Psychol.* *121*, 471–495.
- Kemp, C., Goodman, N.D., and Tenenbaum, J.B. (2010). Learning to learn causal models. *Cogn. Sci.* *34*, 1185–1243.
- Khaligh-Razavi, S.M., and Kriegeskorte, N. (2014). Deep supervised, but not unsupervised, models may explain IT cortical representation. *PLoS Comput. Biol.* *10*, e1003915.
- Kirkpatrick, J., Pascanu, R., Rabinowitz, N., Veness, J., Desjardins, G., Rusu, A.A., Milan, K., Quan, J., Ramalho, T., Grabska-Barwińska, A., et al. (2017). Overcoming catastrophic forgetting in neural networks. *Proc. Natl. Acad. Sci. USA* *114*, 3521–3526.
- Koch, C., and Ullman, S. (1985). Shifts in selective visual attention: towards the underlying neural circuitry. *Hum. Neurobiol.* *4*, 219–227.
- Krakauer, J.W., Ghazanfar, A.A., Gomez-Marín, A., MacIver, M.A., and Poeppel, D. (2017). Neuroscience needs behavior: correcting a reductionist bias. *Neuron* *93*, 480–490.
- Kriegeskorte, N., and Kievit, R.A. (2013). Representational geometry: integrating cognition, computation, and the brain. *Trends Cogn. Sci.* *17*, 401–412.
- Krizhevsky, A., Sutskever, I., and Hinton, G. (2012). ImageNet classification with deep convolutional neural networks. In *Advances in Neural Information Processing Systems* *25*, pp. 1097–1105.

- Kumaran, D., and McClelland, J.L. (2012). Generalization through the recurrent interaction of episodic memories: a model of the hippocampal system. *Psychol. Rev.* *119*, 573–616.
- Kumaran, D., Hassabis, D., and McClelland, J.L. (2016). What learning systems do intelligent agents need? Complementary learning systems theory updated. *Trends Cogn. Sci.* *20*, 512–534.
- Kurth-Nelson, Z., Economides, M., Dolan, R.J., and Dayan, P. (2016). Fast sequences of non-spatial state representations in humans. *Neuron* *91*, 194–204.
- Lake, B.M., Salakhutdinov, R., and Tenenbaum, J.B. (2015). Human-level concept learning through probabilistic program induction. *Science* *350*, 1332–1338.
- Lake, B.M., Ullman, T.D., Tenenbaum, J.B., and Gershman, S.J. (2016). Building machines that learn and think like people. *arXiv*, arXiv:1604.00289.
- Larochelle, H., and Hinton, G. (2010). Learning to combine foveal glimpses with a third-order Boltzmann machine. *NIPS'10 Proceedings of the International Conference on Neural Information Processing Systems*, pp. 1243–1251.
- LeCun, Y., Boser, B., Denker, J.S., Henderson, D., Howard, R.E., Hubbard, W., and Jackel, L.D. (1989). Backpropagation applied to handwritten zip code recognition. *Neural Comput.* *1*, 541–551.
- LeCun, Y., Bengio, Y., and Hinton, G. (2015). Deep learning. *Nature* *521*, 436–444.
- Leibo, J.Z., Liao, Q., Anselmi, F., Freiwald, W.A., and Poggio, T. (2017). View-tolerant face recognition and Hebbian Learning imply mirror-symmetric neural tuning to head orientation. *Curr. Biol.* *27*, 62–67.
- Legg, S., and Hutter, M. (2007). A collection of definitions of intelligence. In *Advances in Artificial General Intelligence: Concepts, Architectures and Algorithms—Proceedings of the AGI Workshop*, B. Goertzel and P. Wang, eds. (Amsterdam IOS), pp. 17–24.
- Lengyel, M., and Dayan, P. (2007). Hippocampal contributions to control: the third way. In *Advances in Neural Information Processing Systems* *20*, pp. 889–896.
- Liao, Q., Leibo, J.Z., and Poggio, T. (2015). How important is weight symmetry in backpropagation? *arXiv*, arXiv:151005067.
- Lillicrap, T.P., Cownden, D., Tweed, D.B., and Akerman, C.J. (2016). Random synaptic feedback weights support error backpropagation for deep learning. *Nat. Commun.* *7*, 13276.
- Lloyd, K., Becker, N., Jones, M.W., and Bogacz, R. (2012). Learning to use working memory: a reinforcement learning gating model of rule acquisition in rats. *Front. Comput. Neurosci.* *6*, 87.
- Marblestone, A.H., Wayne, G., and Kording, K.P. (2016). Toward an integration of deep learning and neuroscience. *Front. Comput. Neurosci.* *10*, 94.
- Marcus, G.F. (1998). Rethinking eliminative connectionism. *Cognit. Psychol.* *37*, 243–282.
- Markram, H. (2006). The blue brain project. *Nat. Rev. Neurosci.* *7*, 153–160.
- Marr, D., and Poggio, T. (1976). From understanding computation to understanding neural circuitry. *A.I. Memo* *357*, 1–22.
- McClelland, J.L., and Rogers, T.T. (2003). The parallel distributed processing approach to semantic cognition. *Nat. Rev. Neurosci.* *4*, 310–322.
- McClelland, J.L., McNaughton, B.L., and O'Reilly, R.C. (1995). Why there are complementary learning systems in the hippocampus and neocortex: insights from the successes and failures of connectionist models of learning and memory. *Psychol. Rev.* *102*, 419–457.
- McCulloch, W., and Pitts, W. (1943). A logical calculus of ideas immanent in nervous activity. *Bull. Math. Biophys.* *5*, 115–133.
- Mnih, V., Heess, N., Graves, A., and Kavukcuoglu, K. (2014). Recurrent models of visual attention. *arXiv*, arXiv:14066247.
- Mnih, V., Kavukcuoglu, K., Silver, D., Rusu, A.A., Veness, J., Bellemare, M.G., Graves, A., Riedmiller, M., Fidjeland, A.K., Ostrovski, G., et al. (2015). Human-level control through deep reinforcement learning. *Nature* *518*, 529–533.
- Moore, T., and Zirnsak, M. (2017). Neural mechanisms of selective visual attention. *Annu. Rev. Psychol.* *68*, 47–72.
- Moravčík, M., Schmid, M., Burch, N., Lisý, V., Morrill, D., Bard, N., Davis, T., Vaughn, K., Johanson, M., and Bowling, M. (2017). DeepStack: expert-level artificial intelligence in heads-up no-limit poker. *Science* *356*, 508–513.
- Nguyen, A., Dosovitskiy, A., Yosinski, J., Borx, T., and Clune, J. (2016). Synthesizing the preferred inputs for neurons in neural networks via deep generator networks. *arXiv*, arXiv:160509304.
- Nishiyama, J., and Yasuda, R. (2015). Biochemical computation for spine structural plasticity. *Neuron* *87*, 63–75.
- O'Doherty, J.P., Dayan, P., Friston, K., Critchley, H., and Dolan, R.J. (2003). Temporal difference models and reward-related learning in the human brain. *Neuron* *38*, 329–337.
- O'Neill, J., Pleydell-Bouverie, B., Dupret, D., and Csicsvari, J. (2010). Play it again: reactivation of waking experience and memory. *Trends Neurosci.* *33*, 220–229.
- O'Reilly, R.C., and Frank, M.J. (2006). Making working memory work: a computational model of learning in the prefrontal cortex and basal ganglia. *Neural Comput.* *18*, 283–328.
- Oh, J., Guo, X., Lee, H., Lewis, R., and Singh, S. (2015). Action-conditional video prediction using deep networks in Atari games. *arXiv*, arXiv:150708750.
- Ólafsdóttir, H.F., Barry, C., Saleem, A.B., Hassabis, D., and Spiers, H.J. (2015). Hippocampal place cells construct reward related sequences through unexplored space. *eLife* *4*, e06063.
- Olshausen, B.A., Anderson, C.H., and Van Essen, D.C. (1993). A neurobiological model of visual attention and invariant pattern recognition based on dynamic routing of information. *J. Neurosci.* *13*, 4700–4719.
- Pfeiffer, B.E., and Foster, D.J. (2013). Hippocampal place-cell sequences depict future paths to remembered goals. *Nature* *497*, 74–79.
- Posner, M.I., and Petersen, S.E. (1990). The attention system of the human brain. *Annu. Rev. Neurosci.* *13*, 25–42.
- Raby, C.R., Alexis, D.M., Dickinson, A., and Clayton, N.S. (2007). Planning for the future by western scrub-jays. *Nature* *445*, 919–921.
- Redish, A.D. (2016). Vicarious trial and error. *Nat. Rev. Neurosci.* *17*, 147–159.
- Reed, S., Zhang, Y., Zhang, Y., and Lee, S. (2015). Deep visual analogy-making. In *NIPS'15 Proceedings of the 28th International Conference on Neural Information Processing Systems*, pp. 1252–1260.
- Reed, S., Akata, Z., Mohan, S., Tenka, S., Schiele, B., and Lee, H. (2016). Learning what and where to draw. *arXiv*, arXiv:161002454.
- Rezende, D., Eslami, A., Mohamed, S., Battaglia, P., Jaderberg, M., and Heess, N. (2016a). Unsupervised learning of 3D structure from images. *arXiv*, arXiv:160700662.
- Rezende, D., Mohamed, S., Danihelka, I., Gregor, K., and Wierstra, D. (2016b). One-shot generalization in deep generative models. *arXiv*, arXiv:160305106.
- Riesenhuber, M., and Poggio, T. (1999). Hierarchical models of object recognition in cortex. *Nat. Neurosci.* *2*, 1019–1025.
- Rosenblatt, F. (1958). The perceptron: a probabilistic model for information storage and organization in the brain. *Psychol. Rev.* *65*, 386–408.
- Rowland, D.C., Roudi, Y., Moser, M.B., and Moser, E.I. (2016). Ten years of grid cells. *Annu. Rev. Neurosci.* *39*, 19–40.
- Rumelhart, D.E., Hinton, G., and Williams, R.J. (1985). Learning internal representations by error propagation. In *Parallel Distributed Processing: Explorations in the Microstructure of Cognition, Volume 1* (MIT Press), pp. 318–362.
- Rumelhart, D.E., McClelland, J.L., and Group, P.R. (1986). *Parallel Distributed Processing: Explorations in the Microstructures of Cognition, Volume 1* (MIT Press).
- Rusu, A.A., Rabinowitz, N., Desjardins, G., Soyer, H., Kirkpatrick, J., Kavukcuoglu, K., Pascanu, R., and Hadsell, R. (2016a). Progressive neural networks. *arXiv*, arXiv:160604671.

- Rusu, A.A., Vecerik, M., Rothorl, T., Heess, N., Pascanu, R., and Hadsell, R. (2016b). Sim-to-real robot learning from pixels with progressive nets. arXiv:161004286.
- Salinas, E., and Abbott, L.F. (1997). Invariant visual responses from attentional gain fields. *J. Neurophysiol.* 77, 3267–3272.
- Santoro, A., Bartunov, S., Botvinick, M., Wierstra, D., and Lillicrap, T. (2016). One-shot Learning with Memory-Augmented Neural Networks. arXiv:160506065.
- Santoro, A., Raposo, D., Barrett, D.G.T., Malinowski, M., Pascanu, R., Battaglia, P., and Lillicrap, T. (2017). A simple neural network module for relational reasoning. arXiv, arXiv:1706.01427, <https://arxiv.org/abs/1706.01427>.
- Saxe, A.M., Ganguli, S., and McClelland, J.L. (2013). Exact solutions to the nonlinear dynamics of learning in deep linear neural networks. arXiv:13126120v3.
- Scellier, B., and Bengio, Y. (2016). Equilibrium propagation: bridging the gap between energy-based models and backpropagation. arXiv, arXiv:160205179.
- Schacter, D.L., Addis, D.R., Hassabis, D., Martin, V.C., Spreng, R.N., and Szpunar, K.K. (2012). The future of memory: remembering, imagining, and the brain. *Neuron* 76, 677–694.
- Schaul, T., Quan, J., Antonoglou, I., and Silver, D. (2015). Prioritized experience replay. bioRxiv, arXiv:1511.05952.
- Schmidhuber, J. (2014). Deep learning in neural networks: an overview. arXiv, 14047828.
- Schultz, W., Dayan, P., and Montague, P.R. (1997). A neural substrate of prediction and reward. *Science* 275, 1593–1599.
- Serre, T., Wolf, L., Bileschi, S., Riesenhuber, M., and Poggio, T. (2007). Robust object recognition with cortex-like mechanisms. *IEEE Trans. Pattern Anal. Mach. Intell.* 29, 411–426.
- Shallice, T. (1988). *From Neuropsychology to Mental Structure* (Cambridge University Press).
- Silver, D., Huang, A., Maddison, C.J., Guez, A., Sifre, L., van den Driessche, G., Schrittwieser, J., Antonoglou, I., Panneershelvam, V., Lanctot, M., et al. (2016). Mastering the game of Go with deep neural networks and tree search. *Nature* 529, 484–489.
- Simonyan, K., Vedaldi, A., and Zisserman, A. (2013). Deep inside convolutional networks: visualising image classification models and saliency maps. arXiv:13126034.
- Singer, A.C., and Frank, L.M. (2009). Rewarded outcomes enhance reactivation of experience in the hippocampus. *Neuron* 64, 910–921.
- Skaggs, W.E., and McNaughton, B.L. (1996). Replay of neuronal firing sequences in rat hippocampus during sleep following spatial experience. *Science* 271, 1870–1873.
- Smith, L.B. (1995). Self-organizing processes in learning to learn words: development is not induction. In *Basic and Applied Perspectives on Learning, Cognition, and Development. The Minnesota Symposia on Child Psychology* (Lawrence Erlbaum Associates), pp. 1–32.
- Solway, A., Diuk, C., Córdova, N., Yee, D., Barto, A.G., Niv, Y., and Botvinick, M.M. (2014). Optimal behavioral hierarchy. *PLoS Comput. Biol.* 10, e1003779.
- Spelke, E.S., and Kinzler, K.D. (2007). Core knowledge. *Dev. Sci.* 10, 89–96.
- Squire, L.R., Stark, C.E., and Clark, R.E. (2004). The medial temporal lobe. *Annu. Rev. Neurosci.* 27, 279–306.
- St. John, M.F., and McClelland, J.L. (1990). Learning and applying contextual constraints in sentence comprehension. *Artif. Intell.* 46, 217–257.
- Stachenfeld, K., Botvinick, M.M., and Gershman, S.J. (2014). Design principles of hippocampal cognitive maps. In *Advances in Neural Information Processing Systems* 27, pp. 2528–2536.
- Sukhbaatar, S., Szlam, A., Weston, J., and Fergus, R. (2015). End-to-end memory networks. arXiv, arXiv:150308895.
- Summerfield, J.J., Lepsien, J., Gitelman, D.R., Mesulam, M.M., and Nobre, A.C. (2006). Orienting attention based on long-term memory experience. *Neuron* 49, 905–916.
- Sutton, R.S. (1991). Dyna, an integrated architecture for learning, planning, and reacting. *ACM SIGART Bull.* 2, 160–163.
- Sutton, R.S., and Barto, A.G. (1981). Toward a modern theory of adaptive networks: expectation and prediction. *Psychol. Rev.* 88, 135–170.
- Sutton, R., and Barto, A. (1998). *Reinforcement Learning* (MIT Press).
- Tesauro, G. (1995). Temporal difference learning and TD-Gammon. *Commun. ACM* 38, 58–68.
- Thrun, S., and Mitchell, T.M. (1995). Lifelong robot learning. *Robot. Auton. Syst.* 15, 25–46.
- Tolman, E.C. (1948). Cognitive maps in rats and men. *Psychol. Rev.* 55, 189–208.
- Tsutsui, K., Grabenhorst, F., Kobayashi, S., and Schultz, W. (2016). A dynamic code for economic object valuation in prefrontal cortex neurons. *Nat. Commun.* 7, 12554.
- Tulving, E. (1985). How many memory systems are there? *American Psychologist* 40, 385–398.
- Tulving, E. (2002). Episodic memory: from mind to brain. *Annu. Rev. Psychol.* 53, 1–25.
- Turing, A.M. (1936). On computable numbers, with an application to the Entscheidungs problem. *Proc. Lond. Math. Soc.* 2, 230–265.
- Turing, A. (1950). Computing machinery and intelligence. *Mind* 236, 433–460.
- van den Oord, A., Dieleman, S., Zen, H., Simonyan, K., Vinyals, O., Graves, A., Kalchbrenner, N., Senior, A., and Kavukcuoglu, K. (2016). WaveNet: a generative model for raw audio. arXiv, arXiv:160903499.
- Vinyals, O., Blundell, C., Lillicrap, T., Kavukcuoglu, K., and Wierstra, D. (2016). Matching networks for one shot learning. arXiv, arXiv:160604080.
- Wang, J., Kurth-Nelson, Z., Tirumala, D., Soyer, H., Leibo, J.Z., Munos, R., Blundell, C., Kumaran, D., and Botvinick, M.M. (2016). Learning to reinforcement learn. arXiv, arXiv:161105763.
- Werbos, P.J. (1974). *Beyond Regression: New Tools for Prediction and Analysis in the Behavioral Sciences* (Harvard University).
- Weston, J., Chopra, S., and Bordes, A. (2014). Memory networks. arXiv, arXiv:14103916.
- Whittington, J.C.R., and Bogacz, R. (2017). An approximation of the error backpropagation algorithm in a predictive coding network with local Hebbian synaptic plasticity. *Neural Comput.* 29, 1229–1262.
- Wu, Y., Schuster, M., Chen, Z., Le, Q.V., Norouzi, M., Macherey, W., Krikun, M., Cao, Y., Gao, Q., Macherey, K., et al. (2016). Google's neural machine translation system: bridging the gap between human and machine translation. arXiv, arXiv:160908144.
- Xu, K., Kiros, J., Courville, A., Salakhutdinov, R., and Bengio, Y. (2015). Show, attend and tell: neural image caption generation with visual attention. arXiv:150203044.
- Yamins, D.L., and DiCarlo, J.J. (2016). Using goal-driven deep learning models to understand sensory cortex. *Nat. Neurosci.* 19, 356–365.
- Yang, G., Pan, F., and Gan, W.B. (2009). Stably maintained dendritic spines are associated with lifelong memories. *Nature* 462, 920–924.
- Zahavy, T., Zrihem, N.B., and Mannor, S. (2016). Graying the black box: understanding DQNs. arXiv, arXiv:160202658.
- Zaremba, W., and Sutskever, I. (2014). Learning to execute. arXiv, arXiv:1410.4615.

Cracking the Neural Code for Sensory Perception by Combining Statistics, Intervention, and Behavior

Stefano Panzeri,^{1,2,6,*} Christopher D. Harvey,^{3,*} Eugenio Piasini,¹ Peter E. Latham,⁴ and Tommaso Fellin^{2,5,*}

¹Neural Computation Laboratory

²Neural Coding Laboratory

Istituto Italiano di Tecnologia, 38068 Rovereto, Italy

³Department of Neurobiology, Harvard Medical School, Boston, MA 02115, USA

⁴Gatsby Computational Neuroscience Unit, University College London, London, W1T 4JG, UK

⁵Optical Approaches to Brain Function Laboratory, Istituto Italiano di Tecnologia, 16163 Genoa, Italy

⁶Lead Contact

*Correspondence: stefano.panzeri@iit.it (S.P.), christopher_harvey@hms.harvard.edu (C.D.H.), tommaso.fellin@iit.it (T.F.)

<http://dx.doi.org/10.1016/j.neuron.2016.12.036>

The two basic processes underlying perceptual decisions—how neural responses encode stimuli, and how they inform behavioral choices—have mainly been studied separately. Thus, although many spatiotemporal features of neural population activity, or “neural codes,” have been shown to carry sensory information, it is often unknown whether the brain uses these features for perception. To address this issue, we propose a new framework centered on redefining the neural code as the neural features that carry sensory information used by the animal to drive appropriate behavior; that is, the features that have an intersection between sensory and choice information. We show how this framework leads to a new statistical analysis of neural activity recorded during behavior that can identify such neural codes, and we discuss how to combine intersection-based analysis of neural recordings with intervention on neural activity to determine definitively whether specific neural activity features are involved in a task.

Introduction

To survive, organisms must both accurately represent stimuli in the outside world and use that representation to generate beneficial behavioral actions. Historically, these two processes—the mapping from stimuli to neural responses and the mapping from neural activity to behavior—have mainly been treated separately. Of the two, the former has received the most attention. Often referred to as the “neural coding problem,” its goal is to determine what features of neural activity carry information about external stimuli. This approach has led to many empirical and theoretical proposals about the spatial and temporal features of neural population activity, or “neural codes,” that represent sensory information (Buonomano and Maass, 2009; Harvey et al., 2012, 2013; Kayser et al., 2009; Luczak et al., 2015; Panzeri et al., 2010; Shamir, 2014). However, there is still no consensus about the neural code for most sensory stimuli in most areas of the nervous system.

The lack of consensus arises in part because, while it is established that certain features of neural population responses carry information about specific stimuli, it is unclear whether the brain uses the information in these features to perform sensory perception (Engineer et al., 2008; Jacobs et al., 2009; Luna et al., 2005; Victor and Nirenberg, 2008). In principle, the link between sensory information that is present and sensory information that is read out to inform choices can be probed using the animal’s behavioral report of sensory stimuli. In addition, improvements in techniques to perturb activity of neural populations during behavior (Boyden et al., 2005; Deisseroth and Schnitzer, 2013; Emiliani et al., 2015; Tehovnik et al., 2006) now make it possible to test causally hypotheses about the neural code, by “writing” on the neural tissue putative information

and then measuring the behavior elicited by this manipulation. However, progress in cracking the neural code has been limited by the lack of a conceptual framework that fully integrates the advantages offered by behavioral, neurophysiological, statistical, and interventional techniques.

Here we elaborate such a conceptual framework, which at its core is based on a change in how a neural code should be defined. We propose that a neural code should be defined as the set of neural response features carrying sensory information that, crucially, is used by the animal to drive appropriate behavior; that is, the set of neural response features that have an intersection between sensory and choice information. In the following, we discuss this framework and its implications for designing and interpreting experiments aimed at cracking the neural code, as well as some theoretical and experimental challenges that arise from it.

What It Takes to Crack the Neural Code Underlying a Sensory Percept

To illustrate our new framework, we consider a perceptual discrimination task in which an animal has to extract information present in the sensory environment and, based on that information, choose an appropriate action. For definiteness, we assume (Figure 1A) a two-alternative forced-choice discrimination task: the animal has to extract color information from a visual stimulus (that is decide whether a green [$s = 1$] or a blue [$s = 2$] stimulus was presented) and choose accordingly to move left (choice $c = 1$) or right ($c = 2$), with the correct choice resulting in a reward (we numbered choices so that $c = 1$ is the correct rewarded choice for $s = 1$ and $c = 2$ is the correct choice for $s = 2$). We suppose that an experimenter is recording the activity of a

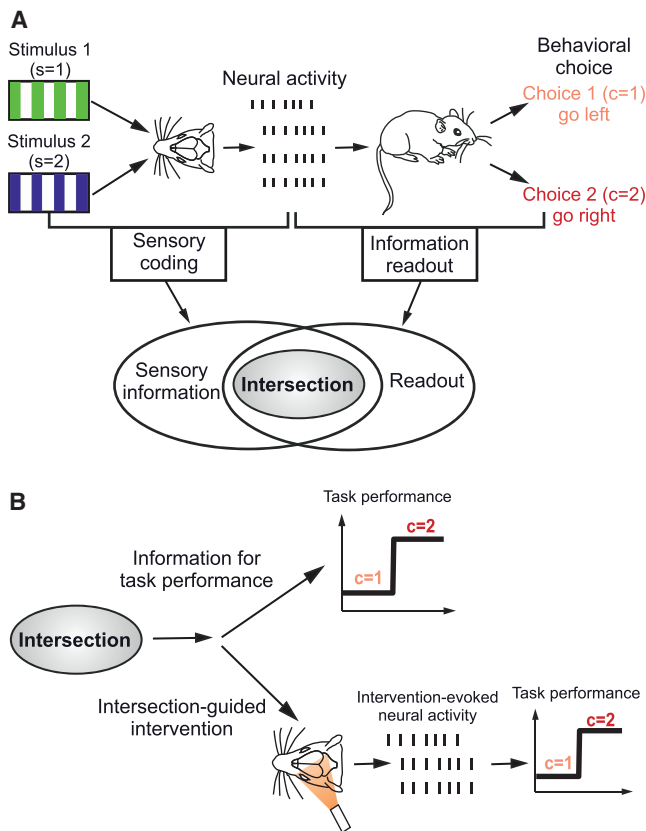


Figure 1. Intersection Information Helps Combining Statistics, Neural Recordings, Behavior, and Intervention to Crack the Neural Code for Sensory Perception

(A) Schematic showing two crucial stages in the information processing chain for sensory perception: sensory coding and information readout. In this example, an animal must discriminate between two stimuli of different color ($s = 1$, green; and $s = 2$, blue) and make an appropriate choice ($c = 1$, pink; and $c = 2$, red). Sensory coding expresses how different stimuli are encoded by different neural activity patterns. Information readout is the process by which information is extracted from single-trial neural population activity to inform behavioral choice. The intersection between sensory coding and information readout is defined as the features of neuronal activity that carry sensory information that is read out to inform a behavioral choice. Note that, as explained in the main text, a neural feature may show both sensory information and choice information but have no intersection information; this is visualized here by plotting the intersection information domain in the space of neural features as smaller than the overlap between the sensory coding and information readout domains.

(B) Only information at the intersection between sensory coding and readout contributes to task performance. Neural population response features that belong to this intersection can be identified by statistical analysis of neural recordings during behavior. Interventional (e.g., optogenetics) manipulations of neural activity informed by statistical analysis of sensory information coding can then be used to causally probe the contribution of neural features to task performance at this intersection.

population of sensory neurons (visual neurons in this example) while the animal performs the task. We would like to determine whether the activity of these neurons contributes causally to the animal's perception and behavioral choice.

The neural code in tasks such as this one involves two crucial stages in the information processing chain (Figure 1A). The first stage is *sensory coding*: the mapping, on each trial, of the sensory stimulus to neural population activity. The second stage is

information readout: the mapping from neural population activity to behavioral choice.

An important observation is that sensory coding and information readout can be based on distinct features: some features of neural activity used to encode sensory information may be ignored when information is read out, and vice versa. For example, suppose that, as is often found (Panzeri et al., 2010; Shriki et al., 2012; Shusterman et al., 2011; Victor, 2000; Zuo et al., 2015), the precise timing of spikes and the spike rate are both informative about the stimulus. Although there is information in spike timing, the downstream neural circuit may be sensitive only to the rate, and thus unable to use information contained in spike timing. Or, the downstream circuit may be sensitive to spike timing, but if extracting spike timing information requires an independent knowledge of the stimulus presentation time to which the downstream circuit does not have access, the readout will not be able to use spike timing information. In a less extreme case, the same features of neural activity may be used for both sensory coding and information readout, but they may be weighted differently by different sets of neurons. For example, the timing of spikes may carry more information about the stimulus than the number of spikes, but the spike rate, defined as the spike count per unit time, may weigh more than spike timing in reaching a behavioral choice.

Although characterizing separately the features of neural activity used for sensory coding and for information readout can provide insight into neural information transmission, we argue that to crack the neural code it is essential to consider the *intersection* between sensory coding and information readout (Figure 1A), defined as the set of neural features carrying sensory information that is read out to inform a behavioral choice. The only information that matters for task performance is the information at this intersection. In fact, only features that lie at this intersection can be used to convert sensory perception into appropriate behavioral actions and can help the animal perform a perceptual discrimination task. We therefore define the neural code that allows the animal to do the task to be the “intersection” features of neural activity carrying sensory information that is read out for behavioral choice.

In the following, we propose a framework for identifying the information at the intersection of sensory coding and information readout. We propose a combination of statistical approaches, behavior, and interventional manipulations (Figure 1B). Statistical approaches can be used on single trials to identify the neural activity features that covary with the sensory stimuli and behavioral choices; they are, therefore, critical for forming hypotheses about the features of the neural activity that both contain sensory information and are used by the information readout. These hypotheses can be tested using experiments in which sensory stimuli are replaced with (or accompanied by) direct manipulation of neural population activity (Figure 1B). The manipulation of the specific features of neural population activity that take part in sensory coding and the examination of how these manipulations affect the animal's behavioral choices probe causally the intersection between sensory information and readout.

Examples of Candidate Neural Codes

Before detailing the concepts behind this proposed framework, we first provide examples to illustrate the types of neural codes

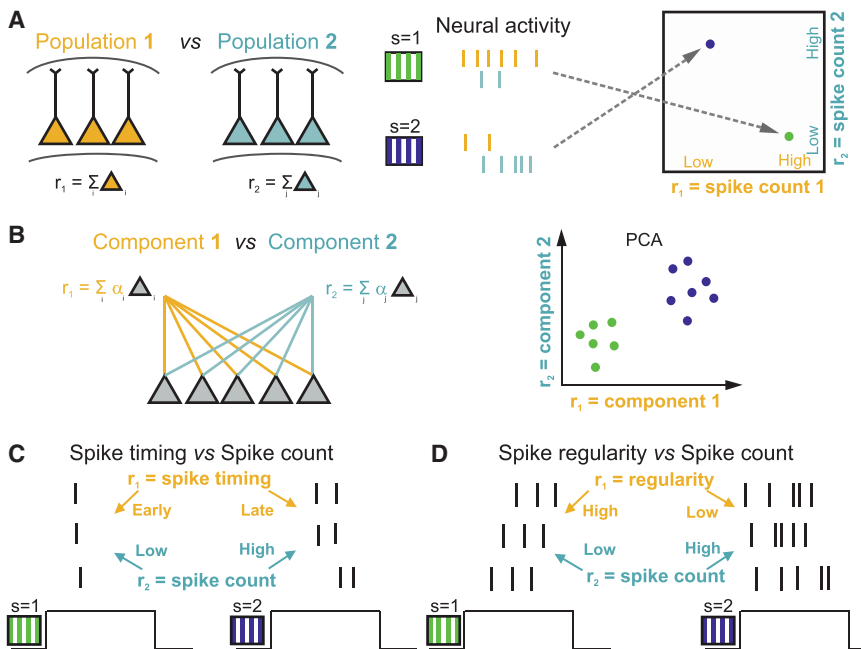


Figure 2. Schematic of Possible Pairs of Neural Population Features Involved in Sensory Perception

(A) Features r_1 and r_2 are the pooled firing rates of two neuronal populations (yellow and cyan) that encode two different visual stimuli ($s = 1$, green; and $s = 2$, blue). Values of single-trial responses of each population can be represented as dots in the two-dimensional plot of spike count variables in the r_1, r_2 space (rightmost panel in A).

(B) Features r_1 and r_2 are low-dimensional projections of large-population activity (computed for example with PCA as weighted sum of the activity of the neurons).

(C) Features r_1 and r_2 are spike timing and spike count of a neuron.

(D) Features r_1 and r_2 are the temporal regularity of the spike train of a neuron and spike count.

and questions that could be addressed. In all these examples, we suppose that we record (either from the same brain location or from multiple locations) neural population activity. That activity consists of n neural features, denoted r_1, \dots, r_n . We would like to determine which of these features, either individually or jointly, carry sensory information that is essential for performing the perceptual discrimination task. For simplicity, hereafter we focus on two features, r_1 and r_2 , but our framework is general enough to deal with an arbitrary number of features (see Supplemental Information).

A common example of studies of population coding (Figure 2A) considers as candidate neural codes two features, r_1 and r_2 , defined respectively as the total spike count of two populations of neurons. This has been the focus of many recent studies designed to test whether activity in specific neural populations is essential for accurate performance in sensory discrimination tasks (Chen et al., 2011; Guo et al., 2014; Hernández et al., 2010; Peng et al., 2015). Those spike counts could be from spatially separated populations in two different brain regions, as shown in Figure 2A, or they could be from different genetically or functionally defined cell classes in the same brain region (Baden et al., 2016; Chen et al., 2013; Li et al., 2015; Wilson et al., 2012). More sophisticated examples of features of neural population activity may involve low-dimensional projections of the activity of large neuronal populations (Cunningham and Yu, 2014). These could be, for example, the first two principal components of neural population activity and would consist of weighted sums of spike counts of the recorded population (Figure 2B). Major open questions that follow from these studies are (Otchy et al., 2015): which populations are instructive for the task (provide sensory information used for perceptual discrimination), which populations are permissive for the task (modulate task performance without directly contributing any specific sen-

sory information), and which populations have no causal role in the sensory discrimination task despite having sensory information? The neural code is expected to be present in instructive populations. In contrast, permissive areas could provide task-relevant modulation that is not related to the sensory stimuli, such as attention or saliency signals. Populations with no causal role may still contain task-related information if it is inherited from instructive regions.

Other questions relevant for population coding regard which neurons are required for sensory information coding and perception (Houweling and Brecht, 2008; Huber et al., 2008; Reich et al., 2001). For example, often only a relatively small fraction of neurons in a population have sharp tuning profiles to the stimuli, whereas the majority of neurons have weak and/or mixed tuning to many different variables (Meister et al., 2013; Rigotti et al., 2013). Information about stimuli can be decoded from both types of neurons, but it remains a major open question whether only the sharply tuned neurons or other neurons as well can contribute to behavioral discrimination (Morcos and Harvey, 2016). A related question is: how many neurons are required for sensory perception? This question can be investigated by determining the smallest subpopulation of neurons that carries all information used for perception.

Another set of questions considers the role of spike timing in sensory coding and perception (Figures 2C and 2D). Spike timing could be measured with respect to the stimulus presentation time, an internal brain rhythm (Kayser et al., 2009; O'Keefe and Recce, 1993), or a rhythmic active sampling process such as sniffing (Shusterman et al., 2011). In many cases both spike timing and spike count carry sensory information (in the example of Figure 2C stimulus $s = 1$ elicits responses with fewer and earlier spikes than does $s = 2$). Although it is accepted that spike timing carries sensory information, whether or not timing is used for behavior has been vigorously debated (Engineer et al., 2008; Harvey et al., 2013; Jacobs et al., 2009; Luna et al., 2005; Zuo et al., 2015). For example, it is still debated whether the sensory information carried by millisecond-scale spike timing is redundant with that provided by the total spike count in a longer

response window of hundreds of milliseconds, whether the information in spike timing measured with respect to stimulus onset can be accessed by a downstream neural decoder, and whether recurrent circuits in higher cortical areas can extract millisecond-scale information.

Also of interest is whether the complex aspects of the temporal structure of spike trains could be part of the neural code. One possibility is that the regularity of spike timing of single neurons or the coordination of spike timing across cells carries information about the stimulus (as in the example of Figure 2D, where stimulus 1 elicits more regular spike trains than stimulus 2). The regularity or temporal coordination across cells may also have a large effect on the readout (Doron et al., 2014; Jia et al., 2013; Nikolić et al., 2013): for example, spikes closer in time may elicit a larger post-synaptic response and so may have a crucial impact on task performance. However, some studies have suggested that temporal coordination does not have a behavioral effect, but instead all spikes are weighted the same by the readout (Histed and Maunsell, 2014).

In what follows, we will consider, for simplicity, two features, and we will generically refer to these features as r_1 and r_2 . These features could refer to spike timing and spike counts, the mean firing rate in two different brain regions, the activity of two different cell types, and so on.

Determining the Single-Trial Intersection between Sensory Information Coding and Information Readout Using Statistical Analysis of Neural Recordings

We now consider how to identify, using statistical measures applied to recordings of neural activity during behavior experiments, three conceptually important domains of interest in the neural information space (Figure 1A): the “sensory information” domain (the features of neural population activity that carry stimulus information), the “readout” domain (the features that influence the computation of choice), and the “intersection” between the two domains (the features that carry sensory information used to compute choice).

Throughout this Perspective, to illustrate neural coding and stimulus and choice domains, we use scatterplots of simulated responses characterized by two features; each dot in the two-dimensional feature plane (r_1, r_2) represents a single-trial response color coded for that trial’s stimulus ($s = 1$: green; $s = 2$, blue) (see also Figure 2A, right panel for a schematization of this representation). Each dot therefore shows the simulated neural response of feature r_1 and r_2 on each individual trial.

A simple way to visualize how neural response features encode sensory stimuli is to compute a sensory decoding boundary (Quiari Quiroga and Panzeri, 2009)—shortened to “*sensory boundary*” hereafter—that best separates trials by stimulus (i.e., that best separates the blue and green dots in the plots in Figure 3). This boundary (black dashed line in the r_1, r_2 plane in Figures 3A₁, 3B₁, and 3C₁) can be used as a rule to decide which stimulus most likely caused a given single-trial neural response. Similarly, we can visualize how neural response features are used to produce a choice with a “*decision boundary*” (Haefner et al., 2013), visualized as a red dashed line in Figures 3A₁, 3B₁, and 3C₁. This decision boundary is the line that best separates trials by choice, and in the specific simulated examples in Figure 3 it

coincides with the actual boundary used to produce choice. Responses that lead to correct choices are shown as filled dots; those leading to incorrect choice are shown as open circles. The orientation of the boundaries determines the relative importance of each feature in sensory coding or choice: a diagonal boundary gives weight to both features, whereas a horizontal or vertical line gives weight only to r_2 or only to r_1 , respectively.

To quantify how well each feature or set of features carries information about stimulus or choice, we use the fraction correct. In terms of the illustrations of Figure 3, the fraction of correctly decoded stimuli is the fraction of green or blue dots that fall on the correct side of the sensory boundary (below or above the sensory boundary for the green, $s = 1$, and blue, $s = 2$, stimulus, respectively). Other measures, such as those based on signal detection theory (Britten et al., 1996; Shadlen et al., 1996) or information theory (Quiari Quiroga and Panzeri, 2009) can be used instead and are discussed in Supplemental Information. We use fraction correct primarily because it is simple and intuitive, but we could use any of the other measures without changing the basic framework. To emphasize the generality of our reasoning, hereafter we often refer to fraction correct as “information.” If the fraction correct refers to the decoded stimulus, we call it “sensory information” or “stimulus information”; if it refers to decoded choice we call it “choice information.”

We say that a neural response feature, r_i , carries sensory or choice information if the value of the presented stimulus or the animal’s choice can be predicted from the single-trial values of this feature. Stimulus information and sensory boundaries are typically computed by presenting two or more different stimuli, and quantifying how well the stimulus-specific distributions of neural response features are separated by sensory boundaries (Quiari Quiroga and Panzeri, 2009). Choice information has been typically computed separately from stimulus information (Britten et al., 1996), by evaluating decision boundaries from distributions of responses with no sensory signal or at fixed sensory stimulus (to eliminate spurious choice variations of neural response arising from their stimulus-related variations).

To understand the neural code associated with a particular task, it is relatively obvious that we need to consider both stimulus and choice information. If a response feature carries stimulus but not choice information, then the sensory information it carries isn’t used for the task. If a response feature carries choice but not stimulus information, then although it may contribute to choice, or relay or execute the result of the decision making, it still cannot be used per se to increase task performance because it does not carry information about the sensory variable to be discriminated (Koulakov et al., 2005). However, a fact that has been underappreciated so far is that a neural feature can carry both sensory and choice information but still not contribute to task performance. This could happen, for example, when features carry both stimulus and choice information, but the rule used to encode sensory information is incompatible with the rule used to read them out.

We illustrate this in Figure 3A. Suppose that in this figure, r_1 and r_2 are the times of the first spike of two different neurons. These features are signal correlated (Averbeck et al., 2006); that is, both neurons spike earlier (corresponding to smaller values of both r_1 and r_2 in the scatterplot in Figure 3A) to the green stimulus

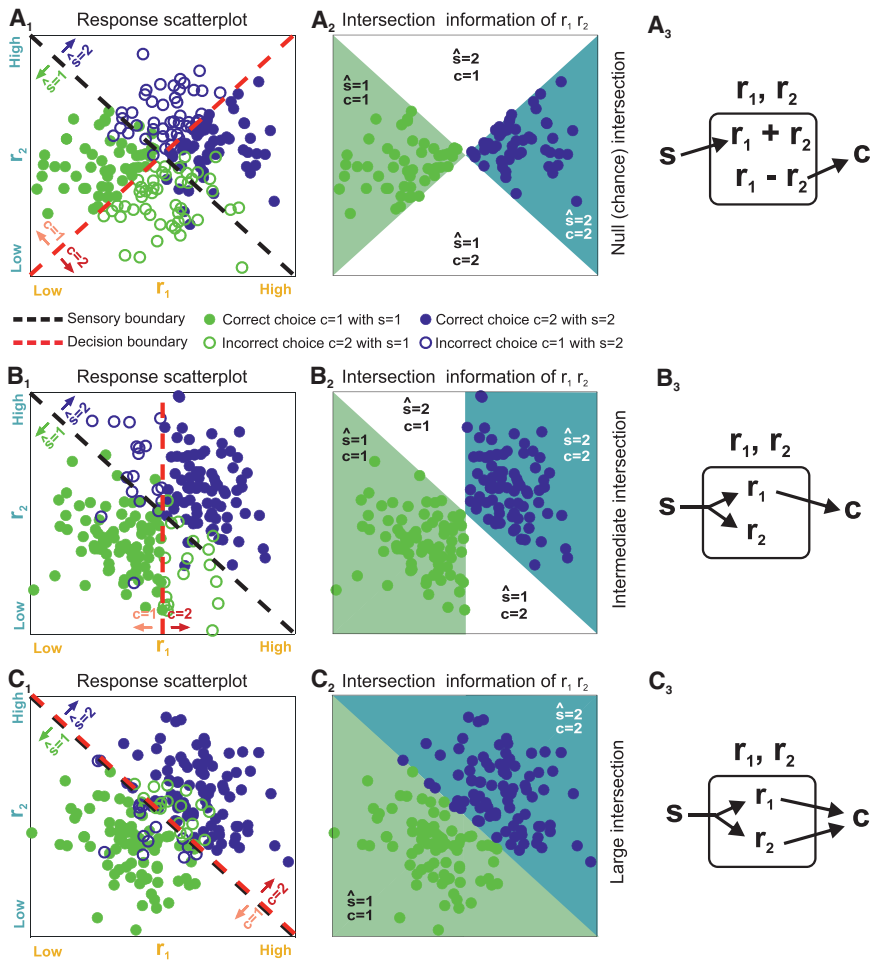


Figure 3. Impact of Response Features on Sensory Coding, Readout, and Intersection Information

In the left panels (A₁), (B₁), and (C₁), we illustrate stimulus and choice dependencies of two hypothetical neural features, r_1 and r_2 , with scatterplots of simulated neural responses to two stimuli, $s = 1$ or $s = 2$. The dots are color coded: green if $s = 1$ and blue if $s = 2$. Dashed black and red lines represent the sensory and decision boundaries, respectively. The region below the sensory boundary corresponds to responses that are decoded correctly from features r_1, r_2 if the green stimulus is shown; the region above the sensory boundary corresponds to responses that are decoded correctly if the blue stimulus is shown. Filled circles correspond to correct behavioral choices; open circles to wrong choices. Panels (A₂), (B₂), and (C₂) plot only the trials that contribute to the calculation of intersection information. Those are the behaviorally correct trials (filled circles) in the two regions of the r_1, r_2 plane regions in which the decoded stimulus \hat{s} and the behavioral choice are both correct. Each region is color coded with the color of the stimulus that contributes to it. White regions indicate the portion of the r_1, r_2 plane that cannot contribute to the intersection because for these responses either the decoded stimulus or choice is incorrect. The larger the colored areas and the number of dots included in panels (A₂), (B₂), and (C₂), the larger the intersection information. Panels (A₃), (B₃), and (C₃) plot a possible neural circuit diagram that could lead to the considered result. In these panels s indicates the sensory stimulus, r_i indicate the neural features and c the readout neural system, and arrows indicate directed information transfer: (A₁–A₃) no intersection information (the sensory and decision boundary are orthogonal); (B₁–B₃) intermediate intersection information (the sensory and decision boundary are partly aligned); (C₁–C₃) large intersection (the sensory and decision boundary are fully aligned).

($s = 1$) and later (corresponding to larger values of r_1 and r_2 in the scatterplot) to the blue stimulus ($s = 2$), with no “noise” correlations (Averbeck et al., 2006) between the activity of these neurons at fixed stimulus. For this encoding scheme, higher values of r_1+r_2 indicate that the blue stimulus is more likely, and so the sensory boundary is anti-diagonal: it is the line $r_1+r_2 = \text{constant}$. Suppose, though, that the readout does not have access to the stimulus time. In such a case, the only information the readout can use is the relative time of firing between the two neurons. This is the difference, r_1-r_2 , and so the decision boundary is $r_1-r_2 = \text{constant}$. In this case, the responses carry information about both stimulus and the choice, but the responses cannot be used to perform the task – the orthogonal sensory and decision boundaries mean the animal’s choice is unrelated to the stimulus.

The case illustrated in Figure 3A could happen also in studying neural population coding rather than spike timing. For example, r_1 and r_2 could be weighted sums of activity of neurons within a large population (as in Figure 2B), with stimulus encoded by the sum of the two neural features and choice by the most active of the two features (which feature is most active is revealed by the sign of r_1-r_2). Also in this “population” interpretation of Figure 3A, none of the stimulus information in population activity could be used to perform the task.

Investigating whether neural stimulus information is usefully read out for task performance requires quantifying whether neural discrimination predicts behavioral discrimination. This has traditionally been addressed by evaluating the similarity between neurometric functions (quantifying the trial-averaged performance in discriminating various pairs of stimuli using one or more neural response features) and psychometric functions (quantifying the animal’s trial-averaged performance in discriminating the same set of pairs of stimuli). If a set of response features contributes to task performance, psychometric and neurometric functions should be similar (stimulus pairs discriminations that are easier for the animal should also be easier for the considered response features, and so on). This approach has provided numerous insights in sensory coding across several modalities (Engineer et al., 2008; Newsome et al., 1989; Romo and Salinas, 2003). For example, it was used to study the role of spike counts and spike times of somatosensory neurons for tactile perception of low-frequency (8–16 Hz) skin vibrations (Romo and Salinas, 2003). Although most such neurons encoded vibration frequency by spike count, some neurons encoded it by spike times fired in phase with skin deflections. However, the neurometric performance of spike counts correlated better to the psychometric one than that of spike times, suggesting that spike rates produce

this sensation (Romo and Salinas, 2003). A similar approach applied to high-frequency vibrations (>100 Hz) suggested that discriminating high-frequency vibrations relies on both spike times and counts (Harvey et al., 2013).

A potential problem with comparing neurometric and psychometric functions is that these functions may be similar even when the sensory and choice information do not intersect at all. The reason why this may happen is that it is based on comparing trial-averaged quantities, rather than comparing sensory information and animal's choice in single trials. To understand the possible problems of only comparing neurometric and psychometric functions, consider a new scenario (Figure S1A). The scenario is in part similar to that of Figure 3A: r_1, r_2 are again the first spike times of two different neurons, and they are tuned to the stimuli and contribute to choice; and, as in Figure 3A, in this new example of Figure S1A both neurons spike earlier to the green stimulus ($s = 1$) and later to the blue one ($s = 2$), leading to an anti-diagonal sensory boundary (line $r_1 + r_2 = \text{constant}$), and the readout uses the relative time of firing $r_1 - r_2$ between the two neurons (the decision boundary projected on the r_1, r_2 plane is $r_1 - r_2 = \text{constant}$). However, suppose that in the example of Figure S1A the actual choice (unlike in Figure 3A) depends also on a third neural feature, r_3 , which we'll take to be the sum of the spike count of the two neurons. Assume also that, crucially, the stimulus dependence of the spike count r_3 is similar to that of both r_1 and r_2 , so that stimulus $s = 1$ elicits both earlier spike and lower counts than stimulus $s = 2$ does. Suppose finally that the experimenter now tunes the task difficulty by varying some "stimulus signal intensity" parameter whose effect on neural firing is to change the separation between the clouds of the $s = 1$ (green) and $s = 2$ (blue) stimulus-specific responses (Figure S1A₂). As the task becomes more difficult, the animal's psychometric performance decreases, as does the decoding neurometric performance (because the blue and green stimulus-specific distributions of points get closer). We can plot neurometric and psychometric performance as a function of signal intensity, and they will have similar shape: both will be near chance when signal intensity is small and the stimulus-specific distributions of r_1, r_2 largely overlap (Figure S1A₃), and will be nearly perfect when signal intensity is high and the stimulus-specific distributions of r_1, r_2 are far apart (Figure S1A₅). Thus, in this example (Figure S1A), statistical analysis will show that spike timing features r_1, r_2 have sensory information (because $r_1 + r_2$ is stimulus dependent), have choice information (even at fixed stimulus, reflecting that $r_1 - r_2$ impacts on choice), and the neurometric function of r_1, r_2 is similar to the psychometric function (because the stimulus dependence of both r_1 and r_2 is similar to that of the firing rate r_3 , which is the only contributor to task performance). Yet r_1, r_2 do not contribute to task performance because none of the sensory information they carry is read due to the orthogonality of the sensory and decision boundaries. That r_1, r_2 do not contribute to task performance can only be discovered by observing that the trial-to-trial fluctuations of the accuracy of sensory information in r_1, r_2 , encoded only by $r_1 + r_2$, does not influence at all behavior, as the decision depends on $r_1 - r_2$. For example, in trials when $r_1 + r_2$ indicates the presence of a stimulus different from that presented, behavior is not less (or more) likely to be correct because of this stimulus coding error (Figures S1A₃–S1A₅).

These examples illustrate a general fact: it is not possible to determine whether sensory information is transmitted to the readout using the trial-averaged stimulus and choice information, either separately or in combination. It is, instead, necessary to investigate the effect of sensory coding on information readout within a single trial. We therefore propose the use of a measure we call intersection information, denoted I . Conceptually, intersection information is large only if the neural features carry a large amount of information about the stimulus and that information is used to inform choice—so that, based on these features, the animal is correct most of the time.

A quantitative description of I was derived in Zuo et al. (2015). The authors reasoned that, if feature r_i contributes to task performance, there should be an association on each trial between the accuracy of sensory information provided through that feature and behavioral choice. In other words, on trials in which r_i provides accurate sensory evidence (stimulus is decoded correctly from r_i), then the likelihood of correct choice should increase. Thus, the simplest operational definition of the intersection information, I , for a particular feature is the probability that on a single trial the stimulus is decoded correctly from r_i and the animal makes the correct choice (see Supplemental Information for additional details, in particular Eq. S7).

Intersection information can be used to rank features according to their potential importance for task performance. Importantly, it is high if there is a large amount of stimulus information and readout is near optimal. It is low, on the other hand, if a neural response feature has only sensory information but very little choice information, or vice versa, or if the rule used for sensory coding is incompatible with the rule used by the readout.

We illustrate intersection information using three examples (Figures 3A₁, 3B₁, and 3C₁), with null (chance-level), intermediate, and high values of intersection information, respectively. In these plots, we divide the r_1, r_2 feature space into four possible areas based on the sensory and decision boundaries: $\hat{s} = 1, c = 1$; $\hat{s} = 1, c = 2$; $\hat{s} = 2, c = 1$; $\hat{s} = 2, c = 2$ (\hat{s} is the decoded stimulus, which can be different from the stimulus, s , presented to the animal). The intersection information is the fraction of trials that are decoded correctly and result in a correct behavioral choice; these trials correspond to the filled dots, indicating a trial with correct choice, shown in the regions in Figures 3A₂, 3B₂, and 3C₂ colored with the decoded stimulus color code. The larger are the colored areas, the larger is the intersection information. Chance level for the intersection measure is when there is no relationship between the stimulus decoded by neural activity and the choice taken by the animal at fixed stimulus (the chance level of intersection equals the product of the probability of a correct behavioral choice and the probability of correctly decoding the stimulus; see Supplemental Information for details). This is the case in Figure 3A, where the sensory and decision boundaries are orthogonal. Because trials that provide faithful stimulus information are just as likely to result in correct as incorrect choices, there is chance-level intersection information (see Figure S1D for the intersection information values in these examples).

Intersection information is intermediate when only some of the features of neural activity carrying sensory information are read out while the information of others is lost before the readout

stage. This is the case in Figure 3B, where both r_1 and r_2 carry sensory information but only r_2 is read out. This may correspond, for example, to a case when both spike count r_1 and spike timing r_2 of a neuron carry information, but only count r_1 is used for behavior (similarly to the case of O'Connor et al., 2013), for example, because the readout mechanism is not sensitive enough to precise spike timing.

Intersection information is largest when the optimal sensory boundary and the decision boundary coincide, as in Figure 3C, so that all sensory information is optimally used to perform the task. This is the case when all measured features of neural activity that carry sensory information directly contribute to the animal's choice. In this example (Figure 3C), trials that lead to correct stimulus decoding from the joint features, r_1 and r_2 (those below the diagonal for the green stimulus, $s = 1$, and those above the diagonal for the blue stimulus, $s = 2$), always lead to correct behavioral choices. Trials leading to incorrect stimulus decoding from r_1 and r_2 (above the diagonal for $s = 1$ and below it for $s = 2$) always lead to incorrect behavioral choices. This situation is reminiscent of texture encoding by somatosensory cortical neurons (Zuo et al., 2015), in which both spike rate and timing seem to carry sensory information that is used for behavioral discrimination.

The above simple reasoning can be extended to provide more refined measurements of the relationship between sensory information in neural activity and behavioral choice. For example, one could also measure (Zuo et al., 2015) what we call the fraction of intersection information fII , defined as the fraction of trials with correct stimulus decoding that have correct behavior. Unlike II , fII is not sensitive to the amount of sensory information (the fraction of trials the stimulus is decoded correctly from neural feature r), but only to the proportion of these correctly decoded trials that lead to correct behavior. Thus, fII is an indicator of the optimality of the readout—in the linear case, the alignment between the sensory and decision boundaries—rather than the total impact of the code on task performance. Measuring both II and fII could be useful to determine whether a moderate amount of intersection information, II , is because the feature has a moderate amount of information but is efficiently read or because the feature has high information but not read out very efficiently. Moreover, given that if a feature r_i contributes to task performance, then, in trials when r_i provides inaccurate evidence (stimulus is decoded incorrectly), the likelihood of correct choice should decrease, an additional separate quantification of the agreement of stimulus information and behavioral choice in incorrect trials would complement intersection measures (see Zuo et al., 2015 and Supplemental Information).

The purely statistical approach to measure intersection information is most straightforward if all response features are statistically independent, because in that case the intersection information approach applied to a set of features would unambiguously identify the contribution of those features to task performance. However, often features are not independent. For example, if the features are the activity of neurons in different brain regions, these features might be partly correlated if there are connections between the two regions. Alternatively, if the features are spike timing and spike count, both involve the same spikes and so may be dependent. The presence of depen-

dencies among features complicates the interpretation of intersection information. In particular, it raises two critical questions. First, does a set of features with intersection information contribute to task performance, or instead reflect only a correlation with other features that truly contributes to task performance? Second, does each neural response feature provide unique intersection information that is not provided by other features?

To illustrate the complications induced by correlations among features, we consider the intersection information from one feature rather than two. We return to Figure 3, for which responses are signal correlated in all panels (that is, responses to $s = 1$ are on average lower than those to $s = 2$ for both features [Averbeck et al., 2006]). We first consider a case (as in Figure 3B) for which both features carry information about the stimulus and are partly correlated (because of signal correlations) but only feature r_1 is read out. Suppose that we apply our statistical analysis to feature r_2 ; that is, we decode the stimulus using only r_2 , which can be done optimally by decoding responses in the lower and upper half of the r_1, r_2 space as $\hat{s} = 1$ and $\hat{s} = 2$, respectively. We will find higher-than-chance intersection and choice information (as shown by the fact that lower values of r_2 are found in trials with choice $c = 1$ than in trials with $c = 2$, see Figure S1B) even though r_2 is not read out. That's only because r_2 is correlated with r_1 , which is the feature that is truly read out.

If we record from both features, we can differentiate, just from statistical analyses of neural recordings, between the case when only one feature is read out (Figure 3B) and the case when both are read out (Figure 3C). If, as in Figure 3C, r_1 and r_2 carry complementary sensory information (the diagonal sensory boundary implies that both features should be used for optimal decoding) and if the readout uses both features (the decision boundary is also diagonal), then intersection information obtained when decoding the stimulus using two features will be larger than the intersection information obtained when decoding the stimulus with either feature alone. This is because decoding the stimulus with only one feature will lose the complementary task information present in the other feature and so the task performance will suffer (Figures S1C and S1D). Thus, a statistical signature that task performance benefits from both features is that using both feature increases the intersection information (Figure S1D). However, if we cannot record both features (and, more generally, all features that carry intersection information), the only way to fully prove which features contribute to task performance is to use interventional methods. That's the subject of the next section.

Causal Interventional Testing of the Neural Code Why Do We Need Intervention?

The statistical methods described above for determining sensory, choice, and intersection information are useful for identifying potential neural coding mechanisms, and for forming hypotheses about information coding and transmission. However, as just discussed, because response features are often correlated and because we do not usually have experimental access to all of them, whether a neural feature carries information in the intersection between sensory coding and readout can ultimately only be proved with intervention. Before discussing how to

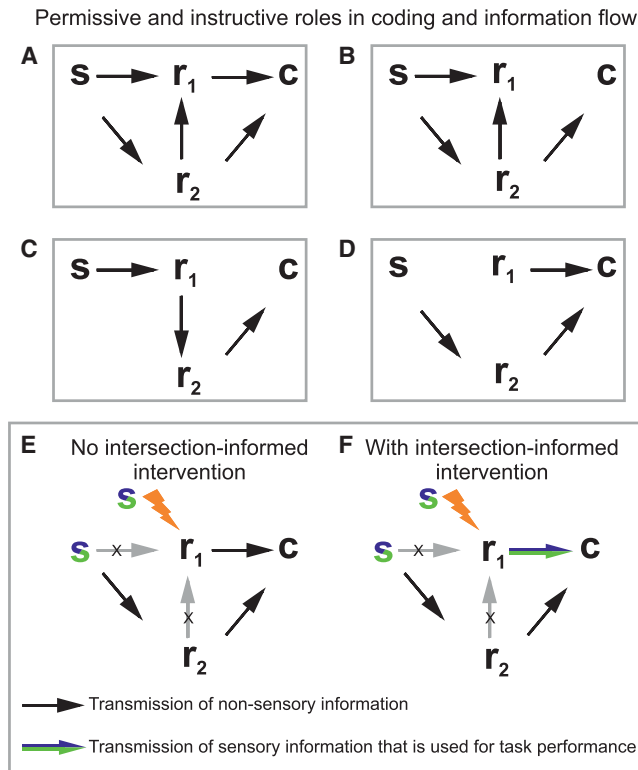


Figure 4. Causal Manipulations to Study the Permissive and Instructive Roles in Coding and Information Flow

(A–D) Interventional approaches can be used to disambiguate among different conditions. (A) The neural features r_1 and r_2 carry significant information about the stimulus, s , and provide essential stimulus information to the decision readout, c . (B) r_1 does not send information to c , but only receives a copy of the information via r_2 , which does send stimulus information to c . (C) r_1 provides instructive information about s to r_2 and r_2 informs c instructively; (D) r_1 influences c but does not directly carry information about s .

(E and F) Interventional approaches can be used to reveal cases in which r_1 informs c but does not send stimulus information that contributes to task performance (black arrow in E) from cases in which r_1 sends stimulus information used for decisions (colored arrow in F).

design interventional experiments that test intersection information, it is useful to consider why interventional manipulations of neural activity are so crucial to prove hypotheses. (In the following, we refer to “statistical” information measures as shorthand for measures of information obtained from recorded natural unperturbed neural activity, and “interventional” information measures to indicate information estimates from neural activity imposed by intervention.)

Suppose that statistical measures like those described in the previous section found that a neural feature, r_1 , carries stimulus, choice, and intersection information. An interpretation of this result is that r_1 provides essential stimulus information to the decision readout (this is indicated in Figure 4A by the arrow from r_1 to the choice, c). However, another interpretation (sketched in Figure 4B), one that is still compatible with these statistical measures, is that r_1 does not transmit information to c (not even indirectly). Instead, it only receives a copy of the information that other neural features (such as r_2 in Figure 4B) do transmit to the choice. In this case, the sensory information in r_1 is not caus-

ally involved in the decision (as indicated by the lack of arrow from r_1 to c in Figure 4B), but r_1 correlates with the decision because it correlates with r_2 , the decision’s cause.

Intervention can disambiguate these two scenarios by imposing a chosen value on r_1 , one that is decided by the experimenter and so is independent of r_2 . By doing that, we break any possible effect of r_2 , or of any other possible variable, on r_1 (Figure 4E). In this case, any observed relationship between r_1 and choice must be due to the causal effect of r_1 on choice (Pearl, 2009).

In the following we discuss how to design a causal intervention experiment that tests whether neural features carry intersection information. We are interested in an intervention design that can tell whether r_1 transmits stimulus information used for decision (as in Figure 4F, indicated by the arrow between r_1 and choice c being colored like a stimulus) or r_1 informs c but does not transmit stimulus information contributing to task performance (as in Figure 4E, indicated by the arrow between r_1 and c not being colored).

Intervention on Neural Activity and Intersection between Sensory Information and Readout

Here we examine cases in which we can both record and manipulate (in the same animal, but not necessarily at the same time) neural features r_1 and r_2 during a perceptual discrimination task.

Let us first consider a causal intervention on the neural features. Suppose that we impose a number of different values of r_1, r_2 in a series of intervention trials (“lightning bolt” symbols in Figure 5, colored by the behavioral choice they elicit) and we measure the choice taken by the animal. In our examples, choice is determined by the red dashed decision boundary in the r_1, r_2 space. Observing the correspondence between the value imposed on r_1, r_2 and the animal’s choice would easily determine the orientation of the decision boundary (Figures 5A–5C). From this interventional decision boundary, choice information can be obtained exactly as in the statistical case.

Applying the same reasoning used for the statistical case, an interventional measure of intersection information is the fraction of trials on which the animal’s choice reports the stimulus that would be decoded (using the sensory boundary acquired with statistical analysis of neural responses) from the imposed neural activity pattern (as above, this can be assessed against chance level). Application of this interventional measure of intersection information to our examples in Figure 5 shows that interventional intersection information captures the alignment of the sensory and decision boundary. It is high when, as in Figure 5C, the animal’s choice ($c = 1$, pink; $c = 2$, dark red) always corresponds to the stimulus decoded from neural activity (in Figure 5C, the case of maximal intersection, all patterns in the $\hat{s} = 1$ “green” decoding region lead to $c = 1$, and the same applies to the $\hat{s} = 2$, $c = 2$ region); it is null (chance-level) when sensory and decision boundaries are mismatched (as in Figure 5A, where half of imposed patterns in either stimulus decoding region lead to choice $c = 1$ and half to $c = 2$).

A critical observation is that the intersection information computed via intervention may be different from that computed using purely statistical analysis. That can happen, as discussed above, if the neural features are correlated with variables that did

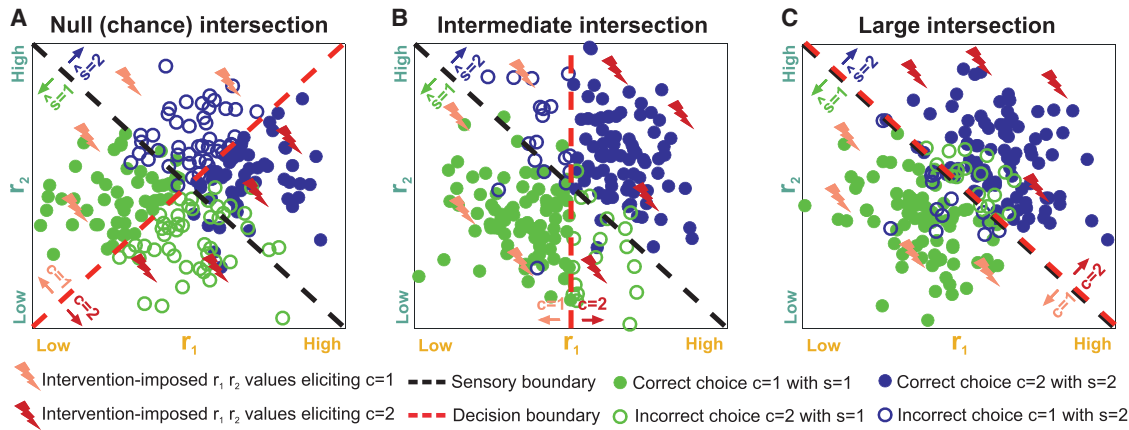


Figure 5. Schematic of an Experimental Design to Probe Intersection Information with Intervention

Three examples of neural responses (quantified by features r_1, r_2) to two stimuli, with conventions as in Figure 3. We assume that some patterns of neural activity are evoked by interventional manipulation in some other trials. The “lightning bolts” indicate activity patterns in r_1, r_2 space evoked by intervention: they are color coded with the choice that they elicited (as determined by the decision boundary—the dashed red line). Choice $c = 1$ is color coded as pink, and $c = 2$ as dark red. The choices evoked by the intervention can be used to determine, in a causal manner, the position of the decision boundary (as the line separating different choices). The correspondence between the stimulus that would be decoded from the neural responses to the intervention-induced choice can be used to compute interventional intersection information.

(A) A case with no interventional intersection information (the sensory and decision boundary are orthogonal).

(B) A case with intermediate intersection (the sensory and decision boundary are partly aligned).

(C) A case with large intersection (the sensory and decision boundary are fully aligned).

carry intersection information, but did not themselves provide any information about choice. For example, if a statistically determined non null choice or intersection information in one feature just reflects a top-down choice signal and not a causal contribution of the feature to choice, this feature will show null (chance-level) intersection information with intervention. Thus, of particular interest are cases in which the decision boundary is orthogonal to the sensory boundary under intervention, but not in trials without an intervention (O’Connor et al., 2013). When that’s the case, the neural features under investigation carry no intersection information and the intersection or choice information determined statistically mean that the considered features only correlate with the true factors that are instructive for task performance.

The values of the interventional evoked neural features in an experiment are arbitrarily determined by the experimenter. The chosen evoked neural features may be designed to drive behavior robustly but may occur very rarely during perception in natural conditions. This may lead to an over-estimation of their importance for task performance. To correct for this problem, when computing interventional intersection information, we should weigh intervention results with the probability distribution over stimuli and responses that occur under natural conditions (see Supplemental Information). Thus, evaluating the causal impact of a neural code with intervention experiments ultimately demands a statistical analysis of the probability of naturally occurring patterns during the presentation of each stimulus while performing the task.

By analogy to what we proposed for the statistical measures, we can design intervention experiments that address whether two neural response features, r_1, r_2 , that are correlated during measures of natural neural activity both contribute causally to choice and to task performance. Suppose that (as in Figures

5B and 5C) we recorded two correlated features in unperturbed (i.e., no intervention) conditions and that we would like to determine interventional whether the readout uses both such sources of sensory information to perform the task. Designing such an experiment requires manipulating both features at the same time, and then comparing interventional intersection information of the joint features and of the individual ones. If the experimenter designs a set of intervention patterns that generate uncorrelated feature values, then only the features that carry sensory information and are read out will show higher-than-chance intersection information. If the experimental design cannot fully decorrelate the features evoked by intervention, then a complementary contribution to task performance of the two features will still be revealed interventional when finding that adding a feature increases the interventional intersection information, exactly as in the statistical analysis case.

Above we argued that statistical analysis is not sufficient to determine whether there is intersection information in a set of neural features. In the following, we argue that causal manipulations of neural activity alone are also not sufficient to determine whether there is intersection information in a set of neural features. Experiments are frequently designed such that an animal is trained to discriminate neural activity patterns that are created artificially using interventional approaches, such as microstimulation or optogenetics, without direct regard to how these patterns may encode sensory stimuli. This approach is extremely powerful for testing the capabilities of the readout. For example, this approach has been used to test the sensitivity of the readout to precisely timed neural activity (Doron et al., 2014; Yang et al., 2008; Yang and Zador, 2012) and also to test the minimal number of neurons or spikes to which a readout could be sensitive (Houweling and Brecht, 2008; Huber et al., 2008). Thus, this approach can be used to infer intersection information indirectly

(by comparing the features that carry sensory information with those that can be detected by the readout). However, this approach is insufficient to determine directly whether a given neural feature is used for performing specific sensory discrimination tasks, and to evaluate how much this feature contributes to sensory discrimination.

Because both statistical and interventional approaches by themselves are not sufficient to test neural codes, we propose a scheme in which statistical analyses must be used to generate hypotheses about neural codes, and interventional experiments must be used to test them.

Neurophysiological Examples of the Potential Advantages of Application of the Statistical and Interventional Concept of Intersection

The foundations underlying intersection between sensory information and readout can be traced back to the work of Newsome and colleagues on visual motion perception in primates (Britten et al., 1996; Newsome et al., 1989). These studies showed that visual area MT encoded visual motion information in its firing rate: higher firing rates indicate motion along the neuron's preferred direction. They established a statistical relationship between the animal's choice in a visual motion discrimination task and the firing rate of MT neurons in the same trial (Britten et al., 1996). The causal role of the firing rate of MT neurons in motion perception was interventionally demonstrated showing that microstimulation of this region biases perception of motion direction (Newsome et al., 1989). Such studies continue today, taking also advantage of modern genetic, optogenetic, and recording techniques. One example is the study of the neural coding of sweet and bitter taste in mice. The authors first established that anatomically separate populations of neurons responded to sweet and bitter taste, and thus carried stimulus information (Chen et al., 2011). An optogenetic intervention was then used to activate the spatially separated "sweet" and "bitter" populations (Peng et al., 2015). These intervention experiments elicited behavioral responses as expected for a mouse's response to sweet and bitter tastes. These studies therefore reveal intersection information in neural codes as spatially segregated response patterns using a combination of stimulus information, statistical analysis, and intervention.

These studies investigated simple properties of an individual neural feature (firing rate of classes of neurons) and followed implicitly part of the logic of the framework proposed here, although they did not measure a single-trial statistical intersection that we propose. Measuring the intersection information becomes, however, crucial in more complex scenarios in which (unlike the cases considered above) either a clear hypothesis about the neural code does not exist a priori (as may happen when analyzing coding of complex natural stimuli, rather than simpler laboratory stimuli) or when there are multiple, perhaps partly correlated, candidate features for the neural code that all seem, statistically, to contribute to choice or stimulus. In these cases, it is necessary to evaluate quantitatively the contribution of each feature to behavior. Below we discuss how the full or partial application of the ideas of our intersection framework in these more complex scenarios could provide further insight into the neural code.

The statistical intersection information framework has been applied to investigate whether millisecond-scale spike timing of somatosensory cortical neurons provides information that is used for performing a whisker-based texture discrimination task (Figures 6A and 6B), above that already carried by spike counts over timescales of tens of milliseconds (Zuo et al., 2015). The authors computed a spike-timing feature by projecting the single-trial spike train onto a timing template (constructed for optimal sensory discrimination) whose shape indicated the weight assigned to each spike depending on its timing (Figure 6C). Computed spike counts corresponded to weighting the spikes with a flat template, which assigns the same weight to spikes independent of their time. This provided timing and count features that had negligible correlation (the temporal distribution of spikes was largely independent from their total number). Both timing and count carried significant sensory (Figure 6D), choice (Figure 6E), and intersection (Figure 6F) information, with timing carrying more information than count for all these types of information, larger than the one carried by either feature alone. These results indicate that in this task sensory information was complementarily multiplexed in spike counts and timing and was also complementarily combined to perform the task. Of the two features, however, timing carried both more sensory information and had a greater influence on the animal's choice. Thus, the statistical intersection framework helped form a very precise hypothesis that multiplexing spike timing and spike count information is the key neural code used to solve the task. A further application of the interventional intersection framework, not yet applied to this experiment, would strongly prove or disprove this multiplexing hypothesis for texture coding.

This example illustrates that the statistical analysis of information intersection may be critical to correctly interpret the results of an interventional experiment and to refine its design. In this case, profound texture-dependent spike timing differences were found even across nearby neurons (Zuo et al., 2015). The cellular-level and millisecond-scale temporal resolution of this information coding revealed by the statistical analysis strongly constrains the interventional experimental design, as it indicates that finely spatially patterned and temporally precise intervention must be used to test whether spike timing is part of the neural code. Also, this example shows how statistical intersection results are essential to interpret successes and failures of interventions. For example, in the presence of such profound neuron-to-neuron differences in spike timing responses to textures, a causal effect of spike timing on behavior would not have been detected using a wide-field optogenetic intervention that activated all neurons simultaneously (see also section Considerations of Interventional Experimental Design). Statistical analysis would be essential to reveal that this failure would not have been because spike timing was not part of the neural code used to perform the task, but because the optogenetically induced activity did not preserve the natural texture-dependent timing differences across neurons.

A study (O'Connor et al., 2013) that implemented an approach close in spirit to the intersection information framework both at the statistical-analysis and interventional level is a recent investigation of the role of spike timing and spike rate coding in

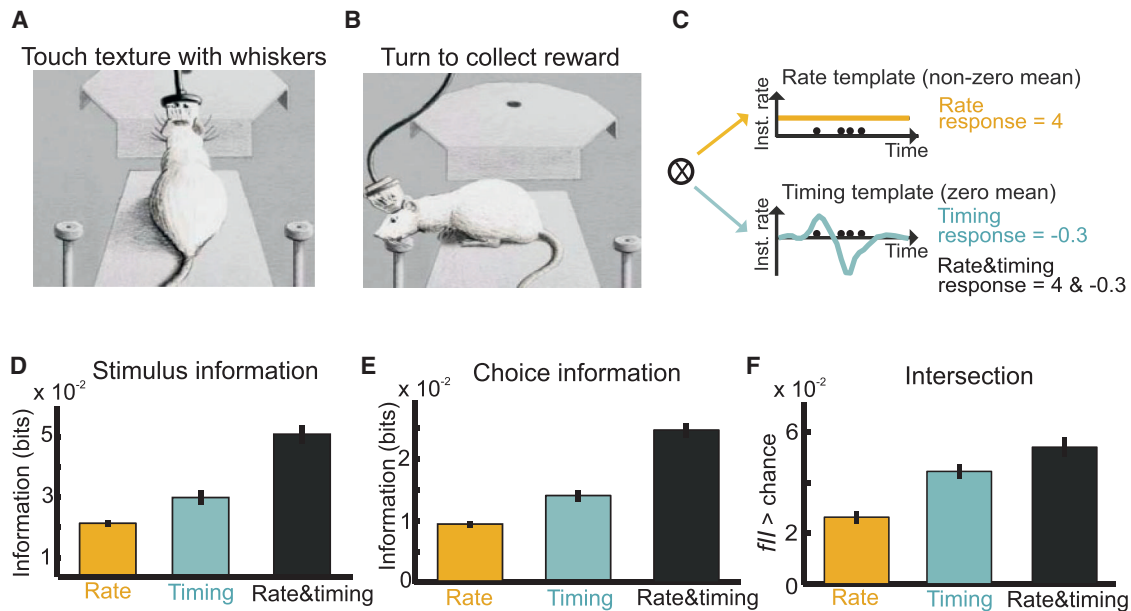


Figure 6. Examples of Statistical Intersection Measures in a Texture Discrimination Task

This figure shows how spike timing and spike count in primary somatosensory cortex encode textures of objects, and how this information contributes to whisker-based texture discrimination.

(A and B) Schematic of the texture discrimination task. (A) On each trial, the rat perched on the edge of the platform and extended to touch the texture with its whiskers. (B) Once the animal identified the texture, it turned to the left or the right drinking spout, where it collected the water reward.

(C) Schematic of the computation of spike count and spike timing signals in single trials.

(D–F) The mean \pm SEM (over $n = 459$ units recorded in rat primary somatosensory cortex) of texture information (D), choice information (E), and fraction of intersection information $f//$ (F). Modified with permission from Zuo et al. (2015).

whisker-based detection task of object location (Figure 7A). The authors found, based on statistical measures, that both timing and rate carried both stimulus and choice information (Figure 7B). The authors then probed the role of timing and rate by replacing the somatosensory object with optogenetic manipulation of layer 4 somatosensory neurons (Figures 7C and 7D). The authors found that using optogenetics to induce neural activity with information in rate caused the animal to report the sensation of a “virtual pole” (Figure 7C), whereas adding to this optogenetic manipulation information in spike timing relative to whisking did not elicit additional behavioral performance in virtual sensation (Figure 7D). When interpreted within our framework, these results suggest that spike times do not carry any intersection information that is additional to that carried by rates. An additional application of the statistical intersection framework to these neurophysiological recordings—not performed in that study—would allow a more precise evaluation of the impact of timing and rate codes on task performance (see previous section) and could provide an important independent confirmation of this hypothesis based on naturally evoked neural activity only.

Considerations of Interventional Experimental Design

Interventional approaches may involve use of one or more experimental techniques such as optogenetic (Lerner et al., 2016) and chemogenetic (Stenerson and Roth, 2014) manipulations, intraparenchymal electrical stimulation (Tehovnik et al., 2006), transcranial direct current stimulation, and transcranial magnetic stimulation (Woods et al., 2016), to name a few. Given its unique

combination of high cell-type specificity and temporal resolution, below we focus mostly on optogenetics.

There are at least two dimensions over which experimental design may be varied. One is how intervention is coupled with sensory stimuli; the other is how intervention is performed. In the following, we consider how these possible experimental variations along these dimensions relate to the intersection framework.

Virtual Sensation Interventional Experiments versus Experiments Overriding or Biasing Natural Sensory Signals

Our framework assumes that we test sensory encoding and information readout using a perceptual discrimination task. An important experimental design question is how to incorporate interventional approaches. Our focus is on understanding the codes that arise from natural sensory cues, and so we mainly consider cases in which interventional trials are interleaved with non-interventional ones.

One practical question for experimental design is whether on intervention trials the sensory stimulus should also be presented, or if the intervention manipulation should be applied in isolation. One possibility is a “virtual sensation” experiment (Figure 8A), in which patterns of neural activity are imposed by intervention in the absence of the sensory stimulus and the animal is asked to report the perception of one of the two sensory stimuli. A classic example is the work of Romo and colleagues (Romo et al., 1998; Romo and Salinas, 2003) demonstrating that cortical microstimulation can entirely substitute for tactile stimulation in a

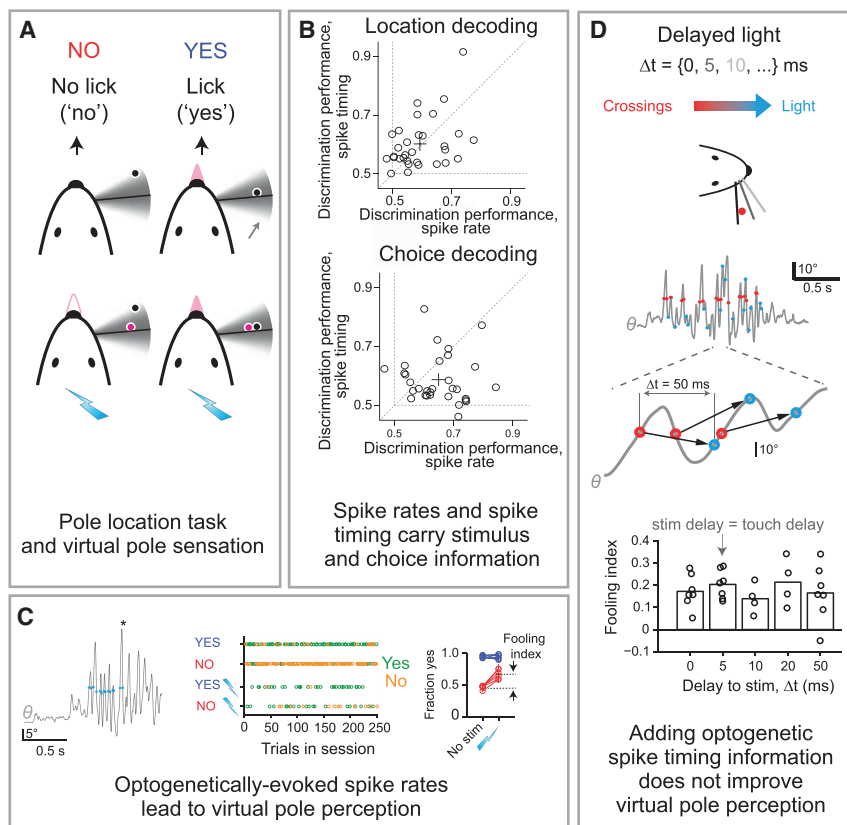


Figure 7. Examples of Statistical and Interventional Intersection Measures with Sensory and Illusory Touches

This figure shows results of the statistical and interventional test of the role of cortical spike timing and spike count in the neural code for whisker-based object location. The test involved closed-loop optogenetic stimulation behavior session depending on pole location and optogenetic stimulation (cyan lightning bolts). A “virtual pole” (magenta) was located within the whisking range (gray area). Mice reported object location by licking or not licking.

(A) Schematic of the task: four trial types during a closed-loop optogenetic stimulation behavior session depending on pole location and optogenetic stimulation (cyan lightning bolts). A “virtual pole” (magenta) was located within the whisking range (gray area). Mice reported object location by licking or not licking.

(B) Decoding object location and behavioral choice from electrophysiologically recorded spikes in layer 4 of somatosensory cortex. Each dot corresponds to the decoding performance (fraction correct) of one neuron.

(C) Optogenetically imposed spike rates evoked virtual pole sensation. Left: optogenetic stimulation (blue circles) coupled to whisker movement (gray, whisking angle θ) during object location discrimination. Asterisk, answer lick. Middle: responses in the four trial types across one behavioral session. Green, yes responses; gold, no responses. Right: optogenetic stimulation in NO trials (red), but not in YES trials (blue), in barrel cortex increases the fraction of yes responses. Lightning bolt and “no stim” labels indicate the presence and absence of optogenetic stimulation, respectively. Error bars, SEM. Each line represents an individual animal.

(D) Adding timing information in the optogenetically evoked activity did not improve virtual pole perception. Top: delayed optogenetic stimulation was triggered by whisker crossing with variable

delays, Δt . Middle: whisker movements with whisker crossing (red circles) and corresponding optogenetic stimuli (cyan circles) for $\Delta t = 50$ ms. Bottom: fooling index (fraction of trials reporting sensing of a virtual pole) as function of Δt . Modified with permission from O’Connor et al. (2013).

frequency discrimination task. Another example of virtual sensation is the induction of an illusory sensation of pole touching during whisking using optogenetic stimulation of cortical primary somatosensory neurons, as discussed above (see Figure 7 and O’Connor et al., 2013). The virtual sensation paradigm is very appealing because it can demonstrate the sufficiency of the considered neural code for creating sensation and for its direct relevance for the development of neural prosthetics.

Another possibility is to impose patterns in the presence of a sensory stimulus. This approach tests whether the imposed pattern can “override” or “bias” (Figure 8B) the signal from the sensory stimulus. A classic example of this approach can be found in the work of Newsome and colleagues (Salzman et al., 1990) showing that MT microstimulation in a visual motion discrimination task can bias the animal’s perception toward the motion direction preferred by the neurons that were activated by microstimulation. A more recent example can be found in the study (also described above) examining the codes for sweet and bitter/salt taste sensation (Peng et al., 2015), where the authors showed that optogenetic activation of the sweet cortical field triggered fictive sweet sensation even in the presence of a salt stimulus. From the point of view of the formalism presented here, successfully overriding the signal from an opposite external stimulus is an appealing proof that the considered neural code provides information that is so crucial to the task that it can

even win over other contrasting sources of information, such as those that may come from different or parallel pathways conveying information from the sensory periphery that contradicts the one injected through intervention of neural activity.

Considerations on How to Perform Intervention on Neural Activity, and the Advantages of Patterned Optogenetics

Imposing a pattern can be done in two conceptually distinct ways. In one, the experimenter mainly tries to “bias” (Guo et al., 2014; Li et al., 2015; O’Connor et al., 2013) the neural activity (Figure 8B). This consists of shifting the endogenous activity in a certain direction (for example, lowering the firing rates of a neural population by imposing a slight hyperpolarization or by exciting a set of inhibitory neurons). This can be done, for example, using wide-field, single-photon optogenetic stimulation of a network of a number of opsin-expressing neurons (this is illustrated in Figure 8C, note that the number of neurons in that sketch is limited to seven for presentation purposes only). A problem with this approach is that it does not completely remove correlations of the patterns evoked by intervention with other brain variables that are present in the endogenous component of the activity (because the evoked activity adds to the endogenous one). This means that this intervention may not entirely break the correlations among features or between

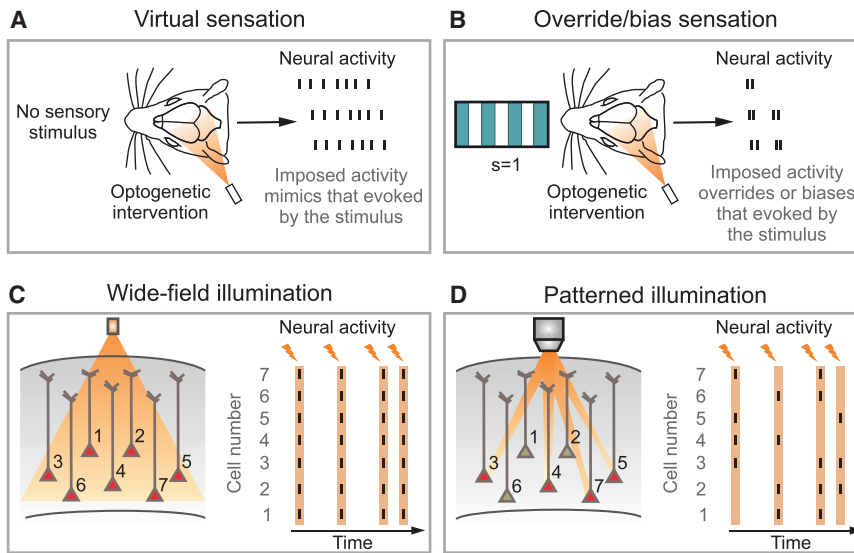


Figure 8. Experimental Configurations for Interventional Optogenetic Approaches

(A) In a virtual sensation experiment, the animal behavior is tested by applying the optogenetic intervention in the absence of the external sensory stimulus.

(B) Alternatively, optogenetic intervention can be paired with sensory stimulation with the aim of overriding or biasing neural activity evoked by the sensory stimulus.

(C) In the wide-field configuration for optogenetic manipulation, light is delivered with no spatial specificity within the illuminated area, resulting in the activation (red cells) of most opsin-positive neurons. Stimulation in this regime may lead to over-synchronous neural responses (right). The orange lightning bolts in the right panel indicate the time at which successive stimuli are applied. The neurons displayed in (C) and (D) are meant to represent a population of N neurons expressing the opsins; their number is here limited to 7 for presentation purposes only.

(D) Patterned illumination permits the delivery of photons precisely in space. When multiple and diverse light patterns are consecutively delivered (orange lightning bolts), optical activation of neural networks with complex spatial and temporal patterns becomes possible (right).

features and non-observed endogenous brain activity that the causal manipulations aim to remove. This is a concern particularly when investigating whether intersection information is complementarily carried by more than one feature, as an interventional bias may affect all features in a correlated way. For example, a general hyperpolarization of the population may both lower the spike rate and delay the latency of neural activity. Given the highly synchronous generation of photocurrents in opsin-expressing cells, wide-field optogenetics may even induce artificial correlations (Figure 8C).

The second interventional approach is to try to impose, or “write down” (Peron and Svoboda, 2011), a target neural activity pattern on a neural population (Figure 8D). This approach is, in principle, ideally suited to test hypotheses about the neural code, because it explicitly aims to overwrite endogenous activity, and so break down all sources of correlation. To crack a neural code, though, it needs to achieve high spatial and temporal precision. Recent optical developments (Bovetti and Fellin, 2015; Emiliani et al., 2015; Grosenick et al., 2015), termed patterned illumination, can deliver light to precise spatial locations (Figure 8D, see also Supplemental Information). When combined with light-sensitive optogenetic actuators, patterned illumination can perturb electrical activity with near cellular resolution (Baker et al., 2016; Carrillo-Reid et al., 2016; Packer et al., 2015; Papagiakoumou et al., 2010; Rickgauer et al., 2014).

Taking full advantage of the intersection framework will depend crucially on further development of improved optogenetics methods to “write” neural activity patterns. Current technologies target simultaneously a few dozen cells with a temporal resolution of few milliseconds (Emiliani et al., 2015). Major areas of future developments include scaling up of the number of stimulated neurons while maintaining single-cell resolution, improving temporal resolution, performing large-scale 3D stimulation, and precisely quantifying tissue photodamage during intervention. In addition, it will, ultimately, be important to imple-

ment these technologies with a closed-loop system (Grosenick et al., 2015), so that intervention can be tied to behavior. This will be useful, among other things, to predict and discount residual effects of endogenous activity (Ahmadian et al., 2011). In fact, both the number of responsive neurons and their functional responses to the sensory stimulus and to the intervention may vary as a function of behavioral variables such as arousal, attention, or locomotion that are reflected in brain states and ongoing neural activity (see also next section Potential Confounds). Coupling functional imaging with optogenetic intervention allows tracking these changes and adapting patterned photostimulation to brain dynamics. Moreover, because patterned illumination requires knowing where the cells to stimulate are, and what pattern to stimulate them with, it will be necessary to combine imaging with patterned photostimulation. Finally, taking full advantage of the intersection approach will require multimodal recording techniques. While electrophysiological recordings have millisecond time resolution, they currently lack the ability to determine accurately where the recorded cells are. Ideally, the best approach is to perform statistical analysis using both electrophysiology and functional imaging in the same area; that way, both high temporal and high spatial resolution could be achieved.

It is important to note that the framework of interventional intersectional information requires knowing precisely which values of the neural response features r_i are elicited by intervention in each trial. This in turn requires measurement of the neural response (r_i) on individual intervention trials. When this is not possible, confounds may arise. For example, in the absence of such measures it would be problematic to rule out a residual correlation between the interventionally elicited neural response and other uncontrolled endogenous brain activity variables that would invalidate the rigor of the causal conclusions, or the elicited activity may be so un-natural (e.g., too synchronized with respect to natural activity patterns) that they may affect in an

un-natural way downstream neural processes. When it is not possible to measure in each trial the elicited neural response, the study should be however accompanied by a rigorous quantification in separate trials or experiments of the precision of manipulated response under various conditions, that is adequate to allow extrapolation to individual trials during the behavioral task and that also characterizes the difference between manipulated and non-manipulated activity.

Potential Confounds: When the Framework May Fail

The result of the intersection framework (and of any experimental approach combining neural recordings and interventional techniques) are potentially confounded by many limitations and factors that must be considered carefully to avoid reaching the wrong conclusions. We have already discussed some of those confounds; in the following we discuss additional ones.

A key requirement for the intersection framework to succeed is that the animal uses the identified stimulus to make choices. This requirement can fail in two important ways. First, in some behaviors, there may be other sensory stimuli that co-vary with the stimuli of interest. In this case, it would be difficult to know which stimulus feature is being used by the animal to drive behavior, a problem exacerbated by the possibility that the stimulus features used by the animal might vary from trial to trial. Second, the animal might have fluctuations in attention, motivation, or arousal, or use non-stimulus features such as reward history, to drive choices. These factors may be present in the two-alternative forced-choice tasks that we discussed in this article, but are likely to be stronger in other task designs, such as go/no go tasks, where our framework could be in principle applied. In all these cases, factors other than the stimulus feature of interest would be involved in driving the animal's choice; that would compromise the proposed framework, since it assumes that the stimulus of interest drives behavior. Such factors can be conceptually formalized by assuming that both the sensory coding and the decision mechanisms may vary across trials, and/or that non-recorded or non-manipulated neurons, may vary across intervention and non-intervention trials (such as r_2 depicted in Figures 4E and 4F when only intervening on feature r_7).

For these reasons, it is important to evaluate whether the variables describing behavior and the non-observed and non-manipulated endogenous variables are in a comparable state during intervention and non-intervention trials. In the presence of variations, a simple strategy could be to down-sample intervention and sensory-evoked trials so that only compatible brain or behavioral states are analyzed. A better solution, however, is to consider tasks in which it is known, based on high behavioral performance and good psychometric curves, that the stimulus feature of interest drives the animal's choice with high reliability. Similarly, the stimulus should be designed so that co-varying stimulus features are avoided. This will probably be easier with simple stimulus sets than with natural stimuli.

Variation of behavior and brain state variables across the experiment, on the other hand, offer an important opportunity to evaluate whether such variables have a "permissive" role on task performance. For example, in the virtual-pole sensation experiment of (O'Connor et al., 2013), the fact that virtual pole perception worked only when the animal whisked suggests a

permissive role of whisker movements for active sensation. A strategy that could take advantage of these variations in state and behavior could be to include (using e.g., simple modeling techniques such as Generalized Linear Models [Park et al., 2014]) behavioral factors such as slow variation across blocks of trials of motivation or reward history or brain states explicitly into the experimenter's sensory coding and decision boundary models. This could potentially lead to explaining the dynamic role of these factors in sensory coding.

Another significant confound can arise for interventional approaches when investigating partly parallel pathways. For example, suppose a behavior is generated by two brain areas that operate in a partly parallel or complementary way, as for example in an "OR" function (Li et al., 2016). In such a case, when inactivating only one area with intervention, one may find little causal effect on behavior. However, interpreting this result as evidence that the inactivated region does not causally contribute much to behavior could be misleading. One way to alleviate these confounds would be to compute both statistical and interventional information intersection. One may use these measures to disambiguate the case in which the two areas contribute complementarily to behavior and so offer complementary intersection information from the case when the two areas operate entirely redundantly and so intersection information from both areas equals intersection information from one area alone. However, accurate interpretation of these measures would require knowledge of the functional anatomy, which, for example, informs the experimenter about the presence or absence of parallel and potentially redundant pathways. Moreover, completeness of activity monitoring and perturbation of the regions involved is also paramount, as this would be, for instance, useful to rule out that a failure to affect behavior by inactivating a region is due to incomplete control of all relevant neurons. We thus anticipate that as approaches move toward understanding larger and larger populations of neurons (Keller and Ahrens, 2015; Sofroniew et al., 2016) and the interconnections between neurons (Lichtman and Denk, 2011), these joint statistical and interventional approaches will become easier to interpret.

Determining the Instructive versus Permissive Role of Neural Codes and Neural Circuit: From Circuit Dissection to Circuit Information Flow

The intersection information framework (both statistical and interventional) has direct application for the dissection of neural circuits underlying behavior. Much work in systems neuroscience has used neurophysiology to identify neural correlates, and, due to recent optogenetics approaches, a wave of new studies has sought to identify which brain regions, cell types, axonal projection pathways, and circuits are required for accurate performance of behavioral tasks (Guo et al., 2014; O'Connor et al., 2013; Peng et al., 2015). It is essential to emphasize that simply measuring the effect of an intervention on choice without regard to stimulus coding precludes understanding a neural circuit's role in task performance. Here we propose that the use of intersection information is crucial to determine whether a neural circuit (or cell type or projection pathway) carries information that is instructive (Otchy et al., 2015) for task performance

(contributes essential information for the task performance that is not provided elsewhere) or if the circuit is permissive for task performance (is required for, or modulates, the behavior but does not provide essential information).

Figures 4A–4D schematizes four cases of different neural circuit architectures in which two neural features, r_1 and r_2 (for example, the activity of neurons in two different brain areas, cell types, or projection pathways), may inform choice. In all four cases, feature r_2 contributes essential information to choice and task performance (r_2 is thus instructive), but the role of r_1 varies. An interventional intersection framework would correctly identify these four circuit architectures. The case of “parallel” information flow (Figure 4A), in which r_1 and r_2 both provide complementary instructive information, could be revealed by finding that the intersection information provided by r_1 and r_2 jointly is larger than that provided by r_1 alone (that is, r_1 and r_2 provide complementary stimulus information to choice). The case of “serial” information flow (Figure 4C), in which r_1 provides instructive information to r_2 and r_2 informs choice, could be discovered by finding that the intersection information provided by r_1 and r_2 jointly equals that provided by r_2 alone. The case in which r_1 provides permissive—but not instructive—information (Figure 4D), could be identified by finding that r_1 carries interventional choice information but not intersection information. Finally, the case when r_1 is not used for choice (Figure 4B) corresponds to the absence of both choice and intersection information in r_1 .

It is important to note that the framework we discussed here is general and can in principle be applied not only to determine how sensory information carried by different codes is used to produce behavior, but it can also be used to study how stimulus information flows across neural populations. For example, the same reasoning expressed above applies to considering a group of brain regions r_1, \dots, r_n (whose activity we can record and manipulate, not necessarily at the same time) and a downstream area c (whose activity we assume we can record at the same time when we manipulate or record r_1, \dots, r_n). In this case, the meaning of intersection information would be that of the amount of information about stimulus s carried by population r_1, \dots, r_n that is transmitted downstream to area c . In essence, we have replaced choice by activity in area c . We could therefore identify the neural response features that influence activity in downstream regions, leading to hypotheses about the mechanisms of information flow in neural circuits.

Ideally, these statistical and causal measures of information flow should be integrated with information about anatomy, response timing, and information dynamics. For example, in the presence of a partly feedforward or hierarchical architecture, anatomy could be used to identify the earliest areas where sensory, choice, and intersection information are developed (Koulakov et al., 2005), and thus better track the computations leading to task performance. Similarly, the timing of stimulus and choice information in neural activity could be used to infer whether, for example, choice signals reflect a neuron’s causal effect on behavioral choice or rather a top-down signal (Nienborg and Cumming, 2009).

Concluding Remarks

We presented a new framework to crack the neural code underlying sensory perception. The framework emphasizes neural

response features that both carry sensory information and lead to appropriate actions, with the emphasis on “appropriate.” These are the neural response features with a large intersection between sensory information and readout. Based on this framework, we provided an initial attempt to formalize statistical ways to identify these features from recordings of neural activity, and to design interventional experiments that can causally test the degree of intersection information. This approach can resolve open debates about the nature of the neural code. Moreover, the ideas we proposed in this framework can guide researchers in the design of experiments, in the design of new statistical tools, and in the development of the new technology, that will lead us to crack the neural code.

SUPPLEMENTAL INFORMATION

Supplemental Information includes Supplemental Experimental Procedures and one figure and can be found with this article online at <http://dx.doi.org/10.1016/j.neuron.2016.12.036>.

ACKNOWLEDGMENTS

We thank the referees for their insightful comments, and members of our laboratories for precious feedback. We are particularly indebted to M.E. Diamond, H. Safaai, D. Chicharro, C. Kayser, and C. Runyan for valuable collaborations on these topics and/or comments on the manuscript. S.P. and E.P. acknowledge the warm hospitality of Harvard Medical School while writing this paper. This work was supported by the Fondation Bertarelli, the European Research Council (ERC, NEURO-PATTERNS), the Flag-Era JTC Human Brain Project (SLOW-DYN), a Burroughs-Wellcome Fund Career Award at the Scientific Interface, the Searle Scholars Program, the New York Stem Cell Foundation, and NIH grants R01-MH107620, R01-NS089521, and U01NS090576. C.D.H. is a New York Stem Cell Foundation Robertson Neuroscience Investigator. Funding for P.E.L. was provided by the Gatsby Charitable Foundation.

REFERENCES

- Ahmadian, Y., Packer, A.M., Yuste, R., and Paninski, L. (2011). Designing optimal stimuli to control neuronal spike timing. *J. Neurophysiol.* *106*, 1038–1053.
- Averbeck, B.B., Latham, P.E., and Pouget, A. (2006). Neural correlations, population coding and computation. *Nat. Rev. Neurosci.* *7*, 358–366.
- Baden, T., Berens, P., Franke, K., Román Rosón, M., Bethge, M., and Euler, T. (2016). The functional diversity of retinal ganglion cells in the mouse. *Nature* *529*, 345–350.
- Baker, C.A., Elyada, Y.M., Parra, A., and Bolton, M.M. (2016). Cellular resolution circuit mapping with temporal-focused excitation of soma-targeted channelrhodopsin. *eLife* *5*, 5.
- Bovetti, S., and Fellin, T. (2015). Optical dissection of brain circuits with patterned illumination through the phase modulation of light. *J. Neurosci. Methods* *247*, 66–77.
- Boyden, E.S., Zhang, F., Bamberg, E., Nagel, G., and Deisseroth, K. (2005). Millisecond-timescale, genetically targeted optical control of neural activity. *Nat. Neurosci.* *8*, 1263–1268.
- Britten, K.H., Newsome, W.T., Shadlen, M.N., Celebri, S., and Movshon, J.A. (1996). A relationship between behavioral choice and the visual responses of neurons in macaque MT. *Vis. Neurosci.* *13*, 87–100.
- Buonomano, D.V., and Maass, W. (2009). State-dependent computations: spatiotemporal processing in cortical networks. *Nat. Rev. Neurosci.* *10*, 113–125.
- Carrillo-Reid, L., Yang, W., Bando, Y., Peterka, D.S., and Yuste, R. (2016). Imprinting and recalling cortical ensembles. *Science* *353*, 691–694.

- Chen, X., Gabbito, M., Peng, Y., Ryba, N.J.P., and Zuker, C.S. (2011). A gustotopic map of taste qualities in the mammalian brain. *Science* 333, 1262–1266.
- Chen, J.L., Carta, S., Soldado-Magraner, J., Schneider, B.L., and Helmchen, F. (2013). Behaviour-dependent recruitment of long-range projection neurons in somatosensory cortex. *Nature* 499, 336–340.
- Cunningham, J.P., and Yu, B.M. (2014). Dimensionality reduction for large-scale neural recordings. *Nat. Neurosci.* 17, 1500–1509.
- Deisseroth, K., and Schnitzer, M.J. (2013). Engineering approaches to illuminating brain structure and dynamics. *Neuron* 80, 568–577.
- Doron, G., von Heimendahl, M., Schlattmann, P., Houweling, A.R., and Brecht, M. (2014). Spiking irregularity and frequency modulate the behavioral report of single-neuron stimulation. *Neuron* 81, 653–663.
- Emiliani, V., Cohen, A.E., Deisseroth, K., and Häusser, M. (2015). All-Optical Interrogation of Neural Circuits. *J. Neurosci.* 35, 13917–13926.
- Engineer, C.T., Perez, C.A., Chen, Y.H., Carraway, R.S., Reed, A.C., Shetake, J.A., Jakkamsetti, V., Chang, K.Q., and Kilgard, M.P. (2008). Cortical activity patterns predict speech discrimination ability. *Nat. Neurosci.* 11, 603–608.
- Grosenick, L., Marshel, J.H., and Deisseroth, K. (2015). Closed-loop and activity-guided optogenetic control. *Neuron* 86, 106–139.
- Guo, Z.V., Li, N., Huber, D., Ophir, E., Gutnisky, D., Ting, J.T., Feng, G., and Svoboda, K. (2014). Flow of cortical activity underlying a tactile decision in mice. *Neuron* 81, 179–194.
- Haefner, R.M., Gerwin, S., Macke, J.H., and Bethge, M. (2013). Inferring decoding strategies from choice probabilities in the presence of correlated variability. *Nat. Neurosci.* 16, 235–242.
- Harvey, C.D., Coen, P., and Tank, D.W. (2012). Choice-specific sequences in parietal cortex during a virtual-navigation decision task. *Nature* 484, 62–68.
- Harvey, M.A., Saal, H.P., Dammann, J.F., 3rd, and Bensmaia, S.J. (2013). Multiplexing stimulus information through rate and temporal codes in primate somatosensory cortex. *PLoS Biol.* 11, e1001558.
- Hernández, A., Náchter, V., Luna, R., Zainos, A., Lemus, L., Alvarez, M., Vázquez, Y., Camarillo, L., and Romo, R. (2010). Decoding a perceptual decision process across cortex. *Neuron* 66, 300–314.
- Histed, M.H., and Maunsell, J.H. (2014). Cortical neural populations can guide behavior by integrating inputs linearly, independent of synchrony. *Proc. Natl. Acad. Sci. USA* 111, E178–E187.
- Houweling, A.R., and Brecht, M. (2008). Behavioural report of single neuron stimulation in somatosensory cortex. *Nature* 451, 65–68.
- Huber, D., Petreanu, L., Ghitani, N., Ranade, S., Hromádka, T., Mainen, Z., and Svoboda, K. (2008). Sparse optical microstimulation in barrel cortex drives learned behaviour in freely moving mice. *Nature* 451, 61–64.
- Jacobs, A.L., Fridman, G., Douglas, R.M., Alam, N.M., Latham, P.E., Prusky, G.T., and Nirenberg, S. (2009). Ruling out and ruling in neural codes. *Proc. Natl. Acad. Sci. USA* 106, 5936–5941.
- Jia, X., Tanabe, S., and Kohn, A. (2013). γ and the coordination of spiking activity in early visual cortex. *Neuron* 77, 762–774.
- Kayser, C., Montemurro, M.A., Logothetis, N.K., and Panzeri, S. (2009). Spike-phase coding boosts and stabilizes information carried by spatial and temporal spike patterns. *Neuron* 61, 597–608.
- Keller, P.J., and Ahrens, M.B. (2015). Visualizing whole-brain activity and development at the single-cell level using light-sheet microscopy. *Neuron* 85, 462–483.
- Koulakov, A.A., Rinberg, D.A., and Tsiganov, D.N. (2005). How to find decision makers in neural networks. *Biol. Cybern.* 93, 447–462.
- Lerner, T.N., Ye, L., and Deisseroth, K. (2016). Communication in Neural Circuits: Tools, Opportunities, and Challenges. *Cell* 164, 1136–1150.
- Li, N., Chen, T.W., Guo, Z.V., Gerfen, C.R., and Svoboda, K. (2015). A motor cortex circuit for motor planning and movement. *Nature* 519, 51–56.
- Li, N., Daie, K., Svoboda, K., and Druckmann, S. (2016). Robust neuronal dynamics in premotor cortex during motor planning. *Nature* 532, 459–464.
- Lichtman, J.W., and Denk, W. (2011). The big and the small: challenges of imaging the brain's circuits. *Science* 334, 618–623.
- Luczak, A., McNaughton, B.L., and Harris, K.D. (2015). Packet-based communication in the cortex. *Nat. Rev. Neurosci.* 16, 745–755.
- Luna, R., Hernández, A., Brody, C.D., and Romo, R. (2005). Neural codes for perceptual discrimination in primary somatosensory cortex. *Nat. Neurosci.* 8, 1210–1219.
- Meister, M.L., Hennig, J.A., and Huk, A.C. (2013). Signal multiplexing and single-neuron computations in lateral intraparietal area during decision-making. *J. Neurosci.* 33, 2254–2267.
- Morcos, A.S., and Harvey, C.D. (2016). History-dependent variability in population dynamics during evidence accumulation in cortex. *Nat. Neurosci.* 19, 1672–1681.
- Newsome, W.T., Britten, K.H., and Movshon, J.A. (1989). Neuronal correlates of a perceptual decision. *Nature* 341, 52–54.
- Nienborg, H., and Cumming, B.G. (2009). Decision-related activity in sensory neurons reflects more than a neuron's causal effect. *Nature* 459, 89–92.
- Nikolić, D., Fries, P., and Singer, W. (2013). Gamma oscillations: precise temporal coordination without a metronome. *Trends Cogn. Sci.* 17, 54–55.
- O'Connor, D.H., Hires, S.A., Guo, Z.V., Li, N., Yu, J., Sun, Q.Q., Huber, D., and Svoboda, K. (2013). Neural coding during active somatosensation revealed using illusory touch. *Nat. Neurosci.* 16, 958–965.
- O'Keefe, J., and Recce, M.L. (1993). Phase relationship between hippocampal place units and the EEG theta rhythm. *Hippocampus* 3, 317–330.
- Otchy, T.M., Wolff, S.B.E., Rhee, J.Y., Pehlevan, C., Kawai, R., Kempf, A., Gobes, S.M.H., and Ölveczky, B.P. (2015). Acute off-target effects of neural circuit manipulations. *Nature* 528, 358–363.
- Packer, A.M., Russell, L.E., Dalgleish, H.W.P., and Häusser, M. (2015). Simultaneous all-optical manipulation and recording of neural circuit activity with cellular resolution in vivo. *Nat. Methods* 12, 140–146.
- Panzeri, S., Brunel, N., Logothetis, N.K., and Kayser, C. (2010). Sensory neural codes using multiplexed temporal scales. *Trends Neurosci.* 33, 111–120.
- Papagiakoumou, E., Anselmi, F., Bègue, A., de Sars, V., Glückstad, J., Isacoff, E.Y., and Emiliani, V. (2010). Scanless two-photon excitation of channelrhodopsin-2. *Nat. Methods* 7, 848–854.
- Park, I.M., Meister, M.L., Huk, A.C., and Pillow, J.W. (2014). Encoding and decoding in parietal cortex during sensorimotor decision-making. *Nat. Neurosci.* 17, 1395–1403.
- Pearl, J. (2009). *Causality* (Cambridge University Press).
- Peng, Y., Gillis-Smith, S., Jin, H., Tränkner, D., Ryba, N.J.P., and Zuker, C.S. (2015). Sweet and bitter taste in the brain of awake behaving animals. *Nature* 527, 512–515.
- Peron, S., and Svoboda, K. (2011). From cudgel to scalpel: toward precise neural control with optogenetics. *Nat. Methods* 8, 30–34.
- Quiñero, R., and Panzeri, S. (2009). Extracting information from neuronal populations: information theory and decoding approaches. *Nat. Rev. Neurosci.* 10, 173–185.
- Reich, D.S., Mechler, F., and Victor, J.D. (2001). Independent and redundant information in nearby cortical neurons. *Science* 294, 2566–2568.
- Rickgauer, J.P., Deisseroth, K., and Tank, D.W. (2014). Simultaneous cellular-resolution optical perturbation and imaging of place cell firing fields. *Nat. Neurosci.* 17, 1816–1824.
- Rigotti, M., Barak, O., Warden, M.R., Wang, X.J., Daw, N.D., Miller, E.K., and Fusi, S. (2013). The importance of mixed selectivity in complex cognitive tasks. *Nature* 497, 585–590.
- Romo, R., and Salinas, E. (2003). Flutter discrimination: neural codes, perception, memory and decision making. *Nat. Rev. Neurosci.* 4, 203–218.

Romo, R., Hernández, A., Zainos, A., and Salinas, E. (1998). Somatosensory discrimination based on cortical microstimulation. *Nature* 392, 387–390.

Salzman, C.D., Britten, K.H., and Newsome, W.T. (1990). Cortical microstimulation influences perceptual judgements of motion direction. *Nature* 346, 174–177.

Shadlen, M.N., Britten, K.H., Newsome, W.T., and Movshon, J.A. (1996). A computational analysis of the relationship between neuronal and behavioral responses to visual motion. *J. Neurosci.* 16, 1486–1510.

Shamir, M. (2014). Emerging principles of population coding: in search for the neural code. *Curr. Opin. Neurobiol.* 25, 140–148.

Shriki, O., Kohn, A., and Shamir, M. (2012). Fast coding of orientation in primary visual cortex. *PLoS Comput. Biol.* 8, e1002536.

Shusterman, R., Smear, M.C., Koulakov, A.A., and Rinberg, D. (2011). Precise olfactory responses tile the sniff cycle. *Nat. Neurosci.* 14, 1039–1044.

Sofroniew, N.J., Flickinger, D., King, J., and Svoboda, K. (2016). A large field of view two-photon mesoscope with subcellular resolution for in vivo imaging. *eLife* 5, 5.

Sternson, S.M., and Roth, B.L. (2014). Chemogenetic tools to interrogate brain functions. *Annu. Rev. Neurosci.* 37, 387–407.

Tehovnik, E.J., Tolias, A.S., Sultan, F., Slocum, W.M., and Logothetis, N.K. (2006). Direct and indirect activation of cortical neurons by electrical microstimulation. *J. Neurophysiol.* 96, 512–521.

Victor, J.D. (2000). How the brain uses time to represent and process visual information(1). *Brain Res.* 886, 33–46.

Victor, J.D., and Nirenberg, S. (2008). Indices for testing neural codes. *Neural Comput.* 20, 2895–2936.

Wilson, N.R., Runyan, C.A., Wang, F.L., and Sur, M. (2012). Division and subtraction by distinct cortical inhibitory networks in vivo. *Nature* 488, 343–348.

Woods, A.J., Antal, A., Bikson, M., Boggio, P.S., Brunoni, A.R., Celnik, P., Cohen, L.G., Fregni, F., Hermann, C.S., Kappenman, E.S., et al. (2016). A technical guide to tDCS, and related non-invasive brain stimulation tools. *Clin. Neurophysiol.* 127, 1031–1048.

Yang, Y., and Zador, A.M. (2012). Differences in sensitivity to neural timing among cortical areas. *J. Neurosci.* 32, 15142–15147.

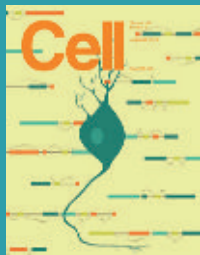
Yang, Y., DeWeese, M.R., Otazu, G.H., and Zador, A.M. (2008). Millisecond-scale differences in neural activity in auditory cortex can drive decisions. *Nat. Neurosci.* 11, 1262–1263.

Zuo, Y., Safaai, H., Notaro, G., Mazzoni, A., Panzeri, S., and Diamond, M.E. (2015). Complementary contributions of spike timing and spike rate to perceptual decisions in rat S1 and S2 cortex. *Curr. Biol.* 25, 357–363.

Introducing
STAR★METHODS

**Empowering methods,
to empower you.**

STAR Methods promote rigor and robustness with an intuitive, consistent framework that integrates seamlessly into the scientific information flow—making reporting easier for the author and replication easier for the reader.



Cell



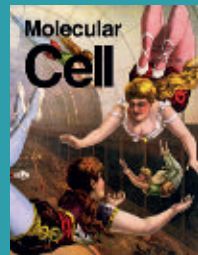
Cell Stem Cell



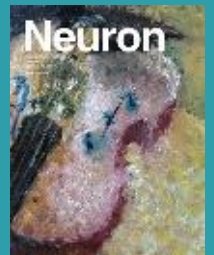
Cell Systems



Developmental Cell



Molecular Cell



Neuron

STAR Methods—a new methods section designed with authors and readers in minds—are now available in Cell Press journals. Learn more about how we're empowering methods.

Visit www.cell.com/star-methods today!

CellPress

Flexible Near-Field Wireless Optoelectronics as Subdermal Implants for Broad Applications in Optogenetics

Gunchul Shin,^{1,17} Adrian M. Gomez,^{2,17} Ream Al-Hasani,^{2,17} Yu Ra Jeong,^{3,17} Jeonghyun Kim,^{1,17} Zhaoqian Xie,^{4,5,17} Anthony Banks,¹ Seung Min Lee,¹ Sang Youn Han,^{1,6} Chul Jong Yoo,⁷ Jong-Lam Lee,⁷ Seung Hee Lee,⁷ Jonas Kurniawan,¹ Jacob Tureb,¹ Zhongzhu Guo,¹ Jangyeol Yoon,¹ Sung-Il Park,⁸ Sang Yun Bang,⁹ Yoonho Nam,¹ Marie C. Walicki,² Vijay K. Samineni,^{2,10} Aaron D. Mickle,^{2,10} Kunhyuk Lee,¹ Seung Yun Heo,¹ Jordan G. McCall,^{2,10} Taisong Pan,¹¹ Liang Wang,¹² Xue Feng,⁵ Tae-il Kim,¹³ Jong Kyu Kim,⁶ Yuhang Li,¹⁴ Yonggang Huang,⁴ Robert W. Gereau IV,^{2,10,15,16} Jeong Sook Ha,^{3,*} Michael R. Bruchas,^{2,10,15,16,18,*} and John A. Rogers^{1,*}

¹Department of Materials Science and Engineering, Frederick Seitz Materials Research Laboratory, University of Illinois at Urbana-Champaign, Urbana, IL 61802, USA

²Division of Basic Research, Department of Anesthesiology, Washington University School of Medicine, St. Louis, MO 63110, USA

³Department of Chemical and Biological Engineering and KU-KIST Graduate School of Converging Science and Technology, Korea University, Seoul 136-701, Republic of Korea

⁴Departments of Civil and Environmental Engineering, Mechanical Engineering, and Materials Science and Engineering, Center for Engineering and Health and Skin Disease Research Center, Northwestern University, Evanston, IL 60208, USA

⁵AML, Department of Engineering Mathematics, Center for Mechanics and Materials, Tsinghua University, Beijing 100084, China

⁶Display Research Center, Samsung Display Co., Yongin, Gyeonggi-do 446-920, Republic of Korea

⁷Department of Materials Science and Engineering, Pohang University of Science & Technology Pohang, Gyeongbuk 790-784, Republic of Korea

⁸Department of Electrical Engineering, Texas A&M University, College Station, TX 77843, USA

⁹Department of Electrical and Computer Engineering, New York University, Brooklyn, NY 11201, USA

¹⁰Washington University Pain Center, Washington University School of Medicine, St. Louis, MO 63110, USA

¹¹State Key Laboratory of Electronic Thin Films and Integrated Devices, University of Electronic Science and Technology of China, Chengdu, Sichuan 610054, People's Republic of China

¹²Institute of Chemical Machinery and Process Equipment, Zhejiang University, Hangzhou 310027, People's Republic of China

¹³School of Chemical Engineering, Sungkyunkwan University, Suwon, Gyeonggi-do 440-746, Republic of Korea

¹⁴Institute of Solid Mechanics, Beihang University, Beijing 100191, China

¹⁵Department of Neuroscience, Washington University School of Medicine, St. Louis, MO 63110, USA

¹⁶Department of Biomedical Engineering, Washington University, St. Louis, MO 63110, USA

¹⁷Co-first author

¹⁸Lead Contact

*Correspondence: jeongsha@korea.ac.kr (J.S.H.), bruchasm@wustl.edu (M.R.B.), jrogers@illinois.edu (J.A.R.)

<http://dx.doi.org/10.1016/j.neuron.2016.12.031>

SUMMARY

In vivo optogenetics provides unique, powerful capabilities in the dissection of neural circuits implicated in neuropsychiatric disorders. Conventional hardware for such studies, however, physically tethers the experimental animal to an external light source, limiting the range of possible experiments. Emerging wireless options offer important capabilities that avoid some of these limitations, but the current size, bulk, weight, and wireless area of coverage is often disadvantageous. Here, we present a simple but powerful setup based on wireless, near-field power transfer and miniaturized, thin, flexible optoelectronic implants, for complete optical control in a variety of behavioral paradigms. The devices combine subdermal magnetic coil antennas connected to microscale, injectable light-emitting diodes (LEDs), with the ability to operate at wavelengths ranging

from UV to blue, green-yellow, and red. An external loop antenna allows robust, straightforward application in a multitude of behavioral apparatuses. The result is a readily mass-producible, user-friendly technology with broad potential for optogenetics applications.

INTRODUCTION

Understanding and controlling the function of the brain is a challenge in modern neuroscience. Techniques in electrical brain stimulation, based on penetrating or surface-mounted electrodes, represent the most traditional means for activating neurons to determine their roles in cognitive function (Campbell et al., 1991; Cogan, 2008; Kozai et al., 2012). Confounding thermal effects, lack of cell-type specificity, the inability to target small numbers of neurons inside electrically conductive tissues, and adverse long-term effects on tissue health are some of the many limitations of these approaches (Aravanis et al., 2007).

Optogenetics avoids these complications through the use of photosensitive ion channels or proteins in genetically modified neurons to allow optical stimulation or inhibition of activity in a highly targeted and controlled fashion (Boyden et al., 2005; Deisseroth, 2011; Fenno et al., 2011; Packer et al., 2013; Siuda et al., 2015a, 2015b; Sparta et al., 2011; Toettcher et al., 2011; Yizhar et al., 2011). This methodology is considered essential for current efforts in neuroscience research largely because of its capabilities for sophisticated functional studies in the central and peripheral nervous systems (Bonin et al., 2016; Boyden et al., 2005; Iyer et al., 2014; Kim et al., 2013; Sparta et al., 2011; Towne et al., 2013). Recent developments in material science and electrical engineering combine this optical control with the use of soft, flexible optoelectronic implants that deliver light directly to regions of interest using ultraminiaturized light-emitting diodes (LEDs), powered and controlled wirelessly (Jeong et al., 2015; Kim et al., 2013; McCall et al., 2013; Park et al., 2015a, 2015b). Such devices enable a range of experiments with untethered, freely behaving animals, in isolation or in social groups, and in simple or elaborate environments. Alternative technologies offer similar capabilities, but in more rigid formats (Montgomery et al., 2015). These wireless platforms bypass the constraints associated with traditional optical fiber interfaces and its external connections; however, even the most advanced wireless systems have drawbacks. These include reliance on: (1) specialized device architectures and unusual combinations of materials that are not easily adapted to mass manufacturing; and (2) wireless operation in radiofrequency (RF) bands that are susceptible to signal reflection, interference and absorption by metallic objects, water features, and other obstructions within or adjacent to the area of interest. As a result, such technologies require expertise in RF electronics for optimized configuration and reliable operation. Options in solar and battery power eliminate some of these disadvantages, but they limit experimental options and add significant weight and bulk (Lee et al., 2015; Park et al., 2015b). In all reported approaches, the accessibility of the implantable devices to the broader community is limited because of the specialized procedures required for their construction.

Here, we demonstrate schemes to circumvent these challenges that leverage ideas associated with recently reported, small-scale, flexible optoelectronic devices that achieve wireless operation by inductive coupling at frequencies (13.56 MHz) (Kim et al., 2015a, 2015b) common to those with near-field communication (NFC) hardware found in commoditized consumer and industrial wireless electronic devices. In particular, we demonstrate that related NFC schemes and miniaturized, flexible wireless receivers can serve as the basis of a versatile technology for optogenetics. Unlike previous wireless systems designed for the UHF (ultrahigh-frequency, 300–3,000 MHz) bands, these inductively coupled antennas operate in the HF (high-frequency, 3–30 MHz) band. These implantable devices, which use the HF band, overcome the limited operational range associated with previously reported systems (Hannan et al., 2014; Harrison et al., 2009). The result enables full wireless coverage across many cage types and environments, with little sensitivity to the presence of objects or physical obstructions, including those environments made of metals or with significant water content.

Reliable operation is, in fact, even possible underwater and/or through metallic cages and/or plates. This level of robustness in function greatly reduces requirements in RF optimization and tuning. In addition to commoditized NFC transmission and control hardware, these implantable components can be mass manufactured in planar geometries using established processes adapted from the flexible printed circuit industry. In addition, the near-field wireless device or system used here can be modified with add-on NFC chips to correspond with sensors or electrodes for additional biological data. Here, we introduce these features in a device that includes ultrathin, injectable needles as supports for microscale inorganic LEDs (μ -ILEDs) (Al-Hasani et al., 2015; Jeong et al., 2015; Kim et al., 2013; McCall et al., 2013; Park et al., 2015a, 2015b; Siuda et al., 2015b; Wu et al., 2015) that implant into targeted regions of the deep brain. An electrically connected sub-system integrates a flexible magnetic loop antenna, rectifier, and indicator LED that mounts sub-dermally on top of the animal's skull, to offer chronic stability (many months) in operation without any observable adverse effects on the animal movement, brain tissue, or general social behavior. Detailed studies of these devices and affiliated external hardware, including demonstrations in vivo for their use in two models of reward-seeking behavior, illustrate key aspects of the technology. The results provide a platform for broad application in studies of freely moving animal behavior within nearly any experimental context.

RESULTS

Designs and Operational Features of Thin, Flexible, Millimeter-Scale Devices for Wireless, Programmed Delivery of Light into Biological Tissues for Optogenetic Experiments

The device incorporates various functional layers (copper metallization), barrier films [parlylene and poly(dimethylsiloxane)], and active components (surface-mounted chips and μ -ILEDs) fabricated on a substrate of polyimide (75 μ m thickness) in an overall planar geometry to facilitate processing by conventional manufacturing techniques. An open architecture allows out-of-plane motion of an injectable needle during manipulation and implantation. This needle incorporates a μ -ILED (270 \times 220 \times 50 μ m) at the tip. Previous studies summarize aspects of the size, shape, and biocompatibility of such needles for deep brain implantation (Al-Hasani et al., 2015; Jeong et al., 2015; Kim et al., 2013; McCall et al., 2013; Park et al., 2015b; Siuda et al., 2015b). The electrical interface consists of a pair of metal lines that pass along a serpentine interconnect trace to allow vertical and horizontal freedom of motion relative to a connected circular coil (9.8 mm diameter, copper traces: 8 turns, 60 μ m width, 18 μ m thickness, and 80 μ m spacing) with surface-mounted chips for power transfer and control via magnetic coupling to a separate RF transmission loop antenna operating at 13.56 MHz (Kim et al., 2015a, 2015b). Here, a capacitor (23 pF) provides impedance matching. A Schottky diode rectifies the received RF signals to yield a current source for the μ -ILEDs.

The system includes two separate LEDs: one with blue emission (470 nm) adjacent to the targeted tissue to serve as the source for optogenetic stimulation; the other with red emission

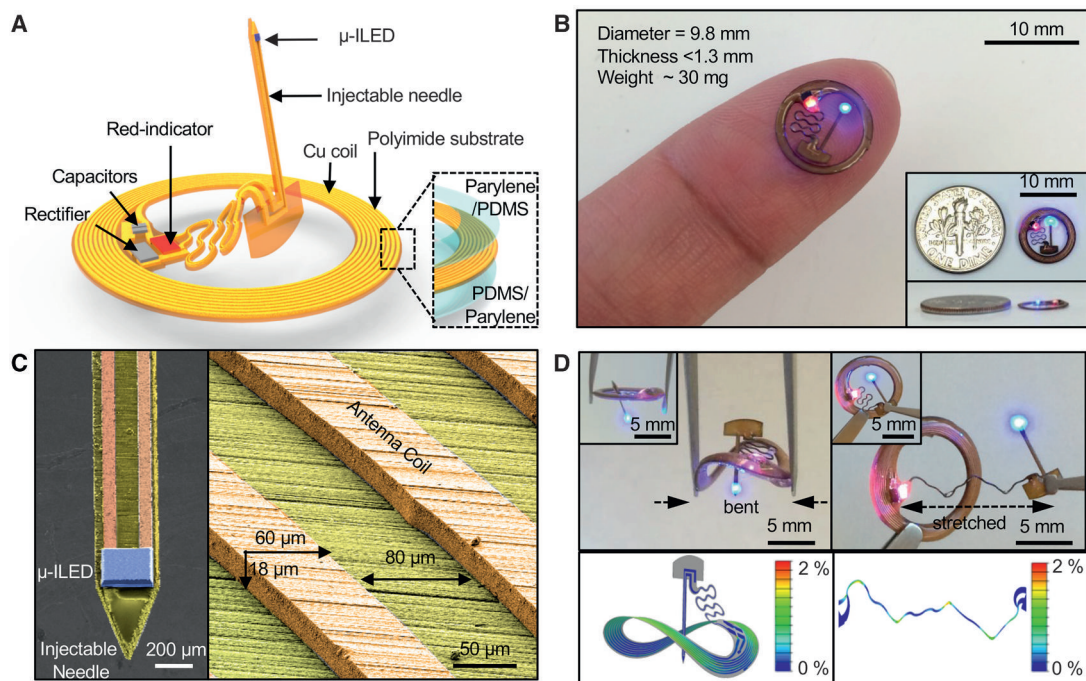


Figure 1. Designs and Operational Features of Thin, Flexible Wireless Optoelectronic Implants for Optogenetic Experiments

(A) Schematic illustration of the overall construction, highlighting a freely adjustable needle with a μ -I-LED at the tip end, connected to a receiver coil with matching capacitors, a rectifier, and a separate μ -I-LED indicator.

(B) Picture of a completed device (diameter \sim 9.8 mm) on top of fingertip and next to a USA dime (diameter, 17.91 mm) (insets) for size comparison.

(C) Scanning electron microscope images of an injectable needle with LED and coil trace with the dimension of $60\ \mu\text{m}$ width, $18\ \mu\text{m}$ thickness, and $80\ \mu\text{m}$ spacing, colorized to highlight the different components (blue: μ -I-LED; yellow: polyimide; orange: copper).

(D) Images and corresponding finite element modeling results of the device before and after bending (left) the body of the device and stretching (right) the serpentine connection to the injectable needle, respectively.

(650 nm) lies just under the skin next to the coil to provide an externally visible signal of system activation, at a wavelength that is essentially invisible to rodents (Conway, 2007; Jacobs et al., 1991, 2007). We refer collectively to this red LED, the coil, and associated components as the body of the device. Additional information about the circuit design and the chip components appears in Figures S1A–S1D. The entire device is depicted next to a USA dime (17.91 mm diameter) to convey a sense of size (Figure 1B) (insets). After encapsulation with a uniform bilayer of parylene ($5\ \mu\text{m}$) and poly(dimethylsiloxane) (PDMS; \sim 0.5–300 μm), the maximum thickness is 1.3 mm (at the location of the chips for the rectifier), similar to that of the dime (1.35 mm); the minimum thickness is 0.5 mm at the position of the coil and associated interconnect wiring. The needle has a total thickness of \sim 80–130 μm and a width of 350 μm (cross-sectional area: \sim 0.028–0.0455 mm^2). These dimensions are comparable with those of conventional optical fiber probes with diameters of 200 μm (cross-sectional area: 0.0314 mm^2). These miniaturized dimensions, the lightweight construction (\sim 30 mg), and the mechanical flexibility represent attractive characteristics as a versatile platform for wireless delivery of light not only into targeted regions of the brain, but also to other organs and tissues. An enlarged image of the μ -I-LED on the tip of the needle (350 μm width) appears in Figure 1C (left). The bottom contact pads of both μ -I-LEDs bond to corresponding copper

features via a solder paste (SMD290SNL250T5; Chip Quik). The colorized SEM image of Figure 1C (right) shows a representative trace of the coil, designed to resonate at 13.56 MHz with a Q factor of \sim 22 and an inductance of \sim 1.8 μH . Figure 1D shows the device bent to a radius of curvature $R = 5\ \text{mm}$ (left column) and with the serpentine trace stretched to 300% (right column), obtained by the finite element analysis (FEA) and experiments, where the color in FEA represents the effective strain. The minimum R of the coil can reach \sim 9 mm, and its maximum stretch can reach \sim 51%, within limits of elastic reversibility (for 0.3% yield strain of copper). For $R = 5\ \text{mm}$ or the serpentine trace stretched to 300%, the maximum effective strain in copper is \sim 2.0%, which is much lower than its fracture strain (\sim 5%).

Electrical, Optical, Mechanical, and Thermal Properties of the Devices

Figure 2 summarizes the essential electrical, optical, mechanical, and thermal properties. The current-voltage response and the optical output power highlight the key operational characteristics, which are all consistent with the requirements for most optogenetic studies. An external loop antenna interface to an RF generator (Feig system; 12 W output power) can wirelessly supply sufficient power for device operation at distances of up to 30 cm. The RF signal can be divided with a multiplexer (ID ISC.ANT.MUX, Feig system) to increase the distance or to operate multiple antennas.

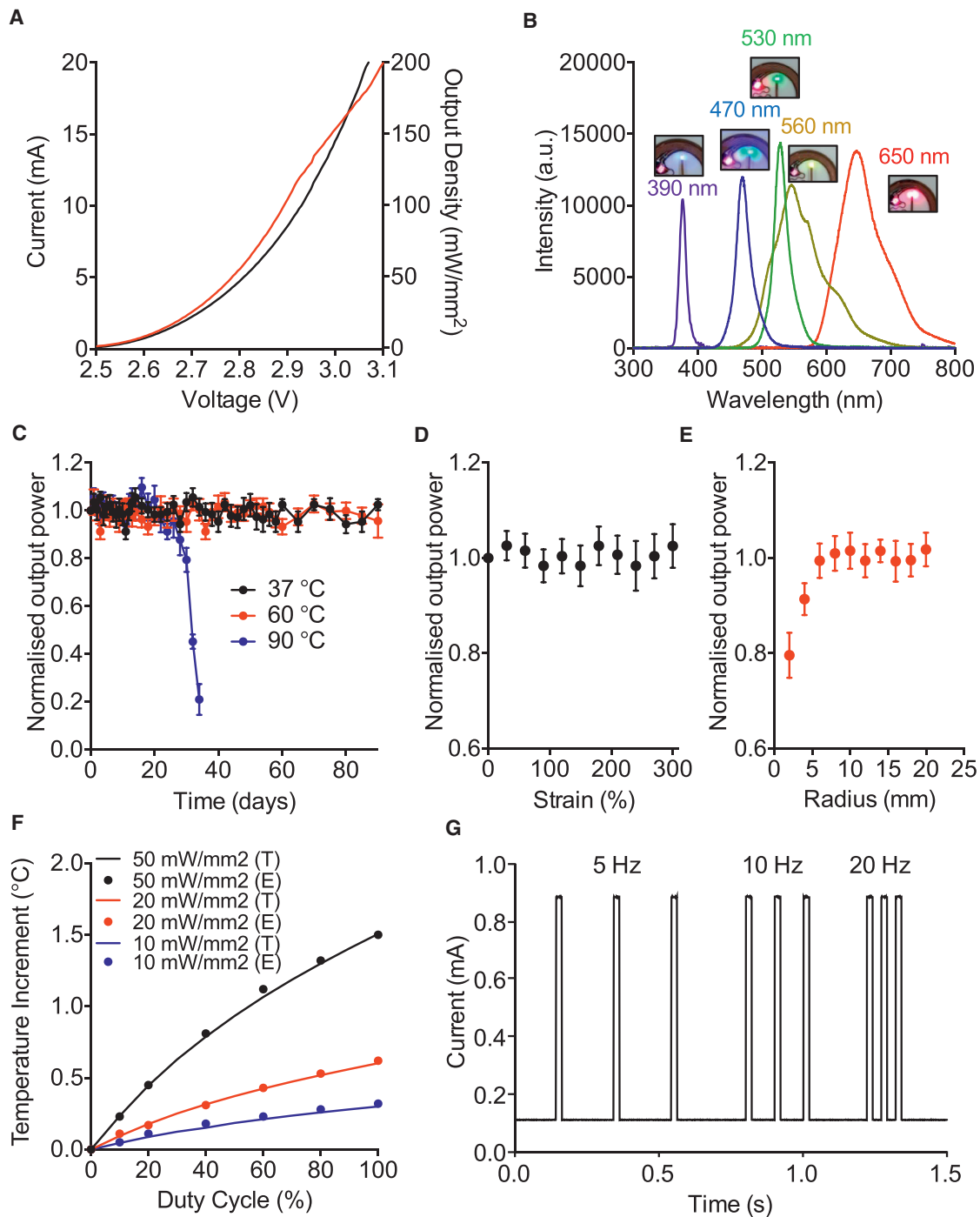


Figure 2. Electrical, Optical, Mechanical, and Thermal Properties

(A) Current-voltage-light output characteristics.

(B) Emission spectra associated with operation of devices built with different μ -ILEDs.

(C) Normalized light optical power as a function time after immersion of devices in warm saline solutions with temperatures of 37°C, 60°C, and 90°C.

(D and E) Normalized light optical as a function (D) of extension of the serpentine interconnect to the injectable needle and (E) of the bending radius of the body of the device, respectively.

(F) Change in temperature adjacent to an operating μ -ILED (T: theoretical, for the case of brain tissue; E: experimental, for the case of a hydrogel) as a function of duty cycle of operation at different peak output powers (10, 20, and 50 mW/mm²).

(G) Current output from a photodiode placed adjacent to a μ -ILED operating at different pulse frequencies (5, 10, and 20 Hz), for a fixed duration of 20 ms. The rise and fall times are \sim 0.1 ms.

The optical output power estimated from the measured current-voltage curve is on the right y axis of Figure 2A. Most optogenetic experiments require powers of $\sim 1\text{--}50\text{ mW/mm}^2$ (Al-Hasani et al., 2015; Aravanis et al., 2007; Boyden et al., 2005; Deisseroth, 2011; Fenno et al., 2011; Jeong et al., 2015; Kim et al., 2013; Montgomery et al., 2015; Park et al., 2015a; Wentz et al., 2011; Yeh et al., 2013; Yizhar et al., 2011), well within the range accessible with these devices, over distances that span the dimensions of most home cage environments and behavioral chambers widely used in small-animal behavior experiments. Optical emission in the UV, blue, green, yellow, and red enables activation of the most popular opsins, including Channelrhodopsin-2 (ChR2) halorhodopsin (eNPHR), and archaerhodopsin (Arch or ArchT), SWTCHR, Opto-XRs, and others (Aravanis et al., 2007; Bonin et al., 2016; Boyden et al., 2005; Deisseroth, 2011; Fenno et al., 2011; Iyer et al., 2014; Kim et al., 2013; Packer et al., 2013; Siuda et al., 2015a, 2015b; Sparta et al., 2011; Toettcher et al., 2011; Towne et al., 2013; Yizhar et al., 2011). This entire wavelength range can be addressed in devices that incorporate appropriate μ -ILEDs, as shown in images and emission spectra in Figure 2B. Fabrication of UV devices (390 nm; $100 \times 100 \times 6\ \mu\text{m}$) exploits previously reported lithographic processes (Kim et al., 2013; McCall et al., 2013). The blue (470 nm; $220 \times 270 \times 50\ \mu\text{m}$) and green (540 nm; $220 \times 270 \times 50\ \mu\text{m}$) devices use commercial μ -ILEDs. The yellow (580 nm; $220 \times 270 \times 50\ \mu\text{m}$) and red (650 nm; $220 \times 270 \times 50\ \mu\text{m}$) devices use yellow and red phosphors (Figures S2A and S2B) coated onto blue μ -ILEDs, respectively.

The encapsulation bilayer of parylene (5 μm)/PDMS ($\sim 0.5\text{--}500\ \mu\text{m}$) extends across all surfaces. Immersion in physiological saline solutions at different temperatures (37°C, 60°C, and 90°C) reveals that these layers provide barrier properties that enable sufficient operational stability. The devices also remain intact, without noticeable degradation of optical power, for at least 90 days at temperatures $<90^\circ\text{C}$ (Figure 2C). Based on Arrhenius scaling, the encapsulated devices are projected to survive up to a year at 37°C in saline solution (Kittel and Kroemer, 1980). Additionally, the optical power is invariant to extension of the serpentine interconnect trace to 300% (Figure 2D) and bending of the coil to a radius of curvature as small as 6 mm (Figure 2E), which is smaller than that of mouse skull ($\sim 7\text{ mm}$) measured with the caudal view of mouse skull (Bab et al., 2007). Detailed modeling results and mechanical characteristics appear in Figure S1. This level of flexibility allows the device to be bent over the curved surface of the skull after injecting the needle into the brain. The device is secured and then the skin is sutured over the device.

Thermal considerations are important to the operation of any active device implanted in the brain or other sensitive biological tissues. Infrared imaging reveals no measurable changes in the temperature across the surfaces of the body of the device, including the coil, the red μ -ILED, the rectifier, and capacitors, during wireless operation of the blue μ -ILED at light output power up to 50 mW/mm^2 in the air (Figures S2C and S2D). Careful measurements of temperature at the surface of the blue μ -ILED (Figure 2F, experimental [E]) as a function of the duty cycle during pulsed operation at three different peak optical powers compare well with those computed using three-dimensional thermal models (Figure 2F, theoretical [T]). Additional modeling results

appear in Figures S2E–S2H. The data indicate only minute increases in temperature ($\sim 0.1^\circ\text{C}$) during operation under typical conditions used for most in vivo applications, e.g., output power of 10 mW/mm^2 and 20 Hz pulsing at a duty cycle of 20%. Here, the RF transmission system that couples to the loop antenna defines the pulsing parameters. Figure 2G shows representative pulse sequences based on square waveforms at various frequencies (5, 10, and 20 Hz), with light output measured using a low-capacitance and high-speed photodiode (PDB-C609-2 Silicon Photodiode; API) placed on top of the operating μ -ILED. The waveforms (controlled via Arduino) have rise and fall times of $<0.1\text{ ms}$.

In addition to the device coil, the transmission loop antenna must be optimized for efficient power transfer. The voltage induced in the receiving coil depends on the distance from the loop and on their relative angular orientations. A single transmission loop with dimensions of $30 \times 30\text{ cm}$ shows uniform in-plane coverage (ratio of output power from the center point > 0.6), although with limited out-of-plane range, such that only 40% of the maximum optical output appears at a vertical distance of 4 cm from the loop (Figure S3B). A double-transmission loop design addresses this limitation. Figure 3A shows a representative configuration, consisting of a double-loop antenna with turns at heights of 4 and 11 cm from the bottom of the animal enclosure. This figure also shows the optical output power, normalized by its value at the center of double-loop antenna (at 3 cm), for a horizontal device at the height of 3, 6, 9, and 12 cm. The power is relatively uniform across the region of interest, with the in-plane ratio of the power to its value at the center (at the same height) >0.6 and out-of-plane ratio (normalized by its value at height 6 cm) >0.8 . Additional experiments for dual loops with spacings of 8, 10, and 13 cm (Figures S3C–S3E) yield reduced uniformity in coverage compared with the 7 cm spacing in Figure 3A.

The power also depends on the orientation of the device with respect to the loop antenna. Figure 3B gives the theoretical (T) and experimental (E) results for the power versus the height at three representative positions (center A; edge B; and corner C) and a wide range of angle from 0° to 80° . Here the power is normalized by its value at the center point (A) with height 3 cm and angle 0° . The normalized power values are $\sim 0.8\text{--}1.5$, $\sim 0.6\text{--}1.4$, $\sim 0.5\text{--}0.9$, and $\sim 0\text{--}0.9$ for angles of 0° , 30° , 60° , and 80° , respectively. The practical significance of these angular variations must be considered in use of these devices for optogenetics experiments. Advanced antennas and RF delivery schemes offer some potential to minimize these effects.

The spatial uniformity can be visualized directly by simultaneous operation of a large collection of devices (13 in this case) placed on a transparent thin substrate inside an enclosure surrounded by a dual-loop antenna ($30 \times 30 \times 15\text{ cm}$), as in Figures 3C–3F. These observations are consistent with those suggested by calculations, and they also illustrate the ability of this system to operate many devices at once, consistent with the expected relationship between the power transfer and the size of the loop antenna (Cannon et al., 2009). Data from such experiments can be captured using a calibrated photodiode to measure the outputs of each μ -ILED. The voltage-output power data, as shown in Figure 2A, yield corresponding operating voltages. At heights of 3, 6, 9, and 12 cm from the bottom, devices at

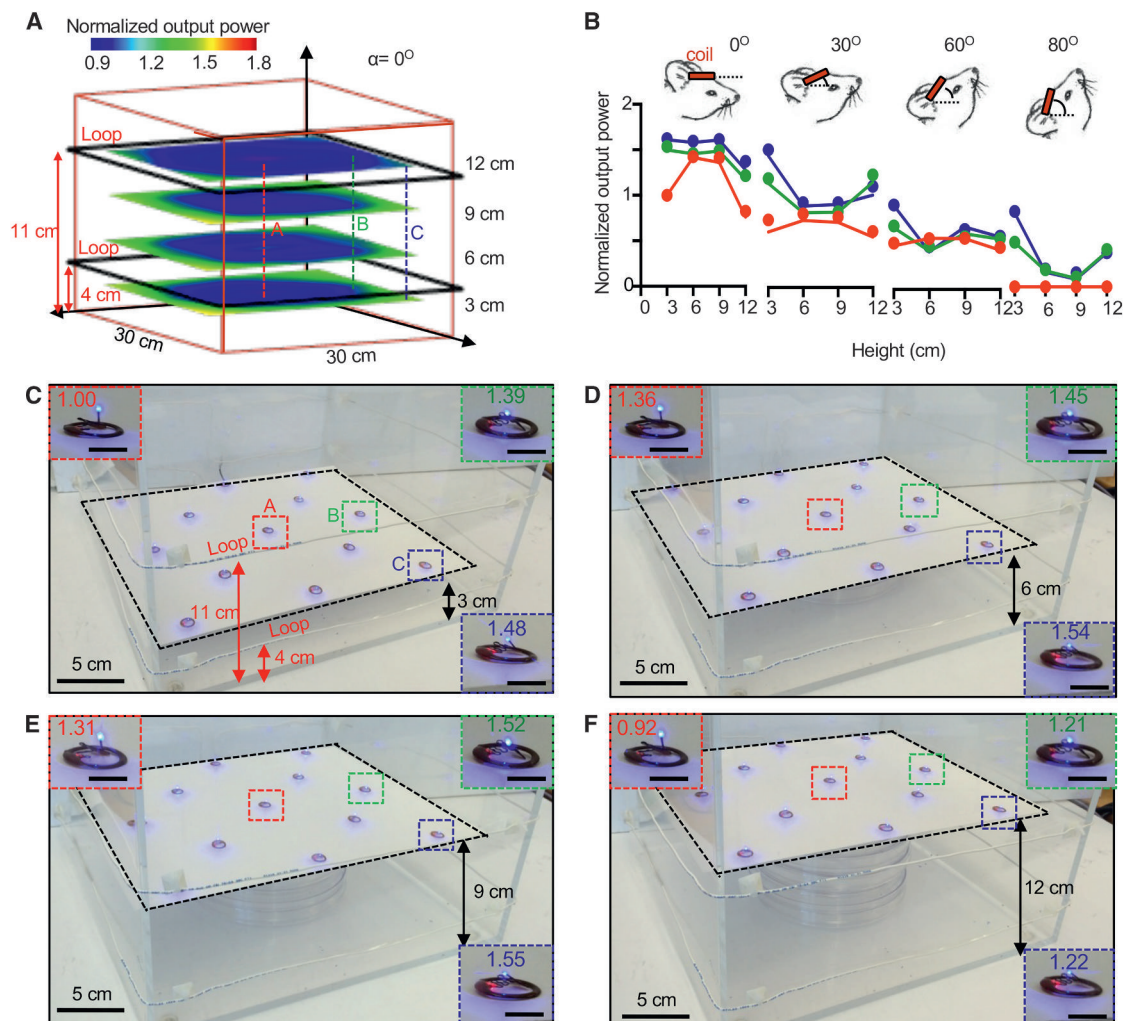


Figure 3. Modeling and Experimental Results for Power Transmission from Loop Antennas with Different Designs

(A) Simulated light output power from a wireless device, as a function of in-plane position at four different heights from the bottom of an enclosure, for the case of a double-loop antenna with turns at heights of 4 and 11 cm.

(B) Theoretical (lines) and experimental (symbols) results for the normalized light output power as a function of height for four different angular orientations between the coil and the loop antennas. The inset cartoons show tilted views of head of the animal.

(C–F) Wireless operation of 13 devices mounted on a thin transparent support, placed at heights of (C) 3, (D) 6, (E) 9, and (F) 12 cm from the bottom. The insets show enlarged images of devices with position of A (red dotted square), B (green dotted square), C (blue dotted square), and normalized light output power.

the same in-plane positions across the enclosure exhibit maximum variations in the output intensity of only 30%.

Surgical Procedure for Device Implantation

Implantation of these devices (Figure 4A) is very similar to implantation of traditional optic fiber ferrules and previous wireless devices (Al-Hasani et al., 2015; Jeong et al., 2015; Kim et al., 2013; McCall et al., 2013; Siuda et al., 2015b). Once the region of interest has been located and a hole drilled through the skull, the device can be lowered using the custom mounting fixture. This fixture holds the needle and the coil, and connects to the arm of a stereotaxic stage from where it can be lowered into the brain (Figures 4B–4F). Once the device has been lowered to the required depth, the needle is secured in place by applying

a small amount of cyanoacrylate gel followed by an accelerant (or approved adhesive, dental cement, etc.). The device can then be released from the fixture by removing the pin (Figure 4G). The coil is then tucked under the skin and can be further secured, although not necessary, with cyanoacrylate gel, and the skin sutured (Figure 4H). These surgeries are substantially faster than the implantation of traditional fiber optics and fully sutured without any open skin so the animals recover faster and experiments can begin 4–5 days post-surgery rather than 7–10 days post-surgery. In addition, these devices have a red LED indicator, which is easily visible through the skin, thereby providing a convenient indicator of operation, which has not been previously possible with any reported implantable optogenetic device (Figure 4I). Figures 4J–4L show an implanted animal at various time

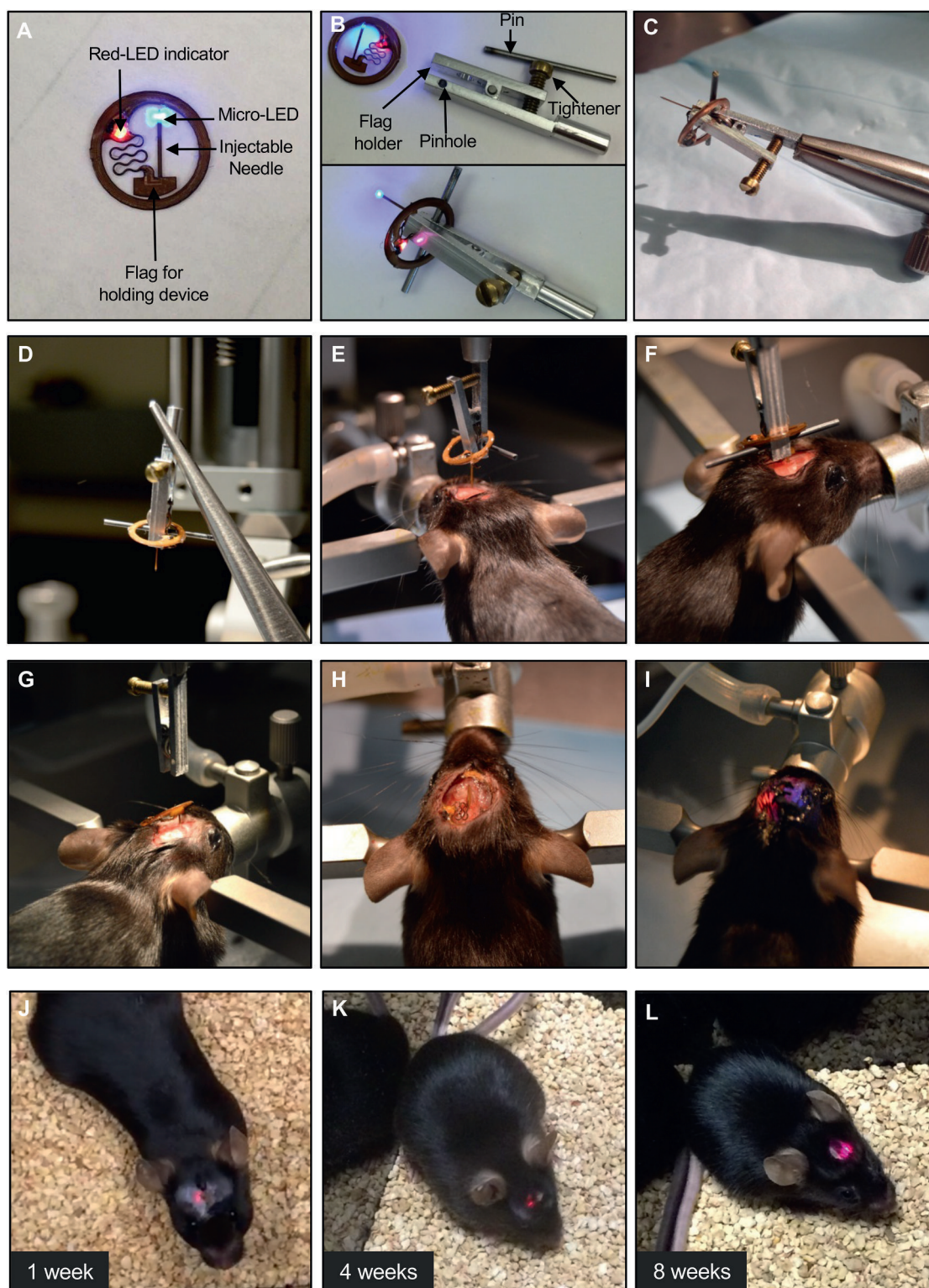


Figure 4. Illustration of Surgical Procedures for Implanting the Device and Recovered Mouse for Operation in the Deep Brain

(A) Representative image of implantable device.
 (B) Images of customized mounting clip and its procedure.
 (C) Image after connecting with stereotaxic arm.

(legend continued on next page)

points after the surgery. Additional images from surgical implantation and data are in Figure S4. In vivo measurements yield qualitatively consistent results. More than 80% (19/23) of successfully implanted devices survived more than 3 months inside the brain and under the skin.

Adaptation and Demonstration of the Devices in Multiple Behavioral Apparatuses

Depending on the dimensions of the animal behavior chamber, double-loop and/or diagonal-loop antennas can increase the volumetric and angular coverage of the near-field wireless coverage (Figure 5). Here, we show wireless operation and robust coverage in multiple representative cages and boxes commonly used for behavioral studies. Conventional fiber-optic approaches or wired hardware cannot be used effectively with enclosed cages (i.e., home cages) or for performing social interaction studies with more than one mouse, because of potential entanglement of the fiber cables or damage to the head stage. Even wireless systems that rely on UHF cannot operate reliably because of their sensitivity to surrounding metal components and/or water pools/reservoirs in or around the cages (Al-Hasani et al., 2015; Kim et al., 2013; Montgomery et al., 2015; Park et al., 2015a; Siuda et al., 2015b; Wentz et al., 2011; Yeh et al., 2013). By contrast, none of these considerations prevents use of the systems we introduce here. In fact, closed-lid home cages with food and water containers are fully compatible, largely independent of materials and structures, suitable for studies of individuals or groups of mice. The home cage shown here has a length of 30 cm, a width of 20 cm, and a height of 20 cm. As in Figure 5A, the loop starts at 4 cm from the bottom of one plane and surrounds the cage twice with 7 cm spacing between these two turns. The right top image of Figure 5B shows that the double loop covers the entire volume, as illustrated by simultaneous operation of 15 devices. Mice with red indicators of operation were able to move with ease freely inside the home cage in the bottom frame of Figure 5B, demonstrating that these devices are highly versatile for use in optogenetics studies.

To demonstrate successful operation in in vivo optogenetic experiments, we characterized the technology in a host of commonly sized animal behavior chambers. In two demonstrations, we optogenetically targeted dopamine projection neurons of the dopaminergic system. This is a commonly targeted pathway and facilitates a combination of behavioral models for testing of dynamic range. Such studies involve a real-time place preference (RTPP) box (2 × 30 × 30 × 30 cm) with a modified double-coil design as shown in Figure 5C. The coils rest under the box at its center region, to eliminate its influence on natural behaviors of freely moving animals within the box. As in Figure 5D, the coil covers the dimensions of 30 cm (length), 30 cm (width), and 15 cm (height), which corresponds to a volume of 13.5 L (13,500 cm³). Mice with working implants appear in the left side of the box in Figure 5D, operated with a modified double-loop antenna. See Movie S1 for real-time operation in the

RTPP box. The Skinner box (Figure 5E), also called an operant conditioning chamber, is widely used for the study and training animals with reward behavior toward various situations and external stimuli. The small, but complex structure of the chamber complicates the operation of wired approaches, specifically with regard to the drug addiction field, where an animal is already tethered to the self-administration line, thus drastically limiting the potential to fully dissect the neural circuitry underlying drug addiction. Additionally, in performing intracranial drug infusions via cannula, one would need two cables, fiber and drug tubing, making these behavioral experiments challenging and difficult to implement. Many metal parts associated with slots on two sides and rod arrays or containers at the bottom can affect the performance and coverage of previously reported wireless systems (Kim et al., 2013; Montgomery et al., 2015; Park et al., 2015a; Wentz et al., 2011; Yeh et al., 2013). In this case, mice often stand and lean on the wall for relatively long times because of the small dimensions of the cage and the functioning parts on the wall. The double-loop antenna around this small cage yields robust coverage inside the box in a manner that also enhances the angular coverage. Figure 5F shows the placement of double coils and the results of evaluations of coverage using nine devices, as well as a freely moving mouse with an implanted device. See Movies S2 and S3 for real-time operation in the operant chamber. The forced swim test (Figure 5G) is another apparatus of interest for behavioral measures of learned helplessness (Porsolt et al., 1977). Here, the animals can swim and/or entirely submerge in the water, with little effect on the performance. A single loop coil around the water tank covers the area up to 4 cm above and below the surface of the water (Figure 5H, top right). Figure S5H shows additional experiments in a large water tank and with submerged devices. Additional cage environments, including those with metal running wheels, can be found in Figure S5.

Wireless Stimulation of Dopaminergic Neurons in the Ventral Tegmental Area or Nucleus Accumbens Promotes Rewarding and Reinforcing Behaviors

To test for the reliable application of these devices in vivo, we targeted the mesolimbic dopaminergic (DA) pathway, a circuit known to facilitate reward and positive reinforcement (Tsai et al., 2009; Witten et al., 2011), by injecting AAV5-DIO-ChR2-eYFP or AAV5-hSyn-FLEX-ChrimsonR-tdTomato into the ventral tegmental area (VTA) of DAT-Cre mice and directing the injectable μ -ILED unilaterally into the nucleus accumbens (NAc) or ventral tegmental area (VTA) (Figure 6A). Both viral approaches were included to demonstrate the feasibility of stimulating different brain regions and the functionality of μ -ILED under different emission (blue and red) spectrums. Characterization of robust ChR2 expression in the VTA and NAc is in Figures 6C and 6D. Here, we demonstrate that within a real-time place preference task, wireless photostimulation (20 Hz, 5 ms pulse width) of DAergic terminals in the NAc, as well as DAergic cell bodies in

(D–F) Images of the surgical steps for (D) holding and (E) positioning the body of the device, and (F) injecting the needle into the deep brain, respectively.

(G and H) Images of mouse (G) after releasing of device from stereotaxic arm and (H) before suturing skin.

(I) Wireless operation of implanted device after suturing the skin.

(J–L) Images of recovered mouse after (J) 1, (K) 4, and (L) 8 weeks from surgery.

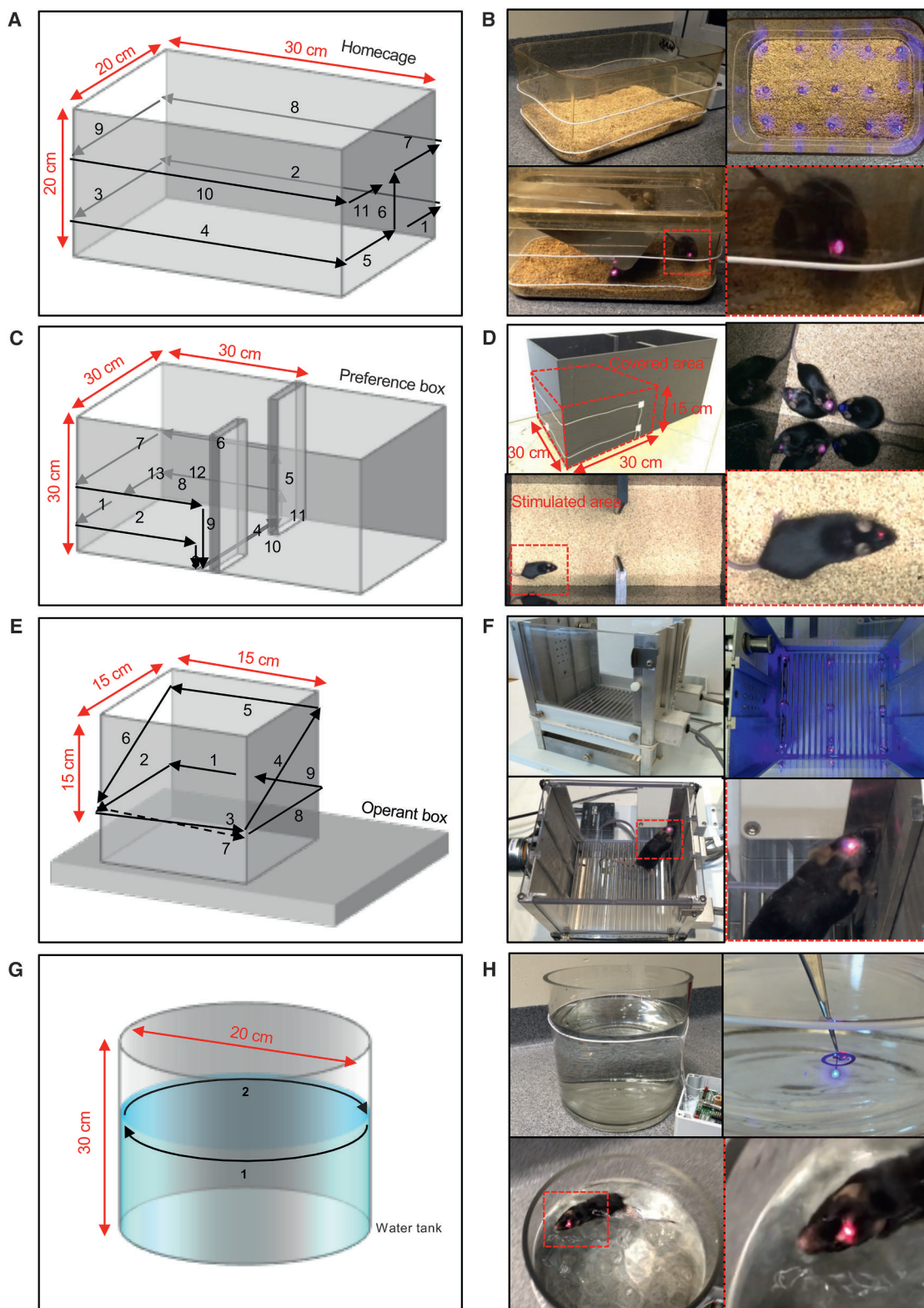


Figure 5. Representative Setup of the Loop Antenna around Various Animal Apparatuses

(A, C, E, and G) The detailed layouts of the loop around a home cage (A), a real-time place preference (RTPP) box (C), an operant conditioning box (E), and a water tank (G).

(legend continued on next page)

the VTA, significantly shifts ChR2- and Chrimson-expressing DAT-Cre mice from no chamber preference to a preference for the stimulation-paired chamber (as measured by time in stimulation side – non-stimulation side and % of time in stimulation side; Figures 6B, 6E, and 6F). There were no observable differences in chamber preference during no stimulation or stimulation test phases in DAT-Cre mice lacking ChR2 or Chrimson (Figures 6B, 6E, and 6G). To further demonstrate the feasibility and application of this novel system, we employed an operant self-stimulation paradigm where the mouse is allowed to trigger μ -ILED stimulations on a fixed-ratio 1 schedule of reinforcement where one nose poke resulted in one photostimulation (Figure 6H). During 7 consecutive days (sessions), both DAT-Cre mice expressing ChR2 and DAT-Cre mice lacking ChR2 were allowed to self-stimulate during 60 min sessions, where a nose poke in the active port resulted in a μ -ILED stimulation (470 nm, 8 mW, 20 Hz, 5 ms pulse width, 1 s burst) of dopaminergic terminals within the NAc, while a nose poke in the inactive port resulted in no stimulation (Figure 6H). ChR2-expressing DAT-Cre mice significantly preferred the active nose poke over the inactive nose poke across seven sessions, as well significantly received more photostimulations than DAT-Cre mice absent of ChR2 expression (Figures 6I–6K). When the stimulation was absent, all DAT-Cre mice expressing ChR2 showed a pronounced decrease in active nose pokes (Figure 6L), further indicating that ChR2-expressing mice were exhibiting photostimulation-maintained responding. Taken together, these *in vivo* assays highlight the ability for wireless spatiotemporal targeting of discrete brain regions for broad application in multiple behavioral contexts with regard to *in vivo* optogenetics.

DISCUSSION

The thin, flexible, and fully implantable wireless optoelectronic technologies reported here have broad applicability across the neuroscience research community. By comparison with alternatives, the robustness of their operation, the scalable methods for their manufacturing, and the relative simplicity of the associated control and power delivery electronics represent key attractive features. The surgical procedures are similar to those used with conventional optical fiber systems (Boyden et al., 2005; Deisseroth, 2011; Fenno et al., 2011; Sparta et al., 2011; Toettcher et al., 2011; Yizhar et al., 2011) and other wireless systems (Al-Hasani et al., 2015; Jeong et al., 2015; Kim et al., 2013; McCall et al., 2013; Siuda et al., 2015b), but with reduced invasiveness associated with implantation. The lightweight, battery-free, sub-dermal nature of this platform also minimizes collisions between bulky head-mounted hardware and various parts of the cage environment (running wheel, food container, lid, and so on) and for avoiding risks that arise from group housing. The sub-dermal configuration allows for long-term functionality as well as simultaneous implantation of the device and the virus during a single surgery rather than two separate surgeries.

With traditional fiber optics, the virus is often injected weeks prior to the fiber optic to allow for viral incubation, while also addressing concerns that the external ferrule may loosen and dislodge the fiber-optic cable.

An associated consequence of the physical form and the bilayer encapsulation scheme is that the devices have exceptional viability, with robust operation consistently for more than 3 months post implantation without performance degradation or any significant immune responses. The near-field coupling scheme, together with the unique optical, electrical, and mechanical characteristics, provide great versatility in all types of optogenetic stimulation and inhibition experiments. Compatibility with a broad range of LEDs (UV, blue, green, yellow, and red), widely controlled optical output powers (~ 0 – 100 mW/mm²), and pulsing parameters with short rise and fall times (< 0.1 ms) support additional options for optogenetic studies using alternate opsins or light-sensitive proteins. Demonstrations in various optogenetic applications with freely moving animals in complex cages, metal surroundings, or also water tanks support these capabilities. Continuous illumination for inhibition may involve challenges in thermal management, perhaps addressable with the addition of copper metallization along the length of the needle to accelerate thermal diffusion away from the μ -ILEDs.

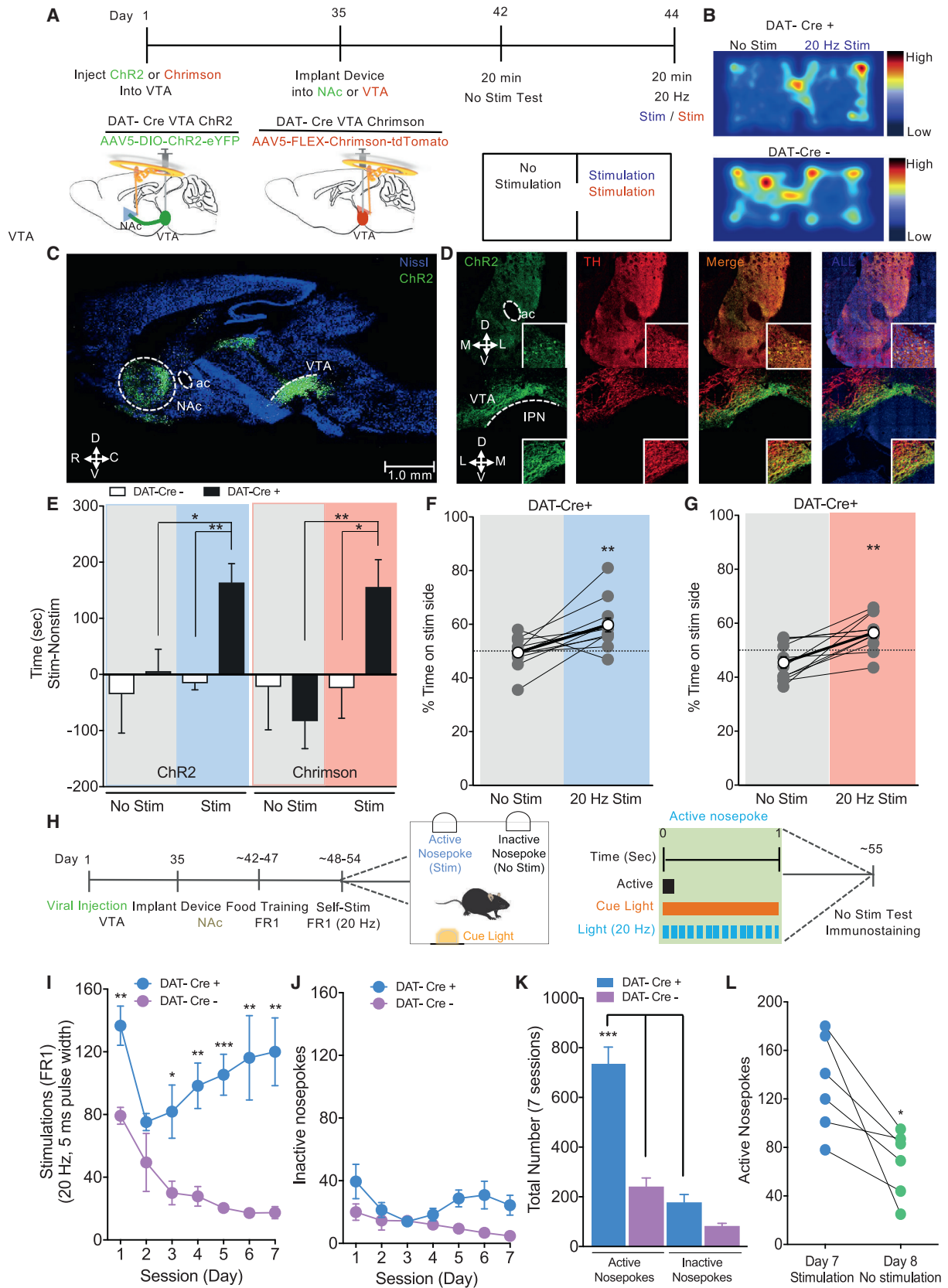
Although the results presented here involve only a single overall device geometry, the designs are easily adaptable for needles with different lengths, matched to targeted regions of the brain, and emerging from different regions of the device relative to the body, potentially to allow bilateral delivery of light in addition to the potential availability to other rodent models (i.e., rats, prairie voles). Advanced versions can be envisioned that involve multiple needle interfaces to a single device body, with single or multiple μ -ILEDs along the length of the shaft. The shapes and the sizes of the antenna coils can also be altered to match the anatomy and the type of animal; larger coils increase the received power, and therefore the operating range beyond the somewhat modest demonstrations reported here. Other alterations will allow application to alternative optogenetic targets, including the spinal cord and sciatic nerve (Montgomery et al., 2015; Park et al., 2015a). Splitter boxes can enable use of a single set of electronics for operation of multiple antennas around multiple cages with different animals, for highly parallel types of experiments or for targeted control of different individual animals within a group. Advanced antenna designs and transmission electronics have the potential to eliminate current limitations associated with angular variations in the received power and to expand the operating range to even larger sizes. Furthermore, the same NFC approach for delivering power to the devices can serve, with advanced electronics, as a wireless capability for data communication. Additionally, with the rapid emergence of sophisticated NFC chips, possibilities such as independent control of multiple μ -ILEDs on a single needle and integration of photodetectors can increase the potential advantages of

(B) Images of the loop and wirelessly operating devices and the corresponding mice with near-field wireless implants in the home cage covered with lid.

(D) Images of double-loop and wirelessly operating devices and corresponding mice with near-field wireless implants in the RTPP box.

(F) Images of mouse with working device in the operant conditioning chamber containing metal components.

(H) Images of water tank with single-loop antenna, working devices under the water, and a swimming mouse that has a working device.



(legend on next page)

these devices. Previously reported, battery-based technologies in wireless drug delivery (Jeong et al., 2015) could also be considered in wireless embodiments. Such types of customized wireless systems (Figures S6A–S6D) in the context of mass-producible device architectures (Figures S6E–S6H) foreshadow widespread use for many purposes in neuroscience research.

STAR★METHODS

Detailed methods are provided in the online version of this paper and include the following:

- KEY RESOURCES TABLE
- CONTACT FOR REAGENT AND RESOURCE SHARING
- EXPERIMENTAL MODEL AND SUBJECT DETAILS
- METHOD DETAILS
 - Fabrication of implants
 - Mechanical modeling
 - The effect of device deformation on the output power
 - Thermal Characteristics
 - Light output power measurements
 - Stereotaxic surgery
 - Real-Time Place Testing (RTPP)
 - Operant Self-Stimulation
 - Immunohistochemistry
- QUANTIFICATION AND STATISTICAL ANALYSIS
- ADDITIONAL RESOURCES

SUPPLEMENTAL INFORMATION

Supplemental Information includes six figures and three movies and can be found with this article online at <http://dx.doi.org/10.1016/j.neuron.2016.12.031>.

AUTHOR CONTRIBUTIONS

Conceptualization, G.S., A.M.G., R.A.-H., J.K., A.B., S.M.L., S.-I.P., J.G.M., R.W.G., M.R.B., and J.A.R.; Methodology, G.S., A.M.G., R.A.-H., Y.R.J., J.K., A.B., J.G.M., T.K., M.R.B., and J.A.R.; Formal Analysis, J.K., Z.X., S.Y.B., K.L., T.P., L.W., X.F., and Y.L.; Investigation, G.S., Y.R.J., A.M.G., R.A.-H.,

J.K., Z.X., J.K., J.T., Z.G., S.Y.H., C.J.Y., J.-L.L., S.H.L., J.Y., Y.N., M.C.W., V.K.S., A.D.M., S.Y.H., and J.K.K.; Writing—Original Draft, G.S., A.M.G., R.A.-H., and Z.X.; Writing—Review & Editing, G.S., A.M.G., R.A.-H., Y.R.J., J.K., Z.X., J.G.M., Y.H., R.W.G., J.S.H., M.R.B., and J.A.R.; Visualization, G.S., A.M.G., R.A.-H., Y.R.J., J.K., and Z.X.; Supervision, J.S.H., R.W.G., M.R.B., and J.A.R.

ACKNOWLEDGMENTS

This work was supported by an NIH Director's Transformative Research Award (NS081707 to J.A.R., R.W.G., and M.R.B.). This work was also supported by the EUREKA Fund (DA037152, DA033396; supplement to A.M.G.) and an K99/R00 Pathway to Independence Award (DA038725 to R.A.-H.). Y.R.J. and J.S.H. were supported by a National Research Foundation of Korea (NRF) grant funded by the Korean government (MEST) (grant NRF-2016R1A2A1A05004935), and J.S.H. also thanks the KU-KIST graduate school program of Korea University. Z.X. and X.F. acknowledge support from the National Basic Research Program of China (grant 2015CB351900) and the National Natural Science Foundation of China (grants 11402134 and 11320101001). Y.H. acknowledges the support from NSF (grants DMR-1121262, CMMI-1300846, and CMMI-1400169) and the NIH (grant R01EB019337). A.D.M. was supported by a McDonnell Center for Cellular and Molecular Neurobiology Postdoctoral Fellowship, and V.K.S. was supported by the Indian American Urological Association/Kailash Kedia, MD Research Scholar Fund. We would also like to thank Karl Deisseroth (Stanford) for sharing ChR2 with us, and Ed Boyden (MIT) for Chrimson with us.

Received: May 16, 2016

Revised: November 3, 2016

Accepted: December 19, 2016

Published: January 26, 2017

REFERENCES

- Al-Hasani, R., McCall, J.G., Foshage, A.M., and Bruchas, M.R. (2013). Locus coeruleus kappa-opioid receptors modulate reinstatement of cocaine place preference through a noradrenergic mechanism. *Neuropsychopharmacology*, 38, 2484–2497.
- Al-Hasani, R., McCall, J.G., Shin, G., Gomez, A.M., Schmitz, G.P., Bernardi, J.M., Pyo, C.-O., Park, S.I., Marcinkiewicz, C.M., Crowley, N.A., et al. (2015). Distinct subpopulations of nucleus accumbens dynorphin neurons drive aversion and reward. *Neuron* 87, 1063–1077.
- Aravanis, A.M., Wang, L.-P., Zhang, F., Meltzer, L.A., Mogri, M.Z., Schneider, M.B., and Deisseroth, K. (2007). An optical neural interface: in vivo control of

Figure 6. Wireless Control of Mesolimbic Reward Circuitry

(A) Cartoon depicting unilateral ChR2 or Chrimson viral injection and near-field wireless device implantation. Timeline outlining real-time place preference behavioral testing.

(B) Heatmaps showing real-time mouse behavior following 20 Hz photostimulation of mice expressing ChR2 in the NAc of DAT-Cre⁺ and DAT-Cre⁻.

(C) Sagittal section highlighting ChR2 viral injection within the ventral tegmental area (VTA) and the targeted projection area of the nucleus accumbens (NAc).

(D) Corresponding coronal sections highlighting ChR2 viral expression within the VTA and NAc. Representative immunohistochemistry showing coronal sections of the NAc and VTA. All images show Nissl (blue), ChR2 (green), and tyrosine hydroxylase (TH, red) staining.

(E) Photostimulation of the NAc in DAT-Cre mice expressing ChR2 or Chrimson increases time spent in stimulation side as measured by stimulation side minus non-stimulation side, compared to DAT-Cre mice absent of ChR2 or Chrimson.

(F and G) DAT-Cre mice expressing ChR2 (F) or Chrimson (G) have increased percent time spent on the stimulation side. Data are represented as mean ± SEM; n = 12 (DAT-Cre⁺) and n = 5 (DAT-Cre⁻) for ChR2; n = 11 (DAT-Cre⁺) and n = 8 (DAT-Cre⁻) for Chrimson.

(H) Timeline outlining operant self-stimulation behavioral testing. Schematic depicting operant box paradigm where an active nose poke results in a 1 s, 20 Hz photostimulation accompanied by a cue light, and an inactive nose poke results in no consequence.

(I and J) DAT-Cre mice expressing ChR2 developed a strong preference for the (I) active nose poke (20 Hz photostimulation) over 7 days in comparison with the (J) inactive nose poke or in comparison with DAT-Cre mice lacking ChR2 expression (one-way repeated-measures ANOVA, main effect of nose poke; main effect on stimulation, Tukey post hoc tests, *p < 0.05, **p < 0.01, ***p < 0.001).

(K) Data showing total number of active and inactive nose pokes in DAT-Cre⁺ and DAT-Cre⁻ mice across 7 days of operant self-stimulation (two-way ANOVA, main effect of nose poke, main effect on cre condition, Bonferroni post hoc tests, ***p < 0.001).

(L) On day 8, ChR2-expressing mice were allowed to nose poke in the absence of photostimulation. All mice showed a reduction in number of active nose pokes in the absence of photostimulation. Data are represented as mean ± SEM; n = 6 (DAT-Cre⁺) and n = 5 (DAT-Cre⁻). *p < 0.05, Student's t test, day 7 stim versus day 8 no stim among DAT-Cre⁺ mice.

- rodent motor cortex with integrated fiberoptic and optogenetic technology. *J. Neural Eng.* 4, S143–S156.
- Bab, I.A., Hajbi-Yonissi, C., Gabet, Y., and Muller, R. (2007). *Micro-tomographic Atlas of the Mouse Skeleton* (Springer Science & Business Media Press).
- Bonin, R.P., Wang, F., Desrochers-Couture, M., Ga Secka, A., Boulanger, M.-E., Côté, D.C., and De Koninck, Y. (2016). Epidural optogenetics for controlled analgesia. *Mol. Pain* 12, 1–11.
- Boyden, E.S., Zhang, F., Bamberg, E., Nagel, G., and Deisseroth, K. (2005). Millisecond-timescale, genetically targeted optical control of neural activity. *Nat. Neurosci.* 8, 1263–1268.
- Campbell, P.K., Jones, K.E., Huber, R.J., Horch, K.W., and Normann, R.A. (1991). A silicon-based, three-dimensional neural interface: manufacturing processes for an intracortical electrode array. *IEEE Trans. Biomed. Eng.* 38, 758–768.
- Cannon, B.L., Hoberg, J.F., Stancil, D.D., and Goldstein, S.C. (2009). Magnetic resonant coupling as a potential means for wireless power transfer to multiple small receivers. *IEEE Trans. Power Electron.* 24, 1819–1825.
- Cogan, S.F. (2008). Neural stimulation and recording electrodes. *Annu. Rev. Biomed. Eng.* 10, 275–309.
- Conway, B.R. (2007). Color vision: mice see hue too. *Curr. Biol.* 17, R457–R460.
- Deisseroth, K. (2011). Optogenetics. *Nat. Methods* 8, 26–29.
- Fenno, L., Yizhar, O., and Deisseroth, K. (2011). The development and application of optogenetics. *Annu. Rev. Neurosci.* 34, 389–412.
- Hannan, M.A., Mutashar, S., Samad, S.A., and Hussain, A. (2014). Energy harvesting for the implantable biomedical devices: issues and challenges. *Biomed. Eng. Online* 13, 79.
- Harrison, R.R., Kier, R.J., Chestek, C.A., Gilja, V., Nuyujukian, P., Ryu, S., Greger, B., Solzbacher, F., and Shenoy, K.V. (2009). Wireless neural recording with single low-power integrated circuit. *IEEE Trans. Neural Syst. Rehabil. Eng.* 17, 322–329.
- Iyer, S.M., Montgomery, K.L., Towne, C., Lee, S.Y., Ramakrishnan, C., Deisseroth, K., and Delp, S.L. (2014). Virally mediated optogenetic excitation and inhibition of pain in freely moving nontransgenic mice. *Nat. Biotechnol.* 32, 274–278.
- Jacobs, G.H., Neitz, J., and Deegan, J.F., 2nd (1991). Retinal receptors in rodents maximally sensitive to ultraviolet light. *Nature* 353, 655–656.
- Jacobs, G.H., Williams, G.A., Cahill, H., and Nathans, J. (2007). Emergence of novel color vision in mice engineered to express a human cone photopigment. *Science* 315, 1723–1725.
- Jeong, J.-W., McCall, J.G., Shin, G., Zhang, Y., Al-Hasani, R., Kim, M., Li, S., Sim, J.Y., Jang, K.-I., Shi, Y., et al. (2015). Wireless optofluidic systems for programmable in vivo pharmacology and optogenetics. *Cell* 162, 662–674.
- Kim, T.I., McCall, J.G., Jung, Y.H., Huang, X., Siuda, E.R., Li, Y., Song, J., Song, Y.M., Pao, H.A., Kim, R.-H., et al. (2013). Injectable, cellular-scale optoelectronics with applications for wireless optogenetics. *Science* 340, 211–216.
- Kim, J., Banks, A., Cheng, H., Xie, Z., Xu, S., Jang, K.-I., Lee, J.W., Liu, Z., Gutruf, P., Huang, X., et al. (2015a). Epidermal electronics with advanced capabilities in near-field communication. *Small* 11, 906–912.
- Kim, J., Banks, A., Xie, Z., Heo, S.Y., Gutruf, P., Lee, J.W., Xu, S., Jang, K.-I., Liu, F., Brown, G., et al. (2015b). Miniaturized flexible electronic systems with wireless power and near-field communication capabilities. *Adv. Funct. Mater.* 25, 4761–4767.
- Kittel, C., and Kroemer, H. (1980). *Thermal Physics*, Second Edition (Macmillan Press).
- Kozai, T.D., Langhals, N.B., Patel, P.R., Deng, X., Zhang, H., Smith, K.L., Lahann, J., Kotov, N.A., and Kipke, D.R. (2012). Ultrasmall implantable composite microelectrodes with bioactive surfaces for chronic neural interfaces. *Nat. Mater.* 11, 1065–1073.
- Lee, S.T., Williams, P.A., Braine, C.E., Lin, D.-T., John, S.W.M., and Irazoqui, P.P. (2015). A miniature, fiber-coupled, wireless, deep-brain optogenetic stimulator. *IEEE Trans. Neural Syst. Rehabil. Eng.* 23, 655–664.
- McCall, J.G., Kim, T.I., Shin, G., Huang, X., Jung, Y.H., Al-Hasani, R., Omenetto, F.G., Bruchas, M.R., and Rogers, J.A. (2013). Fabrication and application of flexible, multimodal light-emitting devices for wireless optogenetics. *Nat. Protoc.* 8, 2413–2428.
- McCall, J.G., Al-Hasani, R., Siuda, E.R., Hong, D.Y., Norris, A.J., Ford, C.P., and Bruchas, M.R. (2015). CRH engagement of the locus coeruleus noradrenergic system mediates stress-induced anxiety. *Neuron* 87, 605–620.
- Montgomery, K.L., Yeh, A.J., Ho, J.S., Tsao, V., Mohan Iyer, S., Grosenick, L., Ferenczi, E.A., Tanabe, Y., Deisseroth, K., Delp, S.L., and Poon, A.S. (2015). Wirelessly powered, fully internal optogenetics for brain, spinal and peripheral circuits in mice. *Nat. Methods* 12, 969–974.
- Packer, A.M., Roska, B., and Häusser, M. (2013). Targeting neurons and photons for optogenetics. *Nat. Neurosci.* 16, 805–815.
- Park, S.-I., Brenner, D.S., Shin, G., Morgan, C.D., Copits, B.A., Chung, H.U., Pullen, M.Y., Noh, K.N., Davidson, S., Oh, S.J., et al. (2015a). Soft, stretchable, fully implantable miniaturized optoelectronic systems for wireless optogenetics. *Nat. Biotechnol.* 33, 1280–1286.
- Park, S.I., Shin, G., Banks, A., McCall, J.G., Siuda, E.R., Schmidt, M.J., Chung, H.U., Noh, K.N., Mun, J.G., Rhodes, J., et al. (2015b). Ultraminiaturized photovoltaic and radio frequency powered optoelectronic systems for wireless optogenetics. *J. Neural Eng.* 12, 056002.
- Porsolt, R.D., Bertin, A., and Jalfre, M. (1977). Behavioral despair in mice: a primary screening test for antidepressants. *Arch. Int. Pharmacodyn. Ther.* 229, 327–336.
- Siuda, E.R., Copits, B.A., Schmidt, M.J., Baird, M.A., Al-Hasani, R., Planer, W.J., Funderburk, S.C., McCall, J.G., Gereau, R.W., 4th, and Bruchas, M.R. (2015a). Spatiotemporal control of opioid signaling and behavior. *Neuron* 86, 923–935.
- Siuda, E.R., McCall, J.G., Al-Hasani, R., Shin, G., Park, S., Schmidt, M.J., Anderson, S.L., Planer, W.J., Rogers, J.A., and Bruchas, M.R. (2015b). Optodynamic simulation of β -adrenergic receptor signalling. *Nat. Commun.* 6, 8480.
- Sparta, D.R., Stamatakis, A.M., Phillips, J.L., Hovelsø, N., van Zessen, R., and Stuber, G.D. (2011). Construction of implantable optical fibers for long-term optogenetic manipulation of neural circuits. *Nat. Protoc.* 7, 12–23.
- Toettcher, J.E., Voigt, C.A., Weiner, O.D., and Lim, W.A. (2011). The promise of optogenetics in cell biology: interrogating molecular circuits in space and time. *Nat. Methods* 8, 35–38.
- Towne, C., Montgomery, K.L., Iyer, S.M., Deisseroth, K., and Delp, S.L. (2013). Optogenetic control of targeted peripheral axons in freely moving animals. *PLoS ONE* 8, e72691.
- Tsai, H.-C., Zhang, F., Adamantidis, A., Stuber, G.D., Bonci, A., de Lecea, L., and Deisseroth, K. (2009). Phasic firing in dopaminergic neurons is sufficient for behavioral conditioning. *Science* 324, 1080–1084.
- Wentz, C.T., Bernstein, J.G., Monahan, P., Guerra, A., Rodriguez, A., and Boyden, E.S. (2011). A wirelessly powered and controlled device for optical neural control of freely-behaving animals. *J. Neural Eng.* 8, 046021.
- Witten, I.B., Steinberg, E.E., Lee, S.Y., Davidson, T.J., Zalocusky, K.A., Brodsky, M., Yizhar, O., Cho, S.L., Gong, S., Ramakrishnan, C., et al. (2011). Recombinase-driver rat lines: tools, techniques, and optogenetic application to dopamine-mediated reinforcement. *Neuron* 72, 721–733.
- Wu, F., Stark, E., Ku, P.-C., Wise, K.D., Buzsáki, G., and Yoon, E. (2015). Monolithically integrated μ LEDs on silicon neural probes for high-resolution optogenetic studies in behaving animals. *Neuron* 88, 1136–1148.
- Yeh, A.J., Ho, J.S., Tanabe, Y., Neofytou, E., Beygui, R.E., and Poon, A.S. (2013). Wirelessly powering miniature implants for optogenetic stimulation. *Appl. Phys. Lett.* 103, 163701.
- Yizhar, O., Fenno, L.E., Davidson, T.J., Mogri, M., and Deisseroth, K. (2011). Optogenetics in neural systems. *Neuron* 71, 9–34.

A person with dark hair, wearing a light blue shirt and grey pants, is sitting on a bed with white linens. They are holding a white mug of coffee in their left hand and looking at a silver laptop in front of them. The laptop screen displays a colorful, abstract pattern. A smartphone is lying on the bed next to the laptop.

OUR NETWORK IS YOUR NETWORK

With Cell Press Webinars, our network is your network!

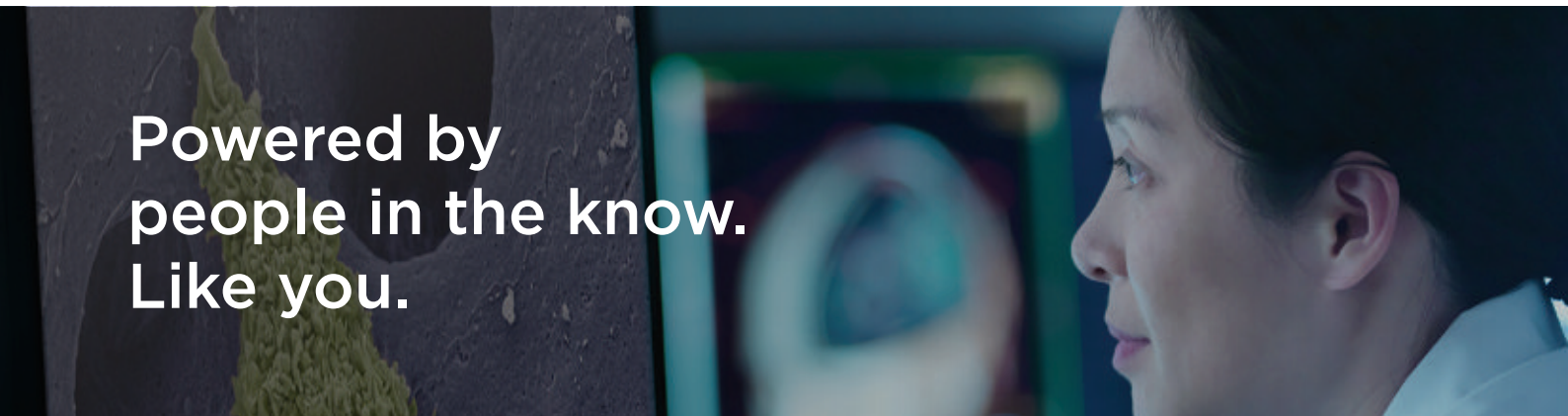
Cell Press Webinars give you access to hot topics in emerging research and the application of new technology.

Watch essential, need-to-know webcasts via live streaming or on demand from the comfort and convenience of your office, lab, or home.

Need-to-know topics, editorially curated

World-class presenters, experts in their field

Moderated by Cell Press editors

A woman with dark hair, wearing a light blue lab coat, is shown in profile, looking intently at a computer screen. The background is a laboratory setting with various pieces of equipment and a blue light source.

Powered by
people in the know.
Like you.

Tap into our network today!
Visit www.cell.com/webinars

CellPress
Webinars

High-Throughput Mapping of Single-Neuron Projections by Sequencing of Barcoded RNA

Justus M. Kechschull,^{1,2} Pedro Garcia da Silva,^{2,3} Ashlan P. Reid,² Ian D. Peikon,^{1,2} Dinu F. Albeanu,² and Anthony M. Zador^{2,*}

¹Watson School of Biological Sciences, Cold Spring Harbor, NY 11724, USA

²Cold Spring Harbor Laboratory, Cold Spring Harbor, NY 11724, USA

³Champalimaud Centre for the Unknown, 1400-038 Lisbon, Portugal

*Correspondence: zador@cshl.edu

<http://dx.doi.org/10.1016/j.neuron.2016.07.036>

SUMMARY

Neurons transmit information to distant brain regions via long-range axonal projections. In the mouse, area-to-area connections have only been systematically mapped using bulk labeling techniques, which obscure the diverse projections of intermingled single neurons. Here we describe MAPseq (Multiplexed Analysis of Projections by Sequencing), a technique that can map the projections of thousands or even millions of single neurons by labeling large sets of neurons with random RNA sequences (“barcodes”). Axons are filled with barcode mRNA, each putative projection area is dissected, and the barcode mRNA is extracted and sequenced. Applying MAPseq to the locus coeruleus (LC), we find that individual LC neurons have preferred cortical targets. By recasting neuroanatomy, which is traditionally viewed as a problem of microscopy, as a problem of sequencing, MAPseq harnesses advances in sequencing technology to permit high-throughput interrogation of brain circuits.

INTRODUCTION

Neurons transmit information to distant brain regions via long-range axonal projections. In some cases, functionally distinct populations of neurons are intermingled within a small region. For example, nearby hypothalamic nuclei regulate basic drives including appetite, aggression, and sexual attraction (Kennedy et al., 2014; Sternson, 2013), and neurons from these nuclei project to distinct targets. In visual cortical area V1, responses to visual stimuli are matched to the properties of the higher visual areas to which the neurons project (Glickfeld et al., 2013; Movshon and Newsome, 1996). Findings such as these suggest that the information transmitted by individual neurons may be tailored to their targets. Such selective routing of information requires an anatomical substrate, but there is currently no high-throughput method for determining the diverse projection patterns of individual neurons.

At present, there is a steep tradeoff between throughput and resolution in anatomical approaches to mapping long-range connections. In conventional anterograde brain mapping studies, a fluorescent or enzymatic label is used to enable visualization of cell bodies and distal projections by light microscopy. Bulk techniques query the projections of many neurons labeled at a single injection site and thus sample the aggregate architecture of an entire neuronal population. There have been several large-scale efforts, including the Allen Brain Projection Atlas (Oh et al., 2014) and the iConnectome (Zingg et al., 2014), to systematically map mesoscopic connectivity. Although fast, such bulk methods obscure the diversity of the many projection neurons labeled in any one experiment. Consider, for example, a single source area that projects to three downstream areas (Figure 1A). This projection pattern enables neurons in the source area to send information to the three downstream areas. However, identical bulk projection patterns could arise in multiple ways: (1) from a one-to-one architecture, in which each neuron targets only a single downstream area (left); (2) from an all-to-all architecture, in which each neuron targets every downstream area (middle); or (3) from a host of more complicated architectures (right). With conventional bulk labeling, these three projection patterns, which have different functional implications, are indistinguishable without further experimentation.

Several alternative methods have been developed to complement conventional anterograde bulk labeling approaches. For example, genetically defined subpopulations of neurons within an area can be targeted by expressing a marker such as Cre recombinase (Gong et al., 2007; Harris et al., 2014; Huang, 2014). Similarly, subpopulations can be defined using retrograde (Lima et al., 2009; Oyibo et al., 2014; Wickersham et al., 2007a) or transsynaptic viruses (DeFalco et al., 2001; Wickersham et al., 2007b). However, because such approaches rely on positing defined subpopulations, they cannot easily be used to screen for the myriad possible complex projection patterns neurons might exhibit.

The most general and unbiased approach to distinguishing among the architectures in Figure 1A relies on single-neuron anterograde tracing. Current methods for achieving single-neuron resolution require individually labeling one or, at most, a few cells per brain (Economo et al., 2016), a labor-intensive approach that affords high resolution at the cost of low throughput. Although single-neuron tracing can be multiplexed by labeling individual neurons with different colored fluorophores (Ghosh et al., 2011; Livet et al., 2007), in practice the extent of

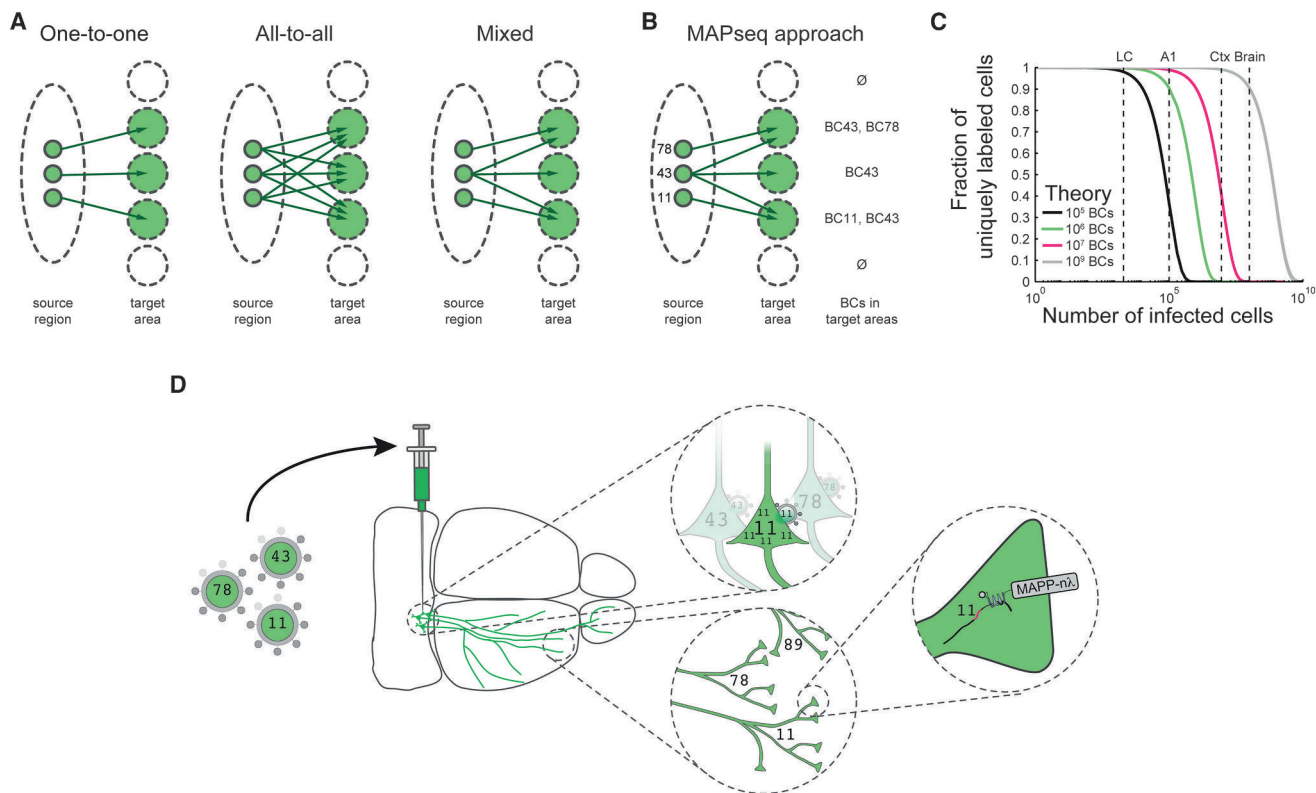


Figure 1. Barcoding Allows High-Throughput Single-Neuron Tracing

(A) Identical bulk mapping results can arise from different underlying projection patterns.

(B) Single-neuron resolution can be achieved by randomly labeling neurons with barcodes and reading out barcodes in target areas.

(C) The expected fraction of uniquely labeled cells is given by $F = (1 - 1/N)^{k-1}$, where N is the number of barcodes and k is the number of infected cells, assuming a uniform distribution of barcodes. The number of neurons for various mouse brain areas is indicated according to references (Herculano-Houzel et al., 2006; Schüz and Palm, 1989) (A1, primary auditory cortex; Ctx, neocortex).

(D) In MAPseq, neurons are infected at low MOI with a barcoded virus library. Barcode mRNA is expressed, trafficked, and can be extracted from distal sites as a measure of single-neuron projections.

multiplexing is limited by the number of colors—at most 5–10—that can be resolved by microscopy.

Here we describe MAPseq (Multiplexed Analysis of Projections by Sequencing), a novel approach in which the speed and parallelization of high-throughput sequencing are exploited for brain mapping (Zador et al., 2012). MAPseq achieves multiplexing by using short, random RNA barcodes to uniquely label individual neurons (Mayer et al., 2015; Walsh and Cepko, 1992; Zador et al., 2012) (Figure 1B). The key advantage of using barcodes is that their diversity grows exponentially with the length of the sequence, overcoming the limited diversity of the resolvable color space. The pool of unique barcode identifiers is effectively infinite; even a 30-nt sequence has a potential diversity of $4^{30} \approx 10^{18}$ barcodes, far surpassing the $\sim 10^8$ neurons in the mouse brain (Herculano-Houzel et al., 2006). Because high-throughput sequencing can quickly and inexpensively distinguish these barcodes, with MAPseq we can potentially read out the projections of thousands or even millions of individual neurons in parallel within a single brain (Figure 1C).

In MAPseq, we uniquely label neurons in a source region by injecting a viral library encoding a diverse collection of barcode

sequences. The barcode mRNA is expressed at high levels and transported into the axon terminals at distal target projection regions (Figure 1D). To read out single-neuron projection patterns, we then extract and sequence barcode mRNA from the injection site, as well as from each target region of interest. Spatial resolution of MAPseq is limited mainly by the precision of target dissection. Although MAPseq, like GFP tracing, does not distinguish fibers of passage, we minimize their contribution by avoiding large fiber bundles during the dissection of target areas. Using this procedure, the brain-wide map of projections from a given area can be determined in less than a week. By reformulating projection mapping as a problem of sequencing, MAPseq harnesses advances in high-throughput sequencing to permit efficient single-neuron circuit tracing.

RESULTS

As a proof of principle, we applied MAPseq to the locus coeruleus (LC), a small nucleus in the brainstem that is the sole source of noradrenaline to the neocortex (Foote and Morrison, 1987). Early bulk tracing experiments revealed that the LC projects broadly

throughout the ipsilateral hemisphere, leading to the view that the LC broadcasts a generalized signal that modulates overall behavioral state (Foote and Morrison, 1987; Foote et al., 1983; Loughlin et al., 1982; Waterhouse et al., 1983). This view has recently been supported by more sophisticated retrograde bulk tracing experiments, which reinforce the idea that LC neurons project largely indiscriminately throughout the entire ipsilateral hemisphere (Schwarz et al., 2015). However, other reports have challenged this model. Using double retrograde labeling methods, these experiments uncovered separate populations of LC neurons projecting to different areas of cortex (Chandler et al., 2014; Chandler and Waterhouse, 2012), raising the possibility that the LC exerts differential control over different cortical areas. To address this controversy, we applied MAPseq to LC to obtain a large number of projection patterns at single-neuron resolution.

In what follows, we first show that long-range projections of neurons can be efficiently and reliably determined using barcode mRNAs, the abundance of which we interpret, like GFP intensity, as a quantitative measure of projection strength. Next, we establish the theoretical and practical foundations of randomly labeling large numbers of neurons with a viral barcode library, critical for ensuring single-cell resolution for MAPseq. We then apply MAPseq to the LC and find that individual neurons have a variety of idiosyncratic projection patterns. Some neurons project almost exclusively to a single preferred target in the cortex or olfactory bulb, whereas others project more broadly. Our findings are consistent with, and reconcile, previous seemingly contradictory results about LC projections. Finally, we show that MAPseq can be multiplexed to two and potentially many injections in the same animal, which will allow the projection patterns from many brain areas to be determined efficiently and in the same brain without the need for registration across animals.

Using RNA to Trace Neurons

Conventional neuroanatomical tracing methods rely on filling neurons with dyes or proteins so that neural processes can be resolved by microscopy. An implicit assumption of these techniques—albeit one that has rarely been rigorously tested—is that the tracer fills the neuron abundantly and uniformly so that the strength of the signal corresponds to the quantity of labeled neural process, independent of distance from the soma. For barcode mRNAs to act as a comparable label in MAPseq, we sought to maximize the abundance and uniformity of barcode mRNA in distal processes. We used two strategies to achieve this goal.

First, we expressed a modified presynaptic protein that was designed to specifically bind to and transport barcode mRNA into axon terminals. We engineered this protein, which we denote MAPP- $n\lambda$, as part of a larger project aiming to read out synaptic connectivity using mRNA. To generate MAPP- $n\lambda$, we began with pre-mGRASP, a protein engineered to localize at the presynaptic terminal due to fusion with trafficking signals from the endogenous presynaptic protein NRXN1 β (Kim et al., 2011). We then inserted four copies of the $n\lambda$ RNA binding domain (Daigle and Ellenberg, 2007) into the cytoplasmic domain of the protein. Derived from the λ phage λ_N protein, the $n\lambda$ domain is a 22-aa peptide that strongly and specifically binds to a 15-nt RNA hairpin, termed boxB. We added four copies of

the boxB hairpin to the barcode mRNA, ensuring coupling of MAPP- $n\lambda$ to the barcode mRNA and thus transport of barcode mRNA into axon terminals (Daigle and Ellenberg, 2007). Second, we delivered the barcode sequence using recombinant Sindbis virus, a virus that can rapidly achieve very high expression levels (Ehrensgruber, 2002). We used a novel Sindbis packaging system that, unlike previous systems, is both neurotropic and propagation incompetent (Kebschull et al., 2016) (Figures S1A–S1G; Supplemental Information, note 1, available online). All components necessary for MAPseq are expressed from a dual promoter virus that generates two subgenomic RNAs (Figure 2A). The first encodes the MAPP- $n\lambda$ protein. The second RNA encodes a random 30-nt barcode, as well as the boxB sequence, downstream of a GFP marker (Figures S1H and S1I). We reasoned that combining these two strategies would maximize our ability to reliably detect barcode mRNA in distal processes.

We injected barcoded virus into right LC (Figures S1J–S1L) and examined barcode localization by *in situ* RNA hybridization 44 hr after injection. We observed robust barcode mRNA localization in the soma and neuronal processes, in a pattern similar to that of co-expressed GFP (Figure 2B). This suggested that barcode mRNA could effectively fill local neuronal processes.

To determine whether the barcode mRNA fills distal neuronal processes uniformly, we exploited the particular anatomy of LC projection neurons. LC neurons that project to cortex send their processes all the way to the rostral end of the brain, before changing direction and moving caudally to innervate cortical areas (Figure 2C). Axons that project to visual cortex are therefore approximately twice as long as those that project to frontal cortices. From bulk tracing studies, it is known that LC innervation is homogeneous along the rostral-caudal axis (Schwarz et al., 2015; Waterhouse et al., 1983). Thus, if barcode mRNA were not efficiently transported to distal processes, we would expect to find more barcode mRNA in rostral regions of cortex. To assess this, we injected barcoded virus into LC, cut 300 μm coronal slices of the entire cortex (Figure 2D), and quantified the amount of barcode mRNA from each ipsilateral and contralateral slice. Consistent with previous results using GFP and other tracing methods (Schwarz et al., 2015; Waterhouse et al., 1983), we found approximately uniform projections throughout the ipsilateral cortex ($p = 0.972$ F-statistic versus constant model; Figure 2E); in particular, we found no evidence that distal processes were more weakly labeled than proximal processes. Also consistent with previous results, we observed much weaker (30.6-fold less; $p = 4 \times 10^{-31}$, paired Student's *t* test) projections to the contralateral cortex (Figure 2F). These results suggest that barcode mRNA fills distal and proximal processes with about equal efficacy so that the barcode mRNA can be interpreted in the same way as the fluorophores and dyes used in conventional tracing studies.

Unique Labeling of Neurons with Barcodes

In conventional single-neuron tracing, the main challenge to multiplexing is the low diversity of labels (fluorophores or enzymes) available to disambiguate individual neurons. To overcome this challenge, MAPseq labels neurons with short, random RNA barcodes delivered by infection with a diverse viral library. Ideally, each labeled neuron should have exactly one unique

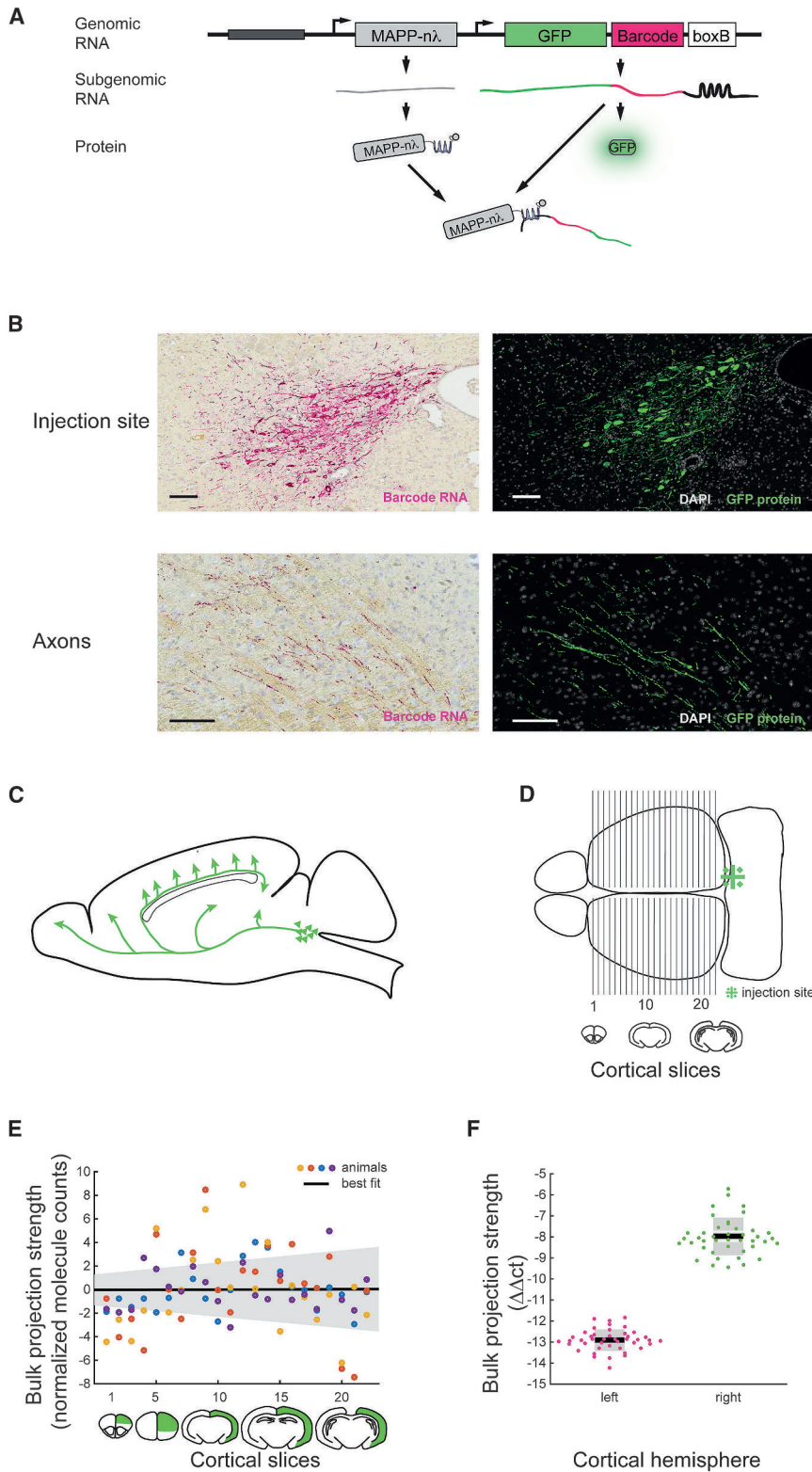


Figure 2. Barcoded Sindbis Virus Can Be Used for Projection Mapping

(A) A dual promoter Sindbis virus was used to deliver barcodes to neurons. The virus encoded GFP, barcodes, and MAPP-nλ.

(B) Barcode mRNA labeling of LC neurons is comparable to GFP labeling of these neurons in an adjacent 6 μm slice both at the injection site (top) and in the axon tract (bottom). Scale bar, 100 μm. Representative data from three animals.

(C) Axons from LC project rostrally from the cell body, before changing direction and innervating cortex. LC axons that project to frontal cortices have thus traveled only about half as long as axons innervating visual cortex.

(D) We injected right LC with MAPseq virus and dissected cortex along the anterior-posterior axis as shown.

(E) Bulk projection strength of LC to ipsilateral cortex as measured by barcode mRNA is independent of the anterior-posterior position of the cortical slice, suggesting a uniform RNA fill of LC axons. N = 4. The shaded area indicates the 95% confidence interval of the fit.

(F) qPCR for barcode mRNA shows approximately 30× stronger LC projections to ipsi- than to contralateral cortex. N = 2 animals and 21 cortical slices per animal. BC, barcodes. The y axis displays $\Delta\Delta\text{Act}$ values, which are equivalent to the $\log_2(\text{foldchange of barcode mRNA per sample})$ normalized to β -actin levels in each sample and to the amount of barcode mRNA in the injection site of each animal (Livak and Schmittgen, 2001). Individual data points are plotted. The mean is indicated by a horizontal bar, SD error bars by a light gray area, and 95% confidence interval by a dark gray area.

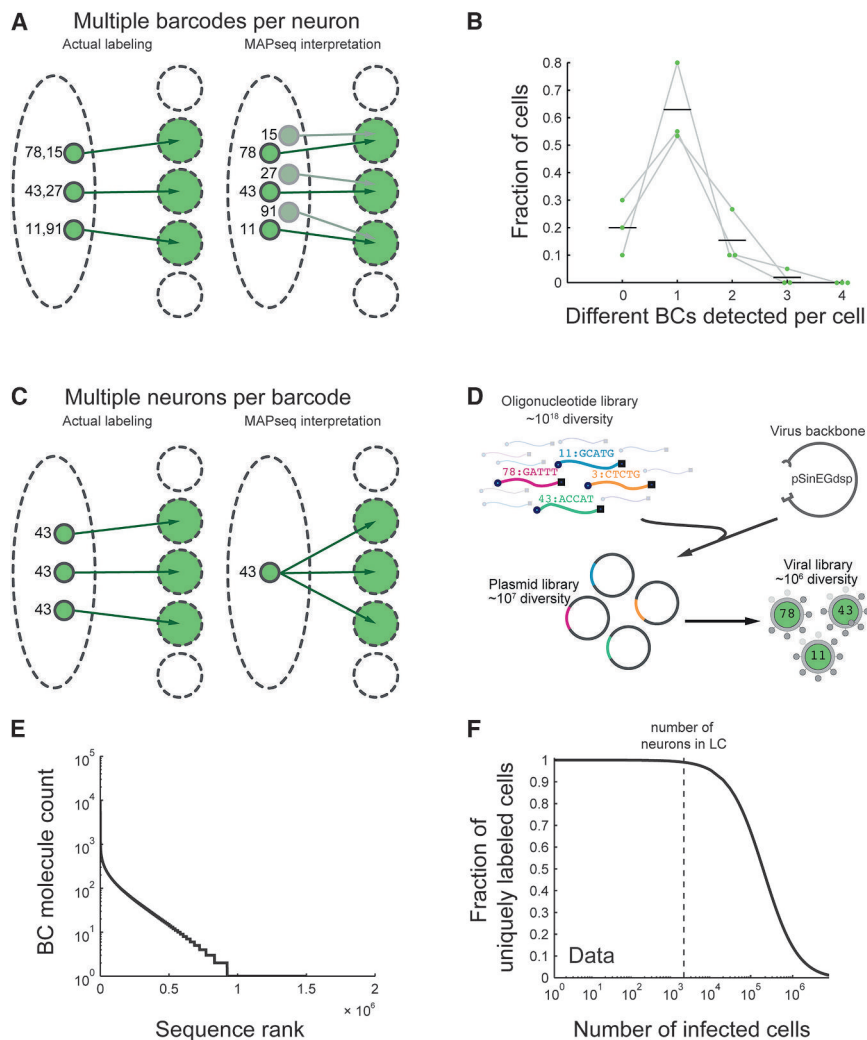


Figure 3. Random Labeling of Neurons with a Barcoded Virus Library Can Achieve Unique Labeling of Many Neurons

(A) When single neurons are labeled with several barcodes, MAPseq will overestimate the number of neurons identified, but will not distort the projection patterns recorded for individual neurons.

(B) Single-cell isolation of GFP-positive, barcoded neurons, followed by sequencing of their barcode complement, reveals a low chance of double infection. We interpret neurons for which no barcodes were recovered as technical failures of cell isolation, rather than biological phenomena. $N = 3$ animals. Mean and individual data points are plotted.

(C) When several neurons share the same barcode, MAPseq misinterprets this as a single neuron whose projection pattern is given by the union of the projection patterns of the two infected neurons.

(D) High-diversity Sindbis virus libraries are produced by shotgun cloning random oligonucleotide sequences into a plasmid followed by virus production.

(E) The virus library used in this work has a diversity of $\sim 10^6$ different barcodes (BC), but the distribution was non-uniform. The sequence rank is a number that ranges from 1 to the total number of barcodes, where 1 corresponds to the most abundant sequence, 2 to the second most abundant, and so on.

(F) Based on the empirically observed non-uniform barcode distribution, we determined that the virus library used is sufficiently diverse to uniquely label all of LC with low error rate.

barcode. Here we consider the factors that could lead to deviations from this ideal scenario: (1) more than one barcode per neuron (multiple labeling) and (2) more than one neuron per barcode (non-unique or degenerate labeling). As discussed below, deviations resulting from multiple labeling are much less of a concern than those resulting from degenerate labeling.

A neuron may express more than one barcode if it is infected by more than one viral particle. Such multiple labeling will lead to an overestimate of the number of neurons identified, but will not distort the projection patterns recorded for individual neurons (Figure 3A). Furthermore, even estimates of the relative abundances of different neuronal classes will, on average, be accurate. Assume, for example, that two neurons A and B are each labeled with ten different barcodes. In this scenario, MAPseq will discover ten instances of neuron A and ten of B, but even though the absolute number of neurons is incorrect, the fact that neurons A and B have distinct projection patterns, and that these patterns occur in a 1:1 ratio, is accurately inferred. Thus, multiple labeling will not, on average, lead to mischaracterization of neuronal classes or of their relative frequency in the population.

Nevertheless, to simplify the interpretation of MAPseq results, we sought to minimize the MOI by titrating the concentration and volume of virus injected. To estimate the MOI, we isolated a total of 45 individual neurons from three animals injected with MAPseq virus into the right LC and sequenced the barcodes within each neuron. On average, infected LC neurons contained 1.2 ± 0.1 barcodes each, implying MOI of 0.43 (Figure 3B). Only $21\% \pm 11\%$ of neurons contained more than one barcode, with most of these neurons carrying two barcode sequences and only $1.7\% \pm 2.9\%$ of neurons containing three barcode sequences.

The second deviation from the ideal scenario is non-unique labeling. If two neurons share the same barcode, then MAPseq misinterprets this as a single neuron whose projection pattern is given by the union of the projection patterns of the two infected neurons (Figure 3C). The probability that two neurons are infected by the same barcode depends on the number of infected cells relative to the number of available barcodes. Trivially, if the number of infected cells is larger than the number of available barcodes, unique labeling of all neurons cannot be achieved. Conversely, if the number of available barcodes is much higher than the number of infected cells, every neuron will be labeled with a different barcode purely by chance.

To determine whether our barcode diversity was sufficient to ensure unique labeling, we first quantified the number of neurons in the LC. We counted $1,985 \pm 132$ ($N = 6$ animals) neurons expressing tyrosine hydroxylase, a noradrenergic marker. The size of this neuronal population is approximately 15 orders of magnitude smaller than the theoretical diversity ($4^{30} \approx 10^{18}$) of a library of 30-nt barcodes, so in theory, unique labeling would be virtually certain. In practice, however, the actual diversity of a virus library is limited by bottlenecks in plasmid and virus generation (Figure 3D), so further analysis was required to determine whether the viral library was sufficiently diverse.

We therefore computed how the fraction of uniquely labeled neurons scaled with the diversity of the viral library. This problem is formally equivalent to a generalization of the classic “birthday problem,” which concerns the probability that in a group of k people (neurons), some pair will have the same birthday (barcode). Assuming that all barcodes are equally abundant in the library, we can express the expected fraction F of uniquely labeled neurons as

$$F = \left(1 - \frac{1}{N}\right)^{k-1},$$

where k is the number of infected neurons (assuming one barcode per cell), and N is the barcode diversity (see Supplemental Information, note 2). Thus, if $k = 1,000$ LC neurons were infected with a library of diversity of $N = 10^6$, on average 99.9% of all neurons would be labeled uniquely. This expression holds only for a library of equally abundant barcodes; if some barcodes are overrepresented, the fraction F of uniquely labeled neurons decreases (in the same way that if birthdays tend to fall on a particular day, the probability of finding a shared birthday in a group increases; Munford, 1977). However, analysis of the actual viral barcode library determined by sequencing (Figure 3E) revealed that in practice, these deviations from uniformity had only a minor effect (Figure S2A). Thus, under our conditions, the vast majority (>99%) of neurons will be uniquely labeled, even taking into account the uneven barcode distribution in the viral library (Figure 3F; Supplemental Information, note 2).

We also used a second, more empirical approach to estimate the extent of degenerate labeling. Since we used the same viral library to infect neurons in different animals, barcode sequences found in more than one animal represent degeneracy. We therefore looked for overlap in the recovered barcodes from four independent injections of the same virus library. Out of the 992 unique barcodes that we recovered from traced neurons, only three barcodes were present in more than one animal, and no barcode was present in more than two animals. This empirically measured rate of degenerate labeling is in close agreement with our expectations based on the theoretical considerations above. Moreover, two of the three repeated barcodes were among the most abundant barcodes in the virus library (Figure S2B), and would thus be expected a priori to have the highest probability of double labeling. This analysis provides an independent confirmation that the error rate due to non-unique labeling by the barcode library is very low in our experiments.

In addition to non-unique barcode labeling, MAPseq is subject to other errors that differ from those associated with conventional tracing approaches. We used several approaches to quan-

tify these errors and find that the overall MAPseq error rate was low both for false positives ($1.4\% \pm 0.8\%$, mean \pm SE) and for false negatives ($8.6\% \pm 6\%$, mean \pm SE) (see Supplemental Information, note 3). MAPseq thus provides a reliable measure of axon projections.

Sequencing of Barcode mRNAs Reveals Diverse Single-Neuron Projection Patterns

The goal of MAPseq is to quantify the projection patterns of large populations of neurons in parallel. We therefore developed a method to determine the amount of each barcode in each dissected target (Figure 4A). Forty-four hours after injection of barcoded virus into right LC, we performed reverse transcription on barcode mRNA extracted from dissected target regions. To overcome distortions introduced during amplification (Kebschull and Zador, 2015), and to allow a precise count of barcode cDNA molecules, we designed reverse transcription primers to tag each individual barcode mRNA molecule with a random 12-nt unique molecular identifier (UMI). We also added a 6-nt slice-specific identifier (SSI) to allow multiplexing of samples within a single high-throughput sequencing flow cell. We then amplified, pooled, and sequenced these SSI-UMI-barcode cDNAs (Figure S3). We developed a conservative computational pipeline to minimize noise due to RNA contamination and to correct for sequencing and other errors (Supplemental Information, note 4). Finally, we converted barcode abundance in the target areas to a matrix of single-neuron projection patterns.

We used MAPseq to determine the projection patterns of a total of 995 barcodes labeled in four animals (249 ± 103 barcodes per animal), roughly corresponding to an equal number of LC neurons. For each animal, we analyzed the barcode mRNAs extracted and amplified from the olfactory bulb and from 22 coronal slices ($300 \mu\text{m}$) taken from the cortex ipsilateral to the LC injection (Figures 4B and 4C). Although, like conventional GFP tracing, MAPseq does not distinguish between synaptic connections and fibers of passage, we minimized the contribution of large fiber tracts in the white matter during dissection, so most of the mRNA barcode signal was likely generated from axons terminating in the regions of interest. Dissection of coronal slices allowed us to probe the organization of projections along the rostral-caudal axis, but we were insensitive to any additional structure along the medio-lateral axis. Because individual barcode cDNA molecules are tagged with a UMI before amplification, we obtained a precise quantification (subject to Poisson counting statistics; see Supplemental Information, note 5) of the amount of each barcode sequence in each dissected target. In this way, we could infer the projection strength—the density of axon per tissue volume—of each neuron to each coronal target area. For example, we recovered 223 copies of BC28 in slice 5, but none in slice 20, indicating that the projection strength to slice 5 is at least a factor of 200 higher than our detection floor (Figure 4D).

Inspection of the projection patterns revealed that in contrast to the simplest prediction from conventional bulk tracing, single neurons did not project uniformly throughout the ipsilateral hemisphere. Instead, neurons projected in diverse and idiosyncratic ways to specific targets, innervating some areas hundreds of times more strongly than others (Figure 4D). Some neurons

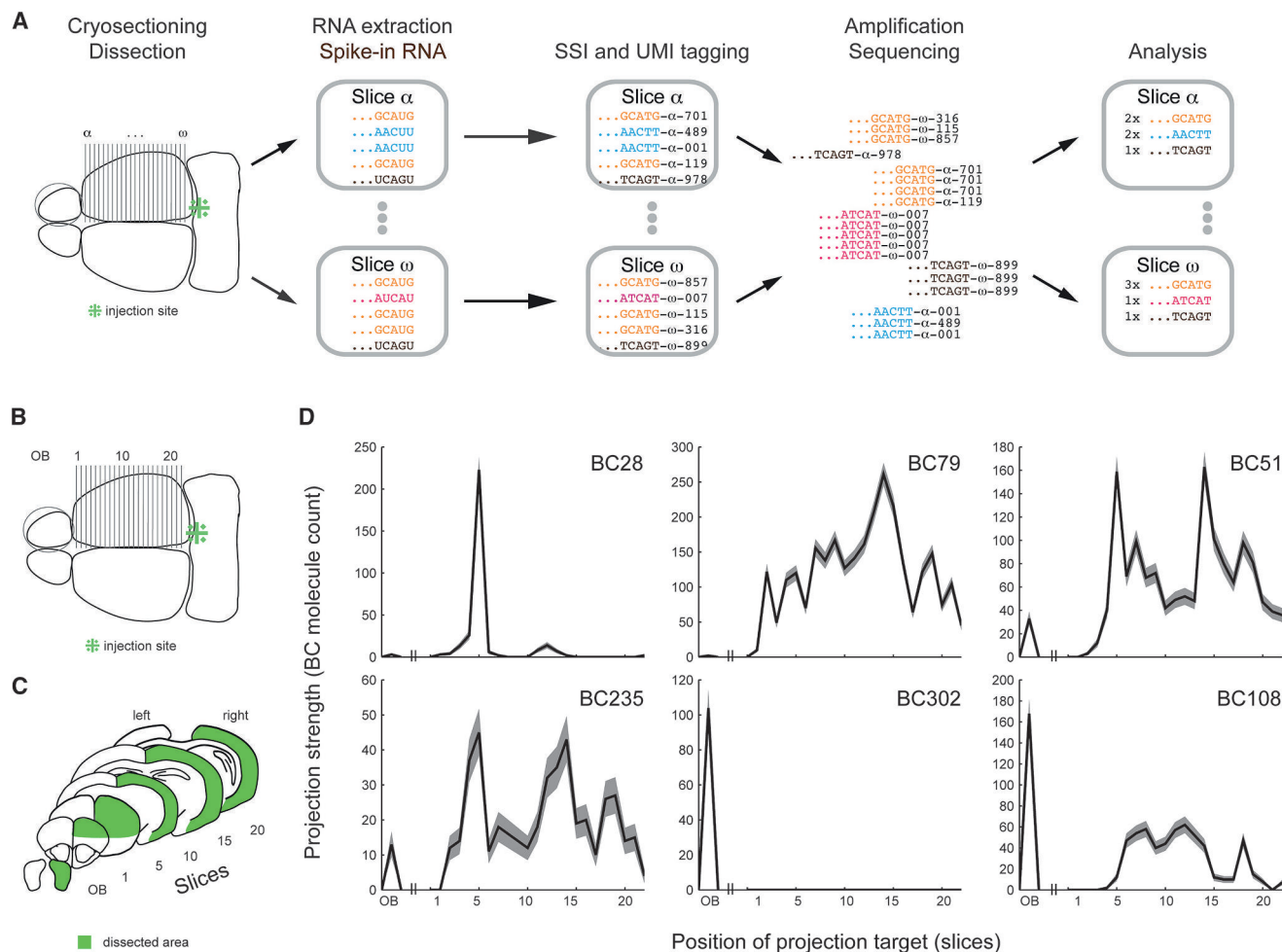


Figure 4. MAPseq Reveals Large Diversity of Projections from LC

(A) Barcode mRNAs from target areas are sequenced as described (SSI, slice specific identifier; UMI, unique molecular identifier).

(B–D) Barcodes from ipsilateral olfactory bulb and cortex (B and C) show projection patterns (D) with single or multiple peaks in cortex and/or olfactory bulb. The shaded area indicates Poisson error bars given by the square root of barcode (BC) counts per slice.

(e.g., BC28) showed specific projections to only a small part of cortex, whereas others (e.g., BC79) projected more broadly, or projected to multiple areas (e.g., BC51 or BC235). Projections to the olfactory bulb appeared independent of projections to cortex, with some neurons projecting exclusively to the olfactory bulb (e.g., BC302), some projecting exclusively to cortex (e.g., BC79), and others projecting to both (e.g., BC108).

The small fraction of multiply infected neurons revealed by single-cell sequencing ($21\% \pm 11\%$; Figure 3B) provided a convenient internal measure of the reliability of MAPseq. Within each animal, we found pairs of very similar projection patterns, as would be expected if they arose from double labeling of the same neuron (Figures 5A and S4A). By comparing the similarity of projection patterns within and across animals, we estimated the total number of barcode pairs arising from doubly labeled neurons ($18.6\% \pm 2\%$; Figures 5B and S4B). The fact that this estimate is in such close agreement with the independent estimate of the number of doubly labeled neurons from single-cell sequencing supports the view that

MAPseq provides a robust measure of single-neuron projection profiles.

To assess the structure of the LC projection to cortex and olfactory bulb, we sorted all traced neurons by their maximum projection (Figure 6A). The maximum projections of individual LC neurons tile the entire cortex. To compare across the population, we normalized the total barcode count of the projection of each neuron to one, although interestingly there was no correlation between expression level in the LC and the maximal projection strength to cortex, as would have been expected if differences across neurons were dominated by expression level ($R = -0.06$; $p = 0.09$; Figure S5A). Only in the aggregate do these projections re-create the apparently homogeneous LC innervation of cortex previously described by bulk methods (Figure 2E). Consistent with previous results (Shipley et al., 1985), a considerable fraction ($23\% \pm 4.7\%$) of all mapped neurons projected to the olfactory bulb.

We then asked if we could find structure, or even stereotypic projection cell types, in the single-cell dataset. We investigated

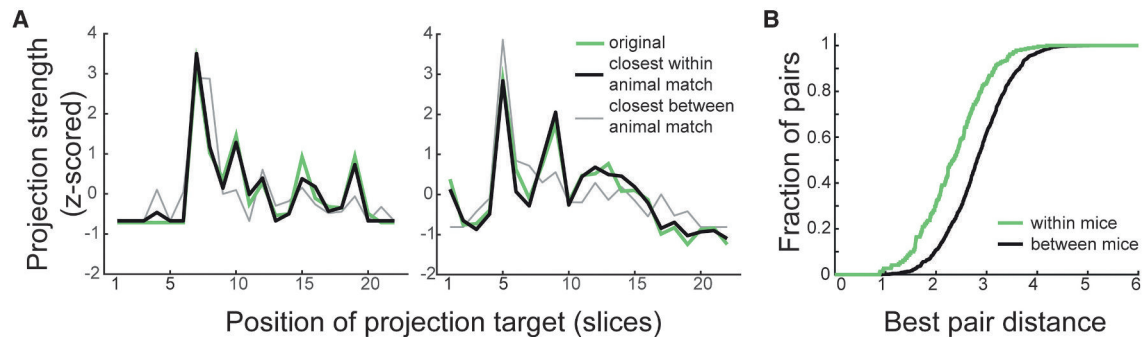


Figure 5. MAPseq Provides a Robust Readout of Single-Neuron Projection Patterns

(A) Two representative pairs of barcodes with projection patterns more similar than expected by chance for two distinct neurons, likely the result of double infection of a single neuron. The close agreement between the two barcode profiles indicates that MAPseq provides a reliable measure of projection patterns. The closest match across animals is indicated in gray for comparison.

(B) Cumulative distribution of distances between the best barcode pairs within one animal and across animals. The shift in the within-animal distribution reflects the higher fraction of closely matched projection profiles, consistent with double infection. Representative data from one animal.

the cortex-wide projection patterns of LC by reducing the dimensionality of the projection dataset using Euclidean distance-based t-SNE (t-distributed stochastic neighbor embedding) (Van der Maaten and Hinton, 2008). Neurons with maximum projections close to each other in physical space along the rostro-caudal axis also fall closely together in t-SNE space (Figure S5B), indicating that the location of the maximum projection target at least partially describes the individual neuron projection patterns. However, hierarchical clustering of the projection profiles of neurons that project to cortex did not uncover distinct cell classes (Figure S5C). Although we cannot rule out the possibility that there is further structure in the projection patterns that would be revealed by higher-resolution dissection, our data suggest the intriguing possibility that LC projections are equipotential for projecting to all targets, and the choice is arbitrary for each neuron. How the circuit might exploit such random connectivity raises interesting computational challenges.

Although many LC axons projected very strongly to a narrow target, these axons often sent minor collaterals to a much broader area, like a plant with a single main stalk and many minor growths. The average number of projection peaks per LC neuron was 1.6 ± 0.8 (Figure S5D), and the fall-off to half the maximum projection strength of individual neurons occurred on average in $<300 \mu\text{m}$ (Figure 6B). Nonetheless, every cortically projecting neuron innervated on average $65\% \pm 23\%$ of cortex at a detectable level (see cumulative distribution of projection widths in Figure 6C). Importantly, this broad, weak innervation of cortex cannot be explained simply by contamination of our dataset by fibers of passage. LC axons innervate cortex starting in the rostral end and moving caudally (Figure 3C). We would therefore expect signals from accidentally dissected fibers of passage to only precede strong projection targets of individual neurons along the rostro-caudal axis. However, we find that strong projection targets are both preceded and followed by low-level projections (e.g., see Figure 4D; BC79 and BC51). We therefore conclude that the observed weaker signals are not the result of fibers of passage but represent real, but weak, projections.

The fact that many neurons had a strong preferred target in cortex or olfactory bulb, but also projected weakly to a much

broader area, provides a way to reconcile apparently conflicting results about the specificity of LC projections. Recent experiments in which retrograde viral labeling was combined with anterograde tracing of axons concluded that as a population, LC neurons project largely indiscriminately throughout cortex and the rest of the brain examined (Schwarz et al., 2015). However, using this approach, a neuron labeled retrogradely from a weak projection is indistinguishable from one labeled from a strong projection, so at the level of the population (i.e., after summing the projection patterns of strongly and weakly projecting neurons), it may appear that projections are nonspecific. Thus, although the results of this study may appear to contradict those obtained by MAPseq at single-neuron resolution, simulations of retrograde labeling in combination with anterograde bulk tracing based on our MAPseq dataset demonstrate that there is no contradiction (Figures S5E and S5F) at the bulk level.

MAPseq Scales to Several Injection Sites

MAPseq can readily be extended to determine the projections of two or more regions in a single animal. As a proof of principle, we injected the same library of MAPseq virus bilaterally into left and right LC, and dissected coronal slices of left and right cortex and the olfactory bulbs, as well as both injection sites (Figure 7A). Each barcode was expressed predominantly in either the left or right LC (Figure 7B); barcode expression at the site contralateral to the injection, due to contralaterally projecting fibers and/or contamination, is much lower. Thus, each barcode can be reliably assigned to the appropriate injection site. As expected, parallel injections recapitulated the projection pattern observed with single injections (Figure 7C). Multiplexing MAPseq to dozens of injections per animal may be feasible, reducing the labor and cost of brain-wide projection mapping efforts, and eliminating the need to map data from multiple animals to an average reference brain (Oh et al., 2014; Zingg et al., 2014).

DISCUSSION

We have described MAPseq, the first application of sequencing to neuroanatomical tracing. MAPseq is a simple, rapid, and

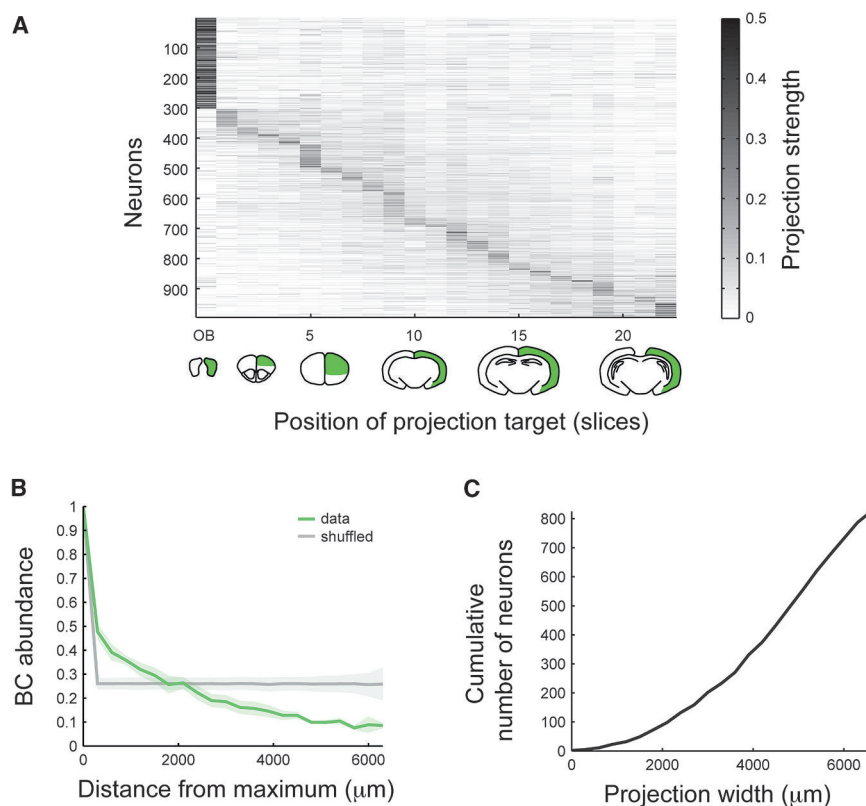


Figure 6. LC Neurons Tile Cortex with Their Maximum Projections, but Innervate Large Areas of Cortex at a Low Level

(A) A heatmap of all 995 projection patterns from four animals shows a strong diagonal component after sorting by maximum projection site. Barcode abundances are normalized to sum to one across target areas and are color coded as indicated.

(B) Average cortical drop-off rate from maximum for all barcodes shows a rapid drop-off and a structure that is different from the drop-off after randomly shuffling slices for all neurons. $N = 4$. The shaded area around the curve indicates the SD across animals.

(C) Cumulative distribution of cortical projection widths indicates a broad, low-intensity innervation of cortex by individual LC neurons. BC, barcode.

inexpensive approach to determining the projection patterns of myriad single neurons at one or more injection sites in a single animal. As a proof of principle, we applied MAPseq to the LC. In contrast to previous bulk labeling studies that reported diffuse and non-specific projections from the LC, this single-neuron resolution analysis reveals that individual LC neurons have idiosyncratic projection patterns with preferred cortical targets, and reconciles a controversy about the specificity of LC projection patterns. MAPseq, which complements rather than replaces conventional approaches, can readily be applied to other brain regions and organisms, and with further development may be combined with information about gene expression and neural activity.

The cost of sequencing the human genome was several billion dollars in 2003, but today it is less than one thousand dollars—a decrease of over six orders of magnitude in just over a dozen years (Hayden, 2014; Sheridan, 2014). This precipitous drop in sequencing costs continues unabated, at a rate faster even than Moore’s law (the rate at which computers improve). At the same time, DNA sequencing has evolved from a specialized tool for determining the sequences of genomes into a versatile technology for determining gene expression levels, discovering new species, tracking cell fates, and understanding cancer growth, among many other applications (Reuter et al., 2015). With advances of technology and novel assays, DNA sequencing has revolutionized disparate areas of biology. By harnessing sequencing for neuroanatomical tracing, MAPseq may accelerate our understanding of neural circuits.

High-Throughput Sequencing and Neuroanatomy

In the present work, we applied the simplest form of MAPseq to LC. We expressed the virus ubiquitously, without any specific targeting to a cell type using, e.g., Cre recombinase, and used gross dissection to probe projections at a spatial resolution of 300 μm coronal sections. Because the LC projects throughout the entire cortex, this relatively low spatial resolution was well suited to address previously unresolved questions about LC anatomy. Gross dissection can achieve somewhat higher spatial resolution ($\sim 1\text{--}2\text{ mm} \times 300\text{ }\mu\text{m} \times$ cortical thickness; Figures S7A and S7B), sufficient to distinguish among cortical areas in the mouse.

The application of MAPseq to the LC highlights both the advantages and the tradeoffs of MAPseq compared with traditional methods. The main advantages of MAPseq are higher throughput and that it is less labor intensive. The total amount of time required to obtain the projection patterns from all labeled LC neurons in a single mouse was under 1 week (dissection 2 days post-injection, followed by 1–2 days of tissue processing to generate sequencing libraries, followed by 1–2 days of sequencing), of which only a relatively small fraction is spent on “hands-on” labor (as opposed to waiting). By comparison, tracing a single neuron’s projections using traditional methods requires a week or more of hands-on labor and even with automation requires days. Processing time with MAPseq does not depend on the number of source (barcoded) neurons—as many as 500,000 neurons can be labeled in a single subject (unpublished data)—and MAPseq can be multiplexed to several injection sites (Figure 7), so the throughput of MAPseq could be five or more orders of magnitude higher than conventional single-neuron tracing.

Therefore, MAPseq is, without any further technical development, well positioned to address questions that depend on single-neuron resolution at the source but do not require very high spatial resolution at the target site. For example, MAPseq could readily be used to systematically and efficiently compare

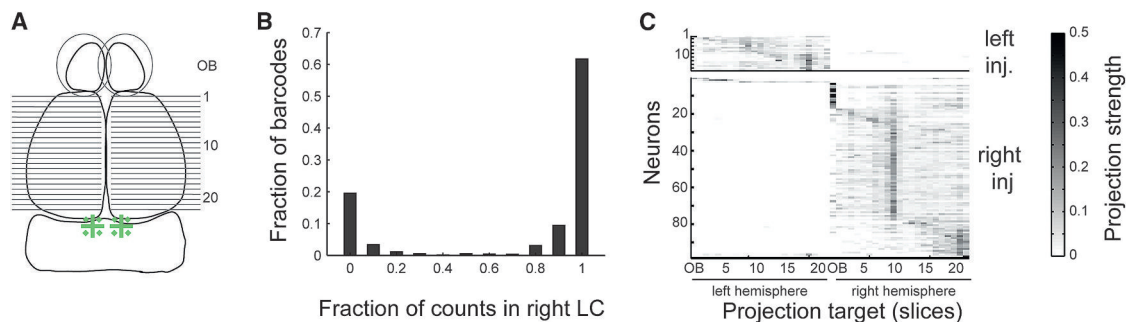


Figure 7. MAPseq Can Be Multiplexed to Several Injection Sites

(A) Following bilateral injection of barcoded Sindbis virus into LC, left and right olfactory bulb and cortex were dissected as before.

(B) Histogram of the fraction of barcode counts in the right versus left injection site across barcodes. Barcodes show strong abundance differences in the left and right injection sites, allowing them to be assigned to one of the two sites.

(C) Bilateral injections produce the projection pattern expected from unilateral injections. Differences in the number of neurons traced from the left and right LC arise from injection variability.

the projection patterns of other neuromodulatory systems, such as cholinergic or serotonergic, to the LC noradrenergic system considered here. MAPseq could also be used to test whether individual neurons in the primary auditory (or somatosensory) cortex project to specific subsets of higher auditory (or somatosensory) areas, analogous to the “ventral” and “dorsal” processing streams in the visual system. Furthermore, the Sindbis virus used to deliver barcodes has a very wide host range (Xiong et al., 1989), from arthropods to mammals (including primates). A particularly appealing application of MAPseq is thus single-neuron tracing in nonhuman primates and in less common model systems, where the cost per specimen renders traditional single-neuron tracing approaches prohibitive, and which benefit from the massive multiplexing achievable in MAPseq. It is easy to envision myriad other applications of MAPseq in its current form.

The main tradeoff of MAPseq compared with conventional methods is spatial resolution. There are several potential paths to achieving higher spatial resolution. One simple extension of the protocol presented here is to use laser-capture microdissection, which can readily resolve MAPseq target areas to several hundred microns (unpublished data), and which in principle can achieve single-neuron resolution (Espina et al., 2006). Using fluorescent in situ sequencing (FISSEQ) (Lee et al., 2014), even higher resolution can be achieved (unpublished data); barcodes can be localized with subcellular resolution, allowing for a kind of “infinite color Brainbow” (Livet et al., 2007). At present, however, FISSEQ is not fully automated and has considerably lower throughput than conventional sequencing.

What are the ultimate limits of MAPseq spatial resolution? The factors limiting MAPseq can be understood by analogy with those limiting optical microscopy. Just as spatial resolution—effective pixel size—in microscopy is limited by the optics and detectors, so is the spatial resolution of MAPseq limited by the spatial precision with which brain regions are sampled—potentially subcellular with FISSEQ. The effective spatial resolution of MAPseq may also be limited by the amount of barcode mRNA in each spatially defined region, analogous to the low-light photon-counting limit in microscopy. The precise spatial

scale at which the barcode mRNA “shot noise” limit is reached in MAPseq is determined by the interplay of several factors, including the diameter of the axonal projections, expression level of the barcode, and the efficiency with which barcodes can be recovered and amplified. Because mRNA shot noise did not appear limiting in the present experiments, we did not invest significant effort in optimizing these parameters. However, the fact that barcodes can be detected even in fine LC axons suggests that MAPseq may achieve relatively high spatial resolution.

MAPseq Extensions

Information about single-neuron projection patterns obtained by MAPseq may be combined with information about other dimensions of neuronal function. For example, single-neuron projection patterns obtained by MAPseq could be associated with information about gene expression. One approach exploits transgenic mice that mark defined neuron classes with Cre recombinase. Although expression of barcodes delivered using the RNA virus Sindbis cannot readily be controlled with Cre, barcodes could be delivered using a DNA virus like AAV or a retrovirus like lentivirus. More general approaches, such as single-cell isolation (Figure S6), might associate several genes or even a whole transcriptome with projection patterns. MAPseq data could also be combined with recordings of neural activity obtained by calcium imaging. Taken together, the combination of connectivity, gene expression, and activity could provide a richer picture of neuronal function than any of these alone (Marblestone et al., 2014).

In its current form, MAPseq provides information about neuronal projections, but not about synaptic connections. MAPseq can tell us, for example, that a given neuron in the thalamus projects to both the amygdala and the cortex, but it cannot resolve whether the cortical target is an excitatory or an inhibitory neuron, or both. In this respect, it is similar to most standard tracing methods, such as GFP, which do not have synaptic specificity. However, the MAPP-n λ protein we engineered includes trafficking signals from the presynaptic protein *NRXN1 β* , and was originally designed to allow us to join pre- and postsynaptic barcodes to detect synaptic connections. The joined barcode

pairs can be sequenced using high-throughput methods and provide an efficient and scalable method for determining the full connectome of a neural circuit (Zador et al., 2012).

Uniformity versus Specificity of LC Projections

The LC sends projections to most ipsilateral brain areas, with the notable exception of the striatum. However, how broadly individual neurons innervate those target areas is subject to debate. Classical retrograde tracing studies suggested a topographic organization of neocortical (Waterhouse et al., 1983) and brain-wide (Loughlin et al., 1986) projection neurons in the LC. Consistent with this, double retrograde labeling studies reported that the LC projections to frontal and motor cortices (Chandler et al., 2014; Chandler and Waterhouse, 2012) overlap minimally. In contrast, other double retrograde studies found overlap between neurons projecting to separate structures along the same processing stream (Simpson et al., 1997), or structures as different as forebrain and cerebellum (Steindler, 1981). More recent work using retrograde viral labeling combined with anterograde tracing concluded that LC neurons project largely indiscriminately throughout both cortex and the rest of the brain (Schwarz et al., 2015).

Our single-cell resolution data reconcile these conflicting datasets. We find that individual LC neurons have very specific projection targets in cortex and olfactory bulb, but are not limited to a single target. We further observe that many LC neurons that project to cortex innervate a large fraction of the cortex at least weakly, in addition to having preferred projection targets. To the extent that retrograde viral tracers may not distinguish between strong and weak projections, it may be this feature of single-neuron projections, in combination with bulk tracing, that leads Schwarz and colleagues (Schwarz et al., 2015) to conclude that LC neurons largely indiscriminately project throughout cortex and the bulb, and indeed we can replicate their results by simulating retrograde tracing on our single-cell dataset.

The LC is the sole source of noradrenaline to the cortex. Noradrenaline exerts a powerful influence on an animal's behavioral state. Noradrenaline levels control the overall level of vigilance; they are lowest during sleep and are increased in response to stimuli such as pain. Noradrenaline gates attention, enhances formation of long-term memory, and is thought to regulate the exploration-exploitation balance (Aston-Jones and Cohen, 2005; Sara, 2009). Traditionally, it has been assumed that the levels of neuromodulators such as noradrenaline represent a global signal, broadcast indiscriminately throughout the cortex. However, the specificity of the single-neuron projections patterns uncovered by MAPseq suggests that different brain regions could be subject to differential control. Whether this potential for differential control is actually realized, and what functional role it plays, remain to be determined.

Conclusion

Applying MAPseq to the LC, we discovered unexpected structure that could not have been resolved by previous methods lacking single-neuron resolution. MAPseq also lays the foundation for using sequencing to decipher local neuron-to-neuron connectivity (Zador et al., 2012). Using DNA sequencing technology, experimenters have gained unprecedented insight into the

heterogeneity of cell populations at the single-cell level (Navin et al., 2011). By leveraging this sequencing technology, MAPseq empowers neuroscience researchers to efficiently do the same for populations of projection neurons examined at the single-neuron level.

EXPERIMENTAL PROCEDURES

Animal procedures were approved by the Cold Spring Harbor Laboratory Animal Care and Use Committee and carried out in accordance with NIH standards.

MAPseq

Forty-four hours after injection of MAPseq virus into LC, we flash froze the brain and cut it into 300 μm coronal sections using a cryostat. We dissected the cortical regions on dry ice and extracted total RNA from each sample. We then performed gene-specific reverse transcription for the barcode mRNA, produced double-stranded cDNA, and PCR amplified it to produce an Illumina sequencing library, which we sequenced at paired end 36 on an Illumina NextSeq sequencing machine.

Data Analysis

We processed the sequencing data to determine the exact copy number of each barcode sequence in each target area and in the injection site, and produced a barcode matrix where each row corresponds to one specific barcode sequence, each column corresponds to a target area or the injection site, and each entry is the copy number of that barcode mRNA in the respective area. All data are expressed as mean \pm SD unless otherwise stated.

For full details on the experimental procedures, please refer to the Supplemental Experimental Procedures.

ACCESSION NUMBERS

All high-throughput sequencing datasets are publicly available under SRA accession codes SRA: SRS1204613 (library ZL067; virus library), SRS1204589 (libraries ZL068, ZL070, ZL071, ZL072; unilateral MAPseq datasets), SRS1204614 (libraries ZL073, ZL074; bilateral MAPseq datasets), and SRS1204626 (libraries ZL075 and ZL078; single-cell dataset).

SUPPLEMENTAL INFORMATION

Supplemental Information includes Supplemental Experimental Procedures seven figures, five notes, and two data files and can be found with this article online at <http://dx.doi.org/10.1016/j.neuron.2016.07.036>.

AUTHOR CONTRIBUTIONS

J.M.K., I.D.P., and A.M.Z. conceived the study. J.M.K. and P.G.S. performed the experiments. J.M.K. and A.P.R. performed the single-cell isolation. J.M.K. and A.M.Z. analyzed the data. J.M.K. and A.M.Z. wrote the paper. A.M.Z. and D.F.A. supervised the project.

ACKNOWLEDGMENTS

The authors would like to acknowledge Vasily Vagin, Fred Marbach, Alex Koulakov, Brittany Cazakoff, and Alexander Vaughan for useful discussions and assistance, and Barry Burbach and Diana Gizatulliana for technical support. We would further like to thank Anirban Paul for help with single-cell isolations. This work was supported by the following funding sources: NIH (5R01NS073129 and 5R01DA036913 to A.M.Z.); Brain Research Foundation (BRF-SIA-2014-03 to A.M.Z.); IARPA (MICrONS to A.M.Z.); Simons Foundation (382793/SIMONS to A.M.Z.); Paul Allen Distinguished Investigator Award (to A.M.Z.); PhD fellowship from the Boehringer Ingelheim Fonds to J.M.K.; PhD fellowship from the Genentech Foundation to J.M.K.; PhD fellowship from the Fundação para a Ciência e Tecnologia, Portugal, to P.G.S.; and

Pew Scholarship and CSHL startup funds to D.F.A. This work was performed with assistance from CSHL Shared Resources, which are funded, in part, by the Cancer Center Support Grant 5P30CA045508.

Received: April 29, 2016

Revised: June 18, 2016

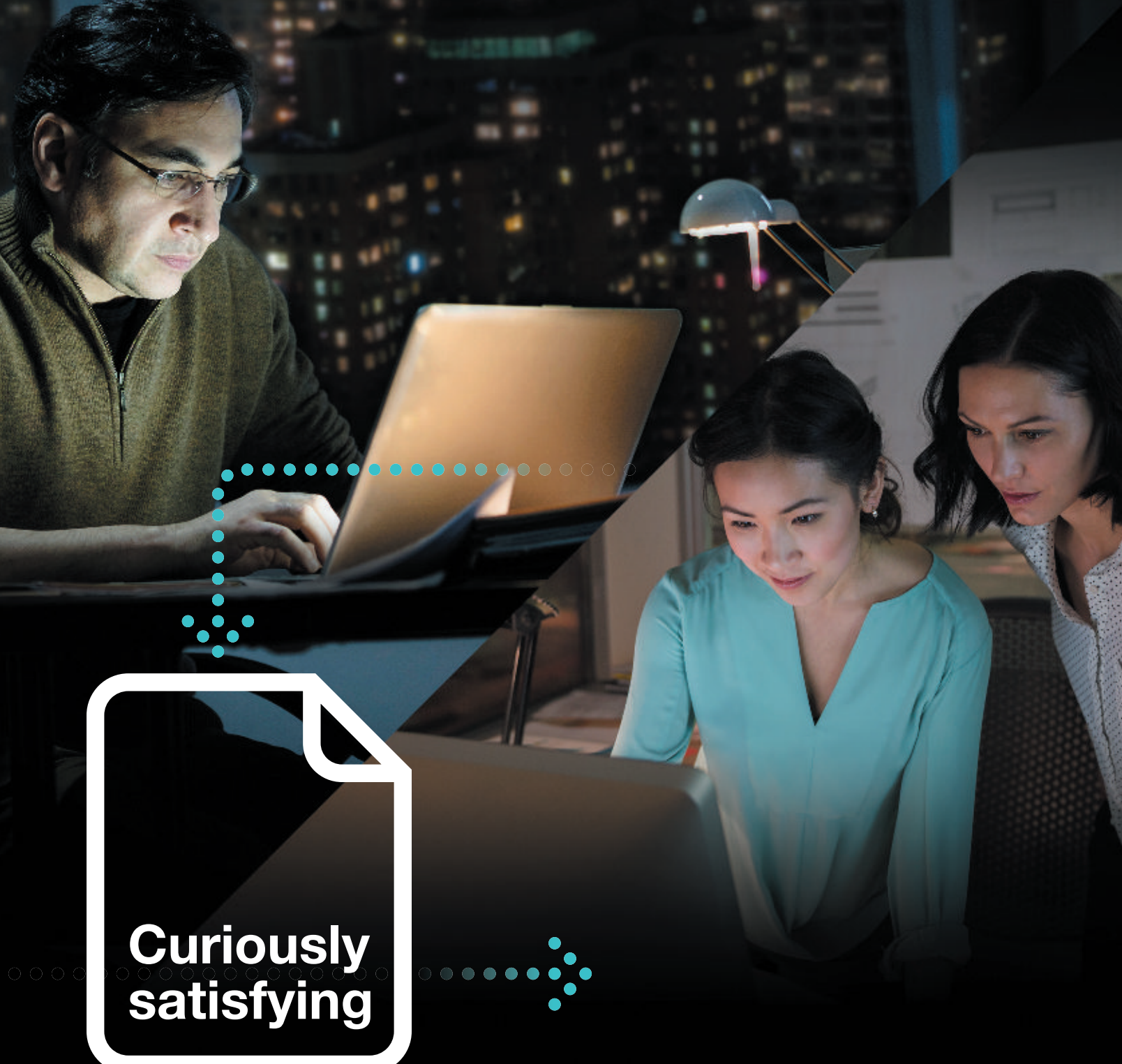
Accepted: July 9, 2016

Published: August 18, 2016

REFERENCES

- Aston-Jones, G., and Cohen, J.D. (2005). An integrative theory of locus coeruleus-norepinephrine function: adaptive gain and optimal performance. *Annu. Rev. Neurosci.* **28**, 403–450.
- Chandler, D., and Waterhouse, B.D. (2012). Evidence for broad versus segregated projections from cholinergic and noradrenergic nuclei to functionally and anatomically discrete subregions of prefrontal cortex. *Front. Behav. Neurosci.* **6**, 20.
- Chandler, D.J., Gao, W.J., and Waterhouse, B.D. (2014). Heterogeneous organization of the locus coeruleus projections to prefrontal and motor cortices. *Proc. Natl. Acad. Sci. USA* **111**, 6816–6821.
- Daigle, N., and Ellenberg, J. (2007). LambdaN-GFP: an RNA reporter system for live-cell imaging. *Nat. Methods* **4**, 633–636.
- DeFalco, J., Tomishima, M., Liu, H., Zhao, C., Cai, X., Marth, J.D., Enquist, L., and Friedman, J.M. (2001). Virus-assisted mapping of neural inputs to a feeding center in the hypothalamus. *Science* **291**, 2608–2613.
- Economo, M.N., Clack, N.G., Lavis, L.D., Gerfen, C.R., Svoboda, K., Myers, E.W., and Chandrashekar, J. (2016). A platform for brain-wide imaging and reconstruction of individual neurons. *eLife* **5**, e10566.
- Ehrengruber, M.U. (2002). Alphaviral gene transfer in neurobiology. *Brain Res. Bull.* **59**, 13–22.
- Espina, V., Wulffkuhle, J.D., Calvert, V.S., VanMeter, A., Zhou, W., Coukos, G., Geho, D.H., Petricoin, E.F., 3rd, and Liotta, L.A. (2006). Laser-capture microdissection. *Nat. Protoc.* **1**, 586–603.
- Foote, S.L., and Morrison, J.H. (1987). Extrathalamic modulation of cortical function. *Annu. Rev. Neurosci.* **10**, 67–95.
- Foote, S.L., Bloom, F.E., and Aston-Jones, G. (1983). Nucleus locus ceruleus: new evidence of anatomical and physiological specificity. *Physiol. Rev.* **63**, 844–914.
- Ghosh, S., Larson, S.D., Hefzi, H., Marnoy, Z., Cutforth, T., Dokka, K., and Baldwin, K.K. (2011). Sensory maps in the olfactory cortex defined by long-range viral tracing of single neurons. *Nature* **472**, 217–220.
- Glickfeld, L.L., Andermann, M.L., Bonin, V., and Reid, R.C. (2013). Cortico-cortical projections in mouse visual cortex are functionally target specific. *Nat. Neurosci.* **16**, 219–226.
- Gong, S., Doughty, M., Harbaugh, C.R., Cummins, A., Hatten, M.E., Heintz, N., and Gerfen, C.R. (2007). Targeting Cre recombinase to specific neuron populations with bacterial artificial chromosome constructs. *J. Neurosci.* **27**, 9817–9823.
- Harris, J.A., Hirokawa, K.E., Sorensen, S.A., Gu, H., Mills, M., Ng, L.L., Bohn, P., Mortrud, M., Ouellette, B., Kidney, J., et al. (2014). Anatomical characterization of Cre driver mice for neural circuit mapping and manipulation. *Front. Neural Circuits* **8**, 76.
- Hayden, E.C. (2014). Technology: The \$1,000 genome. *Nature* **507**, 294–295.
- Herculano-Houzel, S., Mota, B., and Lent, R. (2006). Cellular scaling rules for rodent brains. *Proc. Natl. Acad. Sci. USA* **103**, 12138–12143.
- Huang, Z.J. (2014). Toward a genetic dissection of cortical circuits in the mouse. *Neuron* **83**, 1284–1302.
- Kebschull, J.M., and Zador, A.M. (2015). Sources of PCR-induced distortions in high-throughput sequencing data sets. *Nucleic Acids Res.* **43**, e143.
- Kebschull, J.M., Garcia da Silva, P., and Zador, A.M. (2016). A new defective helper RNA to produce Sindbis virus that infects neurons but does not propagate. *Front. Neuroanat.* **10**, 6439.
- Kennedy, A., Asahina, K., Hoopfer, E., Inagaki, H., Jung, Y., Lee, H., Remedios, R., and Anderson, D.J. (2014). Internal states and behavioral decision-making: toward an integration of emotion and cognition. *Cold Spring Harb. Symp. Quant. Biol.* **79**, 199–210.
- Kim, J., Zhao, T., Petralia, R.S., Yu, Y., Peng, H., Myers, E., and Magee, J.C. (2011). mGRASP enables mapping mammalian synaptic connectivity with light microscopy. *Nat. Methods* **9**, 96–102.
- Lee, J.H., Daugharthy, E.R., Scheiman, J., Kalhor, R., Yang, J.L., Ferrante, T.C., Terry, R., Jeanty, S.S.F., Li, C., Amamoto, R., et al. (2014). Highly multiplexed subcellular RNA sequencing in situ. *Science* **343**, 1360–1363.
- Lima, S.Q., Hromádka, T., Znamenskiy, P., and Zador, A.M. (2009). PINP: a new method of tagging neuronal populations for identification during in vivo electrophysiological recording. *PLoS ONE* **4**, e6099.
- Livak, K.J., and Schmittgen, T.D. (2001). Analysis of relative gene expression data using real-time quantitative PCR and the 2^{-ΔΔC(T)} Method. *Methods* **25**, 402–408.
- Livet, J., Weissman, T.A., Kang, H., Draft, R.W., Lu, J., Bennis, R.A., Sanes, J.R., and Lichtman, J.W. (2007). Transgenic strategies for combinatorial expression of fluorescent proteins in the nervous system. *Nature* **450**, 56–62.
- Loughlin, S.E., Foote, S.L., and Fallon, J.H. (1982). Locus coeruleus projections to cortex: topography, morphology and collateralization. *Brain Res. Bull.* **9**, 287–294.
- Loughlin, S.E., Foote, S.L., and Bloom, F.E. (1986). Efferent projections of nucleus locus coeruleus: topographic organization of cells of origin demonstrated by three-dimensional reconstruction. *Neuroscience* **18**, 291–306.
- Marblestone, A.H., Daugharthy, E.R., Kalhor, R., Peikon, I.D., Kebschull, J.M., Shipman, S.L., Mishchenko, Y., Lee, J.H., Kording, K.P., Boyden, E.S., et al. (2014). Rosetta brains: a strategy for molecularly-annotated connectomics. *arXiv q-bio.NC*. arXiv:1404.5103.
- Mayer, C., Jaglin, X.H., Cobbs, L.V., Bandler, R.C., Streicher, C., Cepko, C.L., Hippenmeyer, S., and Fishell, G. (2015). Clonally related forebrain interneurons disperse broadly across both functional areas and structural boundaries. *Neuron* **87**, 989–998.
- Movshon, J.A., and Newsome, W.T. (1996). Visual response properties of striate cortical neurons projecting to area MT in macaque monkeys. *J. Neurosci.* **16**, 7733–7741.
- Munford, A.G. (1977). A note on the uniformity assumption in the birthday problem. *Am. Stat.* **31**, 119.
- Navin, N., Kendall, J., Troge, J., Andrews, P., Rodgers, L., McIndoo, J., Cook, K., Stepansky, A., Levy, D., Esposito, D., et al. (2011). Tumour evolution inferred by single-cell sequencing. *Nature* **472**, 90–94.
- Oh, S.W., Harris, J.A., Ng, L., Winslow, B., Cain, N., Mihalas, S., Wang, Q., Lau, C., Kuan, L., Henry, A.M., et al. (2014). A mesoscale connectome of the mouse brain. *Nature* **508**, 207–214.
- Oyibo, H.K., Znamenskiy, P., Oviedo, H.V., Enquist, L.W., and Zador, A.M. (2014). Long-term Cre-mediated retrograde tagging of neurons using a novel recombinant pseudorabies virus. *Front. Neuroanat.* **8**, 86.
- Reuter, J.A., Spacek, D.V., and Snyder, M.P. (2015). High-throughput sequencing technologies. *Mol. Cell* **58**, 586–597.
- Sara, S.J. (2009). The locus coeruleus and noradrenergic modulation of cognition. *Nat. Rev. Neurosci.* **10**, 211–223.
- Schüz, A., and Palm, G. (1989). Density of neurons and synapses in the cerebral cortex of the mouse. *J. Comp. Neurol.* **286**, 442–455.
- Schwarz, L.A., Miyamichi, K., Gao, X.J., Beier, K.T., Weissbourd, B., DeLoach, K.E., Ren, J., Ibanes, S., Malenka, R.C., Kremer, E.J., and Luo, L. (2015). Viral-genetic tracing of the input-output organization of a central noradrenergic circuit. *Nature* **524**, 88–92.
- Sheridan, C. (2014). Illumina claims \$1,000 genome win. *Nat. Biotechnol.* **32**, 115.
- Shiple, M.T., Halloran, F.J., and de la Torre, J. (1985). Surprisingly rich projection from locus coeruleus to the olfactory bulb in the rat. *Brain Res.* **329**, 294–299.

- Simpson, K.L., Altman, D.W., Wang, L., Kirifides, M.L., Lin, R.C., and Waterhouse, B.D. (1997). Lateralization and functional organization of the locus coeruleus projection to the trigeminal somatosensory pathway in rat. *J. Comp. Neurol.* **385**, 135–147.
- Steindler, D.A. (1981). Locus coeruleus neurons have axons that branch to the forebrain and cerebellum. *Brain Res.* **223**, 367–373.
- Sternson, S.M. (2013). Hypothalamic survival circuits: blueprints for purposive behaviors. *Neuron* **77**, 810–824.
- Van der Maaten, L., and Hinton, G. (2008). Visualizing data using t-SNE. *J. Mach. Learn. Res.* **9**, 2579–2605.
- Walsh, C., and Cepko, C.L. (1992). Widespread dispersion of neuronal clones across functional regions of the cerebral cortex. *Science* **255**, 434–440.
- Waterhouse, B.D., Lin, C.S., Burne, R.A., and Woodward, D.J. (1983). The distribution of neocortical projection neurons in the locus coeruleus. *J. Comp. Neurol.* **217**, 418–431.
- Wickersham, I.R., Finke, S., Conzelmann, K.-K., and Callaway, E.M. (2007a). Retrograde neuronal tracing with a deletion-mutant rabies virus. *Nat. Methods* **4**, 47–49.
- Wickersham, I.R., Lyon, D.C., Barnard, R.J.O., Mori, T., Finke, S., Conzelmann, K.-K., Young, J.A.T., and Callaway, E.M. (2007b). Monosynaptic restriction of transsynaptic tracing from single, genetically targeted neurons. *Neuron* **53**, 639–647.
- Xiong, C., Levis, R., Shen, P., Schlesinger, S., Rice, C.M., and Huang, H.V. (1989). Sindbis virus: an efficient, broad host range vector for gene expression in animal cells. *Science* **243**, 1188–1191.
- Zador, A.M., Dubnau, J., Oyibo, H.K., Zhan, H., Cao, G., and Peikon, I.D. (2012). Sequencing the connectome. *PLoS Biol.* **10**, e1001411.
- Zingg, B., Hintiryan, H., Gou, L., Song, M.Y., Bay, M., Bienkowski, M.S., Foster, N.N., Yamashita, S., Bowman, I., Toga, A.W., and Dong, H.W. (2014). Neural networks of the mouse neocortex. *Cell* **156**, 1096–1111.



**Curiously
satisfying**

**Introducing Sneak Peek, a preview
of Cell Press papers under review**

Exciting science needs to be shared, and fast. That's why we're introducing Cell Press Sneak Peek, a preview of the papers under review at our primary research journals. Sneak Peek makes papers discoverable earlier in the publication process—so authors can surface their research quickly and readers can build on their work.

**Go on, satisfy your curiosity!
Visit www.cell.com/sneakpeek**

CellPress

Sneak Peek

A PREVIEW OF PAPERS UNDER REVIEW

Human Astrocyte Maturation Captured in 3D Cerebral Cortical Spheroids Derived from Pluripotent Stem Cells

Steven A. Sloan,¹ Spyros Darmanis,^{3,5} Nina Huber,^{2,5} Themasap A. Khan,² Fikri Birey,² Christine Caneda,¹ Richard Reimer,⁴ Stephen R. Quake,³ Ben A. Barres,^{1,6} and Sergiu P. Pașca^{2,6,7,*}

¹Department of Neurobiology, Stanford University School of Medicine, Stanford, CA 94305, USA

²Department of Psychiatry and Behavioral Sciences, Stanford University School of Medicine, Stanford, CA 94305, USA

³Departments of Bioengineering and Applied Physics, Stanford University and Chan Zuckerberg Biohub, Stanford, CA 94305, USA

⁴Department of Neurology and Neurological Science, Stanford University School of Medicine, Stanford, CA 94305, USA

⁵These authors contributed equally

⁶Senior author

⁷Lead Contact

*Correspondence: spasca@stanford.edu

<http://dx.doi.org/10.1016/j.neuron.2017.07.035>

SUMMARY

There is significant need to develop physiologically relevant models for investigating human astrocytes in health and disease. Here, we present an approach for generating astrocyte lineage cells in a three-dimensional (3D) cytoarchitecture using human cerebral cortical spheroids (hCSs) derived from pluripotent stem cells. We acutely purified astrocyte-lineage cells from hCSs at varying stages up to 20 months *in vitro* using immunopanning and cell sorting and performed high-depth bulk and single-cell RNA sequencing to directly compare them to purified primary human brain cells. We found that hCS-derived glia closely resemble primary human fetal astrocytes and that, over time *in vitro*, they transition from a predominantly fetal to an increasingly mature astrocyte state. Transcriptional changes in astrocytes are accompanied by alterations in phagocytic capacity and effects on neuronal calcium signaling. These findings suggest that hCS-derived astrocytes closely resemble primary human astrocytes and can be used for studying development and modeling disease.

INTRODUCTION

Astrocytes comprise the most numerous cell type in the mammalian brain, yet we understand remarkably little about their development and physiological functions. Their juxtaposition to neuronal synapses explains many of their passive roles in the central nervous system (CNS), such as neurotransmitter recycling. Recent evidence, however, suggests that astrocytes also play active roles (Freeman and Rowitch, 2013), including the control of synapse formation (Allen et al., 2012; Christopherson

et al., 2005), function (Eroglu et al., 2009; Tsai et al., 2012), and elimination (Chung et al., 2013). Because of technical limitations, human astrocytes have received particularly little study. Recently, Zhang et al. (2016) reported that human astrocytes exist in at least two distinct stages: a fetal, proliferative, astrocyte progenitor cell (APC) state and an adult, non-proliferative, mature state. Several thousand genes are differentially expressed between fetal and adult human astrocytes (Zhang et al., 2016), and many of these genes have been implicated in functional processes such as synapse formation (*SPARCL1*). Interestingly, in humans, the majority of mature astrocyte markers increase in expression during a time window extending throughout gestation until early postnatal development, which correlates with synapse density in the human cerebral cortex (Huttenlocher, 1979; Huttenlocher et al., 1982) and is thought to be critical for neuropsychiatric disease development. Therefore, elucidating the program underlying human astrocyte maturation and the ability to recapitulate these complex processes in human cellular models are a prerequisite for better understanding astrocyte development and function as well as the role of glia in brain disorders.

Unfortunately, investigating human astrocyte maturation within primary brain tissue is challenging; sample availability is sparse, particularly for critical developmental time periods such as late gestation or early postnatal stages. Human induced pluripotent stem cells (iPSCs) provide a unique platform to investigate neural development *in vitro* (Dolmetsch and Geschwind, 2011; Pașca et al., 2014; Tabar and Studer, 2014) and to elucidate mechanisms of astrocyte development and dysfunction. To date, several groups have developed methods for generating astrocytes from iPSCs in two-dimensional (2D)/monolayer cultures (Emdad et al., 2012; Juopperi et al., 2012; Krencik and Ullian, 2013; Krencik and Zhang, 2011; Roybon et al., 2013; Shaltouki et al., 2013), but these methods have limitations, especially in maintaining long-term cultures and non-reactive states *in vitro*.

To address these issues, we used a 3D differentiation approach that we previously developed for generating cerebral

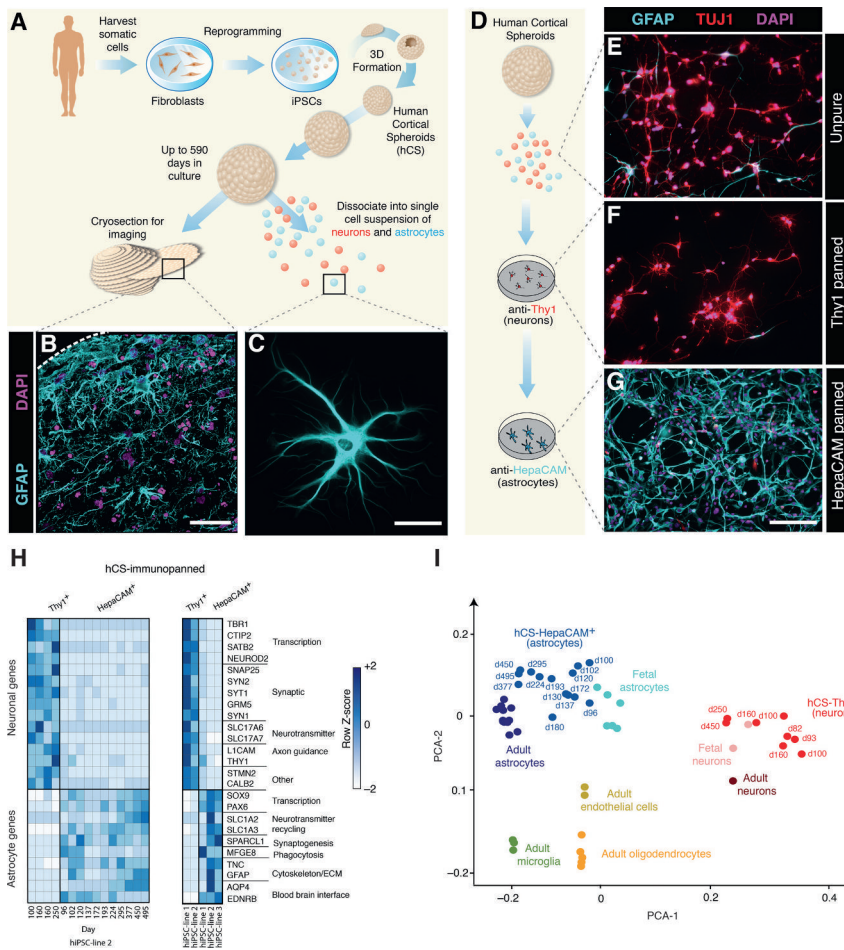


Figure 1. Purification of Astrocytes from hCSs

(A) Schematic for generating hCSs from iPSCs. Single colonies are enzymatically dissociated and suspended in low-attachment plates to form neural spheroids.

(B) GFAP immunostaining of astrocytes in a 10 μ m hCS cryosection at 363 days in culture. Scale bar, 50 μ m.

(C) GFAP staining of an astrocyte isolated from a hCS at 295 days and cultured for 3 days in monolayer. Scale bar, 30 μ m.

(D) hCSs can be immunopanned after single-cell dissociation to isolate neurons with an anti-Thy1 antibody and astrocytes with an anti-HepaCAM antibody.

(E–G) Representative images are shown for cultured samples of unsorted cells (E), Thy1-panned neurons (F), and HepaCAM-panned astrocytes (G). Cells are immunostained with an anti-TUJ1 antibody (red) for neurons and anti-GFAP antibody (cyan) for astrocytes. Scale bar, 150 μ m.

(H) RNA-seq expression data showing enrichment of neuronal and astrocyte-specific genes in bulk Thy1- and HepaCAM- immunopanned samples. Left: variability in immunopanned samples from a single iPSC line across multiple differentiations (HepaCAM: 3–15 hCSs per time point from one iPSC line in 11 differentiation experiments; Thy1: 3–15 hCSs per time-point from one iPSC line from 4 differentiations experiments). Right: variability in immunopanned samples across multiple iPSC lines (HepaCAM: 3–15 hCSs per time point from 3 iPSC lines in 1–11 differentiations per line; Thy1: 3–15 hCSs per time point from 2 iPSC lines in 4 differentiations per line).

(I) PCA using the top two principal components and showing bulk RNA-seq of primary human fetal

and adult CNS cell type samples along with hCS-derived neurons and astrocytes. The top 5,000 over-dispersed genes were used for analysis. hCS-derived cells are labeled by *in vitro* differentiation stage (d, day); 3–15 hCSs were collected from two iPSC lines across 18 differentiation experiments.

cortex-like structures (Paşca et al., 2015) and leveraged the unique ability of these cultures to be maintained for long-term *in vitro* (20 months and beyond) to study their transcriptional and functional maturation. In these floating 3D neural cultures, named human cortical spheroids (hCSs), astrocyte lineage cells are generated spontaneously among a network of cortical neurons. The hCSs grow up to \sim 4 mm in diameter and recapitulate key features of *in vivo* cortical development (Paşca et al., 2015), such as the presence of cortical lamination, abundant synaptogenesis, and robust spontaneous electrical activity. We repurposed strategies for isolating primary human neural and glial cells using immunopanning (Zhang et al., 2016) to purify astrocyte lineage cells directly from hCSs and compared the transcriptional profile of these cells to primary astrocytes isolated from the fetal and adult CNS. We maintained hCSs in long-term cultures up to 590 days *in vitro* and performed a time series of single-cell RNA sequencing (RNA-seq) to capture the dynamics of astrocyte differentiation *in vitro* over a long time window. This enabled us to ask whether astrocyte lineage cells within hCSs mature over time and whether this process is associated with cell-autonomous (synapse phagocytosis) and non-cell-autonomous (calcium signals in neurons) effects.

and non-cell-autonomous (calcium signals in neurons) effects.

RESULTS

Generation and Purification of Astrocyte Lineage Cells from iPSC-Derived hCSs

To generate human astrocytes from human pluripotent stem cells in 3D cultures, we derived hCSs using a previously established approach (Paşca et al., 2015). hCSs are specified and maintained in floating conditions on low attachment and can be either cryosectioned for immunostaining or dissociated into single-cell suspensions for 2D culture, fluorescent-activated cell sorting (FACS), and other downstream analyses (Figure 1A). As previously described (Birey et al., 2017; Deverman et al., 2016; Paşca et al., 2015; Paşca, 2016), immunostainings on hCS cryosections for glial fibrillary acidic protein (GFAP) revealed abundant astrocyte-like cells that were distributed throughout the parenchyma, and 2D culture of dissociated hCSs showed GFAP-expressing cells with characteristic morphological features of astrocytes (Figures 1B and 1C).

We refer to these GFAP-expressing cells as astrocyte lineage cells, an umbrella term that encompasses multiple stages of astrocyte differentiation, which may include radial glia (RG), outer radial glia (oRG), astrocyte progenitor cells (APCs), and mature astrocytes.

To purify astrocyte lineage cells from hCSs, we adapted our existing protocols for immunopanning primary human fetal and adult brain tissue (Zhang et al., 2016). Immunopanning involves passing a single-cell suspension of dissociated tissue over a series of cell culture plates coated with antibodies directed against cell-type-specific antigens. As few as one hCS can be used for immunopanning, with a yield prior to immunopanning of about 500,000–1,000,000 live cells per hCS. Our immunopanning protocol consisted of an anti-Thy1 (Thy1 or CD90) antibody to bind neurons and an anti-hepatic and glial cell adhesion molecule (HepaCAM) antibody to bind astrocytes (Figure 1D). The advantage of using the cell adhesion glycoprotein HepaCAM for immunopanning is that the *HEPACAM* gene is enriched in astrocytes, but it is not as highly expressed by radial glia (Zhang et al., 2016). hCSs contain only neural ectoderm derivatives and therefore do not require depletion of myeloid or vascular populations during the purification protocol as compared to primary brain tissue samples. After binding to antibody-coated plates, the cells of interest were either collected via trypsinization for subsequent culture in 2D or directly scraped off the plate to extract RNA for transcriptional profiling.

To verify the purity of the immunopanning process in hCSs, we cultured immunopanned hCS-derived neurons and astrocyte lineage cells in monolayer for 7 days and immunostained with antibodies against β -tubulin class III (*TUBB3* or TUJ1) to identify neurons and anti-GFAP to identify glial cells (Figures 1E–1G). Whereas unpurified cultures of dissociated hCSs contained both GFAP- and TUJ1-expressing cells, the immunopanned populations were enriched for either neurons (Thy1-panned) or astrocyte lineage cells (HepaCAM-panned), respectively. In line with our previous findings (Paşca et al., 2015), immunopanning of hCSs with the anti-Thy1 antibody isolated numerous neurons as early as 40 days of differentiation *in vitro*, whereas HepaCAM immunopanning became increasingly efficient after 100 days of differentiation *in vitro*. This is suggestive of *in vivo* cell lineage progression in the human dorsal pallium, as well as the delayed onset of astrocyte generation, which typically begins only after the substantive portion of neurogenesis is complete (Freeman and Rowitch, 2013; Sloan and Barres, 2014).

RNA-Seq Transcriptional Profiling of hCS-Derived Astrocyte Lineage Cells and Comparison to Primary Human Cells

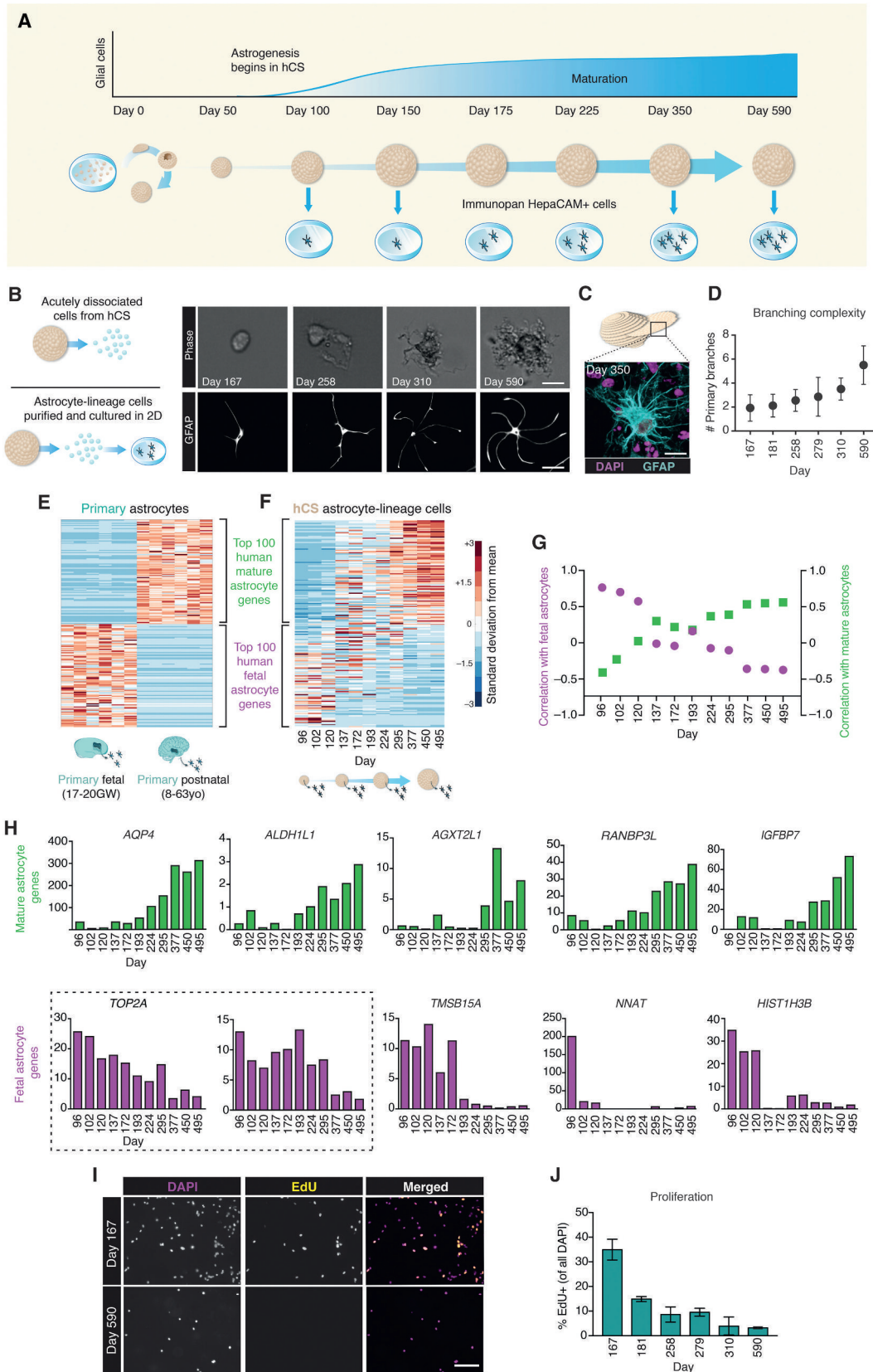
Because GFAP is present in both astrocytes and radial glia in the developing mammalian brain and is often undetected in some mature astrocytes (Middeldorp et al., 2010; Oberheim et al., 2009), we used RNA-seq to verify the level of expression of a series of well-established neuronal and astrocyte markers (Cahoy et al., 2008; Lovatt et al., 2007; Zhang et al., 2016) in HepaCAM-isolated cells as compared to neurons isolated from hCSs. For example, we found high expression of the water trans-

porter Aquaporin-4 (*AQP4*), the transcription factor *SOX9*, and the glial high-affinity glutamate transporter (*SLC1A3*) in hCS-derived astrocyte lineage cells, but not in hCS-derived neurons, which instead showed high expression of neuronal markers such as *TBR1*, *SYN1*, and *L1CAM* (Figure 1H). These findings were consistent across hCSs derived from multiple iPSC lines at various time points and in independent differentiation experiments, as indicated by previous work with this differentiation platform (Paşca et al., 2015).

We next wanted to investigate the transcriptome level fidelity of hCS-derived cells as compared to primary human astrocytes and neurons. We leveraged our primary human RNA-seq transcriptome datasets (Zhang et al., 2016), which include bulk samples of purified forebrain fetal astrocytes, postnatal astrocytes, fetal neurons, postnatal neurons, oligodendrocytes, endothelial cells, and microglia/macrophages, and directly compared these to our hCS-derived samples across multiple *in vitro* differentiation stages (from day 100 to day 450). hCSs can be maintained in floating conditions in ultra-low attachment plates for long periods of time (beyond 25 months in our experience); even after hundreds of days *in vitro*, hCSs were intact, retained a spherical morphology (Figure S1A), and displayed high cell viability (>90%) after dissociation (Figures S1B and S1C). As expected, the relative proportions of glia and neurons within hCSs varied with *in vitro* differentiation stage, and GFAP⁺ cells were found increasingly dispersed throughout the neuropil (Figures S1D–S1F; Paşca et al., 2015). Principal component analysis (PCA) of immunopanned bulk samples showed hCS-derived HepaCAM⁺ cells clustered closely to fetal and mature human primary astrocytes and hCS-derived Thy1⁺ cells clustering closely to fetal and adult human neuronal samples. As expected, the remaining primary human CNS cell type samples (oligodendrocytes, endothelial cells, and microglia) clustered distinctly from hCS-derived astrocyte and neuronal samples (Figure 1I; Figure S1G). This division could be further appreciated from the degree of correlation between hCS-derived and fetal astrocytes ($R^2 = 0.83$, Pearson correlation, $p < 0.0001$) versus the correlation between hCS-derived astrocytes and other human CNS cell types ($R^2 = 0.61$, Pearson correlation, $p < 0.001$) (Figure S1H).

Astrocyte Maturation within hCSs

We next asked whether, over longer time periods *in vitro*, astrocytes within hCSs might undergo a transition from a fetal to a more mature state. We first established a time window for when the transition from fetal to mature astrocytes might occur *in vivo*. We utilized our existing datasets of human astrocytes (Zhang et al., 2016) to identify the top 100 fetal and top 100 mature astrocyte genes that demarcate these two maturation states and that were not expressed in other CNS cell types. We then asked how expression of these astrocyte-specific markers varied in transcriptomic datasets obtained from human brain tissue across numerous regions and developmental periods (Kang et al., 2011). This comparison revealed a consistent trend, in which the expression of the top 100 mature astrocyte markers started to increase as early as 50–100 days post-conception, accelerating around birth and continuing to increase throughout the first several months of the postnatal period. Similarly, fetal astrocyte markers declined rapidly over this same time



(legend on next page)

period (Figure S2). This suggests that the relevant signaling cues responsible for astrocyte maturation likely occur during this critical developmental window. Therefore, we leveraged the ability of hCSs to be maintained for long periods *in vitro* and cultured hCSs for up to 590 days (~20 months) to investigate whether we could capture this maturation process within our system (Figure 2A).

We purified HepaCAM⁺ cells from hCSs at multiple time points ranging from day 100 to day 590. We observed that immediately after dissociation into single cells, the morphologies of older hCS-derived HepaCAM⁺ cells were more complex than those isolated at earlier time points (Figure 2B). This morphological complexity was maintained in monolayer culture and purified cells displayed a significant increase in the number of primary branches with increasing *in vitro* age (Figures 2C and 2D; one-way ANOVA, $F_{(5,143)} = 15.68$, $p < 0.0001$; $n = 15\text{--}38$ cells/time point).

To investigate whether the morphological changes were consistent with transcriptome-level evidence of maturation, we performed RNA-seq on hCS-purified astrocyte lineage cells at each of the above time points. We then identified the top 100 most specifically enriched mature or fetal astrocyte genes from our primary datasets and used this 200-gene barcode as a benchmark of astrocyte maturation. When we chronologically ordered all hCS-derived astrocyte lineage samples from youngest to oldest, we observed a clear trend in the expression pattern of these 200 signature genes: hCS-derived astrocyte lineage cells from days 100–150 were predominantly enriched in the fetal astrocyte cassette of genes, whereas astrocytes from older hCSs, and particularly beyond day 250 *in vitro*, expressed higher levels of nearly all mature astrocyte genes (Figures 2E and 2F). To better quantify the degree of maturation, we calculated correlation values for hCS-derived astrocytes with either primary fetal or mature human astrocytes. The correlation coefficients with mature primary astrocytes increased steadily with *in vitro* age of hCS-derived astrocytes, while the degree of fetal astrocyte correlation declined over the same time course (Figure 2G, Spearman correlations). We then looked

at the expression of individual fetal and mature astrocyte genes over time and observed similar trends in the gradual increase and decrease of mature and fetal genes, respectively (Figure 2H). Based on these data, we hereon refer to astrocyte lineage cells isolated from hCSs after 250 days of *in vitro* differentiation as mature hCS-derived astrocytes, as a respective comparison to those from earlier time points. Despite the close correlation between bulk hCS-derived HepaCAM⁺ cells and primary adult astrocyte samples, we did observe some degree of separation between these two populations. The genes that contribute to this separation, and the respective gene ontological pathways that are specific to primary adult astrocytes versus hCS astrocytes after day 250 *in vitro*, can be found in Table S1.

The well-established proliferative markers *TOP2A* and *MKI67* are highly enriched in fetal astrocytes and steadily decrease with maturation. Previous work has demonstrated that fetal human astrocytes are highly proliferative as compared to mature astrocytes (Zhang et al., 2016). To determine whether this functional difference was maintained across early and late hCS-derived astrocytes, we purified astrocytes from hCSs at various *in vitro* stages. After purification, the cells were grown in monolayer culture with the nucleoside analog 5-ethynyl-2'-deoxyuridine (EdU) to quantify the degree of cell proliferation. After 7 days, the percent of nuclei labeled with DAPI that had undergone at least one cell division declined from $34.9\% \pm 3.4\%$ in day 167 hCSs to only $3.2\% \pm 2.6\%$ in cells harvested from day 590 hCSs (Figures 2I and 2J; one-way ANOVA, $F_{(5,11)} = 49.48$, $p < 0.0001$, $n = 3$ wells per condition). Interestingly, we noticed a slight discrepancy between the expression of mitotic markers (*MKI67* and *TOP2A*) and the proliferation data, which could be related to differences between RNA and protein levels, sensitivity of the two cell proliferation assessments, or cell-culture-related effects.

Single-Cell RNA-Seq of hCSs

To obtain greater resolution into cell type identity and to capture the diversity of hCS-derived glial cells as they transition from fetal progenitors to a more mature state, we performed

Figure 2. Maturation of hCS-Derived Astrocyte Lineage Cells

(A) Schematic predicting the time course of astrogenesis and maturation in hCSs.

(B) Phase images of dissociated astrocytes on the immunopanning plate at various ages (top; scale bar, 12 μm) and after immunostaining with an anti-GFAP antibody following 7 days in monolayer culture (bottom; scale bar, 50 μm).

(C) GFAP immunostain of a cryosection from a hCS at day 350 demonstrates branched morphology of astrocytes within the 3D cytoarchitecture. Scale bar, 10 μm .

(D) Quantification of the number of primary branches in GFAP⁺ cells following 7 days in monolayer culture. One-way ANOVA, $F_{(5,143)} = 15.68$, $p < 0.0001$; $n = 15\text{--}38$ cells/time point.

(E) Heatmap indicating expression of the top 100 fetal and top 100 mature astrocyte-specific genes in primary fetal and astrocyte samples.

(F) Heatmap for the expression of the same 200 genes in hCS-derived astrocytes over *in vitro* culture from day 96 to day 495. The heatmaps are normalized across each gene (row). Cells at the extreme early and late time points express the highest levels of fetal and mature astrocyte genes, respectively, whereas the transitional time points (days 150–300) express more intermediate levels of these genes. Data derived from one iPSC line in 11 differentiation experiments (3–15 hCSs per time point).

(G) Spearman correlations between hCS-derived astrocytes of varying *in vitro* stages and primary fetal (magenta) or mature (green) astrocytes. Values represent Spearman rank correlations on the 200 genes between (F) and (G).

(H) FPKM values of selected mature (top row, green) and fetal (bottom row, purple) astrocyte genes in hCS astrocytes purified at different *in vitro* stages. Boxed graphs highlight the decline in expression of proliferative markers as hCS-derived astrocytes mature.

(I) Representative images from the EdU proliferation assay. Astrocytes were purified from hCSs and grown in monolayer culture with 10 μM EdU for 48 hr and then fixed at 7 days. Scale bar, 100 μm . Data derived from two iPSC lines in seven differentiation experiments (3–15 hCSs per time point).

(J) Quantification of proliferation in culture. Percentages represent the number of EdU-positive cells per total number of DAPI⁺ nuclei. One-way ANOVA, $F_{(5,11)} = 49.48$, $p < 0.0001$; $n = 3$ wells/time point.

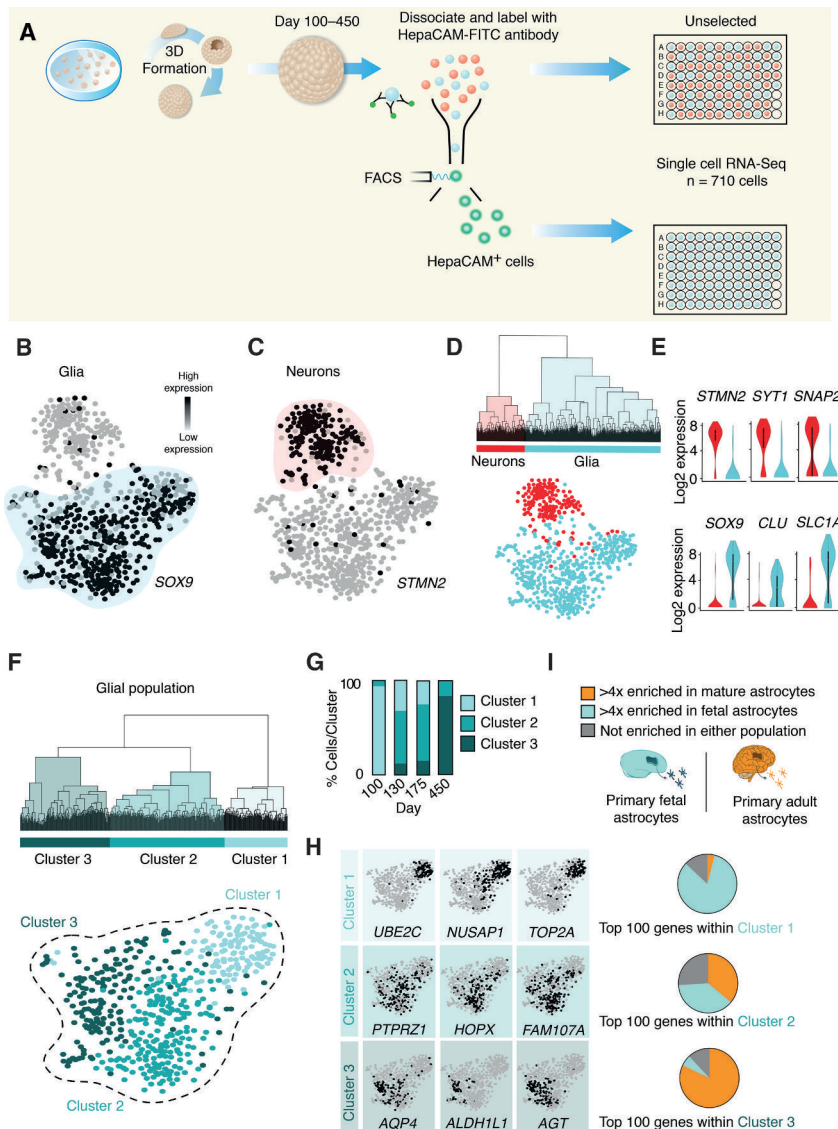


Figure 3. Single-Cell RNA-Seq of iPSC-Derived hCSs

(A) hCSs were dissociated at different *in vitro* stages and single cells were isolated by FACS into 96-well plates (n = 710 cells). Cells were either randomly selected without any immunolabeling or gated by the presence of FITC-conjugated HepaCAM antibodies. Single cells were derived from two iPSC lines from five differentiation experiments (3–7 hCSs per time point).

(B) Glial population (cyan) indicated by *SOX9* gene expression in the t-SNE space of all hCS cells. Dark circles indicate high expression, and gray circles indicate low expression.

(C) Neuronal population (red) indicated by *STMN2* gene expression in the t-SNE space of all hCS cells.

(D) Unsupervised hierarchical clustering (top 1,000 over-dispersed genes) showing separation of glial and neuronal populations.

(E) Violin plots demonstrating expression patterns of generic cell-type-specific markers.

(F) Unsupervised hierarchical clustering of the glial population in (B) and (D) (top 1,000 over-dispersed genes) revealing three clusters (1–3). Glial population (from B and D) are colored by cluster identity.

(G) Distribution of cells from each *in vitro* differentiation stage across clusters 1–3.

(H) Expression of enriched genes within clusters 1–3. (I) The proportion of the top 100 genes in clusters 1–3 that were enriched in adult astrocytes (orange, >4-fold expression increase in primary mature versus primary fetal astrocytes), fetal astrocytes (cyan, >4-fold expression increase in primary fetal versus mature primary astrocytes), or indeterminate (gray).

single-cell RNA-seq on individual cells from the same iPSC line across four different time points (*in vitro* differentiation days 100, 130, 175, and 450). At each of these time points, we dissociated hCSs into a single-cell suspension and collected both unsorted cells, as well as sorted astrocyte lineage cells, using anti-HepaCAM antibodies conjugated to fluorescein isothiocyanate (FITC) (Figure 3A). In total, we extracted sufficient RNA for cDNA library construction on 710 individual cells across these differentiation stages. To minimize batch effects, we collected single cells from multiple *in vitro* differentiation stages in the same sorting experiment, performed library generation on samples in tandem, and sequenced cells from multiple time points simultaneously.

To cluster hCS-derived cells, we first identified over-dispersed genes to calculate a distance matrix for all cells and then used t-distributed stochastic neighbor embedding (t-SNE) dimensionality reduction to condense the data into a 2D space (van der Maaten and Hinton, 2008) (Supplemental Information). The

expressed the astrocyte-related marker *SOX9* and one neuronal that included cells expressing the neuronal marker *STMN2* (Figures 3B and 3C). To take an unbiased approach toward classifying cells, we performed unsupervised hierarchical clustering, which separated the neuronal and glial populations along the same spatial segregation observed using t-SNE (Figures 3D and 3E). As expected, the number of HepaCAM-isolated cells was greatly enriched in the glial population (95%), whereas the neuronal population was largely derived from unselected cells (Figures S3A and S3B). Moreover, the HEPCAM⁺ population contained only a small proportion of ventral RG-like cells (vRGs) as assessed by single-cell profiling and immunocytochemistry (Figures S3C and S3D). Within the *STMN2*⁺ population, we observed neurons expressing deep cortical layer markers (*TBR1* and *ETV1*), as well as neurons expressing upper layer markers (*SATB2* and *TLE1*). As expected, these upper layer markers were primarily derived from hCSs at later stages of *in vitro* differentiation (Figure S3E; Paşca et al., 2015).

To further investigate astrocyte lineage cells, we performed unsupervised hierarchical clustering on the glial cell group. This analysis revealed three primary clusters of cells (Figure 3F), which correlated with *in vitro* differentiation stage (Figure S3F). For example, of the 40 glial cells derived from day 100 hCSs, 39 were assigned to cluster 1, whereas 41 out of 50 cells isolated from hCSs at day 450 were located in cluster 3 (Figure 3G). Cluster 1 contains cells expressing proliferation-related genes, such as *TOP2A*, *NUSAP1*, and *UBE2C*, while cluster 2 and cluster 3 include genes associated with progenitor cells (*HOPX*, *PTPRZ1*, and *FAM107A*) or mature astrocytes (*ALDH1L1*, *AQP4*, and *AGT*), respectively (the top enriched genes per cluster can be found in Table S2). The set of genes that define glial cluster 2 suggested overlap with the recently reported transcriptomic signature of human oRG (Pollen et al., 2015). Therefore, we wondered whether cluster 2 cells might represent a glial lineage of oRGs within hCSs. We directly compared our single-cell RNA-seq data from hCS-derived glia to single-cell data from fetal human brain tissue that was micro-dissected from the ventricular or subventricular zones around gestational weeks 16–18 (GW16–GW18) (Pollen et al., 2015). To control for potential batch effects between these datasets, we normalized FPKMs for each cell via centering and scaling. The resulting t-SNE analysis separated clusters by cell type rather than by experimental origin (Figures S4A–S4C). Subsequent unsupervised hierarchical clustering of hCS-derived glia and primary fetal ventricular/subventricular zone-derived glia produced three distinct clusters (Figures S4D and S4E), which varied in their expression of maturation genes in a pattern similar to what was shown in Figure 3H (Figure S4F). We found that the ventricular zone-dissected primary cells (Pollen et al., 2015) were located almost exclusively within the most immature of these clusters (cluster 1), while subventricular zone-dissected primary cells containing primary oRGs were almost all located in cluster 2. To examine the spatial distribution of oRGs within hCS cytoarchitecture, we performed immunohistochemistry on cross-sections of hCSs and observed expression of the oRG-related *HOPX* marker in the outermost region of the hCS proliferative zones (Figure S4G). Interestingly, none of the primary human fetal tissue cells from GW16–GW18 were found close to the most mature hCS glial cluster 3 (Figures S4H and S4I), which was primarily comprised of hCS-derived astrocytes collected at 450 days of *in vitro* maturation.

These results prompted us to investigate how single-cell data collected from primary adult human brain tissue (Darmanis et al., 2015) might juxtapose with the t-SNE clustering of hCS-derived cells. Comparison to our hCS-derived cells revealed close association of adult primary astrocytes and neurons with respective glial and neuronal populations in hCS at late stages of *in vitro* differentiation (Figures S5A–S5C). We next performed Monocle analysis, which utilizes an unsupervised lineage algorithm to recover single-cell gene expression kinetics over a temporal process such as cell differentiation (Trapnell et al., 2014). The intent of Monocle is to place cells in order of progress through a biological process without *a priori* knowledge of which genes to include. This analysis revealed two clear lineage paths (one neuronal and one glial), whose predicted pseudotime assignments matched closely with *in vitro* differentiation stages of hCSs (Figures S5D and S5E). We used this analysis to identify,

in an unbiased manner, gene modules associated with astrocyte differentiation (Figure S5F; Table S3).

To further verify that cells belonging to the various astrocyte clusters reflect maturation states that have been identified *in vivo*, we correlated the degree of maturation within each population to our primary astrocyte data. We identified the top 100 most specific genes in each glial cluster (as determined from the Wilcoxon signed-rank test for each population) and calculated the enrichment (or depletion) of those genes in primary fetal or mature human astrocytes. We binned each gene into either a fetal (>4-fold enriched in fetal human astrocytes), mature (>4-fold enriched in mature human astrocytes), or unidentified category. We found that the majority of the genes that define the proliferating cluster 1 (83/100) were enriched in fetal astrocytes. This is in contrast to the mature astrocyte population (cluster 3) whose gene signature was defined predominantly by genes enriched in mature human astrocytes (82/100; Figure 3I).

Stage-Dependent Functional Properties of hCS-Derived Astrocytes

To supplement the transcriptomic comparison to primary human astrocytes, we next asked whether hCS astrocyte lineage cells display functional physiological properties similar to what would be expected *in vivo*. In particular, we investigated the ability of hCS-derived HepaCAM-isolated cells to: (1) uptake glutamate via specific excitatory amino acid transporters, (2) phagocytose synaptosomes, (3) induce synapse formation in neurons, and (4) modulate calcium signaling in neurons.

One of the most accepted physiological roles for astrocytes in the CNS is the ability to recycle glutamate that is released at the synaptic cleft (Anderson and Swanson, 2000). To investigate whether excitatory amino acid transporters (EAAT) mediate glutamate uptake in hCS astrocyte lineage cells, we purified HepaCAM⁺ cells from hCSs at day 153 or day 419 and then incubated them with radioactive glutamate (L-[2,3,4-³H] glutamate) in the presence or absence of DL-threo-β-Benzyloxyaspartic acid (TBOA), a competitive non-transportable blocker of excitatory amino acid transporters (Figure S6A). These experiments showed uptake of glutamate in HepaCAM⁺ cells that was significantly reduced by TBOA (Figure S6B; paired t test, *p* = 0.04).

A more recent and intriguing finding about astrocytes is their ability to robustly phagocytose synapses in the rodent brain (Chung et al., 2013). Because synapse pruning has critical relevance to CNS development and disease pathophysiology (Penzes et al., 2011), we asked whether hCS-derived astrocytes could also phagocytose synaptosomes *in vitro*. We purified synaptosomes from mouse brains by differential centrifugation (Dunkley et al., 2008) and labeled them with the fluorescent dextran pHrodoRed, a succinimidyl ester that is non-fluorescent until it is exposed to a low pH environment like the one in phagosomes. This is advantageous as it prevents quantification of synaptosomes that are simply adhering to the outside of cells. We incubated astrocytes purified from day 160 hCSs with pHrodoRed-labeled synaptosomes for 16 hr and imaged them every 15 min with an incubator-mounted system (Incucyte, EssenBiosciences). We observed robust phagocytic activity over this time period with numerous, distinct sites of

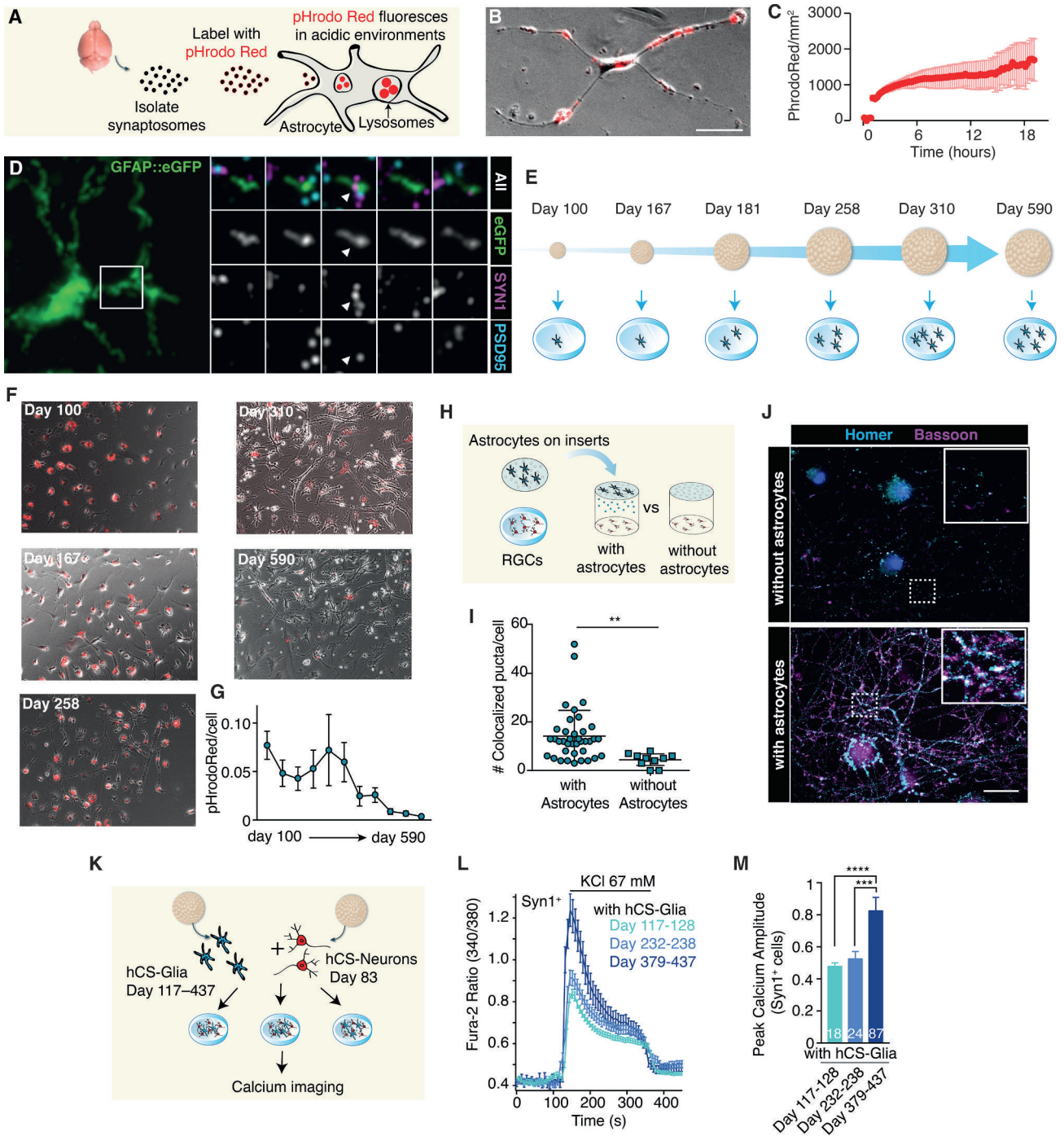


Figure 4. Functional Changes during hCS-derived Astrocyte Maturation In Vitro

(A) Synaptosomes were harvested from the mouse brain and labeled with pHrodoRed, a pH-sensitive indicator that fluoresces only at acidic pH (<6). (B) A representative astrocyte from a hCS (day 150) cultured in monolayer with pHrodoRed-labeled mouse synaptosomes for 2 hr. Phagocytosed synaptosomes fluoresce red and can be seen in multiple locations within the astrocyte. Scale bar, 20 μ m. (C) Quantification of phagocytosis over 16 hr. Synaptosomes were added at $t = 1$ hr, and images were taken every 15 min. Data from three batches of hCSs (3–15 hCSs per batch) derived from one iPSC line in one differentiation. (D) Left: array tomography from an intact hCS that was previously labeled with the hGFAP::eGFP reporter. Right: synaptogram showing the co-localization of pre- and postsynaptic puncta within an astrocyte process. Images represent serial 70 nm sections. (E) Time course of hCS astrocyte purification for functional studies.

(legend continued on next page)

phagocytic uptake on hCS-derived astrocytes (Figures 4A–4C; Figure S6C; Movie S1). Additionally, we investigated whether synapse phagocytosis by hCS-derived astrocytes was occurring endogenously within hCSs during *in vitro* differentiation. We labeled glial cells within hCSs with a hGFAP::eGFP lentivirus and performed array tomography (AT) and immunostaining on ultra-thin cryosections (70 nm) for both presynaptic (SYN1) and postsynaptic markers (PSD95). Using synaptogram reconstructions (Figure 4D), we identified double-positive puncta for SYN1 and PSD95 within individual eGFP⁺ processes of hCS-derived glia, suggesting that endogenous synaptic phagocytosis occurs within hCSs.

We next asked whether astrocyte maturation state correlated with the cell-autonomous functional ability to phagocytose synaptosomes *in vitro*. We purified HepaCAM⁺ cells from several differentiation time points spanning day 100 to day 590 *in vitro* (Figure 4E) and compared their ability to engulf pHrodoRed-labeled synaptosomes. We observed a significant decline in the quantity of phagocytosed synaptosomes as the age of the hCS-derived astrocytes increased (Figures 4F and 4G; one-way ANOVA, $F_{(10,273)} = 2.83$, $p = 0.002$; $n = 9$ fields/time point). Differences in morphology and arborization between hCS-derived astrocytes of different ages were accounted for by normalizing synaptosome engulfment to the total area of the cell (STAR Methods). This age-dependent decline in astrocyte phagocytosis is consistent with *in vivo* observations in mice (Chung et al., 2013). Thus, both mouse and human immature astrocytes display a higher phagocytic ability than mature astrocytes.

In addition to synapse elimination, astrocytes also play a crucial synaptogenic role during CNS development. Therefore, we next asked whether hCS astrocyte lineage cells could induce synapse formation when cultured with retinal ganglion cells (RGCs) (Allen et al., 2012; Christopherson et al., 2005; Ullian et al., 2001). RGCs can be cultured in defined media without astrocytes and therefore are commonly used as a model for assessing synapse formation. As seen in rodent and primary human astrocytes, we observed a robust induction of synapses when RGCs were cultured beneath an insert of hCS-derived astrocytes, which was relatively consistent in hCS-derived astrocytes isolated from 172 to 495 days *in vitro* (Figures 4H–4J; RGCs with astrocytes: 14.2 ± 1.7 synapses/field; RGCs without astrocytes 4.4 ± 0.9 synapses/field; two-tailed t test, $p = 0.006$; mean \pm SEM, Figure S6D). These

data suggest that the decreased phagocytic activity in older hCS-derived astrocytes is unlikely to be a result of decreased cell health, as older hCS-derived astrocytes demonstrated similar synaptogenic properties as astrocytes from younger time points.

Finally, we investigated whether the maturation of hCS-derived astrocyte lineage cells can influence neuronal function. We tested whether depolarization-induced calcium signaling in immature hCS-derived neurons at early *in vitro* stages was affected by the presence of hCS astrocyte lineage cells isolated at early versus late stages of differentiation (Figure 4K). We dissociated human neurons from early hCSs (day 83 of differentiation), infected them with a viral reporter (AAV-DJ, hSyn1::mCherry), and co-cultured them in monolayer with HepaCAM-isolated cells from hCSs of three *in vitro* stages: days 117–128, days 232–238, or days 379–437. We then performed calcium imaging using the ratiometric dye fura-2 and found a significant (~66%) increase in the peak $[Ca^{2+}]_i$ amplitude after depolarization in Syn1⁺ neurons co-cultured with astrocytes isolated from hCSs at days 379–437 as compared to earlier time points (Figures 4L and 4M, one-way ANOVA; $F_{(2, 126)} = 15.69$, $p < 0.0001$; post hoc Bonferroni for days 379–437 versus the other two time points, *** $p < 0.001$, **** $p < 0.0001$). This effect was also present when analyzing all the cells responding to depolarization and not just the more mature Syn1⁺ cells (Figure S6E, one-way ANOVA; $F_{(2, 654)} = 121.8$, $p < 0.0001$; Bonferroni post hoc test, **** $p < 0.0001$).

DISCUSSION

The prolonged time course of human astrogenesis over the first years of life poses an experimental challenge to studying their development and function. We generated astrocyte lineage cells from iPSCs in 3D cerebral cortical cultures and maintained them for very long periods of time *in vitro* (up to ~20 months in this study). We found that hCS-derived astrocytes closely resemble primary *in vivo* human astrocytes in their transcriptional landscapes. Moreover, hCS-derived astrocyte lineage cells display key functional characteristics of astrocytes *in vivo*: they uptake glutamate, promote synapse formation, phagocytose synaptosomes, and augment depolarization-induced calcium signaling in neurons. Lastly, this human 3D culture system using directed differentiation of iPSCs, allows easy maintenance of long-term cultures without significant reactive gliosis,

(F) Representative images of phagocytosis in hCS astrocytes (day 100 to day 590) after 16 hr. Scale bar, 100 μ m. Cells derived from two iPSC lines in 5–10 differentiation experiments (3–15 hCSs per time point).

(G) Quantification of pHrodoRed phagocytosis. One-way ANOVA, $F_{(10, 273)} = 2.83$, $p = 0.002$; $n = 9$ fields/condition.

(H) Astrocyte lineage cells were purified from hCSs and grown on inserts. RGCs were simultaneously purified and cultured either beneath an insert with hCS glia or without any cells on the insert above.

(I) Quantification of co-localized synaptic puncta per cell. Co-localization defined by overlap between the Homer and Bassoon signal as determined by in-house MATLAB image processing software. Two-tailed t test, $p = 0.006$. Cells derived from one iPSC line in six differentiation experiments (3–15 hCSs per time point).

(J) Synaptic immunostainings for the presynaptic (Bassoon) and postsynaptic (Homer) markers in RGCs after 14 days in culture without or with inserts containing hCS-derived astrocytes. Scale bar, 12 μ m. Insets: scale bar, 2 μ m.

(K) Neurons purified from day-83-old hCSs were co-cultured with hCS-derived astrocyte lineage cells at three *in vitro* differentiation stages, and calcium signaling was assessed using the calcium dye fura-2.

(L) Depolarization-induced calcium responses in Syn1⁺ neurons co-cultured with astrocyte lineage cells isolated from hCSs at various *in vitro* stages.

(M) Peak calcium amplitude in Syn1⁺ cells; one-way ANOVA; $F_{(2, 126)} = 15.69$, $p < 0.0001$; post hoc Bonferroni for days 379–437 versus the other two time points, *** $p < 0.001$, **** $p < 0.0001$.

and requires no exogenous factors for coaxing astrogenesis *in vitro*. In addition to enabling fundamental studies of human astrocyte development and function, this preparation has the potential to be a powerful method for elucidating the pathways that promote human astrocyte maturation. Once these pathways are better understood, it may be possible in the future to more rapidly generate human astrocytes *in vitro*.

In vivo maturation of astrocytes involves the progression of fetal APCs to mature, adult astrocytes. A fundamental question is to what extent such a transition could be observed *in vitro* and what functional features are associated with this progression. We observed evidence of maturation in hCS-derived astrocytes in 590-day-long *in vitro* cultures using direct comparison to primary fetal and adult human astrocytes. From a morphological standpoint, astrocyte branching within hCSs and after isolation, in monolayer, are more complex with increasing *in vitro* stage. At the transcriptional level, early-stage hCS astrocytes resemble human APCs, whereas late-stage hCS astrocytes resemble more mature astrocytes. Additionally, single-cell analysis of hCSs over multiple *in vitro* stages revealed a similar temporal progression of astrocyte maturation that involves three states: an actively proliferating population, an intermediate stage, and a mature, non-mitotic population that together comprise a continuum from RGs to APCs and eventually to mature astrocytes. There has been recent discussion regarding the similarities and differences between APCs and oRGs (Pollen et al., 2015; Zhang et al., 2016) due to the considerable overlap in their transcriptional profiles. We found that primary oRGs are similar at the single-cell transcriptional level to the intermediate cluster in hCS-derived HepaCAM⁺ cells. Future studies, including fate-mapping analyses, could elucidate this relationship and bring insights into cortical astrogenesis in humans.

What controls the prolonged timing of human astrocyte maturation? Astrocyte maturation may be governed by numerous factors, including non-cell-autonomous paracrine signals, extrinsic hormonal signals, and/or intrinsic regulation of cell states. Our study offers clues about this process and will be a useful tool for additional studies aimed at understanding the maturation process. Despite an environment that differs considerably from the developing fetal human cortex, astrocyte lineage cells within hCSs mature along a similar time course to what is suggested from primary human data. Furthermore, our findings that astrocytes are maturing in hCSs without blood vessels or other vascular signals suggest either that some of the extrinsic cues for astrocyte maturation are of neural origin and/or that a cell intrinsic signal is responsible for their maturation. Although considerable astrocyte maturation occurs in our cultures, it is not complete, suggesting the possibility for future research that missing cell types, such as microglia or endothelial cells, may contribute to this process. The ability to generate mature human iPSC-derived astrocytes *in vitro* may contribute to the development of strategies for accelerating *in vitro* maturation of neurons and astrocytes, as well as to understanding the role in human CNS disorders of the cellular programs underlying this transition.

What are the functional consequences of astrocyte maturation? In mice and humans, both astrocytes and microglia actively participate in synaptic pruning during development (Chung et al.,

2013; Stevens et al., 2007). In the mouse, the rate of astrocyte synaptic phagocytosis is high in the first postnatal week but then steadily declines as astrocytes mature and stop dividing by about postnatal day 10 (P10) (Chung et al., 2013). Strikingly, we also found that more mature human astrocytes are less efficient at phagocytosing synaptosomes compared to younger, fetal astrocytes. A similar phenomenon was also recently observed *in vivo* in mice, where astrocyte synaptic phagocytosis declined steadily from P4 to P9 during the peak of murine astrocyte maturation (Chung et al., 2013). This decline in synapse phagocytosis could be due to a decrease in available synaptic targets to prune or a cell-autonomous mechanism. When we looked at the expression of phagocytic genes in hCS astrocyte lineage cells over time, we found that *MERTK* is not expressed until human astrocytes mature, whereas *MEGF10* is expressed at both ages but significantly increases upon astrocyte maturation. Interestingly, however, the expression of *SIRP α* , a membrane receptor that strongly inhibits phagocytosis and recognizes the “don’t eat me” signal CD47 (Barclay and Van den Berg, 2014), which is highly concentrated at synapses, is significantly upregulated when astrocytes mature. It is possible that the progressive increase in the expression of *SIRP α* or other phagocytic inhibitors on maturing astrocytes could contribute to reduced phagocytic abilities in these cells, and future studies should explore the role of microglia in modulating this process.

The transition from APCs to mature astrocytes has direct relevance to the fatal astrocytic brain tumor glioblastoma multiforme (GBM). Transcriptome profiles of neoplastic cells harvested from patients with GBM are highly correlated with APCs (Zhang et al., 2016), suggesting that these tumors are largely comprised of fetal-like astrocytes proliferating uncontrollably. Whereas most failed therapeutic attempts to limit GBM progression have focused on restricting vascular supply and/or destroying proliferating cells, new opportunities arise for therapies that address astrocyte maturation/de-differentiation within GBMs. Exploring the detailed molecular pathways underlying astrocyte maturation within hCSs could provide new targets for modulating the transition within GBM tumors from an APC-like proliferative state to a mature, more quiescent phenotype.

Finally, recent work is beginning to implicate abnormal astrocyte development and function in various neurodevelopmental conditions, including autism spectrum disorders and schizophrenias (Ballas et al., 2009; Molofsky et al., 2012; Sloan and Barres, 2014). Because many of the genes involved in synaptogenic and synapse pruning pathways are tightly correlated with astrocyte maturation state, it is possible that the development of abnormal neural circuits in various neurodevelopmental disorders may be related to the inappropriate timing and/or degree of astrocyte maturation.

STAR★METHODS

Detailed methods are provided in the online version of this paper and include the following:

- KEY RESOURCES TABLE
- CONTACT FOR REAGENT AND RESOURCE SHARING

- EXPERIMENTAL MODELS AND SUBJECT DETAILS
 - Human iPSC Lines
 - Fetal and Adult Primary Human Samples
- METHODS DETAILS
 - Generation of hCSs
 - Purification of hCS-Derived Astrocytes and Neurons
 - Bulk RNA-Seq Library Construction and Sequencing
 - Bulk RNA-Seq Read Mapping, Transcript Assembly, and Expression Level Estimation
 - Single-Cell cDNA Synthesis and Library Preparation
 - Single-Cell RNA Sequencing and QC
 - Dimensionality Reduction, Clustering, and Monocle Analysis
 - Unsupervised Hierarchical Clustering
 - Immunocytochemistry
 - Synapse Formation Assay
 - Synaptosome Phagocytosis Assay
 - Calcium Imaging
 - Glutamate Uptake
 - Live/Dead Assay
- QUANTIFICATION AND STATISTICAL ANALYSIS
- DATA AND SOFTWARE AVAILABILITY

SUPPLEMENTAL INFORMATION

Supplemental Information includes six figures, three tables, one movie, and one methods file and can be found with this article online at <http://dx.doi.org/10.1016/j.neuron.2017.07.035>.

AUTHOR CONTRIBUTIONS

S.A.S., B.A.B., and S.P.P. conceived the project. S.A.S., B.A.B., and S.P.P. designed the experiments and wrote the manuscript with input from authors. S.D., S.R.Q., and N.H. aided in the single-cell RNA-seq sorting, sequencing pipeline, and analyses. T.A.K. performed calcium imaging experiments and immunostainings. R.R. performed the glutamate uptake assay, and S.A.S., C.C., and N.H. contributed to other experiments. N.H., T.A.K., and F.B. assisted in generating and maintaining all hCSs and long-term cultures.

ACKNOWLEDGMENTS

We thank J. Andersen, A.M. Paşca, and J.Y. Park in the Paşca lab for experimental support, as well as N. O'Rourke for support with array tomography experiments. This work was supported by the US National Institute of Health (NIH) R01 MH099555 and NS081703 (to B.A.B.); the NIH BRAINS Award (MH107800), the California Institute of Regenerative Medicine (CIRM), the MQ Fellow Award, Donald E. and Delia B. Baxter Foundation Award, the Stanford Neurosciences Institute's Brain Rejuvenation Project, the Kwan Research Fund, and Stanford Start-up Funds (to S.P.P.); NIMH T32GM007365 and F30MH106261, Bio-X Predoctoral Fellowship (to or supporting S.A.S.); the Dean's Postdoctoral Fellowship (N.H.), Child Health Research Institute Postdoctoral Fellowship UL1-TR001085 (N.H. and F.B.), and the NSF Graduate Research Fellowship (T.K.).

Received: March 30, 2017

Revised: June 15, 2017

Accepted: July 28, 2017

Published: August 16, 2017

REFERENCES

Afgan, E., Baker, D., van den Beek, M., Blankenberg, D., Bouvier, D., Čech, M., Chilton, J., Clements, D., Coraor, N., Eberhard, C., et al. (2016). The Galaxy

platform for accessible, reproducible and collaborative biomedical analyses: 2016 update. *Nucleic Acids Res.* *44*, W3–W10.

Allen, N.J., Bennett, M.L., Foo, L.C., Wang, G.X., Chakraborty, C., Smith, S.J., and Barres, B.A. (2012). Astrocyte glypicans 4 and 6 promote formation of excitatory synapses via GluA1 AMPA receptors. *Nature* *486*, 410–414.

Anderson, C.M., and Swanson, R.A. (2000). Astrocyte glutamate transport: review of properties, regulation, and physiological functions. *Glia* *32*, 1–14.

Ballas, N., Liou, D.T., Grunseich, C., and Mandel, G. (2009). Non-cell autonomous influence of MeCP2-deficient glia on neuronal dendritic morphology. *Nat. Neurosci.* *12*, 311–317.

Barclay, A.N., and Van den Berg, T.K. (2014). The interaction between signal regulatory protein alpha (SIRP α) and CD47: structure, function, and therapeutic target. *Annu. Rev. Immunol.* *32*, 25–50.

Barreto-Chang, O.L., and Dolmetsch, R.E. (2009). Calcium imaging of cortical neurons using Fura-2 AM. *J. Vis. Exp.* (23), 1067.

Birey, F., Andersen, J., Makinson, C.D., Islam, S., Wei, W., Huber, N., Fan, H.C., Metzler, K.R.C., Panagiotakos, G., Thom, N., et al. (2017). Assembly of functionally integrated human forebrain spheroids. *Nature* *545*, 54–59.

Cahoy, J.D., Emery, B., Kaushal, A., Foo, L.C., Zamanian, J.L., Christopherson, K.S., Xing, Y., Lubischer, J.L., Krieg, P.A., Krupenko, S.A., et al. (2008). A transcriptome database for astrocytes, neurons, and oligodendrocytes: a new resource for understanding brain development and function. *J. Neurosci.* *28*, 264–278.

Chambers, S.M., Fasano, C.A., Papapetrou, E.P., Tomishima, M., Sadelain, M., and Studer, L. (2009). Highly efficient neural conversion of human ES and iPS cells by dual inhibition of SMAD signaling. *Nat. Biotechnol.* *27*, 275–280.

Christopherson, K.S., Ullian, E.M., Stokes, C.C., Mallowney, C.E., Hell, J.W., Agah, A., Lawler, J., Mosher, D.F., Bornstein, P., and Barres, B.A. (2005). Thrombospondins are astrocyte-secreted proteins that promote CNS synaptogenesis. *Cell* *120*, 421–433.

Chung, W.S., Clarke, L.E., Wang, G.X., Stafford, B.K., Sher, A., Chakraborty, C., Joung, J., Foo, L.C., Thompson, A., Chen, C., et al. (2013). Astrocytes mediate synapse elimination through MEGF10 and MERTK pathways. *Nature* *504*, 394–400.

Darmanis, S., Sloan, S.A., Zhang, Y., Enge, M., Caneda, C., Shuer, L.M., Hayden Gephart, M.G., Barres, B.A., and Quake, S.R. (2015). A survey of human brain transcriptome diversity at the single cell level. *Proc. Natl. Acad. Sci. USA* *112*, 7285–7290.

Deverman, B.E., Pravdo, P.L., Simpson, B.P., Kumar, S.R., Chan, K.Y., Banerjee, A., Wu, W.L., Yang, B., Huber, N., Pasca, S.P., and Gradinaru, V. (2016). Cre-dependent selection yields AAV variants for widespread gene transfer to the adult brain. *Nat. Biotechnol.* *34*, 204–209.

Dolmetsch, R., and Geschwind, D.H. (2011). The human brain in a dish: the promise of iPSC-derived neurons. *Cell* *145*, 831–834.

Dunkley, P.R., Jarvie, P.E., and Robinson, P.J. (2008). A rapid Percoll gradient procedure for preparation of synaptosomes. *Nat. Protoc.* *3*, 1718–1728.

Emdad, L., D'Souza, S.L., Kothari, H.P., Qadeer, Z.A., and Germano, I.M. (2012). Efficient differentiation of human embryonic and induced pluripotent stem cells into functional astrocytes. *Stem Cells Dev.* *21*, 404–410.

Eroglu, C., Allen, N.J., Susman, M.W., O'Rourke, N.A., Park, C.Y., Ozkan, E., Chakraborty, C., Mulinyawe, S.B., Annis, D.S., Huberman, A.D., et al. (2009). Gabapentin receptor alpha2delta-1 is a neuronal thrombospondin receptor responsible for excitatory CNS synaptogenesis. *Cell* *139*, 380–392.

Fan, J., Salathia, N., Liu, R., Kaeser, G.E., Yung, Y.C., Herman, J.L., Kaper, F., Fan, J.B., Zhang, K., Chun, J., and Kharchenko, P.V. (2016). Characterizing transcriptional heterogeneity through pathway and gene set overdispersion analysis. *Nat. Methods* *13*, 241–244.

Freeman, M.R., and Rowitch, D.H. (2013). Evolving concepts of gliogenesis: a look way back and ahead to the next 25 years. *Neuron* *80*, 613–623.

Huttenlocher, P.R. (1979). Synaptic density in human frontal cortex—developmental changes and effects of aging. *Brain Res.* *163*, 195–205.

- Huttenlocher, P.R., de Courten, C., Garey, L.J., and Van der Loos, H. (1982). Synaptogenesis in human visual cortex—evidence for synapse elimination during normal development. *Neurosci. Lett.* **33**, 247–252.
- Juopperi, T.A., Kim, W.R., Chiang, C.H., Yu, H., Margolis, R.L., Ross, C.A., Ming, G.L., and Song, H. (2012). Astrocytes generated from patient induced pluripotent stem cells recapitulate features of Huntington's disease patient cells. *Mol. Brain* **5**, 17.
- Kang, H.J., Kawasawa, Y.I., Cheng, F., Zhu, Y., Xu, X., Li, M., Sousa, A.M., Pletikos, M., Meyer, K.A., Sedmak, G., et al. (2011). Spatio-temporal transcriptome of the human brain. *Nature* **478**, 483–489.
- Kim, D., Pertea, G., Trapnell, C., Pimentel, H., Kelley, R., and Salzberg, S.L. (2013). TopHat2: accurate alignment of transcriptomes in the presence of insertions, deletions and gene fusions. *Genome Biol.* **14**, R36.
- Krencik, R., and Ullian, E.M. (2013). A cellular star atlas: using astrocytes from human pluripotent stem cells for disease studies. *Front. Cell. Neurosci.* **7**, 25.
- Krencik, R., and Zhang, S.C. (2011). Directed differentiation of functional astroglial subtypes from human pluripotent stem cells. *Nat. Protoc.* **6**, 1710–1717.
- Krey, J.F., Paşca, S.P., Shcheglovitov, A., Yazawa, M., Schwemberger, R., Rasmusson, R., and Dolmetsch, R.E. (2013). Timothy syndrome is associated with activity-dependent dendritic retraction in rodent and human neurons. *Nat. Neurosci.* **16**, 201–209.
- Langmead, B., and Salzberg, S.L. (2012). Fast gapped-read alignment with Bowtie 2. *Nat. Methods* **9**, 357–359.
- Lovatt, D., Sonnewald, U., Waagepetersen, H.S., Schousboe, A., He, W., Lin, J.H.C., Han, X., Takano, T., Wang, S., Sim, F.J., et al. (2007). The transcriptome and metabolic gene signature of protoplasmic astrocytes in the adult murine cortex. *J. Neurosci.* **27**, 12255–12266.
- Middeldorp, J., Boer, K., Sluijs, J.A., De Filippis, L., Encha-Razavi, F., Vescovi, A.L., Swaab, D.F., Aronica, E., and Hol, E.M. (2010). GFAPdelta in radial glia and subventricular zone progenitors in the developing human cortex. *Development* **137**, 313–321.
- Molofsky, A.V., Krencik, R., Ullian, E.M., Tsai, H.H., Deneen, B., Richardson, W.D., Barres, B.A., and Rowitch, D.H. (2012). Astrocytes and disease: a neurodevelopmental perspective. *Genes Dev.* **26**, 891–907.
- Oberheim, N.A., Takano, T., Han, X., He, W., Lin, J.H., Wang, F., Xu, Q., Wyatt, J.D., Pilcher, W., Ojemann, J.G., et al. (2009). Uniquely hominid features of adult human astrocytes. *J. Neurosci.* **29**, 3276–3287.
- Paşca, S.P. (2016). Personalized human cortical spheroids. *Am. J. Psychiatry* **173**, 332–333.
- Paşca, S.P., Portmann, T., Voineagu, I., Yazawa, M., Shcheglovitov, A., Paşca, A.M., Cord, B., Palmer, T.D., Chikahisa, S., Nishino, S., et al. (2011). Using iPSC-derived neurons to uncover cellular phenotypes associated with Timothy syndrome. *Nat. Med.* **17**, 1657–1662.
- Paşca, S.P., Panagiotakos, G., and Dolmetsch, R.E. (2014). Generating human neurons in vitro and using them to understand neuropsychiatric disease. *Annu. Rev. Neurosci.* **37**, 479–501.
- Paşca, A.M., Sloan, S.A., Clarke, L.E., Tian, Y., Makinson, C.D., Huber, N., Kim, C.H., Park, J.Y., O'Rourke, N.A., Nguyen, K.D., et al. (2015). Functional cortical neurons and astrocytes from human pluripotent stem cells in 3D culture. *Nat. Methods* **12**, 671–678.
- Penzes, P., Cahill, M.E., Jones, K.A., VanLeeuwen, J.E., and Woolfrey, K.M. (2011). Dendritic spine pathology in neuropsychiatric disorders. *Nat. Neurosci.* **14**, 285–293.
- Picelli, S., Faridani, O.R., Björklund, A.K., Winberg, G., Sagasser, S., and Sandberg, R. (2014). Full-length RNA-seq from single cells using Smart-seq2. *Nat. Protoc.* **9**, 171–181.
- Pollen, A.A., Nowakowski, T.J., Chen, J., Retallack, H., Sandoval-Espinosa, C., Nicholas, C.R., Shuga, J., Liu, S.J., Oldham, M.C., Diaz, A., et al. (2015). Molecular identity of human outer radial glia during cortical development. *Cell* **163**, 55–67.
- Roybon, L., Lamas, N.J., Garcia, A.D., Yang, E.J., Sattler, R., Lewis, V.J., Kim, Y.A., Kachel, C.A., Rothstein, J.D., Przedborski, S., et al. (2013). Human stem cell-derived spinal cord astrocytes with defined mature or reactive phenotypes. *Cell Rep.* **4**, 1035–1048.
- Shaltouki, A., Peng, J., Liu, Q., Rao, M.S., and Zeng, X. (2013). Efficient generation of astrocytes from human pluripotent stem cells in defined conditions. *Stem Cells* **31**, 941–952.
- Sloan, S.A., and Barres, B.A. (2014). Mechanisms of astrocyte development and their contributions to neurodevelopmental disorders. *Curr. Opin. Neurobiol.* **27**, 75–81.
- Stevens, B., Allen, N.J., Vazquez, L.E., Howell, G.R., Christopherson, K.S., Nouri, N., Micheva, K.D., Mehalow, A.K., Huberman, A.D., Stafford, B., et al. (2007). The classical complement cascade mediates CNS synapse elimination. *Cell* **131**, 1164–1178.
- Tabar, V., and Studer, L. (2014). Pluripotent stem cells in regenerative medicine: challenges and recent progress. *Nat. Rev. Genet.* **15**, 82–92.
- Trapnell, C., Williams, B.A., Pertea, G., Mortazavi, A., Kwan, G., van Baren, M.J., Salzberg, S.L., Wold, B.J., and Pachter, L. (2010). Transcript assembly and abundance estimation from RNA-seq reveals thousands of new transcripts and switching among isoforms. *Nat. Biotechnol.* **28**, 511–515.
- Trapnell, C., Cacchiarelli, D., Grimsby, J., Pokharel, P., Li, S., Morse, M., Lennon, N.J., Livak, K.J., Mikkelsen, T.S., and Rinn, J.L. (2014). Pseudo-temporal ordering of individual cells reveals dynamics and regulators of cell fate decisions. *Nat. Biotechnol.* **32**, 381–386.
- Tsai, Y.J., Huang, C.T., Lin, S.C., and Yeh, J.H. (2012). Effects of regional and whole-body hypothermic treatment before and after median nerve injury on neuropathic pain and glial activation in rat cuneate nucleus. *Anesthesiology* **116**, 415–431.
- Ullian, E.M., Sapperstein, S.K., Christopherson, K.S., and Barres, B.A. (2001). Control of synapse number by glia. *Science* **291**, 657–661.
- van der Maaten, L., and Hinton, G. (2008). Visualizing data using t-SNE. *J. Mach. Learn. Res.* **9**, 2579–2605.
- Winzler, A., and Wang, J.T. (2013). Purification and culture of retinal ganglion cells. *Cold Spring Harb. Protoc.* **2013**, 614–617.
- Yazawa, M., Hsueh, B., Jia, X., Paşca, A.M., Bernstein, J.A., Hallmayer, J., and Dolmetsch, R.E. (2011). Using induced pluripotent stem cells to investigate cardiac phenotypes in Timothy syndrome. *Nature* **471**, 230–234.
- Zhang, Y., Sloan, S.A., Clarke, L.E., Caneda, C., Plaza, C.A., Blumenthal, P.D., Vogel, H., Steinberg, G.K., Edwards, M.S., Li, G., et al. (2016). Purification and characterization of progenitor and mature human astrocytes reveals transcriptional and functional differences with mouse. *Neuron* **89**, 37–53.

Mutant Huntingtin Disrupts the Nuclear Pore Complex

Jonathan C. Grima,^{1,2,3} J. Gavin Daigle,^{2,3} Nicolas Arbez,^{1,5} Kathleen C. Cunningham,^{3,4} Ke Zhang,^{2,3} Joseph Ochaba,⁷ Charlene Geater,⁷ Eva Morozko,⁷ Jennifer Stocksdale,⁷ Jenna C. Glatzer,^{2,3} Jacqueline T. Pham,^{2,4} Ishrat Ahmed,¹ Qi Peng,¹ Harsh Wadhwa,³ Olga Pletnikova,⁶ Juan C. Troncoso,^{3,6} Wenzhen Duan,^{1,4,5} Solomon H. Snyder,^{1,5} Laura P.W. Ranum,⁸ Leslie M. Thompson,⁷ Thomas E. Lloyd,^{1,2,3,4} Christopher A. Ross,^{1,5} and Jeffrey D. Rothstein^{1,2,3,4,9,*}

¹Solomon H. Snyder Department of Neuroscience

²Brain Science Institute

³Department of Neurology

⁴Program in Cellular and Molecular Medicine

⁵Department of Psychiatry

⁶Department of Pathology

Johns Hopkins University School of Medicine, Baltimore, MD 21205, USA

⁷Department of Neurobiology and Behavior, University of California, Irvine, Irvine, CA 92697, USA

⁸Center for NeuroGenetics, Departments of Molecular Genetics and Microbiology and Neurology, College of Medicine, Genetics Institute, McKnight Brain Institute, University of Florida, Gainesville, FL 32611, USA

⁹Lead Contact

*Correspondence: jrothstein@jhmi.edu

<http://dx.doi.org/10.1016/j.neuron.2017.03.023>

SUMMARY

Huntington's disease (HD) is caused by an expanded CAG repeat in the *Huntingtin (HTT)* gene. The mechanism(s) by which mutant HTT (mHTT) causes disease is unclear. Nucleocytoplasmic transport, the trafficking of macromolecules between the nucleus and cytoplasm, is tightly regulated by nuclear pore complexes (NPCs) made up of nucleoporins (NUPs). Previous studies offered clues that mHTT may disrupt nucleocytoplasmic transport and a mutation of an NUP can cause HD-like pathology. Therefore, we evaluated the NPC and nucleocytoplasmic transport in multiple models of HD, including mouse and fly models, neurons transfected with *mHTT*, HD iPSC-derived neurons, and human HD brain regions. These studies revealed severe mislocalization and aggregation of NUPs and defective nucleocytoplasmic transport. HD repeat-associated non-ATG (RAN) translation proteins also disrupted nucleocytoplasmic transport. Additionally, overexpression of NUPs and treatment with drugs that prevent aberrant NUP biology also mitigated this transport defect and neurotoxicity, providing future novel therapy targets.

INTRODUCTION

Huntington's disease (HD) is the most common inherited neurodegenerative disorder, caused by an expanded CAG repeat in the first exon of the *Huntingtin (HTT)* gene coding for a polyglutamine (polyQ) tract within the protein Huntingtin (HTT) (Finkbeiner, 2011). This autosomal-dominant disease results in the

selective degeneration of striatal medium spiny projection neurons and cortical pyramidal neurons as well as the formation of intracellular neuronal aggregates. How mutant HTT (mHTT) can induce this selective neuronal loss despite ubiquitous expression throughout the nervous system is unknown. Disease onset and severity are dependent on CAG repeat length, with a longer expansion resulting in an earlier onset and greater severity of illness. The *HTT* gene in asymptomatic individuals contains less than 35 CAG repeats, whereas pathologic expansions contain greater than 39. A juvenile variant exists in which expansion lengths in excess of ~60 or more can result in symptom onset earlier than 20 years of age (Vonsattel and DiFiglia, 1998). The underlying mechanisms by which mHTT causes neurodegeneration have not been fully elucidated. Studies have provided clues that nuclear pore complex (NPC) dysfunction may be a pathogenic contributor (Basel-Vanagaite et al., 2006; Hosp et al., 2015; Liu et al., 2015; Suhr et al., 2001; Woerner et al., 2016), although very little is known about the NPC and the role of nucleocytoplasmic transport defects in human HD or in models of the disease.

The NPC is one of the largest molecular complexes in eukaryotic cells and serves as the main transport conduit between the nucleus and the cytoplasm. NPCs span the entire nuclear envelope and consist of multiple copies of approximately 30 different protein subunits called nucleoporins (NUPs). NUPs differ in functions including protein import, protein export, RNA export, and membrane anchoring and are organized into five unique anatomical regions of the NPC (cytoplasmic ring/filaments, central channel, nuclear ring/basket, transmembrane, and scaffold) (Raices and D'Angelo, 2012; Wenthe and Rout, 2010). The NPC has nucleocytoplasmic transport-independent functions such as regulating genome organization, gene expression, cell differentiation and development, and RNA processing and quality control (Raices and D'Angelo, 2012, 2017). During nuclear import, cargo is released into the nucleus when the transport receptor interacts

with Ran-GTP, a GTP-binding nuclear protein. During nuclear export, cargo is released into the cytoplasm upon GTP hydrolysis of Ran-GTP by RanGAP1, a GTPase-activating protein located on the cytoplasmic filaments of the NPC that is also required for nuclear import. Higher levels of Ran-GTP in the nucleus compared to the cytoplasm are essential for fueling active transport through the NPC and defining nucleocytoplasmic transport directionality (Floch et al., 2014). The proper maintenance of this nuclear/cytoplasmic (N/C) Ran gradient by RanGAP1 is critical, and its loss has been shown to cause cell death within minutes (Hetzer et al., 2002). Finally, molecules less than ~40 kDa can freely migrate through the NPC via passive transport.

Recent work from our group and others has shown that nucleocytoplasmic transport is disrupted by a hexanucleotide repeat expansion (HRE) in the C9orf72 gene, the most common mutation in amyotrophic lateral sclerosis (ALS) and frontotemporal dementia (FTD) and a common cause of HD phenocopies (Freibaum et al., 2015; Hensman Moss et al., 2014; Jovičić et al., 2015; Zhang et al., 2015). A direct interaction between the HRE-containing RNAs and RanGAP1 can cause a disruption of the Ran energy gradient required for active transport. In addition, nucleocytoplasmic transport function can be disrupted by repeat-associated non-ATG (RAN) translation produced polypeptides encoded by the HRE RNAs, which cause NUPs to aggregate (Zhang et al., 2016) or block the central channel of the NPC (Shi et al., 2017). RAN translation occurs not only in diseases with noncoding region repeat expansions like C9orf72 HRE, but recent work has shown that RAN translation also occurs in diseases with coding region expansions, including HD (Bañez-Coronel et al., 2015).

HD is pathologically characterized by intracellular inclusions in the striatum and cortex, which consist of aggregates of HTT, HD-RAN proteins, and other proteins including NUP62 (Suhr et al., 2001). NUP62, located in the central channel of the NPC, plays a direct role in nuclear import of proteins containing a nuclear localization signal (NLS) as well as roles in transcription and chromatin organization (Capelson et al., 2010; Kalverda et al., 2010; Liang and Hetzer, 2011). It is also a member of the phenylalanine-glycine (FG) repeat-containing NUPs, and the FG-rich domain makes NUP62 important for controlling nuclear pore permeability and selective trafficking of macromolecules to and from the nucleus. Many transport receptors like importin- β and NTF2 can traffic cargo containing an NLS or NES (nuclear export signal) through the NPC via dynamic hydrophobic interactions with the FG-rich domain of FG-NUPs (Wente and Rout, 2010). Intriguingly, a mutation in NUP62 causes autosomal-recessive infantile bilateral striatal necrosis (IBSN), a fatal disorder characterized by striatal and globus pallidus degeneration (Basel-Vanagaite et al., 2006). Also, mHTT exhibits preferential binding to RanGAP1 and ribonucleic acid export 1 (RAE1), an mRNA export factor (Hosp et al., 2015). In addition, nuclear membrane distortions can be observed in various cell culture models, transgenic animal models, and ultrastructural studies of HD brain (Brettschneider et al., 2015; Cornett et al., 2005). Perinuclear inclusions of mHTT disrupt the nuclear membrane and cause striatal cell death in mouse and cell models of HD (Liu et al., 2015). Finally, cytoplasmic protein aggregates can

disrupt nucleocytoplasmic trafficking of protein and RNA (Woerner et al., 2016). Given these findings, we hypothesized that mHTT may directly disrupt nucleocytoplasmic transport at the NPC.

We screened several NUPs and NPC-associated proteins from all anatomical regions of the NPC in the R6/2 and zQ175 mouse models of HD and identified a subset that co-localize with mHtt intracellular aggregates. These NUPs also aggregate or mislocalize in HD and juvenile HD (JHD) postmortem human tissue. Using HD induced pluripotent stem cell (iPSC)-derived neurons (iPSNs), primary neurons transfected with full-length *mHTT*, and a *Drosophila* model of HD, we show that several NUPs are severely mislocalized and that there are deficits in both passive and active nucleocytoplasmic transport, and demonstrate correction of these deficits and neurotoxicity using small molecules and overexpression constructs that target the nucleocytoplasmic transport pathway. Finally, we demonstrate that the recently discovered HD-RAN proteins can also directly disrupt nucleocytoplasmic transport. These data suggest that mHTT disrupts nucleocytoplasmic transport directly at the NPC and that targeting this pathway may provide a therapeutic route for HD.

RESULTS

NUPs Aggregate and Co-localize with mHtt in the R6/2 Mouse Model of HD

To analyze the integrity of the NPC in HD, we assessed the localization of the majority of NUPs and NPC-associated proteins (Table S1) in 10-week-old R6/2 mice using immunofluorescence. The R6/2 mouse model expresses exon 1 of human HTT with highly expanded CAG repeats (approximately 125–160 CAGs) and exhibits HD-like symptomology with motor symptom onset at 5 weeks, body weight decline onset at 10 weeks, and a lifespan ranging from 10 to 13 weeks (Pouladi et al., 2013). These animals also develop accumulation of aggregated mHtt. We frequently found that RanGAP1 and NUP62 form intranuclear inclusions that co-localize with EM48+ mHTT aggregates in neurons of the striatum and cortex of these mice (Figures 1A–1D and S1).

We next examined insoluble and soluble mHtt and RanGAP1 levels in the striatum throughout disease progression in the R6/2 mice. We previously showed the presence of an insoluble high molecular weight (HMW) mHtt species along with other modified proteins in the detergent-insoluble fraction from R6/2 striatum (Ochaba et al., 2016); therefore, detergent-soluble and detergent-insoluble proteins were evaluated. The detergent-soluble fraction contains mainly cytoplasmic proteins, monomeric forms of Htt (including the R6/2 *mHTT* fragment encoding human transgene), endogenous mouse full-length Htt, and soluble oligomeric species of Htt, which do not fully resolve on standard PAGE gels (O'Rourke et al., 2013; Sontag et al., 2012). In contrast, the detergent-insoluble fraction contains primarily nuclear proteins such as HMW mHtt species (likely multimers or potentially insoluble oligomers and fibrils) and insoluble accumulated forms of SUMO- and ubiquitin-modified proteins. As anticipated, levels of soluble monomeric transgene mHtt protein significantly decreased throughout disease progression

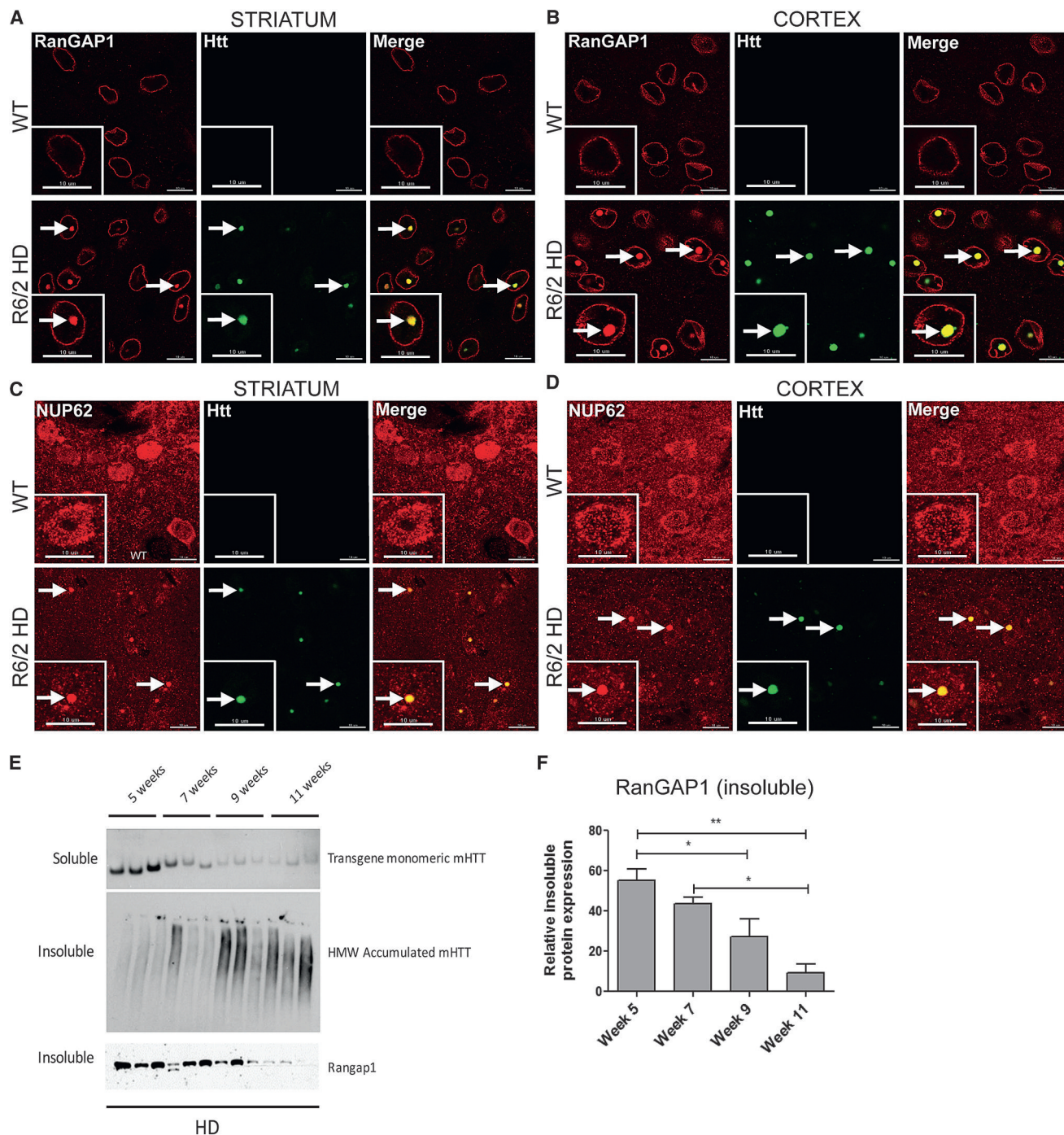


Figure 1. NUPs Aggregate and Co-localize with mHtt in the R6/2 Mouse Model of HD

(A and B) Coronal brain sections from 10-week-old WT and TG R6/2 mice showing aggregates of RanGAP1 (red) that co-localize with EM48+ mHtt aggregates (green) in the striatum (A) and cortex (B) of TG R6/2 mice. N = 5/group.

(C and D) Coronal brain sections from WT and TG R6/2 mice showing aggregates of NUP62 (red) that co-localize with EM48+ mHtt aggregates (green) in the striatum (C) and cortex (D) of TG R6/2 mice. N = 5/group.

(E and F) Insoluble RanGAP1 levels decrease with disease progression in striatum of R6/2 mice (E) and are quantified by densitometry analysis (F). Insoluble RanGAP1 and soluble mHtt transgene levels are significantly reduced and insoluble HMW accumulated mHtt is increased in R6/2 mice from weeks 5 to 11 (E). All data are expressed as western densitometry quantitation. Protein expression was validated for protein loading prior to antibody incubation using reversible protein stain and each samples' corresponding soluble α -tubulin expression.

Data represent mean \pm SEM. * $p < 0.05$, ** $p < 0.01$; one-way ANOVA followed by Bonferroni post-testing was applied. N = 3/time point. Scale bars, 10 μ m (A–D). See also Table S1 and Figures S1 and S2.

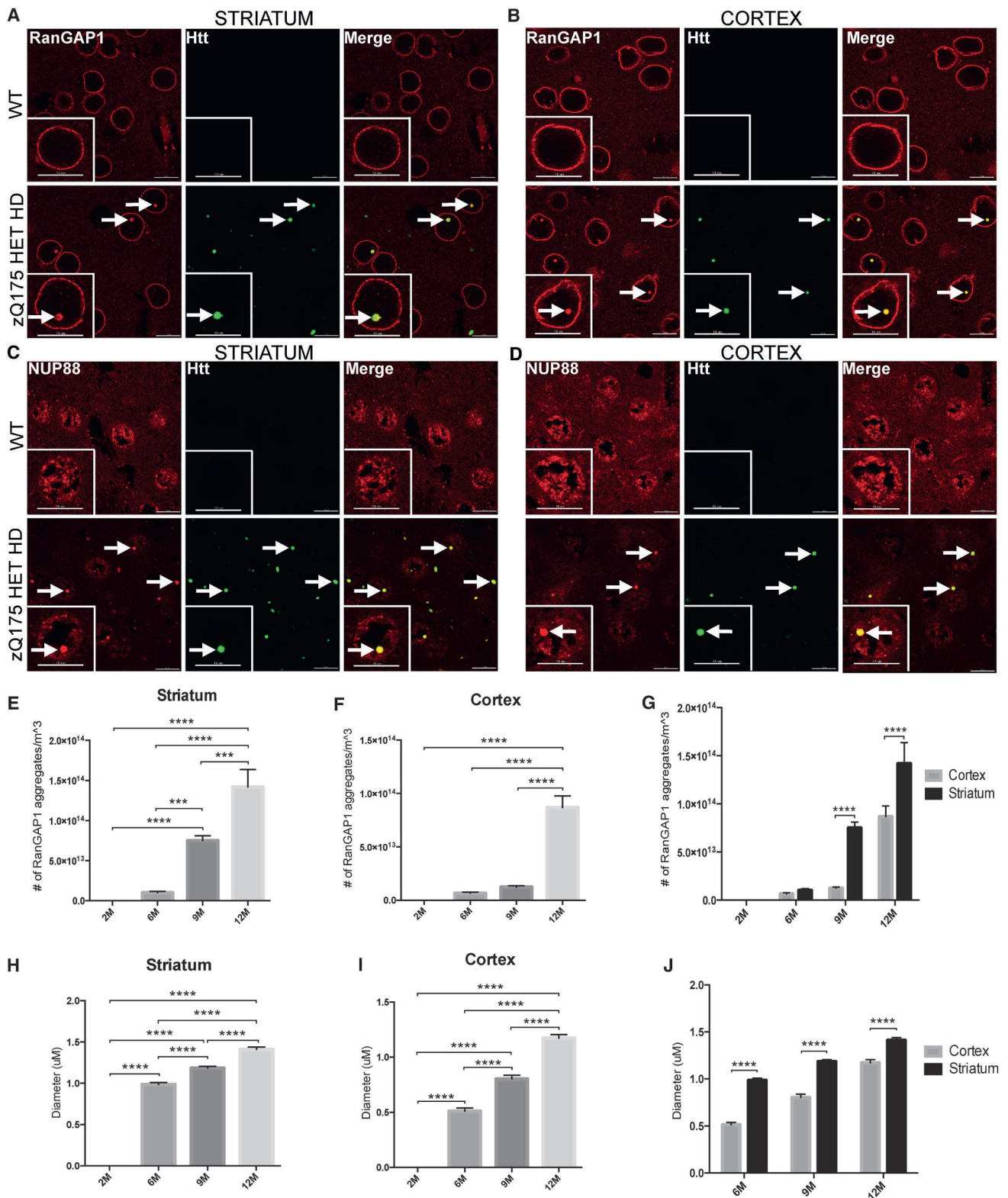


Figure 2. NUPs Aggregate and Co-localize with mHtt in the zQ175 Mouse Model of HD

(A and B) Coronal brain sections from 12-month-old WT and HET zQ175 mice showing aggregates of RanGAP1 (red) that co-localize with EM48+ mHtt aggregates (green) in the striatum (A) and cortex (B) of HET zQ175 mice.

(legend continued on next page)

(Figure 1E), with a corresponding age-dependent increase of an insoluble, HMW accumulated species of mHtt (Figure 1E). Notably, levels of insoluble RanGAP1 significantly decreased throughout the progression of the disease, with little RanGAP1 observed by 11 weeks of age in this fraction from R6/2 striatum (Figures 1E and 1F). This likely reflects a decrease in the levels of nuclear envelope RanGAP1.

If chronic expression of mHtt causes the mislocalization and nuclear envelope reduction of RanGAP1, then a molecular intervention that reduces the aberrant accumulation of HMW mHtt species in R6/2 mice might restore nuclear envelope RanGAP1 levels. Therefore, we evaluated striatal tissues from mice that had been treated with microRNA (miRNA) directed against PIAS1, an E3-SUMO ligase that modulates SUMO-1 and SUMO-2/3 modification of HTT (O'Rourke et al., 2013; Ochaba et al., 2016). Reduction of PIAS1 through intrastriatal injection of a PIAS1-directed miRNA in vivo in R6/2 mice reduces formation of the HMW species of mHtt. Using the same fractionation procedure, the detergent-insoluble fraction of non-transgenic (NT) and R6/2 striatum plus and minus PIAS1 knockdown (miPIAS1.3 treatment) at 10 weeks was analyzed for the presence of insoluble RanGAP1 (Figures S2A and S2B). Treatment significantly restored levels of nuclear RanGAP1 to normal (NT) levels in R6/2 striatum compared to miSAFE (control)-treated mice. There were no significant differences either by genotype or treatment for soluble RanGAP1 levels (Figure S2A). We also assessed whether RanGAP1 was correspondingly reduced in mHtt aggregates using a filter retardation assay to examine levels of RanGAP1 that may be caught up in insoluble fibrils. We found that RanGAP1 levels were higher in aggregates resolved on filter blots in miSAFE-treated R6/2 striatum than in miPIAS1.3 (Figure S2C), suggesting again the restoration of RanGAP1 dyshomeostasis upon PIAS1 knockdown and that RanGAP1 may be sequestered in aberrant protein inclusions and complexes in the disease state.

NUPs Aggregate and Co-localize with mHtt in the zQ175 Mouse Model of HD

We next assessed the localization of many NUPs and NPC-associated proteins (Table S1) in the zQ175 mouse model of HD at 2, 6, 9, and 12 months. This knockin mouse model contains the human HTT exon 1 sequence with an ~ 193 CAG (193 ± 7) repeat tract, replacing the mouse Htt exon 1 within the native mouse Htt gene (Pouladi et al., 2013). Heterozygous zQ175 mice begin exhibiting motor symptoms after 3 months of age and demonstrate significant brain atrophy by 8 months. We found that RanGAP1 and NUP88 form intracellular inclusions that co-localize with EM48+ mHtt aggregates in the striatum and cortex of these mice (Figures 2A–2D). On average, $\sim 70\%$ of all RanGAP1 aggregates co-localize with EM48+ mHtt aggregates at 12 months (Figure S3). Using the spot detection function

in IMARIS software, these RanGAP1 aggregates increase in frequency with age in both the striatum and cortex but are significantly more prevalent in the striatum (Figures 2E–2G). Similarly, quantification of the size of these inclusions indicates that the diameter increases with age in both brain regions but is significantly greater in the striatum (Figures 2H–2J).

NUP Pathology in Human HD and JHD Brain Tissue

To determine whether RanGAP1 and NUP62 mislocalization and/or aggregation occurs in human disease, we assessed post-mortem human brain tissue from HD and JHD patients. Brain cells in HD and JHD frontal cortex and striatum commonly exhibit either a mislocalization (arrow heads) or aggregation (arrows) of RanGAP1 compared to smooth perinuclear staining observed in controls (Figures 3A and 3B; Table S2). Similar pathology was detected in HD and JHD cerebellum (Figure S4A). Quantitatively, the pathologic mislocalization or aggregation of RanGAP1 was more common in JHD than in adult-onset HD brain regions, which might be predicted given that greater *mHTT* CAG repeats are found in JHD. We then investigated whether NUP62 also exhibited abnormal localization and/or aggregation. Although we did not detect NUP62 aggregation, NUP62 was dramatically mislocalized to either the cytoplasm (arrows) or inside the nucleus (arrow heads) in HD and JHD striatum, but not in cortex (except slightly for JHD) (Figure 3C) or cerebellum (Figure S4B). This is consistent with the observations that human mutations in NUP62 cause selective striatal pathology in IBSN (Basel-Vanagaite et al., 2006). NUP62 cytoplasmic or intranuclear mislocalization was also more pronounced in JHD than in adult-onset HD brains regions (Figure 3C). Additionally, we saw no pathology in translocated promoter region (TPR) (data not shown), an NUP located in the nuclear basket of the NPC and involved in nuclear export of N-terminal Htt (Cornett et al., 2005). This was expected given that polyQ expansion and aggregation of mHtt decrease its interaction with TPR (Cornett et al., 2005) and would presumably render TPR unaffected.

Nucleocytoplasmic Transport Defects in Human HD iPSNs

To validate our observations in human HD patient neurons (Table S3), we quantified nuclear and cytoplasmic (N/C) endogenous Ran in HD iPSNs via immunofluorescence. Higher levels of Ran-GTP in the nucleus compared to the cytoplasm are required to fuel canonical active transport through the NPC. We observed a significant reduction in the N/C ratio of endogenous Ran in our HD iPSN lines, suggesting that active transport is deficient in HD (Figure 4A). We next assessed passive transport through the NPC by quantifying N/C MAP2 via immunofluorescence. MAP2 (~ 70 kDa) is a cytoplasmic protein that is normally excluded from the nucleus by the NPC (~ 40 kDa passive diffusion limit) (Izant and McIntosh, 1980). We found a significant increase in

(C and D) Coronal brain sections from 12-month-old WT and HET zQ175 mice showing aggregates of NUP88 (red) that co-localize with EM48+ mHtt aggregates (green) in the striatum (C) and cortex (D) of HET zQ175 mice.

(E–G) Quantification of number of RanGAP1 aggregates in the striatum (E) and cortex (F) of HET zQ175 mice at 2, 6, 9, and 12 months (G).

(H–J) Quantification of diameter of RanGAP1 aggregates in the striatum (H) and cortex (I) of HET zQ175 mice at 2, 6, 9, and 12 months (J).

Data (E–J) are presented as mean \pm SEM. *** $p < 0.001$ and **** $p < 0.0001$ as analyzed by one-way ANOVA followed by Tukey's post hoc analysis. $N = 3/\text{age group}$. Scale bars, 10 μm (A–D). See also Table S1 and Figure S3.

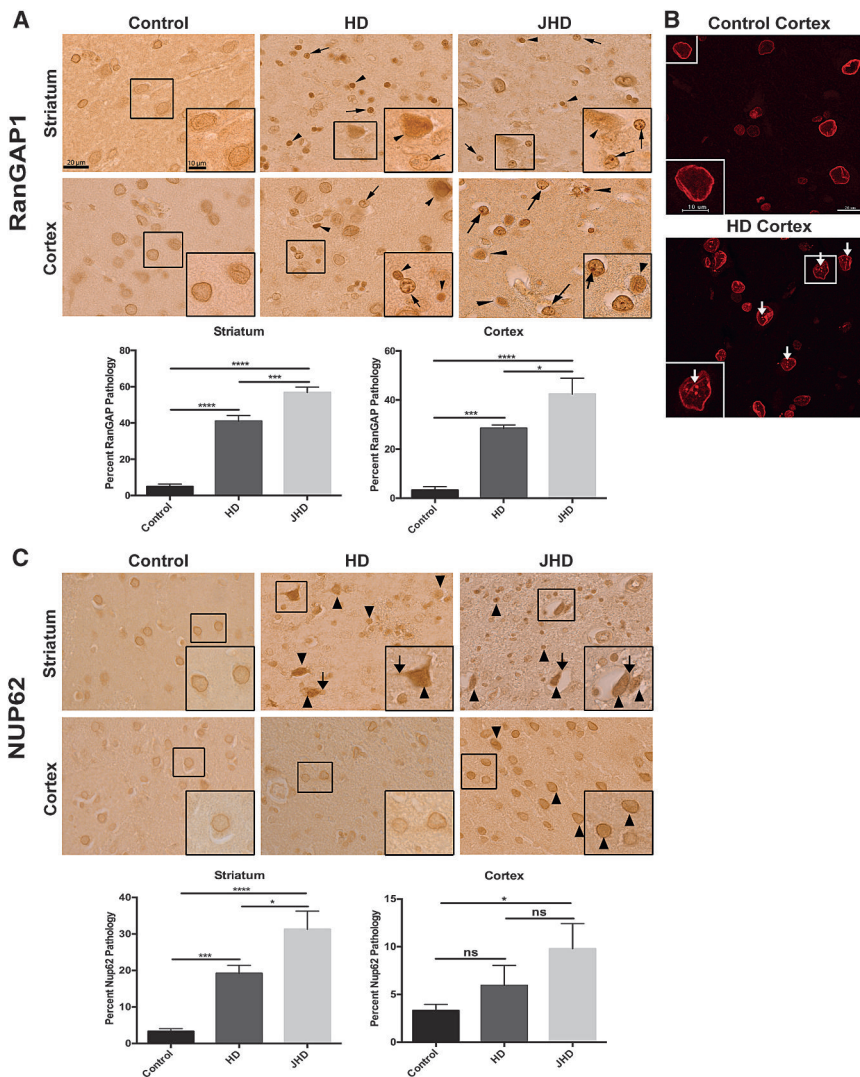


Figure 3. NUP Pathology in Human HD and JHD Brain Tissue

(A) Immunohistochemical RanGAP1 staining in non-neurological disease control ($n = 10$), HD ($n = 5$), and JHD ($n = 5$) striatum and frontal cortex showing aberrant nuclear aggregates (arrows) and intense nuclear mislocalization (arrowheads). Quantitation of percent of RanGAP1-positive cells with RanGAP1 pathology (nuclear aggregates or intense nuclear mislocalization) for each brain region shown below images.

(B) Immunofluorescence RanGAP1 staining in non-neurological disease control and HD frontal cortex showing aberrant nuclear aggregates (arrows).

(C) Immunohistochemical NUP62 staining in non-neurological disease control ($n = 10$), HD ($n = 5$), and JHD ($n = 5$) striatum and frontal cortex showing intense cytoplasmic (arrows) and nuclear (arrowheads) mislocalization. Quantitation of percent of NUP62-positive cells with NUP62 pathology (intense nuclear or cytoplasmic mislocalization) for each brain region shown below images.

Data are presented as mean \pm SEM. * $p < 0.05$, *** $p < 0.001$, and **** $p < 0.0001$ as analyzed by one-way ANOVA followed by Tukey's post hoc analysis. Scale bars, 20 and 10 μm (zoom inset). See also Table S2 and Figure S4.

the N/C ratio of endogenous MAP2, indicating that the NPC may be leaky and compromised in HD (Figure 4B). We next quantified the N/C ratio of RanGAP1 and NUP62 via immunofluorescence and found significant decreases in both, providing additional evidence that these NUPs and NPC-associated proteins are severely mislocalized in HD (Figures 4C and 4D).

Nucleocytoplasmic Transport Defects in Primary Neurons Transfected with Full-Length *mHTT*

As an additional model system, we investigated the disruption of neuronal nucleocytoplasmic transport by employing rodent cortical neurons transfected at 5 days in vitro (DIV5) with full-length *HTT* 22Q (control) or *HTT* 82Q (HD) and examined active nucleocytoplasmic transport via assessment of the Ran N/C gradient. We observed a marked mislocalization of Ran (green) to the cytoplasm in primary cortical neurons transfected with *HTT* 82Q, with an $\sim 50\%$ decrease in the Ran N/C gradient upon quantification compared to cortical neurons transfected with *HTT* 22Q (Figure 5A). To directly measure the nucleocyto-

plasmic transport of a protein reporter, we co-transfected primary cortical neurons at DIV5 with *HTT* 22Q or *HTT* 82Q and NLS-tdTomato-NES, a tdTomato protein fused with a classical NLS and NES, and measured the N/C ratio of NLS-tdTomato-NES. Again, we observed mislocalization of NLS-tdTomato-NES (red) to the cytoplasm in primary cortical neurons transfected with *HTT* 82Q and an $\sim 50\%$ loss of nuclear stain (Figure 5B). Collectively, these results may indicate that nuclear import is especially deficient in HD.

HD-RAN Proteins Disrupt Nucleocytoplasmic Transport

It was recently demonstrated that in addition to the *HTT* polyGln-expansion protein, four additional homopolymeric expansion proteins (polyAla, polySer, polyLeu, and polyCys) are generated in HD (Bañez-Coronel et al., 2015) from the nucleotide repeat. These sense and antisense HD-RAN proteins are also toxic to neural cells. In order to initially assess whether HD-RAN proteins can alter nucleocytoplasmic transport, we transfected cortical primary neurons with a CAG *HTT*-exon 1 minigene with a 6x STOP codon cassette (two stops in each frame) upstream of *HTT* exon1 (Bañez-Coronel et al., 2015) to generate these HD-RAN proteins (Figure S5) and quantified N/C Ran (active transport) and N/C MAP2 (passive transport) via immunofluorescence. We observed a significant reduction in the N/C ratio of endogenous Ran (Figure 6A) and a significant

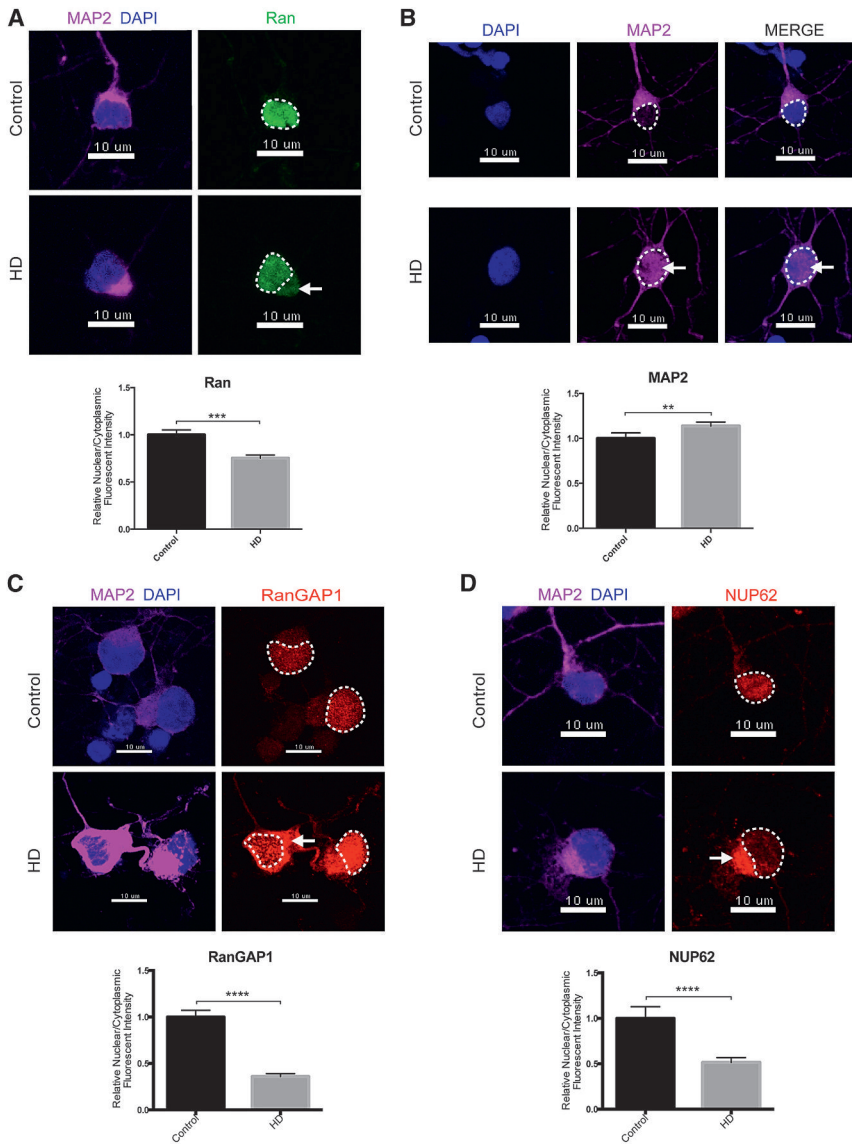


Figure 4. Nucleocytoplasmic Transport Defects in Human HD iPSNs

(A) iPSNs from control and HD patients showing mislocalization of Ran (green) to the cytoplasm in HD iPSNs. Quantification of N/C Ran gradient in neurons from one control (110 neurons) and two HD (144 neurons) iPSN lines when normalized to control shown below representative image. N/C Ran ratio is reduced in HD neurons. Bar indicates mean N/C Ran.

(B) iPSNs from control and HD patients showing leakage of MAP2 (magenta) to the nucleus in HD iPSNs. Quantification of N/C MAP2 gradient in neurons from one control (110 neurons) and two HD (296 neurons) iPSN lines when normalized to control shown below representative image. Bar indicates mean N/C MAP2.

(C) iPSNs from control and HD patients showing mislocalization of RanGAP1 (red) to the cytoplasm in HD iPSNs. Quantification of N/C RanGAP1 gradient in neurons from one control (30 neurons) and two HD (110 neurons) iPSN lines when normalized to control shown below representative image. Bar indicates mean N/C RanGAP1.

(D) iPSNs from control and HD patients showing mislocalization of NUP62 (red) to the cytoplasm in HD iPSNs. Quantification of N/C NUP62 gradient in neurons from one control (100 neurons) and two HD (186 neurons) iPSN lines when normalized to control shown below representative image. Bar indicates mean N/C NUP62.

Data are presented as mean \pm SEM. Each independent experiment represents the average of six wells total per condition per line repeated over three separate differentiations. ** $p < 0.01$, *** $p < 0.001$, **** $p < 0.0001$ as analyzed by unpaired Student's *t* test with Welch's correction. Scale bars, 10 μ m. See also Table S3.

increase in the N/C ratio of endogenous MAP2 (Figure 6B), indicating that HD-RAN proteins can cause defects in both active and passive nucleocytoplasmic transport. Finally, we co-expressed the aforementioned HD-RAN construct with a tdTomato protein tagged with an NLS and NES and quantified N/C NLS-tdTomato-NES. We observed a significant decrease in the N/C ratio of NLS-tdTomato-NES (Figure 6C), indicating that HD-RAN proteins may also contribute to defects in nuclear import.

Overexpression of Ran and RanGAP1 Is Neuroprotective in HD

To assess the extent to which the nucleocytoplasmic transport pathway may contribute to HD, we overexpressed a functional RanGAP1-GFP fusion protein in primary mouse cortical neurons that were co-transfected with either full-length *HTT* 22Q (control) or *HTT* 82Q (HD) and eGFP and performed a nuclear

condensation assay to assess cell death (Figure 7A). We found that overexpression of RanGAP1-GFP significantly reduced cell death in primary cortical neurons that were transfected with *HTT* 82Q (Figure 7A). Overexpression of a functional Ran-GFP fusion protein also significantly reduced cell death (Figure 7B) and significantly increased cell viability as assessed with the alamarBlue assay (Figure 7C). Finally, to test whether overexpression of Ran could modulate the mHTT phenotype in vivo, we tested the genetic interaction of Ran with Htt in an HD expanded repeat *Drosophila* model (Figure 7D). Using the GAL4/UAS system to express an N-terminal fragment of the human HTT protein in *Drosophila* tissues results in HTT aggregate formation and neurodegeneration (Lee et al., 2004). Expression of *HTT* 128Q, but not *HTT* 0Q, in the eye using GMR-GAL4 produced disruption in the external eye morphology including ommatidial disorganization and loss of pigment consistent with previous observations, a phenotype not observed upon expression of *HTT* 0Q. These phenotypes are rescued when we overexpress wild-type (WT) Ran and enhanced when we express a dominant-negative (DN) form of Ran (Figure 7D). To confirm

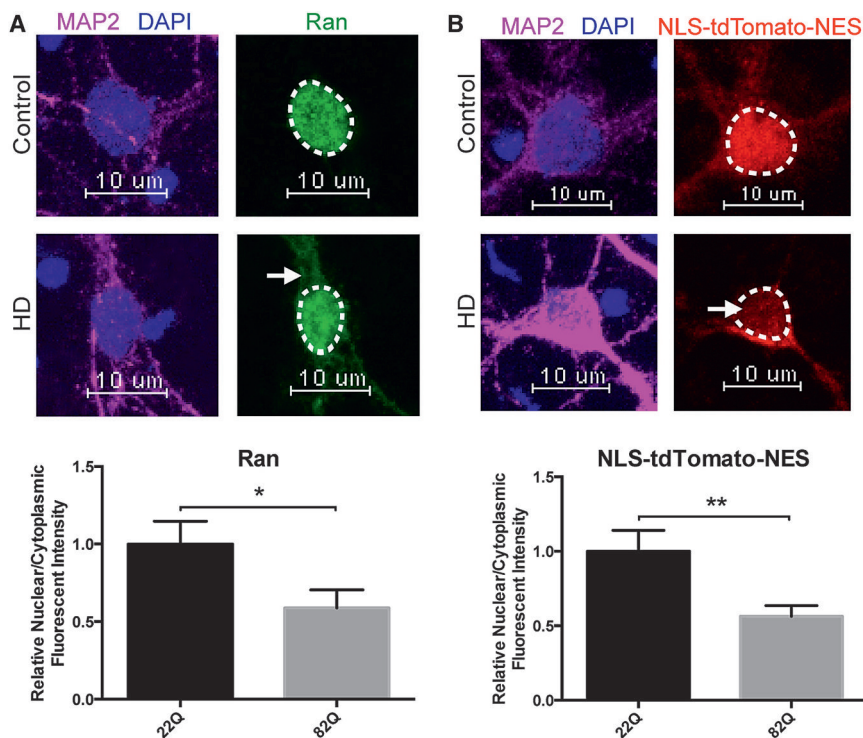


Figure 5. Nucleocytoplasmic Transport Defects in Primary Neurons Transfected with Full-Length *mHTT*

(A) Primary cortical neurons transfected at DIV5 with *HTT* 22Q (control) or *HTT* 82Q showing mislocalization of Ran (green) to the cytoplasm in primary cortical neurons transfected with *HTT* 82Q. Quantification of N/C Ran gradient in neurons transfected with 22Q (25 neurons) and 82Q (23 neurons) when normalized to control shown below representative image. Bar indicates mean N/C Ran. Experiment represents the average of three wells.

(B) Primary cortical neurons cotransfected at DIV5 with *HTT* 22Q (control) or *HTT* 82Q (HD) and NLS-tdTomato-NES showing mislocalization of NLS-tdTomato-NES (red) to the cytoplasm in primary cortical neurons transfected with *HTT* 82Q. Quantification of N/C NLS-tdTomato-NES gradient in neurons transfected with 22Q (48 neurons) and 82Q (54 neurons) when normalized to control shown below representative image. N/C NLS-tdTomato-NES is reduced in primary cortical neurons transfected with 82Q. Bar indicates mean N/C NLS-tdTomato-NES. Experiment represents average of nine wells.

Data are presented as mean \pm SEM. * $p < 0.05$ and ** $p < 0.01$ as analyzed by unpaired Student's *t* test with Welch's correction. Scale bars, 10 μ m.

this genetic interaction in another neuronal subtype, we expressed *HTT* 128Q in motor neurons using the OK371-GAL4 driver causing complete pupal lethality (Figure 7E). However, when WT Ran without GFP or DN Ran is coexpressed with Htt 128Q, there is a marked rescue of lethality with \sim 40% of flies surviving to adulthood.

Pharmacological Rescue of Nucleocytoplasmic Transport Defects and Neurotoxicity in HD

We next evaluated two additional pathways that might regulate function of NUPs and NPC-associated proteins and restore their proper homeostasis. First, O-GlcNAcylation is a post-translational modification in which β -N-acetylglucosamine (GlcNAc) is added to serine or threonine residues within intracellular proteins (Zachara and Hart, 2006). Interestingly, NUPs are the most heavily O-GlcNAc-modified proteins and are among the best substrates of O-GlcNAc transferase (OGT), the enzyme that catalyzes the addition of O-GlcNAc to proteins (Li and Kohler, 2014; Ruba and Yang, 2016). Because O-GlcNAcylation is essential for NPC integrity and function as well as maintenance of the pore selectivity filter (Zhu et al., 2016), and ten O-GlcNAc residues have been detected on NUP62, we quantified the nuclear levels of O-GlcNAc found specifically on NUPs using immunofluorescence in the cortex of 12-month-old zQ175 animals (Figure 8A). Using the RL2 antibody that predominantly recognizes this post-translational modification on NUPs (Li and Kohler, 2014), we observed that O-GlcNAc is significantly decreased in cortical cells of Het zQ175 mice (Figure 8A). This suggests that NUPs like NUP62, which is mislocalized in HD cultured neurons (Figure 4D) and in rodent (Figures 1C and 1D) and human

brain (Figure 3C), may be susceptible to mislocalization due to decreased levels and/or misregulation of O-GlcNAc. We therefore treated primary cortical neurons cotransfected with full-length *HTT* 22Q (control) or *HTT* 82Q (HD) and eGFP with Thiamet-G (0.5 μ M). Thiamet-G is a potent selective inhibitor of O-GlcNAcase (OGA) that catalyzes the removal of O-GlcNAc, resulting in elevated levels of O-GlcNAc (Yuzwa et al., 2014). We observed that treatment with Thiamet-G significantly reduced cell death in primary cortical neurons transfected with Htt 82Q (Figure 8B) and increased cell viability (Figure S6A). Treatment with Thiamet-G also rescued nucleocytoplasmic trafficking defects with the nuclear restoration of both endogenous Ran (Figure 8C) and exogenous NLS-tdTomato-NES (Figure 8D).

Next, we assessed the therapeutic potential of KPT-350, a potent inhibitor of Exportin-1 (XPO1 or CRM1), an NPC-associated protein responsible for the nuclear export of proteins bearing a leucine-rich NES and RNAs (Wente and Rout, 2010). KPT-350 was recently shown to be neuroprotective in models of inflammatory demyelination (Haines et al., 2015), and KPT-276, a closely related molecule, was shown to be neuroprotective in C9orf72-ALS models (Zhang et al., 2015). Treatment with KPT-350 (0.01 and 0.1 μ M) significantly reduced cell death in primary cortical neurons transfected with *HTT* 82Q (Figure 8E) and significantly increased cell viability (Figure S6B). Treatment with KPT-350 also rescued nucleocytoplasmic trafficking defects as seen with nuclear restoration of exogenous NLS-tdTomato-NES (Figure 8F). This suggests that inhibiting nuclear export may be neuroprotective and able to mitigate nucleocytoplasmic transport defects in HD by compensating for disrupted nuclear import.

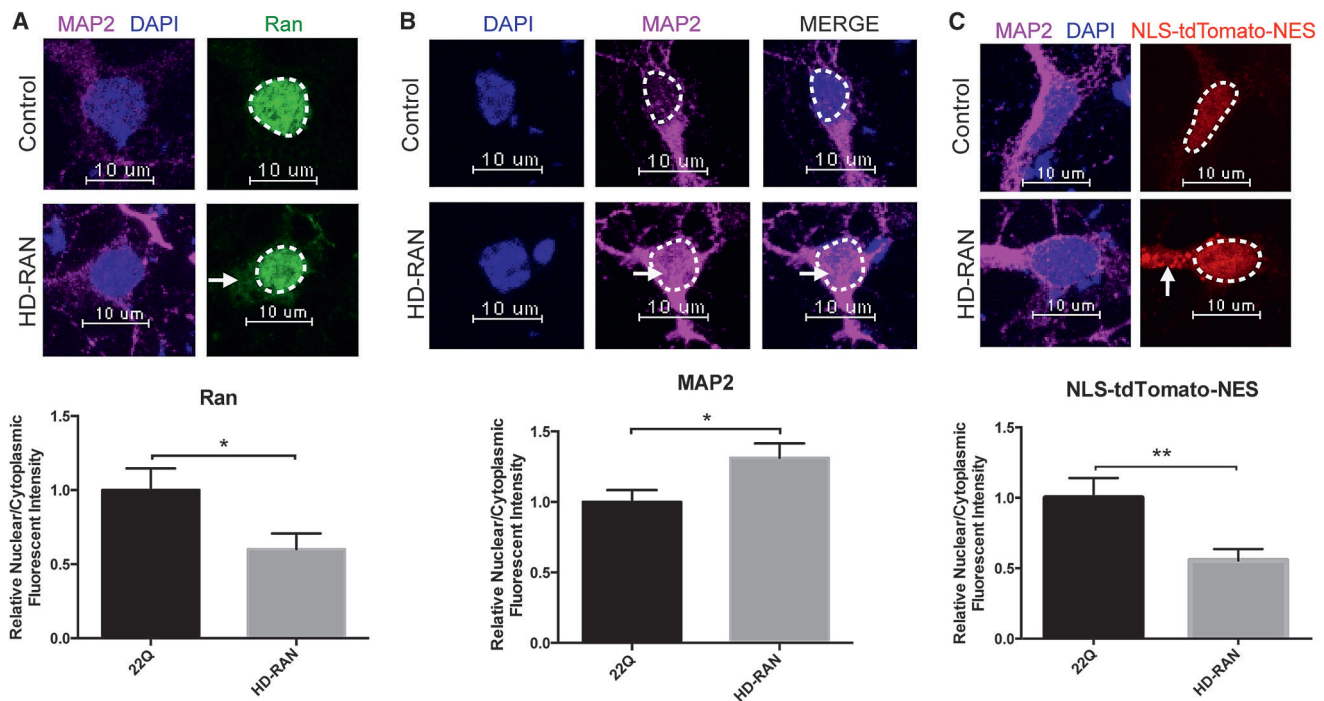


Figure 6. HD-RAN Proteins Disrupt Nucleocytoplasmic Transport

(A) Primary cortical neurons transfected at DIV5 with *HTT* 22Q (control) or 6xStop-(CAG)80 (HD-RAN) showing mislocalization of Ran (green) to the cytoplasm in primary cortical neurons transfected with 6xStop-(CAG)80. Quantification of N/C Ran gradient in neurons transfected with 22Q (25 neurons) and 6xStop-(CAG)80 (27 neurons) when normalized to control shown below representative image. Bar indicates mean N/C Ran. Experiment represents average of two wells.

(B) Primary cortical neurons transfected at DIV5 with *HTT* 22Q (control) or 6xStop-(CAG)80 (HD-RAN) showing leakage of MAP2 (magenta) to the nucleus in primary cortical neurons transfected with 6xStop-(CAG)80. Quantification of N/C MAP2 gradient in neurons transfected with 22Q (50 neurons) and 6xStop-(CAG)80 (54 neurons) when normalized to control shown below representative image. Bar indicates mean N/C MAP2. Experiment represents average of six wells.

(C) Primary cortical neurons cotransfected at DIV5 with *HTT* 22Q (control) or 6xStop-(CAG)80 (HD-RAN) and NLS-tdTomato-NES showing mislocalization of NLS-tdTomato-NES (red) to the cytoplasm in primary cortical neurons transfected with 6xStop-(CAG)80. Quantification of N/C NLS-tdTomato-NES gradient in neurons transfected with 22Q (48 neurons) and 6xStop-(CAG)80 (51 neurons) when normalized to control shown below representative image. Bar indicates mean N/C NLS-tdTomato-NES. Experiment represents average of six wells.

Data are presented as mean \pm SEM. * $p < 0.05$ and ** $p < 0.01$ as analyzed by unpaired Student's *t* test with Welch's correction. Scale bars, 10 μ m. See also Figure S5.

DISCUSSION

Using mouse models, postmortem human tissue, a *Drosophila* model, human patient-derived neurons, and primary neurons transfected with full-length *mHTT*, we demonstrate that products of the CAG triplet repeat expansion within the HD gene cause disruption of the NPC and nucleocytoplasmic transport. First, multiple proteins of the NPC, particularly those from the cytoplasmic ring/filaments and central channel regions, mislocalize and/or aggregate in the striatum and cortex of both an N-terminal mutant *HTT* transgenic and full-length mutant *Htt* knockin mouse model of HD, human HD, and JHD postmortem tissue, iPSNs from HD human patients, and primary neurons transfected with full-length *mHTT*. These NUP aggregates colocalize with mHtt and increase in frequency and diameter with disease progression. Second, the insoluble levels of one of these proteins, RanGAP1, which is essential for maintaining the energy gradient (Ran) that fuels active nucleocytoplasmic transport, decreases in the nuclear-enriched fraction with disease progression. This can be rescued when knocking down

levels of PIAS1, which was recently shown to decrease aberrant mHtt accumulation (Ochaba et al., 2016) and thus may free up proteins like NUPs that are caught up in insoluble protein aggregates and complexes. Third, iPSNs from human HD patients and primary neurons transfected with full-length *mHTT* show a disruption in the Ran gradient and increased permeability of the NPC, indicating that both active and passive nucleocytoplasmic transport is disrupted in HD. Also, exogenous NLS-tdTomato-NES mislocalizes to the cytoplasm in primary neurons transfected with full-length *mHTT*, suggesting that nuclear protein import may be especially deficient in HD. Additionally, recently discovered HD-RAN proteins can also contribute to deficits in nucleocytoplasmic transport. Finally, we can rescue cell death, increase cell viability, and restore nucleocytoplasmic transport function when overexpressing RanGAP1 or Ran in primary neurons transfected with full-length *mHTT* and in a *Drosophila* model of HD as well as when treating with Thiamet-G, an inhibitor that increases O-GlcNAc levels that highly regulate NPC homeostasis, or KPT-350, an inhibitor of canonical nuclear export.

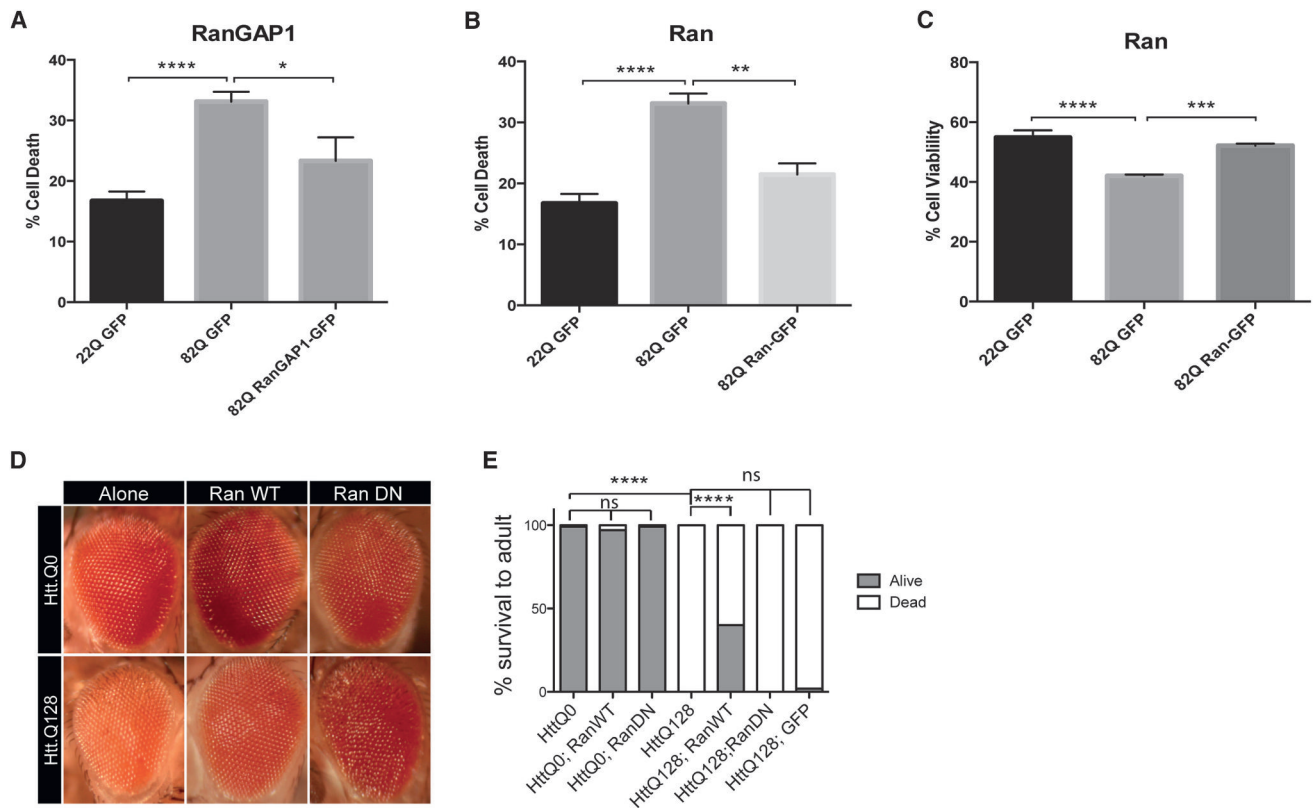


Figure 7. Overexpression of Ran and RanGAP1 Is Neuroprotective in HD

(A and B) Overexpression of *HTT* 82Q-eGFP in primary cortical neurons causes significant cell death compared to neurons transfected with *HTT* 22Q-eGFP (A and B), and cell death is significantly reduced when overexpressing RanGAP1-GFP (A) or Ran-GFP (B). Experiment represents the average of four wells per condition.

(C) Overexpression of *HTT* 82Q and eGFP in primary cortical neurons causes a significant reduction in cell viability compared to neurons transfected with *HTT* 22Q and eGFP, and is rescued when overexpressing Ran-GFP. Experiment represents the average of four wells total per condition over the course of two separate experiments.

Data (A–C) are presented as mean \pm SEM. * $p < 0.05$, ** $p < 0.01$, *** $p < 0.001$, and **** $p < 0.0001$ as analyzed by one-way ANOVA followed by Tukey's post hoc analysis.

(D) Overexpression in the *Drosophila* eye of *HTT.Q0* or *HTT.Q128* using GMR-Gal4. Co-expressing wild-type (WT) Ran rescues this disorganization, whereas co-expression of a dominant-negative (DN) Ran allele enhances this disorganization phenotype.

(E) Overexpression of *HTT.Q128* in motor neurons using OK371-Gal4 causes lethality at the pupal stage (Fisher's exact test, $p < 0.0001$), whereas overexpression of *HTT.Q0* has no phenotype alone or with Ran alleles. Co-expression of RanWT is sufficient to partially rescue the lethality caused by *HTT.Q128* expression (Fisher's exact test, $p < 0.0001$), whereas co-expression of RanDN or GFP alone was not sufficient to rescue.

There are prior clues to support our hypothesis that a disruption of nuclear events by mHTT is important for expanded CAG-repeat-mediated pathophysiology. Previous studies showed that adding an exogenous NLS to polyQ expanded proteins such as small HTT amino-terminal fragments (Schilling et al., 2004) and full-length HTT (Saudou et al., 1998) results in increased toxicity in cell and animal models, suggesting that nuclear localization of HTT polyQ expansions contributes to its toxicity. Additionally, adding an NES to full-length HTT, restricting it to the cytoplasm, reduces toxicity. However, the real target of nuclear disruption remained unknown. The comprehensive studies that we have amassed in human brain and multiple human cell and animal models, in vivo and in vitro, strongly suggest that mHTT compromises the gatekeeper of the nucleus, the NPC, and ultimately nucleocytoplasmic transport function. This pathophysiology may extend to other polyQ diseases given

that nuclear shuttling and accumulation are common to the majority of polyQ disease proteins such as ataxin-2 in spinocerebellar ataxia 2 (SCA2) (La Spada and Taylor, 2010). This may partially explain why the R6/2 mouse model exhibits such an extreme phenotype. This model uniquely expresses just the N-terminal fragment of HTT, which contains no classic NLS or HEAT repeats but may be small enough to readily cross the NPC into the nucleus and potentially sequester significantly more NUPs compared to full-length Htt mouse models. In fact, the current study indicates that NUP aggregates are larger in diameter in the R6/2 mouse model compared to zQ175; alternatively, this could also be due to different expression levels of HTT. Further comparative studies in different animal models are needed.

Nucleocytoplasmic transport, the trafficking of protein and RNA between the nucleus and cytoplasm, is critical for the

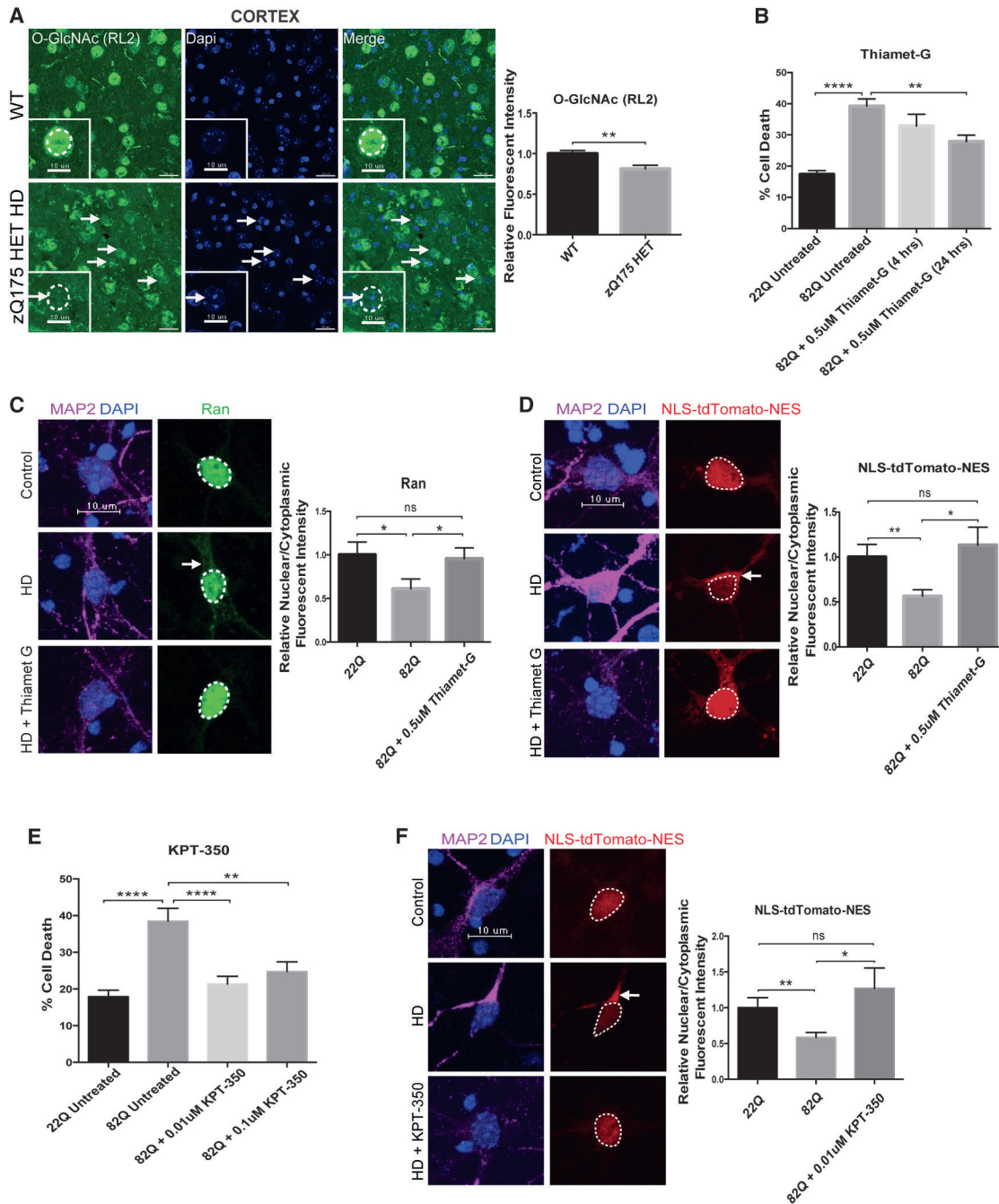


Figure 8. Pharmacological Rescue of Nucleocytoplasmic Transport Defects and Neurotoxicity in HD

(A) Coronal brain sections from WT and HET zQ175 mice showing decreased relative nuclear fluorescent intensity of O-GlcNAc (RL2) in the cortex of 12M HET zQ175 mice. Quantification of relative nuclear fluorescent intensity of O-GlcNAc (RL2) in cortical cells from three WT (150 neurons; 50 neurons each) and three zQ175 HET (150 neurons; 50 neurons each) when normalized to WT shown next to representative image. Bar indicates mean nuclear O-GlcNAc (RL2). Data are presented as mean \pm SEM. ** $p < 0.01$ as analyzed by unpaired Student's *t* test with Welch's correction.

(B) Overexpression of *HTT* 82Q and eGFP in primary cortical neurons causes significant cell death compared to neurons transfected with *HTT* 22Q and eGFP, and cell death is significantly reduced when treating cells with 0.5 μ M Thiamet-G for 24 hr beginning 24 hr after transfection. Experiment represents the average of four wells.

(C) Overexpression of *HTT* 82Q and eGFP in primary cortical neurons causes significant mislocalization of Ran (green) to the cytoplasm, which is rescued back to control levels upon treatment with 0.5 μ M Thiamet-G for 4 hr beginning 44 hr after transfection. Quantification of N/C Ran gradient in neurons transfected with 22Q (25 neurons), 82Q (23 neurons), and 82Q + Thiamet G (30 neurons) when normalized to control shown next to representative image. Bar indicates mean N/C Ran. Experiment represents the average of three wells.

(legend continued on next page)

proper functioning of cells. This regulated and efficient communication of macromolecules is essential for signal transduction, neuronal plasticity, glial function, and overall cellular survival (Dickmanns et al., 2015; Schachtrup et al., 2015). Altered nucleocytoplasmic distribution of proteins such as transcription factors is commonly seen across several neurodegenerative diseases and may be the result of defective nucleocytoplasmic transport. Examples include mislocalization of activating transcription factor 2 (ATF2), nuclear factor E2-related factor 2 (Nrf2), and importin- α 1 in Alzheimer's disease (AD) (Lee et al., 2006; Yamada et al., 1997); phosphorylated cyclic AMP response element-binding protein (pCREB) and phosphorylated extracellular signal-regulated kinase 1/2 (pERK1/2) in Parkinson's disease (PD) (Chalovich et al., 2006; Ferrer et al., 2001); and TAR DNA binding protein 43 (TDP-43) in FTD and ALS (Neumann et al., 2006). Recent work from our group and others, using human, fly, and yeast models, revealed that an expanded hexanucleotide (GGGGCC) repeat (HRE) within a non-coding region of the C9orf72 gene causes dysfunction in nuclear import, which may explain the hallmark cytoplasmic accumulation of TDP-43 in ALS and FTD (Zhang et al., 2015). Given these prior studies in ALS, FTD, and now HD, as well as a recent study demonstrating that certain cytoplasmic protein aggregates can interfere with nucleocytoplasmic trafficking of protein and RNA (Woerner et al., 2016), dysfunction in nucleocytoplasmic transport may be a shared common defect across multiple neurodegenerative disorders. Whether this pathway contributes to sporadic forms of these age-related degenerative diseases awaits further research.

Interestingly, altering NPC function has been shown to impact longevity (Lord et al., 2015). The NPC regulates not only nucleocytoplasmic transport but also genome organization, gene expression, cell differentiation, and development, and may be fundamental to brain aging. Some of the longest-lived proteins in the mammalian brain are components of the NPC and thus may represent a "weak link" in the aging proteome (Savas et al., 2012; Toyama et al., 2013). Because these NUPs persist for so long without being recycled, they have been shown to accumulate molecular damage over time, and this age-related deterioration results in an increase in nuclear permeability and the leaking of cytoplasmic proteins and toxins inside the nucleus (D'Angelo et al., 2009). In fact, the current study provides evidence of nuclear leakage of MAP2, a cytoplasmic protein, in several *in vitro* models of HD, indicating a dysfunctional NPC. This could result in alterations in DNA and cellular aging. Given

that aging is an independent risk factor for neurodegeneration, defects in the NPC may underlie neurodegeneration, and this injury may be mitigated by utilizing small molecules that act on this pathway such as Thiamet-G and KPT-350, as detailed in the current studies. In fact, Thiamet-G has already been shown to be neuroprotective in models of AD (Borghgraef et al., 2013; Yuzwa et al., 2012, 2014), and KPT-350 and related SINE (selective inhibitor of nuclear export) compounds were recently shown to be neuroprotective in models of C9orf72-ALS (Zhang et al., 2015) and inflammatory demyelination (Haines et al., 2015). Therefore, these compounds may also prove therapeutic for other diseases that involve defects in NPC and nucleocytoplasmic transport function.

A question that often arises when studying neurodegeneration is why only some cells undergo injury when the mutant proteins or pathways are often ubiquitous. Very little is known about the neurobiology of the NPC in the CNS. Although the overall structure of the NPC is conserved across different cell types, studies suggest that cells may express unique combinations of NUPs to generate NPCs with specialized functions (Ori et al., 2013). There is evidence to suggest that individual NUPs may be responsible for the trafficking of unique macromolecules, thus adding a layer of diversity and specificity to the NPC (Raices and D'Angelo, 2012). This is best supported by the fact that mutations in various NUPs result in tissue-specific diseases. For instance, a missense mutation in NUP62 (Q391P) causes IBSN, an autosomal-recessive neurodegenerative disease that results in the selective degeneration of the corpus striatum in infants (Basel-Vanagaite et al., 2006). This suggests that NUP62 may play a critical role for the proper functioning of the corpus striatum. We now show that NUP62 mislocalizes and/or aggregates in several HD animal models, HD human tissue, and HD iPSCs. In fact, NUP62 pathology was primarily found in HD human striatum, not cortex or cerebellum. Purified HTT fragment polyQ aggregates have been shown to sequester NUP62 (Suhr et al., 2001). The mechanism that underlies sequestration of NUP62 may mediate the selective degeneration of the striatum in HD. Future studies could address whether the composition of the NPC is different across the CNS at a regional and cellular level, yielding NPCs with distinct properties and specialized functions given brain cell-type-specific constraints and context-dependent needs. If the composition of the NPC differs across CNS cell types and tissues, this may provide a plausible explanation for tissue-specific neurological diseases that arise from mutations in various NUPs like GLE1 in fetal motoneuron disease

(D) Overexpression of *HTT* 82Q and eGFP in primary cortical neurons causes significant mislocalization of exogenous NLS-tdTomato-NES (red) to the cytoplasm, which is rescued back to control levels upon treatment with 0.5 μ M Thiamet-G for 4 hr beginning 44 hr after transfection. Quantification of N/C NLS-tdTomato-NES gradient in neurons transfected with 22Q (48 neurons), 82Q (54 neurons), and 82Q + Thiamet G (32 neurons) when normalized to control shown next to representative image. Bar indicates mean N/C NLS-tdTomato-NES. Experiment represents average of nine wells.

(E) Overexpression of *HTT* 82Q and eGFP in primary cortical neurons causes significant cell death compared to neurons transfected with *HTT* 22Q and eGFP, and cell death is significantly reduced when treating cells with either 0.01 μ M or 0.1 μ M KPT-350 at the time of transfection for 48 hr. Experiment represents the average of four wells per condition.

(F) Overexpression of *HTT* 82Q and eGFP in primary cortical neurons causes significant mislocalization of endogenous NLS-tdTomato-NES (red) to the cytoplasm, which is rescued back to control levels upon treatment with 0.01 μ M KPT-350 at the time of transfection for 48 hr. Quantification of N/C NLS-tdTomato-NES gradient in neurons transfected with 22Q (48 neurons), 82Q (54 neurons), and 82Q + KPT-350 (20 neurons) when normalized to control shown next to representative image. Bar indicates mean N/C NLS-tdTomato-NES. Experiment represents average of three wells.

Data (B–F) are presented as mean \pm SEM. * $p < 0.05$, ** $p < 0.01$, and **** $p < 0.0001$ as analyzed by one-way ANOVA followed by Tukey's post hoc analysis. Scale bars, 20 (A) and 10 μ m (A, zoom inset, C, D, and F). See also Figure S6.

(Nousiainen et al., 2008) and rare forms of ALS (Kaneb et al., 2015) and NUP62 in IBSN.

Our findings highlighting the contribution of O-GlcNAc and NPC proteins in HD provide a new avenue for investigation and therapeutics discovery. While we cannot rule out that our Thiamet-G treatment may have also modified other O-GlcNAc-modified proteins that indirectly altered nucleocytoplasmic transport to mitigate the injury observed, the current studies do show that altering nucleocytoplasmic transport function is one such candidate and not previously studied. Also, the O-GlcNAc antibody used in the current study, “RL2,” predominantly recognizes the O-GlcNAc modification on NPC proteins, and these NUPs are the most heavily O-GlcNAc-modified proteins and are among the best substrates for O-GlcNAc transferase (OGT) (Li and Kohler, 2014; Ruba and Yang, 2016). For example, downregulation of O-GlcNAcylation selectively affects NUP62 and NUP88, but not TPR, in vitro (Mizuguchi-Hata et al., 2013), which directly supports what we observe in our HD models. NUP88 homeostasis is also regulated through its interaction with O-GlcNAcylated NUP62, which suggests that the NPC defect in HD could be initiated with NUP62 mislocalization. O-GlcNAc also helps maintain NPC homeostasis by preventing the inappropriate aggregation and degradation of NUPs by decreasing ubiquitination or disturbing the ubiquitin-proteasomal degradation pathway (Zhu et al., 2016). Given the relationship between O-GlcNAc and NUP homeostasis and the fact that O-GlcNAc integrates metabolic information (Bond and Hanover, 2015; Hart, 2014), it is enticing to speculate whether distinct metabolic profiles across different regions of the brain (Magistretti and Allaman, 2015) may dictate NPC composition via O-GlcNAc signaling. Lastly, recent work showed that cytoplasmic aggregates such as tau can disrupt nucleocytoplasmic transport of protein and RNA (Woerner et al., 2016). Given we now show that Thiamet-G can restore nucleocytoplasmic transport function, it may also provide an additional explanation as to why Thiamet-G has already been shown to be neuroprotective against tauopathy (Borghgraef et al., 2013).

Overall, the current study provides compelling and comprehensive new data using multiple model systems and human brain, implicating aberrant NPC function, specifically its role in regulating nucleocytoplasmic transport, in the pathogenesis of HD and potentially other polyQ-expansion and neurodegenerative disorders. The mHTT polyQ protein is sufficient to induce nucleocytoplasmic trafficking deficits; however, future studies are required to further elucidate the contribution of newly discovered HD-RAN proteins in altering nucleocytoplasmic transport function. Although we demonstrate that the HD-RAN proteins can generally alter nucleocytoplasmic transport, it is still unknown as to which one of these specific protein(s) (polyAla, polySer, polyLeu, and polyCys) is/are mostly mediating this dysfunction. Interestingly, HD-RAN proteins appear to be more abundant in the cerebellum than the polyQ aggregates (Bañez-Coronel et al., 2015) and thus may be selectively responsible for the mislocalization or aggregation of RanGAP1 detected in HD, but mostly JHD, cerebellum in the current studies. This is consistent with recent reports demonstrating cerebellar pathology and atrophy in both adult and juvenile HD cases, which may explain

some of the balance and gait abnormalities found in patients (Rüb et al., 2013).

Lastly, future work should not only focus on further elucidating the role of nucleocytoplasmic transport in HD but also on other critical functions mediated by the NPC such as potential genome organization and gene expression alterations. Given the crucial role that the NPC plays in regulating the transport of macromolecules to and from the nucleus and local transcription, these new studies suggest that defects in the NPC may be playing a substantial role in HD pathogenesis and provide a new target for therapeutic interventions.

STAR★METHODS

Detailed methods are provided in the online version of this paper and include the following:

- KEY RESOURCES TABLE
- CONTACT FOR REAGENT AND RESOURCE SHARING
- EXPERIMENTAL MODEL AND SUBJECT DETAILS
 - Ethics Statement
 - HD Mouse Models
 - iPS Cell Culture
 - Primary Neuron Culture
 - *Drosophila* Genetics
- METHOD DETAILS
 - Immunofluorescence in Mouse Brain Tissue
 - Immunocytochemistry in Primary and iPS Neurons
 - Immunohistochemistry in Human Brain Tissue
 - Immunofluorescence in Human Brain Tissue
 - Histological Quantification Strategy
 - Neuronal Differentiation
 - Microscopy and Image Analysis
 - Constructs
 - Cell Death and Viability Assays
 - Soluble/Insoluble Fractionation Experiments
 - Filter Retardation Assay
 - Experimental Design
- QUANTIFICATION AND STATISTICAL ANALYSIS

SUPPLEMENTAL INFORMATION

Supplemental Information includes six figures and three tables and can be found with this article online at <http://dx.doi.org/10.1016/j.neuron.2017.03.023>.

AUTHOR CONTRIBUTIONS

Conceptualization, J.C. Grima and J.D.R.; Methodology, J.C. Grima; Investigation, J.C. Grima, J.G.D., N.A., K.C.C., K.Z., J.O., C.G., E.M., J.S., J.C. Glatzer, J.T.P., I.A., Q.P., and H.W.; Writing – Original Draft, J.C. Grima; Writing – Review & Editing, all authors; Resources, O.P., J.C.T., W.D., S.H.S., L.P.W.R., L.M.T., T.E.L., C.A.R., and J.D.R.; Funding Acquisition, J.C. Grima, J.O., C.G., W.D., S.H.S., L.P.W.R., L.M.T., T.E.L., C.A.R., and J.D.R.; Supervision, J.D.R.

ACKNOWLEDGMENTS

Funded by grants from the NIH (R01NS094239 and R01NS085207 to J.D.R., C.A.R., L.M.T., L.P.W.R., S.H.S., and T.E.L.), National Science Foundation Graduate Research Fellowship Award (J.C. Grima), Thomas Shortman

Training Fund Graduate Award (J.C. Grima), Axol Science Award (J.C. Grima), NIH Training in Neurotherapeutics Discovery and Development for Academic Scientists (J.C. Grima), MDI Biological Laboratory QFM Chroma Fellowship Award (J.C. Grima), National Science Foundation (J.O.), CIRM Training Grant (C.G.) and the Johns Hopkins Brain Science Institute (J.D.R.). Drs. Ross, Troncoso, and Pletnikova provided human tissue and demographics. We wish to thank Michael J. Matunis for helpful discussions, Svetlana Videnskey for construct preparations and technical support, Natasha Zachara and the CardioPEG Core at Johns Hopkins (NHLBI PO1 HL107153) for providing Thiamet-G, Uzma Hussain for technical assistance, and Sharon Tamir/Karyopharm Therapeutics for supplying KPT-350.

Received: September 28, 2016

Revised: January 30, 2017

Accepted: March 13, 2017

Published: April 5, 2017

REFERENCES

- Bañez-Coronel, M., Ayhan, F., Tarabochia, A.D., Zu, T., Perez, B.A., Tusi, S.K., Pletnikova, O., Borchelt, D.R., Ross, C.A., Margolis, R.L., et al. (2015). RAN translation in Huntington disease. *Neuron* **88**, 667–677.
- Basel-Vanagaite, L., Muncher, L., Straussberg, R., Pasmanik-Chor, M., Yahav, M., Rainshtein, L., Walsh, C.A., Magal, N., Taub, E., Drasinover, V., et al. (2006). Mutated nup62 causes autosomal recessive infantile bilateral striatal necrosis. *Ann. Neurol.* **60**, 214–222.
- Bond, M.R., and Hanover, J.A. (2015). A little sugar goes a long way: the cell biology of O-GlcNAc. *J. Cell Biol.* **208**, 869–880.
- Borghgraef, P., Menuet, C., Theunis, C., Louis, J.V., Devijver, H., Maurin, H., Smet-Nocca, C., Lippens, G., Hilaire, G., Gijssen, H., et al. (2013). Increasing brain protein O-GlcNAc-ylation mitigates breathing defects and mortality of Tau.P301L mice. *PLoS ONE* **8**, e84442.
- Brettschneider, J., Del Tredici, K., Lee, V.M.-Y., and Trojanowski, J.Q. (2015). Spreading of pathology in neurodegenerative diseases: a focus on human studies. *Nat. Rev. Neurosci.* **16**, 109–120.
- Capelson, M., Liang, Y., Schulte, R., Mair, W., Wagner, U., and Hetzer, M.W. (2010). Chromatin-bound nuclear pore components regulate gene expression in higher eukaryotes. *Cell* **140**, 372–383.
- Chalovich, E.M., Zhu, J.H., Caltagarene, J., Bowser, R., and Chu, C.T. (2006). Functional repression of cAMP response element in 6-hydroxydopamine-treated neuronal cells. *J. Biol. Chem.* **281**, 17870–17881.
- Cornett, J., Cao, F., Wang, C.-E., Ross, C.A., Bates, G.P., Li, S.-H., and Li, X.-J. (2005). Polyglutamine expansion of huntingtin impairs its nuclear export. *Nat. Genet.* **37**, 198–204.
- D'Angelo, M.A., Raices, M., Panowski, S.H., and Hetzer, M.W. (2009). Age-dependent deterioration of nuclear pore complexes causes a loss of nuclear integrity in postmitotic cells. *Cell* **136**, 284–295.
- Dickmanns, A., Kehlenbach, R.H., and Fahrenkrog, B. (2015). Nuclear pore complexes and nucleocytoplasmic transport: from structure to function to disease. *Int. Rev. Cell Mol. Biol.* **320**, 171–233.
- Ferrer, I., Blanco, R., Carmona, M., Puig, B., Barrachina, M., Gómez, C., and Ambrosio, S. (2001). Active, phosphorylation-dependent mitogen-activated protein kinase (MAPK/ERK), stress-activated protein kinase/c-Jun N-terminal kinase (SAPK/JNK), and p38 kinase expression in Parkinson's disease and Dementia with Lewy bodies. *J. Neural Transm (Vienna)* **108**, 1383–1396.
- Finkbeiner, S. (2011). Huntington's Disease. *Cold Spring Harb. Perspect. Biol.* **3**, a007476.
- Floch, A.G., Palancade, B., and Doye, V. (2014). Fifty years of nuclear pores and nucleocytoplasmic transport studies: multiple tools revealing complex rules. *Methods Cell Biol.* **122**, 1–40.
- Freibaum, B.D., Lu, Y., Lopez-Gonzalez, R., Kim, N.C., Almeida, S., Lee, K.-H., Badders, N., Valentine, M., Miller, B.L., Wong, P.C., et al. (2015). GGGGCC repeat expansion in C9orf72 compromises nucleocytoplasmic transport. *Nature* **525**, 129–133.
- Haines, J.D., Herbin, O., de la Hera, B., Vidaurre, O.G., Moy, G.A., Sun, Q., Fung, H.Y., Albrecht, S., Alexandropoulos, K., McCauley, D., et al. (2015). Nuclear export inhibitors avert progression in preclinical models of inflammatory demyelination. *Nat. Neurosci.* **18**, 511–520.
- Hart, G.W. (2014). Minireview series on the thirtieth anniversary of research on O-GlcNAcylation of nuclear and cytoplasmic proteins: Nutrient regulation of cellular metabolism and physiology by O-GlcNAcylation. *J. Biol. Chem.* **289**, 34422–34423.
- Hensman Moss, D.J., Poulter, M., Beck, J., Hehir, J., Polke, J.M., Campbell, T., Adamson, G., Mudanohwo, E., McColgan, P., Haworth, A., et al. (2014). C9orf72 expansions are the most common genetic cause of Huntington disease phenocopies. *Neurology* **82**, 292–299.
- Hetzer, M., Gruss, O.J., and Mattaj, I.W. (2002). The Ran GTPase as a marker of chromosome position in spindle formation and nuclear envelope assembly. *Nat. Cell Biol.* **4**, E177–E184.
- Hosp, F., Vossfeldt, H., Heinig, M., Vasiljevic, D., Arumughan, A., Wyler, E., Landthaler, M., Hubner, N., Wanker, E.E., Lannfelt, L., et al.; Genetic and Environmental Risk for Alzheimer's Disease GERAD1 Consortium (2015). Quantitative interaction proteomics of neurodegenerative disease proteins. *Cell Rep.* **11**, 1134–1146.
- Izant, J.G., and McIntosh, J.R. (1980). Microtubule-associated proteins: a monoclonal antibody to MAP2 binds to differentiated neurons. *Proc. Natl. Acad. Sci. USA* **77**, 4741–4745.
- Jovčić, A., Mertens, J., Boeynaems, S., Bogaert, E., Chai, N., Yamada, S.B., Paul, J.W., 3rd, Sun, S., Herdy, J.R., Bieri, G., et al. (2015). Modifiers of C9orf72 dipeptide repeat toxicity connect nucleocytoplasmic transport defects to FTD/ALS. *Nat. Neurosci.* **18**, 1226–1229.
- Kalverda, B., Pickersgill, H., Shloma, V.V., and Fornerod, M. (2010). Nucleoporins directly stimulate expression of developmental and cell-cycle genes inside the nucleoplasm. *Cell* **140**, 360–371.
- Kaneb, H.M., Folkmann, A.W., Belzil, V.V., Jao, L.-E., Leblond, C.S., Girard, S.L., Daoud, H., Noreau, A., Rochefort, D., Hince, P., et al. (2015). Deleterious mutations in the essential mRNA metabolism factor, hGle1, in amyotrophic lateral sclerosis. *Hum. Mol. Genet.* **24**, 1363–1373.
- Kumita, J.R., Helmfors, L., Williams, J., Luheshi, L.M., Menzer, L., Dumoulin, M., Lomas, D.A., Crowther, D.C., Dobson, C.M., and Brorsson, A.C. (2012). Disease-related amyloidogenic variants of human lysozyme trigger the unfolded protein response and disturb eye development in *Drosophila melanogaster*. *FASEB J.* **26**, 192–202.
- La Spada, A.R., and Taylor, J.P. (2010). Repeat expansion disease: progress and puzzles in disease pathogenesis. *Nat. Rev. Genet.* **11**, 247–258.
- Lee, W.C., Yoshihara, M., and Littleton, J.T. (2004). Cytoplasmic aggregates trap polyglutamine-containing proteins and block axonal transport in a *Drosophila* model of Huntington's disease. *Proc. Natl. Acad. Sci. USA* **101**, 3224–3229.
- Lee, H.G., Ueda, M., Miyamoto, Y., Yoneda, Y., Perry, G., Smith, M.A., and Zhu, X. (2006). Aberrant localization of importin alpha1 in hippocampal neurons in Alzheimer disease. *Brain Res.* **1124**, 1–4.
- Li, B., and Kohler, J.J. (2014). Glycosylation of the nuclear pore. *Traffic* **15**, 347–361.
- Liang, Y., and Hetzer, M.W. (2011). Functional interactions between nucleoporins and chromatin. *Curr. Opin. Cell Biol.* **23**, 65–70.
- Liu, K.-Y., Shyu, Y.-C., Barbaro, B.A., Lin, Y.-T., Chern, Y., Thompson, L.M., James Shen, C.-K., and Marsh, J.L. (2015). Disruption of the nuclear membrane by perinuclear inclusions of mutant huntingtin causes cell-cycle re-entry and striatal cell death in mouse and cell models of Huntington's disease. *Hum. Mol. Genet.* **24**, 1602–1616.
- Lord, C.L., Timney, B.L., Rout, M.P., and Wente, S.R. (2015). Altering nuclear pore complex function impacts longevity and mitochondrial function in *S. cerevisiae*. *J. Cell Biol.* **208**, 729–744.
- Magistretti, P.J., and Allaman, I. (2015). A cellular perspective on brain energy metabolism and functional imaging. *Neuron* **86**, 883–901.

- Mizuguchi-Hata, C., Ogawa, Y., Oka, M., and Yoneda, Y. (2013). Quantitative regulation of nuclear pore complex proteins by O-GlcNAcylation. *Biochim. Biophys. Acta* *1833*, 2682–2689.
- Neumann, M., Sampathu, D.M., Kwong, L.K., Truax, A.C., Micsenyi, M.C., Chou, T.T., Bruce, J., Schuck, T., Grossman, M., Clark, C.M., et al. (2006). Ubiquitinated TDP-43 in frontotemporal lobar degeneration and amyotrophic lateral sclerosis. *Science* *314*, 130–133.
- Nousiainen, H.O., Kestilä, M., Pakkasjärvi, N., Honkala, H., Kuure, S., Tallila, J., Vuopala, K., Ignatius, J., Herva, R., and Peltonen, L. (2008). Mutations in mRNA export mediator GLE1 result in a fetal motoneuron disease. *Nat. Genet.* *40*, 155–157.
- O'Rourke, J.G., Gareau, J.R., Ochaba, J., Song, W., Raskó, T., Reverter, D., Lee, J., Monteys, A.M., Pallos, J., Mee, L., et al. (2013). SUMO-2 and PIAS1 modulate insoluble mutant huntingtin protein accumulation. *Cell Rep.* *4*, 362–375.
- Ochaba, J., Monteys, A.M., O'Rourke, J.G., Reidling, J.C., Steffan, J.S., Davidson, B.L., and Thompson, L.M. (2016). PIAS1 regulates mutant huntingtin accumulation and Huntington's disease-associated phenotypes in vivo. *Neuron* *90*, 507–520.
- Ori, A., Banterle, N., Iskar, M., Andrés-Pons, A., Escher, C., Khanh Bui, H., Sparks, L., Solis-Mezarino, V., Rinner, O., Bork, P., et al. (2013). Cell type-specific nuclear pores: a case in point for context-dependent stoichiometry of molecular machines. *Mol. Syst. Biol.* *9*, 648.
- Pouladi, M.A., Morton, A.J., and Hayden, M.R. (2013). Choosing an animal model for the study of Huntington's disease. *Nat. Rev. Neurosci.* *14*, 708–721.
- Raices, M., and D'Angelo, M.A. (2012). Nuclear pore complex composition: a new regulator of tissue-specific and developmental functions. *Nat. Rev. Mol. Cell Biol.* *13*, 687–699.
- Raices, M., and D'Angelo, M.A. (2017). Nuclear pore complexes and regulation of gene expression. *Curr. Opin. Cell Biol.* *46*, 26–32.
- Ratovitski, T., Arbez, N., Stewart, J.C., Chighladze, E., and Ross, C.A. (2015). PRMT5-mediated symmetric arginine dimethylation is attenuated by mutant huntingtin and is impaired in Huntington's disease (HD). *Cell Cycle* *14*, 1716–1729.
- Rüb, U., Hoche, F., Brunt, E.R., Heinsen, H., Seidel, K., Del Turco, D., Paulson, H.L., Bohl, J., von Gall, C., Vonsattel, J.P., et al. (2013). Degeneration of the cerebellum in Huntington's disease (HD): possible relevance for the clinical picture and potential gateway to pathological mechanisms of the disease process. *Brain Pathol.* *23*, 165–177.
- Ruba, A., and Yang, W. (2016). O-GlcNAc-ylation in the nuclear pore complex. *Cell. Mol. Bioeng.* *9*, 227–233.
- Saudou, F., Finkbeiner, S., Devys, D., and Greenberg, M.E. (1998). Huntingtin acts in the nucleus to induce apoptosis but death does not correlate with the formation of intranuclear inclusions. *Cell* *95*, 55–66.
- Savas, J.N., Toyama, B.H., Xu, T., Yates, J.R., 3rd, and Hetzer, M.W. (2012). Extremely long-lived nuclear pore proteins in the rat brain. *Science* *335*, 942.
- Schachtrup, C., Ryu, J.K., Mammadzada, K., Khan, A.S., Carlton, P.M., Perez, A., Christian, F., Le Moan, N., Vagena, E., Baeza-Raja, B., et al. (2015). Nuclear pore complex remodeling by p75(NTR) cleavage controls TGF- β signaling and astrocyte functions. *Nat. Neurosci.* *18*, 1077–1080.
- Schilling, G., Savonenko, A.V., Klevytska, A., Morton, J.L., Tucker, S.M., Poirier, M., Gale, A., Chan, N., Gonzales, V., Slunt, H.H., et al. (2004). Nuclear-targeting of mutant huntingtin fragments produces Huntington's disease-like phenotypes in transgenic mice. *Hum. Mol. Genet.* *13*, 1599–1610.
- Shi, K.Y., Mori, E., Nizami, Z.F., Lin, Y., Kato, M., Xiang, S., Wu, L.C., Ding, M., Yu, Y., Gall, J.G., and McKnight, S.L. (2017). Toxic PRn poly-dipeptides encoded by the C9orf72 repeat expansion block nuclear import and export. *Proc. Natl. Acad. Sci. USA* *114*, E1111–E1117.
- Sontag, E.M., Lotz, G.P., Yang, G., Sontag, C.J., Cummings, B.J., Glabe, C.G., Muchowski, P.J., and Thompson, L.M. (2012). Detection of mutant huntingtin aggregation conformers and modulation of SDS-soluble fibrillar oligomers by small molecules. *J. Huntingtons Dis.* *1*, 119–132.
- Suhr, S.T., Senut, M.C., Whitelegge, J.P., Faull, K.F., Cuizon, D.B., and Gage, F.H. (2001). Identities of sequestered proteins in aggregates from cells with induced polyglutamine expression. *J. Cell Biol.* *153*, 283–294.
- Toyama, B.H., Savas, J.N., Park, S.K., Harris, M.S., Ingolia, N.T., Yates, J.R., 3rd, and Hetzer, M.W. (2013). Identification of long-lived proteins reveals exceptional stability of essential cellular structures. *Cell* *154*, 971–982.
- Vonsattel, J.P., and DiFiglia, M. (1998). Huntington disease. *J. Neuropathol. Exp. Neurol.* *57*, 369–384.
- Wanker, E.E., Scherzinger, E., Heiser, V., Sittler, A., Eickhoff, H., and Lehrach, H. (1999). Membrane filter assay for detection of amyloid-like polyglutamine-containing protein aggregates. *Methods Enzymol.* *309*, 375–386.
- Watkin, E.E., Arbez, N., Waldron-Roby, E., O'Meally, R., Ratovitski, T., Cole, R.N., and Ross, C.A. (2014). Phosphorylation of mutant huntingtin at serine 116 modulates neuronal toxicity. *PLoS ONE* *9*, e88284.
- Wente, S.R., and Rout, M.P. (2010). The nuclear pore complex and nuclear transport. *Cold Spring Harb. Perspect. Biol.* *2*, a000562.
- Woerner, A.C., Frottin, F., Hornburg, D., Feng, L.R., Meissner, F., Patra, M., Tatzelt, J., Mann, M., Winklhofer, K.F., Hartl, F.U., and Hipp, M.S. (2016). Cytoplasmic protein aggregates interfere with nucleocytoplasmic transport of protein and RNA. *Science* *351*, 173–176.
- Yamada, T., Yoshiyama, Y., and Kawaguchi, N. (1997). Expression of activating transcription factor-2 (ATF-2), one of the cyclic AMP response element (CRE) binding proteins, in Alzheimer disease and non-neurological brain tissues. *Brain Res.* *749*, 329–334.
- Yuzwa, S.A., Shan, X., Macauley, M.S., Clark, T., Skorobogatko, Y., Vosseller, K., and Vocadlo, D.J. (2012). Increasing O-GlcNAc slows neurodegeneration and stabilizes tau against aggregation. *Nat. Chem. Biol.* *8*, 393–399.
- Yuzwa, S.A., Shan, X., Jones, B.A., Zhao, G., Woodward, M.L., Li, X., Zhu, Y., McEachern, E.J., Silverman, M.A., Watson, N.V., et al. (2014). Pharmacological inhibition of O-GlcNAcase (OGA) prevents cognitive decline and amyloid plaque formation in bigenic tau/APP mutant mice. *Mol. Neurodegener.* *9*, 42.
- Zachara, N.E., and Hart, G.W. (2006). Cell signaling, the essential role of O-GlcNAc. *Biochim. Biophys. Acta* *1761*, 599–617.
- Zhang, K., Donnelly, C.J., Haeusler, A.R., Grima, J.C., Machamer, J.B., Steinwald, P., Daley, E.L., Miller, S.J., Cunningham, K.M., Vidensky, S., et al. (2015). The C9orf72 repeat expansion disrupts nucleocytoplasmic transport. *Nature* *525*, 56–61.
- Zhang, Y.J., Gendron, T.F., Grima, J.C., Sasaguri, H., Jansen-West, K., Xu, Y.F., Katzman, R.B., Gass, J., Murray, M.E., Shinohara, M., et al. (2016). C9ORF72 poly(GA) aggregates sequester and impair HR23 and nucleocytoplasmic transport proteins. *Nat. Neurosci.* *19*, 668–677.
- Zhu, Y., Liu, T.W., Madden, Z., Yuzwa, S.A., Murray, K., Cecioni, S., Zachara, N., and Vocadlo, D.J. (2016). Post-translational O-GlcNAcylation is essential for nuclear pore integrity and maintenance of the pore selectivity filter. *J. Mol. Cell Biol.* *8*, 2–16.

De Novo Coding Variants Are Strongly Associated with Tourette Disorder

A. Jeremy Willsey,^{1,2,12} Thomas V. Fernandez,^{3,12} Dongmei Yu,^{4,5,13} Robert A. King,^{3,13} Andrea Dietrich,^{6,13} Jinchuan Xing,^{7,13} Stephan J. Sanders,¹ Jeffrey D. Mandell,^{1,2} Alden Y. Huang,^{8,9} Petra Richer,^{3,10} Louw Smith,¹ Shan Dong,¹ Kaitlin E. Samocha,^{4,5} Tourette International Collaborative Genetics (TIC Genetics), Tourette Syndrome Association International Consortium for Genetics (TSAICG), Benjamin M. Neale,^{4,5} Giovanni Coppola,^{8,9} Carol A. Mathews,^{11,14} Jay A. Tischfield,^{7,14} Jeremiah M. Scharf,^{4,5,14,*} Matthew W. State,^{1,14,15,*} and Gary A. Heiman^{7,14,*}

¹Department of Psychiatry, UCSF Weill Institute for Neurosciences, University of California San Francisco, San Francisco, CA 94143, USA

²Institute for Neurodegenerative Diseases, UCSF Weill Institute for Neurosciences, University of California San Francisco, San Francisco, CA 94143, USA

³Yale Child Study Center and Department of Psychiatry, Yale University School of Medicine, New Haven, CT 06520, USA

⁴Center for Genomic Medicine, Department of Neurology, Massachusetts General Hospital, Harvard Medical School, Boston, MA 02114, USA

⁵Psychiatric and Neurodevelopmental Genetics Unit, Department of Psychiatry, Massachusetts General Hospital, Harvard Medical School, Boston, MA 02114, USA

⁶University of Groningen, University Medical Center Groningen, Department of Child and Adolescent Psychiatry, 9713GZ Groningen, the Netherlands

⁷Rutgers, the State University of New Jersey, Department of Genetics and the Human Genetics Institute of New Jersey, Piscataway, NJ 08854, USA

⁸Department of Neurology, University of California Los Angeles, Los Angeles, California, CA 90095, USA

⁹Department of Psychiatry and Biobehavioral Sciences, University of California Los Angeles, Los Angeles, CA 90095, USA

¹⁰Sewanee: The University of the South, Sewanee, TN 37383, USA

¹¹Department of Psychiatry, University of Florida School of Medicine, Gainesville, FL 32611, USA

¹²These authors contributed equally

¹³These authors contributed equally

¹⁴Senior author

¹⁵Lead Contact

*Correspondence: jscharf@partners.org (J.M.S.), matthew.state@ucsf.edu (M.W.S.), heiman@dls.rutgers.edu (G.A.H.)
<http://dx.doi.org/10.1016/j.neuron.2017.04.024>

SUMMARY

Whole-exome sequencing (WES) and de novo variant detection have proven a powerful approach to gene discovery in complex neurodevelopmental disorders. We have completed WES of 325 Tourette disorder trios from the Tourette International Collaborative Genetics cohort and a replication sample of 186 trios from the Tourette Syndrome Association International Consortium on Genetics (511 total). We observe strong and consistent evidence for the contribution of de novo likely gene-disrupting (LGD) variants (rate ratio [RR] 2.32, $p = 0.002$). Additionally, de novo damaging variants (LGD and probably damaging missense) are over-represented in probands (RR 1.37, $p = 0.003$). We identify four likely risk genes with multiple de novo damaging variants in unrelated probands: *WWC1* (WW and C2 domain containing 1), *CELSR3* (Cadherin EGF LAG seven-pass G-type receptor 3), *NIPBL* (Nipped-B-like), and *FN1* (fibronectin 1). Overall, we estimate that de novo damaging vari-

ants in approximately 400 genes contribute risk in 12% of clinical cases.

INTRODUCTION

Tourette disorder (TD) is an often-disabling developmental neuropsychiatric syndrome characterized by persistent motor and vocal tics. Onset is typically in early childhood, and estimates of the worldwide prevalence are between 0.3% and 1% (Centers for Disease Control and Prevention, 2009; Robertson, 2008; Scharf et al., 2015). The vast majority of children and adults who present for medical attention have other impairing co-occurring psychiatric disorders, including obsessive-compulsive disorder (OCD) (do Rosário and Miguel Filho, 1997; Ghanizadeh and Mosallaei, 2009; Hounie et al., 2006), attention-deficit/hyperactivity disorder (ADHD) (Burd et al., 2005; Leckman, 2003; Roessner et al., 2007), and mood and anxiety disorders (Cavanna et al., 2009; Hirschtritt et al., 2015). Rates of OCD-like conditions, such as trichotillomania and pathologic skin picking (Lochner et al., 2005), are likewise elevated.

Current treatments for tics and TD have limited efficacy and pharmacotherapies may carry significant long-term adverse effects. A fundamental obstacle to identifying novel therapeutic

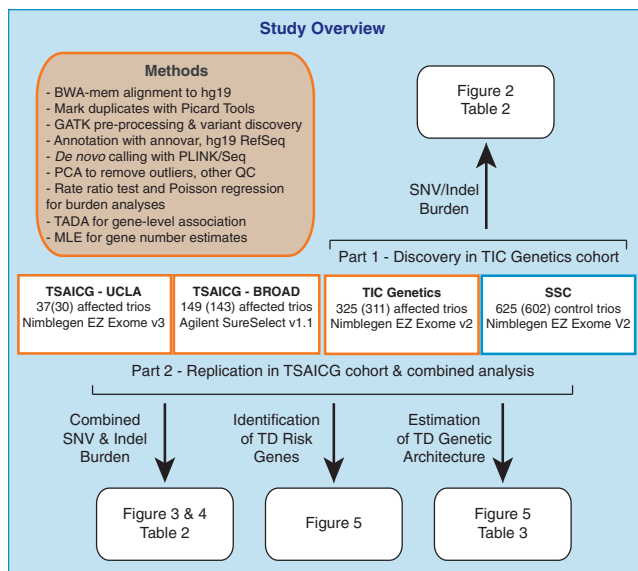


Figure 1. Study Overview

Using WES, we assessed the burden of de novo variants in Tourette disorder (TD) in the Tourette International Collaborative Genetics group (TIC Genetics; <http://tic-genetics.org>) and the Tourette Syndrome Association International Collaboration for Genetics (TSAICG; <https://www.findtsgene.org/>) cohorts. We performed an initial analysis of de novo single-nucleotide variant (SNV) and insertion-deletion variants (indel) in the TIC Genetics cohort ($n = 325$, 311 in parentheses passed quality control [QC]). This was followed by replication in the TSAICG cohort ($n = 186$, 173 passed QC: 143 of 149 samples sequenced at the Broad Institute and 30 of 37 samples sequenced at UCLA) and then a combined analysis ($n = 484$ trios). We obtained control trios, consisting of unaffected parents and unaffected sibling controls, from the Simons Simplex Collection (SSC; $n = 625$, 602 passed QC). In this figure, affected cohorts are outlined in an orange box and control trios in blue. After assessing the contribution of de novo variants to TD risk, we assessed the number of TD genes that contribute to TD risk via damaging de novo variants (likely gene disrupting, a.k.a. LGD, and probably damaging missense, a.k.a. missense 3 or Mis3). We then utilized the TADA algorithm (He et al., 2013) to identify TD risk genes based on per-gene burden of de novo variants. Finally, we predicted the gene discovery yield as additional TD trios are sequenced. See Table S1 for detailed sample- and cohort-level information, Table S2 for a list of annotated de novo variants, and Table S4 for TADA gene association p and q values.

targets is a limited understanding of underlying pathophysiology. There is widespread agreement that genetics plays a significant role in TD etiology based on twin and family studies (Browne et al., 2015; Mataix-Cols et al., 2015; Pauls et al., 1981, 1991; Price et al., 1985). To date, non-parametric linkage analyses (The Tourette Syndrome Association International Consortium for Genetics, 1999, 2007) and a genome-wide association study (Scharf et al., 2013) have not yet led to reproducible, statistically significant findings. Studies of rare pedigrees have identified putative risk genes expressed in the developing striatum and mediating neurite outgrowth (Abelson et al., 2005; Stillman et al., 2009) or involved in histaminergic neurotransmission (Ercan-Sencicek et al., 2010), signal transduction and cell adhesion (Lawson-Yuen et al., 2008; Verkerk et al., 2003), or serotonin transport (Moya et al., 2013). None of these findings can yet be considered definitive.

Our group and others have reported on copy number variations (CNVs) in TD (Fernandez et al., 2012; McGrath et al., 2014; Nag et al., 2013; Sundaram et al., 2010), confirming a role for rare structural variants and showing a trend toward enrichment of de novo events. These findings also provide additional support for the involvement of histaminergic neurotransmission, as well as dopaminergic neurotransmission, in the pathogenesis of TD (Ercan-Sencicek et al., 2010; Fernandez et al., 2012) and suggest a potential overlap with CNVs contributing to other neurodevelopmental syndromes (Malhotra and Sebat, 2012).

Studies of de novo sequence variation using whole-exome sequencing (WES) have proven to be a powerful approach to systematic gene discovery in genetically complex neurodevelopmental disorders (NDDs) apart from TD (Bilgüvar et al., 2010; de Ligt et al., 2012; Deciphering Developmental Disorders Study, 2015, 2017; Epi4K Consortium, 2016; Allen et al., 2013; EuroEPINOMICS-RES Consortium et al., 2014; Rauch et al., 2012), particularly autism spectrum disorders (ASDs) (De Rubeis et al., 2014; Dong et al., 2014; Iossifov et al., 2014; Iossifov et al., 2012; Neale et al., 2012; O’Roak et al., 2011, 2012; Sanders et al., 2012, 2015; Willsey et al., 2013). In light of these findings and our previous results suggesting a role for de novo CNVs, we performed WES in 325 (311 after quality control) TD parent-child trios from the Tourette International Collaborative Genetics group (TIC Genetics; <http://tic-genetics.org>) to identify de novo single-nucleotide variants (SNVs) and insertion-deletion variants (indels). We observe significant evidence for the contribution of de novo likely gene-disrupting (LGD) variants (insertion of premature stop codon, frameshift, or canonical splice-site variant) to TD. We then replicate these findings in WES data from 186 parent-child trios (173 after quality control) from the Tourette Syndrome Association International Consortium for Genetics (TSAICG; <https://www.findtsgene.org/>). We also observe evidence for the contribution of de novo damaging variants (LGD and probably damaging missense). Overall, we estimate that 12% of clinical cases will carry a de novo damaging variant mediating TD risk and that approximately 400 genes are vulnerable to these variants. Finally, a combined analysis identifies one high-confidence TD (hcTD) risk gene (false discovery rate [FDR] < 0.1), *WWC1* (WW and C2 domain containing 1), and three additional probable TD (pTD) risk genes (FDR < 0.3) *CELSR3* (Cadherin EGF LAG seven-pass G-type receptor 3), *NIPBL* (Nipped-B-like), and *FN1* (fibronectin 1). See Figure 1 for an overview of this study.

RESULTS

De Novo LGD Variants Are Associated with TD Risk in the TIC Genetics Cohort

We first conducted WES of 325 TIC Genetics trios. Dietrich et al. (2015) have previously described ascertainment and phenotyping of this cohort. We utilized the SeqCap EZ Human Exome v2.0 library kit (Roche NimbleGen) to capture exomes from whole-blood-derived DNA and then sequenced with Illumina HiSeq 2000 technology. In all analyses, we compared TD trios passing quality control to control trios from the Simons Simplex Collection (SSC) (Fischbach and Lord, 2010). The SSC consists of simplex

families: two unaffected parents with a single child affected with autism spectrum disorder (ASD). Approximately 80% of these families also include one or more unaffected siblings. Therefore, our control trios consist of two unaffected parents and an unaffected sibling. We randomly selected 625 control trios from among the 96.9% ($n = 2,438$ of 2,517) of SSC families that had been captured with the same library used for the TIC Genetics cohort and sequenced using Illumina technology. 311 TD trios (311/325, 95.7%) and 602 SSC trios (602/625, 96.3%) passed quality control (Table 1; Table S1). We summarize sequencing metrics in Table 1 and detail all sample- and cohort-level data in Table S1. The distribution of de novo coding variants per individual in the TIC Genetics cohort and in the SSC siblings follow an expected Poisson distribution (Figure S1), as has been observed in other disorders (e.g., Fromer et al., 2014; Homsy et al., 2015; Neale et al., 2012; Sanders et al., 2012; Xu et al., 2012).

We conducted Sanger-sequencing-based validation for all de novo variants predicted in TD probands and observed confirmation rates of 97.2% in the TIC Genetics trios (97.8% for SNVs and 60% for indels). We did not do so in SSC controls, and consequently, for all burden analyses, we compared unconfirmed de novo variants identified using identical methods from both cohorts. For analysis of recurrent mutations in probands, we relied solely on confirmed variants. See Table S2 for detailed annotations of each predicted de novo variant, including validation status.

We compared the rate of de novo mutation per base pair (bp), restricting these analyses to base pairs covered at $\geq 20\times$ in all members of a trio (our minimum criteria for de novo calling; Sanders et al., 2012). We calculated the rate per base pair as the total number of variants observed within this target region. More specifically, for the overall (coding plus non-coding) mutation rate (e.g., Table 2), this encompassed the exome capture array intervals plus the 100 bp of interval padding added during GATK processing (denoted as “total callable” in Table 1). For coding mutation rate (e.g., Table 2; Figures 2A, 2B, 3A, and 3B), this encompassed the intersection of these intervals with the coding portion of the exome based on RefSeq hg19 gene definitions (“total callable exome” in Table 1). This strategy normalizes for differences in capture array design and coverage distribution across the exome.

We calculated the mutation rate per base pair for each individual. For Figures 2 and 3, we plotted the mean of these rates by cohort, along with the 95% confidence intervals (see also Table 2). To estimate rate ratios and p values, we utilized a one-sided rate ratio test, comparing the number of variants per the number of callable base pairs assessed (Table S3).

Based on consistent observations in other NDDs and our TD CNV analyses, we hypothesized that de novo LGD variants would be significantly overrepresented in TD cases versus controls. We confirmed this expectation, with de novo LGD variants showing a significantly elevated rate ratio in TD probands (rate ratio [RR] 2.14, 95% CI 1.28–3.61, $p = 0.006$; Figure 2A; Table 2). De novo missense (Mis) variants, particularly those predicted to be damaging by PolyPhen2 (Missense 3 or Mis3; PolyPhen2 [HumDiv] score ≥ 0.957 ; Adzhubei et al., 2010, 2013), are also enriched in probands (RR 1.27, 95% CI 1.03–1.57, $p = 0.03$; Figure 2A). As a group, therefore, damaging de novo variants (Mis3

and LGD variants) occur at a significantly higher rate in coding regions in TD probands versus SSC controls (RR 1.38, 95% CI 1.14–1.67, $p = 0.003$). No differences were seen in the rate of de novo synonymous variants (RR 0.91, 95% CI 0.70–1.17, $p = 0.8$) nor in the rate of in-frame indels (RR 0.45, 95% CI 0.019–3.48, $p = 0.9$). A one-sided binomial exact test, which is typically used in WES studies to assess the significance of observed burden differences in cases versus controls (e.g., Iossifov et al., 2014; Sanders et al., 2012; Willsey et al., 2013), produced consistent results (Figure S2). Indeed, these results more strongly support the association of de novo variants with TD. However, as the distribution of callable base pairs per sample varied across the cohorts due to differences in experimental design (e.g., library capture protocol or sequencing coverage; Table 1; Figure S3), we felt the rate ratio test would provide a more accurate estimate of the significance of true variant burden. This approach compares the number of variants while also controlling for the per sample differences in the number of base pairs with sufficient coverage and quality for de novo detection.

We also estimated the theoretical number of variants per individual (exome) based on the total size of RefSeq hg19 coding intervals (33,828,798 bp); this is shown as a second axis on the same plots (Figures 2A and 2B). We reasoned this would provide a second and potentially more accurate comparison metric versus the rate of observed de novo variants per individual because the callable exome differed by cohort (Figure S3). The theoretical rate also has the advantage of providing an estimate of the total number of expected de novo variants under 100% coverage, as opposed to the number of observed variants per individual, and is therefore a useful metric for comparing across sequencing studies.

Analysis of the TSAICG Cohort Replicates Association of De Novo Likely Gene-Disrupting Variants

We next evaluated 186 TD trios ascertained through the Tourette Syndrome Association International Consortium for Genetics (TSAICG). Scharf et al. (2013) have previously described the ascertainment and phenotyping of this cohort. We compared the 173/186 (93.0%) trios passing our quality control metrics (Table S1) to the same set of 602 SSC control trios (Table 2; Figures 3A and 3B). Within the TSAICG cohort, we attempted validation on only a subset of de novo variants based on their validation likelihood (De Rubeis et al., 2014). Within the variants from the TSAICG cohort prioritized for validation, 94.3% of de novo variants confirmed, with 96.4% of SNVs and 60% of indels confirmed (Table S2). Again, all burden analyses were based on unconfirmed de novo variants in both TD and control cohorts. The distribution of de novo coding variants per individual in the TSAICG also follows an expected Poisson distribution (Figure S1).

This analysis replicates the association of de novo LGD variants with TD (RR 1.97, 95% CI 1.03–3.68, $p = 0.04$, one-sided rate ratio test; Figure 3A; Table 2). Again, neither synonymous de novo variants (RR 1.10, 95% CI 0.81–1.47, $p = 0.3$) nor de novo in-frame indels (RR 1.67, 95% CI 0.22–8.97, $p = 0.4$) showed any differences between TD and controls.

There is a male:female sex bias in both the TIC Genetics (3.64; Table 1) and TSAICG (4.97) cohorts but not in the SSC sibling trios

Table 1. Cohort-Level Information, Quality Control, and Sequencing Metrics

| Cohort | TIC Genetics | TSAICG–Broad | TSAICG–UCLA | SSC Siblings |
|--------------------------------------------------|--------------------------|-------------------------|--------------------------|--------------------------|
| Samples sequenced (trios) | 975 (325) | 447 (149) | 111 (37) | 1,875 (625) |
| Samples passing QC (trios) ^a | 933 (311) | 429 (143) | 90 (30) | 1,806 (602) |
| Male:Female (sex ratio) ^b | 244:67 (3.64) | 115:28 (4.11) | 29:1 (29.0) | 275:327 (0.84) |
| Paternal age ^c | 32.83 (±0.61) | 33.29 (±0.81) | 31.25 (±2.20) | 32.99 (±0.47) |
| Exome capture platform | Nimblegen EZ Exome V2 | Agilent SureSelect v1.1 | Nimblegen EZ Exome V3 | Nimblegen EZ Exome V2 |
| Size of capture region | 44,001,748 bp | 32,760,120 bp | 63,564,965 bp | 44,001,748 bp |
| RefSeq hg19 coding region covered ^d | 32,586,393 bp | 31,844,591 bp | 33,644,238 bp | 32,586,393 bp |
| % Refseq hg19 coding region covered | 96.33% | 94.13% | 99.45% | 96.33% |
| Mean callable exome (million bp) | 27.52 (±0.66) | 26.84 (±1.11) | 27.09 (±3.63) | 25.80 (±1.06) |
| Total callable exome (million bp) | 8,560.01 | 3,838.13 | 812.71 | 15,529.00 |
| Total callable exome + other (million bp) | 17,108.37 | 6,549.29 | 2,089.62 | 28,584.79 |
| Mean total reads per sample (million) | 99.03 (±1.42) | 86.45 (±2.68) | 105.17 (±3.71) | 111.33 (±1.89) |
| Mean read length | 76 (±0) | 75.98 (±0.004) | 100 (±0) | 77.64 (±0.71) |
| Passing unique aligned reads (million) | 93.64 (±1.33) | 73.40 (±2.04) | 86.17 (±3.04) | 102.43 (±1.64) |
| % passing, unique reads aligned | 99.76% (±0.01%) | 98.70% (±0.03%) | 99.68% (±0.03%) | 98.95% (±0.12%) |
| Number of bases in target (million) ^e | 2,748.94 (±39.20) | 2,505.88 (±66.45) | 1,964.89 (±67.91) | 2,256.09 (±41.76) |
| % Duplicate reads | 5.17% (±0.07%) | 13.19% (±0.35%) | 17.52% (±1.39%) | 6.46% (±0.20%) |
| Mean coverage in target ^e | 80.79 (±1.15) | 73.65 (±1.95) | 57.75 (±2.00) | 66.31 (±1.23) |
| Median coverage in target ^e | 67.72 (±1.00) | 62.41 (±1.68) | 46.19 (±1.60) | 55.73 (±1.05) |
| % target at 2× ^e | 94.89% (±0.05%) | 92.53% (±0.03%) | 96.49% (±0.07%) | 94.76% (±0.07%) |
| % target at 10× ^e | 90.20% (±0.13%) | 87.72% (±0.14%) | 92.38% (±0.25%) | 88.34% (±0.13%) |
| % target at 20× ^e | 83.76% (±0.22%) | 81.57% (±0.31%) | 84.72% (±0.95%) | 79.51% (±0.30%) |
| % target at 40× ^e | 68.77% (±0.40%) | 66.41% (±0.81%) | 57.97% (±1.97%) | 59.37% (±0.63%) |
| Fold 80 vase penalty | 3.27 (±0.03) | 3.29 (±0.01) | 2.37 (±0.02) | 3.65 (±0.37) |
| Het SNP quality | 10.97 (±0.04) | 9.27 (±0.05) | 12.68 (±0.10) | 11.08 (±0.04) |
| Base pair error rate | 0.0034 (±0.0001) | 0.0043 (±0.0001) | 0.0043 (±0.0001) | 0.0044 (±0.0001) |
| Novel transition/transversion ratio | 2.01 (±0.02) | 2.30 (±0.02) | 2.23 (±0.05) | 2.13 (±0.01) |
| Novel insertion/deletion ratio | 0.51 (±0.01) | 0.31 (±0.02) | 0.52 (±0.03) | 0.42 (±0.01) |

We sequenced two Tourette disorder (TD) cohorts in this study: TIC Genetics and TSAICG. Two different locations sequenced the TSAICG—the Broad Institute and UCLA. We compared these cohorts to control trios from the Simons Simplex Collection (SSC). Three different library kits captured exomes with different target sizes and, therefore, varying coverage of RegSeq hg19 coding regions. Mean and median coverage differed across the cohorts. To control for these factors, we determined the number of “callable” bp, or the number of bp in each family that have $\geq 20\times$ coverage in all family members. We summed these lengths across all families within a given cohort to determine the “total callable” bp. We then intersected these coordinates with RefSeq hg19 coding exons to determine the “total callable exome,” or the number of bp within RefSeq coding exons that had sufficient coverage for de novo calling. Picard Tools (<https://broadinstitute.github.io/picard/>) generated capture, sequencing, alignment, and variant level quality metrics, and GATK DepthOfCoverage generated coverage metrics for the exome intervals. We remove samples with excess de novo variants (>5). A panel of informative genotypes confirmed familiarity, and trios were removed if expected family relationships did not confirm or if there were unexpected relationships within or across families. If any family member failed QC, we removed all family members from the analysis. Principal-component analysis (PCA) revealed outliers, which we removed from analysis (Figure S4). Where applicable, sequencing metrics include $\pm 95\%$ confidence intervals. We provide quality control information and detailed sequencing metrics for all subjects in Table S1.

^aSequencing metrics and statistics summarized in this table are from samples passing QC only

^bCalculated from children only. Mutation rates were not significantly different between males and females in the TIC Genetics ($p = 0.4$, two-sided rate ratio test, STAR Methods), combined TSAICG ($p = 0.9$), or SSC siblings cohorts ($p = 0.3$). See also Table S1

^cCalculated from parents only

^dSize determined from intersection of exome capture array intervals plus 100 bp interval padding (added during GATK processing) with RefSeq hg19 coding intervals

^eTarget refers to entire Refseq hg19 coding regions (33,828,798 bp)

(0.84); however, mutation rates were not significantly different between males and females in the TIC Genetics ($p = 0.4$, two-sided rate ratio test; Table S1), TSAICG ($p = 0.9$), or SSC siblings ($p = 0.3$) cohorts. Therefore, despite the differences in sex ratio, the direc-

tion of effect suggests that, if anything, there is a slightly higher rate of de novo variants in females, and therefore, a male-biased TD cohort and a non-male-biased control cohort should result in conservative burden estimates.

Table 2. Distribution of De Novo SNVs and Indels in TD Cases and Controls

| Variant Type | Total # Variants | Mean Rate per bp ($\times 10^{-6}$) ($\pm 95\%$ CI) | Theoretical Rate per Individual ($\pm 95\%$ CI) | Rate Ratio ($\pm 95\%$ CI) | p value | | | |
|------------------------------|------------------|--------------------------------------------------------|--------------------------------------------------|-----------------------------|------------------------|-------------------------|-------------------|-----------|
| Cohort | | | | | | | | |
| TIC Genetics | | | | | | | | |
| | TIC Gen | Control | TIC Gen | Control | | | | |
| | (n = 311) | (n = 602) | (n = 311) | (n = 602) | | | | |
| All | 525 | 862 | 1.53 (1.41–1.65) | 1.50 (1.40–1.60) | N/A ^c | 1.02 (0.93–1.12) | p = 0.4 | |
| Coding | 301 ^a | 484 ^b | 1.75 (1.56–1.95) | 1.56 (1.42–1.70) | 1.19 (1.06–1.32) | 1.05 (0.96–1.15) | 1.13 (1.00–1.28) | p = 0.05 |
| Synonymous | 67 | 134 | 0.39 (0.30–0.49) | 0.43 (0.36–0.50) | 0.27 (0.20–0.33) | 0.29 (0.24–0.34) | 0.91 (0.70–1.17) | p = 0.8 |
| Nonsynonymous | 233 | 343 | 1.36 (1.18–1.53) | 1.10 (0.99–1.22) | 0.92 (0.8–1.03) | 0.75 (0.67–0.83) | 1.23 (1.07–1.42) | p = 0.008 |
| Missense (Mis) | 207 | 321 | 1.21 (1.04–1.37) | 1.03 (0.92–1.15) | 0.82 (0.70–0.93) | 0.70 (0.62–0.78) | 1.17 (1.01–1.36) | p = 0.04 |
| Missense 3 (Mis3) | 111 | 158 | 0.65 (0.53–0.77) | 0.51 (0.43–0.59) | 0.44 (0.36–0.52) | 0.34 (0.29–0.40) | 1.27 (1.03–1.57) | p = 0.03 |
| Likely Gene Disrupting (LGD) | 26 | 22 | 0.15 (0.092–0.21) | 0.071 (0.042–0.10) | 0.10 (0.062–0.14) | 0.048 (0.028–0.068) | 2.14 (1.28–3.61) | p = 0.006 |
| Damaging (LGD + Mis3) | 137 | 180 | 0.80 (0.67–0.93) | 0.58 (0.49–0.67) | 0.54 (0.45–0.63) | 0.39 (0.33–0.45) | 1.38 (1.14–1.67) | p = 0.003 |
| LGD SNV | 16 | 19 | 0.092 (0.048–0.14) | 0.061 (0.034–0.088) | 0.063 (0.033–0.093) | 0.041 (0.023–0.060) | 1.53 (0.82–2.82) | p = 0.1 |
| LGD FS Indel | 10 | 3 | 0.058 (0.022–0.093) | 0.0095 (–0.0013–0.020) | 0.039 (0.015–0.063) | 0.0064 (–0.00086–0.014) | 6.05 (1.85–25.65) | p = 0.003 |
| In-Frame Indel | 1 | 4 | 0.0058 (–0.0056–0.017) | 0.012 (0.00022–0.024) | 0.0039 (–0.0038–0.012) | 0.0081 (0.00015–0.016) | 0.45 (0.02–3.48) | p = 0.9 |
| Cohort | | | | | | | | |
| TSAICG | | | | | | | | |
| | TSAICG | Control | TSAICG | Control | | | | |
| | (n = 173) | (n = 602) | (n = 173) | (n = 602) | | | | |
| All | 258 | 862 | 1.49 (1.31–1.67) | 1.50 (1.40–1.60) | N/A ^c | N/A ^c | 0.99 (0.88–1.11) | p = 0.6 |
| Coding | 153 | 484 ^b | 1.64 (1.39–1.9) | 1.56 (1.42–1.70) | 1.11 (0.94–1.29) | 1.05 (0.96–1.15) | 1.06 (0.90–1.23) | p = 0.3 |
| Synonymous | 44 | 134 | 0.47 (0.34–0.61) | 0.43 (0.36–0.50) | 0.32 (0.23–0.41) | 0.29 (0.24–0.34) | 1.10 (0.81–1.47) | p = 0.3 |
| Nonsynonymous | 109 | 343 | 1.17 (0.95–1.39) | 1.10 (0.99–1.22) | 0.79 (0.64–0.94) | 0.75 (0.67–0.83) | 1.06 (0.88–1.28) | p = 0.3 |
| Missense (Mis) | 96 | 321 | 1.03 (0.82–1.24) | 1.03 (0.92–1.15) | 0.70 (0.56–0.84) | 0.70 (0.62–0.78) | 1.00 (0.82–1.21) | p = 0.5 |
| Missense 3 (Mis3) | 49 | 158 | 0.53 (0.36–0.70) | 0.51 (0.43–0.59) | 0.36 (0.25–0.47) | 0.34 (0.29–0.40) | 1.04 (0.78–1.37) | p = 0.4 |
| Likely Gene Disrupting (LGD) | 13 | 22 | 0.14 (0.059–0.21) | 0.071 (0.042–0.10) | 0.092 (0.040–0.14) | 0.048 (0.028–0.068) | 1.97 (1.03–3.68) | p = 0.04 |
| Damaging (LGD + Mis3) | 62 | 180 | 0.67 (0.49–0.84) | 0.58 (0.49–0.67) | 0.45 (0.33–0.57) | 0.39 (0.33–0.45) | 1.15 (0.89–1.48) | p = 0.2 |
| LGD SNV | 8 | 19 | 0.083 (0.026–0.14) | 0.061 (0.034–0.088) | 0.056 (0.018–0.094) | 0.041 (0.023–0.060) | 1.41 (0.62–2.98) | p = 0.3 |
| LGD FS Indel | 5 | 3 | 0.053 (0.0068–0.10) | 0.0095 (–0.0013–0.020) | 0.036 (0.0046–0.068) | 0.0064 (–0.00086–0.014) | 5.56 (1.36–26.71) | p = 0.02 |
| In-Frame Indel | 2 | 4 | 0.021 (–0.0081–0.050) | 0.012 (0.00022–0.024) | 0.014 (–0.0055–0.034) | 0.0081 (0.00015–0.016) | 1.67 (0.22–8.97) | p = 0.4 |
| Cohort | | | | | | | | |
| Combined | | | | | | | | |
| | TD | Control | TD | Control | | | | |
| | (n = 484) | (n = 602) | (n = 484) | (n = 602) | | | | |
| All | 783 | 862 | 1.52 (1.42–1.62) | 1.51 (1.40–1.60) | N/A ^c | N/A ^c | 1.01 (0.93–1.10) | p = 0.4 |
| Coding | 454 ^d | 484 ^b | 1.72 (1.56–1.87) | 1.56 (1.42–1.70) | 1.16 (1.06–1.26) | 1.05 (0.96–1.15) | 1.10 (0.99–1.23) | p = 0.07 |
| Synonymous | 111 | 134 | 0.42 (0.35–0.50) | 0.43 (0.36–0.50) | 0.29 (0.23–0.34) | 0.29 (0.24–0.34) | 0.97 (0.78–1.21) | p = 0.6 |
| Nonsynonymous | 342 | 343 | 1.29 (1.15–1.43) | 1.10 (0.99–1.22) | 0.87 (0.78–0.96) | 0.75 (0.67–0.83) | 1.17 (1.03–1.33) | p = 0.02 |

(Continued on next page)

Table 2. Continued

| Variant Type | Total # Variants | Mean Rate per bp ($\times 10^{-6}$) ($\pm 95\%$ CI) | Theoretical Rate per Individual ($\pm 95\%$ CI) | Rate Ratio ($\pm 95\%$ CI) | p value |
|------------------------------|------------------|--------------------------------------------------------|--------------------------------------------------|-----------------------------|-----------|
| Missense (Mis) | 303 | 1.14 (1.01–1.28) | 0.77 (0.69–0.86) | 1.11 (0.97–1.27) | p = 0.1 |
| Missense 3 (Mis3) | 160 | 0.61 (0.51–0.70) | 0.41 (0.34–0.48) | 1.19 (0.98–1.44) | p = 0.07 |
| Likely Gene Disrupting (LGD) | 39 | 0.15 (0.099–0.19) | 0.10 (0.067–0.13) | 2.08 (1.31–3.37) | p = 0.004 |
| Damaging (LGD + Mis3) | 199 | 0.75 (0.65–0.85) | 0.51 (0.44–0.58) | 1.30 (1.09–1.55) | p = 0.006 |
| LGD SNV | 24 | 0.089 (0.054–0.12) | 0.060 (0.037–0.084) | 1.48 (0.86–2.59) | p = 0.1 |
| LGD FS Indel | 15 | 0.056 (0.028–0.084) | 0.038 (0.019–0.057) | 5.88 (1.95–23.82) | p = 0.001 |
| In-Frame Indel | 3 | 0.011 (–0.0015–0.024) | 0.0075 (–0.0010–0.016) | 0.88 (0.17–4.04) | p = 0.7 |

We annotated de novo variants with Anovar according to RefSeq hg19 gene definitions. “Missense 3” are missense variants with a PolyPhen2 (HumDiv) score ≥ 0.957 (probably damaging). “Likely Gene Disrupting (LGD)” are nonsense variants, canonical splice site variants, and frameshift indels. We estimated the per base mutation rates for each class of variant by dividing the number of variants by the total number of callable base pairs (either within coding regions [“callable exome”] or within all regions [“total callable”]; Table 1). We further divided this rate by two in order to account for the diploid genome. We also estimated the theoretical number of each type of coding variant per individual (exome) based on the mutation rates per bp and the total size of all RefSeq hg19 coding intervals (33,828,798 bp). We determined rate ratios by dividing the observed rate per bp in TD probands by the observed rate per bp in the SSC controls and estimated p values with a one-sided rate ratio test. See also Table S3.

^aOne (1) coding variant (301 total) is annotated as “unknown” effect by Anovar and therefore is not present in the synonymous (67) or nonsynonymous (233) counts (total = 300)

^bSeven (7) coding variants (484 total) are annotated as “unknown” effect by Anovar and therefore are not present in the synonymous (134) or nonsynonymous (343) counts (total = 477)

^cWe did not estimate the theoretical rate per individual for all de novo variants, because the size of the total possible target varies by capture array (see Table 1)

^dOne (1) coding variant (454 total) is annotated as “unknown” effect by Anovar and therefore is not present in the synonymous (111) or nonsynonymous (342) counts (total = 453)

Managing Batch Effects across Multiple Cohorts and Array Types

We hypothesized that batch effects might confound the combined analyses due to the use of three different exome capture arrays and sequencing at different centers (Table 1). Indeed, the three cohorts have different coverage distributions (Figure S3) and cluster separately in principal-component analysis (PCA) based on sequencing quality metrics (Figure S4). Likewise, we observed that “naïve” estimates of de novo variant rates were highly divergent across cohorts (Figure S5). However, we did not observe a significant difference in the “normalized” de novo variant rates between TIC Genetics, TSAICG, and the SSC control trios, suggesting that we adequately controlled for these confounds in our analyses.

Nonetheless, to ensure that the observed increases in de novo burden were not due to additional batch effects, we also performed a Poisson regression (Figure 4) to control for other factors potentially influencing de novo variant rate and detection. In iterative univariate multiple regression analyses, we observed that paternal age, sequencing coverage (percent of exome at 2 \times coverage), sequencing coverage uniformity (fold 80 base penalty), heterozygous SNP quality, and the number of de novo synonymous variants provided the best model for de novo nonsynonymous coding variants. We used the size of the callable coding exome as an offset (Table 1; Table S1; Figure S3). The correlation between paternal age and de novo variant rate has been previously observed (e.g., lossifov et al., 2012, 2014; Kong et al., 2012; Neale et al., 2012; O’Roak et al., 2012; Sanders et al., 2012). Sex was not a significant predictor (Table S1). After controlling for these additional covariates in the Poisson multiple regression, de novo LGD variants still remained significantly associated with TD risk (Figure 4; RR 2.20, 95% CI 1.19–4.08, p = 0.01; RR 2.23, 95% CI 1.04–4.82, p = 0.04 in TIC Genetics and TSAICG, respectively). Additionally, de novo damaging variants (LGD + Mis3) showed enrichment in the TIC Genetics cohort (RR 1.38, 95% CI 1.08–1.76, p = 0.009) and a trend toward enrichment in the TSAICG cohort (RR 1.37, 95% CI 0.98–1.92, p = 0.07). Mis3 variants alone were no longer significantly associated in either cohort, although we still observed evidence of modest effects in the TIC Genetics (RR 1.27, 95% CI 0.97–1.65, p = 0.08) cohort.

Combined Analysis Estimates a Rate Ratio of 2.32 for De Novo LGD Variants

Having observed that putatively deleterious de novo variants are overrepresented in both TIC Genetics and TSAICG probands separately, and that the overall rate of de novo mutations was not significantly different by cohort (Figure S5), we combined the TIC Genetics and TSAICG cohorts (484 TD trios) to obtain an overall estimate for de novo variant burden in TD (Figure 4). We observed a significant excess of de novo LGD variants (RR 2.32, 95% CI 1.37–3.93, p = 0.002, Poisson regression) and de novo damaging (LGD + Mis3) variants (RR 1.37, 95% CI 1.11–1.69, p = 0.003). Mis3 variants alone again showed a trend toward enrichment in the combined data (RR 1.24, 95% CI 0.98–1.55, p = 0.07). We observed similar results with the binomial exact and rate ratio tests (Figures 3A and 3B; Table 2; Table S2), as well as a Fisher exact test normalizing for the rate of de novo synonymous variants (Figure S6).

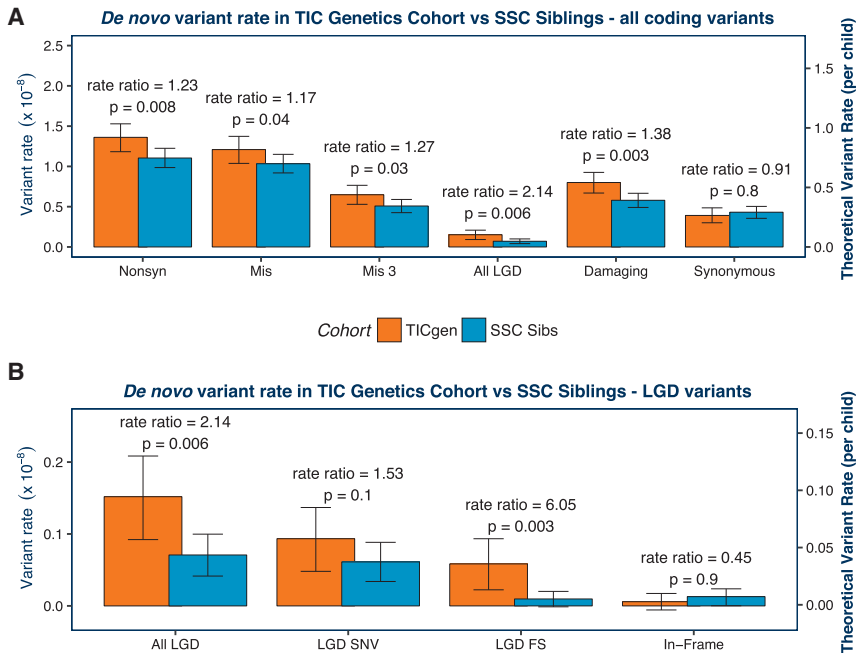


Figure 2. De Novo Variants Are Associated with Risk in the TIC Genetics Cohort

We first compared the rate of de novo mutation per base pair (bp) in the TIC Genetics and SSC cohorts. We determined the “total callable exome” for each TD proband or SSC sibling (Table 1; Table S1). We then calculated the mutation rate per bp for each individual based on the observed number of de novo variants and the size of the callable exome. The mean of these rates ($\pm 95\%$ CI) is plotted by cohort in (A) and (B) (see left y axis; see also Table 2). To estimate rate ratios and p values, we compared the number of mutations observed per the number of callable bp assessed using a one-sided rate ratio test. We estimated the theoretical rate of coding de novo variants per individual by multiplying the variant rate by the size of the “coding” exome (RefSeq hg19 coding exons; 33,828,798 bp). We display this as the right y axis in (A) and (B). We compare the main classes of variants in (A). All classes of de novo non-synonymous variants show a significantly elevated rate ratio in TD probands (orange) versus SSC siblings (blue). As expected, de novo synonymous variants are not significantly overrepresented in TD probands ($p = 0.8$). We compare subclasses of LGD variants in (B). Frameshift (FS) indels trend toward a higher rate ratio (RR) than LGD SNVs (RR 6.0, $p = 0.003$

versus RR 1.5, $p = 0.1$). In-frame indels, which are not expected to have marked biological impact, are not significantly overrepresented in TD probands ($p = 0.9$). A one-sided binomial exact test to assess the significance of the observed burden differences in TD cases versus controls produced consistent results (Figure S2). Mis3, missense variants predicted to be damaging by PolyPhen (Missense 3 or Mis3; PolyPhen2 HumDiv score ≥ 0.957).

De Novo Damaging Variants Contribute to TD Risk in Approximately 12% of Cases

As previously noted, we can estimate the theoretical de novo variant rate per individual (exome) by multiplying the observed rate per base pair by the total size of all RefSeq hg19 coding regions. By subtracting the theoretical rate, per exome, of de novo variants in controls from the theoretical rate in probands, we can then estimate the percentage of probands in whom a de novo variant is contributing to TD risk (Iossifov et al., 2014; Sanders et al., 2015). Based on this calculation, we estimate that 5.0% (95% CI 1.3%–8.7%) of cases have a de novo LGD variant and 11.6% (95% CI 2.4%–20.8%) of cases have a de novo damaging variant contributing to TD risk (Table 3). Similarly, 6.9% (95% CI 4.9%–8.9%) of ASD cases have a de novo LGD variant mediating ASD risk (Sanders et al., 2015).

We can also estimate the fraction of observed proband de novo variants that contribute to TD risk (Iossifov et al., 2014; Sanders et al., 2015) by dividing the difference in theoretical rate by the theoretical rate in probands. Using this approach, we estimate that 51.3% (95% CI 13.7%–89.0%) of de novo LGD and 22.9% (95% CI 4.8%–41.0%) of de novo damaging variants carry TD risk (Table 3). Again, the estimate for de novo LGD variants in TD is similar to that for ASD (45.9%, 95% CI 31.8%–55.5%) (Sanders et al., 2015).

Maximum Likelihood Estimation Predicts that Approximately 400 Genes Contribute TD Risk

We next utilized a maximum likelihood estimation (MLE) procedure to estimate the number of genes contributing risk to TD, based on vulnerability to de novo damaging variants, as

has been done recently in congenital heart disease (Homsy et al., 2015). We observed 192 confirmed damaging de novo variants in 484 TD probands. Therefore, for every possible number of risk genes, from 1 to 2,500, we simulated 192 variants. 50,000 permutations were conducted: in each permutation, we randomly selected risk genes and then, based on the fraction of damaging variants estimated to carry risk, randomly assigned a percentage of variants to the risk genes and the rest of the variants to the non-risk genes. We weighted the probability of variation by gene size and GC content (He et al., 2013). We then determined the combined number of risk and non-risk genes harboring multiple de novo variants and recorded when the number of genes with two variants and the number of genes with three or more variants in the simulated data matched the number observed in our study (4 and 1, respectively). Based on the frequency of these occurrences versus gene number, we determined the MLE of the number of TD risk genes to be 420 genes (Figure 5A). Alternatively, based on methods we have used previously to evaluate target size in ASD (Sanders et al., 2011, 2012), we estimate 447 genes (95% CI 136.7–932.7).

Recurrent De Novo Variants Identify Four Candidate Genes

We next asked whether de novo variants cluster within specific genes. Here we considered only de novo damaging variants that confirmed using Sanger sequencing (Table S2). We chose to focus on de novo damaging variants because both LGD and Mis3 variants showed evidence of TD association. We identified five genes with multiple (two or more) de novo LGD or Mis3 variants. None of these had two de novo LGD variants. Based on our

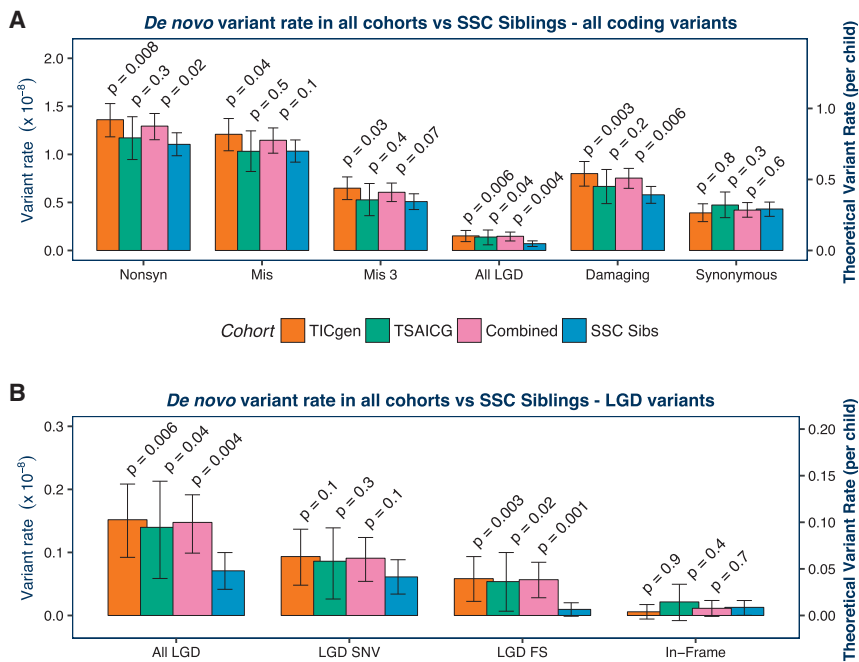


Figure 3. Association of De Novo Variants with TD Is Confirmed in the TSAICG Cohort

We next repeated the analyses in a non-overlapping cohort, ascertained and characterized by the TSAICG. De novo mutation rate per bp and theoretical mutation rate per child ($\pm 95\%$ CI) were calculated as in Figure 2. The TIC Genetics cohort is in orange, TSAICG in green, the “Combined” TD cohort of TIC Genetics and TSAICG in pink, and the SSC control trios in blue. We compared the rate of de novo variants within the total callable exome with a one-sided rate ratio test (see Figure 2; Table 1). (A) As in the TIC Genetics cohort, de novo LGD variants are elevated in TSAICG TD probands ($p = 0.04$). De novo damaging variants as a group (LGD + Mis3) showed a trend toward enrichment in probands ($p = 0.2$). (B) Again, FS indels occur at a substantially elevated rate ($p = 0.02$). Neither synonymous de novo variants ($p = 0.3$; A) nor de novo in-frame indels ($p = 0.4$; B) showed any differences between TD and controls. Finally, we combined the TIC Genetics and TSAICG cohorts to obtain an overall estimate for de novo variant burden in TD (pink bars in A and B). De novo LGD variants are strongly associated with TD risk, occurring 2-fold more frequently in TD probands (RR 2.1, 95% CI 1.3–3.4, $p = 0.004$). De novo damaging variants (LGD + Mis3) are also associated (RR 1.3, 95% CI 1.1–1.5, $p =$

0.006). The distribution of de novo coding variants per individual in the TIC Genetics and TSAICG cohorts, as well as in the SSC siblings, follows an expected Poisson distribution (Figure S1). Mis3, missense variants predicted to be damaging by PolyPhen (Missense 3 or Mis3; PolyPhen2 [HumDiv] score ≥ 0.957).

MLE of 420 risk genes, we estimated the per-gene p and q values for these observations with TADA, using the de novo only algorithm (He et al., 2013). According to previously established q value thresholds (FDR thresholds) (De Rubeis et al., 2014; He et al., 2013; Sanders et al., 2015), one of these genes is a high-confidence TD (hcTD) gene ($q < 0.1$): *WWC1* (WW and C2 domain containing 1); and three of these genes are probable TD (pTD) risk genes ($q < 0.3$): *CELSR3* (Cadherin EGF LAG seven-pass G-type receptor 3), *NIPBL* (Nipped-B-like), and *FN1* (fibronectin 1) (Figure 5B).

Prediction of the Number of Risk Genes Identified by Cohort Size

We also utilized our MLE of the number of genes involved in TD risk to predict the likely future gene discovery yield from WES. We fixed the gene number at 420 and varied the cohort size. Therefore, we calculated the number of variants in each iteration based on the cohort size and the observed variant rate per proband. In each iteration, we randomly selected 420 TD risk genes and then assigned a fraction of the permuted variants to these TD risk genes and the leftover fraction to the remaining non-TD risk genes. This allocation was determined based on the fraction of variants estimated to carry risk. We performed 10,000 permutations at each cohort size, separately randomly generating LGD and Mis3 variants, using their observed rates and per-gene likelihoods. These data were then combined, and each permutation was run through the TADA de novo algorithm to assess the per gene q values. We then recorded the number of pTD genes ($q < 0.3$) and hcTD genes ($q < 0.1$) observed at each cohort size (Figure 5C). Based on the smoothed curves, the predicted

number of probable genes for the cohort presented in this study (484 trios) tracked very closely with our empirical results: we predict 2.8 pTD genes (we observed 3) and 0.69 hcTD genes (we observed 1). Moreover, we can further predict that, at 1,000 trios, we will identify approximately 11.8 pTD genes and 3.2 hcTD genes and, at 2,000 trios, will identify 39.8 pTD genes and 13.4 hcTD genes.

DISCUSSION

Exome sequencing of TD trios establishes the increased rate of de novo LGD variants in cases versus controls. We observe this excess burden in two independently ascertained cohorts: TIC Genetics and TSAICG. We also observe evidence for enrichment of de novo Mis3 variants in TD probands, though statistical significance is not reached in all tests. Sequencing of additional trios is certain to clarify this result. As has been well established in exome studies of other NDDs, these results provide a highly reliable avenue for gene discovery based on the recurrence of damaging de novo mutations. In the current dataset, one gene, *WWC1*, meets the threshold for high-confidence association and three genes meet the threshold for probable association.

The four likely TD genes span a range of biological pathways and functional ontologies and are all clearly brain expressed (Kang et al., 2011; Kapushesky et al., 2012; Petryszak et al., 2014, 2016). Indeed, these genes provide interesting avenues for additional investigations: *WWC1*, also known as *KIBRA* (kidney and brain expressed protein), is a cytoplasmic phosphoprotein that shows evidence of interaction with multiple proteins and pathways (Kremerskothen et al., 2003; Rebhan et al., 1997;

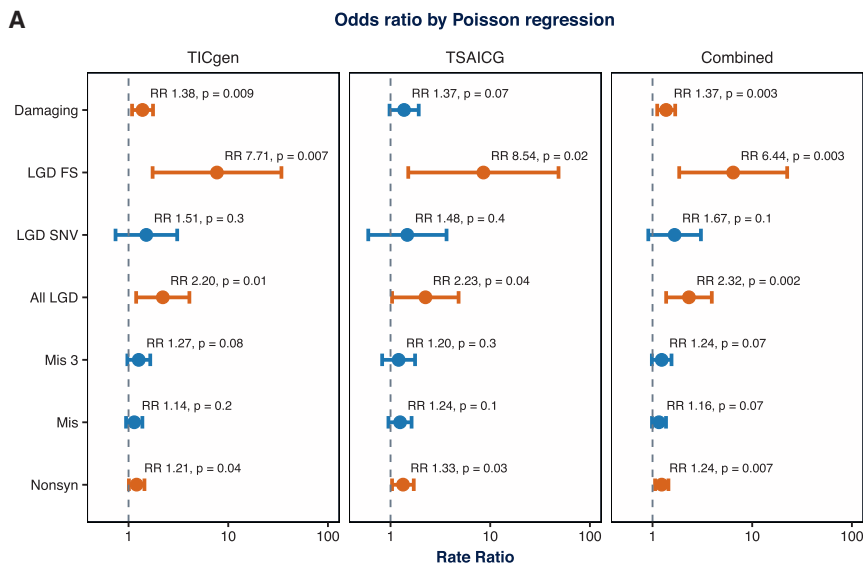


Figure 4. Poisson Regression to Control for Paternal Age and Sequencing Coverage Confirms Association of De Novo LGD Variants

To ensure that the observed differences in burden were not due to additional batch effects (Figures S3–S5), we performed a Poisson regression to control for other factors influencing de novo variant rate and detection. We first confirmed that the distribution of de novo coding variants per individual in the TIC Genetics and TSAICG cohorts, as well as in the SSC siblings, follow an expected Poisson distribution (Figure S1). Next, after several model building steps, we selected paternal age, sequencing coverage (percent of exome at 2× coverage), sequencing coverage uniformity (fold 80 base penalty), heterozygous SNP quality, and the number of de novo synonymous variants as covariates, along with affected status, in the regression analysis (Figure S3). The size of the callable coding exome served as the offset, and the number of de novo variants in a particular class was the response variable. The resulting rate ratios ($\pm 95\%$ CI) are plotted in (A). After controlling for

these covariates, de novo LGD variants remained associated with TD risk in both cohorts, and in the combined cohort we estimate the rate ratio as 2.32 (95% CI 1.37–3.93, $p = 0.002$). Additionally, de novo damaging variants (LGD + Mis3) showed enrichment in the TIC Genetics cohort, a trend toward enrichment in the TSAICG cohort, and are significantly enriched overall with a rate ratio of 1.37 (95% CI 1.11–1.69, $p = 0.003$). Using this approach to analysis, Mis3 variants alone are not significantly associated in either cohort but show a trend toward enrichment in the combined data (rate ratio 1.24, 95% CI 0.98–1.55, $p = 0.07$). Other approaches to correct for batch effects consistently supported an increased burden of de novo LGD and damaging variants in TD probands (see Figures S2 and S6 for details). Mis3, missense variants predicted to be damaging by PolyPhen (Missense 3 or Mis3; PolyPhen2 [HumDiv] score ≥ 0.957).

Zhang et al., 2014). For instance, it may be a transcriptional co-activator of estrogen receptor 1 (*ESR1*), regulate the collagen-stimulated activation of ERK-MAPK cascade, and regulate the Hippo/SWH signaling pathway (Zhang et al., 2014). It has been demonstrated to have roles in cell polarity, migration, and trafficking, as well as learning and memory (Schneider et al., 2010). It is also likely regulated by *PRKCZ* (protein kinase C zeta), a kinase known to play a role in synaptic plasticity and memory formation (Büther et al., 2004).

CELSR3 belongs to the flamingo subfamily of non-classic cadherins, which are defined by non-interaction with catenins and seven transmembrane domains (Feng et al., 2012). The protein encoded by this gene may be involved in the regulation of contact-dependent neurite outgrowth (Chai et al., 2015). In mice, *Celsr3* appears to be critical for axon pathfinding in the central nervous system, with cortico-cortical and cortico-subcortical connections defective in mutant mice (Tissir et al., 2005; Zhou et al., 2008). Moreover, the role of *Celsr3* in steering motor axons innervating the dorsal hindlimb and in the anterior-posterior patterning of monoaminergic neurons has also recently been demonstrated (Chai et al., 2014; Fenstermaker et al., 2010).

NIPBL, also known as *Delangin*, appears to have two critical functions: (1) it is essential for loading the cohesin complex onto sister chromatids during meiosis I and DNA double-stranded break repair (Peters et al., 2008) and (2) it may influence gene expression during development (Zuin et al., 2014). Variants in *NIPBL* are associated with Cornelia de Lange syndrome (CdLS), a developmental disorder characterized by slow growth, moderate to severe intellectual disability, and abnormalities of bones in the arms, hands, and fingers (Brachmann, 1916; De Lange, 1933). Many affected individuals also have behavior

problems, including compulsive repetition, anxiety, OCD, and ADHD (Mulder et al., 2017; Oliver et al., 2008). Given that approximately 60% of CdLS cases have a heterozygous *NIPBL* variant (Mannini et al., 2013), we were surprised to observe variants in this gene in our subjects. However, we only observed Mis3 variants, perhaps suggesting that these variants have less severe consequences. Indeed, cdLS severity is highly correlated to the expression levels of *NIPBL* (Kaur et al., 2016), and the de novo Mis3 variants that we observed were in exons 29 and 47 whereas exon 10 has the greatest proportion of pathogenic CdLS variants (Mannini et al., 2013). In addition, both patients have some phenotypic aspects that are consistent with CdLS: (1) the TIC Genetics proband has failure to thrive in childhood with adult short stature (final height in the fifth percentile for males), generalized anxiety, and irritable bowel, and (2) the TSAICG proband has developmental delay, intellectual disability, and mild hearing loss, although birthweight, height, and weight were within normal limits.

FN1 codes for two types of fibronectin-1 protein: a soluble plasma protein, mainly produced by the liver and involved in blood clotting and wound healing; and an insoluble protein released to the extracellular space, helping with formation of fibrils and the extracellular matrix (Frantz et al., 2010; Pankov and Yamada, 2002; Rebhan et al., 1997). Both types of proteins are involved in cell adhesion, spreading, migration, and differentiation (Frantz et al., 2010; Pankov and Yamada, 2002). It is therefore possible that this gene will be similarly involved in neurite outgrowth or a similar process during brain development. Indeed, homozygous knockout mice display neural tube defects and shortened anterior-posterior axes (George et al., 1993). Variants in *FN1* also appear to be involved in glomerulopathy with

Table 3. Contribution of De Novo SNVs to TD Risk

| Variant Type | Theoretical rate per child ($\pm 95\%$ CI) ^a | | % of cases with mutation mediating risk ($\pm 95\%$ CI) | % of mutations carrying risk ($\pm 95\%$ CI) |
|------------------------------|----------------------------------------------------------|-----------------------|----------------------------------------------------------|-----------------------------------------------|
| | TD (n = 484) | Control (n = 602) | | |
| Likely Gene Disrupting (LGD) | 0.098 (0.067 – 0.13) | 0.048 (0.028 – 0.067) | 5.0% (1.3%–8.7%) | 51.3% (13.7%–89.0%) |
| Damaging (LGD + Mis3) | 0.51 (0.44 – 0.58) | 0.39 (0.33 – 0.45) | 11.6% (2.4%–20.8%) | 22.9% (4.8%–41.0%) |

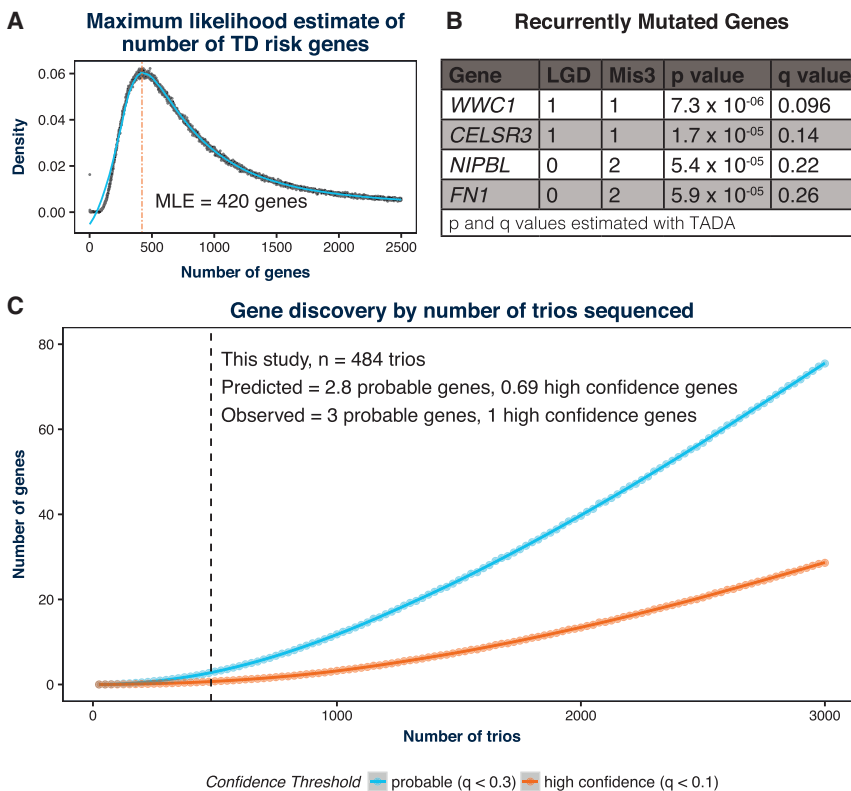
To estimate the percentage of probands in whom a de novo variant is contributing to TD risk, we subtracted the theoretical rate, per exome, of de novo variants in controls from the theoretical rate in probands (Iossifov et al., 2014; Sanders et al., 2015). We predict that 5.0% (95% CI 1.3%–8.7%) of cases have a de novo LGD variant and 11.6% (95% CI 2.4%–20.8%) of cases have a de novo damaging variant contributing TD risk. To estimate the fraction of observed proband de novo variants that contribute to TD risk, we divided the difference in theoretical rate by the theoretical rate in probands (Iossifov et al., 2014; Sanders et al., 2015). Based on this approach, we predict that 51.3% (95% CI 13.7%–89.0%) of de novo LGD and 22.9% (95% CI 4.8%–41.0%) of de novo damaging variants carry TD risk.

^aTheoretical rate per child was calculated per individual. Mean theoretical rate and 95% CI was then calculated per cohort based on individual rates (see STAR Methods and Table 2 for more details)

fibronectin deposits (Castelletti et al., 2008). Unlike the probands with *NIPBL* variants, affected individuals do not appear to have overlapping phenotypic characteristics, although this disorder has a late onset (Castelletti et al., 2008).

Given the current results, a comparison to recent studies of ASD may be instructive: to date 2,517 simplex SSC ASD families have been reported, and both de novo LGD and Mis3 variants

have been associated with ASD risk, with mutation rates and effect sizes consistent with those observed here (e.g., rate ratio of 2.08 versus 1.74 for de novo LGD variants in TD versus ASD) (Iossifov et al., 2014). Of note, the ascertainment strategies used in both TD cohorts did not restrict to apparently simplex families, as was done in the SSC. Given the evidence for an increased burden of de novo variation in simplex versus multiplex families

**Figure 5. Recurrent De Novo Damaging Variants Identify Four Likely TD Risk Genes**

(A) Given the number of confirmed damaging de novo variants observed in 484 TD probands (192) and an empirical estimate of the fraction of these carrying risk, we used a maximum likelihood estimation (MLE) procedure to estimate the total number of “target” genes. After 50,000 permutations, we estimate that 420 genes contribute to TD risk based on vulnerability to de novo damaging variants. We identified five genes with recurrent de novo LGD or Mis3 variants confirmed using PCR and Sanger sequencing (Table S2).

(B) We estimated the per-gene p values and q values for recurrence with TADA using the de novo only algorithm (He et al., 2013). Based on previously established q value (false discovery rate) thresholds (see De Rubeis et al., 2014; He et al., 2013; Sanders et al., 2015), one of these genes, *WWC1*, is a high-confidence TD (hcTD) risk gene ($q < 0.1$), and three of these genes are probable TD (pTD) risk genes ($q < 0.3$; shown in A). The fifth gene, *TTN*, did not meet this threshold ($q = 0.76$), as expected given its large size.

(C) The estimate of 420 genes derived from (A) was utilized to predict the likely future gene discovery yield as additional TD trios are whole-exome sequenced. For each of 10,000 permutations, we ran simulated variants through the TADA de novo algorithm to assess per-gene q values. We then recorded the number of pTD genes ($q < 0.3$) and hcTD genes ($q < 0.1$) observed at each cohort size and plotted the smoothed trend line using local

polynomial regression fitting. The regression model also predicted the number of genes identified at a given number of trios. The predicted number of TD genes for the cohort presented in this study (484 trios) tracked very closely with our empirical results: we predict 2.8 pTD genes (we observed 3) and 0.69 hcTD genes (we observed 1). Mis3, missense variants predicted to be damaging by PolyPhen (Missense 3 or Mis3; PolyPhen2 [HumDiv] score ≥ 0.957).

in ASD (e.g., Leppa et al., 2016), it would be reasonable to hypothesize that the current analysis may underestimate the rate ratios for de novo variants in simplex TD families.

The widespread success in gene discovery leveraging de novo variation in ASD (De Rubeis et al., 2014; Dong et al., 2014; Iossifov et al., 2012, 2014; Neale et al., 2012; O’Roak et al., 2011, 2012; Sanders et al., 2012, 2015; Willsey et al., 2013) strongly argues for additional WES in TD. The current gene discovery by cohort size curves predict that increasing our study size to 2,517 trios would lead to the identification of ~21 hcTD genes, which is a similar order of magnitude to the 27 hcASD genes identified from 2,517 trios in Iossifov et al. (2014). Moreover, the integration of de novo CNV data should further increase the yield of risk genes (Sanders et al., 2015). The discovery of a large number of TD-associated genes will provide a critical substrate for model systems and systems-biological studies aimed at understanding the spatial, temporal, and cell-level dynamics of TD pathology (Parikshak et al., 2013; Willsey et al., 2013; Willsey and State, 2015; Xu et al., 2014) and, importantly, for the development of novel, more effective therapeutic targets.

STAR★METHODS

Detailed methods are provided in the online version of this paper and include the following:

- KEY RESOURCES TABLE
- CONTACT FOR REAGENT AND RESOURCE SHARING
- EXPERIMENTAL MODEL AND SUBJECT DETAILS
 - Sample Selection
- METHOD DETAILS
 - Whole Exome Sequencing
 - Burden Analyses
 - TADA
 - Estimation of Number of TS Genes
- QUANTIFICATION AND STATISTICAL ANALYSIS
- DATA AND SOFTWARE AVAILABILITY
 - Data
 - Software
- ADDITIONAL RESOURCES

SUPPLEMENTAL INFORMATION

Supplemental Information includes six figures, four tables, and consortium member names and can be found with this article online at <http://dx.doi.org/10.1016/j.neuron.2017.04.024>.

A video abstract is available at <http://dx.doi.org/10.1016/j.neuron.2017.04.024#mmc6>.

CONSORTIA

The members of the Tourette International Collaborative Genetics (TIC Genetics) consortium are: Mohamed Abdulkadir, Julia Bohnenpoll, Yana Bromberg, Lawrence W. Brown, Keun-Ah Cheon, Barbara J. Coffey, Li Deng, Andrea Dietrich, Shan Dong, Lonnie Elzerman, Thomas V. Fernandez, Odette Fründt, Blanca Garcia-Delgar, Erika Gedvilaite, Donald L. Gilbert, Dorothy E. Grice, Julie Hagstrom, Tammy Hedderly, Gary A. Heiman, Isobel Heyman, Pieter J. Hoekstra, Hyun Ju Hong, Chaim Huyser, Laura Ibanez-Gomez, Young Key Kim, Young Shin Kim, Robert A. King, Yun-Joo Koh, Sodahm Kook, Samuel Kuperman, Andreas Lamerz, Bennett Leventhal, Andrea G. Ludolph, Claudia Lührs da Silva, Marcos Madruga-Garrido, Jeffrey D. Mandell,

Athanasios Maras, Pablo Mir, Astrid Morer, Alexander Münchau, Tara L. Murphy, Cara Nasello, Thaira J. C. Openner, Kerstin J. Plessen, Petra Richer, Veit Roessner, Stephan Sanders, Eun-Young Shin, Deborah A. Sival, Louw Smith, Dong-Ho Song, Jungeun Song, Matthew W. State, Anne Marie Stolte, Nawei Sun, Jay A. Tischfield, Jennifer Tübing, Frank Visscher, Michael F. Walker, Sina Wanderer, Shuoguo Wang, A. Jeremy Willsey, Martin Woods, Jinchuan Xing, Yeting Zhang, Anbo Zhou, and Samuel H. Zinner. The members of the Tourette Syndrome Association International Consortium for Genetics (TSAICG) are: Cathy L. Barr, James R. Batterson, Cheston Berlin, Ruth D. Bruun, Cathy L. Budman, Danielle C. Cath, Sylvain Chouinard, Giovanni Coppola, Nancy J. Cox, Sabrina Darrow, Lea K. Davis, Yves Dion, Nelson B. Freimer, Marco A. Grados, Matthew E. Hirschtritt, Alden Y. Huang, Cornelia Illmann, Robert A. King, Roger Kurlan, James F. Leckman, Gholson J. Lyon, Irene A. Malaty, Carol A. Mathews, William M. McMahon, Benjamin M. Neale, Michael S. Okun, Lisa Osiecki, David L. Pauls, Danielle Posthuma, Vasily Ramensky, Mary M. Robertson, Guy A. Rouleau, Paul Sandor, Jeremiah M. Scharf, Harvey S. Singer, Jan Smit, Jae-Hoon Sul, and Dongmei Yu.

AUTHOR CONTRIBUTIONS

Conceptualization, A.J.W., T.V.F., S.J.S., B.M.N., G.C., C.A.M., J.A.T., J.M.S., M.W.S., and G.A.H.; Methodology, A.J.W., T.V.F., D.Y., A.Y.H., K.E.S., B.M.N., G.C., J.M.S., and M.W.S.; Software, A.J.W., J.D.M., and L.S.; Validation, A.J.W., T.V.F., D.Y., A.Y.H., P.R., G.C., and J.M.S.; Formal Analysis, A.J.W., T.V.F., D.Y., J.X., J.D.M., and S.D.; Investigation, A.J.W., T.V.F., D.Y., J.D.M., A.Y.H., P.R., L.S., G.C., J.M.S., and M.W.S.; Resources, TIC Genetics, TSAICG, A.D., R.A.K., J.X., C.A.M., J.A.T., J.M.S., M.W.S., and G.A.H.; Data Curation, A.J.W., T.V.F., D.Y., A.D., R.A.K., J.X., J.D.M., TIC Genetics, TSAICG, J.M.S., and G.A.H.; Writing – Original Draft, A.J.W., T.V.F., and M.W.S.; Writing – Review & Editing, A.J.W., T.V.F., D.Y., A.Y.H., TIC Genetics, TSAICG, G.C., C.A.M., J.A.T., J.M.S., M.W.S., and G.A.H.; Visualization, A.J.W.; Supervision, R.A.K., G.C., C.A.M., J.A.T., J.M.S., M.W.S., and G.A.H.; Project Administration, J.A.T., J.M.S., M.W.S., and G.A.H.; Funding Acquisition, G.C., C.A.M., J.A.T., J.M.S., M.W.S., and G.A.H.

ACKNOWLEDGMENTS

We wish to thank the families who have participated in and contributed to this study. We also thank the NIMH Repository and Genomics Resource (U24MH068457 to J.A.T.) at RUCDR Infinite Biologics for transforming cell lines and providing DNA samples and the Simons Foundation for providing genotyping and sequencing data used as controls in this study. This study was supported by grants from the National Institute of Mental Health (R01MH092290 to L.W. Brown; R01MH092291 to S. Kuperman; R01MH092292 to B.J. Coffey; R01MH092293 to G.A.H. and J.A.T.; R01MH092513 to S.H. Zinner; R01MH092516 to D.E. Grice; R01MH092520 to D.L. Gilbert; R01MH092289 to M.W.S.; K08MH099424 to T.V.F.; K23MH085057 to J.M.S.), the National Institute of Neurological Disorders and Stroke (U01NS40024-09S1 and K02 NS085048 to J.M.S.), the Harvard Clinical and Translational Science Center (UL TR001102 to J.M.S.), the Tourette Association of America (to C.A.M. and J.M.S.), the New Jersey Center for Tourette Syndrome and Associated Disorders (NJCTS; to G.A.H. and J.A.T.), and the Overlook International Fund (to M.W.S.). We are also grateful to the NJCTS for facilitating the inception and organization of the TIC Genetics study. The content is solely the responsibility of the authors and does not necessarily represent the official views of the National Institutes of Health. This work was additionally supported by grants from Spain (to P. Mir): the Instituto de Salud Carlos III (PI10/01674, PI13/01461), the Consejería de Economía, Innovación, Ciencia y Empresa de la Junta de Andalucía (CVI-02526, CTS-7685), the Consejería de Salud y Bienestar Social de la Junta de Andalucía (PI-0741/2010, PI-0437-2012, and PI-0471-2013), the Sociedad Andaluza de Neurología, the Fundación Alicia Koplowitz, the Fundación Mutua Madrileña, and the Jaques and Gloria Gossweiler Foundation; grants from Germany (to A. Münchau): Deutsche Forschungsgemeinschaft (DFG: MU 1692/3-1, MU 1692/4-1, and project C5 of the SFB 936). This research was supported by the NIHR Great Ormond Street Hospital Biomedical Research Centre (GOSH BRC). The views expressed are those of the author(s) and not necessarily those of the NHS, the NIHR, or the Department of Health.

This research was also supported in part by an Informatics Starter Grant from the PhRMA Foundation (to Y. Bromberg). We thank all of the individuals involved in recruitment and assessment of the subjects reported in this study: Denmark: Nikoline Frost and Heidi B. Biernat (Copenhagen); Germany: Stephanie Enghardt, Yvonne Friedrich, Christiane Michel (Dresden), Jenny Schmalfeld (Lübeck), Hanife Kling, and Ariane Saccarello (Ulm); Spain: María T. Cáceres, Fátima Carrillo, Marta Correa, Pilar Gómez-Garre, and Laura Vargas (Sevilla); the Netherlands: Vivian op de Beek (Amsterdam), Marieke Meschendorp (Groningen), Nicole Driessen, Nadine Schalk (Nijmegen), Noor Tromp (Alkmaar), Els van den Ban (Utrecht), Jolanda Blom, Rudi Bruggemans, and MariAnne Overdijk (Barendrecht); UK: Anup Kharod (London GOSH); USA: Sarah Jacobson (Cincinnati), Angie Cookman (Iowa City), Zoey Shaw (Mount Sinai/NKI), Julia Brillante, Daniela B. Colognori, Joseph Conerty, Alycia Davis, Joanne O'Brien, Carolyn Spiro, Donna Tischfield (Rutgers), Shannon Granillo, and JD Sandhu (Seattle Children's). Finally, we thank Adife Gulhan Ercan-Sencicek (Yale), Xin He (University of Chicago), Kathryn Roeder (CMU), Bernie Devlin (University of Pittsburgh), Helen Willsey (UCSF), the Willsey lab (UCSF), and all who may not have been mentioned.

Received: January 21, 2017

Revised: April 15, 2017

Accepted: April 18, 2017

Published: May 3, 2017

REFERENCES

- Abelson, J.F., Kwan, K.Y., O'Roak, B.J., Baek, D.Y., Stillman, A.A., Morgan, T.M., Mathews, C.A., Pauls, D.L., Rasin, M.-R., Gunel, M., et al. (2005). Sequence variants in SLITRK1 are associated with Tourette's syndrome. *Science* **310**, 317–320.
- Adzhubei, I.A., Schmidt, S., Peshkin, L., Ramensky, V.E., Gerasimova, A., Bork, P., Kondrashov, A.S., and Sunyaev, S.R. (2010). A method and server for predicting damaging missense mutations. *Nat. Methods* **7**, 248–249.
- Adzhubei, I., Jordan, D.M., and Sunyaev, S.R. (2013). Predicting functional effect of human missense mutations using PolyPhen-2. *Curr. Protoc. Hum. Genet. Chapter 7*, Unit7.20.
- Allen, A.S., Berkovic, S.F., Cossette, P., Delanty, N., Dlugos, D., Eichler, E.E., Epstein, M.P., Glauser, T., Goldstein, D.B., Han, Y., et al.; Epi4K Consortium; Epilepsy Phenome/Genome Project (2013). De novo mutations in epileptic encephalopathies. *Nature* **501**, 217–221.
- American Psychiatric Association (2000). *Diagnostic and Statistical Manual of Mental Disorders, DSM-IV-TR edn* (American Psychiatric Association).
- Bilgüvar, K., Oztürk, A.K., Louvi, A., Kwan, K.Y., Choi, M., Tatli, B., Yalnizoğlu, D., Tüysüz, B., Çağlayan, A.O., Gökben, S., et al. (2010). Whole-exome sequencing identifies recessive WDR62 mutations in severe brain malformations. *Nature* **467**, 207–210.
- Brachmann, W. (1916). Ein fall von symmetrischer monodaktylie durch Ulnadefekt, mit symmetrischer flughautbildung in den ellenbeugen, sowie anderen abnormitäten (zwerghaftogkeit, halsrippen, behaarung). *Jarb Kinder Phys Erzie* **84**, 225–235.
- Browne, H.A., Hansen, S.N., Buxbaum, J.D., Gair, S.L., Nissen, J.B., Nikolajsen, K.H., Schendel, D.E., Reichenberg, A., Parner, E.T., and Grice, D.E. (2015). Familial clustering of tic disorders and obsessive-compulsive disorder. *JAMA Psychiatry* **72**, 359–366.
- Burd, L., Freeman, R.D., Klug, M.G., and Kerbeshian, J. (2005). Tourette Syndrome and learning disabilities. *BMC Pediatr.* **5**, 34.
- Büther, K., Plaas, C., Barnekow, A., and Kremerskothen, J. (2004). KIBRA is a novel substrate for protein kinase Czeta. *Biochem. Biophys. Res. Commun.* **317**, 703–707.
- Castelletti, F., Donadelli, R., Banterla, F., Hildebrandt, F., Zipfel, P.F., Bresin, E., Otto, E., Skerka, C., Renieri, A., Todeschini, M., et al. (2008). Mutations in FN1 cause glomerulopathy with fibronectin deposits. *Proc. Natl. Acad. Sci. USA* **105**, 2538–2543.
- Cavanna, A.E., Servo, S., Monaco, F., and Robertson, M.M. (2009). The behavioral spectrum of Gilles de la Tourette syndrome. *J. Neuropsychiatry Clin. Neurosci.* **21**, 13–23.
- Centers for Disease Control and Prevention (CDC) (2009). Prevalence of diagnosed Tourette syndrome in persons aged 6–17 years - United States, 2007. *MMWR Morb. Mortal. Wkly. Rep.* **58**, 581–585.
- Chai, G., Zhou, L., Manto, M., Helmbacher, F., Clotman, F., Goffinet, A.M., and Tissir, F. (2014). Celsr3 is required in motor neurons to steer their axons in the hindlimb. *Nat. Neurosci.* **17**, 1171–1179.
- Chai, G., Goffinet, A.M., and Tissir, F. (2015). Celsr3 and Fzd3 in axon guidance. *Int. J. Biochem. Cell Biol.* **64**, 11–14.
- De Lange, C. (1933). Sur un type nouveau de dégénération (typus Amstelodamensis). *Arch Med Enfants* **36**, 713–719.
- de Ligt, J., Willemsen, M.H., van Bon, B.W., Kleefstra, T., Yntema, H.G., Kroes, T., Vulto-van Silfhout, A.T., Koolen, D.A., de Vries, P., Gilissen, C., et al. (2012). Diagnostic exome sequencing in persons with severe intellectual disability. *N. Engl. J. Med.* **367**, 1921–1929.
- De Rubeis, S., He, X., Goldberg, A.P., Poultney, C.S., Samocha, K., Cicek, A.E., Kou, Y., Liu, L., Fromer, M., Walker, S., et al.; DDD Study; Homozygosity Mapping Collaborative for Autism; UK10K Consortium (2014). Synaptic, transcriptional and chromatin genes disrupted in autism. *Nature* **515**, 209–215.
- Deciphering Developmental Disorders Study (2015). Large-scale discovery of novel genetic causes of developmental disorders. *Nature* **519**, 223–228.
- Deciphering Developmental Disorders Study (2017). Prevalence and architecture of de novo mutations in developmental disorders. *Nature* **542**, 433–438.
- DePristo, M.A., Banks, E., Poplin, R., Garimella, K.V., Maguire, J.R., Hartl, C., Philippakis, A.A., del Angel, G., Rivas, M.A., Hanna, M., et al. (2011). A framework for variation discovery and genotyping using next-generation DNA sequencing data. *Nat. Genet.* **43**, 491–498.
- Dietrich, A., Fernandez, T.V., King, R.A., State, M.W., Tischfield, J.A., Hoekstra, P.J., Heiman, G.A., and Group, T.I.C.G.C.; TIC Genetics Collaborative Group (2015). The Tourette International Collaborative Genetics (TIC Genetics) study, finding the genes causing Tourette syndrome: objectives and methods. *Eur. Child Adolesc. Psychiatry* **24**, 141–151.
- do Rosário, M.C., and Miguel Filho, E.C. (1997). Obsessive-compulsive disorder and Tourette syndrome: is there a relationship? *Sao Paulo Med. J.* **115**, 1410–1411.
- Dong, S., Walker, M.F., Carriero, N.J., DiCola, M., Willsey, A.J., Ye, A.Y., Waqar, Z., Gonzalez, L.E., Overton, J.D., Frahm, S., et al. (2014). De novo insertions and deletions of predominantly paternal origin are associated with autism spectrum disorder. *Cell Rep.* **9**, 16–23.
- Epi4K Consortium (2016). De novo mutations in SLC1A2 and CACNA1A are important causes of epileptic encephalopathies. *Am. J. Hum. Genet.* **99**, 287–298.
- Ercan-Sencicek, A.G., Stillman, A.A., Ghosh, A.K., Bilguvar, K., O'Roak, B.J., Mason, C.E., Abbott, T., Gupta, A., King, R.A., Pauls, D.L., et al. (2010). L-histidine decarboxylase and Tourette's syndrome. *N. Engl. J. Med.* **362**, 1901–1908.
- EuroEPINOMICS-RES Consortium; Epilepsy Phenome/Genome Project; Epi4K Consortium (2014). De novo mutations in synaptic transmission genes including DNM1 cause epileptic encephalopathies. *Am. J. Hum. Genet.* **95**, 360–370.
- Feng, J., Han, Q., and Zhou, L. (2012). Planar cell polarity genes, Celsr1-3, in neural development. *Neurosci. Bull.* **28**, 309–315.
- Fenstermaker, A.G., Prasad, A.A., Bechara, A., Adolfs, Y., Tissir, F., Goffinet, A., Zou, Y., and Pasterkamp, R.J. (2010). Wnt/planar cell polarity signaling controls the anterior-posterior organization of monoaminergic axons in the brainstem. *J. Neurosci.* **30**, 16053–16064.
- Fernandez, T.V., Sanders, S.J., Yurkiewicz, I.R., Ercan-Sencicek, A.G., Kim, Y.S., Fishman, D.O., Raubeson, M.J., Song, Y., Yasuno, K., Ho, W.S.C., et al. (2012). Rare copy number variants in tourette syndrome disrupt genes in histaminergic pathways and overlap with autism. *Biol. Psychiatry* **71**, 392–402.

- Fischbach, G.D., and Lord, C. (2010). The Simons Simplex Collection: a resource for identification of autism genetic risk factors. *Neuron* 68, 192–195.
- Frantz, C., Stewart, K.M., and Weaver, V.M. (2010). The extracellular matrix at a glance. *J. Cell Sci.* 123, 4195–4200.
- Fromer, M., Pocklington, A.J., Kavanagh, D.H., Williams, H.J., Dwyer, S., Gormley, P., Georgieva, L., Rees, E., Palta, P., Ruderfer, D.M., et al. (2014). De novo mutations in schizophrenia implicate synaptic networks. *Nature* 506, 179–184.
- George, E.L., Georges-Labouesse, E.N., Patel-King, R.S., Rayburn, H., and Hynes, R.O. (1993). Defects in mesoderm, neural tube and vascular development in mouse embryos lacking fibronectin. *Development* 119, 1079–1091.
- Ghanizadeh, A., and Mosallaei, S. (2009). Psychiatric disorders and behavioral problems in children and adolescents with Tourette syndrome. *Brain Dev.* 31, 15–19.
- He, X., Sanders, S.J., Liu, L., De Rubeis, S., Lim, E.T., Sutcliffe, J.S., Schellenberg, G.D., Gibbs, R.A., Daly, M.J., Buxbaum, J.D., et al. (2013). Integrated model of de novo and inherited genetic variants yields greater power to identify risk genes. *PLoS Genet.* 9, e1003671.
- Hirschtritt, M.E., Lee, P.C., Pauls, D.L., Dion, Y., Grados, M.A., Illmann, C., King, R.A., Sandor, P., McMahon, W.M., Lyon, G.J., et al.; Tourette Syndrome Association International Consortium for Genetics (2015). Lifetime prevalence, age of risk, and genetic relationships of comorbid psychiatric disorders in Tourette syndrome. *JAMA Psychiatry* 72, 325–333.
- Homsy, J., Zaidi, S., Shen, Y., Ware, J.S., Samocha, K.E., Karczewski, K.J., DePalma, S.R., McKean, D., Wakimoto, H., Gorham, J., et al. (2015). De novo mutations in congenital heart disease with neurodevelopmental and other congenital anomalies. *Science* 350, 1262–1266.
- Hounie, A.G., do Rosario-Campos, M.C., Diniz, J.B., Shavitt, R.G., Ferrão, Y.A., Lopes, A.C., Mercadante, M.T., Busatto, G.F., and Miguel, E.C. (2006). Obsessive-compulsive disorder in Tourette syndrome. *Adv. Neurol.* 99, 22–38.
- Iossifov, I., Ronemus, M., Levy, D., Wang, Z., Hakker, I., Rosenbaum, J., Yamrom, B., Lee, Y.H., Narzisi, G., Leotta, A., et al. (2012). De novo gene disruptions in children on the autistic spectrum. *Neuron* 74, 285–299.
- Iossifov, I., O’Roak, B.J., Sanders, S.J., Ronemus, M., Krumm, N., Levy, D., Stessman, H.A., Witherspoon, K.T., Vives, L., Patterson, K.E., et al. (2014). The contribution of de novo coding mutations to autism spectrum disorder. *Nature* 515, 216–221.
- Kang, H.J., Kawasawa, Y.I., Cheng, F., Zhu, Y., Xu, X., Li, M., Sousa, A.M., Pletikos, M., Meyer, K.A., Sedmak, G., et al. (2011). Spatio-temporal transcriptome of the human brain. *Nature* 478, 483–489.
- Kapushesky, M., Adamusiak, T., Burdett, T., Culhane, A., Farne, A., Filippov, A., Holloway, E., Klebanov, A., Kryvych, N., Kurbatova, N., et al. (2012). Gene Expression Atlas update—a value-added database of microarray and sequencing-based functional genomics experiments. *Nucleic Acids Res.* 40, D1077–D1081.
- Kaur, M., Mehta, D., Noon, S.E., Deardorff, M.A., Zhang, Z., and Krantz, I.D. (2016). NIPBL expression levels in CdLS probands as a predictor of mutation type and phenotypic severity. *Am. J. Med. Genet. C. Semin. Med. Genet.* 172, 163–170.
- Kong, A., Frigge, M.L., Masson, G., Besenbacher, S., Sulem, P., Magnusson, G., Gudjonsson, S.A., Sigurdsson, A., Jonasdottir, A., Jonasdottir, A., et al. (2012). Rate of de novo mutations and the importance of father’s age to disease risk. *Nature* 488, 471–475.
- Kremerskothen, J., Plaas, C., Büther, K., Finger, I., Veltel, S., Matanis, T., Liedtke, T., and Barnekow, A. (2003). Characterization of KIBRA, a novel WW domain-containing protein. *Biochem. Biophys. Res. Commun.* 300, 862–867.
- Lawson-Yuen, A., Saldivar, J.S., Sommer, S., and Picker, J. (2008). Familial deletion within NLGN4 associated with autism and Tourette syndrome. *Eur. J. Hum. Genet.* 16, 614–618.
- Leckman, J.F. (2003). Phenomenology of tics and natural history of tic disorders. *Brain Dev.* 25 (Suppl 1), S24–S28.
- Leppa, V.M., Kravitz, S.N., Martin, C.L., Andrieux, J., Le Caignec, C., Martin-Coignard, D., DyBuncio, C., Sanders, S.J., Lowe, J.K., Cantor, R.M., and Geschwind, D.H. (2016). Rare inherited and de novo CNVs reveal complex contributions to ASD risk in multiplex families. *Am. J. Hum. Genet.* 99, 540–554.
- Li, H., and Durbin, R. (2009). Fast and accurate short read alignment with Burrows-Wheeler transform. *Bioinformatics* 25, 1754–1760.
- Lochner, C., Hemmings, S.M., Kinnear, C.J., Niehaus, D.J., Nel, D.G., Corfield, V.A., Moolman-Smook, J.C., Seedat, S., and Stein, D.J. (2005). Cluster analysis of obsessive-compulsive spectrum disorders in patients with obsessive-compulsive disorder: clinical and genetic correlates. *Compr. Psychiatry* 46, 14–19.
- Malhotra, D., and Sebat, J. (2012). CNVs: harbingers of a rare variant revolution in psychiatric genetics. *Cell* 148, 1223–1241.
- Mannini, L., Cucco, F., Quarantotti, V., Krantz, I.D., and Musio, A. (2013). Mutation spectrum and genotype-phenotype correlation in Cornelia de Lange syndrome. *Hum. Mutat.* 34, 1589–1596.
- Mataix-Cols, D., Isomura, K., Pérez-Vigil, A., Chang, Z., Rück, C., Larsson, K.J., Leckman, J.F., Serlachius, E., Larsson, H., and Lichtenstein, P. (2015). Familial risks of Tourette syndrome and chronic tic disorders. A population-based cohort study. *JAMA Psychiatry* 72, 787–793.
- McGrath, L.M., Yu, D., Marshall, C., Davis, L.K., Thiruvahindrapuram, B., Li, B., Cappi, C., Gerber, G., Wolf, A., Schroeder, F.A., et al. (2014). Copy number variation in obsessive-compulsive disorder and tourette syndrome: a cross-disorder study. *J. Am. Acad. Child Adolesc. Psychiatry* 53, 910–919.
- McKenna, A., Hanna, M., Banks, E., Sivachenko, A., Cibulskis, K., Kernytsky, A., Garimella, K., Altshuler, D., Gabriel, S., Daly, M., and DePristo, M.A. (2010). The Genome Analysis Toolkit: a MapReduce framework for analyzing next-generation DNA sequencing data. *Genome Res.* 20, 1297–1303.
- Moya, P.R., Wendland, J.R., Rubenstein, L.M., Timpano, K.R., Heiman, G.A., Tischfield, J.A., King, R.A., Andrews, A.M., Ramamoorthy, S., McMahon, F.J., and Murphy, D.L. (2013). Common and rare alleles of the serotonin transporter gene, SLC6A4, associated with Tourette’s disorder. *Mov. Disord.* 28, 1263–1270.
- Mulder, P.A., Huisman, S.A., Hennekam, R.C., Oliver, C., van Balkom, I.D., and Piening, S. (2017). Behaviour in Cornelia de Lange syndrome: a systematic review. *Dev. Med. Child Neurol.* 59, 361–366.
- Nag, A., Bochukova, E.G., Kremeyer, B., Campbell, D.D., Muller, H., Valencia-Duarte, A.V., Cardona, J., Rivas, I.C., Mesa, S.C., Cuartas, M., et al.; Tourette Syndrome Association International Consortium for Genetics (2013). CNV analysis in Tourette syndrome implicates large genomic rearrangements in COL8A1 and NRXN1. *PLoS ONE* 8, e59061.
- Neale, B.M., Kou, Y., Liu, L., Ma’ayan, A., Samocha, K.E., Sabo, A., Lin, C.F., Stevens, C., Wang, L.S., Makarov, V., et al. (2012). Patterns and rates of exonic de novo mutations in autism spectrum disorders. *Nature* 485, 242–245.
- O’Roak, B.J., Deriziotis, P., Lee, C., Vives, L., Schwartz, J.J., Girirajan, S., Karakoc, E., Mackenzie, A.P., Ng, S.B., Baker, C., et al. (2011). Exome sequencing in sporadic autism spectrum disorders identifies severe de novo mutations. *Nat. Genet.* 43, 585–589.
- O’Roak, B.J., Vives, L., Girirajan, S., Karakoc, E., Krumm, N., Coe, B.P., Levy, R., Ko, A., Lee, C., Smith, J.D., et al. (2012). Sporadic autism exomes reveal a highly interconnected protein network of de novo mutations. *Nature* 485, 246–250.
- Oliver, C., Arron, K., Sloneem, J., and Hall, S. (2008). Behavioural phenotype of Cornelia de Lange syndrome: case-control study. *Br. J. Psychiatry* 193, 466–470.
- Pankov, R., and Yamada, K.M. (2002). Fibronectin at a glance. *J. Cell Sci.* 115, 3861–3863.
- Parikshak, N.N., Luo, R., Zhang, A., Won, H., Lowe, J.K., Chandran, V., Horvath, S., and Geschwind, D.H. (2013). Integrative functional genomic analyses implicate specific molecular pathways and circuits in autism. *Cell* 155, 1008–1021.

- Pauls, D.L., Cohen, D.J., Heimbuch, R., Detlor, J., and Kidd, K.K. (1981). Familial pattern and transmission of Gilles de la Tourette syndrome and multiple tics. *Arch. Gen. Psychiatry* *38*, 1091–1093.
- Pauls, D.L., Raymond, C.L., Stevenson, J.M., and Leckman, J.F. (1991). A family study of Gilles de la Tourette syndrome. *Am. J. Hum. Genet.* *48*, 154–163.
- Peters, J.M., Tedeschi, A., and Schmitz, J. (2008). The cohesin complex and its roles in chromosome biology. *Genes Dev.* *22*, 3089–3114.
- Petryszak, R., Burdett, T., Fiorelli, B., Fonseca, N.A., Gonzalez-Porta, M., Hastings, E., Huber, W., Jupp, S., Keays, M., Kryvych, N., et al. (2014). Expression Atlas update—a database of gene and transcript expression from microarray- and sequencing-based functional genomics experiments. *Nucleic Acids Res.* *42*, D926–D932.
- Petryszak, R., Keays, M., Tang, Y.A., Fonseca, N.A., Barrera, E., Burdett, T., Füllgrabe, A., Fuentes, A.M., Jupp, S., Koskinen, S., et al. (2016). Expression Atlas update—an integrated database of gene and protein expression in humans, animals and plants. *Nucleic Acids Res.* *44* (D1), D746–D752.
- Price, R.A., Kidd, K.K., Cohen, D.J., Pauls, D.L., and Leckman, J.F. (1985). A twin study of Tourette syndrome. *Arch. Gen. Psychiatry* *42*, 815–820.
- Quinlan, A.R., and Hall, I.M. (2010). BEDTools: a flexible suite of utilities for comparing genomic features. *Bioinformatics* *26*, 841–842.
- Rauch, A., Wiczorek, D., Graf, E., Wieland, T., Ende, S., Schwarzmayr, T., Albrecht, B., Bartholdi, D., Beygo, J., Di Donato, N., et al. (2012). Range of genetic mutations associated with severe non-syndromic sporadic intellectual disability: an exome sequencing study. *Lancet* *380*, 1674–1682.
- Rebhan, M., Chalifa-Caspi, V., Prilusky, J., and Lancet, D. (1997). GeneCards: integrating information about genes, proteins and diseases. *Trends Genet.* *13*, 163.
- Robertson, M.M. (2008). The prevalence and epidemiology of Gilles de la Tourette syndrome. Part 1: the epidemiological and prevalence studies. *J. Psychosom. Res.* *65*, 461–472.
- Roessner, V., Becker, A., Banaschewski, T., Freeman, R.D., and Rothenberger, A.; Tourette Syndrome International Database Consortium (2007). Developmental psychopathology of children and adolescents with Tourette syndrome—impact of ADHD. *Eur. Child Adolesc. Psychiatry* *16* (Suppl 1), 24–35.
- Sanders, S.J., Ercan-Sencicek, A.G., Hus, V., Luo, R., Murtha, M.T., Moreno-De-Luca, D., Chu, S.H., Moreau, M.P., Gupta, A.R., Thomson, S.A., et al. (2011). Multiple recurrent de novo CNVs, including duplications of the 7q11.23 Williams syndrome region, are strongly associated with autism. *Neuron* *70*, 863–885.
- Sanders, S.J., Murtha, M.T., Gupta, A.R., Murdoch, J.D., Raubeson, M.J., Willsey, A.J., Ercan-Sencicek, A.G., DiLullo, N.M., Parikshak, N.N., Stein, J.L., et al. (2012). De novo mutations revealed by whole-exome sequencing are strongly associated with autism. *Nature* *485*, 237–241.
- Sanders, S.J., He, X., Willsey, A.J., Ercan-Sencicek, A.G., Samocha, K.E., Cicek, A.E., Murtha, M.T., Bal, V.H., Bishop, S.L., Dong, S., et al.; Autism Sequencing Consortium (2015). Insights into Autism Spectrum Disorder genomic architecture and biology from 71 risk loci. *Neuron* *87*, 1215–1233.
- Scharf, J.M., Yu, D., Mathews, C.A., Neale, B.M., Stewart, S.E., Fagerness, J.A., Evans, P., Gamazon, E., Edlund, C.K., Service, S.K., et al.; North American Brain Expression Consortium; UK Human Brain Expression Database (2013). Genome-wide association study of Tourette's syndrome. *Mol. Psychiatry* *18*, 721–728.
- Scharf, J.M., Miller, L.L., Gauvin, C.A., Alabiso, J., Mathews, C.A., and Ben-Shlomo, Y. (2015). Population prevalence of Tourette syndrome: a systematic review and meta-analysis. *Mov. Disord.* *30*, 221–228.
- Schneider, A., Huentelman, M.J., Kremerskothen, J., Duning, K., Spoelgen, R., and Nikolich, K. (2010). KIBRA: a new gateway to learning and memory? *Front. Aging Neurosci.* *2*, 4.
- Stillman, A.A., Krsnik, Z., Sun, J., Rasin, M.R., State, M.W., Sestan, N., and Louvi, A. (2009). Developmentally regulated and evolutionarily conserved expression of SLITRK1 in brain circuits implicated in Tourette syndrome. *J. Comp. Neurol.* *513*, 21–37.
- Sundaram, S.K., Huq, A.M., Wilson, B.J., and Chugani, H.T. (2010). Tourette syndrome is associated with recurrent exonic copy number variants. *Neurology* *74*, 1583–1590.
- The Tourette Syndrome Association International Consortium for Genetics (1999). A complete genome screen in sib pairs affected by Gilles de la Tourette syndrome. *Am. J. Hum. Genet.* *65*, 1428–1436.
- Tissir, F., Bar, I., Jossin, Y., De Backer, O., and Goffinet, A.M. (2005). Protocadherin Celsr3 is crucial in axonal tract development. *Nat. Neurosci.* *8*, 451–457.
- The Tourette Syndrome Association International Consortium for Genetics (2007). Genome scan for Tourette disorder in affected-sibling-pair and multi-generational families. *Am. J. Hum. Genet.* *80*, 265–272.
- Van der Auwera, G.A., Carneiro, M.O., Hartl, C., Poplin, R., Del Angel, G., Levy-Moonshine, A., Jordan, T., Shakir, K., Roazen, D., Thibault, J., et al. (2013). From FastQ data to high confidence variant calls: the Genome Analysis Toolkit best practices pipeline. *Curr. Protoc. Bioinformatics* *43*, 11.10.1–33.
- Verkerk, A.J., Mathews, C.A., Joosse, M., Eussen, B.H., Heutink, P., and Oostra, B.A.; Tourette Syndrome Association International Consortium for Genetics (2003). CNTNAP2 is disrupted in a family with Gilles de la Tourette syndrome and obsessive compulsive disorder. *Genomics* *82*, 1–9.
- Wang, K., Li, M., and Hakonarson, H. (2010). ANNOVAR: functional annotation of genetic variants from high-throughput sequencing data. *Nucleic Acids Res.* *38*, e164.
- Willsey, A.J., and State, M.W. (2015). Autism spectrum disorders: from genes to neurobiology. *Curr. Opin. Neurobiol.* *30*, 92–99.
- Willsey, A.J., Sanders, S.J., Li, M., Dong, S., Tebbenkamp, A.T., Muhle, R.A., Reilly, S.K., Lin, L., Fertuzinhos, S., Miller, J.A., et al. (2013). Coexpression networks implicate human midfetal deep cortical projection neurons in the pathogenesis of autism. *Cell* *155*, 997–1007.
- Xu, B., Ionita-Laza, I., Roos, J.L., Boone, B., Woodrick, S., Sun, Y., Levy, S., Gogos, J.A., and Karayiorgou, M. (2012). De novo gene mutations highlight patterns of genetic and neural complexity in schizophrenia. *Nat. Genet.* *44*, 1365–1369.
- Xu, X., Wells, A.B., O'Brien, D.R., Nehorai, A., and Dougherty, J.D. (2014). Cell type-specific expression analysis to identify putative cellular mechanisms for neurogenetic disorders. *J. Neurosci.* *34*, 1420–1431.
- Zhang, L., Yang, S., Wennmann, D.O., Chen, Y., Kremerskothen, J., and Dong, J. (2014). KIBRA: in the brain and beyond. *Cell. Signal.* *26*, 1392–1399.
- Zhou, L., Bar, I., Achouri, Y., Campbell, K., De Backer, O., Hebert, J.M., Jones, K., Kessar, N., de Rouvroit, C.L., O'Leary, D., et al. (2008). Early forebrain wiring: genetic dissection using conditional Celsr3 mutant mice. *Science* *320*, 946–949.
- Zuin, J., Franke, V., van Ijcken, W.F., van der Sloot, A., Krantz, I.D., van der Reijden, M.I., Nakato, R., Lenhard, B., and Wendt, K.S. (2014). A cohesin-independent role for NIPBL at promoters provides insights in CdLS. *PLoS Genet.* *10*, e1004153.

Tau Prion Strains Dictate Patterns of Cell Pathology, Progression Rate, and Regional Vulnerability In Vivo

Sarah K. Kaufman,^{1,3,5} David W. Sanders,^{1,3,5} Talitha L. Thomas,³ Allison J. Ruchinskas,³ Jaime Vaquer-Alicea,³ Apurwa M. Sharma,^{3,4} Timothy M. Miller,² and Marc I. Diamond^{3,6,*}

¹Program in Neuroscience

²Department of Neurology

Washington University in St. Louis, St. Louis, MO 63130, USA

³Center for Alzheimer's and Neurodegenerative Diseases, University of Texas Southwestern Medical Center, Dallas, TX 75390, USA, USA

⁴Program in Biochemistry, Washington University in St. Louis, St. Louis, MO 63130, USA

⁵Co-first author

⁶Lead Contact

*Correspondence: marc.diamond@utsouthwestern.edu

<http://dx.doi.org/10.1016/j.neuron.2016.09.055>

SUMMARY

Tauopathies are neurodegenerative disorders that affect distinct brain regions, progress at different rates, and exhibit specific patterns of tau accumulation. The source of this diversity is unknown. We previously characterized two tau strains that stably maintain unique conformations in vitro and in vivo, but did not determine the relationship of each strain to parameters that discriminate between tauopathies such as regional vulnerability or rate of spread. We have now isolated and characterized 18 tau strains in cells based on detailed biochemical and biological criteria. Inoculation of PS19 transgenic tau (P301S) mice with these strains causes strain-specific intracellular pathology in distinct cell types and brain regions, and induces different rates of network propagation. In this system, strains alone are sufficient to account for diverse neuropathological presentations, similar to those that define human tauopathies. Further study of these strains can thus establish a structural logic that governs these biological effects.

INTRODUCTION

Tauopathies are a diverse group of neurodegenerative diseases characterized by clinical heterogeneity, progressive deposition of tau protein aggregates in characteristic brain regions, and distinct cellular pathologies (Lee et al., 2001). The etiology of this clinical and pathological diversity is unknown, but may hold the key to accurate diagnosis, prognosis, and therapy. Tauopathies include Alzheimer's disease (AD), frontotemporal dementias (FTDs), corticobasal degeneration (CBD), progressive supranuclear palsy (PSP), and others (Lee et al., 2001). Most tauopathies are sporadic, but dominantly inherited mutations in the *MAPT* gene, which encodes the tau protein, lead to specific

FTD syndromes (Hutton et al., 1998). Disease-associated mutations enhance the ability of tau to form amyloids, which are ordered protein assemblies rich in cross beta sheet structure (Knowles et al., 2014), and support a causal role for tau aggregation in pathogenesis (Barghorn et al., 2000).

In AD, the most common tauopathy (Lee et al., 2001), tau amyloid deposition occurs in an orderly fashion, beginning in the transentorhinal cortex, spreading to synaptically connected regions such as the hippocampus, and eventually moving to more distant regions of the neocortex (Braak and Braak, 1991). Multiple studies have now documented tau aggregate uptake, "seeding" (i.e., aggregate serving as a template for the conversion of monomer to a fibrillar form) and transfer of aggregates among cultured cells (Frost et al., 2009a; Guo and Lee, 2011; Holmes et al., 2013; Nonaka et al., 2010). Experimental evidence suggests that "propagation", or the movement of tau aggregates between connected neurons with seeding of tau monomer in recipient cells, mediates this progression in vivo (Sanders et al., 2016; Walker and Jucker, 2015). Importantly, injection of tau aggregates into mice that express human tau protein induces tau pathology that spreads outward along known brain networks (Clavaguera et al., 2009; Iba et al., 2013). Transgenic mice that limit the expression of tau to the entorhinal cortex also show spread of tau pathology to distant, connected brain regions (de Calignon et al., 2012; Liu et al., 2012). Together, these studies suggest that propagation of an aggregated state underlies the progression of tau pathology. These observations match the established mechanisms of propagation of pathological prion protein (PrP) (Prusiner, 1998).

The pathology of tauopathies occurs in distinct brain regions (Arnold et al., 2013), involves disparate brain networks (Raj et al., 2012; Zhou et al., 2012), and features unique tau inclusions in various cell types (Kovacs, 2015). Individuals may develop rapid or slow neurodegeneration even within the same syndrome (Armstrong et al., 2014; Thalhauser and Komarova, 2012). The basis of these diverse disease patterns is unknown.

We initially observed that tau adopts multiple, stably propagating conformers in vitro and speculated that structural variation in amyloids could underlie different tauopathies (Frost

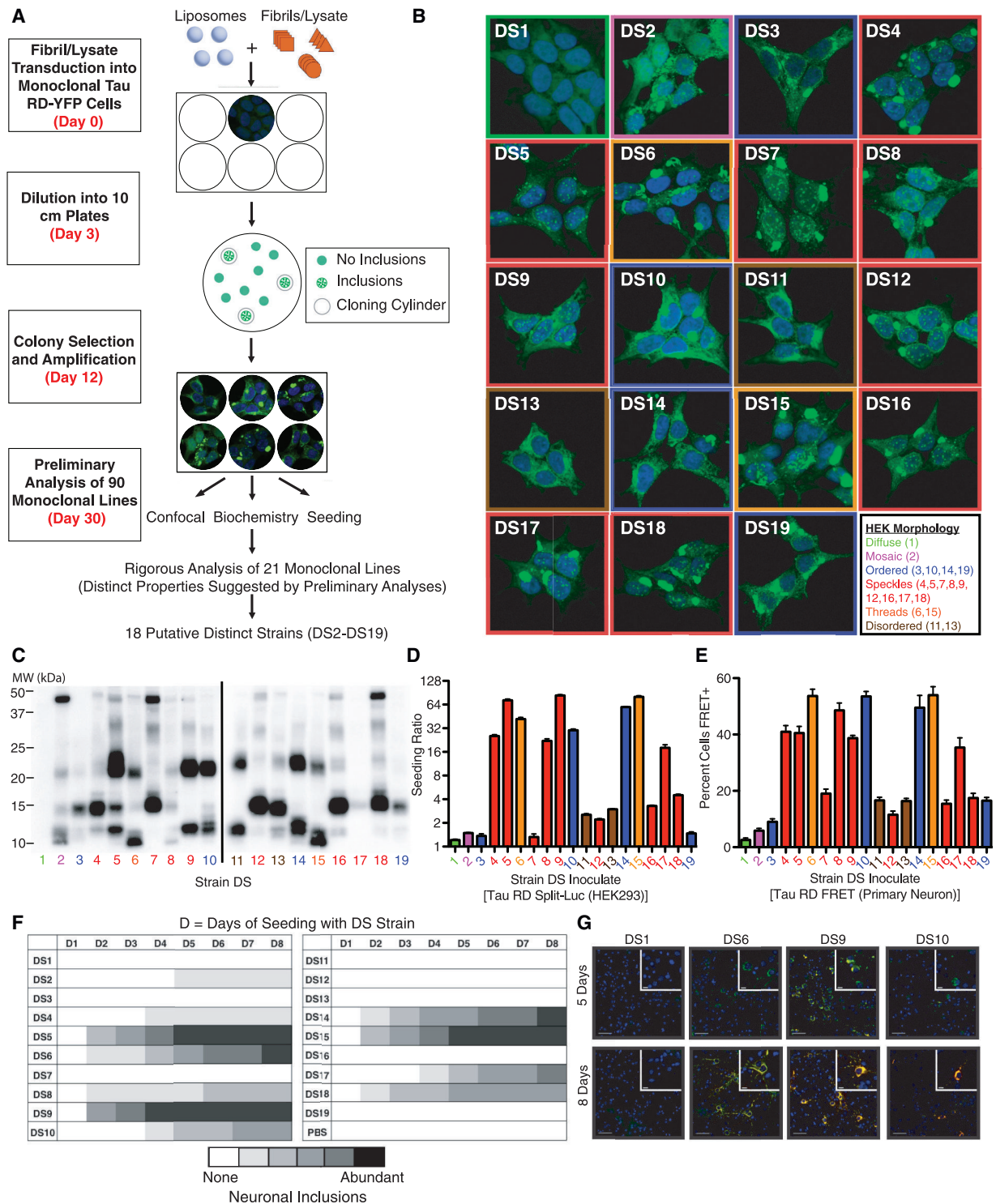


Figure 1. Generation and Characterization of a Tau Prion Strain Library

(A) A monoclonal HEK293 line stably expressing tau RD(P301L/V337M) (“LM”)-YFP (DS1) was treated with diverse sources of fibrillar tau seeds. 90 monoclonal lines that stably propagated tau inclusions were derived and characterized by the indicated metrics. 18 strains were differentiated based on their unique properties in the indicated assays. See Figure S1A for origin of inoculates used to derive each strain.

(B) Several tau inclusion phenotypes were identified in the monoclonal strains: mosaic (magenta), ordered (blue), speckles (red), threads (orange), and disordered (brown). With the exception of the mosaic phenotype, these inclusion phenotypes stably propagate to daughter cells over months of division. A negative control cell line (DS1) features diffuse tau (green). See Figures S2F–S2H for data regarding stability of specific strains upon passage into DS1.

(legend continued on next page)

et al., 2009b). We subsequently determined that tau forms discrete prion “strains” that propagate with remarkable fidelity through living systems (Sanders et al., 2014). The concept of prion strains derived from a realization that PrP prions can induce distinct transmissible spongiform encephalopathies with reproducible incubation times and patterns of neuropathology (Collinge and Clarke, 2007). It is now clear that PrP prion strains derive from different PrP amyloid conformations and produce predictable incubation times and neurodegenerative phenotypes upon serial passage *in vivo*. Moreover, distinct PrP strains probably account for the myriad features of individual PrP prion diseases (Collinge et al., 1996). The concept of a strain as a stably propagating structure that induces a specific and reproducible phenotype is critical, as it anticipates and enables mechanistic, diagnostic, and therapeutic insights based on knowledge of a defined molecular assembly (Sanders et al., 2016).

In addition to the distinct morphologies of tau fibrils and isoform composition of amyloid deposits in tauopathies (Lee et al., 2001), prior studies have suggested that unique tau amyloid structures might account for some aspects of clinical variation. Injection of homogenate from different tauopathy brains into a mouse model that expresses full-length human tau induced pathology that closely resembled that of the human source cases (Clavaguera et al., 2013). In a similar study, tau aggregates purified either from AD or CBD brains induced distinct patterns of tau pathology that affected different cell populations in transgenic mice that express 1N4R tau with a P301S mutation (PS19) (Boluda et al., 2015). However, both works relied upon a limited number of patient samples that likely contain a heterogeneous mixture of tau aggregate conformations (Sanders et al., 2014). Thus, the structure and biochemical properties of injected tau aggregates could not be well defined, making it impossible to directly link an amyloid structure to pathology.

Like PrP, tau forms bona fide prion strains that propagate in cells and animals (Sanders et al., 2014). We have now isolated 18 putative tau prion strains derived from recombinant, mouse, or human sources. We have studied them extensively *in vivo* and find that they can account for diverse and predictable patterns of neuropathology. This work thus develops a framework to understand the relationship of tau prion structure to distinct tauopathy syndromes.

RESULTS

Generation of a Library of Tau Strains

We previously created a monoclonal HEK293 cell line (Clone 1/DS1) that stably expresses the repeat domain (amino acids 244–372) of 2N4R tau with two disease-associated mutations (P301L and V337M), which allows us to indefinitely propagate tau prion strains derived from a variety of sources (Sanders et al., 2014). We treated DS1 cells with tau aggregates from diverse recombinant, mouse, and human brain samples (Figure 1A). We isolated and amplified 90 monoclonal cell lines that stably propagated tau aggregates and froze them for later study. Following preliminary analyses by several assays (inclusion morphology, limited proteolysis, and seeding by tau split-luciferase complementation, as described previously; Sanders et al., 2014), we isolated 18 putatively distinct strains (DS2–DS19; see Figure S1A for origin of each strain). These strains featured several striking differences in their subcellular distribution of aggregated tau (Figure 1B): a single, large juxtanuclear inclusion (ordered: DS3, DS10, DS14, and DS19), prominent nuclear inclusions (speckles: DS4, DS5, DS7, DS8, DS9, DS12, DS16, DS17, and DS18), aggregated tau that failed to organize into ordered inclusions (disordered: DS11 and DS13), fibril-like ribbons of aggregated tau throughout the cytoplasm (threads: DS6 and DS15), and one strain that sectorized with time, reverting from the aggregated state to the soluble diffuse state (mosaic: DS2). Importantly, with the exception of the mosaic strain DS2, every daughter cell featured the same inclusion morphology even after months of passage, suggesting that each monoclonal cell line stably propagated a single strain.

To examine whether the tau inclusions were composed of structurally distinct tau amyloids, we used limited proteolysis, an assay previously shown to differentiate prion strains derived from PrP (Bessen and Marsh, 1994) and tau (Sanders et al., 2014). We thus determined a “fingerprint” for each putative strain based on the regions of tau protected from digestion by pronase (Figure 1C). These digestion patterns were stable even upon dilution with HEK lysate (Figure S1B), confirming their independence from the amount of aggregated tau present in each sample. This assay suggested that while cell lines with different inclusion morphologies always propagated different

(C) Limited proteolysis using pronase differentiates the protected fibrillar cores in individual tau strains. Unique fingerprints along with other metrics indicated structurally distinct tau prion strains. See Figure S1B for pronase digestion of strains diluted with HEK lysate.

(D) Seeding activity of strains in a split-luciferase assay. A tau RD(P301S) split-luciferase assay based on enzymatic complementation following aggregation demonstrates differences in strain seeding activities following introduction into the cytoplasm using lipofectamine. The seeding ratio indicates luminescence relative to sham treatment. The biological quadruplicates with saturating quantities of lysate were averaged. The error bars represent SEM for biological quadruplicates.

(E) Strain seeding activities replicate in primary neurons expressing tau RD. Primary hippocampal neurons expressing tau RD(P301S)-CFP and tau RD(P301S)-YFP were treated with lysates derived from various strains. After 96 hr, neurons were fixed and the percentage of cells featuring seeded aggregates was determined by FRET flow cytometry. The error bars represent SEM for biological quintuplicates.

(F) Strain seeding activities replicate in primary neurons expressing full-length tau. Primary hippocampal neurons expressing 1N4R tau(P301S)-YFP were exposed to lysates from each strain and the extent of seeding was semiquantitatively determined at various time points (D = number of days) based on the extent of visible YFP puncta (0–5: 0 = none and 5 = abundant inclusions). The strains show variable lag times and extent of seeding, which correlates with the split-luciferase complementation assay.

(G) Strains differentially induce the formation of insoluble tau aggregates in primary neurons. Triton X-100 was used to remove soluble tau, and the primary neurons were stained for conformationally altered tau (MC1) 5 or 8 days following seeding. The strains show significant differences in seeding of aggregation in neurons. This parallels differences in the split-luciferase complementation assay. The scale bars represent 50 μm for the wide view and 10 μm for the inset images. See Figure S1C for representative images for all strains.

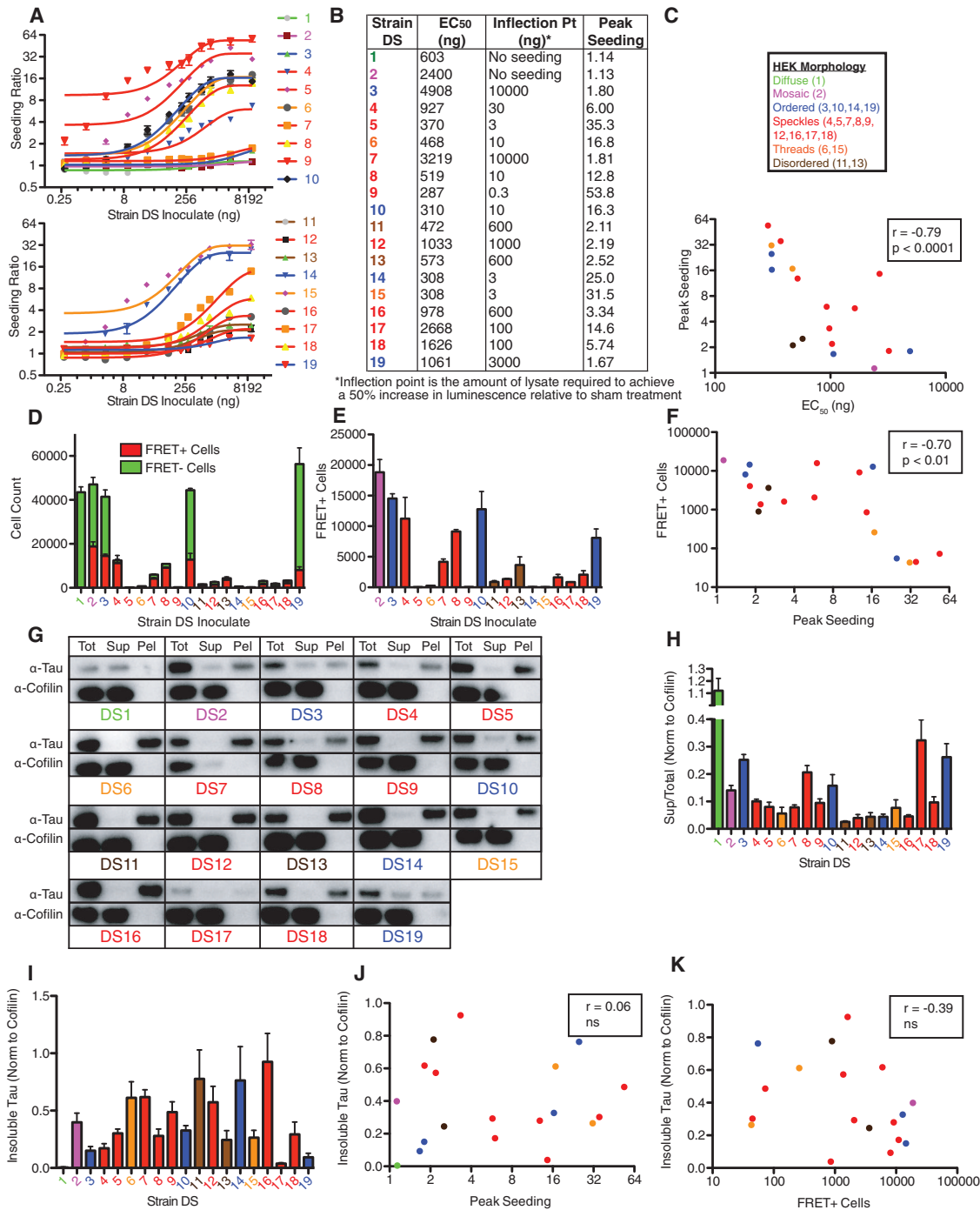


Figure 2. Seeding Activity, but Not Insoluble Tau, Correlates with Strain Toxicity In Vitro

(A) Strains have large differences in seeding of monomeric tau as determined by a tau split-luciferase complementation assay. The strain lysates were transduced into tau RD(P301S) split-luciferase cells, the seeding ratios relative to sham treatment were determined, and the titration curves were plotted using non-linear regression with a one-phase decay fit. The curves are plotted on two separate graphs for clarity. The error bars represent SEM for biological quadruplicates.

(B) Based on titration curves in the tau split-luciferase complementation assay, the EC₅₀, infection point, and peak seeding ratio were determined for each strain. The infection point represents the amount of lysate required to achieve a 50% increase in luminescence relative to sham treatment.

(C) Peak seeding significantly correlates with EC₅₀s for the strain library in the tau split-luciferase complementation assay.

(D) Strains display significant differences in toxicity. The strains were transduced in biological triplicates into cells overexpressing both tau RD(LM)-CFP and tau RD(LM)-YFP. After 72 hr, equivalent numbers of aggregate-containing (FRET+) cells were sorted for each condition by FRET flow cytometry. For the negative control (DS1), aggregate-negative (FRET-) cells were sorted. The sorted cells were allowed to proliferate in technical sextuplicates for 1 week.

(legend continued on next page)

conformations, inclusion morphology alone could not discriminate all strains.

Tau Strains Show Unique Seeding Profiles in Dividing Cells and Neurons

Next, we examined the ability of each putative strain to seed tau monomer using a cell line that expresses tau RD(P301S) fused to the N or C terminus of click beetle green luciferase enzyme (Mirbaha et al., 2015; Sanders et al., 2014). When saturating concentrations of lysate were transduced directly into the cytoplasm of these cells, induction of luminescence ranged from 0.3- to 80-fold increase in seeding at saturation versus background, termed the “seeding ratio” (Figure 1D). We observed no association between inclusion morphology and seeding. For example, the four ordered strains showed different seeding activity (DS3, DS10, DS14, and DS19). The relative seeding abilities of individual tau strains were largely recapitulated when lysates were applied to primary hippocampal neurons expressing tau RD(P301S) fluorescence resonance energy transfer (FRET) biosensor proteins (Holmes et al., 2014) (Figure 1E). We also observed these relative differences upon exposure of strains to primary neurons expressing full-length 1N4R P301S-YFP, suggesting common effects on either truncated or full-length tau. Strains also showed different lag phases to induce inclusions in neurons that express full-length tau (Figures 1F, 1G, and S1C).

Seeding Activity Correlates with Toxicity in Dividing Cells

To investigate the relationship between seeding activity and toxicity, we first performed a detailed titration of cell lysates (30 pg to 10 μ g) from the 18 putatively distinct strains. We determined the EC_{50} and peak seeding ratio for each strain using the tau split-luciferase complementation assay. Strains differentially seeded tau monomer in cell culture as reflected by their peak seeding ratios (Figures 2A and 2B). Different strains displayed $>10\times$ range for EC_{50} (DS9: 287 ng and DS3: 4908 ng) (Figure 2B). Peak seeding and EC_{50} strongly anti-correlated (Figure 1C), suggesting that peak seeding accurately reflects a strain’s potency in triggering tau aggregation.

We then compared the toxicity of each putative strain to their seeding potential. We generated a cell line (LM10) that expresses

a mutant tau RD FRET pair (CFP/YFP) at high levels and assessed the growth potential of cells propagating various strains after first isolating aggregate-positive cells by FRET fluorescence-activated cell sorting (FACS) (Holmes et al., 2014). Several ordered and mosaic strains (DS2, DS3, DS10, and DS19) lost the aggregated state (“sectored”) with repeated cell division (Figure 2D). All others stably propagated the aggregated state, but exhibited growth defects relative to LM10 cells that lacked tau aggregates (Figure 2E). Strains that sectored, a possible correlate of low seeding, were the least toxic. All three seeding metrics (peak seeding, EC_{50} and inflection point) correlated with inhibition of growth (Figures 2F, S2A, and S2B). In other words, strains that seeded more efficiently were significantly more toxic to cells that express high levels of monomeric tau.

We next performed sedimentation analyses to determine the level of soluble, insoluble, and total tau for all 18 putative strains (Figure 2G). While each strain (DS2–DS19) contained the majority of tau in the insoluble fraction (Figures 2G and 2H), different strains featured variable levels of insoluble (Figure 2I) and total (Figure S2C) tau. Neither total nor insoluble tau levels correlated with seeding (Figures 2J and S2D) or toxicity (Figures 2K and S2E). Thus, structural differences among strains, rather than soluble/insoluble tau levels per se, account for seeding activity and toxicity in dividing cells.

Diversity of Pathology Induced by Tau Strains

We hypothesized that to account for variation in tauopathies, individual tau strains should produce a wide array of pathological phenotypes *in vivo*. To test whether these putative strains can produce such diversity, we inoculated cell lysate from each line (DS1–DS19) into the PS19 mouse model that expresses 1N4R tau with the FTDP-17-associated P301S mutation from the prion promoter (Yoshiyama et al., 2007) (Figure 3A) and examined tau pathology induced 8 weeks after inoculation (Figures 3B–3J).

Pathology varied greatly between putative strains and was often, but not always, consistent with seeding activity observed in culture (Figures 1D–1G). Strains with low seeding activity (DS2, DS3, DS11, and DS19) produced a “rare seeding” phenotype *in vivo*, with limited AT8 pathology localized in CA1 of the ipsilateral hippocampus (Figures 3G and S3A). These strains appear

Aggregate-positive (FRET+) and aggregate-negative (FRET-) cells were then quantified by flow cytometry. The presence of FRET- cells in certain conditions reflects the fact that some strains lose the aggregated state with cell division. Technical sextuplicates were averaged for each biological replicate. The error bars represent SEM of biological triplicates.

(E) Aggregate-positive (FRET+) cells were quantified and plotted after 1 week of growth. This highlights the variable growth defects in aggregate-containing cells. The error bars represent SEM of biological triplicates.

(F) Toxicity correlates with seeding activity. The number of aggregate-positive (FRET+) cells for a strain was plotted against its peak seeding ratio in the tau split-luciferase complementation assay. The strains that seed more efficiently are associated with reduced growth of aggregate-positive cells. See Figures S2A and S2B for data indicating the correlation between a strain’s toxicity, EC_{50} , and inflection point in the seeding assay.

(G) Sedimentation analysis of strains. Lysates were ultracentrifuged and tau as well as a loading control protein (cofilin) were probed in the total, supernatant, and pellet fractions (total = Tot, supernatant = Sup, and pellet = Pel). The blots are representative of biological quadruplicates.

(H) Strains feature the majority of tau in the insoluble fraction. Densitometric analysis of tau in the total, supernatant, and pellet fractions was used to calculate supernatant to total ratios (a higher ratio indicates a smaller proportion of tau in the insoluble pellet). The error bars represent SEM of biological quadruplicates.

(I) Densitometric analyses highlight variation in insoluble tau in the various strains. The error bars represent SEM of biological quadruplicates. See Figure S2C for quantification of tau in the total fractions.

(J) Lack of correlation between insoluble tau and seeding activity as measured by peak seeding ratio. See Figure S2D for data indicating lack of correlation between total tau and seeding.

(K) Lack of correlation between total tau and seeding activity. See Figure S2E for data indicating lack of correlation between total tau and toxicity.

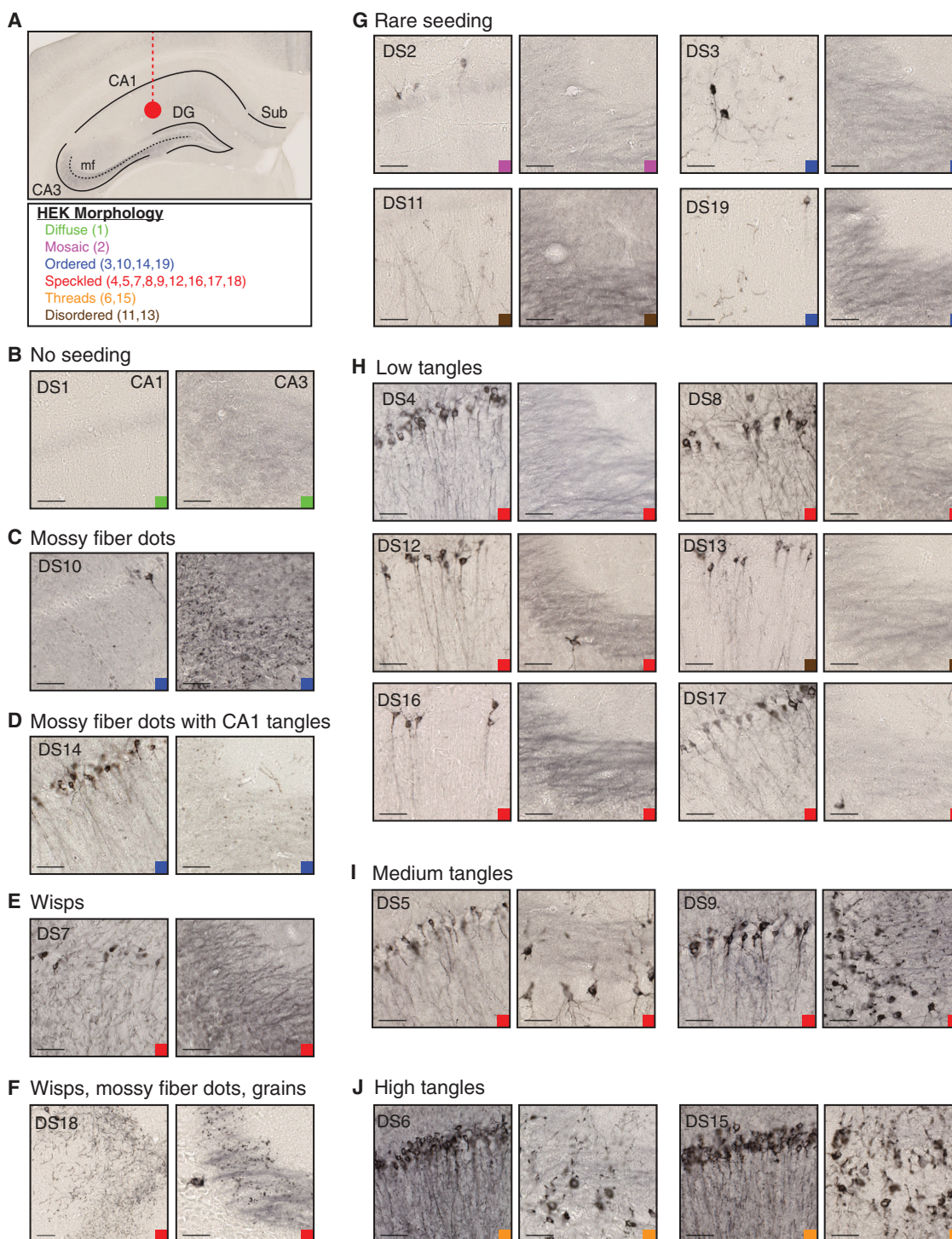


Figure 3. Tau Prion Strains Induce Diverse Patterns of Hippocampal Tau Pathology

(A) Tau strains (10 μ g) were injected into the left hippocampus of young PS19 mice ($n = 3$ per condition, see Table S1). Mouse brains were collected 8 weeks after injection. The relevant regions are indicated on a representative mouse hippocampus (dentate gyrus, DG; mossy fibers, mf; and subiculum, Sub). The HEK morphology table indicates the inclusion patterns in various strains, grouped by text color. The color-coded squares indicate these HEK cell-associated patterns in all images (B–J).

(B) DS1 injection produces no AT8 tau pathology. The representative images of CA1 and CA3 are displayed. The scale bars represent 50 μ m. See Figure S3A for whole hippocampal images for DS1–DS19.

(legend continued on next page)

different in terms of their AT8 subcellular localization (soma versus axonal pathology in DS2 and DS11), but this may reflect different levels of maturation of tau aggregates (e.g., pretangles and tangles). Several strains induced low level, yet consistent, tangle-like pathology in CA1 of the hippocampus (DS4, DS8, DS12, DS13, DS16, and DS17) (Figures 3H and S3A). Strains with the highest seeding activity in culture (DS5, DS6, DS9, and DS15) caused widespread tangle-like tau pathology throughout several hippocampal regions (Figures 3I and 3J). Pathology from these robust strains spread to distant regions such as the entorhinal cortex (EC) and contralateral hippocampus (Figure S3B).

Several putative strains induced unique pathology in the hippocampus. DS10 typically produced AT8-positive “dots” in the mossy fiber tracts of the ipsilateral and contralateral hippocampus, while mostly sparing CA1 pyramidal neurons (Figures 3C and S3C) as was observed in previous work (Sanders et al., 2014). DS14, which shared the same ordered cellular phenotype as DS10, also produced mossy fiber dots (Figure 3D). However, this strain showed higher seeding activity in culture and additionally induced CA1 tangle-like pathology in the ipsilateral and contralateral hippocampus (Figure S3C).

DS7 produced “wisps” that resemble neuropil threads (Figure 3E), while inducing weaker AT8 pathology in the main axon branches. This contrasted with several other speckled phenotype strains, which primarily induced AT8 pathology in the main axon (Figures 3H and 3I). DS18 produced wisps, mossy fiber dots, and “grains”, which are AT8 positive puncta found throughout the hippocampus (Figure 3F). DS18-inoculated mice also developed grain pathology in the contralateral hippocampus and wisps in the EC, indicating these specific phenotypic features can spread to distant regions (Figure S3D).

Critically, strains with matching limited proteolysis fingerprints produced similar histopathology in vivo (DS3 and 19; DS6 and DS15; and DS12 and DS16) (Figures 3F, 3G, and 3I). These pairs of similar strains (which may propagate identical tau aggregate conformations) displayed similar seeding activity and toxicity levels and induced similar phenotypes in primary neuron culture. Importantly, DS6 and DS15 derive from distinct aggregate sources (aged PS19 mice and recombinant fibrils, respectively), indicating that these strain-based phenotypes are conformation-specific rather than source-specific.

Stability of Distinct Tau Prion Strains

We previously demonstrated that DS9 and DS10 propagate unique conformations and produce identical phenotypes upon reintroduction into DS1 cells. To test whether other strains meet these same criteria for stable prion strains (Sanders et al., 2014), we transduced cell lysate from strains with distinct cellular morphology, seeding activity, and/or in vivo phenotypes into naive DS1 cells (DS1, DS4, DS6, DS7, DS9, DS10, or DS11). We first performed a blinded analysis of cell morphology from a polyclonal population at 5 and 8 days after transduction. The original DS1 and secondary polyclonal DS1 cell lines contained no aggregate-positive cells (Figures S2F–S2H). Blinded counts of DS4, DS7, and DS9 demonstrated the polyclonal population maintained the nuclear speckled phenotype, while DS10 and DS11 secondary lines were readily scored as ordered and disordered. DS6 threads that project from a large juxtanuclear aggregate are only readily apparent when assessing morphology on a population level rather than within individual cells. However, transduction of this cell line reliably induced overt “threads” in the vast majority of secondary cells at 5 days after transduction. By 8 days, tau aggregates in DS6 secondary cells appeared to mature, and the cellular morphology and blinded scoring results resembled that of the original DS6 cell line (Figures S2F–S2H).

To further examine the stability of each strain phenotype, monoclonal secondary cell lines that stably propagate aggregates were isolated by unbiased single-cell sorting at 4 days after transduction of DS4, DS6, DS7, DS9, DS10, and DS11 into the LM1 cell line. Secondary strains displayed the same cellular morphology as the original cell lines (Figure S7A). We tested the seeding activity of each secondary cell line compared to the original strains by transducing cell lysate into a biosensor cell line that expresses tau RD(P301S)-CFP/YFP and quantifying FRET by flow cytometry (Holmes et al., 2014). Secondary cell lines produced seeding activity similar to their respective source strain (Figure S7C). Thus, these are stable strains that induce unique cellular phenotypes even upon serial passage in culture.

Specific Strains Reliably Induce Astrocytic Pathology

Several tauopathies, including CBD and PSP, feature unique glial cell pathology (Kovacs, 2015). While the mechanisms that underlie these patterns are not known, previous work suggested that inoculation of CBD patient lysate into PS19 mice is sufficient to

(C) DS10 produces AT8 positive mossy fiber dot pathology, with limited CA1 pathology as observed previously (Sanders et al., 2014). See Figure S3C for contralateral mf pathology.

(D) DS14 seeds mossy fiber dots similar to DS10, as well as tangle-like pathology, indicating that it is a distinct strain despite its other similar features to DS10. See Figure S3C for contralateral mossy fiber and CA1 pathology.

(E) DS7 induces wisps that resemble neuropil threads, but may fall within axon terminals and the dendritic tree of pyramidal neurons.

(F) DS18 pathology includes wisps and mossy fiber dots similar to DS7 and DS10, respectively, as well as grains that are found throughout much of the hippocampus. See Figure S3D for data indicating that these phenotypes spread to distant synaptically connected locations including the entorhinal cortex.

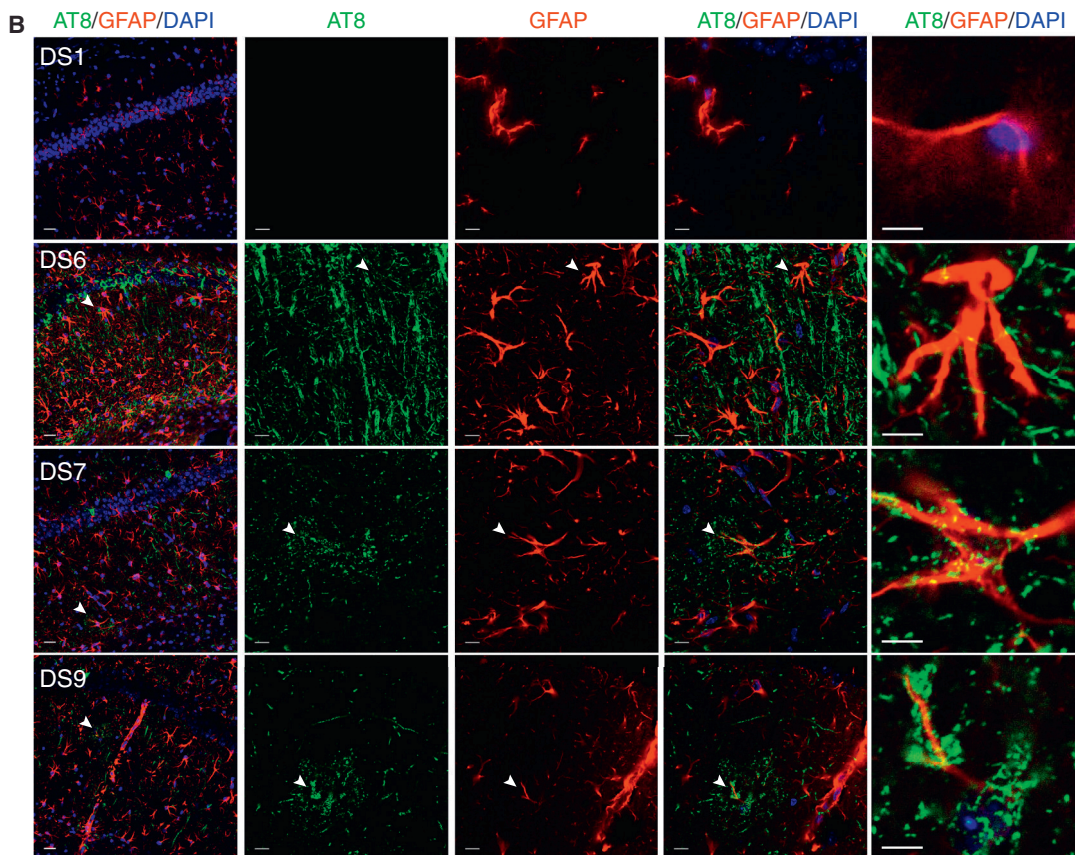
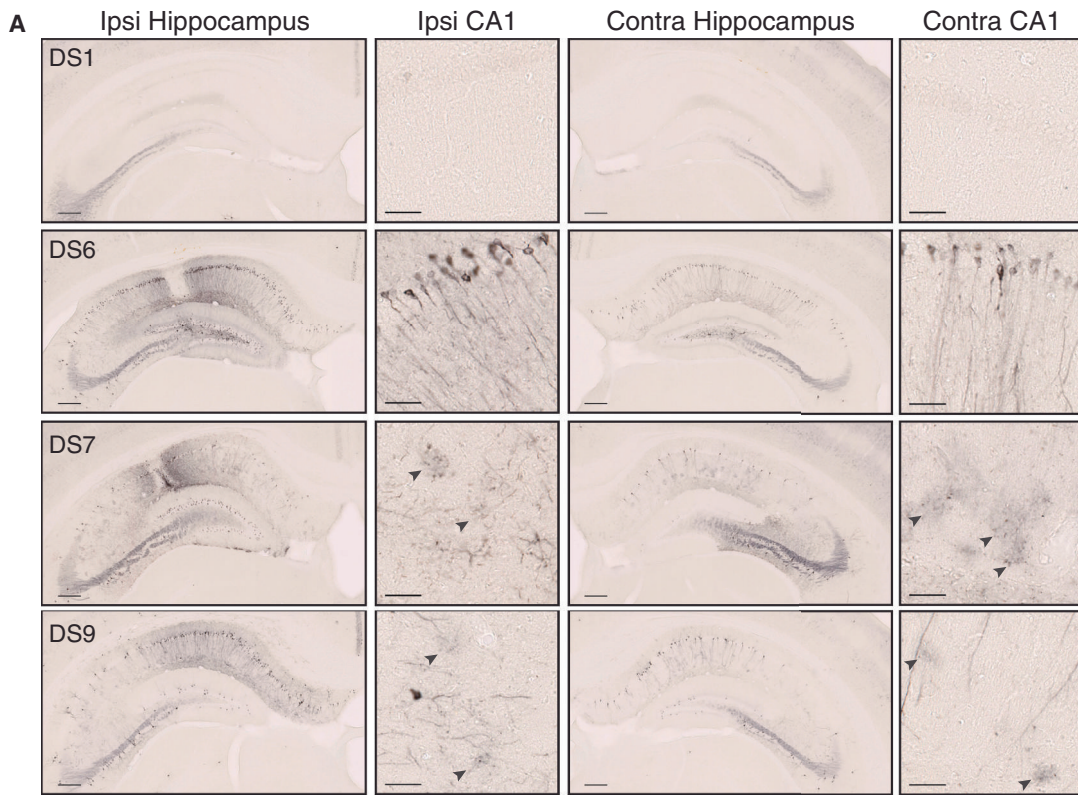
(G–J) Several strains produce different levels of tangle-like AT8 pathology in CA1 and CA3 of the hippocampus.

(G) DS2, DS3, DS11, and DS19 induce rare AT8 pathology in pyramidal CA1 neurons. The localization of AT8 staining varies in certain cases (cell body versus axonal pathology in DS2 and DS11, respectively).

(H) DS4, DS8, DS12, DS13, DS16, and DS17 induce slightly stronger tangle-like pathology in CA1 of the hippocampus (“low tangles”). CA3 shows limited or no tangle pathology at this time point.

(I) DS5 and DS9 produces AT8 tangle-like tau pathology that reaches CA3 of the hippocampus as well as CA1 pyramidal cells (“medium tangles”). Tangles appear relatively consolidated within the soma of neurons. See Figure S3B for spread of tau pathology to the contralateral hippocampus and ipsilateral EC.

(J) DS6 and DS15 display the highest level of tangle-like AT8 pathology (“high tangles”). Highly consolidated pathology was observed throughout cell bodies and axons of CA1 and CA3 neurons. See Figure S3B for spread of tau pathology to the contralateral hippocampus and ipsilateral EC.



(legend on next page)

induce astrocytic pathology (Boluda et al., 2015). Interpretation of this result was limited by the potential for individual patient brains to contain multiple strains (Sanders et al., 2014). Further, two different paradigms were used for purification of AD versus CBD derived tau, which might also have affected the observed phenotypes (Boluda et al., 2015). We thus assessed astrocytic pathology after inoculation with isolated, individual tau strains.

At 8 weeks after inoculation with DS7 and DS9, we observed tau pathology reminiscent of astrocytic plaques in multiple animals, as noted by small AT8-positive inclusions arranged in ring-like structures (Figure 4A) (Yoshida, 2014). Strains that produced higher levels of tau pathology such as DS6 did not show similar plaque pathology at this time point (Figure 4A). Co-staining with GFAP and AT8 indicated that these accumulations consist of phospho-tau within or directly adjacent to astrocytes as is typical of astrocytic plaques (Figure 4B) (Yoshida, 2014). DS12, DS15, DS16, and DS18 induced a small degree of astrocytic plaque-like pathology at 8 weeks (Figures S4A and S4B). Given these findings, we retrospectively quantified the number of animals with astrocytic plaque-like pathology after completion of the time course injection experiment described below. DS7 or DS9 inoculations induced astrocytic plaque-like pathology in the majority of inoculated mice by 8 weeks (Figure S4A). In contrast, DS4 and DS6 induced limited plaque pathology by 12 weeks, which was far less robust than the level observed in DS7 and DS9 inoculated animals (Figures S4A and S4C). Thus, this phenotype is likely independent of seeding activity and suggests specific tau conformations preferentially and predictably induce astrocytic tau pathology.

While two CBD-derived strains showed a small degree of astrocytic plaque-like pathology (DS12 and DS16), they were sparse at this time point (Figures S4A and S4B). We examined mice inoculated with DS12 and DS16 at 6 months after injection and observed increased levels of astrocytic pathology (Figure S4D). This suggests these two CBD-derived strains produce robust astrocytic plaque pathology after an extended incubation period compared to DS7 or DS9. DS11 and DS13, which were also isolated from CBD patients, did not induce astrocytic plaque pathology 8 weeks after injection. Individual CBD patients likely have multiple tau strains present in their brains (Sanders et al., 2014), which may give rise to the overall pattern of histopathology observed in patients. Alternatively, DS11 and DS13 may simply require more time to produce robust astrocytic plaque pathology in this mouse model, as was observed for DS12 and DS16 (Figures S4B and S4D).

Regional Vulnerability to Specific Strains

Tauopathies feature accumulation of tau pathology in distinct brain regions (Arnold et al., 2013), yet the mechanisms that un-

derlie these patterns are not well understood. To test whether strains differentially induce pathology in specific brain regions, we inoculated DS1, DS4, DS6, DS7, DS9, DS10, or DS11 into six locations per mouse: sensory cortex (SC), caudate/putamen (CP), visual cortex (VC), hippocampus (Hip), thalamus (Thal), and inferior colliculus (IC) (Figure 5A). We chose these strains based on their unique limited proteolysis patterns, different tau pathology induced in the hippocampus, and their low (DS7 and DS11), medium (DS4 and DS10), or high (DS6 and DS9) seeding activity in culture. Further, DS4 and DS11 derive from AD and CBD brain homogenates, respectively. Patients with these diseases have different patterns of tau deposition (Arnold et al., 2013).

After 5 weeks, we quantified the level of AT8 pathology these strains induced at each injection site in a blinded fashion (Figure 5B). All produced hippocampal pathology consistent with the previous injection paradigm, illustrating the reproducibility of these phenotypes (Figure 5C). Strains with the strongest seeding activity in culture (DS6 and DS9) produced pathology in every injected region. DS4, a medium-seeding strain, induced moderate pathology in each region except the IC. DS11 pathology was entirely limited to the hippocampus (Figures 5B and 5C).

DS10 again induced pathology specific to the mossy fiber tracts of the hippocampus (Figure S5A), with limited pathology in the caudate/putamen and thalamus. Of note, it did not produce any pathology in the injected cortical regions. In contrast, DS7 produced limited AT8 pathology in each targeted brain region (Figures 5B and 5C). The specificity of DS10, despite its strong seeding activity, and promiscuity of DS7, despite its weak seeding activity (Figures 1D–1G), were remarkable. These studies indicate tropism of certain strains for specific brain regions (mossy fiber tracts, cortical structures, and IC) that is independent of simple metrics such as seeding activity.

Strains Induce Different Rates of Spread of Tau Pathology along Neuronal Networks

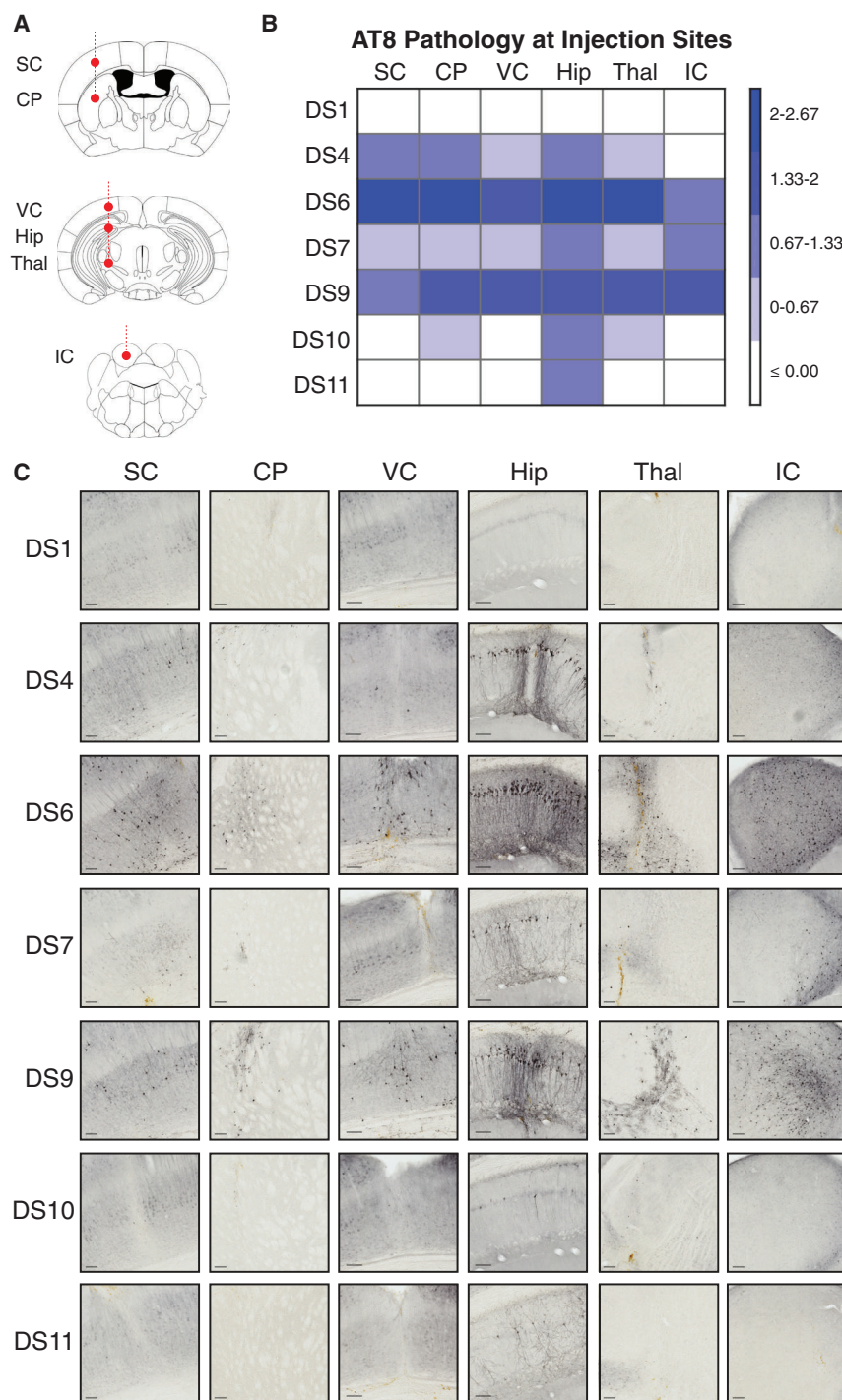
Even within a single clinical syndrome, tauopathy patients experience rapid or slow rates of progression (Armstrong et al., 2014; Thalhauser and Komarova, 2012). PrP strains show different lag phases and rates of neurodegeneration in animal models of prion diseases (Collinge and Clarke, 2007), suggesting this phenomenon may be linked to specific aggregate conformations. While several factors may contribute to the rate of degeneration observed in tauopathy patients, rapid spread of tau pathology likely accelerates this process. Thus, we tested the relationship between strain characteristics and rates of spread of tau pathology.

To control for differences in insoluble material, we first quantified the insoluble tau present in lysate from DS1, DS4, DS6, DS7, DS9, and DS10 prepared for this time course experiment. As

Figure 4. Specific Strains Induce Astrocytic Tau Pathology

(A) AT8 tau pathology 8 weeks after injection with DS1, DS6, DS7, or DS9. DS1 does not induce tau pathology. DS6, DS7, and DS9 develop strong AT8 staining in ipsilateral and contralateral hippocampi. DS7 and DS9 develop diffuse, circular-shaped accumulations of AT8 staining that do not appear to localize to a neuronal cell body (black arrow heads). The scale bars represent 250 μ m for the whole hippocampus and 50 μ m for CA1.

(B) Co-staining of AT8 (green) for phospho-tau, GFAP (red) for astrocytes, and DAPI (blue) for cell nuclei. DS1 shows limited GFAP staining and no AT8 pathology. DS6 shows strong AT8 staining with limited overlap of AT8 staining. DS7 and DS9 injected mice display astrocytic plaque-like pathology that either deposits within or around GFAP-positive processes of astrocytes. The scale bars represent 25 μ m for left column and 10 μ m for all remaining images. For further quantification and representative images of other strains that display limited astrocytic plaque pathology, see Figure S4.



expected, each strain contained a large amount of insoluble tau (Figures 6A and 6B). We hypothesized that a strain's ability to seed aggregation of endogenously expressed monomeric tau would primarily determine the rate of spread of pathology. We predicted that strains such as DS6 and DS9 with high seeding activity in culture and in vivo (Figures 1D, 5B, and 5C) would produce rapid spread of pathology even after inoculation of reduced

hippocampus until 12 weeks (Figures 6D and 6E). Thus, stronger strains induced more rapid spread of pathology even with a reduced amount of insoluble tau inoculum, presumably due to more efficient seeding and spread of endogenous tau aggregates.

While these inoculations induced robust neuronal tau pathology and strain-specific patterns of astrocytic tau pathology, we

Figure 5. Tau Strains Preferentially Seed Pathology in Specific Brain Regions

(A) Six tau strains were injected simultaneously into six brain regions: SC; CP; VC; Hip; Thal; and IC (5 μ g per region). The mice that received DS1 (negative control), DS4, DS6, DS7, DS9, DS10, or DS11 strain injections were kept for 5 weeks post-inoculation before assessment of AT8 tau pathology (n = 3 per condition).

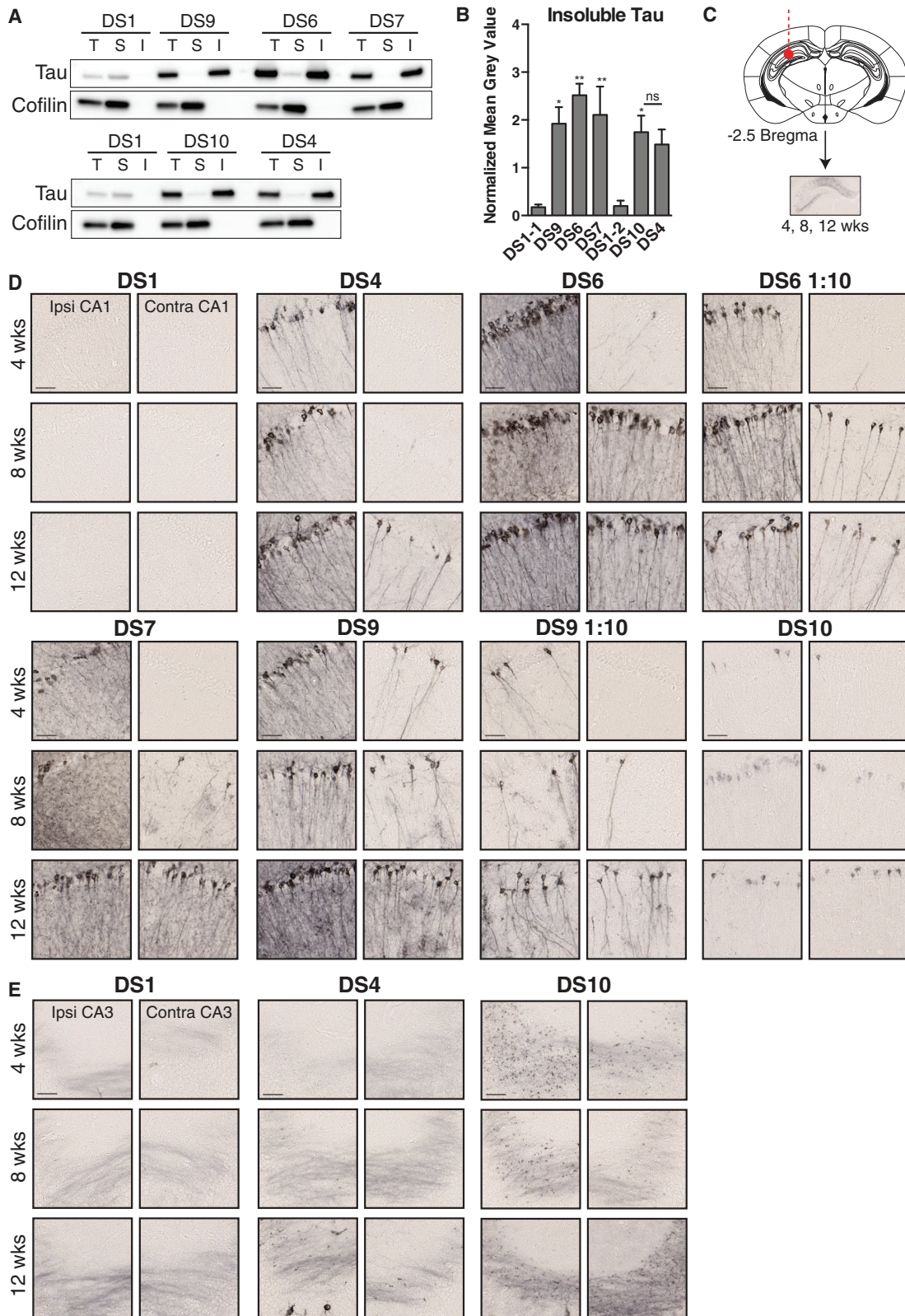
(B) Strains preferentially induced tau pathology in specific brain regions. Slices that contained the injection sites were stained for AT8 phospho-tau. Each injection site was assessed in a blinded fashion for tau pathology on a 0–3 scale (none, low, medium, and high). The level of background AT8 pathology at each injection site was accounted for by subtracting the level of pathology present in DS1 mice within each brain region. A binned heatmap represents the level of pathology observed at the injection site for each strain. Note differences in regional vulnerability.

(C) Representative images are displayed for each brain region injected with the different tau strains. The scale bars represent 100 μ m. DS10 mossy fiber pathology is shown in Figure S5A.

levels of insoluble tau. To test this hypothesis, we included DS6 and DS9 lysate diluted 1:10 as part of this time course experiment.

We injected cell lysate from each condition into the hippocampus of young PS19 mice and collected brains at 4, 8, and 12 weeks post-injection (Figure 6C). While each strain induced tau pathology in the contralateral hippocampus, this occurred at different time points (Figures 6D and 6E). DS6 and DS9 pathology progressed rapidly to the contralateral hippocampus, beginning as early as 4 weeks (Figure 6D). DS10 induced mossy fiber dots and limited CA1 pathology in the ipsilateral and contralateral hippocampus by 8 weeks (Figures 6D and 6E). DS7 wispy pathology also spread to the contralateral hippocampus by 8 weeks (Figure 6D).

While dilution of DS6 and DS9 decreased the initial level of pathology induced upon inoculation, we observed tau pathology in the contralateral hippocampus at 8 weeks. In contrast, DS4 did not show tau pathology in the contralateral



(legend on next page)

did not observe overt neuronal loss at these time points (data not shown). However, to begin to assess the functional effects of distinct strains, we examined the patterns of microglial pathology induced at 12 weeks after inoculation. Compared to DS1 inoculated mice, several strains displayed Iba1-positive rod microglial phenotype, with elongated projections that align along axons of CA1 pyramidal neurons (Figures S6A–S6C). We performed blinded quantification of ramified and rod microglia ipsilateral and contralateral to the site of inoculation. DS6 induced the largest degree of rod microgliosis, while DS7 produced very limited rod microglial pathology. DS4, DS9, and DS10 also produced rod microglia, but we observed this phenotype in the contralateral hippocampus primarily in DS6 and DS10 inoculated mice.

To test the stability of tau strains *in vivo*, we transduced brain homogenate from the hippocampus of mice at 8 weeks after inoculation into the naive DS1 cell line. DS4, DS6, DS9, and DS10 produced morphologies consistent with the original inoculum (Figures S2F–S2H and S7D). However, brain-derived DS7 produced a mixture of cellular morphologies. This is in contrast to DS7 cell lysate, which stably induces its cellular phenotype in culture, suggesting DS7 may imperfectly template its conformation onto full-length P301S tau in this mouse model.

We isolated monoclonal lines derived from inoculated mouse tissue by transducing brain homogenate into the DS1 line and sorting single aggregate-containing cells. Tau derived from mice inoculated with DS6 strain readily produced thread-containing inclusions in the population of converted cells (Figures S2F and S7D). However, isolation of monoclonal lines was not possible due to toxicity (0/36 individual colonies survived). In contrast, transduction of mouse-derived tissue inoculated with DS7 produced few inclusions in the population overall, with only one resultant monoclonal line. This is consistent with the low seeding activity of the original DS7 line. Multiple secondary lines were derived from brains originally inoculated with DS4, DS9, and DS10 (Figure S7B). FRET-based seeding activity of the secondary cell lines resembled that of the original lines (Figure S7C). Thus, several of these strains stably propagate their phenotype even upon passage through mice.

To assess AT8 pathology induced by each strain, we performed a blinded analysis of AT8 staining in slices at the level

of the locus coeruleus, hippocampal injection site, and caudate/putamen. We averaged AT8 pathology rankings for each region and displayed them as a heatmap to visualize the spread of tau pathology (Figure 7A). We subsequently created a limited heatmap for each strain that focuses on specific brain regions, several of which developed pathology over time (Figure 7B). DS10 once again displayed marked neuronal specificity, with strong pathology only in the mossy fiber tracts (Figures 7A and 7B). Blinded analysis also confirmed that DS4 exhibits slower kinetics than DS6 or DS9 even when the latter strains are diluted 10-fold (Figure 7B). DS4 did not develop strong pathology outside the ipsilateral hippocampus until 12 weeks after injection, while the stronger strains showed AT8 staining in distant brain regions by 8 weeks. DS7 induced robust pathology at the injection site as observed previously (Figures 3 and 5). However, the spread of DS7 pathology was relatively slow and appeared limited to the hippocampus (Figures 7A and 7B).

DS6 and 9 spread pathology rapidly to specific brain regions after 4 weeks. DS6 strongly targeted the ipsilateral retrosplenial cortex and LC, while DS9 pathology spread most strongly to the ipsilateral entorhinal cortex and thalamus. Despite these initial differences, by 8 weeks the patterns of pathology induced by these strains largely resembled one another (Figure 7B). While diluted lysate of DS6 and DS9 induced lower levels of pathology at early time points, they induced pathology that spread faster and farther than DS4, DS7, or DS10 and followed similar patterns to that of undiluted DS6 and DS9 lysate (Figure 7B).

We next performed a seeding assay on tissue from the ipsilateral and contralateral hippocampus, thalamus, and sensory cortex at 8 weeks after injection as a second metric of tau pathology. We transduced homogenized brain regions into the FRET biosensor cell line (Holmes et al., 2014) and quantified seeding after 2 days in culture. We have observed that all seeding activity measured after inoculation of DS9 into the hippocampus of tau knockout mice completely dissipates by approximately 6 weeks (data not shown), which suggests any signal identified at this time point likely derives from induced aggregation of endogenous tau expressed in this mouse line.

Several strains displayed robust seeding in the ipsilateral hippocampus (DS4, DS6, DS9, DS10, and 1:10 diluted DS6 and

Figure 6. Strains Induce Different Rates of Tau Pathology Spread

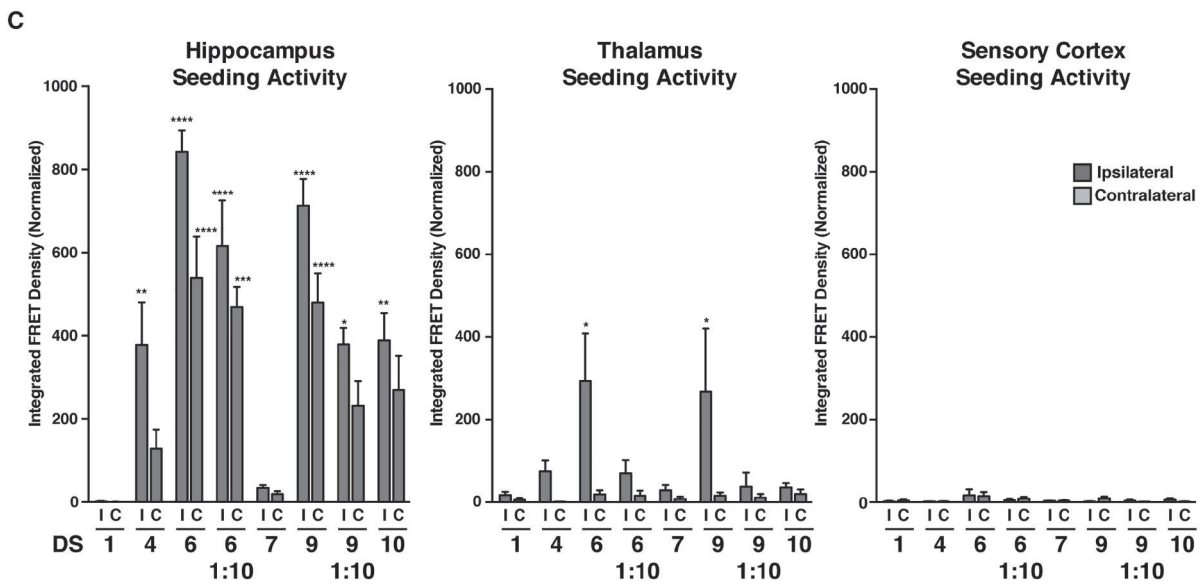
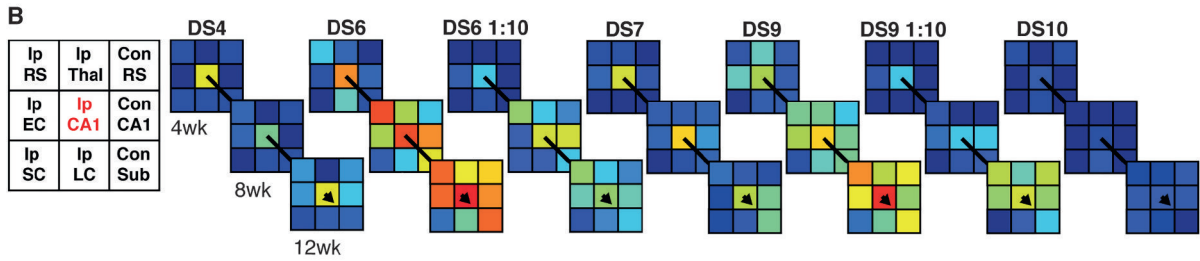
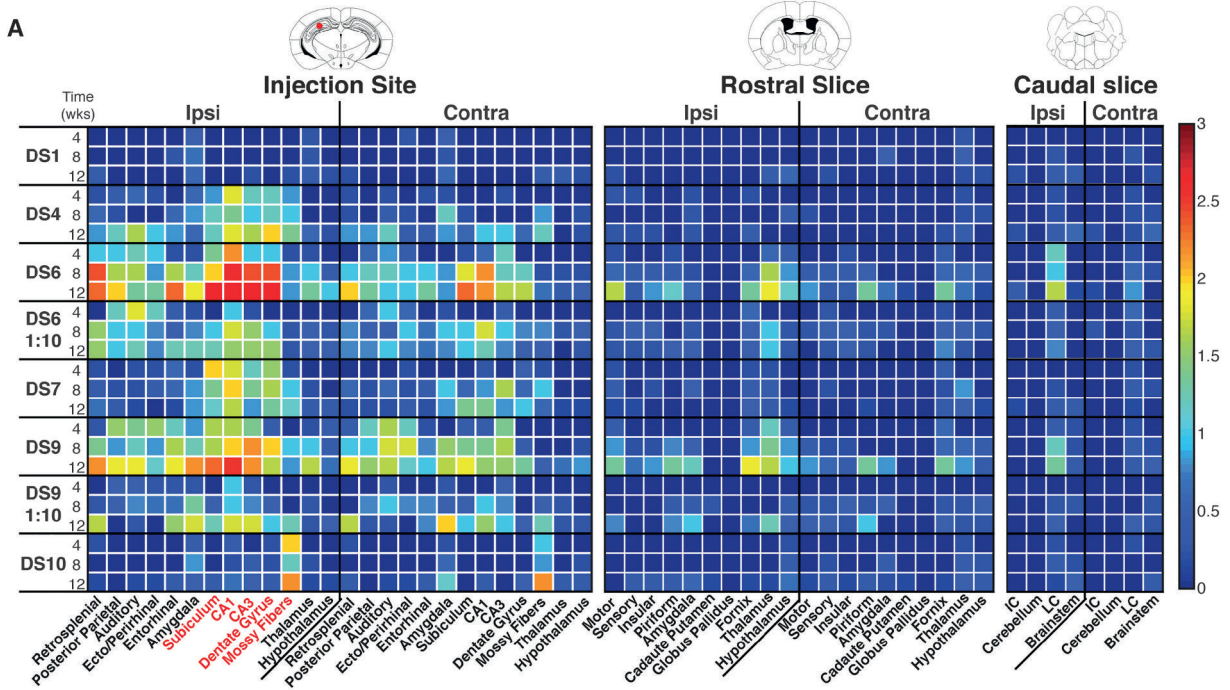
(A) Sedimentation analysis was performed on cell lysate used for the time course inoculation experiment. Each strain contains a large amount of insoluble material (total, T; soluble, S; and insoluble, I). Western blot analysis of insoluble tau was performed on three biological replicates. For each experiment, the soluble fraction was loaded at 2× the concentration of the total and insoluble fractions. A cofilin loading control was performed on the blots to verify the same amount of cell lysate was added for each strain.

(B) The level of insoluble tau present in each strain was quantified by measuring the mean gray value of the insoluble tau western blot band. The samples were normalized to the mean gray value of cofilin in the total cell lysate fraction. DS1-1 and DS1-2 represent biological replicates of DS1. ANOVA shows strains have significantly more insoluble tau than DS1. A two-way t test demonstrates DS10 and DS4 do not contain significantly different levels of insoluble tau (ns for $p > 0.5$; * for $p \leq 0.05$; and ** for $p \leq 0.01$). The error bars represent SEM of biological triplicates.

(C) Strains were inoculated into the hippocampus of young PS19 mice ($n = 5$ – 6 per condition per time point, see Table S1). DS6 and DS9 lysate diluted 1:10 in HEK293 cell lysate were also injected ($n = 4$ – 5 per condition per time point). The mice were collected at 4, 8, or 12 weeks.

(D) Representative images of ipsilateral and contralateral CA1 are displayed for each strain at 4, 8, and 12 weeks post-injection. AT8-positive tau pathology spreads to the contralateral hippocampus at different time points. The diluted DS6 and DS9 lysate show faster spread than concentrated DS4 and more robust spread than DS7 and DS10 at 8 weeks post-injection. The scale bars represent 50 μm . See Figure S6 for data regarding strain-specific rod microglial phenotype present at 12 weeks after inoculation.

(E) Spread of mossy fiber dot pathology occurs by 8 weeks in DS10 mice. The dot pathology appears eventually to develop in DS4 mice, but spread appears delayed compared to DS10.



(legend on next page)

DS9). While each of these strains spread to the contralateral hippocampus, DS4 showed distinctly less contralateral seeding activity as a percentage of the ipsilateral hippocampus (Figure 7C). Further, DS6 and DS9 showed variable yet significant seeding activity in the ipsilateral thalamus. The level of seeding observed in DS1 inoculated mice is consistent with the level observed in this mouse model at 4–5 months of age, suggesting this signal is due to spontaneous aggregation of endogenous tau that normally occurs within this model (Holmes et al., 2014). DS7 showed remarkably low seeding activity, while DS10 induced relatively robust seeding from the hippocampus despite only inducing mossy fiber AT8 tau pathology (Figures 6E and 7C). This is consistent with the seeding activity for the original inoculum as observed by the split-luciferase assay (Figures 1D and 2G–2I). These results are also consistent with the different rates of spread observed by AT8 immunohistochemistry for DS4 versus DS6 and DS9, while providing a separate metric to quantify the spread of pathology for strains such as DS10.

DISCUSSION

Overview of Findings

We have tested whether specific tau prion strains can account for critical neuropathological features that are used to discriminate tauopathies. We characterized strains by various biochemical and biological metrics, including inclusion morphology, seeding activity in dividing cells and primary neurons, detergent solubility, cellular toxicity, limited proteolysis, and reintroduction into reporter cells. We inoculated all 18 strains individually into the hippocampi of a transgenic tauopathy mouse model, causing distinct patterns of tau pathology in cell bodies, axons, and dendrites. To test for regional vulnerability, we injected six strains into six different brain regions and waited 5 weeks to evaluate pathology. Many induced pathology in all regions (DS6, DS7, and DS9), while others exhibited restricted patterns in which very little or no pathology occurred despite direct exposure of neurons to a particular strain (DS4, DS10, and DS11). We next tested whether strains exhibited unique rates of propagation through the brain. In this case, we observed correlations with *in vitro* parameters: strains with high seeding activity tended to spread more rapidly through the brain, with one important exception—strain DS10—which only spread to the contralateral mossy fiber tracts of the hippocampus. These observations suggest that distinct tau prion strains could

account for many of the features observed in human tauopathies.

Limitations of this Experimental Approach

It is impossible at this time to directly control tau strain production *in vivo* using transgenic mice or to propagate strains faithfully and indefinitely *in vitro* without using cultured cells. This work relies on a cell model that expresses a truncated form of tau with a fluorescent protein tag, an imperfect system that has nonetheless allowed us to propagate distinct tau prion strains indefinitely. Likewise, in mice, we utilized a model that expresses full-length human tau (1N4R) that contains a disease-associated mutation (P301S) (Yoshiyama et al., 2007). While this obviously deviates from sporadic tauopathy that occurs in most individuals, it has enabled us to rapidly and reliably induce unique tau pathology based on local inoculation. We cannot exclude the possibility that inoculated tau prions themselves are moving throughout the brain and inducing pathology based on local uptake rather than true trans-neuronal propagation (Rey et al., 2013). Nonetheless, our observations suggest a fundamental disease mechanism whereby strain-specific differences govern seeding, propagation, and specific regional vulnerability.

The Utility of Studying Isolated Strains

Our prior work has indicated that human tauopathy brains, even those carefully defined by histopathology, exhibit enormously diverse strain content within and between individuals (Sanders et al., 2014). Thus syndromes that appear to be clinically and neuropathologically identical are potentially quite distinct in terms of their strain composition. This presents obvious challenges when attempting to define strains present in human disease based principally on inoculation of purified aggregates into mice. Fibril preparations created *in vitro* also exhibit tremendous conformational heterogeneity, as clearly illustrated by studies of α -synuclein in which one dominant fibril structure shifts to another upon serial seeding reactions (Guo et al., 2013). In this work, we have stably propagated strains with specific biochemical properties in a simple culture system based on expression of tau RD-YFP. While technical limitations have restricted our ability to define the specific structures of tau aggregates present in these strains, this work suggests a single dominant structure is faithfully propagated in each line. This has enabled us to make predictions about phenotypes *in vivo* based on properties observed *in vitro*.

Figure 7. Strain Dictates the Rate and Pattern of Spread of Tau Pathology

(A) Slices from mice injected with each strain at each time point were stained for AT8 pathology. Tau pathology was quantified in a blinded fashion on a 0–3 scale and averaged for each location within a given condition ($n = 5–6$ per condition). A continuous heatmap was generated. Note differential rates of spread and regional vulnerability. The regions are listed on the x axis and conditions/time points are on the y axis.

(B) Limited heatmaps were generated from the above data set (Figure 7A). Ipsilateral (Ip) and contralateral (Con) regions were included to assess patterns and rates of spread of pathology (retrosplenial cortex, RS; EC; SC; Thal; CA1 of hippocampus, CA1; locus coeruleus, LC; and subiculum, Sub). Time points are arranged in order from earliest (4 weeks) to latest (12 weeks). Diluted DS6 and DS9 lysates are also displayed (DS6 1:10 and DS9 1:10).

(C) Homogenized tissue from the hippocampus, thalamus, or sensory cortex of mice 8 weeks after inoculation with strains was applied to tau biosensor cell lines. After 48 hr, cells were collected and flow cytometry was performed to quantify the level of seeding activity in each region by integrated FRET density (percent FRET-positive cells*median fluorescent intensity of FRET positive cells = IFD) (Holmes et al., 2014). DS4 induces lower spread of seeding activity to the contralateral hippocampus at 8 weeks. DS10 induces high seeding activity despite limited AT8 pathology, while DS7 induces low seeding activity despite high AT8 pathology. DS6 and DS9 also induce seeding activity in the ipsilateral thalamus. A one-way ANOVA with Bonferroni correction for multiple comparisons was performed between ipsilateral DS1 and every other sample within a given region (* $p \leq 0.05$; ** $p \leq 0.01$; *** $p \leq 0.001$; and **** $p \leq 0.0001$). The error bars represent SEM, $n = 4–5$. See Figure S7 for data regarding secondary cell line isolation of strains derived from inoculated mice or strain cell lysate.

Prion Strains Characterized In Vitro

PrP prion strains have distinct, yet reproducible patterns of incubation time, neuropathology, and behavioral phenotypes (Collinge and Clarke, 2007). Strains are presumably distinct amyloid structures that faithfully replicate in a living system and produce well-defined pathology. Thus, if a strain is identified, it is possible to predict incubation time and resultant pathology (Collinge and Clarke, 2007). In this work, we characterized multiple tau strains from recombinant, mouse, and patient sources *in vitro* and *in vivo*. Their detailed characterization *in vitro* using several metrics (inclusion morphology, solubility, seeding efficiency, and limited proteolysis) allowed us to make predictions regarding their effects *in vivo*. For instance, DS6 and DS9 induced robust spread of tau pathology even upon dilution, which was predicted by *in vitro* seeding activity. Importantly, while seeding activity correlated best with induction of local and distant pathology, this is an imperfect metric. For example, DS10 inoculation produces very limited pathology *in vivo* despite its relatively strong seeding activity *in vitro*. This indicates a major influence of other as yet unidentified strain-specific parameters. With further, more detailed study, we hope to link specific structural characteristics to various steps in pathogenesis, *i.e.*, to define the “logic” that predicts biological effects. For instance, cell-type specificity (or at least preference) might be based on differential strain binding affinities to heparan sulfate proteoglycans (Holmes et al., 2013). Likewise, post-translational modifications of monomeric tau within a target cell might render it more or less vulnerable to conversion by a specific strain.

Distinct Cellular Pathologies In Vivo

Tauopathies are defined histopathologically by several criteria, especially the pattern of intracellular tau accumulation: neurofibrillary tangles, Pick bodies, threads, grains, axonal puncta, etc. (Kovacs, 2015). Although we have readily observed patterns of pathology reminiscent of those described in patients, we have not attempted to link human patterns of pathology to those in P301S mice, which express only a single isoform of mutant tau. Instead, we wish to emphasize how conformational differences in tau prion strains are sufficient to create an enormous pathological diversity: neurofibrillary tangles, soma versus axonal accumulation, grain-like structures, dendritic and axonal terminal deposits that resemble threads, and astrocytic plaques.

The presence or absence of specific glial pathology also contributes to the definition of tauopathies (Yoshida, 2014). We observed that certain strains produce AT8-positive pathology in patterns reminiscent of astrocytic plaques described in tauopathies, with localization of phospho-tau inclusions along the processes of GFAP-positive astrocytes (Yoshida, 2014). We cannot attribute these effects to tau seeding activity or toxicity, as we observed these phenomena in DS7 (low seeding and low toxicity) and DS9 (high seeding and high toxicity). Distinct strains also induced different levels of rod microglial pathology.

Given that inoculates were identical with the exception of tau structure, and the transgenic mouse model expresses only a single tau isoform, we conclude that tau prion strains them-

selves dictate the resultant glial pathology. Further, three strain pairs (DS3/DS19; DS12/DS16; and DS6/DS15) that displayed similar biochemical features and limited proteolysis patterns produced similar patterns of neuropathology *in vivo*. These strains served to internally validate the methods we developed and highlight the close relationship of strain type to induced pathology.

Rates of Propagation In Vivo

Neurodegenerative diseases progress at different rates for unknown reasons. Similar to previous observations regarding PrP prion strains (Legname et al., 2006), our data indicate that the characteristics of an individual tau prion strain are sufficient to dictate the rate at which pathology spreads throughout the nervous system. Seeding activity correlates with this phenomenon, but cannot completely explain it. Instead, the rate of spread appears to reflect a unique interaction of specific strains with vulnerable cells. For example, strain DS10 seeds very strongly *in vitro*, but fails to propagate pathology outside of the hippocampal mossy fibers. Likewise, DS6 seeds very strongly *in vitro*, but exhibits a longer lag phase as it spreads to specific brain regions such as the entorhinal cortex versus the retrosplenial cortex. In contrast, DS9 showed more rapid spread to the entorhinal than the retrosplenial cortex. Taken together, our results suggest that the rate of propagation must be strongly influenced by raw seeding potential, *i.e.*, the ability to convert monomeric tau upon direct introduction to the cytoplasm via lipofectamine, but also the ability of a given strain to spontaneously enter and replicate within a vulnerable cell.

Distinct Regional Vulnerabilities

Regional or “selective” neuronal vulnerability in neurodegenerative diseases has long mystified investigators. PrP prion strains appear to account for differential regional involvement of the brain (Collinge and Clarke, 2007). Within the limits of our experimental system, our identification and characterization of distinct tau strains has allowed us to test whether aggregate structure itself defines regional vulnerability. We have found striking strain-specific regional differences, both in the pattern of spread from a single hippocampal inoculum and also in vulnerability to a direct injection. These effects correlated with individual tau strains, independent of an inoculum dose that could have accounted for vulnerability. For example, 10-fold dilution of a potent strain, DS9, produced patterns of spreading pathology very similar to a full dose. Further, low-dose DS9 spread at a faster rate than a full dose of DS4, even though the initial “seed burden” of DS9 was less. By contrast, strain DS10 has relatively high seeding activity, yet it selectively targets the mossy fibers of the hippocampus and does not convert tau in several other brain regions even after direct inoculation.

Others previously observed that different tau fibril preparations produce unique patterns of pathology based on inoculation of tau purified from tauopathy brains or crude homogenates (Boluda et al., 2015; Clavaguera et al., 2013), and two groups have inoculated unique α -synuclein preparations (Bousset et al., 2013; Guo et al., 2013; Peelaerts et al., 2015). However, no prior studies can attribute these effects to a specific, well-characterized strain or structure and make predictions about

the behavior of a strain in vivo from the biochemical properties of that inoculum. Given that we can now link specific pathology patterns to single tau prion strains, the experiments described here should enable new approaches to define how the structural characteristics of prions dictate neuronal vulnerability.

Implications for Diagnosis and Therapy

We propose that tau prion strains will explain the diversity of human neuropathology and will be required for mechanistic understanding of disease. Precise diagnosis of tauopathy now depends on histopathology, yet we have observed different strain composition patterns in putatively identical pathological syndromes (Sanders et al., 2014). Further, diversity and evolution may confound efforts to target a specific strain, as for PrP (Giles et al., 2010; Weissmann et al., 2011). Tau prion strains as defined by their specific conformations should have enormous power to help elucidate the structural determinants that underlie and predict the pathological patterns of diverse human tauopathies and to devise appropriate therapies.

EXPERIMENTAL PROCEDURES

Generation of Monoclonal Strain Library

Cells stably expressing tau RD(P301L/V337M) fused to YFP (DS1) were treated with recombinant tau fibrils or cell/brain homogenate. Resultant monoclonal lines were isolated and analyzed for inclusion morphology, seeding by split luciferase assay, and protease digestion as previously described (Sanders et al., 2014). These analyses identified 18 putatively distinct strains (DS2–DS19).

Limited Proteolysis

Cell lysates (60 μ g) in PBS/Triton X-100 were digested with pronase (30 μ g/mL) for 1 hr at 37°C, then resolved by SDS-PAGE and western blot probed with primary anti-tau antibody 2B11.

Sedimentation Analysis of Strain Library

Cell lysates were spun at 186,000 $\times g$ for 60 min. Pellets were washed with 1 mL lysis buffer and spun for an additional 30 min. Samples were resolved by SDS-PAGE and western blot using rabbit polyclonal anti-tau antibody ab64193 (Abcam).

Toxicity and Seeding Assay

LM10 cells, a monoclonal cell line expressing high levels of tau RD(P301L/V337M)-CFP and tau RD(P301L/V337M)-YFP, were transduced with 20 μ g of clarified cell lysate. After 72 hr, FRET-positive cells were sorted by FACS (Holmes et al., 2014) and replated. After 7 days, the number of FRET-positive and FRET-negative cells was quantified by flow cytometry.

Animal Maintenance and Inoculation Experiments

PS19 mice expressing 4R1N P301S human tau under the murine prion promoter (Yoshiyama et al., 2007) were used. Strains were inoculated intracerebrally via 10 μ L gas-tight Hamilton syringes. All experiments involving animals were approved by the University of Texas Southwestern Medical Center Institutional Animal Care and Use Committee.

Histology and Quantification of AT8 Pathology

50 μ m frozen sections were used. For DAB stain, biotinylated AT8 primary antibody (Thermo Scientific) was used. Images of AT8-stained slices were collected via Olympus Nanoscope 2.0-HT (Hamamatsu). The level of tau pathology present in each region was determined by blinded analysis with a semiquantitative 0–3 scale (no pathology, mild, moderate, and severe). Pathology was averaged among biological replicates and plotted as a heatmap using MATLAB as described.

SUPPLEMENTAL INFORMATION

Supplemental Information includes Supplemental Experimental Procedures, seven figures, and three tables and can be found with this article online at <http://dx.doi.org/10.1016/j.neuron.2016.09.055>.

AUTHOR CONTRIBUTIONS

S.K.K. designed and performed all in vivo and primary neuron experiments, inoculum sedimentation analysis, secondary cell line isolation and characterization, and brain immunohistochemistry. D.W.S. designed and performed all in vitro cell culture and biochemistry experiments to characterize DS1–DS19. Both authors assisted in data analysis, writing, and figure preparation for this manuscript. T.L.T. provided technical assistance with stereotaxic injections, tissue collection, sectioning, and immunohistochemistry. A.R. conducted blinded scoring of AT8 pathology and microglial pathology. A.M.S. performed limited proteolysis experiments. J.V.-A. assisted with development of primary neuron culture experiments and MATLAB analysis of pathology. T.M.M. provided guidance and reagents for in vivo experiments. M.I.D. provided guidance for in vitro and in vivo experiments and assisted in the writing and preparation of figures for this manuscript.

ACKNOWLEDGMENTS

We thank Ann McKee, Bill Seeley, and Lea Grinberg for providing invaluable reagents for this study. We thank Peter Davies for providing MC1 antibody. We thank Matthew Brier, Jennifer Furman, Brandon Holmes, Suzanne Schindler, and Niall Prendergast for providing guidance and critiques during the preparation of this manuscript. This work was funded by NIH/NIA grant F30AG048653 (S.K.K.); NIH grant F31NS086251 (D.W.S.); NIH/NIA R01AG048678, NIH/NINDS R01NS071835, the Tau Consortium, and the Cure Alzheimer's Fund (M.I.D.). This work was supported by the Hope Center Alafi Neuroimaging Laboratory at Washington University in St. Louis, Neuro-Models Facility, Whole Brain Microscopy Facility, Moody Foundation Flow Cytometry Facility, and High Throughput Screening Core at University of Texas Southwestern.

Received: March 22, 2016

Revised: July 22, 2016

Accepted: September 23, 2016

Published: October 27, 2016

REFERENCES

- Armstrong, M.J., Castellani, R.J., and Reich, S.G. (2014). "Rapidly" progressive supranuclear palsy. *Mov. Disord. Clin. Pract. (Hoboken)* 1, 70–72.
- Arnold, S.E., Toledo, J.B., Appleby, D.H., Xie, S.X., Wang, L.-S., Baek, Y., Wolk, D.A., Lee, E.B., Miller, B.L., Lee, V.M.-Y., and Trojanowski, J.Q. (2013). Comparative survey of the topographical distribution of signature molecular lesions in major neurodegenerative diseases. *J. Comp. Neurol.* 527, 4339–4355.
- Barghorn, S., Zheng-Fischhöfer, Q., Ackmann, M., Biernat, J., von Bergen, M., Mandelkow, E.M., and Mandelkow, E. (2000). Structure, microtubule interactions, and paired helical filament aggregation by tau mutants of frontotemporal dementias. *Biochemistry* 39, 11714–11721.
- Bessen, R.A., and Marsh, R.F. (1994). Distinct PrP properties suggest the molecular basis of strain variation in transmissible mink encephalopathy. *J. Virol.* 68, 7859–7868.
- Boluda, S., Iba, M., Zhang, B., Raible, K.M., Lee, V.M.-Y., and Trojanowski, J.Q. (2015). Differential induction and spread of tau pathology in young PS19 tau transgenic mice following intracerebral injections of pathological tau from Alzheimer's disease or corticobasal degeneration brains. *Acta Neuropathol.* 129, 221–237.
- Bousset, L., Pieri, L., Ruiz-Arlandis, G., Gath, J., Jensen, P.H., Habenstein, B., Madiona, K., Olieric, V., Böckmann, A., Meier, B.H., and Melki, R. (2013).

- Structural and functional characterization of two alpha-synuclein strains. *Nat. Commun.* **4**, 2575.
- Braak, H., and Braak, E. (1991). Neuropathological staging of Alzheimer-related changes. *Acta Neuropathol.* **82**, 239–259.
- Clavaguera, F., Bolmont, T., Crowther, R.A., Abramowski, D., Frank, S., Probst, A., Fraser, G., Stalder, A.K., Beibel, M., Staufenbiel, M., et al. (2009). Transmission and spreading of tauopathy in transgenic mouse brain. *Nat. Cell Biol.* **11**, 909–913.
- Clavaguera, F., Akatsu, H., Fraser, G., Crowther, R.A., Frank, S., Hench, J., Probst, A., Winkler, D.T., Reichwald, J., Staufenbiel, M., et al. (2013). Brain homogenates from human tauopathies induce tau inclusions in mouse brain. *Proc. Natl. Acad. Sci. USA* **110**, 9535–9540.
- Collinge, J., and Clarke, A.R. (2007). A general model of prion strains and their pathogenicity. *Science* **318**, 930–936.
- Collinge, J., Sidle, K.C.L., Meads, J., Ironside, J., and Hill, A.F. (1996). Molecular analysis of prion strain variation and the aetiology of ‘new variant’ CJD. *Nature* **383**, 685–690.
- de Calignon, A., Polydoro, M., Suárez-Calvet, M., William, C., Adamowicz, D.H., Kopeikina, K.J., Pittstick, R., Sahara, N., Ashe, K.H., Carlson, G.A., et al. (2012). Propagation of tau pathology in a model of early Alzheimer’s disease. *Neuron* **73**, 685–697.
- Frost, B., Jacks, R.L., and Diamond, M.I. (2009a). Propagation of tau misfolding from the outside to the inside of a cell. *J. Biol. Chem.* **284**, 12845–12852.
- Frost, B., Ollesch, J., Wille, H., and Diamond, M.I. (2009b). Conformational diversity of wild-type Tau fibrils specified by templated conformation change. *J. Biol. Chem.* **284**, 3546–3551.
- Giles, K., Glidden, D.V., Patel, S., Korh, C., Groth, D., Lemus, A., DeArmond, S.J., and Prusiner, S.B. (2010). Human prion strain selection in transgenic mice. *Ann. Neurol.* **68**, 151–161.
- Guo, J.L., and Lee, V.M.-Y. (2011). Seeding of normal Tau by pathological Tau conformers drives pathogenesis of Alzheimer-like tangles. *J. Biol. Chem.* **286**, 15317–15331.
- Guo, J.L., Covell, D.J., Daniels, J.P., Iba, M., Stieber, A., Zhang, B., Riddle, D.M., Kwong, L.K., Xu, Y., Trojanowski, J.Q., and Lee, V.M. (2013). Distinct α -synuclein strains differentially promote tau inclusions in neurons. *Cell* **154**, 103–117.
- Holmes, B.B., DeVos, S.L., Kfoury, N., Li, M., Jacks, R., Yanamandra, K., Ouidja, M.O., Brodsky, F.M., Marasa, J., Bagchi, D.P., et al. (2013). Heparan sulfate proteoglycans mediate internalization and propagation of specific tauopathic seeds. *Proc. Natl. Acad. Sci. USA* **110**, E3138–E3147.
- Holmes, B.B., Furman, J.L., Mahan, T.E., Yamasaki, T.R., Mirbaha, H., Eades, W.C., Belaygorod, L., Cairns, N.J., Holtzman, D.M., and Diamond, M.I. (2014). Proteopathic tau seeding predicts tauopathy in vivo. *Proc. Natl. Acad. Sci. USA* **111**, E4376–E4385.
- Hutton, M., Lendon, C.L., Rizzu, P., Baker, M., Froelich, S., Houlden, H., Pickering-Brown, S., Chakraverty, S., Isaacs, A., Grover, A., et al. (1998). Association of missense and 5’-splice-site mutations in tau with the inherited dementia FTDP-17. *Nature* **393**, 702–705.
- Iba, M., Guo, J.L., McBride, J.D., Zhang, B., Trojanowski, J.Q., and Lee, V.M.-Y. (2013). Synthetic tau fibrils mediate transmission of neurofibrillary tangles in a transgenic mouse model of Alzheimer’s-like tauopathy. *J. Neurosci.* **33**, 1024–1037.
- Knowles, T.P.J., Vendruscolo, M., and Dobson, C.M. (2014). The amyloid state and its association with protein misfolding diseases. *Nat. Rev. Mol. Cell Biol.* **15**, 384–396.
- Kovacs, G.G. (2015). Invited review: Neuropathology of tauopathies: principles and practice. *Neuropathol. Appl. Neurobiol.* **41**, 3–23.
- Lee, V.M., Goedert, M., and Trojanowski, J.Q. (2001). Neurodegenerative tauopathies. *Annu. Rev. Neurosci.* **24**, 1121–1159.
- Legname, G., Nguyen, H.-O.B., Peretz, D., Cohen, F.E., DeArmond, S.J., and Prusiner, S.B. (2006). Continuum of prion protein structures enciphers a multitude of prion isolate-specified phenotypes. *Proc. Natl. Acad. Sci. USA* **103**, 19105–19110.
- Liu, L., Drouet, V., Wu, J.W., Witter, M.P., Small, S.A., Clelland, C., and Duff, K. (2012). Trans-synaptic spread of tau pathology in vivo. *PLoS ONE* **7**, e31302.
- Mirbaha, H., Holmes, B.B., Sanders, D.W., Bieschke, J., and Diamond, M.I. (2015). Tau trimers are the minimal propagation unit spontaneously internalized to seed intracellular aggregation. *J. Biol. Chem.* **290**, 14893–14903.
- Nonaka, T., Watanabe, S.T., Iwatsubo, T., and Hasegawa, M. (2010). Seeded aggregation and toxicity of alpha-synuclein and tau: cellular models of neurodegenerative diseases. *J. Biol. Chem.* **285**, 34885–34898.
- Peelaerts, W., Bousset, L., Van der Perren, A., Moskalyuk, A., Pulizzi, R., Giugliano, M., Van den Haute, C., Melki, R., and Baekelandt, V. (2015). α -Synuclein strains cause distinct synucleinopathies after local and systemic administration. *Nature* **522**, 340–344.
- Prusiner, S.B. (1998). Prions. *Proc. Natl. Acad. Sci. USA* **95**, 13363–13383.
- Raj, A., Kuceyeski, A., and Weiner, M. (2012). A network diffusion model of disease progression in dementia. *Neuron* **73**, 1204–1215.
- Rey, N.L., Petit, G.H., Bousset, L., Melki, R., and Brundin, P. (2013). Transfer of human α -synuclein from the olfactory bulb to interconnected brain regions in mice. *Acta Neuropathol.* **126**, 555–573.
- Sanders, D.W., Kaufman, S.K., DeVos, S.L., Sharma, A.M., Mirbaha, H., Li, A., Barker, S.J., Foley, A.C., Thorpe, J.R., Serpell, L.C., et al. (2014). Distinct tau prion strains propagate in cells and mice and define different tauopathies. *Neuron* **82**, 1271–1288.
- Sanders, D.W., Kaufman, S.K., Holmes, B.B., and Diamond, M.I. (2016). Prions and protein assemblies that convey biological information in health and disease. *Neuron* **89**, 433–448.
- Thalhauser, C.J., and Komarova, N.L. (2012). Alzheimer’s disease: rapid and slow progression. *J. R. Soc. Interface* **9**, 119–126.
- Walker, L.C., and Jucker, M. (2015). Neurodegenerative diseases: expanding the prion concept. *Annu. Rev. Neurosci.* **38**, 87–103.
- Weissmann, C., Li, J., Mahal, S.P., and Browning, S. (2011). Prions on the move. *EMBO Rep.* **12**, 1109–1117.
- Yoshida, M. (2014). Astrocytic inclusions in progressive supranuclear palsy and corticobasal degeneration. *Neuropathology* **34**, 555–570.
- Yoshiyama, Y., Higuchi, M., Zhang, B., Huang, S.-M., Iwata, N., Saido, T.C., Maeda, J., Suhara, T., Trojanowski, J.Q., and Lee, V.M.-Y. (2007). Synapse loss and microglial activation precede tangles in a P301S tauopathy mouse model. *Neuron* **53**, 337–351.
- Zhou, J., Gennatas, E.D., Kramer, J.H., Miller, B.L., and Seeley, W.W. (2012). Predicting regional neurodegeneration from the healthy brain functional connectome. *Neuron* **73**, 1216–1227.

Dorsal Raphe Dopamine Neurons Modulate Arousal and Promote Wakefulness by Salient Stimuli

Jounghong Ryan Cho,¹ Jennifer B. Treweek,² J. Elliott Robinson,² Cheng Xiao,² Lindsay R. Bremner,² Alon Greenbaum,² and Viviana Gradinaru^{2,3,*}

¹Computation and Neural Systems

²Division of Biology and Biological Engineering
California Institute of Technology, Pasadena, CA 91125, USA

³Lead Contact

*Correspondence: viviana@caltech.edu

<http://dx.doi.org/10.1016/j.neuron.2017.05.020>

SUMMARY

Ventral midbrain dopamine (DA) is unambiguously involved in motivation and behavioral arousal, yet the contributions of other DA populations to these processes are poorly understood. Here, we demonstrate that the dorsal raphe nucleus DA neurons are critical modulators of behavioral arousal and sleep-wake patterning. Using simultaneous fiber photometry and polysomnography, we observed time-delineated dorsal raphe nucleus dopaminergic (DRN^{DA}) activity upon exposure to arousal-evoking salient cues, irrespective of their hedonic valence. We also observed broader fluctuations of DRN^{DA} activity across sleep-wake cycles with highest activity during wakefulness. Both endogenous DRN^{DA} activity and optogenetically driven DRN^{DA} activity were associated with waking from sleep, with DA signal strength predictive of wake duration. Conversely, chemogenetic inhibition opposed wakefulness and promoted NREM sleep, even in the face of salient stimuli. Therefore, the DRN^{DA} population is a critical contributor to wake-promoting pathways and is capable of modulating sleep-wake states according to the outside environment, wherein the perception of salient stimuli prompts vigilance and arousal.

INTRODUCTION

In mammals, behavioral arousal fluctuates as inputs are received from both the external environment (e.g., food availability, predator threat) and internal milieu (e.g., hunger, mating drive, homeostatic sleep demand) (Garey et al., 2003; Brown et al., 2012). While the neural circuits that encode these individual stimuli can be highly stimulus specific or tuned to a specific valence (positive or negative), their activation often promotes more general effects on arousal and electrocortical wakefulness through diverse wake-promoting neurons (Aston-Jones and Bloom, 1981; Szymusiak and McGinty, 2008). Akin to how the noradrenergic (NA) neurons of the locus coeruleus (LC) regulate circadian

sleep-wake cycling (Takahashi et al., 2010) and promote vigilance during wake (Aston-Jones and Bloom, 1981), multiple neural circuits play roles in electrocortical wakefulness and behavioral arousal to motivationally relevant situations, including cholinergic neurons of the pons and basal forebrain (Jones, 1991; Xu et al., 2015; Pinto et al., 2013), the corticotrophin-releasing hormone (CRH) and hypocretin (orexin) neuropeptide systems (Sakurai et al., 1998; Winsky-Sommerer et al., 2005), and the mesolimbic dopamine (DA) system (Eban-Rothschild et al., 2016; Taylor et al., 2016).

Several lines of basic research and clinical observations converge upon DA as a crucial modulator of wake drive, but the neuroanatomical underpinnings have resisted detailed characterization. For example, persistent elevation of DA tone via pharmacology (i.e., amphetamine [Daberkow et al., 2013], modafinil [Qu et al., 2008]) or genetic ablation of the dopamine transporter gene (*Slc6a3*) (Wisor et al., 2001) is associated with behavioral arousal, but these manipulations are diffuse and brain-wide rather than localized to a certain region. Recent work has revealed a role for ventral tegmental area (VTA) DA neurons in electrocortical arousal and sleep-wake patterning (Eban-Rothschild et al., 2016; Taylor et al., 2016), which complements its long-standing role in behavioral arousal to motivationally relevant stimuli (Cohen et al., 2012; Lammel et al., 2014; Matsumoto and Hikosaka, 2009). In contrast, diminished DA signaling from the substantia nigra pars compacta (SNc) is associated with insomnia, a major symptom in Parkinson's disease (Gjerstad et al., 2007). Considering the functional (Morales and Margolis, 2017), genetic (Poulin et al., 2014), and anatomical (Lammel et al., 2011, 2012; Margolis et al., 2008) heterogeneity of midbrain DA neurons, distinct DA subgroups may exert diverging effects on sleep-wake regulation.

Previously, a small population of DA neurons (~1,000 cells in rats) in the dorsal raphe nucleus (DRN; or "A10 dc" or "ventral/ventrolateral periaqueductal gray"; herein referred to as the DRN^{DA}) (Hokfelt et al., 1984; Descarries et al., 1986; Dougalis et al., 2012) was observed to be wake promoting (Lu et al., 2006). Chemical lesion of these cells precipitated profound hypersomnia (~20% increase in sleep), while prolonged wakefulness elicited increased *c-fos* expression (Lu et al., 2006; but see Léger et al., 2010). Compared to other DA populations, little is known about the natural dynamics of DRN^{DA} cells, such as whether their activity contributes to the valuation of external

cues and whether this valuation is predictive of the corresponding behavioral response. Contrary to VTA^{DA}-driven reward circuits, optogenetic activation of DRN^{DA} neurons fails to reinforce operant responding (McDevitt et al., 2014) but instead conveys a negative affective state and promotes social seeking via a negative reinforcement mechanism (Matthews et al., 2016). Given these seemingly disparate roles of DRN^{DA} cells, namely to promote wakefulness (Lu et al., 2006) and encode a “loneliness-like” state (Matthews et al., 2016), we hypothesized that DRN^{DA} neurons may signal arousal on a more general level, including awakening from sleep, maintenance of wakefulness, and promoting arousal in response to behaviorally relevant cues.

Here, we performed longitudinal monitoring of DRN^{DA} activity by calcium imaging via fiber photometry (Gunaydin et al., 2014) and of sleep-wake states via electroencephalography (EEG) and electromyography (EMG) recordings, in conjunction with optogenetics and chemogenetics for reversible, spatially specific control of neural activity (Rajasekharan et al., 2016; Urban and Roth, 2015). We found that DRN^{DA} neurons are wake-active, showing higher population activity during wakefulness over sleep states, and that endogenous DRN^{DA} activity correlates with state transitions and with external stimulus-driven behaviors. Furthermore, reversible and bi-directional manipulations of DRN^{DA} firing support the sufficiency and necessity of these neurons in promoting vigilance and arousal. Taken together, our results provide evidence that DRN^{DA} pathways provide a circuit for modulating behavioral states and salience-induced arousal in mammals.

RESULTS

DRN^{DA} Neurons Are Activated by Arousal-Provoking Salient Cues

To investigate the natural dynamics of DRN^{DA} neurons during awake-behaving states, we monitored DRN^{DA} population activity in subjects exposed to a diverse array of salient stimuli and environmental settings. In vivo activity of DRN^{DA} neurons was recorded using fiber photometry (Gunaydin et al., 2014), which can measure bulk Ca²⁺-dependent fluorescence of GCaMP6, a genetically encoded calcium indicator (Chen et al., 2013), through a single optical fiber positioned in deep brain structures (Figures S1A, S1G, and S1H). Our photometry setup utilized a 490 nm beam to activate Ca²⁺-dependent GCaMP6 fluorescence, as well as a 405 nm beam to image an isosbestic reference signal, which compensates for photo-bleaching and movement-related artifacts (Lerner et al., 2015). For specific targeting of DRN^{DA} neurons, we stereotaxically injected an adeno-associated virus (AAV) encoding GCaMP6f in a Cre-dependent manner (AAV5-Syn-FLEX-GCaMP6f) into the DRN of tyrosine hydroxylase (TH)::IRES-Cre mice (Figures 1A and 1B). Control animals were injected with AAV encoding the fluorescent marker EGFP (AAV5-hSyn-DIO-EGFP). An optical fiber was implanted over the DRN to acquire population fluorescence emitted from DRN^{DA} neurons (Figures 1A and S1A). We confirmed that GCaMP6f-expressing neurons emitted dynamic fluorescence fluctuations, while EGFP-expressing cells showed minimal fluorescence variation (Figures S1B and S1C).

We quantified the efficiency and specificity of GCaMP6f+ neurons in the DRN of TH-Cre mice. Transfection was highly efficient (94.2%, *n* = 407/432 neurons). Similar to previous reports that used the identical mouse line or others targeting TH or the *Slc6a3* promoter (Matthews et al., 2016), 74.9% (*n* = 407/543) of GCaMP6f+ neurons were co-localized with TH in the DRN. These neurons are not noradrenergic, as they lack dopamine beta-hydroxylase, which converts dopamine to norepinephrine (Nagatsu et al., 1979). Importantly, GCaMP6f+ or TH+ neurons never overlapped with serotonergic neurons (Figures 1B and S1D; Lu et al., 2006; Matthews et al., 2016), a major population in the DRN that is hypothesized to regulate arousal states (Jouvet, 1999). It is possible that GCaMP6f+/TH− neurons may express TH at a level below immunohistochemical detection limit but sufficient to drive Cre expression.

We first tested DRN^{DA-GCaMP6f} mice in a social interaction paradigm, in which physical contact with conspecifics after social isolation has been demonstrated to activate DRN^{DA} neurons (Matthews et al., 2016). We observed the robust activation of DRN^{DA} neurons in single-housed male DRN^{DA-GCaMP6f} mice when they first interacted with female intruders (Figures 1C and 1D). Similar activation was observed with juvenile mice (Figure S2A; Movie S1; Matthews et al., 2016) and also when they displayed aggressive behavior toward adult male intruders (Figure S2B). Beyond social interaction, we also observed prominent DRN^{DA} activity when mice consumed palatable food (Figures 1E and 1F; Movie S2). To further characterize the valence tuning of DRN^{DA} cells, we also challenged DRN^{DA-GCaMP6f} mice in assays with negative contexts. Surprisingly, DRN^{DA} neurons showed phasic activation upon delivery of unexpected electric footshocks (Figures 1G and 1H), air puffs (Figure S2C), or motivated responding (mobility/struggling) in tail suspension tests (Figure S2D) and during investigation of predator odor TMT (component of fox urine; Figure S2E). Furthermore, they showed sustained activation when subjects were physically restrained (Figure S2F).

In contrast, DRN^{DA} activity showed minimal change when mice interacted with novel or familiar objects (Figures 1I–1L, first encounters), which are less salient than social targets, food, or aversive cues. Indeed, DRN^{DA} activation during female interaction, chocolate consumption, and footshock was significantly larger than that during object investigation (Figure 1M). Furthermore, the second and third bouts of female interaction and aggressive behavior continued to provoke a significant elevation in DRN^{DA} activity, whereas it remained relatively unchanged from baseline with repeated novel object encounters, suggesting rapid habituation toward physically salient but motivationally neutral cues (Figures S2G–S2I).

These findings did not vary with subject social history, as similar patterns of DRN^{DA} activation were seen in group-housed mice (Figures S2J–S2L). Furthermore, DRN^{DA} neuronal activation was not correlated with locomotion, which argues against the observed DRN^{DA} activity resulting from the motor response alone (Figures S2M–S2O). Taken together, these findings suggest that DRN^{DA} neurons are activated by a broad array of arousal-provoking stimuli, paralleling animals' heightened environmental awareness that accompanies exposure to such motivationally salient stimuli.

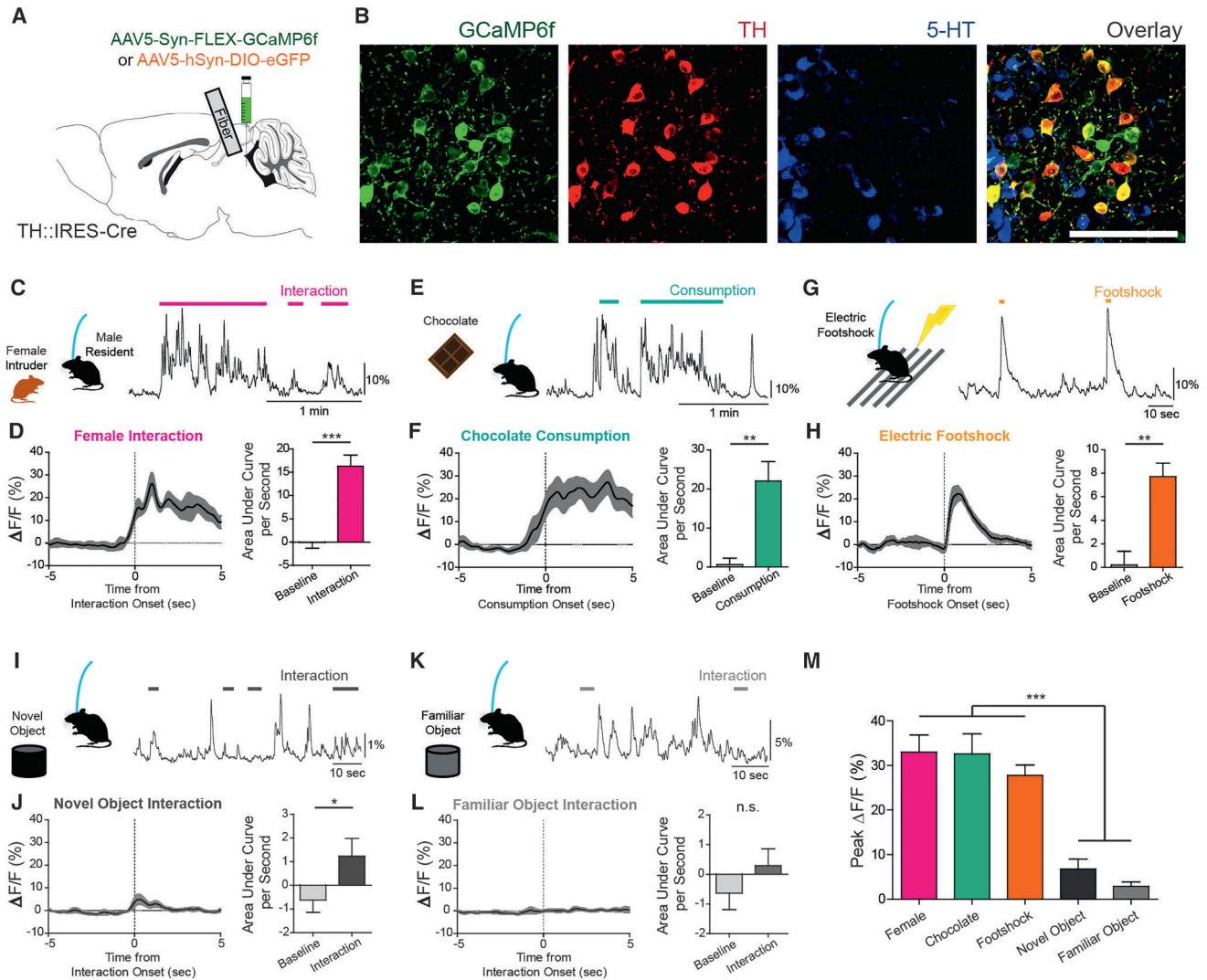


Figure 1. DRN^{DA} Neurons Are Activated upon Exposure to Salient Stimuli or Behavioral Challenge

(A) TH-Cre mice were injected with AAV5-Syn-FLEX-GCaMP6f or AAV5-hSyn-DIO-eGFP and implanted with an optical fiber into the DRN for fiber photometry. (B) Confocal images of GCaMP6f+ (green) neurons show co-localization with TH+ neurons (red), but no overlap with 5-HT+ neurons (blue). Scale bar, 100 μ m. (C) Social interaction between a male DRN^{DA-GCaMP6f} resident mouse and a female intruder were associated with increased DRN^{DA} activity; the trace is a representative recording with interaction bouts indicated. (D) Left: female interaction caused an increase in fluorescence at the onset (first interactions only). Right: quantification of the area under the curve per second (AUC) during the interaction (0–5 s) shows that social interaction caused significant increase in DRN^{DA} activity from baseline (–5 to 0 s) ($n = 7$ DRN^{DA-GCaMP6f} mice; paired t test, $t_6 = 11.97$, $***p < 0.001$). (E) Chocolate consumption by a DRN^{DA-GCaMP6f} mouse increased DRN^{DA} activity; representative recording. (F) Left: DRN^{DA} activity was increased upon chocolate consumption. Right: AUC quantification during consumption (0–5 s) compared with baseline (–5 to 0 s) shows that food consumption is associated with significant fluorescence increase ($n = 7$ DRN^{DA-GCaMP6f} mice; paired t test, $t_6 = 4.273$, $**p < 0.01$). (G) Electric footshocks (0.25 mA, 1 s) were delivered; representative DRN^{DA} trace during two consecutive footshocks. (H) Left: footshock induced phasic DRN^{DA} activation. Right: DRN^{DA} activity after footshock (0–5 s) was significantly increased relative to baseline (–5 to 0 s) ($n = 7$ DRN^{DA-GCaMP6f} mice; paired t test, $t_6 = 5.763$, $**p < 0.01$). (I) DRN^{DA-GCaMP6f} mouse was allowed to interact with a novel object; representative recording during interactions. (J) Left: first interaction of a novel object was associated with DRN^{DA} activity increase. Right: DRN^{DA} activity after first interaction (0–5 s) was significantly increased relative to baseline (–5 to 0 s) ($n = 7$ DRN^{DA-GCaMP6f} mice; paired t test, $t_6 = 3.614$, $*p < 0.05$). (K) A familiar object was introduced; representative DRN^{DA} trace with interaction bouts. (L) Left: first interaction bout was not associated with any change in DRN^{DA} fluorescence. Right: there was no change in DRN^{DA} activity across familiar object interaction ($n = 7$ DRN^{DA-GCaMP6f} mice; paired t test, $t_6 = 2.205$, $p > 0.05$). (M) Peak DRN^{DA} fluorescence values during female interaction, chocolate consumption, and electric footshocks were significantly higher than those during novel and familiar object interaction ($n = 7$ DRN^{DA-GCaMP6f} mice; one-way ANOVA, $F_{4,30} = 22.77$, $p < 0.0001$, Bonferroni post hoc analysis, $***p < 0.001$). Data represent mean \pm SEM.

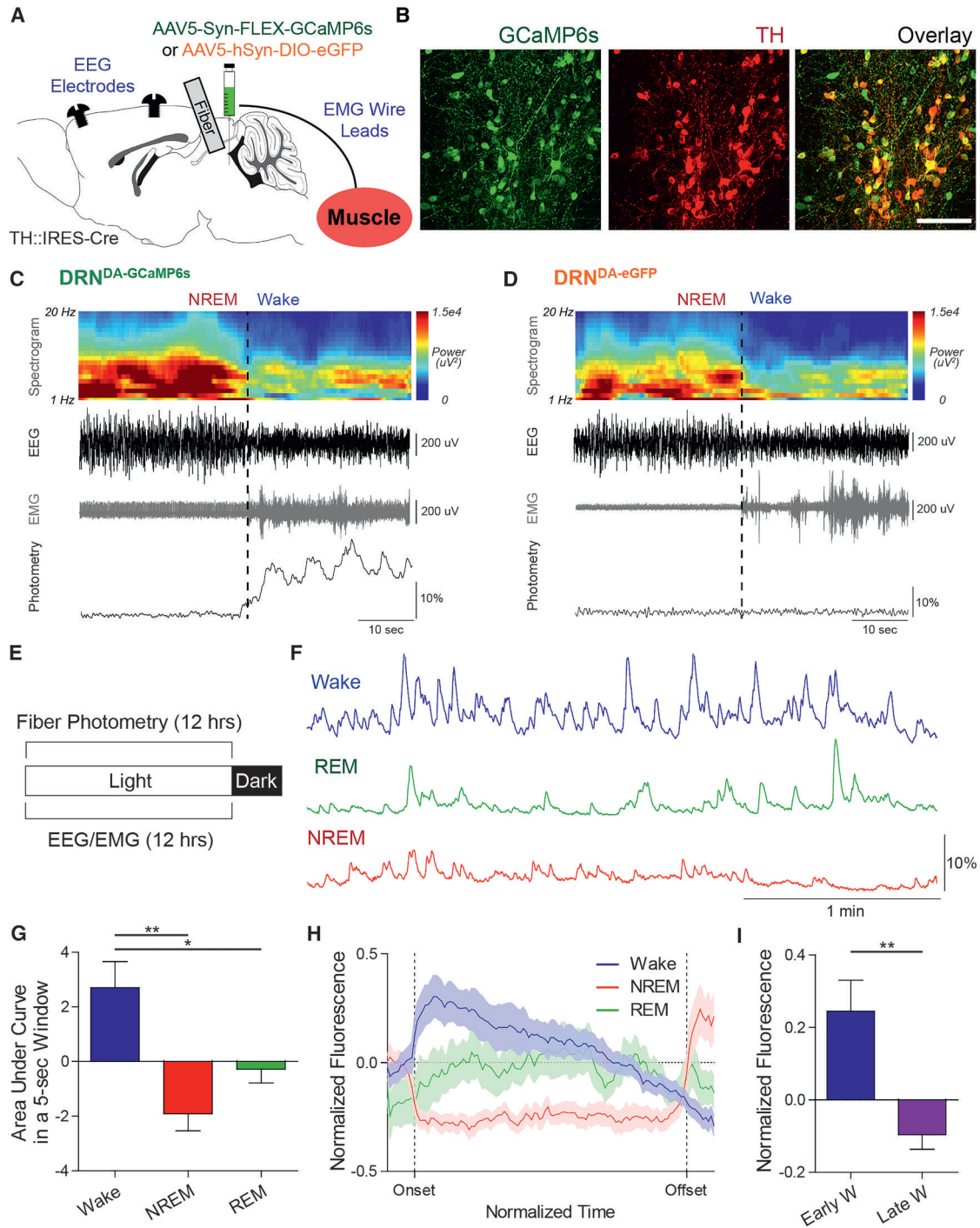


Figure 2. Simultaneous Fiber Photometry and EEG/EMG Recordings Reveal a Correlation between DRN^{DA} Neuronal Activity and Sleep-Wake States

(A) In addition to fiber photometry, EEG screw electrodes and EMG wires were implanted to classify sleep-wake states. (B) Representative confocal images of GCaMP6s+ neurons (green) co-localized with TH+ neurons (red). Scale bar, 100 μ m. (C) Representative example of an NREM-to-wake transition from a DRN^{DA}-GCaMP6s mouse with EEG spectrogram, EEG, EMG, and photometry traces. Note DRN^{DA} fluorescence was increased at the wake onset, when EEG desynchronized from delta (0.5–4 Hz) and EMG amplitude increased. (D) Same as (C), but from a DRN^{DA}-EGFP mouse. No change in photometry was observed. (E) Synchronized photometry and EEG/EMG recordings were performed during the entire light phase. (F) Representative photometry traces at distinct sleep-wake states (blue, wake; green, REM sleep; red, NREM sleep).

(legend continued on next page)

DRN^{DA} Population Activity Correlates with Sleep-Wake States

That DRN^{DA} neurons were activated by exposure to a variety of salient cues expands their previous description as a socio-centric pathway (Matthews et al., 2016). It seems plausible that DRN^{DA} neurons convey more generalized arousal signals across broad temporal scales, especially given that chemogenetic activation promotes analgesia (Li et al., 2016) and selective lesion causes hypersomnia (Lu et al., 2006).

To test this hypothesis, we prepared TH-Cre mice for simultaneous and synchronized recording of DRN^{DA-GCaMP6s} fluorescence (AAV5-Syn-FLEX-GCaMP6s, EGFP for control animals; DRN optical fiber insertion; Figures 2A and 2B) and polysomnography signals (implantation of EEG electrodes and EMG wires; Figure 2A). Sleep-wake states, which were manually classified in 5 s windows based on the visual and spectral characteristics of the EEG/EMG signals, were correlated to fluctuations in DRN^{DA} population activity (Figures 2C and S3A). Variations in fluorescent signal were absent in control DRN^{DA-EGFP} mice (Figures 2D and S3B), and viral delivery of transgenes (here and in all subsequent experiments) did not alter the basic sleep-wake architecture (Figures S1E and S1F).

To record DRN^{DA} activity over many episodes of distinct sleep-wake states, we collected fiber photometry and EEG/EMG across the entire light (inactive) phase (Figure 2E). DRN^{DA-GCaMP6s} mice showed normal EEG spectral characteristics and sleep-wake patterns, even in the presence of GCaMP6s excitation light (Figures S3C and S3D). Over long recording sessions, GCaMP6s bleaching was observed, but it could be effectively removed by subtracting the linearly scaled control signal from 405 nm excitation (Figure S3E). To examine the correlation of DRN^{DA} activity with sleep-wake states, we calculated the area under the curve (AUC) for non-overlapping 5 s windows of photometry data during each state as an index of the estimated DRN^{DA} population firing rate (Figure 2F). AUC values were significantly higher during wakefulness (Figure 2G). For further characterization, Ca²⁺ peak events were detected (Figure S3F), and their quantitative features were compared across states. The peak amplitude and summed AUC values of detected events were highest during wakefulness, but there was no significant difference in their frequency or duration across distinct states (Figures S3G–S3J). Altogether, these results suggest that DRN^{DA} neurons are wake-active and that their activity profile correlates with arousal states.

To examine the temporal dynamics of DRN^{DA} activity during each state, we normalized the variable durations of sleep-wake states to a unit-less time from 0 (onset) to 1 (offset) and accordingly down-sampled the normalized photometry traces. During wakefulness, DRN^{DA} population fluorescence peaked soon after wake onset and gradually decreased toward wake offset (Figure 2H). Indeed, the DRN^{DA} activity at the early 20th percentile

of a wake episode was significantly larger than at the late 20th percentile (Figure 2I). In contrast, DRN^{DA} activity was continuously suppressed during NREM sleep and showed minimal variations during REM sleep (Figure 2H). We additionally verified that wake episodes whose durations were similar to sleep episodes demonstrated similar dynamics (Figure S3K), suggesting that the observed DRN^{DA} wake dynamics did not originate from photobleaching over time. In sum, the activity level of DRN^{DA} populations not only varies across sleep-wake states but also shows dynamic changes within wakefulness, showing highest activity after wake onset and gradual decrease toward sleep onset.

Next, we examined DRN^{DA} activity during state transitions. DRN^{DA} fluorescence increased significantly at NREM to wake (Figure 3A; when wake duration >60 s). There was no significant fluorescence change at REM-to-wake transitions (Figure 3B; when wake duration >60 s). Conversely, DRN^{DA} activity decreased when animals fell asleep (Figure 3C). We also observed a gradual increase of DRN^{DA} activity across NREM-to-REM transitions (Figure 3D). When a brief period of wake (<15 s) intervened in transition from REM to NREM, DRN^{DA} activity exhibited a corresponding decrease across the brief wake and NREM onset (Figure S3L).

Interestingly, we observed that the duration of wake episodes varied as a function of the change in DRN^{DA} activity across the wake onset. The net fluctuation in DRN^{DA} fluorescence across sleep-to-wake transitions (from both NREM and REM) was significantly larger when mice were awake for a longer period (“long”: >60 s) than when mice were briefly awake (“short”: <30 s; “intermediate”: between 30 and 60 s; Figures 3E and 3F). This suggests that DRN^{DA} activity at wake onset is positively correlated with the duration of the following wake episode. In sum, these results provide correlative evidence that endogenous DRN^{DA} firing is highest during wakefulness and that DRN^{DA} activity is dynamic across state transitions.

Optogenetic Activation of DRN^{DA} Neurons Promotes Wakefulness

To reveal a causal relationship between DRN^{DA} activity and wakefulness, we tested for sufficiency using a Cre-dependent excitatory opsin to stimulate transduced DRN^{DA} cells (AAV5-Ef1a-DIO-ChR2-eYFP, EGFP for controls; polysomnography for stage classification; Figures 4A and 4B). ChR2-eYFP expression was limited to the DRN and caudal linear nucleus, and never found in retrorubral field or VTA (Figures S4N and S4O). To avoid potential ceiling effects, we applied optogenetic stimulation to DRN^{DA} neurons during the light phase (Figure 4C). As endogenous firing characteristics of DRN^{DA} cells are unknown (one neuron reported by juxtacellular recording [Schweimer and Ungless, 2010]), we used stimulus parameters commonly adopted for photoactivation of ventral midbrain DA neurons (Tsai et al., 2009), which operate in phasic and tonic firing modes. We

(G) Quantification of AUC per 5 s window revealed higher DRN^{DA} activity during wakefulness over NREM and REM sleep ($n = 6$ DRN^{DA-GCaMP6s} mice; one-way ANOVA, $F_{2,15} = 10.58$, $p < 0.01$; Bonferroni post hoc analysis, * $p < 0.05$, ** $p < 0.01$).

(H) Temporal dynamics of normalized DRN^{DA} activity during wake (blue), NREM (red), and REM (green) episodes within normalized time.

(I) Normalized DRN^{DA} activity at early wake (first 20th percentile) was significantly increased from late wake period (last 20th percentile) ($n = 6$ DRN^{DA-GCaMP6s} mice; paired t test, $t_5 = 5.672$, ** $p < 0.01$).

Data represent mean \pm SEM.

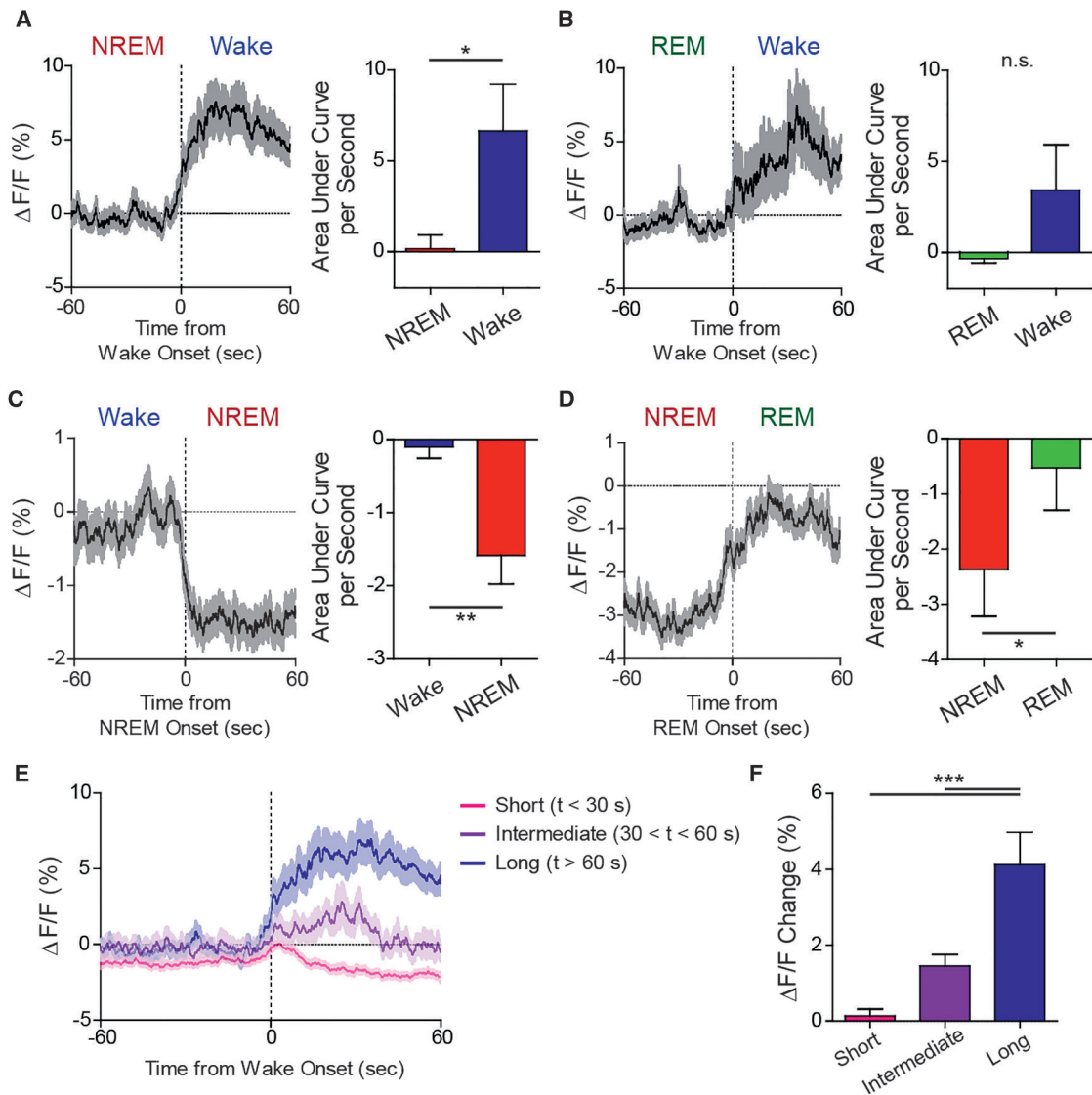


Figure 3. DRN^{DA} Neuronal Dynamics across State Transitions

(A) Left: DRN^{DA} activity increased across NREM-to-wake transitions. Right: DRN^{DA} activity after transitions (wake) was significantly greater than before transitions (NREM) ($n = 6$ DRN^{DA-GCaMP6s} mice; paired t test, $t_5 = 3.052$, $*p < 0.05$).

(B) Left: DRN^{DA} activity did not change across REM-to-wake transitions. Right: DRN^{DA} fluorescence was not different across transitions ($n = 6$ DRN^{DA-GCaMP6s} mice; paired t test, $t_5 = 1.556$, $p > 0.1$).

(C) Left: DRN^{DA} activity decreased at wake-to-NREM transitions. Right: the AUC values after transitions (NREM) were significantly lower than before transitions (wake) ($n = 6$ DRN^{DA-GCaMP6s} mice; paired t test, $t_5 = 4.516$, $**p < 0.01$).

(D) Left: DRN^{DA} fluorescence increased across NREM-to-REM transitions. Right: DRN^{DA} activity significantly increased during NREM to REM transitions ($n = 6$ DRN^{DA-GCaMP6s} mice; paired t test, $t_5 = 3.192$, $*p < 0.05$).

(E) DRN^{DA} activity increase across sleep-to-wake transitions was more prominent when mice spent longer time awake (> 60 s, blue) than when mice were awake for intermediate (between 30 and 60 s, purple) or short (< 30 s, pink) period.

(F) Fluorescence increase across wake onsets was significantly larger for long-duration wake episodes than for intermediate- or short-duration wake episodes ($n = 366$ short, 158 intermediate, and 185 long wake episodes; one-way ANOVA, $F_{2,706} = 21.85$, $p < 0.0001$; Bonferroni post hoc analysis, $***p < 0.001$).

Data represent mean \pm SEM.

applied both phasic (a train of ten 30 Hz pulses, 10 ms pulse width, every 5 s) and tonic (continuous 2 Hz pulses, 10 ms pulse width) stimulation patterns (Figures 4C and S4D). These specific parameters were designed to expose subjects to the same total number of light pulses with distinct temporal structures. We veri-

fied that DRN^{DA} neurons were capable of faithfully following phasic pulse trains in whole-cell patch clamp recordings (Figure S4A).

Two minutes of phasic stimulation caused immediate transitions to and maintenance of wakefulness from both NREM and

REM sleep in DRN^{DA-ChR2} mice, but not in control DRN^{DA-EGFP} mice (Figures 4D–4F, S4B, and S4C). By contrast, 2 min of tonic stimulation could only induce waking from REM sleep (Figures S4D–S4G). Because phasic stimulation more reliably evoked stage changes, we employed this paradigm in subsequent experiments. Phasic activation was effective in inducing immediate NREM-to-wake transitions even after 4 hr of sleep deprivation, suggesting that DRN^{DA} activation can promote instantaneous arousal in face of high sleep pressure (Figure 4G). Phasic stimulation caused a significant change in cortical EEG in DRN^{DA-ChR2}, but not in control DRN^{DA-EGFP} mice, as revealed by spectral analysis (Figures 4H, 4I, S4H, and S4I); delta (0.5–4 Hz) and high-frequency (40–100 Hz) EEG powers were decreased and increased, respectively, upon DRN^{DA} activation (Figures 4J and 4K).

We next sought to examine the effect of longer, sustained activation of DRN^{DA} neurons on behavioral states. A 1 hr epoch of phasic stimulation was applied 4 hr into the subject's light phase when sleep pressure is high. Photostimulation resulted in a net increase in time awake relative to unstimulated epochs, due to the extension of wake episodes (Figures 4L and 4M). Spectral analysis revealed that delta (0.5–4 Hz) power was significantly diminished while high-frequency (40–100 Hz) activity was enhanced in ChR2-expressing mice (Figures 4N–4P). This spectral change from DRN^{DA} activation could not be attributed to increased locomotion, which can also affect cortical activity and arousal (Vinck et al., 2015), because optogenetic manipulations did not affect locomotion in either the light or dark phase (open field test; Figure S4L). Moreover, the sustained increase in wakefulness from DRN^{DA} activation was directly mediated by DA, as systemic administration of D1 and D2 receptor antagonists (SCH-23390 and eticlopride, respectively, 1 mg/kg) prior to stimulation abolished the wake-promoting effect of phasic stimulation in DRN^{DA-ChR2} mice but caused no overall effect in control mice (Figures S4J–S4K).

In sum, phasic stimulation of DRN^{DA} neurons can affect sleep-wake state patterning and promote arousal by inducing immediate sleep-to-wake transitions and prolonging wake duration. DRN^{DA} activity also causes electrocortical arousal, bi-directionally modulating low- and high-frequency rhythms across both minutes-short and hour-long temporal scales.

Chemogenetic Inhibition of DRN^{DA} Neurons Reduces Wakefulness

To interrogate the necessity of DRN^{DA} signaling for wake maintenance, we used a chemogenetic (Urban and Roth, 2015) approach to reversibly inhibit DRN^{DA} activity during polysomnographic recordings (Figure 5A). Here, DRN^{DA} cell recruitment via expression of the inhibitory DREADD (AAV2-hSyn-DIO-hM4Di-mCherry; Figures 5A and 5B) rather than the analogous opsin is not limited to light spread from optical fibers, and long-term suppression of DRN^{DA} activity carries no potential for phototoxicity. We confirmed with *ex vivo* whole-cell patch-clamp recordings that bath application of 1 μ M clozapine-N-oxide (CNO) reversibly reduced the firing of hM4Di-expressing DRN^{DA} neurons via hyperpolarization but showed no effect on EGFP-positive cells in control mice (Figures S5B–S5E). We also verified that the hM4Di vector was not anterogradely or retrogradely

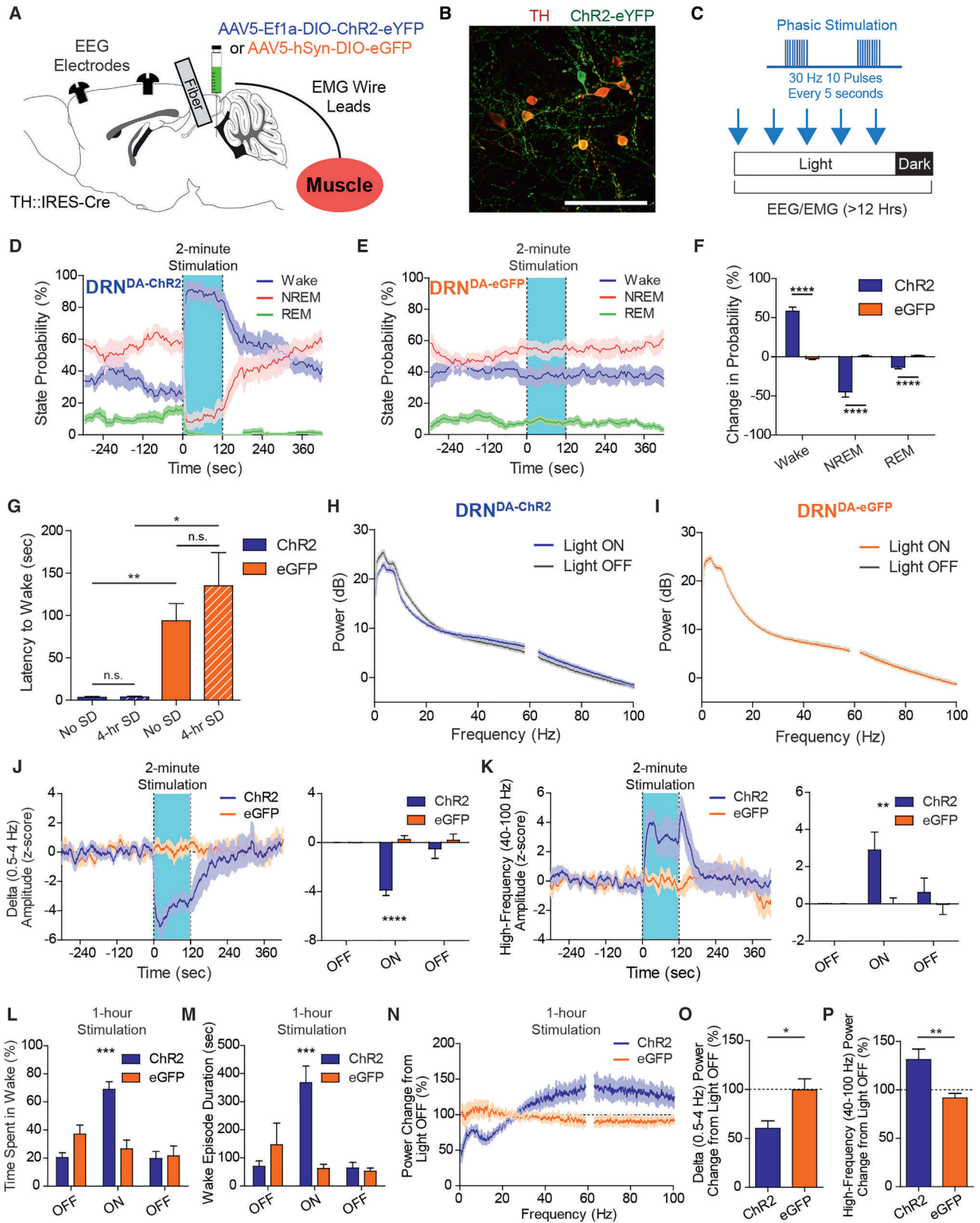
transported from the DRN to other TH+ neurons (across a 4-week window; Figures S5F–S5I), some of which have been shown to have reciprocal connections (Lu et al., 2006).

DRN^{DA-hM4Di} and DRN^{DA-EGFP} mice were habituated to experimenter handling for three days prior to intraperitoneal injection of saline or CNO (1 mg/kg) 3 hr into their dark (active) cycle, and EEG/EMG recordings took place for 2 hr afterward (Figure 5C). Compared to saline, CNO injection led to a marked reduction in wakefulness (Figures 5D and 5E). At the group level, DRN^{DA} inhibition decreased the time spent in wakefulness and increased NREM sleep time (Figure 5F). Specifically, CNO injection into the DRN^{DA-hM4Di} mice increased NREM sleep duration (Figure 5G) but had no effect on the number of episodes of each state (Figure 5H). Importantly, saline or CNO injection into control mice did not affect sleep-wake proportions (Figures 5F–5H). A change was also evident in cortical EEG (Figure 5I); contrary to optogenetic activation, chemogenetic inhibition was associated with increased delta (0.5–4 Hz) power (Figure 5J) and decreased high-frequency (40–100 Hz) activity (Figure 5K) relative to vehicle injection. To test whether CNO-induced sleep-wake states have normal EEG architecture, we verified that the EEG spectrum in each state after CNO injection was not distinguishable from those after saline injection (Figures S5J–S5L). Thus, our findings indicate that DRN^{DA} neuronal activity is required for supporting wakefulness in normal physiological conditions.

DRN^{DA} Neuronal Activity Supports Wakefulness in the Presence of Salient Stimuli

Since diverse salient stimuli activated DRN^{DA} neurons (Figure 1) and their firing promoted wakefulness (Figures 4 and 5), we asked whether DRN^{DA} neurons are necessary for maintaining arousal in the face of environmental salience by chemogenetically inhibiting their activity (Figure 6A). We introduced female mouse and predator odor TMT to the subject's home cage during the dark cycle while monitoring behavioral states. These two stimuli, which were shown to induce robust DRN^{DA} activity (Figures 1C, 1D, and S2E), hold ethological relevance and are of opposite valence. CNO injection into the DRN^{DA-hM4Di} mice reduced the time spent awake and promoted NREM sleep in both assays, contrary to other conditions where mice remained awake (Figures 6B and 6C). More broadly, DRN^{DA} inhibition during these assays caused a shift in cortical EEG spectra; CNO treatment of DRN^{DA-hM4Di} mice led to an increase in delta (0.5–4 Hz) power and decreases in high-theta (8–12 Hz) and high-frequency (40–100 Hz) power relative to saline condition, which was absent in control mice (Figures 6D–6G).

We further asked if the unexpected presentation of arousing or alerting stimuli (e.g., loud noises) during sleep could induce immediate wake transitions with DRN^{DA} firing. DRN^{DA-GCaMP6s} mice were exposed to randomized auditory stimuli (65 dB, 2–5 kHz, 2 Hz pulse frequency, 250 ms width, 10 s duration) throughout their light phase while recording GCaMP6s fluorescence and EEG/EMG signals (Figure S6A). We observed time-locked DRN^{DA} activity upon tone onset, which was most prominent when subjects immediately (within 10 s) switched from sleep to wake (Figures S6B and S6C). There was no detectable difference in DRN^{DA} activity increase between NREM- and REM-to-wake transitions (Figures S6D and S6E). To test



(legend on next page)

for a causal contribution of DRN^{DA} activity to cued arousal, we repeated the above experiment on mice expressing archaerhodopsin-3 (Arch; Mattis et al., 2011), which allows for time-locked reversible inhibition (Figures S6F and S6G). When DRN^{DA} neurons were exposed to a continuous 20 s light pulse (532 nm, 10 mW) centered on tone delivery (70 dB), the probability of cued waking from NREM (Figures S6H–S6K), but not from REM sleep (Figures S6L–S6O), significantly decreased. DRN^{DA} inhibition did not completely block NREM-to-wake transitions, which suggests that multiple pathways likely work together to sustain full arousal, including, but not limited to, noradrenergic or cholinergic neurons (Aston-Jones and Bloom, 1981; Xu et al., 2015). In sum, these data indicate that DRN^{DA} activity is required for maintaining salience-induced wakefulness and for triggering cued waking from sleep.

DISCUSSION

Using simultaneous calcium imaging and polysomnography in conjunction with optogenetic and chemogenetic manipulations, we demonstrated that DRN^{DA} neurons respond to external salient events of positive and negative valence, show correlative fluctuations at the population level across distinct sleep-wake states, and promote wakefulness. Furthermore, DRN^{DA} activity is necessary to maintain normal levels of wakefulness and support arousal in response to the perception of salient stimuli. These findings support a role for wake-promoting DRN^{DA} neurons that parallels the arousal-promoting function of isolated DA cells in invertebrates (Pimentel et al., 2016), as well as a

more expansive role for DRN^{DA} signaling beyond promoting social interaction via negative reinforcement (Matthews et al., 2016) or mediating anti-nociceptive effects (Li et al., 2016).

Our photometry data demonstrate not only that social interaction robustly enhances DRN^{DA} spiking (female interaction, male intruder; Figures 1 and S2), akin to previous findings (juvenile interaction; Matthews et al., 2016), but also that these neurons respond to the perception of highly salient, non-social stimuli (Figures 1 and S2). DRN^{DA} activation by a wide variety of rewarding and aversive stimuli, both social and non-social, occurred irrespective of the subject's social history, as the stimulus-evoked change in DRN^{DA} fluorescence was not influenced by chronic separation from cage-mates (Figures S2J–S2M). Given the subtleties in how various forms of social deprivation (e.g., maternal separation, acute or chronic social isolation) can differentially alter physiology and behavior (George et al., 2010; Whitaker et al., 2013), the extent to which a subject's social environment and rank causes plasticity in DRN^{DA} neurons will require further investigation. Based on the documented heterogeneity of ventral midbrain DA groups (Bromberg-Martin et al., 2010; Morales and Margolis, 2017), it is plausible that DRN^{DA} cells may also be heterogeneous and individually tuned to specific classes of stimuli. For example, some DRN^{DA} neurons may play a general role in social engagement or may be more susceptible to changes in social history, while other subsets may fire selectively for arousing, non-social stimuli. Since we and Matthews et al. (2016) used different fiber-placement methods (angled versus perpendicular, respectively), we may have sampled distinct, non-overlapping DRN^{DA} subsets.

Figure 4. Optogenetic Stimulation of DRN^{DA} Neurons Promotes Wakefulness

- (A) TH-Cre mice injected with AAV5-Ef1a-DIO-ChR2-eYFP or AAV5-hSyn-DIO-EGFP and implanted with an optical fiber received optogenetic stimulation during sleep-wake state monitoring.
- (B) Confocal images of ChR2-eYFP+ neurons (green) co-localized with TH+ neurons (red). Scale bar, 100 μ m.
- (C) Two-minute blocks (blue arrows) of phasic stimulations were delivered with intervals of 20 to 25 min throughout the light phase to photo-activate DRN^{DA} neurons.
- (D) Probability of being awake was dramatically increased upon onset of the phasic stimulation, with concurrent reduction of both NREM and REM state probability in DRN^{DA-ChR2} mice.
- (E) Same as (D), but no change was observed in DRN^{DA-EGFP} mice.
- (F) The increase in wake probability in DRN^{DA-ChR2} mice compared with DRN^{DA-EGFP} mice was significant, as were the decreases in NREM and REM sleep probability ($n = 8$ per group; unpaired t test, **** $p < 0.0001$).
- (G) There was no difference in the latency to wake onset even after 4 hr of sleep deprivation in both groups ($n = 4$ per group; paired t test, $p > 0.2$). Regardless of sleep deprivation, latency to wake after stimulation was significantly shorter in DRN^{DA-ChR2} mice compared to controls (unpaired t test, * $p < 0.05$, ** $p < 0.01$).
- (H) Power spectral density of frontal EEG shows reduced power in low-frequency range and increased power in high-frequency range during light ON (blue) compared to light OFF (gray) conditions in DRN^{DA-ChR2} mice.
- (I) Same as (H), but power spectral density showed no difference across light ON (orange) and OFF (gray) conditions in DRN^{DA-EGFP} mice.
- (J) Left: time-varying spectral analysis showed that the amplitude of delta (0.5–4 Hz) rhythms was decreased upon phasic stimulation. Right: delta amplitude during the light ON epoch was significantly decreased compared to baseline OFF epochs ($n = 8$ per group; two-way ANOVA revealed group \times epoch interaction, $F_{2,26} = 17.06$, $p < 0.0001$; Bonferroni post hoc analysis, **** $p < 0.0001$).
- (K) Left: the amplitude of high-frequency (40–100 Hz) rhythms was increased upon phasic stimulation. Right: high-frequency amplitude was significantly increased during the light ON epoch compared to the OFF epochs ($n = 8$ per group; two-way ANOVA revealed group \times epoch interaction, $F_{2,26} = 5.096$, $p < 0.05$; Bonferroni post hoc analysis, ** $p < 0.01$).
- (L) 1 hr of phasic DRN^{DA} stimulation significantly increased the time spent in wakefulness during the light ON hour compared to the light OFF hours ($n = 6$ per group; two-way ANOVA revealed group \times epoch interaction, $F_{2,20} = 15.99$, $p < 0.0001$; Bonferroni post hoc analysis, *** $p < 0.001$).
- (M) 1 hr of phasic stimulation significantly increased the duration of wake episodes ($n = 6$ per group; two-way ANOVA revealed group \times epoch interaction, $F_{2,20} = 12.16$, $p < 0.001$; Bonferroni post hoc analysis, *** $p < 0.001$).
- (N) Power spectral density revealed decrease in low-frequency power and increase in high-frequency power in DRN^{DA-ChR2} mice during light ON compared to the light OFF hours, but no changes were observed in DRN^{DA-EGFP} mice.
- (O) Stimulation-induced delta (0.5–4 Hz) power reduction was significantly larger in DRN^{DA-ChR2} mice ($n = 6$ per group; unpaired t test, * $p < 0.05$).
- (P) Stimulation-induced high-frequency (40–100 Hz) power increase was significantly larger in DRN^{DA-ChR2} mice ($n = 6$ per group; unpaired t test, ** $p < 0.01$).
- Data represent mean \pm SEM.

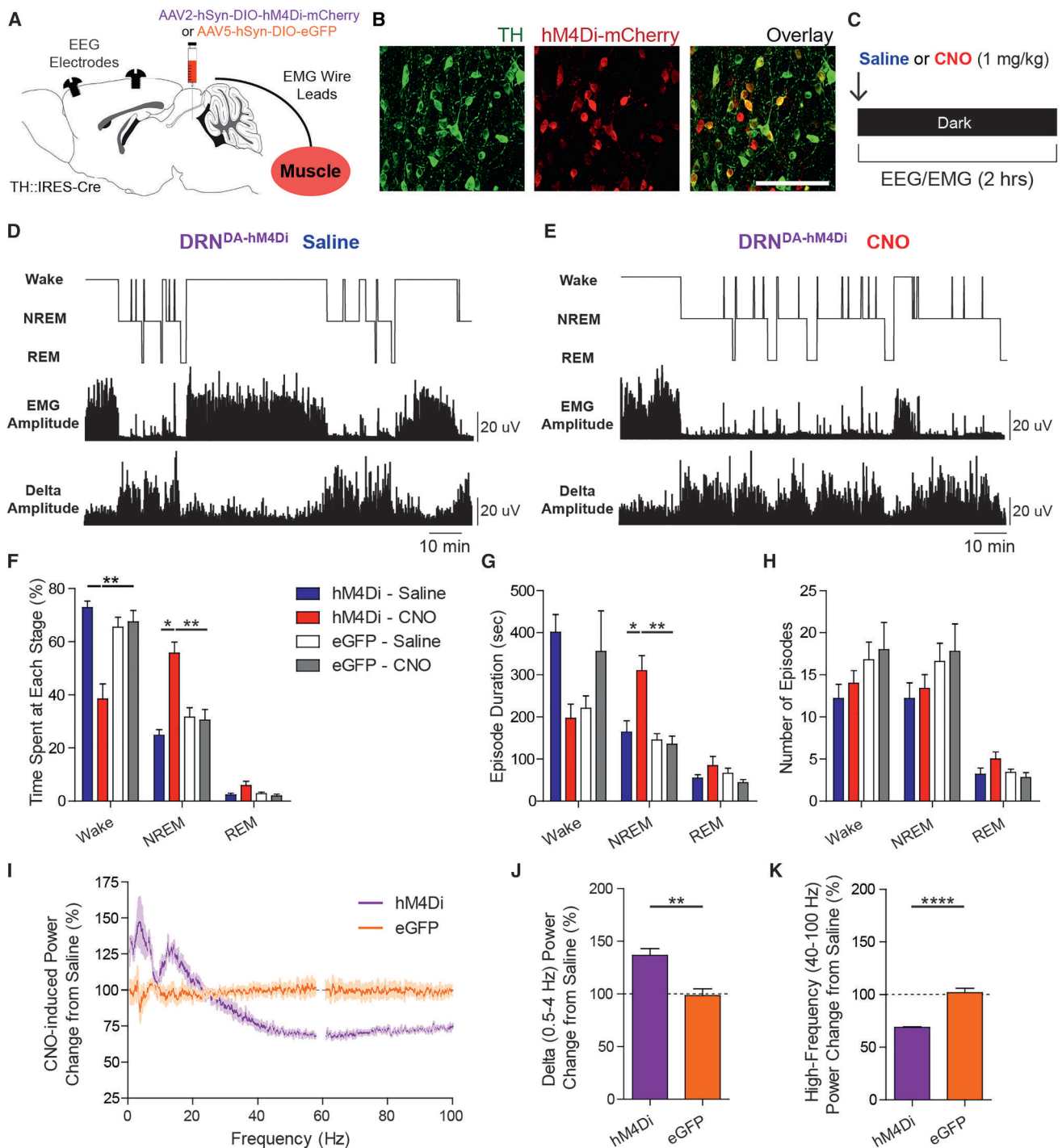


Figure 5. Chemogenetic Inhibition of DRN^{DA} Neurons Reduces Wakefulness

(A) AAV2-hSyn-DIO-hM4Di-mCherry or EGFP vectors were injected to the DRN of TH-Cre mice, and EEG/EMG electrodes were implanted for sleep-wake state classification.

(B) Confocal images of TH+ (green) neurons co-localized with hM4Di-mCherry (red) expression. Scale bar, 100 μ m.

(C) Saline or CNO (1 mg/kg) was intraperitoneally injected to inhibit DRN^{DA} neurons during the dark phase. EEG/EMG recordings were performed for 2 hr afterward.

(D) Representative hypnogram (top), EMG amplitude (middle, in 5 s windows), and delta amplitude (bottom, in 5 s windows) from a DRN^{DA}-hM4Di mouse after saline injection.

(E) Same as (D), but with CNO injection. CNO injection caused reduced wakefulness, accompanied by lower EMG and higher delta amplitudes.

(legend continued on next page)

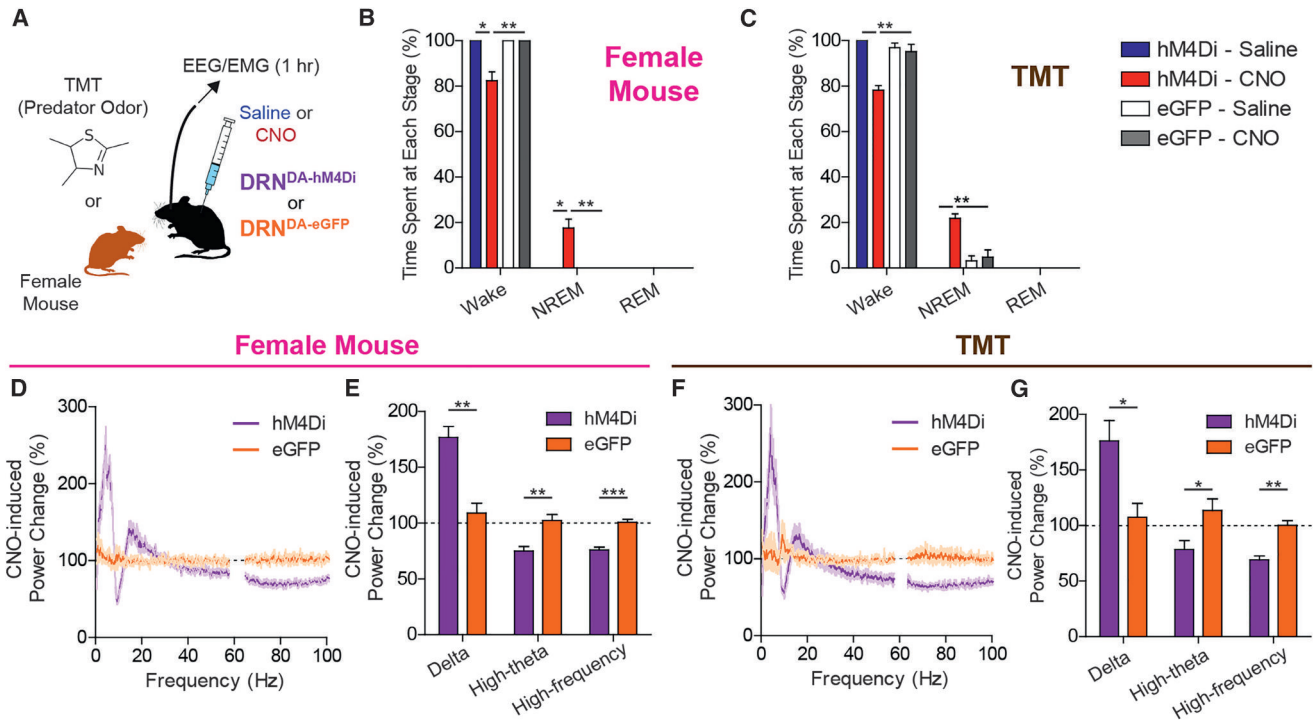


Figure 6. DRN^{DA} Firing Supports Wakefulness upon Exposure to Salient Stimuli

(A) DRN^{DA-hM4Di} and DRN^{DA-eGFP} mice were systemically administered with saline or CNO (1 mg/kg) 45 min prior to the introduction of a female mouse or a filter paper with predator odor TMT. EEG/EMG recordings were carried out for 1 hr after salient stimuli presentation.

(B) While the introduction of a female mouse induced robust wakefulness in other conditions, CNO-injected DRN^{DA-hM4Di} mice spent significantly reduced time in wakefulness at the cost of NREM sleep (n = 4 per group; two-way ANOVA revealed a group × drug interaction, $F_{1,15}$ [wake, NREM] = 20.83, $p < 0.01$, Bonferroni post hoc analysis, * $p < 0.05$, ** $p < 0.01$).

(C) Similar to (B), but a filter paper with predator odor TMT was introduced to home-cages. Compared to other conditions, CNO-injected DRN^{DA-hM4Di} mice spent significantly reduced time in wakefulness and increased time in NREM sleep (n = 4 per group; two-way ANOVA revealed a group × drug interaction, $F_{1,15}$ [wake, NREM] = 26.88, $p < 0.01$, Bonferroni post hoc analysis, ** $p < 0.01$).

(D) Power spectral density analysis during female mouse interaction revealed CNO-induced increase in low-frequency power and decrease in high-theta (8–12 Hz) and high-frequency power in DRN^{DA-hM4Di} mice with respect to the saline condition but no change in control mice.

(E) CNO-induced increase in delta (0.5–4 Hz) power and decrease in high-theta (8–12 Hz) and high-frequency (40–100 Hz) power were significantly larger in DRN^{DA-hM4Di} mice than in controls (n = 4 per group; unpaired t test, ** $p < 0.01$, *** $p < 0.001$).

(F) Same as (D), but for the TMT condition. A similar trend was observed as (D).

(G) CNO-induced increase in delta (0.5–4 Hz) power and decrease in high-theta (8–12 Hz) and high-frequency (40–100 Hz) power were significantly larger in DRN^{DA-hM4Di} mice than in controls (n = 4 per group; unpaired t test, * $p < 0.05$, ** $p < 0.01$).

Data represent mean ± SEM.

Matthews et al. (2016) further demonstrated that DRN^{DA} neurons signal aversion, a trend that was also corroborated, albeit weakly, by our data (Figure S4M). This is in stark contrast with

wake-promoting VTA^{DA} neurons, whose activity supports robust place preference and operant responding (Tsai et al., 2009; Witten et al., 2011). That neural circuits may be involved in two

(F) CNO injections into the DRN^{DA-hM4Di} mice decreased the time spent in wake and increased the time spent in NREM sleep (n = 5 per group; two-way ANOVA revealed a group × drug interaction in wake and NREM, $F_{1,19}$ [wake] = 20.96, $p < 0.01$, $F_{1,19}$ [NREM] = 28.34, $p < 0.001$, $F_{1,19}$ [REM] = 2.07, $p > 0.1$; Bonferroni post hoc analysis, * $p < 0.05$, ** $p < 0.01$).

(G) Duration of NREM sleep was significantly increased when DRN^{DA-hM4Di} mice were administered with CNO (n = 5 per group; two-way ANOVA revealed a group × drug interaction in NREM, $F_{1,19}$ [wake] = 3.84, $p > 0.05$, $F_{1,19}$ [NREM] = 10.78, $p < 0.05$, $F_{1,19}$ [REM] = 0.26, $p > 0.6$; Bonferroni post hoc analysis, ** $p < 0.01$, * $p < 0.05$).

(H) There was no difference in the number of episodes in all states (n = 5 per group; two-way ANOVA revealed no group × drug interaction, $F_{1,19}$ [wake] = 0.88, $F_{1,19}$ [NREM] = 0.52, $F_{1,19}$ [REM] = 0.55, all $p > 0.3$).

(I) Power spectral density analysis revealed CNO-induced increase in low-frequency power and decrease in high-frequency power in DRN^{DA-hM4Di} mice with respect to saline condition, but no change in controls.

(J) CNO-induced delta (0.5–4 Hz) power increase was significantly larger in DRN^{DA-hM4Di} mice compared to controls (n = 5 per group; unpaired t test, ** $p < 0.01$).

(K) CNO-induced high-frequency (40–100 Hz) power decrease was significantly larger in DRN^{DA-hM4Di} mice compared to controls (n = 5 per group; unpaired t test, **** $p < 0.0001$).

Data represent mean ± SEM.

seemingly unrelated roles, valence encoding and sleep-wake regulation, is not unique to midbrain DA groups; wake-promoting LC NA neurons and CRH inputs also convey negative valence (McCall et al., 2015). Considering the involvement of hypocretin and VTA^{DA} systems in reward behavior (España, 2012; Wise, 2004), there may be dichotomous wake-promoting pathways signaling positive or negative valence upon their activation. That DRN^{DA} neurons can simultaneously send arousal and anti-nociceptive signals (Li et al., 2016) can be understood by considering DRN^{DA} connectivity with the bed nucleus of stria terminalis (BNST; Figure S4Q), which is a critical regulator of pain perception (Minami and Ide, 2015).

Compared to ventral midbrain DA counterparts (Schultz, 1997; Ungless et al., 2004; Matsumoto and Hikosaka, 2009; Cohen et al., 2012; Lerner et al., 2015; Kim et al., 2016), the natural dynamics of DRN^{DA} neurons are much less characterized. Due to their relative low number and shared projection targets, DRN^{DA} neurons have been assumed to be functionally similar to VTA^{DA} neurons and hence termed the dorso-caudal extension of the VTA (A10) or A10 dc group (Hokfelt et al., 1984). Several pieces of evidence argue against their treatment as a mere extension of the VTA. Unlike the well-studied dorsal or lateral VTA^{DA} neurons, which fire bursts in response to rewarding or reward-predicting stimuli and are inhibited by punishment (Schultz, 1997; Ungless et al., 2004; Cohen et al., 2012; Kim et al., 2016), or the ventromedial VTA^{DA} neurons, which are selectively excited by aversive stimuli (Brischoux et al., 2009), DRN^{DA} neurons appear to be activated by any alerting or salient stimulus, regardless of valence (Figures 1 and S2). Also, they appear to be minimally affected by physically salient but motivationally neutral cues, such as novel or familiar objects (Figure 1). Since both rewarding and aversive stimuli elicit arousal and motivated responding, the VTA^{DA} system may address this challenge of dual positive (Schultz, 1997) and negative (Brischoux et al., 2009; Matsumoto and Hikosaka, 2009; Zweifel et al., 2011) valence coding in part through segregating to functionally and electrophysiologically distinct subgroups split across anatomical gradients (Brischoux et al., 2009; Bromberg-Martin et al., 2010) or projection targets (Lammel et al., 2011). The DRN^{DA} population, from our observations, showed bimodal activation at the population level, responding to both positive and negative stimuli. Whether individual DRN^{DA} neurons are uniformly excited by positive and negative valence (therefore encoding salience), or whether they are oppositely tuned and intermingled within the DRN, will require future single-cell recording techniques.

DRN^{DA} and VTA^{DA} populations diverge significantly in downstream targets, which may help to explain their functional heterogeneity. Optogenetic excitation of VTA^{DA} neurons, especially those projecting to the nucleus accumbens, supports both appetitive conditioning and positive reinforcement behavior (Wise, 2004; Witten et al., 2011; Steinberg et al., 2014), whereas stimulation of DRN^{DA} neurons produces neutral or mild aversion (Figure S4M; Matthews et al., 2016). These observations may be indicative of differences in downstream connectivity between these neuronal populations. Although DRN^{DA} and VTA^{DA} neurons share overlap in some of their downstream targets (e.g., the prefrontal cortex and the basolateral amygdala), DA neurons projecting to cortical and striatal regions predominantly arise

from the VTA (Björklund and Dunnett, 2007). DRN^{DA} terminals, however, are biased toward the extended amygdala, such as the BNST and central nucleus of the amygdala (CeA) (Figures S4P–S4S; Hasue and Shammah-Lagnado, 2002). Thus, as a major source of excitatory DA drive to the BNST and CeA (Matthews et al., 2016), two regions known to bi-directionally affect motivated behavior and regulate complex emotional states (Jennings et al., 2013), DRN^{DA} neurons are uniquely positioned to provide excitatory signals about environmental salience and internal arousal state to downstream nuclei, which can in turn initiate appropriate behavior, including triggering vigilance or patterning sleep-wake states.

Although DA has been implicated in sleep-wake regulation by pharmacological (Lin et al., 1992), genetic (Wisor et al., 2001), and clinical (Lima, 2013) studies, the precise circuits mediating such actions have been elusive. Single-unit recordings of VTA^{DA} and SNc^{DA} neurons have indicated that they do not change their mean firing rate across distinct sleep-wake states (Miller et al., 1983; Dahan et al., 2007). Here, we show that DRN^{DA} neurons are wake-active (Figures 2 and 3), whereas VTA^{DA} neurons exhibited increased burst firing or Ca²⁺ signals during REM sleep over wakefulness (Dahan et al., 2007; Eban-Rothschild et al., 2016). While the role of VTA^{DA} firing during REM sleep remains elusive, optogenetic activation of VTA^{DA} neurons can promote behavioral and electrocortical arousal (Eban-Rothschild et al., 2016; Taylor et al., 2016). Unlike the DRN^{DA} or VTA^{DA} populations, other DA groups appear to promote sleep rather than wakefulness. For example, chemical lesion of the SNc^{DA} neurons projecting to the dorsal striatum (DS) promotes wakefulness, and optogenetic stimulation of SNc^{DA} terminals in the DS increases NREM sleep (Qiu et al., 2016). Outside the midbrain, A13 zona incerta DA neurons express *c-fos* after REM sleep rebound (Léger et al., 2010). Taken together, these studies indicate that anatomically segregated DA populations may play functionally heterogeneous or even opposing roles in regulating sleep-wake states, and the DRN^{DA} as well as VTA^{DA} systems represent key arousal-promoting DA populations.

As shown here (Figures 6 and S6), external factors can influence sleep-wake patterns, and DRN^{DA} neurons contribute to these processes. Our findings that DRN^{DA} activity tracks the arousal states over broad temporal scales and that DRN^{DA} neurons respond to salient external cues position the DRN^{DA} system at the interface between internal (e.g., wake/sleep drive) and external (e.g., salient stimuli) influences in regulating sleep-wake states. While this evolutionarily conserved trait is advantageous for organism survival, its dysfunction may have negative implications in humans, in which sleep disorders triggered by the malfunctioning of arousal-promoting circuits represent a highly morbid societal burden (Sanford et al., 2015). DRN^{DA} neurons are not well studied in humans, but it has been shown that they degenerate in patients with multiple systems atrophy and Lewy body dementia, which commonly cause excessive daytime sleepiness (Benarroch et al., 2009). Going forward, therapeutic strategies targeting DRN^{DA} activity may have utility in the treatment of primary sleep-wake disorders and sleep/arousal disturbances secondary to myriad neuropsychiatric diseases (Sateia et al., 2000), including major depressive disorder, bipolar affective disorder, and schizophrenia.

STAR★METHODS

Detailed methods are provided in the online version of this paper and include the following:

- KEY RESOURCES TABLE
- CONTACT FOR REAGENT AND RESOURCE SHARING
- EXPERIMENTAL MODEL AND SUBJECT DETAILS
 - Surgeries for viral delivery, optical fiber and EEG/EMG implantation
 - Fiber photometry
 - Behavioral experiments
 - EEG/EMG data acquisition, processing, and sleep-wake state classification
 - Optogenetic and chemogenetic modulation of behavioral states and locomotion
 - Auditory cue arousal test
 - Data analysis
 - Ex vivo electrophysiology
 - Histology
- QUANTIFICATION AND STATISTICAL ANALYSIS

SUPPLEMENTAL INFORMATION

Supplemental Information includes six figures and two movies and can be found with this article online at <http://dx.doi.org/10.1016/j.neuron.2017.05.020>.

AUTHOR CONTRIBUTIONS

J.R.C., J.B.T., and V.G. conceived and designed the project. J.R.C. performed and collected data from EEG/EMG recording, fiber photometry, and optogenetic, chemogenetic, and behavioral experiments. C.X. and J.E.R. performed ex vivo slice recordings. J.R.C., J.B.T., and V.G. analyzed data and made figures. J.R.C. and A.G. assembled the fiber photometry setup and wrote scripts for processing. J.R.C. and L.R.B. set up the EEG and EMG recording system. J.R.C., J.B.T., and V.G. wrote the manuscript with significant contributions from J.E.R. and L.R.B. All authors read and approved the final manuscript. V.G. supervised all aspects of the project.

ACKNOWLEDGMENTS

We would like to acknowledge Drs. Karl Deisseroth and Tom Davidson for the fiber photometry setup. We appreciate the entire Gradinaru lab and Dr. David Anderson for helpful discussions. This work was supported by the NIH (Director's New Innovator grants IDP20D017782-01 and PECASE), the NIH/NIA (grants 1R01AG047664-01 and NIH BRAIN 1U01NS090577), the Heritage Medical Research Institute (HMRI-15-09-01), the Pew Charitable Trust (00026171), the Michael J. Fox Foundation (RRIA 2013), Caltech-GIST (CG2013), and the Sloan Foundation (FR2015-65471, to V.G.). J.B.T. is a Colvin postdoctoral fellow. J.E.R. is supported by the Children's Tumor Foundation (2016-01-006). C.X. was partly supported by the Michael J. Fox Foundation.

Received: October 6, 2016

Revised: March 31, 2017

Accepted: May 11, 2017

Published: June 8, 2017

REFERENCES

Aston-Jones, G., and Bloom, F.E. (1981). Activity of norepinephrine-containing locus coeruleus neurons in behaving rats anticipates fluctuations in the sleep-waking cycle. *J. Neurosci.* *1*, 876–886.

Benarroch, E.E., Schmeichel, A.M., Dugger, B.N., Sandroni, P., Parisi, J.E., and Low, P.A. (2009). Dopamine cell loss in the periaqueductal gray in multiple system atrophy and Lewy body dementia. *Neurology* *73*, 106–112.

Björklund, A., and Dunnett, S.B. (2007). Dopamine neuron systems in the brain: an update. *Trends Neurosci.* *30*, 194–202.

Brischoux, F., Chakraborty, S., Brierley, D.I., and Ungless, M.A. (2009). Phasic excitation of dopamine neurons in ventral VTA by noxious stimuli. *Proc. Natl. Acad. Sci. USA* *106*, 4894–4899.

Bromberg-Martin, E.S., Matsumoto, M., and Hikosaka, O. (2010). Dopamine in motivational control: rewarding, aversive, and alerting. *Neuron* *68*, 815–834.

Brown, R.E., Basheer, R., McKenna, J.T., Strecker, R.E., and McCarley, R.W. (2012). Control of sleep and wakefulness. *Physiol. Rev.* *92*, 1087–1187.

Chen, T.W., Wardill, T.J., Sun, Y., Pulver, S.R., Renninger, S.L., Baohan, A., Schreiter, E.R., Kerr, R.A., Orger, M.B., Jayaraman, V., et al. (2013). Ultrasensitive fluorescent proteins for imaging neuronal activity. *Nature* *499*, 295–300.

Cohen, J.Y., Haesler, S., Vong, L., Lowell, B.B., and Uchida, N. (2012). Neuron-type-specific signals for reward and punishment in the ventral tegmental area. *Nature* *482*, 85–88.

Daberkow, D.P., Brown, H.D., Bunner, K.D., Kraniotis, S.A., Doellman, M.A., Ragozzino, M.E., Garris, P.A., and Roitman, M.F. (2013). Amphetamine paradoxically augments exocytotic dopamine release and phasic dopamine signals. *J. Neurosci.* *33*, 452–463.

Dahan, L., Astier, B., Vautrelle, N., Urbain, N., Kocsis, B., and Chouvet, G. (2007). Prominent burst firing of dopaminergic neurons in the ventral tegmental area during paradoxical sleep. *Neuropsychopharmacology* *32*, 1232–1241.

Descarries, L., Berthelet, F., Garcia, S., and Beaudet, A. (1986). Dopaminergic projection from nucleus raphe dorsalis to neostriatum in the rat. *J. Comp. Neurol.* *249*, 511–520, 484–515.

Dougalis, A.G., Matthews, G.A., Bishop, M.W., Brischoux, F., Kobayashi, K., and Ungless, M.A. (2012). Functional properties of dopamine neurons and co-expression of vasoactive intestinal polypeptide in the dorsal raphe nucleus and ventro-lateral periaqueductal grey. *Eur. J. Neurosci.* *36*, 3322–3332.

Eban-Rothschild, A., Rothschild, G., Giardino, W.J., Jones, J.R., and de Lecea, L. (2016). VTA dopaminergic neurons regulate ethologically relevant sleep-wake behaviors. *Nat. Neurosci.* *19*, 1356–1366.

España, R.A. (2012). Hypocretin/orexin involvement in reward and reinforcement. *Vitam. Horm.* *89*, 185–208.

Garey, J., Goodwillie, A., Frohlich, J., Morgan, M., Gustafsson, J.A., Smithies, O., Korach, K.S., Ogawa, S., and Pfaff, D.W. (2003). Genetic contributions to generalized arousal of brain and behavior. *Proc. Natl. Acad. Sci. USA* *100*, 11019–11022.

George, E.D., Bordner, K.A., Elwafi, H.M., and Simen, A.A. (2010). Maternal separation with early weaning: a novel mouse model of early life neglect. *BMC Neurosci.* *11*, 123.

Gjerstad, M.D., Wentzel-Larsen, T., Aarsland, D., and Larsen, J.P. (2007). Insomnia in Parkinson's disease: frequency and progression over time. *J. Neurol. Neurosurg. Psychiatry* *78*, 476–479.

Gunaydin, L.A., Grosenick, L., Finkelstein, J.C., Kauvar, I.V., Fenno, L.E., Adhikari, A., Lammel, S., Mirzabekov, J.J., Airan, R.D., Zalocusky, K.A., et al. (2014). Natural neural projection dynamics underlying social behavior. *Cell* *157*, 1535–1551.

Hasue, R.H., and Shammah-Lagnado, S.J. (2002). Origin of the dopaminergic innervation of the central extended amygdala and accumbens shell: a combined retrograde tracing and immunohistochemical study in the rat. *J. Comp. Neurol.* *454*, 15–33.

Hokfelt, T., Martensson, R., Björklund, A., Kleinau, S., and Goldstein, M. (1984). Distribution Maps of Tyrosine-Hydroxylase-Immunoreactive Neurons in the Rat Brain (Elsevier).

Jennings, J.H., Sparta, D.R., Stamatakis, A.M., Ung, R.L., Pleil, K.E., Kash, T.L., and Stuber, G.D. (2013). Distinct extended amygdala circuits for divergent motivational states. *Nature* *496*, 224–228.

- Jones, B.E. (1991). Paradoxical sleep and its chemical/structural substrates in the brain. *Neuroscience* 40, 637–656.
- Jouvet, M. (1999). Sleep and serotonin: an unfinished story. *Neuropsychopharmacology* 21 (2, Suppl), 24S–27S.
- Kim, C.K., Yang, S.J., Pichamoorthy, N., Young, N.P., Kauvar, I., Jennings, J.H., Lerner, T.N., Berndt, A., Lee, S.Y., Ramakrishnan, C., et al. (2016). Simultaneous fast measurement of circuit dynamics at multiple sites across the mammalian brain. *Nat. Methods* 13, 325–328.
- Lammel, S., Ion, D.I., Roeper, J., and Malenka, R.C. (2011). Projection-specific modulation of dopamine neuron synapses by aversive and rewarding stimuli. *Neuron* 70, 855–862.
- Lammel, S., Lim, B.K., Ran, C., Huang, K.W., Betley, M.J., Tye, K.M., Deisseroth, K., and Malenka, R.C. (2012). Input-specific control of reward and aversion in the ventral tegmental area. *Nature* 491, 212–217.
- Lammel, S., Lim, B.K., and Malenka, R.C. (2014). Reward and aversion in a heterogeneous midbrain dopamine system. *Neuropharmacology* 76 (Pt B), 351–359.
- Léger, L., Sapin, E., Goutagny, R., Peyron, C., Salvert, D., Fort, P., and Luppi, P.H. (2010). Dopaminergic neurons expressing Fos during waking and paradoxical sleep in the rat. *J. Chem. Neuroanat.* 39, 262–271.
- Lerner, T.N., Shilyansky, C., Davidson, T.J., Evans, K.E., Beier, K.T., Zalocusky, K.A., Crow, A.K., Malenka, R.C., Luo, L., Tomer, R., and Deisseroth, K. (2015). Intact-brain analyses reveal distinct information carried by SNc dopamine subcircuits. *Cell* 162, 635–647.
- Li, C., Sugam, J.A., Lowery-Gionta, E.G., McElligott, Z.A., McCall, N.M., Lopez, A.J., McKlveen, J.M., Pleil, K.E., and Kash, T.L. (2016). Mu opioid receptor modulation of dopamine neurons in the periaqueductal gray/dorsal raphe: a role in regulation of pain. *Neuropsychopharmacology* 41, 2122–2132.
- Lima, M.M. (2013). Sleep disturbances in Parkinson's disease: the contribution of dopamine in REM sleep regulation. *Sleep Med. Rev.* 17, 367–375.
- Lin, J.S., Roussel, B., Akaoka, H., Fort, P., Debilly, G., and Jouvet, M. (1992). Role of catecholamines in the modafinil and amphetamine induced wakefulness, a comparative pharmacological study in the cat. *Brain Res.* 597, 319–326.
- Lu, J., Zhou, T.C., and Saper, C.B. (2006). Identification of wake-active dopaminergic neurons in the ventral periaqueductal gray matter. *J. Neurosci.* 26, 193–202.
- Margolis, E.B., Mitchell, J.M., Ishikawa, J., Hjelmstad, G.O., and Fields, H.L. (2008). Midbrain dopamine neurons: projection target determines action potential duration and dopamine D(2) receptor inhibition. *J. Neurosci.* 28, 8908–8913.
- Matsumoto, M., and Hikosaka, O. (2009). Two types of dopamine neuron distinctly convey positive and negative motivational signals. *Nature* 459, 837–841.
- Matthews, G.A., Nieh, E.H., Vander Weele, C.M., Halbert, S.A., Pradhan, R.V., Yosafat, A.S., Glober, G.F., Izadmehr, E.M., Thomas, R.E., Lacy, G.D., et al. (2016). Dorsal raphe dopamine neurons represent the experience of social isolation. *Cell* 164, 617–631.
- Mattis, J., Tye, K.M., Ferenczi, E.A., Ramakrishnan, C., O'Shea, D.J., Prakash, R., Gunaydin, L.A., Hyun, M., Fenno, L.E., Gradinaru, V., et al. (2011). Principles for applying optogenetic tools derived from direct comparative analysis of microbial opsins. *Nat. Methods* 9, 159–172.
- McCall, J.G., Al-Hasani, R., Siuda, E.R., Hong, D.Y., Norris, A.J., Ford, C.P., and Bruchas, M.R. (2015). CRH engagement of the locus coeruleus noradrenergic system mediates stress-induced anxiety. *Neuron* 87, 605–620.
- McDevitt, R.A., Tiran-Cappello, A., Shen, H., Balderas, I., Britt, J.P., Marino, R.A., Chung, S.L., Richie, C.T., Harvey, B.K., and Bonci, A. (2014). Serotonergic versus nonserotonergic dorsal raphe projection neurons: differential participation in reward circuitry. *Cell Rep.* 8, 1857–1869.
- Miller, J.D., Farber, J., Gatz, P., Roffwarg, H., and German, D.C. (1983). Activity of mesencephalic dopamine and non-dopamine neurons across stages of sleep and waking in the rat. *Brain Res.* 273, 133–141.
- Minami, M., and Ide, S. (2015). How does pain induce negative emotion? Role of the bed nucleus of the stria terminalis in pain-induced place aversion. *Curr. Mol. Med.* 15, 184–190.
- Morales, M., and Margolis, E.B. (2017). Ventral tegmental area: cellular heterogeneity, connectivity and behaviour. *Nat. Rev. Neurosci.* 18, 73–85.
- Nagatsu, I., Inagaki, S., Kondo, Y., Karasawa, N., and Nagatsu, T. (1979). Immunofluorescent studies on the localization of tyrosine hydroxylase and dopamine-beta-hydroxylase in the mes-, di-, and telencephalon of the rat using unperfused fresh frozen section. *Acta Histochem. Cytochem.* 12, 20–37.
- Pimentel, D., Donlea, J.M., Talbot, C.B., Song, S.M., Thurston, A.J., and Miesenböck, G. (2016). Operation of a homeostatic sleep switch. *Nature* 536, 333–337.
- Pinto, L., Goard, M.J., Estandian, D., Xu, M., Kwan, A.C., Lee, S.H., Harrison, T.C., Feng, G., and Dan, Y. (2013). Fast modulation of visual perception by basal forebrain cholinergic neurons. *Nat. Neurosci.* 16, 1857–1863.
- Poulin, J.F., Zou, J., Drouin-Ouellet, J., Kim, K.Y., Cicchetti, F., and Awatramani, R.B. (2014). Defining midbrain dopaminergic neuron diversity by single-cell gene expression profiling. *Cell Rep.* 9, 930–943.
- Qiu, M.H., Yao, Q.L., Vetrivelan, R., Chen, M.C., and Lu, J. (2016). Nigrostriatal dopamine action on globus pallidus regulates sleep. *Cereb. Cortex* 26, 1430–1439.
- Qu, W.M., Huang, Z.L., Xu, X.H., Matsumoto, N., and Urade, Y. (2008). Dopaminergic D1 and D2 receptors are essential for the arousal effect of modafinil. *J. Neurosci.* 28, 8462–8469.
- Rajasethupathy, P., Ferenczi, E., and Deisseroth, K. (2016). Targeting neural circuits. *Cell* 165, 524–534.
- Sakurai, T., Amemiya, A., Ishii, M., Matsuzaki, I., Chemelli, R.M., Tanaka, H., Williams, S.C., Richardson, J.A., Kozlowski, G.P., Wilson, S., et al. (1998). Orexins and orexin receptors: a family of hypothalamic neuropeptides and G protein-coupled receptors that regulate feeding behavior. *Cell* 92, 573–585.
- Sanford, L.D., Suchecki, D., and Meerlo, P. (2015). Stress, arousal, and sleep. *Curr. Top. Behav. Neurosci.* 25, 379–410.
- Sateia, M.J., Greenough, G., and Nowell, P. (2000). Sleep in neuropsychiatric disorders. *Semin. Clin. Neuropsychiatry* 5, 227–237.
- Schultz, W. (1997). Dopamine neurons and their role in reward mechanisms. *Curr. Opin. Neurobiol.* 7, 191–197.
- Schweimer, J.V., and Ungless, M.A. (2010). Phasic responses in dorsal raphe serotonin neurons to noxious stimuli. *Neuroscience* 171, 1209–1215.
- Steinberg, E.E., Boivin, J.R., Saunders, B.T., Witten, I.B., Deisseroth, K., and Janak, P.H. (2014). Positive reinforcement mediated by midbrain dopamine neurons requires D1 and D2 receptor activation in the nucleus accumbens. *PLoS ONE* 9, e94771.
- Szymusiak, R., and McGinty, D. (2008). Hypothalamic regulation of sleep and arousal. *Ann. N Y Acad. Sci.* 1129, 275–286.
- Takahashi, K., Kayama, Y., Lin, J.S., and Sakai, K. (2010). Locus coeruleus neuronal activity during the sleep-waking cycle in mice. *Neuroscience* 169, 1115–1126.
- Taylor, N.E., Van Dort, C.J., Kenny, J.D., Pei, J., Guidera, J.A., Vlasov, K.Y., Lee, J.T., Boyden, E.S., Brown, E.N., and Solt, K. (2016). Optogenetic activation of dopamine neurons in the ventral tegmental area induces reanimation from general anesthesia. *Proc. Natl. Acad. Sci. USA* 113, 12826–12831.
- Tsai, H.C., Zhang, F., Adamantidis, A., Stuber, G.D., Bonci, A., de Lecea, L., and Deisseroth, K. (2009). Phasic firing in dopaminergic neurons is sufficient for behavioral conditioning. *Science* 324, 1080–1084.
- Ungless, M.A., Magill, P.J., and Bolam, J.P. (2004). Uniform inhibition of dopamine neurons in the ventral tegmental area by aversive stimuli. *Science* 303, 2040–2042.

- Urban, D.J., and Roth, B.L. (2015). DREADDs (designer receptors exclusively activated by designer drugs): chemogenetic tools with therapeutic utility. *Annu. Rev. Pharmacol. Toxicol.* *55*, 399–417.
- Vinck, M., Batista-Brito, R., Knoblich, U., and Cardin, J.A. (2015). Arousal and locomotion make distinct contributions to cortical activity patterns and visual encoding. *Neuron* *86*, 740–754.
- Whitaker, L.R., Degoulet, M., and Morikawa, H. (2013). Social deprivation enhances VTA synaptic plasticity and drug-induced contextual learning. *Neuron* *77*, 335–345.
- Winsky-Sommerer, R., Boutrel, B., and de Lecea, L. (2005). Stress and arousal: the corticotrophin-releasing factor/hypocretin circuitry. *Mol. Neurobiol.* *32*, 285–294.
- Wise, R.A. (2004). Dopamine, learning and motivation. *Nat. Rev. Neurosci.* *5*, 483–494.
- Wisor, J.P., Nishino, S., Sora, I., Uhl, G.H., Mignot, E., and Edgar, D.M. (2001). Dopaminergic role in stimulant-induced wakefulness. *J. Neurosci.* *21*, 1787–1794.
- Witten, I.B., Steinberg, E.E., Lee, S.Y., Davidson, T.J., Zalocusky, K.A., Brodsky, M., Yizhar, O., Cho, S.L., Gong, S., Ramakrishnan, C., et al. (2011). Recombinase-driver rat lines: tools, techniques, and optogenetic application to dopamine-mediated reinforcement. *Neuron* *72*, 721–733.
- Xu, M., Chung, S., Zhang, S., Zhong, P., Ma, C., Chang, W.C., Weissbourd, B., Sakai, N., Luo, L., Nishino, S., and Dan, Y. (2015). Basal forebrain circuit for sleep-wake control. *Nat. Neurosci.* *18*, 1641–1647.
- Zweifel, L.S., Fadok, J.P., Argilli, E., Garelick, M.G., Jones, G.L., Dickerson, T.M., Allen, J.M., Mizumori, S.J., Bonci, A., and Palmiter, R.D. (2011). Activation of dopamine neurons is critical for aversive conditioning and prevention of generalized anxiety. *Nat. Neurosci.* *14*, 620–626.

A Map of Anticipatory Activity in Mouse Motor Cortex

Tsai-Wen Chen,^{1,2} Nuo Li,^{1,3} Kayvon Daie,¹ and Karel Svoboda^{1,4,*}

¹Janelia Research Campus, HHMI, Ashburn, VA 20147, USA

²Institute of Neuroscience, National Yang-Ming University, Taipei, 112 Taiwan

³Present address: Baylor College of Medicine, One Baylor Plaza, Room T632, Houston, TX 77030, USA

⁴Lead Contact

*Correspondence: svobodak@janelia.hhmi.org

<http://dx.doi.org/10.1016/j.neuron.2017.05.005>

SUMMARY

Activity in the mouse anterior lateral motor cortex (ALM) instructs directional movements, often seconds before movement initiation. It is unknown whether this preparatory activity is localized to ALM or widely distributed within motor cortex. Here we imaged activity across motor cortex while mice performed a whisker-based object localization task with a delayed, directional licking response. During tactile sensation and the delay epoch, object location was represented in motor cortex areas that are medial and posterior relative to ALM, including vibrissal motor cortex. Preparatory activity appeared first in deep layers of ALM, seconds before the behavioral response, and remained localized to ALM until the behavioral response. Later, widely distributed neurons represented the outcome of the trial. Cortical area was more predictive of neuronal selectivity than laminar location or axonal projection target. Motor cortex therefore represents sensory, motor, and outcome information in a spatially organized manner.

INTRODUCTION

The motor cortex plays roles in planning and executing voluntary movements (Shenoy et al., 2013). Activating different regions of the motor cortex causes movements of specific body parts (Kobayashi et al., 2010; Li et al., 2015; Matyas et al., 2010; Neafsey et al., 1986; Tennant et al., 2011; Travers et al., 1997). Consistent with a role in controlling movement, motor cortex neurons encode variables related to movement, such as movement direction and speed as well as muscle force (Scott, 2008). Motor cortex activity also anticipates movement. In delayed response tasks, motor cortex neurons show preparatory activity, which predicts specific movements, including arm movements (Crutcher and Alexander, 1990; Riehle and Requin, 1989; Tanji and Evarts, 1976), eye movements (Bruce and Goldberg, 1985), body orienting (Erich et al., 2011), and tongue movements (Guo et al., 2014b), often seconds before initiation of the move-

ment (Churchland et al., 2010). Disrupting preparatory activity can bias movement direction (Guo et al., 2014b; Li et al., 2015) or delay movement onset (Churchland and Shenoy, 2007). Preparatory activity is therefore considered a neural correlate of motor preparation, also referred to as motor planning.

During decision making, the brain evaluates sensory input and recent reward history to choose an action. Preparatory activity is an early neural correlate of behavioral choice. The cortical area showing the earliest preparatory activity is likely part of a neural circuit that selects and initiates the action, a critical step in decision making (Sul et al., 2011). Identifying areas showing the earliest preparatory activity is thus critical for mechanistic analyses of decision making and motor preparation. Preparatory activity has been reported in multiple parts of motor cortex (Bruce and Goldberg, 1985; Crutcher and Alexander, 1990; Erlich et al., 2011; Guo et al., 2014b; Hernández et al., 2010) and other brain areas (Goard et al., 2016; Maimon and Assad, 2006; Tanaka, 2007). It is not known whether preparatory activity originates in one locus and then spreads to other areas, or whether preparatory activity appears concurrently in multiple areas within the motor cortex.

Recently developed delayed response tasks for rodents are beginning to allow a more comprehensive and mechanistic analysis of motor preparation (Erich et al., 2011, 2015; Goard et al., 2016; Guo et al., 2014b; Li et al., 2015, 2016). In one such task mice report the location of an object, sensed with their whiskers by directional licking (Guo et al., 2014a). Brief and localized optogenetic silencing experiments identified the anterior lateral motor cortex (ALM; centered on 2.5 mm anterior, 1.5 mm lateral) as a hub for planning voluntary licking in mice (Guo et al., 2014b; Li et al., 2016). A large proportion of ALM neurons exhibit persistent and ramping preparatory activity during the delay epoch before the movement (Guo et al., 2014b; Li et al., 2015, 2016). Preparatory activity coding for different movement directions is distributed across both ALM hemispheres, similar to preparatory activity in human premotor cortex (Fried et al., 2011). Maintenance of preparatory activity requires reverberations in a cortico-thalamocortical loop (Guo et al., 2017).

Three types of manipulation experiment show that preparatory activity in ALM and connected subcortical structures instructs future directed licking. First, unilateral inactivation of ALM, but not surrounding cortical areas, during motor preparation impairs upcoming licking in the contralateral direction, without impairing licking in general (Guo et al., 2014b). The effects of unilateral inactivation are similar to the spatial contralesional neglect

observed after unilateral lesion of the primate premotor cortex (Kerkhoff, 2001; Rizzolatti et al., 1983). Second, transient unilateral activation of ALM pyramidal tract neurons has persistent effects on ALM population activity and biases the direction of future licking in the contralateral direction (Li et al., 2015). Third, brief bilateral inactivation destroys ALM preparatory activity on average and randomizes future licking direction; but on a trial-by-trial basis, licking direction can still be predicted based on ALM population activity before movement onset (Li et al., 2016). These experiments establish a causal link between ALM preparatory activity and licking direction.

Other studies have found preparatory activity outside of ALM in the rodent motor cortex. A more posterior and medial area, referred to as frontal orienting field (Erlich et al., 2011) and vibrissal motor cortex (Brecht, 2011; Hill et al., 2011; Hooks et al., 2011, 2013; Mao et al., 2011; Matyas et al., 2010) can show preparatory activity for orienting movements (Erlich et al., 2011). This area also overlaps with the anterior part of the somatic forelimb motor cortex (Tennant et al., 2011). Here we refer to this multimodal motor cortex area as medial motor cortex (MM) (mouse coordinates centered on, 1.5 mm anterior, 1 mm lateral). Together these studies suggest that preparatory activity might be widely distributed across motor cortex. One confounding issue is that comparisons across multiple regions of motor cortex have rarely been made within the same task (but see Crutcher and Alexander, 1990; Hernández et al., 2010; Sul et al., 2011).

Other experiments have described coding for touch (Ferezou et al., 2007; Huber et al., 2012; Kleinfeld et al., 2002; Petreanu et al., 2012), visual input (Goard et al., 2016), and whisker movement (Hill et al., 2011; Huber et al., 2012; Petreanu et al., 2012) in mouse motor cortex. The diverse patterns of behavior-related activity, including preparatory activity, seen in motor cortex could be distributed differentially across cell types within a motor cortical area. Evidence for cell-type-specific coding has come from recordings from the two major projection neuron classes in motor cortex (Li et al., 2015; Turner and DeLong, 2000; Sommer and Wurtz, 2000): intratelencephalic (IT) neurons that project to other cortical areas and pyramidal tract (PT) neurons that project out of the cortex, including the superior colliculus, brainstem, and spinal cord (Shepherd, 2013). IT neurons connect to other IT neurons and excite PT neurons, but not vice versa. PT neurons are thus at the output end of the local motor cortex circuit (Brown and Hestrin, 2009; Hooks et al., 2013; Kiritani et al., 2012; Morishima and Kawaguchi, 2006). ALM PT neurons in layer 5B project to subcortical structures that control facial movements, including the contralateral intermediate nucleus of the reticular formation, which is presynaptic to the hypoglossal nucleus and the intrinsic and extrinsic muscles of the tongue (Komiya et al., 2010; Stanek et al., 2014; Travers et al., 1997). A comparison of IT and PT neuron activity in ALM suggests that both populations show preparatory activity, but activity consistent with a movement command is specific to PT neurons. How selectivity is distributed across IT and PT neurons in other parts of the motor cortex during behavior is not known.

Here we map behavior-related activity across the motor cortex while mice performed a tactile delayed directional licking task. Our goal was to address two related questions. First, is prepara-

tory activity limited to, most prevalent in, or earliest in ALM? Second, are neural activity patterns most correlated with membership of motor cortical area, cortical layer, or neuronal projection type? To address these questions, we used cellular imaging in transgenic mice expressing the protein calcium indicator GCaMP6s (Chen et al., 2013; Dana et al., 2014). This allowed us to measure encoding of behavior-related variables in tens of thousands of neurons distributed across the motor cortex in an unbiased manner. Parallel experiments were performed using silicon probe recordings in ALM and MM. We observed diverse task-related activity in both ALM and MM. A whisker-related persistent representation of trial type emerged in superficial and deep MM. Neurons showing preparatory activity selective for upcoming licking directions emerged first in the deep layers of ALM. Preparatory activity was largely confined to ALM in the delay epoch and spread to superficial ALM layers and other parts of motor cortex at the time of movement. Correlating cortical location, cortical depth, and axonal projection type with encoding revealed a strong effect of cortical location in explaining the diversity of neuronal response compared to other factors.

RESULTS

We imaged behavior-related population activity across the motor cortex in mice performing a whisker-based object location discrimination task with a delay epoch (Guo et al., 2014b; Li et al., 2015). In each trial, a vertical pole (“object”) was presented in one of two positions (anterior or posterior) during a sample epoch (duration, 1.2 s) (Figure 1). Mice discriminated object locations using their whiskers. During a subsequent delay epoch, mice planned the upcoming response. An auditory “go” cue (0.1 s) signaled the beginning of the response epoch, and mice reported object location by licking one of two ports (posterior → lick right; anterior → lick left) (Figures 1A and 1B). Because calcium imaging provides a low-pass filtered report of neural activity (decay time in GP4.3 mice, ~350 ms; Dana et al., 2014), we used a long delay epoch (3 s). This allowed us to isolate neural activity related to distinct behavioral epochs using calcium imaging. In addition, a parallel set of experiments was performed using single unit measurements with silicon probe electrodes (Figure 7).

We considered four trial types: on correct trials, mice licked as instructed by the object location (correct right [CR]; correct left [CL]) and were rewarded; on error trials, mice licked the other lickport (error right [ER]; error left [EL]) and were not rewarded (Figure 1C). Trials in which the mice licked early during the delay epoch (13.3% ± 10%) were not analyzed. Since mice had all of their whiskers, relatively small whisker movements were sufficient to touch the pole and thus discriminate object location.

Mapping Neural Activity Using Wide-Field Imaging

We tracked behavior-related activity on the mesoscale using wide-field calcium imaging (Vanni and Murphy, 2014). An imaging window was made over the left frontal cortex, covering MM, ALM (Guo et al., 2014b; Li et al., 2016), and other motor cortical areas (Figure 2A). Changes in fluorescence relative to baseline were measured as changes in behavior-related activity

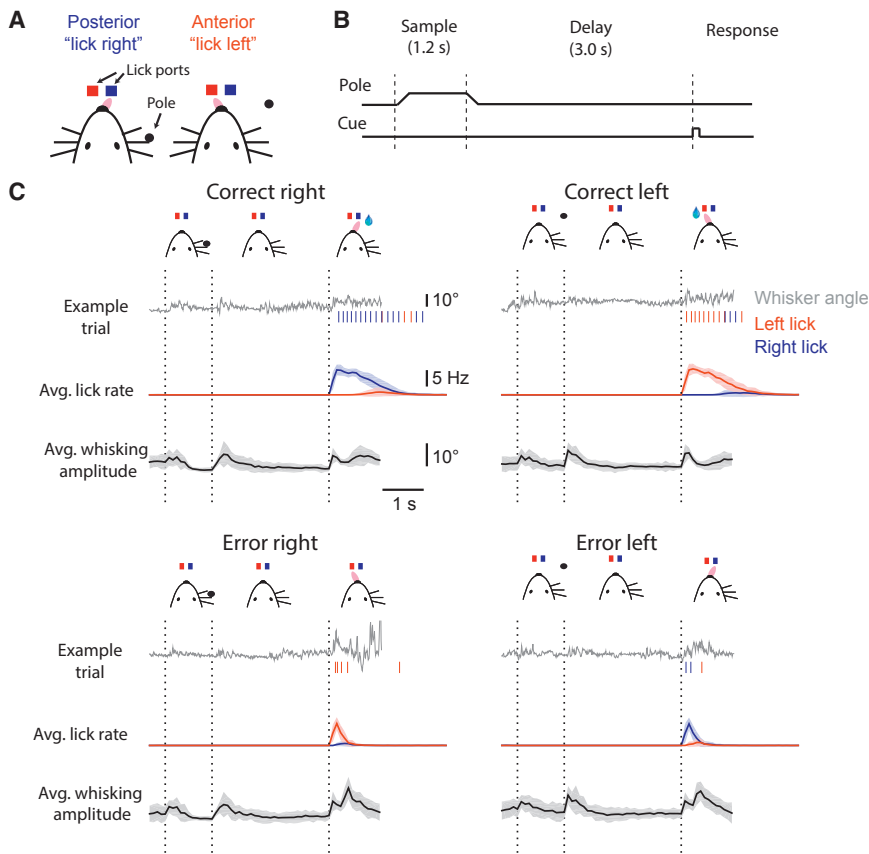


Figure 1. Tactile Object Localization

(A) Mice were trained to lick the right (blue) lickport for the posterior pole location or the left (red) lickport for the anterior pole location.

(B) The pole was within reach of the whiskers during the sample epoch (1.2 s). Mice responded with licking after a delay (3 s) and an auditory cue. Licking the correct port was rewarded with water. Licking the wrong port was neither rewarded nor punished.

(C) Whisker and tongue movements tracked for the four trial types (correct right, CR; correct left, CL; error right, ER; error left, EL). Shaded area indicates standard deviation (SD).

(STAR Methods). During the sample and early parts of the delay epoch, activity was most pronounced in MM (Figures 2B–2D), contralateral to the whiskers touching the object (Figure S1). As the delay epoch progressed, activity spread forward and lateral to ALM (Figures 2B–2D), across both ALM hemispheres (Figure S1). Behavior-related activity therefore shifts from MM to ALM before the behavioral response (Figure 2D). After the behavioral response, activity increased across a large part of the motor and somatosensory cortex.

Mapping Activity Using Two-Photon Calcium Imaging

The wide-field calcium imaging experiments suggest that ALM and MM might encode distinct types of information during different phases of the task. We used two-photon calcium imaging to track behavior-related information encoded by representative populations of individual neurons (Huber et al., 2012). Neurons were sampled across MM, ALM, and surrounding areas. For each mouse ($n = 6$), we collected data from 1 to 3 image locations ($n = 12$ locations in total, Figure 2E), each containing multiple (8.8 ± 2.6) image planes ($600 \mu\text{m} \times 600 \mu\text{m}$) spanning depths from $100 \mu\text{m}$ (layer [L] 2) to $600 \mu\text{m}$ (L5) (Figures 2F and S2).

Each image plane ($n = 105$, Figure 2F and S2) was sampled at 14 Hz while mice performed the task for 92 ± 26 trials, with performance at $73\% \pm 9\%$ trials correct. Mice typically performed 300–500 trials per behavioral session, allowing sequential imaging of 3 ± 1 planes per session (range 1–6, Figure S2). Behavioral performance was stable across planes of a session (Figure S2).

each imaged location was aligned to the surface blood vessels pattern in the window. The stereotactic coordinate of each imaged cell can then be derived from the known stereotactic coordinates of vascular landmarks recorded during surgery.

We measured activity of each neuron across all four trial types (Figure S2, average number of trials per imaged plane: CR: 34 ± 13 , CL: 36 ± 14 ; ER: 12 ± 5 , EL: 10 ± 4). Neuropil signals were small compared to task-related cellular responses (Figure S3) and were subtracted (STAR Methods). Consistent with previous studies, the activity of a large proportion of neurons distinguished between trial types in MM (23%, 1,523/6,594) (Erich et al., 2011; Goard et al., 2016; Huber et al., 2012) and ALM (31%, 2,754/8,837) (Guo et al., 2014b; Li et al., 2015). Consistent with the wide-field imaging experiments (Figure 2), the peak of activity shifted from MM to ALM over the course of the delay epoch (Figure S4).

Analysis of Behavior-Related Activity

The four trial types differ in the location of the presented object (anterior or posterior), the direction of the answer lick (left or right) and the trial outcome (correct, rewarded; error, unrewarded) (Figure 3A, left). For each neuron, the pattern of neuronal responses across the four trial types could reflect coding (selectivity) for one or a combination of these three task-related variables (Figure 3A, right). For example, selectivity for object location implies a different response in trials with posterior object location (CR, ER) compared to trials with anterior

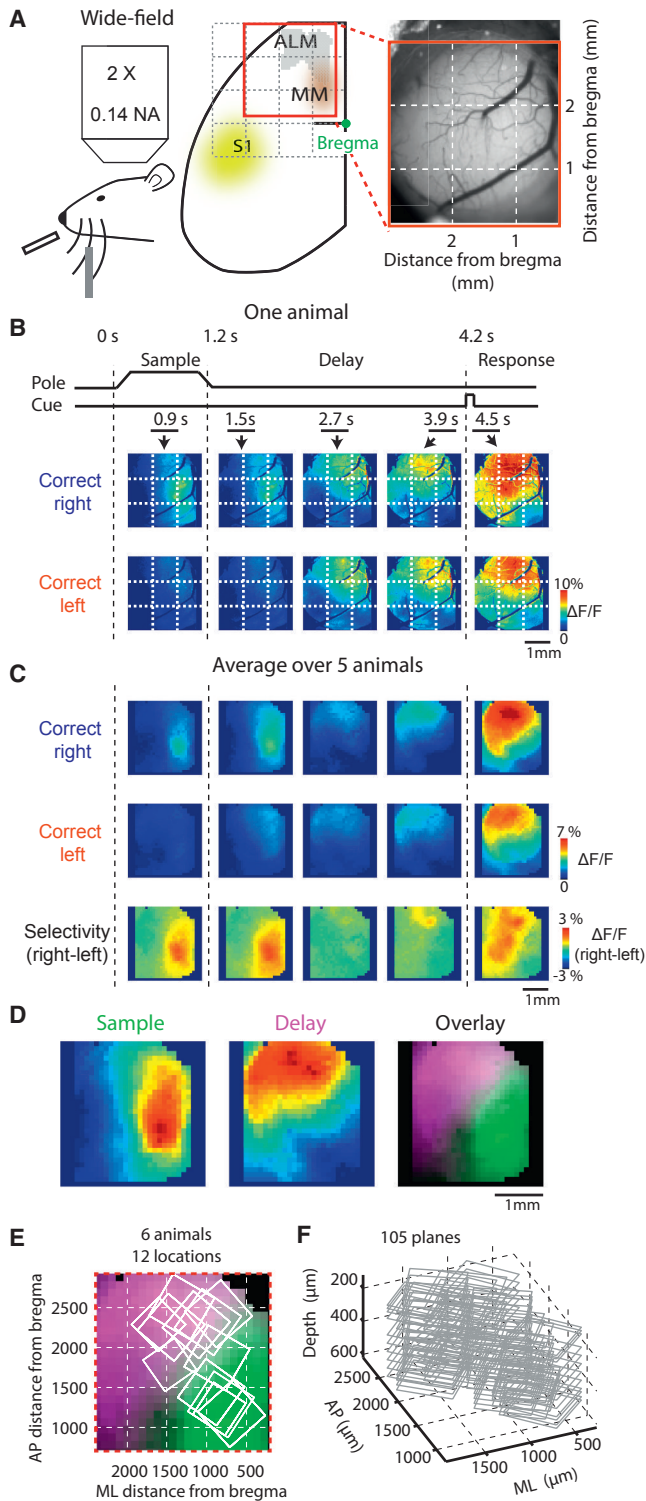


Figure 2. Wide-Field Calcium Imaging

(A) Wide-field fluorescence imaging (left), the location of the imaged area (middle), and an example image (right). The border of ALM was defined as a spatially deconvolved region where photo inactivation affects behavior (Li et al., 2016); the center of MM was defined approximately by the projection zone of vS1 axons (Mao et al., 2011).

object location (CL, EL) (Figure 3A, neuron 1). On the other hand, selectivity for lick direction implies a different response in lick left trials (CR, EL) compared to lick right trials (CL, ER) (Figure 3A, neuron 2). Finally, selectivity for outcome implies different responses for correct (CR, CL) and error (ER, EL) trials (neuron 3 in Figure 3A).

We modeled the trial-type-specific $\Delta F/F$ of each neuron as a linear combination of object location (α), lick direction, (β) and outcome (γ) effects, together with a non-selective, trial-type independent term (μ) (STAR Methods). For each time point t relative to trial start, we decomposed $\Delta F/F(t)$ into $\alpha(t)$, $\beta(t)$, $\gamma(t)$, $\mu(t)$. Selectivity was determined by testing for significant contributions of $\alpha(t)$, $\beta(t)$, $\gamma(t)$ using three-way analysis of variance (ANOVA). The selectivity of most neurons can be attributed to one of the three coefficients, especially during the early part of the trial (Figure S5). This implies that most neurons mainly encode one of the three behavioral variables at any given time.

A large number of neurons were selective for licking direction (Figure 4A), consistent with electrophysiological (Guo et al., 2014b; Li et al., 2015, 2016) and previous imaging (Li et al., 2015) studies in ALM. Individual neurons coded for lick direction at different times during the task. Some neurons were selective during the sample and delay epochs, long before onset of licking, a key signature of preparatory activity (Guo et al., 2014b; Li et al., 2015; Tanji and Evarts, 1976) (Figure 4A, left). Other neurons became selective during the response epoch, after mice indicated their decision by licking (Figure 4A, middle). Some neurons even represented licking direction after the animal stopped consuming water (Figure 4A, right). Thus, different neurons represented information about lick direction during different task epochs.

We also found abundant neurons selective for object location (Figure 4B). Many of these neurons were selective during the sample epoch when mice explored the object (Figure 4B, left). However, a subset of neurons coded object location primarily during the delay epoch, after the pole was removed (Figure 4B, middle, right). Some of these neurons carried information about object location up to the end of the delay epoch, seconds after the stimulus (Figure 4B, right), representing a memory of object location (Hernández et al., 2010; Huber et al., 2012; Petreanu et al., 2012).

A third group of neurons was selective for trial outcome (Figure 4C). These neurons typically became selective after the answer lick. A subset of the outcome-selective neurons responded preferentially during correct trials (Figure 4C, right), whereas others responded strongly during error trials (Figure 4C, left, middle). Some neurons persistently represented trial

(B) Example maps of fluorescence response ($\Delta F/F$) at indicated time points relative to trial start. Each image shows the average response at 0.33 s intervals, averaged over all trials of the same type (correct right: 54 trials; correct left: 49 trials).

(C) Same as (B), averaged across 5 mice.

(D) Averaged activity during sample and delay epoch (peak normalized).

(E) Locations imaged with two-photon calcium imaging, aligned to a common reference frame and overlaid on the wide-field response map (2D).

(F) 3D positions of 105 imaging planes (4–12 per imaged location).

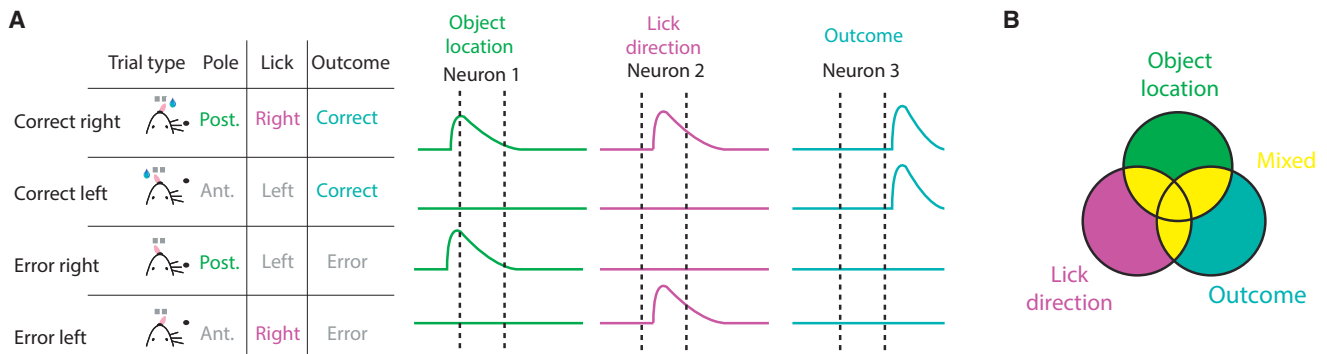


Figure 3. Analysis of Neuronal Selectivity

(A) Hypothetical neurons and their responses during the four trial types (correct, right, CR; correct left, CL; error right, ER; error left, EL). (B) Individual neurons were classified independently in each time bin (66.7 ms) as “object location,” “lick direction,” or “outcome” selective if α , β , or γ were the only significant factor at that time, respectively (STAR Methods). Neurons were classified as “mixed” selective (yellow) if more than one factor was significant.

outcome long after the trial ended (Figure 4C, middle). Thus, in the motor cortex, object location, lick direction, and trial outcome are encoded in different neuronal populations during multiple task epochs.

We also observed neurons with activity patterns that cannot be explained by a single coefficient alone (Hernández et al., 2010; Rigotti et al., 2013). Most of these neurons with “mixed” selectivity were observed during the response epoch. A subset responded during only one of the four trial types (Figure 5A). A few neurons switched their selectivity during the trial (Figure 5B). For example, some neurons encoding object location early during the task later encode trial outcome during the response epoch (Figure 5B, cell 1). Other neurons encoded object location early in the trial, and licking direction late in the trial (Figure 5B, cell 2–4).

Spatial Map of Behavior-Related Activity

We mapped the spatial distribution of neurons with different types of selectivity over time (Figure 6). During the sample and the early part of the delay epoch, representation of object location was prominent, mainly in MM (Figures 6B, 6C, 6D, S6, and S7). This is consistent with coding of tactile signals in MM (Ferezou et al., 2007; Huber et al., 2012; Petreanu et al., 2012). Neurons selective for lick direction appeared first in the deep layers of ALM, early in the delay epoch (Figures 6D, 6E, and S6). Lick-direction selectivity, including number of neurons and the strength of coding, continued to increase and spread across ALM layers and to a minor extent into MM (Figure S7), reaching a maximum after the go cue (Figures 6F–6I).

Outcome-selective neurons, which were observed only during the response epoch, were scattered approximately uniformly throughout ALM and MM (Figures 6G–6I). “Mixed” neurons were also observed primarily during the response epoch in both ALM and MM (Figures 6G–6I). Throughout the trial, preparatory activity, quantified either as fraction of lick direction-selective neuron (Figures 6H and 6I) or as average coding coefficient (Figures S6 and S8), was most pronounced in ALM, whereas object location related selectivity was mainly limited to MM (Figures 6H and S6–S8). Consistently, the effects of optogenetic inactivation during the delay epoch on lick direction were greater in ALM compared

to MM (Figure S9; Discussion). These measurements show that within motor cortex, preparatory activity arises first in ALM.

Comparison with Extracellular Electrophysiology

Cellular calcium imaging produces a biased representation of the underlying spike rates. The fluorescence signal is a low-pass filtered (Chen et al., 2013; Dana et al., 2014) and non-linear (Akerboom et al., 2012) readout of neural activity. In addition, decreases in activity produce a slowly changing fluorescence signal, which is more difficult to detect than the more rapid fluorescence changes associated with increases in activity. Although deconvolution and spike rate inference can overcome some of these problems in ideal situations (i.e., zero baseline spike rate and infinite signal-to-noise ratio) (Pnevmatikakis et al., 2016; Vogelstein et al., 2009; Theis et al., 2016), these methods are not easily applicable to situations where the spike rate varies by 50-fold across the neural population (Guo et al., 2014b; Li et al., 2015, 2016).

We performed parallel experiments using silicon probes. We recorded single units ($n = 567$, 3 mice) in the left ALM and MM under identical behavioral conditions as the imaging experiments. The spikes rates of 393 neurons distinguished trial types during either sample ($n = 115$), delay ($n = 182$), or response epoch ($n = 309$). Similar to the imaging experiments, we found neurons selective for distinct task variables during different task epochs (Figures 7A–7C). The majority of object location-, lick direction-, and outcome-selective neurons were observed during sample, delay/response, and response epochs, respectively (Figure 7D). Neurons selective for object location were observed most frequently in MM; neurons selective for lick direction were mainly observed in ALM; neurons selective for outcome and mixed neurons were numerous in both ALM and MM (Figure 7D). We observed neurons that appeared to carry a memory for task-related variables. This includes neurons representing object location after the object had been removed (Figure 7B, object location cell 2 and 3), lick direction after animals stopped licking (Figure 7A, lick direction cell 3), and neurons representing trial outcome after the trial was over (Figure 7C, outcome cell 2).

Using both imaging and electrophysiology data, we calculated the fraction of object location, lick direction, outcome, and mixed

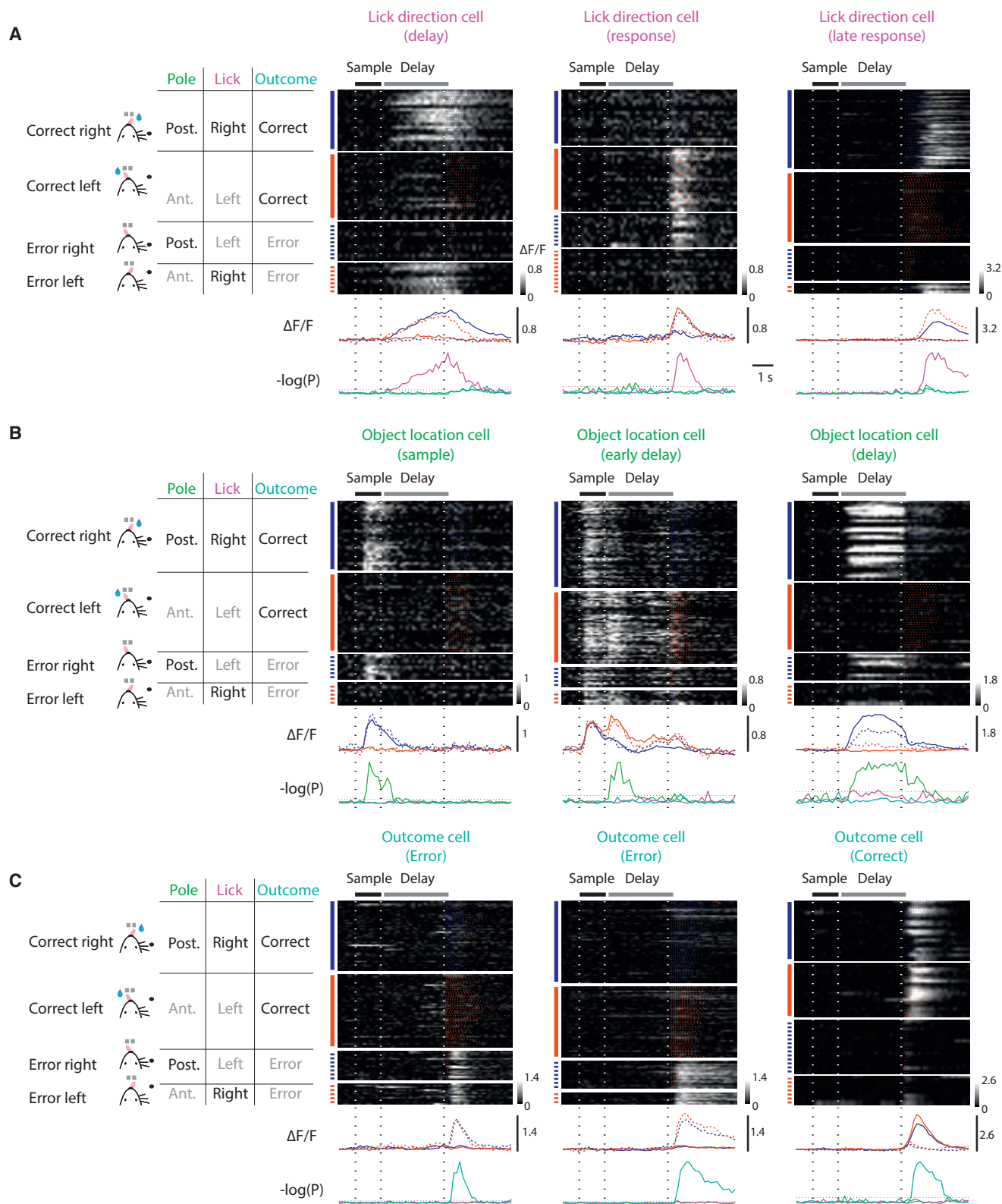


Figure 4. Example Neurons Coding for Lick Direction, Object Location, and Trial Outcome

(A) Example cells showing lick direction selectivity during different trial epochs. Each row in the black and white images shows the $\Delta F/F$ response of one trial. Each of the four groups of rows shows one trial type, indicated by the vertical lines to the left. Blue solid line, correct right; red solid line, correct left; blue dashed lines, error right; red dashed lines, error left. (legend continued on next page)

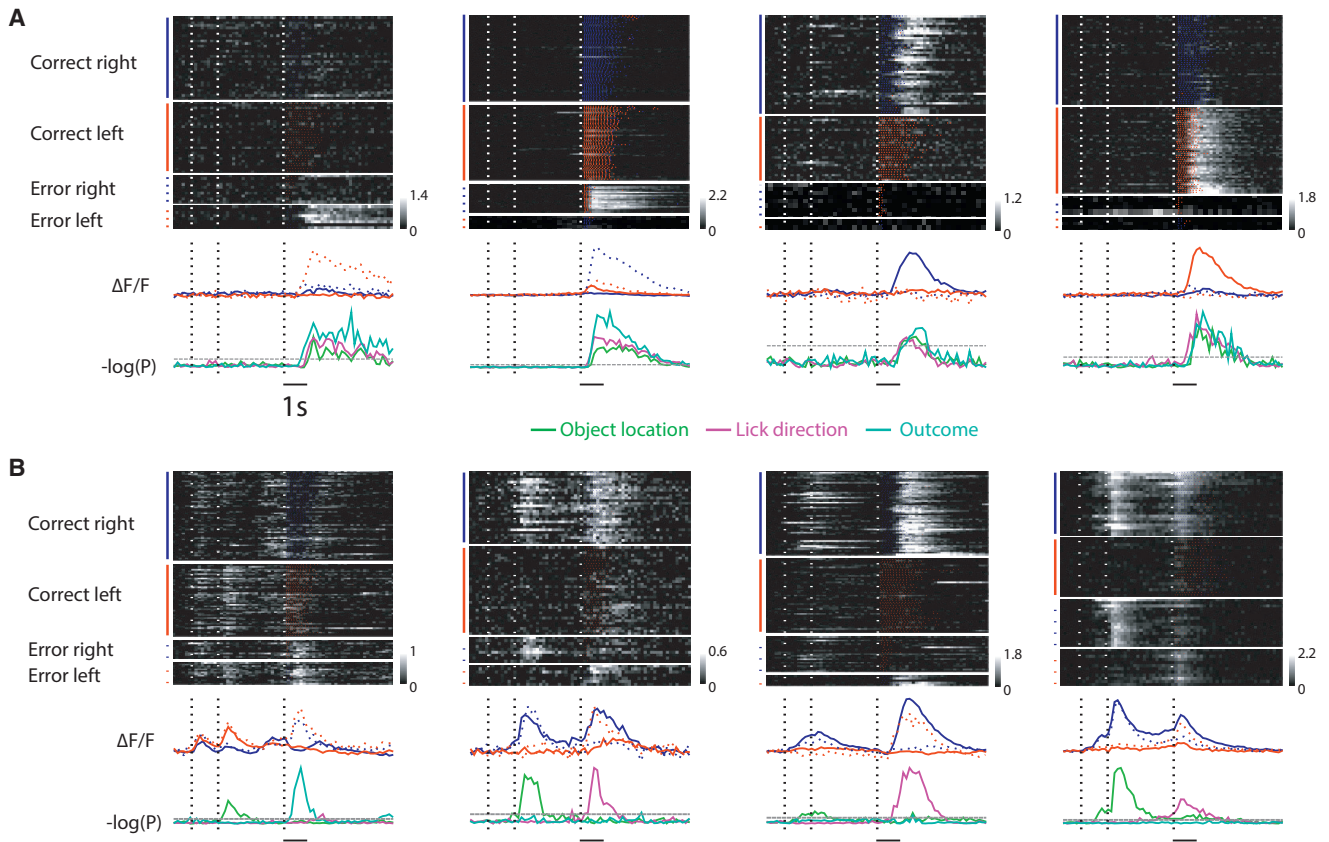


Figure 5. Example Neurons with Mixed Selectivity

(A) Four example neurons with mixed selectivity that responded mainly during one specific trial type. Each row in the black and white images shows the $\Delta F/F$ response of one trial. Each of the four groups of rows shows one trial type, indicated by the vertical lines to the left. Blue solid line, correct right; red solid line, correct left; blue dashed lines, error right; red dashed line, error left. The three dotted vertical lines demarcate the sample and delay epochs. The blue and red dots on the black and white image indicate the time of right and left licks, respectively. Bottom: the blue and red traces show the average $\Delta F/F$ response for right and left trials (solid for correct, dashed for error trials). Significance ($-\log(p \text{ value})$) of the object location, lick direction, and outcome selectivity are shown as green, magenta, and cyan traces. Horizontal dashed line indicates $p = 0.05$.

(B) Example neurons that switched the modality of selectivity during the trial.

neurons and compared their abundance in ALM and MM (Figures 6H, 6I, 7D, and S8). Neurons selective for object location were concentrated in MM during the sample and early delay epochs. Neurons selective for lick direction were concentrated in ALM during the delay epoch. They were encountered in both MM and ALM during the response epoch. Neurons selective for trial outcome were observed in both ALM and MM. Similarly, mixed neurons were observed both in ALM and MM during the response epoch.

Projection-Specific Coding

The diverse neuronal responses in ALM (Li et al., 2015) and primary motor cortex (Turner and DeLong, 2000) correlate with

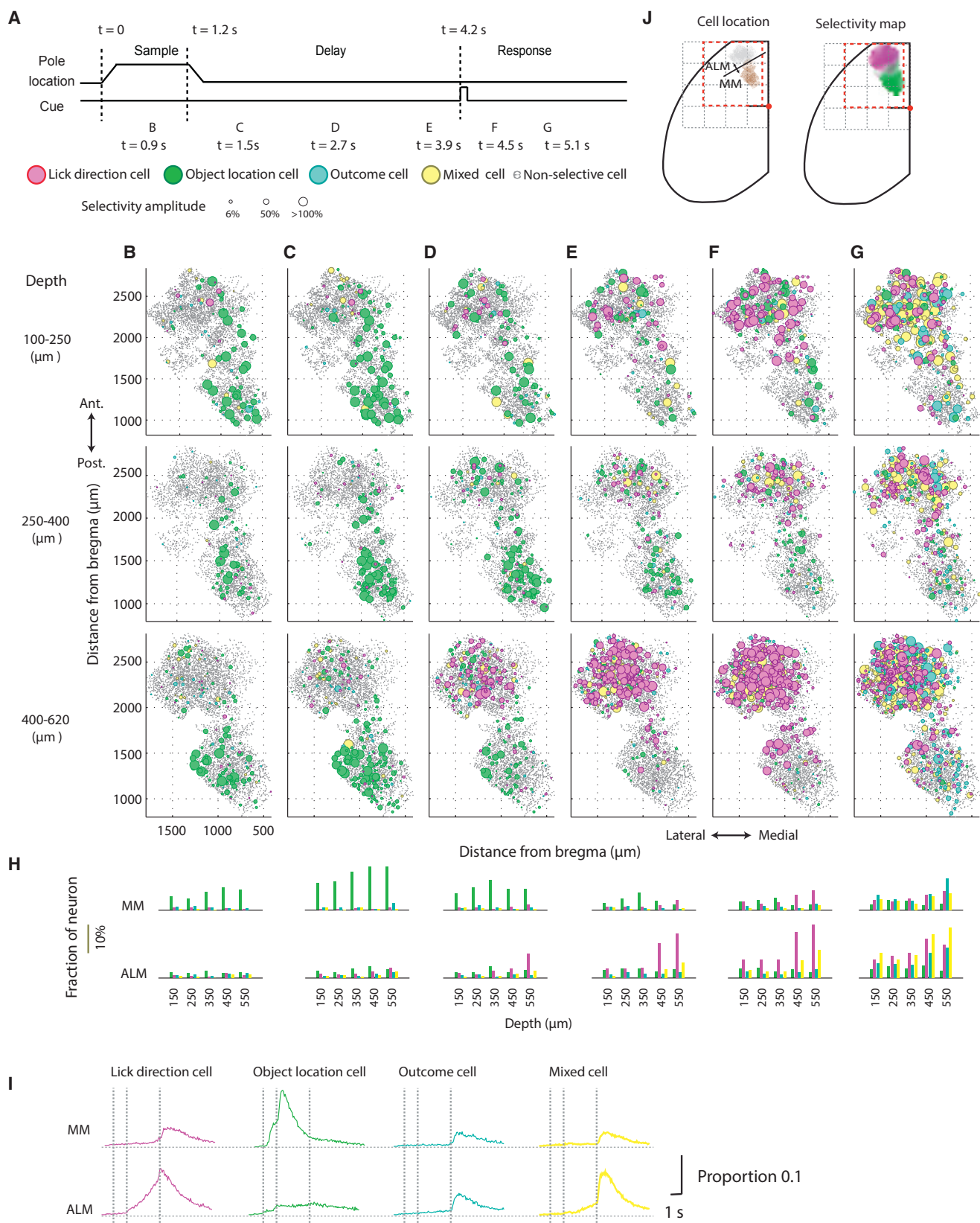
specific neuronal projection types. We asked whether projection type and cortical layer explain differences in responses across neurons. In three mice, we combined retrograde labeling of pyramidal tract (PT) ($n = 719$) and intratelencephalic (IT) ($n = 2,631$) neurons with two-photon calcium imaging (Figure 8A). We divided cortical depth into superficial ($<350 \mu\text{m}$ deep; including L1–3) and deep ($>350 \mu\text{m}$ deep; including L5A and 5B) layers (Hooks et al., 2013; Li et al., 2015; Mao et al., 2011). IT neurons were found in both superficial and deep layers, whereas PT neurons were exclusively in deep layers (Figure 8C).

In ALM, the strongest lick direction selectivity was observed in the deep layers (Figures 8D and S10), where PT and IT neurons were intermingled. A contra bias during the delay epoch was

error right; red dashed line, error left. The three dotted vertical lines demarcate the sample and delay epochs. The blue and red dots on the black and white image indicate the time of right and left licks, respectively. Bottom: the blue and red traces show the average $\Delta F/F$ response for right and left trials (solid for correct, dashed for error trials). Significance ($-\log(p \text{ value})$) of the object location, lick direction, and outcome selectivity are shown as green, magenta, and cyan traces. Horizontal dashed line indicates $p = 0.05$.

(B) Same as (A) for three examples of object location-selective cells.

(C) Same as (A) for three examples of outcome-selective cells.



(legend on next page)

observed in PT neurons (Figure 8D), consistent with previous electrophysiological recordings (Li et al., 2015). The magnitude of lick direction selectivity ($|\beta|$) appeared stronger and earlier in PT than in IT neurons (delta onset time; time when selectivity rose to >6 SD above baseline = 1.4 ± 0.6 s; $p < 0.01$, bootstrap; Figure 8D). However, this difference in lick direction selectivity onset was not detected in an electrophysiology dataset recorded under similar conditions (Li et al., 2015) (Discussion).

ALM neurons displayed prominent lick direction selectivity and little object location selectivity. In contrast, MM neurons displayed strong object location selectivity in both superficial and deep layers, and in both PT and IT cells. PT neurons in MM also displayed strong object location selectivity particularly during the early delay period (Figure 8D). This is surprising because, compared to IT neurons, PT neurons receive only weak input from the somatosensory cortex (Hooks et al., 2013; Mao et al., 2011). Neither PT nor IT neurons in MM displayed prominent lick direction selectivity before licking movement.

Our results suggest that coding of PT and IT neurons is primarily determined by their location in the motor cortex. We quantified response variance explained by cortical area, cell depth, and projection type (STAR Methods). Cortical area (i.e., ALM versus MM) and cell depth (superficial $z < 350$ versus deep $z > 350$) explained the majority of response variability (Figures 8E and 8F). Motor cortex neurons projecting to a common target therefore carry distinct information depending on the location of the source neuron.

DISCUSSION

We mapped activity across the motor cortex while mice performed a whisker-based object localization task with a delayed licking response. As a function of time during the behavior, task-related activity spread from medial motor cortex (MM) to anterior lateral motor cortex (ALM). Preparatory activity predicting the licking response was first detected in deep layers of ALM, seconds before the movement. Preparatory activity began and increased during the delay epoch. During the response epoch, lick direction-selective activity was also seen in superficial neurons and in MM. Our data show that preparatory activity is most pronounced in ALM.

In previous experiments we used optogenetic methods to inactivate parts of the cortex during the delay epoch and measured the directional response bias during the response epoch (Guo et al., 2014b). The bias was largest when inactivation was centered 2.5 mm anterior of bregma and 1.5 mm lateral to the midline, defining the center of ALM. The behavioral effects of photoinhibition decreased as the photostimulus was moved

to more posterior and medial parts of the motor cortex (Figure S9). Inactivation of anterior parts of MM also biased the behavior, but to a lesser extent compared to ALM. The behavioral effect during silencing MM could be explained by the finite resolution of the inactivation methods. The optogenetic manipulation reduced activity by 50% one millimeter from the center of the photostimulus (1.5 mW average power) (Guo et al., 2014b). The centers of ALM and MM are separated by less than 2 mm in the mouse and inactivation of anterior parts of MM likely also silenced parts of ALM. To better define the brain areas controlling motor preparation, Li et al. used deconvolution methods to correct for the spatial extent of inactivation (Li et al., 2016). This analysis suggests that ALM (approximate diameter, 1.5 mm) controls motor preparation in the delayed directional licking task.

ALM shows pronounced preparatory activity, the neural correlate of motor preparation. Little preparatory activity was seen in MM. Together the imaging and inactivation studies provide a parsimonious view of ALM as a center of motor preparation for directional licking.

Our experiments do not yet determine the origin of preparatory activity. Preparatory activity could be expressed in other cortical areas that were not probed here. Furthermore, preparatory activity has been observed in structures of the brain that are directly or indirectly coupled to ALM, such as thalamus (Guo et al., 2017; Tanaka, 2007), cerebellum (Ohmae et al., 2013), striatum (Ding and Gold, 2010), and the basal ganglia (Howe et al., 2013). ALM is part of a multi-regional loop that produces and maintains preparatory activity (Guo et al., 2017).

Previous studies found preparatory activity in MM neurons in a task involving orienting movements (Erlich et al., 2011, 2015). Another recent study reported delay epoch activity in MM during delayed go-nogo behavior (Goard et al., 2016). In both studies, inactivation of MM degraded behavioral performance. However, the inactivation experiments do not clearly distinguish between MM and ALM. In the Erlich et al. experiments, muscimol likely silenced a large area of frontal cortex (Krupa et al., 1999), including parts of ALM. Similarly, Goard et al. used very powerful photoinhibition, approximately 10-fold stronger than in Guo et al. (20 mW versus 1.5 mW average power), and thus likely inactivated an area with radius larger than 2 mm, including MM and ALM (Guo et al., 2014b; Figure 2). Neither study investigated the relative prevalence of selective delay period activity across brain areas. Additional experiments are required to determine whether ALM plays a role in these other behavioral tasks.

It is currently unclear whether ALM is critical for planning movements in general or is specialized for orofacial movements. Multiple lines of evidence argue that ALM might be specialized

Figure 6. Spatial Distribution of Task-Related Variables across Time

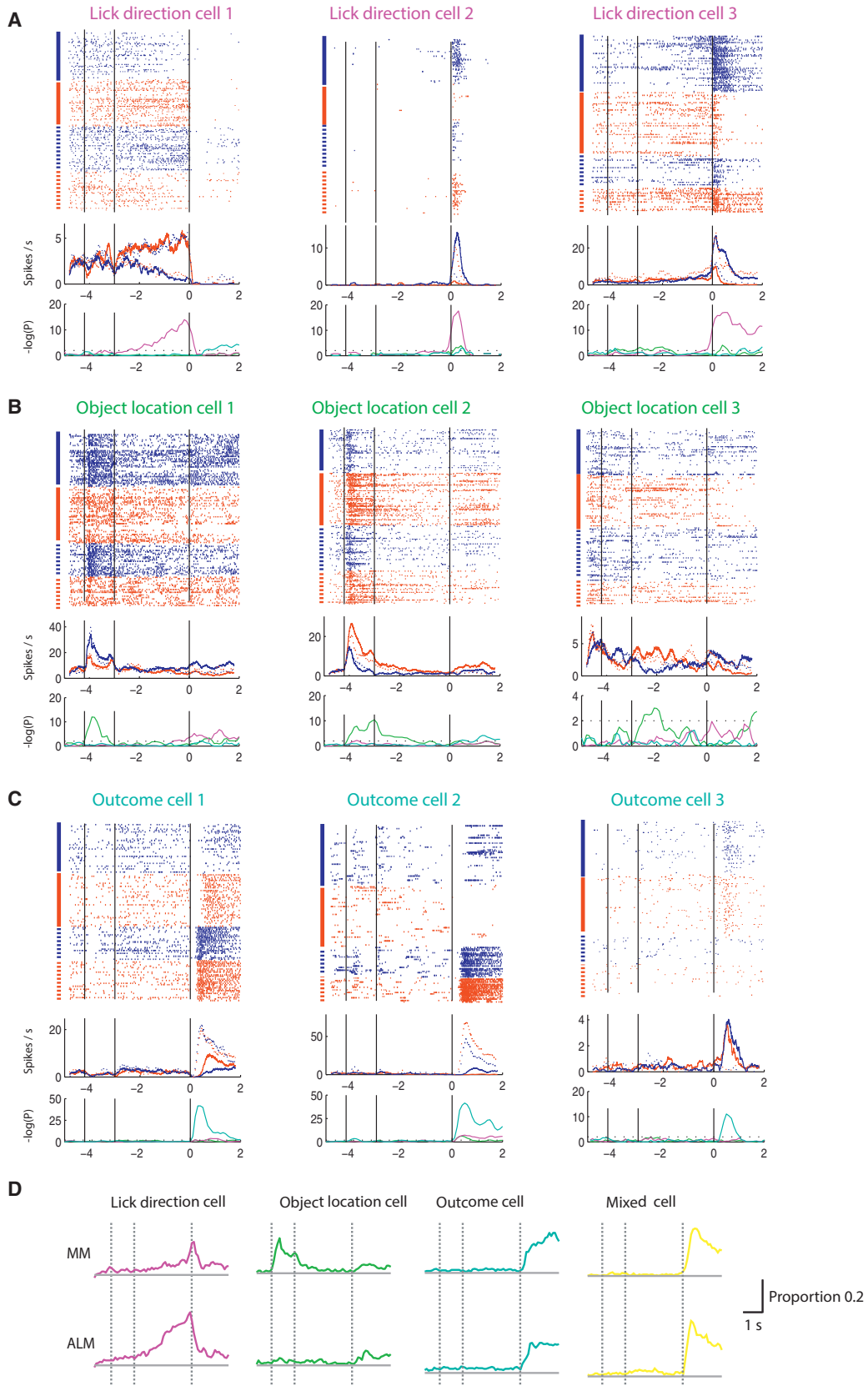
(A) Timeline of the data presented in panels B–G.

(B–G) Spatial distribution of selective cells as a function of time within the trial. Object location, green; lick direction, magenta; outcome, cyan; mixed, yellow. The size of the marker indicates the strength of the respective effect size (i.e., the values of α , β , or γ). The histograms at the bottom of each panel indicate the fraction of selective cells at different depths in ALM and MM.

(H) The proportion of object location (green), lick direction (magenta), outcome (cyan), and mixed (yellow) cells at different depths and times for ALM and MM.

(I) The proportion of lick direction, object location, outcome, and complex cells as a function of time for ALM and MM.

(J) Left: spatial distribution of imaged neurons (ALM gray, MM brown). Right: distribution of object location-selective cells at time point C (green) and lick direction-selective cells at time point E (magenta).



(legend on next page)

for *executing* orofacial movements. First, the projections of ALM PT neurons overlap with regions of superior colliculus (Rossi et al., 2016) and the reticular formation (Li et al., 2015) that have been implicated in the control of licking. Second, bilateral silencing of ALM can prevent task-related licking (Komiya et al., 2010) (H. Inagaki, personal communication). Third, ALM was first identified as the brain area with the lowest microstimulation threshold for activating rhythmic licking in rats (Travers et al., 1997) and mice (Komiya et al., 2010). Unilateral photostimulation of ALM neurons evokes directional rhythmic licking, even in untrained mice (Li et al., 2015), showing that ALM can control licking direction. ALM may play roles in controlling cognitive aspects of tongue movements, similar to the roles of frontal eye fields in the control of eye movements (Bruce and Goldberg, 1985; Funahashi et al., 1989; Schall and Thompson, 1999).

MM shows little preparatory activity. However, MM neurons display early selectivity for the tactile stimulus (i.e., object location). Neurons were more active in posterior trials, when the pole was within reach of the whiskers, than in the anterior location, when the pole was out of reach (Figure 8D). The stronger response during the posterior trials likely reflects touch-evoked activity transmitted by projections from the vibrissal somatosensory cortex directly to MM (Chakrabarti et al., 2008; Ferezou et al., 2007; Hooks et al., 2013; Kleinfeld et al., 2002; Mao et al., 2011). Previous recordings in MM also reported activity related to whisker movement (Hill et al., 2011; Huber et al., 2012). In our experiments, whisker movements were similar across trial types (Figure 1) and neurons encoding whisker movements were likely classified as “non-selective.” In more challenging object localization tasks in which mice have to actively search for the object, whisker movements differed across trial types and MM activity shows encoding of whisker movement, even during the delay epoch (S. Peron, personal communication).

Object location selectivity in MM persisted into the delay epoch, after the removal of the tactile stimulus. Although some delay epoch selectivity may be caused by “spillover” of sample epoch selectivity (Figure 4B, left) caused by the finite GCaMP6s decay time (~350 ms half decay time in GP4.3 line; Dana et al., 2014), this clearly does not explain all delay epoch selectivity in MM. For example, some neurons showed persistent object location selectivity throughout the entire delay period, which is several fold longer than the GCaMP6s decay time (Figure 4B, right). Other neurons only developed object location selectivity during the delay epoch (Figure 4B, middle, right). Some of these delayed, object location-selective neurons preferred the anterior pole location (Figure 4B, middle). These neuronal activity patterns represent a memory of object location. Persistent object

location signals have previously been reported in MM (Huber et al., 2012) and in MM neuron axons projecting to somatosensory cortex (Petreanu et al., 2012). Activity related to working memory has also been reported in primate motor cortex (Hernández et al., 2010). Motor cortex thus might play complex roles during cognitive behavior that are conserved across species. Despite this rich task-related activity in MM, our inactivation experiments suggested that MM is not required to perform the task (Guo et al., 2014b; Li et al., 2016). Moreover, photoinhibiting MM during the delay epoch produced behavioral effects that were inconsistent with a critical role in stimulus perception (Figure S9). Instead, photoinhibition perturbed behavioral choice, consistent with spillover of inactivation into ALM.

The photoinhibition experiments do not prove that MM activity is irrelevant in the delayed response task. Coding for object location is likely distributed across multiple brain areas. In addition to MM (vS1 → MM → ALM), somatosensory information could impinge onto ALM via the secondary somatosensory cortex (vS1 → S2 → ALM), the posterior nucleus of the thalamus (vS1 → PO → ALM), or the basal ganglia (vS1 → BG → thalamus → ALM). This redundancy might manifest itself as robustness to localized inactivation.

We also observed neurons representing trial outcome in both ALM and MM (Figures 6 and 8). Some of these neurons responded specifically during correct trials, whereas others responded during error trials (Figures 4C and 7C). Overall, neurons preferring error trials outnumbered neurons preferring correct trials (Figure 8D). Neurons encoding reward and error have previously been reported in multiple frontal cortical areas (Matsumoto et al., 2007; Amiez et al., 2006), including pre-motor cortex (Stuphorn et al., 2000; Amador et al., 2000). Discovering the precise nature and function of these outcome responses will require additional experiments with targeted behavioral manipulations.

We analyzed neuronal selectivity with respect to cortical location, cortical depth, and axonal projection type. Preparatory activity related to future licking direction was first detected in deep ALM, where PT and IT neurons were intermingled. PT neurons appeared to display stronger and earlier lick direction selectivity than IT neurons, but this difference was not detected in a previous electrophysiology dataset (Li et al., 2015). Several explanations are possible. First, even in ALM, less than 20% of PT or IT cells displayed lick direction selectivity at any given time (Figures 6, 8, and S10), and the onset timing was variable. It is possible that the sample size of the electrophysiology data (PT/IT cells; electrophysiology, 45/27; imaging, 719/2,631) was not sufficient to detect a difference in onset timing. Alternatively, a substantial part of early IT selectivity reflects spike rate

Figure 7. Silicon Probe Recordings

(A) Three example neurons classified as lick direction selective. Top: spike raster. Each row shows one trial. Trial types are indicated by the vertical lines on the left. Blue solid line, correct right; red solid line, correct left; blue dashed lines, error right; red dashed line, error left. The three vertical lines demarcate the sample and delay epochs (Figure 1C). Middle: mean spike rate. The red and blue traces show the average response for each trial type (solid for correct, dashed for error trials). Bottom: significance ($-\log(p \text{ value})$) of the object location, lick direction, and outcome selectivity are shown as green, magenta, and cyan traces. Horizontal dashed line indicates $p = 0.05$.

(B) Object location-selective neurons.

(C) Outcome-selective neurons.

(D) The proportion of neurons recorded with silicon probes showing lick direction, object location, outcome, and complex selectivity in MM and ALM as a function of time.

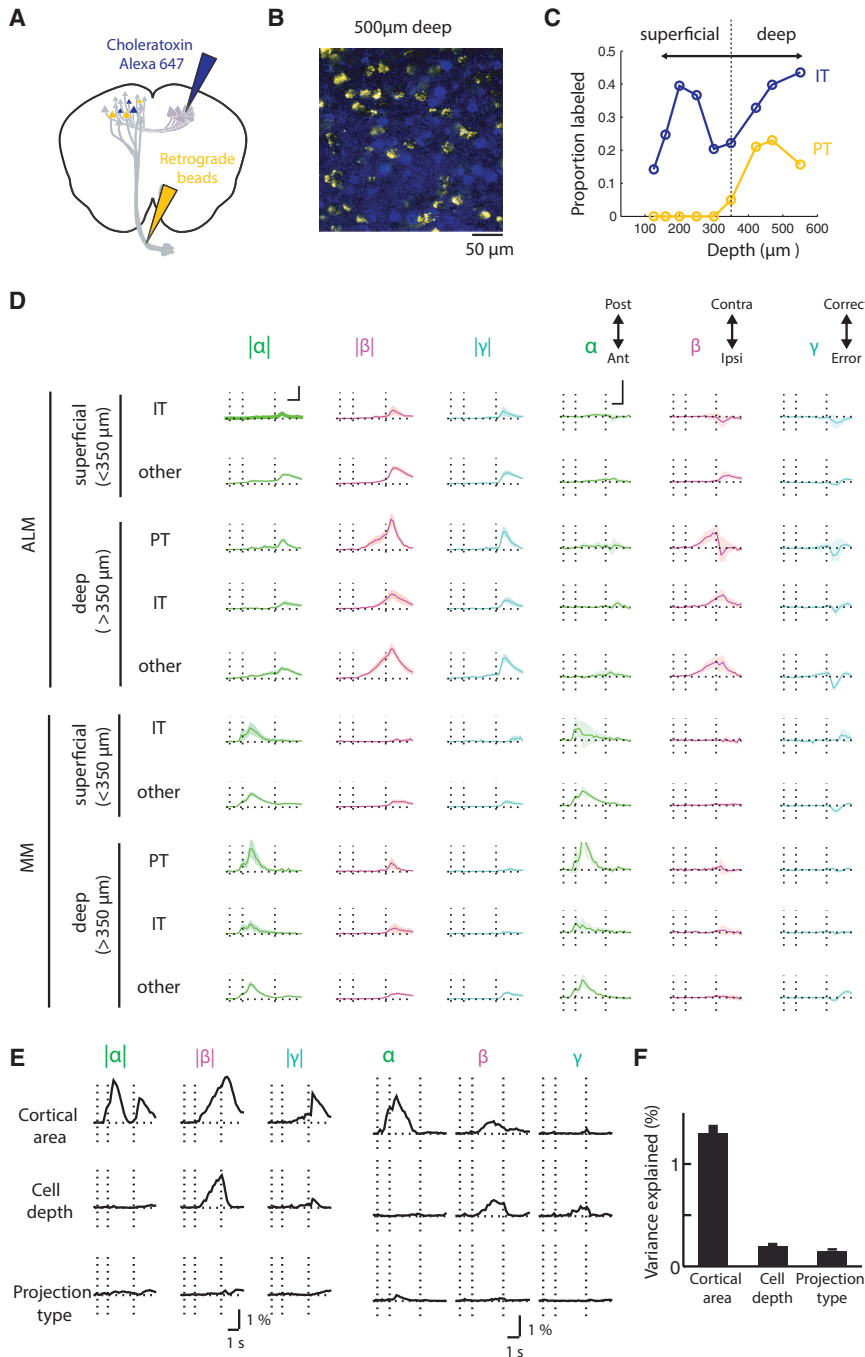


Figure 8. Projection-Specific Analysis of Neural Coding

(A) Labeling pyramidal tract (PT, orange) and intralenticular (IT, blue) neurons with fluorescent retrograde tracers. (B) Example image showing labeled cells in the intact brain. (C) Proportion of imaged cells identified as PT or IT as a function of depth. (D) Coefficients (α , β , γ) and their absolute values ($|\alpha|$, $|\beta|$, $|\gamma|$) averaged for different subpopulation of neurons (STAR Methods): ALM versus MM; superficial, $<350 \mu\text{m}$ versus deep, $z > 350 \mu\text{m}$; PT versus IT. The coefficients of non-significant cells were set to zero before computing the average. Shaded area around the curve represents standard error of the mean estimated by bootstrapping. (E) Variance of neuronal selectivity accounted for by imaged location (ALM versus MM), cell depth (superficial $z < 350 \mu\text{m}$ versus deep, $z > 350 \mu\text{m}$), or projection type (PT, IT, and others). (F) Total variance of absolute selectivity coefficients summed over the entire trial period accounted for by imaged location, cell depth, or projection type.

MM (Mao et al., 2011). However, among MM neurons, PT cells in layer 5B receive only weak input from somatosensory cortex (Hooks et al., 2013), yet they displayed strongest object location selectivity, particularly during the early delay period. This suggests that amplification by cortical microcircuits contributes to MM selectivity. Representation of object location in MM PT neurons also suggests that corticofugal projections in the motor cortex may convey rich information about the external world, beyond motor commands.

We combined transgenic mice (Dana et al., 2014) with high-speed two-photon imaging (Peron et al., 2015) to map the behavior-related activity in large populations of neurons across multiple parts of the motor cortex. Recent and future advances in transgenic mouse technology (Madisen et al., 2015), protein sensors for neural activity (Dana et al., 2016),

and mesoscale, high-resolution imaging (Sofroniew et al., 2016) will make even larger cortical activity maps routine.

suppression (Li et al., 2015), which is more difficult to detect in calcium imaging compared to increases in spike rate. This could cause an underestimation of early selectivity in IT neurons by calcium imaging. Finally, calcium-spike relationships could depend on cell type (Lin et al., 2007). It is possible that IT cells display smaller calcium changes per spike, leading to an underestimation of its selectivity (but see Lur et al., 2016).

Object location selectivity was widespread in MM in superficial and deep neurons, both in PT and IT cells. This likely reflects a prominent projection from somatosensory cortex to

and mesoscale, high-resolution imaging (Sofroniew et al., 2016) will make even larger cortical activity maps routine.

STAR★METHODS

Detailed methods are provided in the online version of this paper and include the following:

- KEY RESOURCES TABLE
- CONTACT FOR REAGENT AND RESOURCE SHARING

● METHOD DETAILS

- Tracer injection and window surgery
- Wide field calcium imaging
- Two-photon calcium imaging
- Image analysis
- Electrophysiology
- Electrophysiology data analysis

SUPPLEMENTAL INFORMATION

Supplemental Information includes ten figures and one movie and can be found with this article online at <http://dx.doi.org/10.1016/j.neuron.2017.05.005>.

AUTHOR CONTRIBUTIONS

T.W.C. and K.S. conceived the project. T.W.C. performed imaging experiments with help from K.D. N.L. performed silicon probe recordings. T.W.C., N.L., and K.S. analyzed the data. T.W.C. and K.S. wrote the paper with comments from other authors.

ACKNOWLEDGMENTS

We thank Simon Peron, Aaron Kerlin, Hidehiko Inagaki, and Ziqiang Wei for comments on the manuscript and Zengcai Guo for useful discussions. This work was funded by Howard Hughes Medical Institute. T.W.C. is supported by a career development grant (NHRI-ex-105-10509NC) from the Taiwan National Health Research Institute. N.L. and K.D. are Helen Hay Whitney Foundation postdoctoral fellows.

Received: October 14, 2016

Revised: January 29, 2017

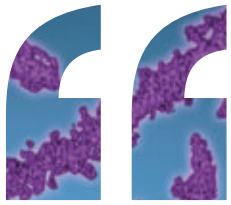
Accepted: May 1, 2017

Published: May 17, 2017

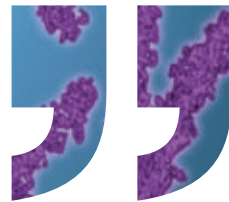
REFERENCES

- Akerboom, J., Chen, T.W., Wardill, T.J., Tian, L., Marvin, J.S., Mutlu, S., Calderón, N.C., Esposti, F., Borghuis, B.G., Sun, X.R., et al. (2012). Optimization of a GCaMP calcium indicator for neural activity imaging. *J. Neurosci.* *32*, 13819–13840.
- Amador, N., Schlag-Rey, M., and Schlag, J. (2000). Reward-predicting and reward-detecting neuronal activity in the primate supplementary eye field. *J. Neurophysiol.* *84*, 2166–2170.
- Amiez, C., Joseph, J.P., and Procyk, E. (2006). Reward encoding in the monkey anterior cingulate cortex. *Cereb. Cortex* *16*, 1040–1055.
- Brecht, M. (2011). Movement, confusion, and orienting in frontal cortices. *Neuron* *72*, 193–196.
- Brown, S.P., and Hestrin, S. (2009). Intracortical circuits of pyramidal neurons reflect their long-range axonal targets. *Nature* *457*, 1133–1136.
- Bruce, C.J., and Goldberg, M.E. (1985). Primate frontal eye fields. I. Single neurons discharging before saccades. *J. Neurophysiol.* *53*, 603–635.
- Chakrabarti, S., Zhang, M., and Alloway, K.D. (2008). M1 neuronal responses to peripheral whisker stimulation: relationship to neuronal activity in si barrels and septa. *J. Neurophysiol.* *100*, 50–63.
- Chen, T.-W. (2008). A Systems level analysis of neuronal network function in the olfactory bulb: coding, connectivity, and modular organization. PhD Thesis (University of Göttingen).
- Chen, T.W., Wardill, T.J., Sun, Y., Pulver, S.R., Renninger, S.L., Baohan, A., Schreiter, E.R., Kerr, R.A., Orger, M.B., Jayaraman, V., et al. (2013). Ultrasensitive fluorescent proteins for imaging neuronal activity. *Nature* *499*, 295–300.
- Churchland, M.M., and Shenoy, K.V. (2007). Delay of movement caused by disruption of cortical preparatory activity. *J. Neurophysiol.* *97*, 348–359.
- Churchland, M.M., Cunningham, J.P., Kaufman, M.T., Ryu, S.I., and Shenoy, K.V. (2010). Cortical preparatory activity: representation of movement or first cog in a dynamical machine? *Neuron* *68*, 387–400.
- Crutcher, M.D., and Alexander, G.E. (1990). Movement-related neuronal activity selectively coding either direction or muscle pattern in three motor areas of the monkey. *J. Neurophysiol.* *64*, 151–163.
- Dana, H., Chen, T.-W., Hu, A., Shields, B.C., Guo, C., Looger, L.L., Kim, D.S., and Svoboda, K. (2014). Thy1-GCaMP6 transgenic mice for neuronal population imaging in vivo. *PLoS ONE* *9*, e108697.
- Dana, H., Mohar, B., Sun, Y., Narayan, S., Gordus, A., Hasseman, J.P., Tsegaye, G., Holt, G.T., Hu, A., Walpita, D., et al. (2016). Sensitive red protein calcium indicators for imaging neural activity. *eLife* *5*, 5.
- Ding, L., and Gold, J.I. (2010). Caudate encodes multiple computations for perceptual decisions. *J. Neurosci.* *30*, 15747–15759.
- Erich, J.C., Bialek, M., and Brody, C.D. (2011). A cortical substrate for memory-guided orienting in the rat. *Neuron* *72*, 330–343.
- Erich, J.C., Brunton, B.W., Duan, C.A., Hanks, T.D., and Brody, C.D. (2015). Distinct effects of prefrontal and parietal cortex inactivations on an accumulation of evidence task in the rat. *eLife* *4*, 4.
- Ferezou, I., Haiss, F., Gentet, L.J., Aronoff, R., Weber, B., and Petersen, C.C. (2007). Spatiotemporal dynamics of cortical sensorimotor integration in behaving mice. *Neuron* *56*, 907–923.
- Fried, I., Mukamel, R., and Kreiman, G. (2011). Internally generated preactivation of single neurons in human medial frontal cortex predicts volition. *Neuron* *69*, 548–562.
- Funahashi, S., Bruce, C.J., and Goldman-Rakic, P.S. (1989). Mnemonic coding of visual space in the monkey's dorsolateral prefrontal cortex. *J. Neurophysiol.* *61*, 331–349.
- Goard, M.J., Pho, G.N., Woodson, J., and Sur, M. (2016). Distinct roles of visual, parietal, and frontal motor cortices in memory-guided sensorimotor decisions. *eLife* *5*, 5.
- Guo, Z.V., Hires, S.A., Li, N., O'Connor, D.H., Komiyama, T., Ophir, E., Huber, D., Bonardi, C., Morandell, K., Gutnisky, D., et al. (2014a). Procedures for behavioral experiments in head-fixed mice. *PLoS ONE* *9*, e88678.
- Guo, Z.V., Li, N., Huber, D., Ophir, E., Gutnisky, D., Ting, J.T., Feng, G., and Svoboda, K. (2014b). Flow of cortical activity underlying a tactile decision in mice. *Neuron* *81*, 179–194.
- Guo, Z.V., Inagaki, H., Daie, K., Druckmann, S., Gerfen, C.R., and Svoboda, K. (2017). Maintenance of persistent activity in a frontal thalamocortical loop. *Nature*. Published online May 3, 2017. <http://dx.doi.org/10.1038/nature22324>.
- Hernández, A., Nácher, V., Luna, R., Zainos, A., Lemus, L., Alvarez, M., Vázquez, Y., Camarillo, L., and Romo, R. (2010). Decoding a perceptual decision process across cortex. *Neuron* *66*, 300–314.
- Hill, D.N., Curtis, J.C., Moore, J.D., and Kleinfeld, D. (2011). Primary motor cortex reports efferent control of vibrissa motion on multiple timescales. *Neuron* *72*, 344–356.
- Hooks, B.M., Hires, S.A., Zhang, Y.X., Huber, D., Petreanu, L., Svoboda, K., and Shepherd, G.M. (2011). Laminar analysis of excitatory local circuits in vibrissal motor and sensory cortical areas. *PLoS Biol.* *9*, e1000572.
- Hooks, B.M., Mao, T., Gutnisky, D.A., Yamawaki, N., Svoboda, K., and Shepherd, G.M. (2013). Organization of cortical and thalamic input to pyramidal neurons in mouse motor cortex. *J. Neurosci.* *33*, 748–760.
- Howe, M.W., Tierney, P.L., Sandberg, S.G., Phillips, P.E., and Graybiel, A.M. (2013). Prolonged dopamine signalling in striatum signals proximity and value of distant rewards. *Nature* *500*, 575–579.
- Huber, D., Gutnisky, D.A., Peron, S., O'Connor, D.H., Wiegert, J.S., Tian, L., Oertner, T.G., Looger, L.L., and Svoboda, K. (2012). Multiple dynamic representations in the motor cortex during sensorimotor learning. *Nature* *484*, 473–478.
- Juneak, S., Chen, T.W., Alevra, M., and Schild, D. (2009). Activity correlation imaging: visualizing function and structure of neuronal populations. *Biophys. J.* *96*, 3801–3809.
- Kerkhoff, G. (2001). Spatial hemineglect in humans. *Prog. Neurobiol.* *63*, 1–27.

- Kerlin, A.M., Andermann, M.L., Berezovskii, V.K., and Reid, R.C. (2010). Broadly tuned response properties of diverse inhibitory neuron subtypes in mouse visual cortex. *Neuron* 67, 858–871.
- Kiritani, T., Wickersham, I.R., Seung, H.S., and Shepherd, G.M. (2012). Hierarchical connectivity and connection-specific dynamics in the cortico-spinal-corticostriatal microcircuit in mouse motor cortex. *J. Neurosci.* 32, 4992–5001.
- Kleinfeld, D., Sachdev, R.N., Merchant, L.M., Jarvis, M.R., and Ebner, F.F. (2002). Adaptive filtering of vibrissa input in motor cortex of rat. *Neuron* 34, 1021–1034.
- Komiyama, T., Sato, T.R., O'Connor, D.H., Zhang, Y.X., Huber, D., Hooks, B.M., Gabitto, M., and Svoboda, K. (2010). Learning-related fine-scale specificity imaged in motor cortex circuits of behaving mice. *Nature* 464, 1182–1186.
- Krupa, D.J., Ghazanfar, A.A., and Nicolelis, M.A. (1999). Immediate thalamic sensory plasticity depends on corticothalamic feedback. *Proc. Natl. Acad. Sci. USA* 96, 8200–8205.
- Li, N., Chen, T.W., Guo, Z.V., Gerfen, C.R., and Svoboda, K. (2015). A motor cortex circuit for motor planning and movement. *Nature* 519, 51–56.
- Li, N., Daie, K., Svoboda, K., and Druckmann, S. (2016). Robust neuronal dynamics in premotor cortex during motor planning. *Nature* 532, 459–464.
- Lin, B.J., Chen, T.W., and Schild, D. (2007). Cell type-specific relationships between spiking and [Ca²⁺]_i in neurons of the *Xenopus* tadpole olfactory bulb. *J. Physiol.* 582, 163–175.
- Lur, G., Vinck, M.A., Tang, L., Cardin, J.A., and Higley, M.J. (2016). Projection-Specific Visual Feature Encoding by Layer 5 Cortical Subnetworks. *Cell Rep.* 14, 2538–2545.
- Madisen, L., Garner, A.R., Shimaoka, D., Chuong, A.S., Klapoetke, N.C., Li, L., van der Bourg, A., Niino, Y., Ego, L., Monetti, C., et al. (2015). Transgenic mice for intersectional targeting of neural sensors and effectors with high specificity and performance. *Neuron* 85, 942–958.
- Maimon, G., and Assad, J.A. (2006). A cognitive signal for the proactive timing of action in macaque LIP. *Nat. Neurosci.* 9, 948–955.
- Mao, T., Kusefoglu, D., Hooks, B.M., Huber, D., Petreanu, L., and Svoboda, K. (2011). Long-range neuronal circuits underlying the interaction between sensory and motor cortex. *Neuron* 72, 111–123.
- Matsumoto, M., Matsumoto, K., Abe, H., and Tanaka, K. (2007). Medial prefrontal cell activity signaling prediction errors of action values. *Nat. Neurosci.* 10, 647–656.
- Matyas, F., Sreenivasan, V., Marbach, F., Wacongne, C., Barsy, B., Mateo, C., Aronoff, R., and Petersen, C.C. (2010). Motor control by sensory cortex. *Science* 330, 1240–1243.
- Morishima, M., and Kawaguchi, Y. (2006). Recurrent connection patterns of corticostriatal pyramidal cells in frontal cortex. *J. Neurosci.* 26, 4394–4405.
- Neafsey, E.J., Bold, E.L., Haas, G., Hurley-Gius, K.M., Quirk, G., Sievert, C.F., and Terrence, R.R. (1986). The organization of the rat motor cortex: a microstimulation mapping study. *Brain Res.* 396, 77–96.
- Ohmae, S., Uematsu, A., and Tanaka, M. (2013). Temporally specific sensory signals for the detection of stimulus omission in the primate deep cerebellar nuclei. *J. Neurosci.* 33, 15432–15441.
- Peron, S., Chen, T.W., and Svoboda, K. (2015). Comprehensive imaging of cortical networks. *Curr. Opin. Neurobiol.* 32, 115–123.
- Petreanu, L., Mao, T., Sternson, S.M., and Svoboda, K. (2009). The subcellular organization of neocortical excitatory connections. *Nature* 457, 1142–1145.
- Petreanu, L., Gutnisky, D.A., Huber, D., Xu, N.L., O'Connor, D.H., Tian, L., Looger, L., and Svoboda, K. (2012). Activity in motor-sensory projections reveals distributed coding in somatosensation. *Nature* 489, 299–303.
- Pneumatikakis, E.A., Soudry, D., Gao, Y., Machado, T.A., Merel, J., Pfau, D., Reardon, T., Mu, Y., Lacefield, C., Yang, W., et al. (2016). Simultaneous denoising, deconvolution, and demixing of calcium imaging data. *Neuron* 89, 285–299.
- Pologruto, T.A., Sabatini, B.L., and Svoboda, K. (2003). ScanImage: flexible software for operating laser scanning microscopes. *Biomed. Eng. Online* 2, 13.
- Riehle, A., and Requin, J. (1989). Monkey primary motor and premotor cortex: single-cell activity related to prior information about direction and extent of an intended movement. *J. Neurophysiol.* 61, 534–549.
- Rigotti, M., Barak, O., Warden, M.R., Wang, X.J., Daw, N.D., Miller, E.K., and Fusi, S. (2013). The importance of mixed selectivity in complex cognitive tasks. *Nature* 497, 585–590.
- Rizzolatti, G., Matelli, M., and Pavesi, G. (1983). Deficits in attention and movement following the removal of postarcuate (area 6) and prearcuate (area 8) cortex in macaque monkeys. *Brain* 106, 655–673.
- Rossi, M.A., Li, H.E., Lu, D., Kim, I.H., Bartholomew, R.A., Gaidis, E., Barter, J.W., Kim, N., Cai, M.T., Soderling, S.H., and Yin, H.H. (2016). A GABAergic nigrothalamic pathway for coordination of drinking behavior. *Nat. Neurosci.* 19, 742–748.
- Schall, J.D., and Thompson, K.G. (1999). Neural selection and control of visually guided eye movements. *Annu. Rev. Neurosci.* 22, 241–259.
- Scott, S.H. (2008). Inconvenient truths about neural processing in primary motor cortex. *J. Physiol.* 586, 1217–1224.
- Shenoy, K.V., Sahani, M., and Churchland, M.M. (2013). Cortical control of arm movements: a dynamical systems perspective. *Annu. Rev. Neurosci.* 36, 337–359.
- Shepherd, G.M. (2013). Corticostriatal connectivity and its role in disease. *Nat. Rev. Neurosci.* 14, 278–291.
- Sofroniew, N.J., Flickinger, D., King, J., and Svoboda, K. (2016). A large field of view two-photon mesoscope with subcellular resolution for in vivo imaging. *eLife* 5, 5.
- Sommer, M.A., and Wurtz, R.H. (2000). Composition and topographic organization of signals sent from the frontal eye field to the superior colliculus. *J. Neurophysiol.* 83, 1979–2001.
- Stanek, E., 4th, Cheng, S., Takatoh, J., Han, B.X., and Wang, F. (2014). Monosynaptic premotor circuit tracing reveals neural substrates for oro-motor coordination. *eLife* 3, e02511.
- Stuphorn, V., Taylor, T.L., and Schall, J.D. (2000). Performance monitoring by the supplementary eye field. *Nature* 408, 857–860.
- Sul, J.H., Jo, S., Lee, D., and Jung, M.W. (2011). Role of rodent secondary motor cortex in value-based action selection. *Nat. Neurosci.* 14, 1202–1208.
- Tanaka, M. (2007). Cognitive signals in the primate motor thalamus predict saccade timing. *J. Neurosci.* 27, 12109–12118.
- Tanji, J., and Evarts, E.V. (1976). Anticipatory activity of motor cortex neurons in relation to direction of an intended movement. *J. Neurophysiol.* 39, 1062–1068.
- Tennant, K.A., Adkins, D.L., Donlan, N.A., Asay, A.L., Thomas, N., Kleim, J.A., and Jones, T.A. (2011). The organization of the forelimb representation of the C57BL/6 mouse motor cortex as defined by intracortical microstimulation and cytoarchitecture. *Cereb. Cortex* 21, 865–876.
- Theis, L., Berens, P., Froudarakis, E., Reimer, J., Román Rosón, M., Baden, T., Euler, T., Tolias, A.S., and Bethge, M. (2016). Benchmarking spike rate inference in population calcium imaging. *Neuron* 90, 471–482.
- Thévenaz, P., Ruttimann, U.E., and Unser, M. (1998). A pyramid approach to subpixel registration based on intensity. *IEEE Trans. Image Process.* 7, 27–41.
- Trachtenberg, J.T., Chen, B.E., Knott, G.W., Feng, G., Sanes, J.R., Welker, E., and Svoboda, K. (2002). Long-term in vivo imaging of experience-dependent synaptic plasticity in adult cortex. *Nature* 420, 788–794.
- Travers, J.B., Dinardo, L.A., and Karimnamazi, H. (1997). Motor and premotor mechanisms of licking. *Neurosci. Biobehav. Rev.* 21, 631–647.
- Turner, R.S., and DeLong, M.R. (2000). Corticostriatal activity in primary motor cortex of the macaque. *J. Neurosci.* 20, 7096–7108.
- Vanni, M.P., and Murphy, T.H. (2014). Mesoscale transcranial spontaneous activity mapping in GCaMP3 transgenic mice reveals extensive reciprocal connections between areas of somatomotor cortex. *J. Neurosci.* 34, 15931–15946.
- Vogelstein, J.T., Watson, B.O., Packer, A.M., Yuste, R., Jedynek, B., and Paninski, L. (2009). Spike inference from calcium imaging using sequential Monte Carlo methods. *Biophys. J.* 97, 636–655.



We will help you make it shine.



Our editors will work with you to ensure that the paper you publish meets the highest possible standards.

When you choose Cell Press you get the attention you deserve.

For more information visit: www.cell.com/values

Your **work** is our **life**





SPEAKERS THAT MINGLE

Connect with the best and the brightest at Cell Symposia

At Cell Symposia, you can engage with world-renowned experts and colleagues in your field. We offer events to encourage networking and facilitate collaboration.

Make sure the time you spend away from the lab is quality time, register for a Cell Symposia. Our editors curate symposia on a broad range of topics.

See for yourself at www.cell.com/symposia

It's happening at Cell Symposia!

CellSymposia

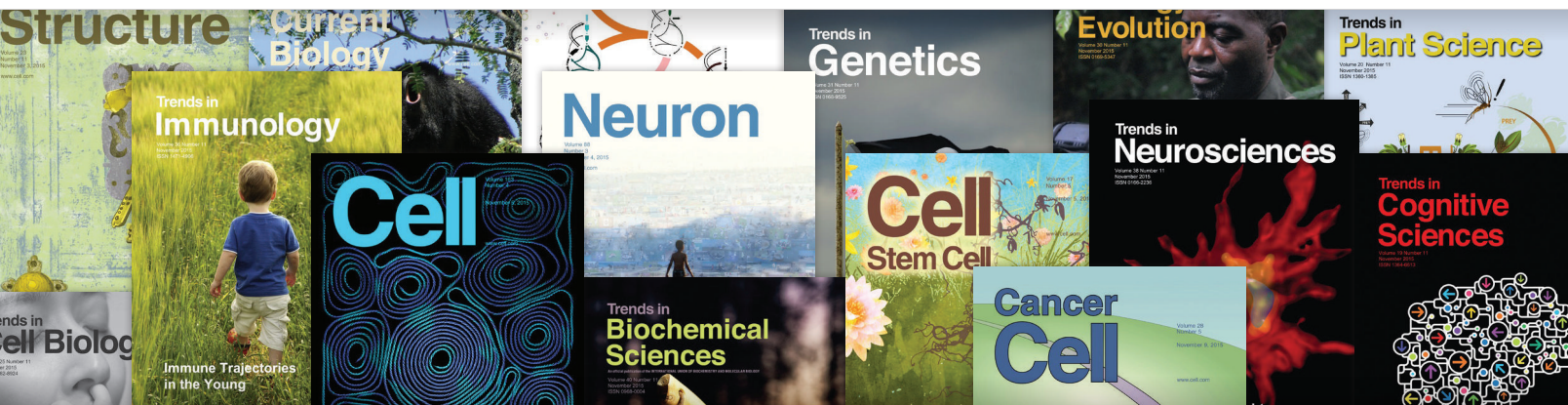


**DON'T BE THE
LAST TO KNOW**

Give your research a boost with alerts from Cell Press. You'll be glad you did.

Get first access with immediate, regular electronic table of contents (eToCs) alerts delivered directly to your desktop, free of charge, that keep you informed of breakthroughs in your field.

Exciting extra features like video abstracts, podcasts, and blog posts give you additional depth and context and you can access news and commentary, normally not accessible online, in advance of publication.



Register today
Visit cell.com/alerts

CellPress

Revolutionizing your confocal imaging.

ZEISS LSM 880 with Airyscan



// INNOVATION
MADE BY ZEISS

Your new standard for fast and gentle confocal imaging

Discover ZEISS LSM 880 with Airyscan: this unique confocal laser scanning microscope delivers perfect optical sections with 120 nm resolution in x/y and 350 nm in z. You get 4–8× higher sensitivity for gentle superresolution imaging. Use the additional Fast mode with acquisition speeds of 27 fps (at 480 × 480 pixels) to follow even the most dynamic processes in your samples.



www.zeiss.com/lsm880



Accelerate your neuropathology research

Identify novel interactions across 23 key pathways in less than 24 hours

nCounter[®] Neuropathology Gene Expression Panel

23 neurodegenerative pathways and processes

15 mins hands on time, publishable data in less than 24 hours

770 genes with option to add custom content

Profile disease mechanisms, response to drug treatment and biomarker characterization

View the gene list at nanosttring.com/neuro

FOR RESEARCH USE ONLY. Not for use in diagnostic procedures.
© 2017 NanoString Technologies, Inc. All rights reserved.

nanosttring